CRANFIELD UNIVERSITY
LIBRARY

Cranfield UNIVERSITY

Cranfield College of Aeronautics

Department of Aerospace Sciences

PhD Thesis
Academic Years 1996-1997

Konstantinos Kontis

PROJECTILE AERODYNAMICS: MEASUREMENT AND COMPUTATION

Supervisor: Emeritus Professor JL Stollery

October 1997

This thesis is submitted in partial fulfilment of the requirements for the Degree of Doctor of Philosophy

Cranfield UNIVERSITY
CRANFIELD UNIVERSITY LIBRARY

KONSTANTINOS KONTIS

PROJECTILE AERODYNAMICS: MEASUREMENT AND COMPUTATION

CRANFIELD COLLEGE OF AERONAUTICS

PhD THESIS

Abstract

An experimental study has been performed at M_∞=8.2 and Re_∞/cm=93000 to examine:
1. *The effect of strakes on the aerodynamic characteristics and performance on slender elliptic cone missile configurations.* Some information regarding the shock layer was obtained from schlieren pictures. Detailed flow properties in the shock layer were obtained, for some elliptic cone configurations with and without strakes, using a three-dimensional, high resolution, iterative, finite volume parabolized Navier-Stokes solver. Surface flow visualisation, using an oil-dot technique, and pressure measurements were made on one of the models to determine the effect of strakes. Lift, drag and pitching moment characteristics for the elliptic cones with and without strakes were obtained using a three component strain-gauge balance.
No gross external flow differences were detected from the schlieren pictures for models tested due to the addition of strakes. Oil-dot visualisation demonstrates that the strakes alter the surface flow characteristics and tended to inhibit the cross-flow. The addition of strakes caused a reduction of pressure on the leeward side and an increase of pressure on the windward side. The strakes produced a significant increase in the lift and drag coefficients, in the incidence range of 0° to 20°. The right elliptic cone without strakes with its major axis horizontal exhibits higher lift coefficients than the cone with its major axis vertical.
The numerical study predicted the complex flowfield surrounding the right elliptic cone with its major axis horizontal, gave a better understanding of the complicated nature of the flow and good indications of the shock shape and vortex core positions. An estimation model of the aerodynamic forces and moments for the right elliptic cone with and without strakes was developed based on the standard Newtonian theory. The model successfully predicted the experimental trends in the aerodynamic coefficients.
2. *The aerodynamic effectiveness of a cylinder-flare body at zero incidence under laminar and turbulent boundary layer conditions.* Two nose geometries, namely a 10° half-angle sharp cone and a hemisphere, were used. The surface flow over the cylinder-flare body was studied using oil-dot and liquid crystal techniques. Some information regarding the shock layer was obtained from schlieren pictures. The effects of entropy layer and boundary layer state on flare effectiveness were deduced from pressure measurements over the cylinder and the flare.
The most important difference between the laminar and turbulent boundary layer interaction is that a much smaller angle is necessary to cause laminar separation than that necessary for turbulent separation. The determination of incipient separation is very sensitive to the detection method employed. The existence of a small scale separation bubble can explain the differences in the determination of incipient separation angles if different experimental methods are used. The addition of a hemisphere nose reduces the surface pressure and heat transfer levels on the flare. This is due to loss of reservoir pressure across the bow shock wave. The reduction of flare pressure also reduces the separated flow lengths for the laminar case, whereas for the turbulent case the separated flow lengths are increased. This may be due to the boundary layer along the cylinder body not being fully developed. The effect of Mach shear on the flare pressures distribution has been calculated theoretically. The model predicted the experimental results satisfactorily.

To

my father Spiros, my mother Helen

and Keiko

"...και όταν φτάσει η στιγμή αυτή, που πίσω δεν μπορείς να κάνεις, πρόσεξε πολύ, γιατί ο δρόμος είναι ανηφορικός, η λάμψη μπορεί να σε τυφλώσει και η ζέστα τα φτερά να σου λιώσει. Κι' αν ο δρόμος στενεύσει, μην φοβάσαι, έχε πίστη δυνατή, θυμήσου, σκέψου και πορεύσου..."

"...and when that moment of no-return has arrived, be very careful, because the path is steep, the brightness may blind you and the comfort may melt yours wings. And if the path is getting narrow, do not worry, have strong faith, remember, think and proceed..."

Κόντης Κωνσταντίνος
3η Οκτώβρίου του 1994

Acknowledgements

I am indebted to my supervisor, Emeritus Professor JL Stollery, for his continual guidance, encouragement and inspiration throughout the duration of my studies. I wish to thank him for giving me the opportunity to be one of his students and making this work possible. A big dept of thanks goes to Dr N Qin for his invaluable help and guidance on the computational side of the study and for allowing me to work with him, sometimes late Saturday evenings.

I am thankful to the Defence Evaluation and Research Agency for their financial support in the form of a contract, which helped to sponsor the experimental investigation on the elliptic cones with and without strakes. I must not neglect to mention the encouragement of Professor JA Edwards, the monitor for the Defence Evaluation and Research Agency contract and the useful suggestions of Professor GR Inger of Iowa State University and Dr A Kokkalis of Westland Helicopters.

I am grateful to Cranfield College of Aeronautics staff, in particular Emeritus Professor JL Stollery, Professor I Poll, and Dr K Gary, for allowing me to complete the research through their financial, technical and spiritual contribution for the work on cylinder-flare body.

Special thanks must go to Dr A Singh for his help during those difficult days in the gun tunnel facility and Mr S Shaw for his programming suggestions. I would like to thank Mr W Osbourn and Mr R Wadher for ensuring the operation of the gun tunnel. The help of the workshop staff of Cranfield College of Aeronautics deserves mention, especially Mr M Goodridge, Mr D Giles, Mr P Dancer and Mr C Boddington for model fabrication, their technical advice on model design and their patience in dealing with many problems incurred during development of the models. Many thanks also go to the Royal Aeronautical Society, the Defence Evaluation and Research Agency and the Cranfield College of Aeronautics for their generosity which enabled me to participate in many conferences around the world and present my papers.

I am grateful to Keiko, for her ever available help. I have to add a special big thanks to my best friends Elias, George and Thanasis for making my life since junior school even more interesting and enjoyable. Finally, I am indebted to my parents, Spiros and Helen, and my grandparents, Panagiotis and Aggeliki, for their constant moral, spiritual and financial support, encouragement and guidance throughout my life.

THANK YOU!

Table of Contents

ABSTRACT ii
ACKNOWLEDGEMENTS iv
TABLE OF CONTENTS v
LIST OF FIGURES viii
LIST OF TABLES xiii
NOMENCLATURE xiv

CHAPTER 1 INTRODUCTION 1
1.1 Historical Overview 1
1.2 Characteristic Features of Hypersonic Flow 2
1.3 Program of Study 3

CHAPTER 2 LITERATURE SURVEY 8
2.1 Boundary Layer Separation 8
2.2 Boundary Layer Transition 8
2.3 Parameters Affecting Separation 9
2.4 Incipient Separation for Laminar Interactions 10
2.5 The Effect of Transition on Incipient Separation 11
2.6 Incipient Separation for Turbulent Interactions 12
2.7 Parameters Affecting the Scale of Separation Interaction Region 15
2.8 Leading Edge Bluntness Effect on Separation 18
2.9 Slender Bodies 21
2.9.1 Slender Circular Bodies 21
2.9.2 Slender Elliptic Bodies 24
2.9.3 Slender Bodies with Wings, Fins or Strakes 27
2.10 PNS Computations for Slender Body Configurations 31

CHAPTER 3 METHODS AND PROCEDURES 32
3.1 Computational Tool 32
3.2 Gun Tunnel Facility 34
3.2.1 Description of the Gun Tunnel Facility 34
3.2.2 Flow Establishment Time 36
3.3 Test Conditions 36
3.4 Models and Supports 36
3.4.1 Right Elliptic Cone Without Strakes, $L_{cone}/d_{minor}=15$ 36
3.4.2 Half-Power-Law Elliptic Cone With and Without Strakes, $L_{cone}/d_{minor}\approx 11.2$ 37
3.4.3 Right Elliptic Cone With and Without Strakes, $L_{cone}/d_{minor}=7.5$ 37
3.4.4 Axisymmetric Body 38
3.4.5 Model Supports 40
3.5 Flow Visualisation 40
3.5.1 Schlieren Technique 40
3.5.2 Oil-Dot Flow Technique 41

3.5.3 Liquid-Crystal Technique 43
3.6 Data Acquisition and Instrumentation **44**
3.6.1 Force Measurement System 46
3.6.1.1 Calibration of the Force Balance 48

CHAPTER 4 RESULTS AND DISCUSSION
ELLIPTIC CONES WITH AND WITHOUT STRAKES **50**
4.1 Right Elliptic Cone Without Strakes, L_{cone}/d_{minor}=15 **50**
4.1.1 Experimental Investigation 50
4.1.2 Computational Investigation 54
4.2 Half-Power-Law Elliptic Cone With and Without Strakes, L_{cone}/d_{minor}=11.2 **55**
4.2.1 Schlieren and Force Measurements 57
4.3 Right Elliptic Cone With and Without Strakes, L_{cone}/d_{minor}=7.5 **60**
4.3.1 Theoretical Estimation of Pressure Distribution 61
4.3.1.1 Cone Theory of Leung and Emanuel[163] 61
4.3.1.2 Newtonian Theory 62
4.3.2 Estimation Model of Aerodynamic Forces and Moments 63
4.3.3 Results and Discussion for Configuration 4 67
4.3.3.1 Navier-Stokes Study 67
4.3.3.2 Schlieren and Oil-Dot Visualisation Studies 69
4.3.3.3 Pressure Measurements 73
4.3.3.4 Forces and Moment Measurements 76
4.3.3.5 Comparison of Forces and Moment Measurements with Other Data 80
4.3.4 Results and Discussion for Configuration 5 81
4.3.4.1 Schlieren and Oil-Dot Visualisation Studies 81
4.3.4.2 Forces and Moment Measurements 82

CHAPTER 5 RESULTS AND DISCUSSION
FLARE CONTROL EFFECTIVENESS **87**
5.1 Cylinder-Flare Body **87**
5.2 Hemisphere-Cylinder, Theoretical Correlations **87**
5.2.1 Blast Wave Theory 87
5.2.2 Alpha Code 89
5.2.3 Flowfield around a Hemisphere-Cylinder Body 91
5.2.4 Boundary Layer Edge Mach Number 92
5.2.5 Entropy-Layer Mach Profile Prediction 93
5.3 Sharp Cone-Cylinder Correlations **94**
5.3.1 Flowfield about a Sharp Cone-Cylinder Body 94
5.3.2 Pressure Distribution Estimation 95
5.4 Boundary-Layer Thickness Estimation Methods **96**
5.5 The Effect of Mach-Shear and Area-Change on Flare Pressure **97**
5.6 Flare Pressure Distribution Estimation Methods **101**
5.7 Sharp Cone-Cylinder-Flare Laminar Boundary Layer Studies **103**
5.7.1 Sharp Cone-Cylinder Body 103
5.7.2 The Effect of Flare Deflection (Attached Flows) 103
5.7.3 The Effect of Flare Deflection (Separated Flows) 104

5.8 Hemisphere-Cylinder-Flare Laminar Boundary Layer Studies **109**
5.8.1 Hemisphere-Cone-Cylinder Body 109
5.8.2 The Effect of Bluntness (Attached Flows) 109
5.8.3 The Effect of Bluntness (Separated Flows) 111
5.8.4 The Effect of Hemisphere Nose on Incipient Separation 113
5.8.5 Mach Shear Interaction Effect 113
5.9 Sharp Cone-Cylinder-Flare Turbulent Boundary Layer Studies **114**
5.9.1 Sharp Cone-Cylinder Body 114
5.9.2 Effect of Flare Angle Variation (Cone-Cylinder-Flare with Vortex Generators) 115
5.9.3 The Effect of Boundary Layer Turbulence on Incipient Separation 117
5.9.4 Flare Pressure Prediction (Attached Flows) 119
5.10 Hemisphere-Cylinder-Flare Turbulent Boundary Layer Studies **119**
5.10.1 Hemisphere-Cone-Cylinder Body 119
5.10.2 The Effect of Bluntness 120
5.11 Correlations **124**

CHAPTER 6 CONCLUDING REMARKS **127**
6.1 Elliptic Cones With and Without Strakes **127**
6.2 Flare Control Effectiveness **128**

TABLES **130**
REFERENCES **135**
FIGURES

APPENDIX A
APPENDIX B
APPENDIX C
AWARDS
LIST OF PUBLICATIONS
PAPERS
1.Control Effectiveness of a Jet-Slender Body Combination at Hypersonic Speeds
2.Hypersonic Effectiveness of Slender Lifting Elliptic Cones With and Without Strakes
3.Computational and Experimental Investigation of Hypersonic Performance of Lifting Elliptic Cone With and Without Strakes

List of Figures

Fig. 2.1 Incipient separation angles for laminar and turbulent separation (ref. 29)
Fig. 2.2 Variation of separation length in vicinity of 2-D compression corner (ref. 41)
Fig. 2.3 Model of Elfstrom (ref. 37)
Fig. 2.4 2-D compression corner incipient separation data
Fig. 2.5 Incipient separation at a wedge compression corner
Fig. 2.6 The effect of Mach number on the transition of conical and quasi two dimensional boundary layers
Fig. 2.7 The effect of incidence on the local Mach number over a flat plate
Fig. 2.8 The effect of incidence on the local unit Reynolds number over a flat plate
Fig. 2.9 Correlation between the effect of leading edge bluntness on the length of separated flow and on the reattachment pressure ratio (ref. 79, $\alpha=0^{\circ}$, $\beta=25^{\circ}$)
Fig. 2.10 The effect of "small" and "large" bluntness on the onset of transition in planar and conical boundary layers
Fig. 3.1 A sketch of the gun-tunnel
Fig. 3.2 Variation of Mach number along the axis of the nozzle (ref. 137)
Fig. 3.3 Variation of reservoir temperature with the driver to barrel pressure ratio (ref. 76)
Fig. 3.4 Pitot pressure measurements along and off the axis of Mach 8.2 nozzle (ref. 140)
Fig. 3.5a Mach number survey along and off the axis of Mach 8.2 nozzle (ref. 140)
Fig. 3.5b Mach number survey along a vertical line normal to the axis of the Mach 8.2 nozzle (ref. 140)
Fig. 3.6 A typical pressure transducer output signal
Fig. 3.7a A sketch of the elliptic cone without strakes, $L_{cone}/d_{minor}=15$
Fig. 3.7b A sketch of the power-law elliptic cone with and without strakes
Fig. 3.7c A sketch of the elliptic cone with and without strakes, $L_{cone}/d_{minor}=7.5$
Fig. 3.7d A sketch of the cylinder-flare body
Fig. 3.8a Photographs of the elliptic cone models
Fig. 3.8b Photographic detail of the base region of the pressure model, (elliptic cone with and without strakes, $L_{cone}/d_{minor}=7.5$)
Fig. 3.9a Photograph of the cylinder-flare model
Fig. 3.9b Photograph of the instrumented flares with pressure tappings
Fig. 3.9c Photograph of the instrumented cylinder-flare model with pressure tappings
Fig. 3.10 Photograph of the vortex generators
Fig. 3.11a Photograph of the horizontally rotatable rigid mounting
Fig. 3.11b Photograph of the V-shape mounting block
Fig. 3.11c Photograph of the pedestal support
Fig. 3.12 Typical schlieren picture of flow separation and reattachment (sharp cone-cylinder-30°-flare body without vortex generators)
Fig. 3.13 Schematic of the set-up for the liquid crystal technique as viewed along the direction of the flow
Fig. 3.14 Photograph of the system used for pressure and force data acquisition
Fig. 3.15 Photograph of the force balance

Fig. 3.16a Typical unfiltered signal trace of the strain gauge balance (normal force component)
Fig. 3.16b Typical filtered signal trace of the strain gauge balance (normal force component)
Fig. 3.17 Set-up used for calibration of gun-tunnel 3-component force balance
Fig. 3.18 Calibration bar
Fig. 4.1 Schlieren and oil-dot pictures for configuration 1
Fig. 4.2 Schlieren and oil-dot pictures for configuration 5
Fig. 4.3 Effect of incidence to the windward shock angle (angle was determined from the schlieren pictures and was measured from the body centre axis)
Fig. 4.4 Effect of sharp-cone half-angle to the shock angle ($\alpha=0^{\circ}$, $M_{\infty}=8.2$)
Fig. 4.5 Base flowfield computational results for configuration 1 at $\alpha=10^{\circ}$
Fig. 4.6 Proposed flow field model for configuration 1 at $\alpha=10^{\circ}$
Fig. 4.7 Forces and pitching moment sign convention
Fig. 4.8 Comparison of the schlieren pictures (strakes on and off) for the power-law body at $\alpha=12^{\circ}$
Fig. 4.9 Schlieren photographs of power-law body (strakes off)
Fig. 4.10 Effect of strakes on the aerodynamic characteristics of the power-law body
Fig. 4.11 Comparison of present force data (strakes off) with other experimental results (ref. 103)
Fig. 4.12 Comparison of present force data (strakes off) with a theoretical minimum-wave-drag body (ref. 103)
Fig. 4.13 Experimental level of scattering in the location of the centre of pressure
Fig. 4.14 Grid used for the discretization of the flowfield of the elliptic cone (strakes on and off)
Fig. 4.15 Sensitivity of numerical results to grid density
Fig. 4.16 Comparison of the schlieren pictures (strakes on and off) of configuration 4 at $\alpha=15^{\circ}$
Fig. 4.17 Comparison of the base flowfield computational results of configuration 4
Fig. 4.18 Oil-dot pictures of configuration 4 (strakes off and on)
Fig. 4.19 Schlieren photographs of configuration 4 (strakes on)
Fig. 4.20 Proposed flow field models for configuration 4 (strakes off and on)
Fig. 4.21 Comparison of the schlieren pictures ($\alpha=10^{\circ}$, 15° and 20°) with the numerical results
Fig. 4.22 Detail of the flow field near the strakes region (PNS)
Fig. 4.23 Comparison of the oil-dot flow visualisation and numerical streamline results for the cone with and without strakes at $\alpha=15^{\circ}$
Fig. 4.24 Proposed near flow field analogy
Fig. 4.25 Initial pressure measurements on the elliptic cone without strakes
Fig. 4.26 Effect of strakes on the pressure distributions along the windward and leeward sides
Fig. 4.27 Comparison of numerical results with experimental pressure measurements (strakes on and off, windward and leeward sides)
Fig. 4.28 Comparison of theoretical results with experimental pressure measurements (strakes off, windward side)
Fig. 4.29 Effect of strakes on the aerodynamic characteristics of configuration 4

Fig. 4.30 Comparison of present force data (strakes off) with other experimental results (ref. 103)
Fig. 4.31 Comparison of present aerodynamic characteristics with those of the power-law body (see section 4.2.1)
Fig. 4.32 Comparison of the schlieren pictures (strakes on and off) of configuration 5 at $\alpha=15^{o}$
Fig. 4.33 Oil-dot pictures of configuration 5 (strakes off and on)
Fig. 4.34 Schlieren photographs of configuration 5 (strakes on)
Fig. 4.35 Proposed flow field for configuration 5 (strakes off and on)
Fig. 4.36 Effect of strakes on the aerodynamic characteristics of configuration 5
Fig. 4.37 Comparison of present measurements with those of configuration 4 (see section 4.3.3.4)
Fig. 5.1a Pressure distributions on the hemisphere cylinder ($M_{\infty}=8.2$)
Fig. 5.1b Shock-wave shape around the hemisphere cylinder
Fig. 5.2 Predicted pressure distribution along the hemisphere nose and cylinder body ($M_{\infty}=8.2$, $r_n=8.5$ mm)
Fig. 5.3a Schlieren photo of the hemisphere cylinder ($M_{\infty}=8.2$, Re_{∞}/cm=93000, laminar boundary layer)
Fig. 5.3b Comparison of the experimental pressure distribution along the cylinder body with a prediction model ($M_{\infty}=8.2$, $r_n=8.5$ mm)
Fig. 5.4 Flow structure over a hemisphere cylinder
Fig. 5.5 Predicted streamline pattern around a hemisphere cylinder (ref. 189)
Fig. 5.6a Predicted local boundary layer edge Mach number distribution of the present hemisphere cylinder at various Mach numbers
Fig. 5.6b Comparison of experimentally predicted local boundary layer edge Mach number distribution with theory
Fig. 5.7 Predicted entropy-layer Mach profile ($M_{\infty}=8.2$, Re_{∞}/cm=93000, $d_{cyl}=1.7$ cm)
Fig. 5.8a Flow structure over a sharp cone-cylinder body and streamline pattern
Fig. 5.8b Schlieren photo of the sharp cone cylinder ($M_{\infty}=8.2$, Re_{∞}/cm=93000, laminar boundary layer)
Fig. 5.9 Pressure distributions on the sharp cone cylinder ($M_{\infty}=8.2$, Re_{∞}/cm=93000)
Fig. 5.10 Inviscid flow structure over a hemisphere-cylinder-flare body
Fig. 5.11a Wave reflection from a shock wave
Fig. 5.11b Variation of the reflected coefficient with the strength of the Mach shear
Fig. 5.12a Kuehn's[9] laminar Mach profiles (10^{o} semi-vertex sharp cone and hemisphere noses, $M_{\infty}=4.76$, Re_{∞}/cm=40000)
Fig. 5.12b Attached flow pressure distribution over the hemisphere-cylinder-flare body ($M_{\infty}=8.2$, Re_{∞}/cm=93000, turbulent boundary layer, $\beta=10^{o}$)
Fig. 5.13 Predicted inviscid Mach profile (derived from a seventh power law profile)
Fig. 5.14 Oil-dot photo of the sharp cone cylinder ($M_{\infty}=8.2$, Re_{∞}/cm=93000, laminar boundary layer)
Fig. 5.15 Liquid-crystal photos of the sharp cone cylinder ($M_{\infty}=8.2$, Re_{∞}/cm=93000, laminar and turbulent boundary layers)
Fig. 5.16 Schematic diagram of the effect of flare deflection on local flowfield in laminar unseparated flow

Fig. 5.17 Skin friction distribution along a flat plate-wedge model (ref. 27, M_∞=19.8, Re_∞/in=8.7x10^3)
Fig. 5.18 The effect of flare deflection on the location of separation and reattachment in laminar flows (M_∞=8.2, Re_∞/cm=93000, L_{cyl}=15.3 cm, sharp cone nose)
Fig. 5.19a Cross-plot of Kuehn's[9] laminar incipient separation data
Fig. 5.19b Determination of incipient separation angle (laminar boundary layer, sharp cone nose)
Fig. 5.20 Liquid-crystal and oil-dot flow visualisation and pressure measurements on control flare configurations (M_∞=8.2, Re_∞/cm=93000, L_{cyl}=15.3 cm, d_{cyl}=1.7 cm, sharp cone nose, laminar boundary layer)
Fig. 5.21 Direct comparison of the pressure distributions along the cylinder body with sharp cone and hemisphere noses under laminar and turbulent boundary layer conditions (M_∞=8.2, Re_∞/cm=93000, L_{cyl}=15.3 cm, d_{cyl}=1.7 cm)
Fig. 5.22 Oil-dot picture of the hemisphere cylinder (M_∞=8.2, Re_∞/cm=93000, laminar boundary layer)
Fig. 5.23 Comparison of liquid crystal pictures of the sharp cone and hemisphere cylinder bodies (M_∞=8.2, Re_∞/cm=93000, laminar boundary layer)
Fig. 5.24 The effect of bluntness on flare shock structure at supersonic and hypersonic speeds
Fig. 5.25 The effect of hemisphere nose on the flare shock structure (β=10°, M_∞=8.2, Re_∞/cm=93000, laminar boundary layer)
Fig. 5.26 The effect of hemisphere nose on the pressure distribution (β=10°, M_∞=8.2, Re_∞/cm=93000, laminar boundary layer)
Fig. 5.27 The effect of hemisphere nose on the oil-dot flow visualisation (β=10°, M_∞=8.2, Re_∞/cm=93000, laminar boundary layer)
Fig. 5.28 The effect of hemisphere nose on the liquid crystal flow visualisation (β=10°, M_∞=8.2, Re_∞/cm=93000, laminar boundary layer)
Fig. 5.29 Liquid-crystal and oil-dot flow visualisation and pressure measurements on hemisphere nose control flare configurations (M_∞=8.2, Re_∞/cm=93000, laminar boundary layer)
Fig. 5.30 The effect of hemisphere nose on the pressure distributions of control flare configurations (M_∞=8.2, Re_∞/cm=93000, laminar boundary layer)
Fig. 5.31 The effect of hemisphere nose on the schlieren flow visualisation of control flare configurations (M_∞=8.2, Re_∞/cm=93000, laminar boundary layer)
Fig. 5.32 The effect of hemisphere nose on the oil-dot flow visualisation of control flare configurations (M_∞=8.2, Re_∞/cm=93000, laminar boundary layer)
Fig. 5.33 The effect of hemisphere nose on the liquid-crystal flow visualisation of control flare configurations (M_∞=8.2, Re_∞/cm=93000, laminar boundary layer)
Fig. 5.34 Determination of incipient separation angle (laminar boundary layer, hemisphere nose)
Fig. 5.35 The effect of entropy layer Mach shear interaction on the flare pressure distribution (M_∞=8.2, Re_∞/cm=93000, laminar boundary layer, hemisphere nose)
Fig. 5.36 Schlieren photo of the sharp cone cylinder (M_∞=8.2, Re_∞/cm=93000, turbulent boundary layer)

Fig. 5.37 The effect of turbulent boundary layer on the oil-dot flow visualisation of the sharp cone cylinder (M_∞=8.2, Re_∞/cm=93000)
Fig. 5.38 The effect of turbulent boundary layer on the liquid-crystal flow visualisation of the sharp cone cylinder (M_∞=8.2, Re_∞/cm=93000)
Fig. 5.39 The progress of vortex development and final break down (ref. 187)
Fig. 5.40 Schlieren, liquid-crystal and oil-dot flow visualisation and pressure measurements on sharp cone nose control flare configurations (M_∞=8.2, Re_∞/cm=93000, L_{cyl}=15.3 cm, turbulent boundary layer)
Fig. 5.41 Composite of pressure distributions (M_∞=8.2, Re_∞/cm=93000, sharp cone nose cylinder, turbulent boundary layer)
Fig. 5.42 Flowfield of a separated hypersonic turbulent boundary layer (ref. 37)
Fig. 5.43 Determination of incipient separation angle (turbulent boundary layer, sharp cone nose)
Fig. 5.44 Comparison of the experimental pressure distribution along the 10° flare with Elfstrom's[37] prediction model (M_∞=8.2, Re_∞/cm=93000, sharp cone nose, turbulent boundary layer)
Fig. 5.45 Comparison of the experimental pressure distribution along the 20° flare with Elfstrom's[37] prediction model (M_∞=8.2, Re_∞/cm=93000, sharp cone nose, turbulent boundary layer)
Fig. 5.46 The effect of turbulent boundary layer on the oil-dot and liquid-crystal flow visualisation of the hemisphere cylinder (M_∞=8.2, Re_∞/cm=93000)
Fig. 5.47 Schlieren, liquid-crystal and oil-dot flow visualisation and pressure measurements on hemisphere nose control flare configurations (M_∞=8.2, Re_∞/cm=93000, L_{cyl}=15.3 cm, d_{cyl}=1.7 cm, turbulent boundary layer)
Fig. 5.48 Composite of pressure distributions (M_∞=8.2, Re_∞/cm=93000, hemisphere nose, turbulent boundary layer)
Fig. 5.49 Determination of incipient separation angle (turbulent boundary layer, hemisphere cone nose)
Fig. 5.50 Correlation of supersonic and hypersonic laminar incipient axisymmetric data
Fig. 5.51 Correlation of supersonic and hypersonic turbulent incipient axisymmetric data
Fig. 5.52 Comparison of incipient separation angles for axi-symmetric configurations with 2-D results

List of Tables

Table 1 Power-law body design co-ordinates
Table 2 The location of the pressure orifices on the cylinder-flare body
Table 3 Temperature profile of the liquid crystal (ref. 195)
Table 4 Laminar supersonic and hypersonic axisymmetric incipient separation data
Table 5 Turbulent supersonic and hypersonic axisymmetric incipient separation data

Nomenclature

A	area
A	axial force
a	length of major axis of an elliptic cross-section
a	side length of a square
a	speed of sound
b or d_{minor}	length of minor axis of an elliptic cross-section
C	calibration constant
C	Chapman-Rubesin constant
C_A	axial force coefficient based on the body planform area
C_D	drag coefficient based on the body planform area
C_{D_B}	base drag coefficient
C_{Dn}	nose drag coefficient
C_{D_f}	skin-friction drag coefficient
c_f	local skin friction coefficient
CG	centre of gravity
C_L	lift coefficient based on the body planform area
C_{Lbasic_cone}	lift coefficient due to cone only
$C_{Lstrake}$	lift coefficient due to strakes only
C_m	pitching moment coefficient measured at the moment reference point based on the planform area and the total length of the body
C_N	normal force coefficient based on the body planform area
C_p	pressure coefficient
d	diameter
D	drag
d_{cyl}	diameter of cylinder
e	eccentricity, $(a^2-b^2)^{1/2}/a$
G_{cal}	gain of amplifier used during transducer calibration
G_{run}	gain of amplifier used during the tunnel run
H	flux tensor
i, j, k	Cartesian unit vectors
K_ϑ	hypersonic similarity parameter, $M_\infty\vartheta$
$K\beta_c$	hypersonic similarity parameter, $M_\infty\beta_c$
$K\delta_e$	hypersonic similarity parameter, $M_\infty\delta_e$
$K\vartheta_s$	hypersonic similarity parameter, $M_\infty\vartheta_s$
k_1	constant
L	length of flat plate or nose-cylinder body up to hingeline
L	lift
L_{cone}	length of cone
L_{cyl}	length of cylinder
L_{flare}	length of flare
LIF	Laser induced fluorescence
L_s	length of strake

L_s	measured distance from separation point to hingeline, (Fig. 2.2)
L_s^*	characteristic separation length
L_{sep}	measured distance from separation to reattachment point
M	Mach number
M	pitching moment
M^*	characteristic Mach number, (Fig. 2.3)
n	index of the velocity profile, $u/u_\infty=(y/\delta)^n$
N	normal force
n	power-law exponent
n	unit vector normal to surface
o/p	output
p or P	pressure
P_r	Prandtl number
q	heat transfer rate
Q	vector of conserved variables
q_∞	freestream dynamic pressure, $\frac{1}{2}\gamma p_\infty M_\infty^2$
r	radius
R	residual
Re	Reynolds number
$\Re_v$	reflection pressure coefficient
r_f	recovery factor
S	surface area
T	temperature
t	time
u	velocity measured along x-axis
v	velocity measured along y-axis
V	voltage
V	volume
V_∞	freestream velocity
V_{FS}	full voltage scale
W	weight
x	measured distance in x-direction
x	transient recorder reading
x_{cp}	distance to centre of pressure from nose
x_{moment_centre}	distance to balance moment centre from base
Y	distance along radial or spanwise direction
y	measured distance in y-direction
Greek letters	
α	incidence
β	flare angle
β	angle of sideslip
β_s	small-scale separation flare angle
β^*	flare angle for normal shock formation at the line $M=M^*$, (Fig. 2.3)
Γ	Mach number coefficient
γ	ratio of specific heats
δ	shock stand-off distance

δ^*	boundary layer displacement thickness
δ_e	equivalent cone half angle
$\delta_{entropy}$	entropy layer thickness
δ	boundary layer thickness
Δ	incremental change
ε	density ratio across a normal shock, $(\gamma-1)/(\gamma+1)$
η	angle between the unit normal and wind vectors
θ	angle on nose from stagnation point
ϑ_m	maximum cone semi-angle for an attached shock wave
ϑ_s	shock angle
θ_{xz}	elliptic cone half-angle measured in vertical plane
ϑ_c	cone semivertex angle
μ	dynamic viscosity
ρ	density
Φ	ray angle of cone
x, ρ, φ	cylindrical polar co-ordinates
χ	viscous interaction parameter
subscripts	
∞	freestream
1	conditions ahead the normal shock
2	conditions ahead the flare shock
3	conditions behind the flare shock
atm	atmospheric conditions
aw	adiabatic wall
b	base
c	cone
e	local conditions ahead hingeline
f	final
HL	hingeline
i	initial
incip	incipient
max	maximum
n	nose
o or total	total conditions
o	start of interaction
o∞	freestream stagnation conditions
o1	reservoir conditions behind of normal shock
p	platform
r	reattachment
r	recovery
ref or *	reference
s	strong
tr	transition
INV	inviscid
w	wall

Chapter 1

Introduction

1.1 Historical Overview

In 1933, the Austrian engineer Eugen Sänger published a design of a rocket-aeroplane that would fly at high altitudes (60-70 km), with an airspeed of 10,000 km/h. Pushed by the start of the Second Word War, Sänger altered this design. He made a mathematical model of a bomber, which after launch from a sled, the rocket engines would accelerate the vehicle to a final velocity of 6 km/s at an altitude of 160 km. After completing its mission, it would, after bouncing a few times on the atmosphere, land some 24,000 km from the launch site. During the Second World War, Wernher von Braun worked on the A-4 ballistic missile, also known as the V-2. To enhance the range of this missile, the design was altered in 1945, and two swept wings were added. This rocket reached speeds up to Mach 4, which made this rocket the first winged vehicle to fly faster than the speed of sound. The first man-made object to reach hypersonic speeds was a second stage rocket that had been added to a V-2. This took place on February 24th, 1949 at White Sands, USA[1].

The 1950's and 1960's saw extensive and pioneering research in the aerodynamics of bodies flying at hypersonic speeds. The effort was fuelled by the need for intercontinental ballistic missiles and for manned space flight. Until 1980, the main applications for hypersonic aerodynamics were missile aerodynamics and spacecraft re-entry into the earth's atmosphere. The re-entry scene was dominated by Apollo class modules, which were primarily blunt objects and followed near ballistic re-entry trajectories with little control over their flight path.

In 1980, Space Shuttle became the first reusable re-entry vehicle resembling an aircraft with significant flight path control. This has lead to the revival in the research of hypersonic flow phenomena, with challenging hypersonic research programs. Examples are Hotol, Hermes and Sänger in Europe, NASP (National Aerospace Plane) in USA and Hope and Himes in Japan. This revival was mainly supported by positive economic development in the industrialised nations. However, in the 1990's, budget cuts as a result of slowing down of the growth of economies of the countries involved, and the apparent absence of any serious military threat, has led to slow progress of these projects. The inherent very high cost of developing any future hypersonic vehicles and the limited world market that they would command, means that such programmes would have to be based on some co-operative arrangement of the countries interested. The present reduced funding for hypersonic research does not deny the role that hypersonic aerodynamics is going to play in the near future transportation systems.

Apart from the field of space flight, weapons technology has experienced increasing interest in aerothermodynamics. It is expected that future generations of missiles and projectiles will enter the domain of hypersonic Mach numbers and similar problems to the ones highlighted by research into spacecraft and hypersonic planes will be encountered.

1.2 Characteristic Features of Hypersonic Flow

Flight above a Mach number of 5 is considered to be hypersonic. The reason for this definition is that a Mach number of 5 is the lower limit of the flight regime in which real gas effects begin to appear. Stagnation temperatures reach levels at which: a constant specific heat assumption is no longer valid, aeroheating becomes a problem with respect to structural temperatures and strong shock interactions can occur on various parts of the vehicle.

A very important feature of hypersonic flow past a body is the formation of very strong shock waves close to the body surface. In the absence of intense radiation, the effect of the body is felt only downstream of the bow shock, and it is the flow field between the body and the shock that is of interest. The region between the surface of the body and the shock is called the shock layer. The bow shock may be attached if the body is slender

and pointed, or it may stand off from the surface if the vertex angle of the pointed body is too large or if the nose or leading edge is blunt. For curved shocks, vorticity is generated in the flow and the entropy varies from streamline to streamline.

Viscous effects are more pronounced for hypersonic flows. Close to the surface where the flow velocity is low, large temperatures develop. Therefore, the viscosity is high and the density is low and the boundary-layer thickness may be much larger than for corresponding situations at the same external-stream Reynolds number in subsonic or supersonic flows. Boundary-layer displacement effects may significantly modify the inviscid flow in the shock layer. The influence of the boundary layer on the outer flow is called viscous interaction.

For a sharp 2-dimensional wedge, the inviscid flow properties remain constant inside the shock layer. If the leading edge is blunt, an entropy layer is formed next to the surface of the body and the flow properties are not constant. The detached bow shock, formed at the leading edge, is highly curved because of the interaction between the shock wave and expansion waves created around the leading edge. Streamlines have different flow properties depending upon the part of the shock through which they have been processed. The streamlines passing through the near normal (stronger) portion of the shock wave have higher entropy but lower stagnation pressure than those passing through the weaker portions of the shock wave.

Although heat-transfer effects do not differ in principle from slower-speed flows, greater temperature differences exist across the boundary layers and can cause large changes in the gas properties. Heat-transfer rates become intense at sharp leading edges and pointed noses, and, consequently, blunted leading edges and noses are required in order to avoid these high heat-transfer rates. Blunted leading edges and noses are easier to manufacture and may satisfy other system requirements, for example, radar or infra-red signal distortion reduction[2].

1.3 Program of Study

Future defence weapons may include very high speed projectiles flying and manoeuvring over a wide incidence range. The flowfield about them can be very complex and may feature extensive areas of separated flow and vortices. The designer must be aware of

these effects, so that a suitable control system can be developed to manoeuvre the vehicle.

In the conceptual design phase, a simple description of the aerodynamic characteristics is sufficient to assess candidate configurations. As the development process carries on, the complexity and detail required increases and the source of the data changes, from an almost exclusive reliance on engineering prediction methods, to a high dependence on results from detailed wind tunnel tests. There are obvious advantages in being able to proceed further with weapon development before limitations of available prediction methods force the designer to resort to expensive and time consuming wind tunnel tests.

In recent years an increasing number of new weapon designs have included features, such as non-circular cross-section bodies, air intakes, or novel control concepts, which cannot usually be addressed using engineering prediction methods. These points, coupled with developments in computer technology and numerical methods, have focused attention on the application of computational fluid dynamics to weapon configurations.

Although in recent years the design of flight vehicles has been based increasingly upon computational simulation, wind tunnel experiments continue to play the major role in aerodynamic analysis and design. However, for a small class of supersonic and hypersonic flow problems, high-quality numerical solutions are now believed to represent the physics of the problem more accurately than a wind tunnel experiment can simulate the free flight conditions. An example of this is the supersonic or hypersonic, laminar, perfect gas flow over a simple geometry at low angle of attack.

The realisation that certain flow fields can be computed more accurately than they can be measured experimentally must begin to change the relationship between computational and experimental aerodynamics. This thesis addresses this changing relationship and seeks to improve the synergism between computational aerodynamics and wind tunnel experimentation. The physical and numerical approaches can each gain by using the strengths of one approach to offset the weaknesses of the other, and vice versa.

The present study is divided in two parts:

a) Slender lifting elliptic cones with and without strakes

(This part of the study was supported under contract by the Defence Establishment and Research Agency of the United Kingdom.)

Slender elliptic planform cones are of interest as gun fired projectiles. As it has been pointed out by Van Dyke[3], the elliptic cone can be used as a standard of comparison for supersonic flow past bodies without axial symmetry, just as the circular cone is used as a standard of comparison for supersonic flow past bodies of revolution. Elliptic cones may have important aerodynamic advantages over circular cones. Theoretical and experimental investigations[4-7] have shown that an elliptic cone may have significantly higher lift/drag ratios than a circular cone of the same cross-sectional area per unit length.

An experimental and numerical investigation has been made to determine the effect of strakes on the aerodynamic characteristics and performance on slender elliptic cone missile configurations.

The present investigation aims:

1. to compare a right elliptic cone with a power-law body, (see Figs. 3.7b and 3.7c);
2. to determine the effect of strakes on both a right elliptic cone and a power-law body and to access whether improvements in lift coefficient are significant due to the containment of the windward flowfield;
3. to provide data for code validation and further CFD analysis;
4. to assist in the future design of realistic shapes for slender manoeuvring bodies;
5. to improve the synergism between computational aerodynamics and wind tunnel experimentation (CFD provides more details in the present case).

Some information regarding the shock layer was obtained from schlieren pictures. Detailed flow properties in the shock layer were obtained, for some elliptic cone configurations with and without strakes, using a three-dimensional, high resolution, iterative, finite volume parabolized Navier-Stokes solver, based on the Osher approximate Riemann solver. This program (Cranfield PNS3D) has been developed by Dr N Qin at Cranfield. Surface flow visualisation, using an oil-dot technique, and pressure measurements were made on one of the models to determine the effect of strakes. Lift, drag and pitching moment characteristics for the elliptic cones with and without strakes were obtained using a three component strain-gauge balance.

b) Cylinder-flare body

(This part of the study was supported by the Cranfield College of Aeronautics, Cranfield University, UK.)

Boundary layer separation is of interest in many phases of aerodynamics. The presence of separation causes sudden changes in pressure and heat transfer distributions and aerodynamic forces. For the occurrence of separation to be predicted, information on the conditions which cause separation should be available. When separation occurs, the designer must be able to judge the acceptability and desirability of the separated boundary layer by knowing the flow characteristics, i.e. extent of separation, pressure distribution, heat transfer and boundary layer steadiness.

Boundary layer separation is caused by the formation of a strong adverse pressure gradient. This is present, in supersonic flows, because of compression waves generated either by shock impingement or a local change of surface slope. For the latter case the compression waves originate from the edge of the subsonic portion of the boundary layer and deflect its supersonic portion as well as the inviscid flow around the local protuberance. The local wall skin-friction distribution determines the penetration ability of the boundary layer in an adverse pressure gradient. The local flow properties of Mach and Reynolds number, wall to freestream temperature ratio and its laminar, transitional or turbulent character, all affect the skin-friction distribution.

The cylinder-flare configuration has many advantages as a space vehicle and missile: The nose shape can be adjusted to suit different thermal protection materials and to produce the required drag for a given trajectory; the centerbody length can be adjusted for payload size; and the flare angle and length can be varied to produce a stable configuration.

An experimental study has been performed to examine the aerodynamic effectiveness of a cylinder-flare body at M_∞=8.2 and it has been inspired by the work of Kuehn[8-9]. The present investigation aims:

1. to analyse the effects of an entropy layer, generated by a hemispherical nose, on the performance of an axisymmetric cylinder-flare body;
2. to investigate the effects of laminar and turbulent boundary layer on flow properties close to the body;

3. to provide data for code validation and further CFD analysis;
4. to complement the existing database on boundary layer separation for three dimensional bodies.

The surface flow over the cylinder-flare body was studied using oil-dot and liquid crystal techniques. Some information regarding the shock layer was obtained from schlieren pictures. The effects of entropy layer and boundary layer state on flare effectiveness were deduced from pressure measurements over the cylinder and the flare.

This thesis contains six chapters. These chapters cover:

1. Historical overview, characterisation of hypersonic flow and program of study;
2. Existing literature pertinent to the study;
3. Computational methods and experimental facilities and techniques used;
4. Elliptic cones with and without strakes;
5. Flare control effectiveness;
6. Conclusions of the research and suggestions for future work.

Chapter 2

Literature Survey

2.1 Boundary Layer Separation

The flow over a hypersonic vehicle is likely to separate where the surface pressure is rising rapidly. These pressure changes may be due to gradients in the surface geometry, displacement effects associated with the ejection of reaction control gases or due to external agencies such as impinging shockwaves. The incident flow is required to tolerate a pressure gradient associated with the flow field modification. Separation occurs when the low momentum fluid contained in the lower portions of the boundary layer is unable to penetrate the external pressure gradient. It results in a considerable modification of the attached-flow-field pressure and heat transfer distributions and thus of the aerothermal loads on the surface. For wedge and flare type flows, an adverse pressure gradient is generated by the change in the wall geometry. The interaction between the wall skin friction and the adverse pressure gradient determines whether the flow separates.

2.2 Boundary Layer Transition

Boundary layer transition is critical to the aerodynamic optimisation of hypersonic vehicles. Transition affects a number of surface properties such as heat transfer and skin friction as well as the drag and payload performance of the vehicle. Natural transition arises from the amplification of very small disturbances to the boundary layer. Stetson[10,11] has shown experimentally that this is followed by the linear and non-linear amplification of selected disturbances (within a mean flow boundary layer which exhibits laminar characteristics). Following a considerable amplification of the disturbances,

White[12] and Malik[13] suggest that intense local fluctuations or turbulent spots appear randomly within the boundary layer. From these, true turbulence (in the form of high frequency eddies) is generated and convected downstream. The random generation and passing of these concentrated regions of turbulence over surface mounted sensors produces an intermittent increase in the amplitude of fluctuation on the surface, seen as an increase in the RMS (Root Mean Square) component.

The increased frequency of synthesis of turbulent spots in the transition region results in an increase in intermittency. This increases until the spots coalesce at which point a peak in the intermittency is observed. Following the merger of the spots, the boundary layer is made up of high frequency turbulent eddies (originally present within the confines of the spot). The frequencies of these eddies are outside the sensing range of surface mounted sensors, the fluctuations are not registered and the fluctuating component of the signal is reduced.

2.3 Parameters Affecting Separation

Experiments by Coleman et al[14], Kuehn[15,8,9], Gray[16] and Ginoux[17] have emphasised the close similarity between axisymmetric and two-dimensional separated flows. This similarity suggests that criteria evolved from the large amount of available two-dimensional data may be relevant to the analysis of axisymmetric interactions. The main factors governing the two-dimensional interaction between a shock wave and a boundary layer according to Popinski and Ehrlich[18] are the boundary layer state (laminar, transitional or turbulent), Mach number, Reynolds number and overall pressure rise. Chapman et al[19] and Delery et al[20], amongst many others, have shown that the state of the boundary layer is the most important factor governing the properties of the interaction. The state of the boundary layer produces four classifications of the interaction region according to the relative location of transition to the point of separation. These classifications are:

1. purely laminar: a laminar separation with transition occurring well downstream of the interaction region. In these cases, the boundary layer is laminar at separation and reattachment;

2. transitional type 1: transition beginning between the separation and reattachment points. In these cases, the boundary layer is laminar at separation but reattachment is either transitional or turbulent;
3. transitional type 2: transition beginning upstream of the separation with fully turbulent conditions developing either downstream of separation or downstream of reattachment;
4. purely turbulent: transition being complete and a fully turbulent boundary layer being established well upstream of separation.

2.4 Incipient Separation for Laminar Interactions

For low flare deflection angles, Kuehn[15,9], Gray[16], Becker et al[21], Ferguson et al[22] have shown that the flow remains attached. Similarly for low flap deflection angles, Kumar et al[23], Bloy[24], Needham et al[25] and Holden[26] have shown that the flow remains attached. The flow structure resembles that for inviscid flows with a single flap or flare shock present at the hingeline. An increase in the flap or flare deflection angle increases the associated pressure gradient and causes the incipient separation condition to be attained. At this condition, the wall skin friction at the hingeline is reduced to zero. The heat transfer is reduced locally in the corner and in the separated flow regions away from reattachment.

Experimental studies by Needham and Stollery[25] of incipient separation in hypersonic flow have shown that for a sharp leading edge flat plate of length L with a trailing edge flap at angle β:

$$M_\infty \beta_{incip} = 80 \overline{\chi}_{\infty L}^{1/2} \qquad (2.1)$$

where $\overline{\chi}_{\infty L} \equiv M_\infty^3 \sqrt{C} / \sqrt{Re_L}$. This variation is also given by Hankey and Holden[27] and by Delery et al[20].

Inger[28] has shown, using a triple deck formulation of the incipient separation interaction region, that this experimental correlation has a sound theoretical basis and extended the incipient separation model to supersonic Mach numbers. He gives the incipient separation flap deflection angle as:

$$M_\infty \beta_{incip} = k_1 \left[\frac{\sqrt{M_\infty^2 - 1}}{M_\infty} C_{ref}^{\frac{1}{2}} \overline{\chi}_{\infty L} \right]^{\frac{1}{2}} \tag{2.2}$$

Needham and Stollery's[29] experiments have shown that a wall temperature reduction increases the incipient separation flap angle. The same effect of wall temperature on the incipient separation flare angle was also deduced by Ferguson et al[22] on experiments with flared bodies. Inger's formulation suggests that the wall temperature effect is governed by the Chapman-Rubesin constant which is:

$$C_{ref} = \left[0.5 + 0.5\frac{T_w}{T_\infty} + 0.039 M_\infty^2 \right]^{\varpi - 1} \tag{2.3}$$

where $0.5 \le \overline{\omega} \le 0.7$.

According to Simeonides[30], Delery et al[20] and Katzer[31], the flap pressure rise, required for laminar incipient separation, can be scaled according to the laws of free interaction:

$$\frac{p_{incip} - p_o}{q_o} = F[\overline{X}] \frac{(2c_{f,o})^{\frac{1}{2}}}{(M_o^2 - 1)^{\frac{1}{4}}} \tag{2.4a}$$

where suffix *o* corresponds to the interaction origin and F is a dimensionless correlation function of the scaled streamwise distance:

$$\overline{X} = \frac{X - X_o}{L} \tag{2.4b}$$

The length scale L obeys a law of the form:

$$L \propto \delta_o^* c_{f,o} (M_o^2 - 1)^{-\frac{1}{4}} \tag{2.4c}$$

and F takes values of 0.81 to 1.

2.5 The Effect of Transition on Incipient Separation

Gray[16] has shown experimentally that on laminar configurations with ramps or flares, with $\beta = \beta_{incip}$, an increase in Reynolds number will eventually promote transition of the flap or flare boundary layer. Potter et al[32] have shown that boundary layer transition on a flat plate is accompanied by an increase in boundary layer thickness. According to Coles[33], the thickening of the boundary layer causes an increase in viscous/inviscid

interaction which causes an increase in static pressure. Because of that pressure rise the overall flap or flare pressure will increase further, and hence separation will be promoted[14]. Further increasing the Reynolds number will promote transition well upstream of the hingeline. The increased energisation of the boundary layer, well ahead of the hingeline, will delay separation and hence increase the incipient separation flap or flare deflection angle[16], (see Fig. 2.1). Needham[34] and Needham and Stollery[25] studies provide further information about these effects.

2.6 Incipient Separation for Turbulent Interactions

Kuehn[8] has shown that the qualitative effects of geometry and test conditions on the *occurrence* of turbulent separation are very similar to those found for laminar boundary layers. However, it is now well established that in a well separated turbulent flow there is an *increase* in heat transfer in the separated region in contrast to the laminar case in which the heat transfer is reduced in the separated region. This is one of the most significant differences between laminar and turbulent flow. With respect to the *occurrence* of separation, the only important difference between the laminar and turbulent boundary layers is that a much higher flare is necessary to cause turbulent separation than that for laminar separation. Kuehn[35] has shown that incipient separation marks a distinct change in the shape of the wall static pressure distribution. He used the appearance of a kink in the wall pressure distribution to detect incipient separation. Various researchers[36,8,14,37,38] have found that very high incipient separation angles ($\cong 30^{\circ}$) are possible in hypersonic flow under turbulent conditions.

Coleman et al[14] have shown that the incipient separation angle for axisymmetric flow is slightly higher than for the planar two-dimensional case. The same was deduced by Kuehn[35,8] and Appels et al[39]. Coleman et al[14] have also observed a close similarity between the surface pressure and heat transfer rate distributions for the two cases. Rose et al[40] conducted an experimental investigation of the incipient separation pressure rise for a turbulent boundary layer that developed on the wall of an axially symmetric nozzle and supersonic ($M_{\infty}=3.8$) test section. The experimental arrangement is shown in Diagram 2.1.

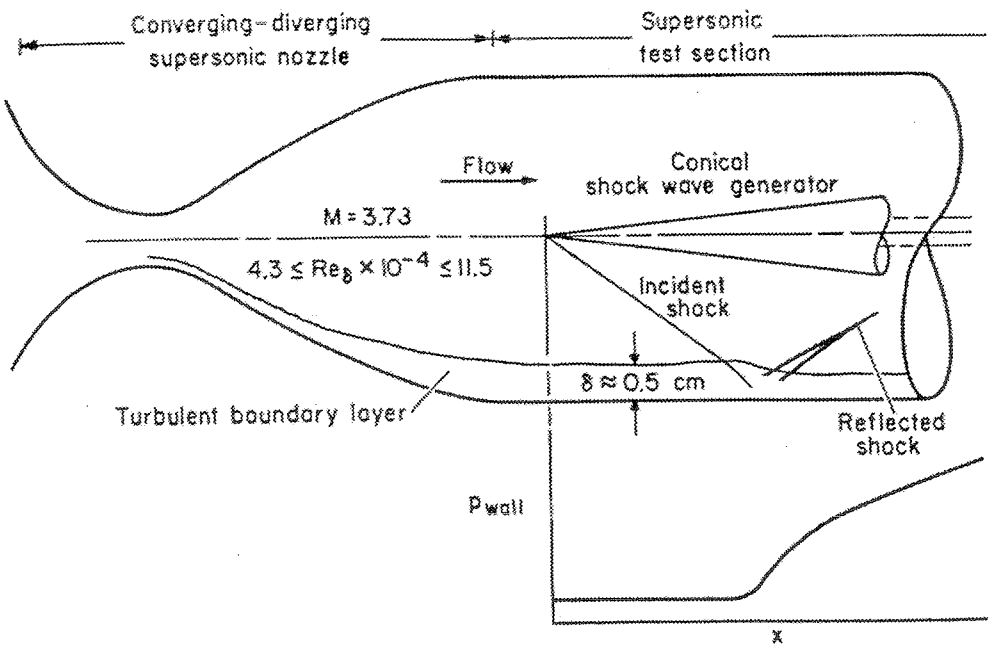

Diagram 2.1 Rose's et al[40] experimental arrangement

The data presented by Rose et al[40] indicate that the incipient separation pressure ratios in axially symmetric flows are much lower than those indicated by Kuehn's[35,8], Coleman's et al[14] and Appels et al[39] planar, two-dimensional data. This may be due to the sensitivity of the determination of incipient separation to the detection method used and the possible fundamental difference between incipient separation on internal and external surfaces.

Zheltovodov[41] has indicated that before the unseparated flow develops to a fully steady separation, it acquires an intermediate separation state. Appels et al[39], Spaid et al[42] and Settles et al[43] have shown the existence of small separation bubbles at very low flap deflection angles, Fig. 2.2. Such small scale separations were observed by Babinsky et al[44] from experiments using a cylinder-flare configuration and were predicted computationally by Edwards et al[45].

Examining Fig. 2.2, when $\beta_s \leq \beta \leq \beta^*$ a small-scale separation arises in the laminar sublayer and develops within the near-wall part of the boundary layer, its length changing up to some characteristic value L_s^*. A further increase of β will cause the separation region to

extend to the external part of the boundary layer, large-scale separation, where the rate of L_s variation is higher[41]. The value of β_{incip} close to β^*, obtained by extrapolation of the external part of the curve at $L_s \rightarrow 0$, is commonly used as a practical criterion of incipient separation. It should be noted that the large-scale separation region starts to be formed when $\beta=\beta_{incip}$ whereas the birth of the small-scale separation takes place when the deflection angle is close to β_s (ref. 41).

Elfstrom[37] was the first to use the assumption that the large-scale separation can be borne at the instant of the normal shock formation at $\beta=\beta^*$ at the line $M=M^*$, which is the interface between the near-wall and external parts of the boundary layer[†] as shown in Fig. 2.3. In the simplified model suggested by Elfstrom a close value M_w is used instead of M^*. It is obtained by extrapolation to the wall of the external part of the Mach number profile over the boundary layer thickness, Fig. 2.3. The incipient separation angle is then defined as the deflection angle needed to detach an inviscid flow at M_w. This approach allows a good description of experimental data for the incipient separation angle β_{incip} as found by Korkegi[46], Spaid el al[42], Settles et al[43] and Appels et al[39] (see Fig. 2.4). The calculated values, for the Reynolds number range $Re_{\delta L}=10^5$-10^7, lie within the band bounded by the dashed lines.

A collection of incipient separation data is shown in Fig. 2.5. The correlation and explanation of all the data presented is impossible because of the difficulty in defining the incipient separation condition in turbulent flow. Taking into account the work of Dolling et al[47], that turbulent separated flow is unsteady, most measurements in Fig. 2.5 reflect a mean value of β_{incip} which varies with the technique chosen to detect incipient separation. The same figure shows the trend reversal of β_{incip} with $Re_{\delta L}$ at high values of Reynolds number. Elfstrom[37] has given an explanation, based on his model explained above, of this trend reversal. The slowly increasing β_{incip} with $Re_{\delta L}$ was attributed to the fact that the various parts of a fully developed turbulent profile grow at different rates so that the Mach number M_w increases slightly with Reynolds number. The reason for the decreasing β_{incip} with $Re_{\delta L}$ at low values of $Re_{\delta L}$ was attributed to the slow development of the wake component of the turbulent velocity profile.

[†] M^* is the Mach number at the point of inflection of the Mach profile curve i.e Fig. 2.3

Stollery and Bates[53] have shown that the strong viscous interaction parameter for turbulent flow is:

$$\overline{\chi}_S \equiv \left\{\frac{M_\infty^9 C}{Re_x}\right\}^{\frac{2}{7}} \tag{2.5a}$$

and they have suggested that by analogy to the laminar case:

$$M_\infty^2 \beta_{incip}^2 \sim \left(\frac{M_\infty^9 C}{Re_L}\right)^{\frac{2}{7}} \tag{2.5b}$$

However, the experimental data described in Fig. 2.5 shows that the real picture is far more complex but many experiments show β_{incip} increasing with M_∞.

Elfstrom[37], Kilburg et al[54] and Back et al[55] have found that wall cooling reduces the streamwise extent of the interaction region. Delery[56], in experiments executed with a heated wall ($T_w/T_r>1$), found that a rise in wall temperature induced a substantial increase of the interaction extent, which is consistent with the above findings. Zheltovodov et al[57] have shown that the incipient separation stage for the two-dimensional cases as well as three-dimensional shock wave/turbulent boundary layer interaction with conical and cylindrical symmetry may be predicted on the basis of the classical free interaction analysis of Chapman[17]:

$$\frac{p_{incip} - p_o}{q_o} = F[\overline{X}]\frac{(2c_{f,o})^{\frac{1}{2}}}{(M_o^2 - 1)^{\frac{1}{4}}} \tag{2.4a}$$

and F takes the value of 4.2.

2.7 Parameters Affecting the Scale of Separation Interaction Region

1.Flap or flare deflection

Kumar et al[23], Needham et al[29], Miller et al[59], Kuehn[15,9] and Ferguson et al[22] have shown that flap or flare deflection promotes separation and increase the length of the separation interaction region of a laminar boundary layer. Simeonides[30], Smith[60], Becker et al[21] and Gray[16] have shown a similar trend for transitional type 1 and 2 interactions, as have Elfstrom[37], Coleman et al[36], Appels[61], Kuehn[8] and Inouye et al[62], for turbulent

interactions. Needham and Stollery[25] suggested that the scale of the separation interaction region is mainly determined by the pressure rise associated with the reattachment process. The increase in inviscid flap pressure ratio with flap deflection is responsible for the promotion of separation for laminar, transitional and turbulent interactions. A similar suggestion was given by Kuehn[8,9,15] for experiments using cylinder-flare configurations under both laminar and turbulent conditions.

2.Mach number

Experiments by Miller et al[59], Needham et al[29], Hankey and Holden[27] and Kuehn[9,15] have shown, for fully laminar interactions, that an increase in Mach number (whilst maintaining a constant flap or flare deflection angle and freestream unit Reynolds number) reduces the separation length. For transitional type 1 interactions, Gray[16] and Kaufman[63] have shown that the length of the separation interaction region increases with Mach number, which is due to transition delay by increased Mach number halting the spread of turbulence reducing the energisation of the shear layer by transition.

The delaying effect of increasing Mach number on the onset of transition of a laminar boundary layer on a sharp flat plate has been studied by Korkegi[64], Potter et al[32] and Coleman[65] (above M=4 see Fig. 2.6). An investigation by Nagamatsu et al[66] on a cone attained a similar conclusion. The results of these tests also showed that for both flat plate and conical boundary layers, the length of the transition region increased with Mach number. In the hypersonic regime, the length of the transition was of the order of the length of the laminar region. These results are shown in Fig. 2.6. The observed delay in transition with Mach number may be due to the slower growth rates of disturbances, e.g. Tollmien-Schlichting waves and Gortler instabilities within the boundary layer, as suggested by Spall et al[67] and Mack[68] experimentally and theoretically.

Kuehn[8,35] and Roshko et al[58] found, for turbulent interaction, that an increase in Mach number inhibits separation and reduces the separation length once separation has occured. Roshko et al[58] also suggested that for large flare angle the separation region upstream of the flare had free interaction characteristics.

3.Incidence

The effect of incidence in the separated interaction region is very complex because changing incidence changes the local Reynolds number and Mach number therefore an understanding of the effect of incidence on the hingeline Mach and Reynolds numbers is important. In the absence of strong viscous interaction effects, these parameters are dependent on the strength of the leading edge shock. This is a function of the freestream Mach number and the geometrical incidence of model.

For a given freestream Mach number, incidence increases the strength of the leading edge shock. This reduces the reservoir pressure behind the shock (the pressure attained if the flow is reduced isentropically to rest) and thus decreases the local Mach number. The rate of decrease of the local Mach number with incidence increases with freestream Mach number. This is due to the increase in reservoir pressure loss sustained at the leading edge. The effects described above can be seen in Fig. 2.7.

The ratio of the local to freestream unit Reynolds number is:

$$\frac{\mathrm{Re}_e}{\mathrm{Re}_\infty} = \left[\frac{\rho_e}{\rho_\infty}\right]\left[\frac{M_e}{M_\infty}\sqrt{\frac{T_e}{T_\infty}}\right]\left[\frac{\mu_\infty}{\mu_e}\right] \tag{2.6}$$

Assuming a linear viscosity-temperature relationship ($\mu \propto T$) and a perfect gas flow, the unit Reynolds number ratio becomes:

$$\frac{\mathrm{Re}_e}{\mathrm{Re}_\infty} = \frac{\rho_e}{\rho_\infty}\frac{M_e}{M_\infty}\left[\frac{T_\infty}{T_e}\right]^{\frac{1}{2}} \tag{2.7}$$

From the above relationship is obvious that the effect of incidence on the local unit Reynolds number is a combination of the effects of incidence on the changes in pressure, temperature and Mach number across the leading edge shock, which are function of the leading edge shock. The pressure and temperature ratio across an oblique shock increase with incidence while Mach number ratio decreases with incidence. Fig. 2.8 shows the complex behaviour of the unit Reynolds number with incidence. At low incidence, the increase in pressure dominates and produces an increase in unit Reynolds number. At high incidences, the effects of the heating from the strong leading edge shock become dominant and result in a decrease in the unit Reynolds number.

2.8 Leading Edge Bluntness Effect on Separation

1."Small" bluntness

Pressure distribution measurements conducted by Vermeulen et al[194] at M_∞=6 on a compression corner with a slightly blunt leading edge showed the promotion of separation due to bluntness. Heat transfer tests on corresponding configurations showed that bluntness decreased the heat transfer rate for some distance downstream of the reattachment compression. This was attributed to an increased resistance to transition in the reattachment region due to bluntness, (pressure and heat transfer reduced because of the entropy layer). The measurements on the flat plate upstream of the interaction region correlated with heat transfer predictions for laminar boundary layers. Promotion of separation by leading edge bluntness was also observed by Edwards et al[71] in low density tests at M_∞=12.5 and Re_∞/cm=6.2x10^2. The freestream conditions indicate a laminar boundary layer at the hingeline. In summary, for entirely laminar flow bluntness promotes separation.

The delaying of transition by "small" bluntness has been observed by Brinich[72], Potter et al[32], Deem et al[73] and Richards[74]. Stetson[75] observed that disturbances present within the boundary layer on a sharp cone were absent on a cone with small bluntness. For the latter, the measurements showed large disturbances to be present in the entropy layer. The growth of the boundary layer and the subsequent swallowing of the entropy layer moved these disturbances into the boundary layer. Following the swallowing, the disturbances entered and forced the transition of the boundary layer. For small bluntness, an increase in leading edge diameter increases the thickness of the entropy layer. This delays the entry of the disturbances into the boundary layer and hence delays transition of the boundary layer. Small bluntness delays transition and hence may promote separation.

2."Large" bluntness

In tests at M_∞=8.2 and Re_∞/cm=9.x10^4 on a compression corner, Kumar et al[76] found that the introduction of bluntness reduces the pressure recovered on the flap due to losses in reservoir pressure through the bow shock at the leading edge. Transition of the flap boundary layer is promoted by large bluntness. The reduction in flap pressure reduces laminar and turbulent heat transfer rates on the flap and substantially delays

separation of the boundary layer. In tests at M_∞=10.0 and Re_∞/cm=8.4x10^4 on a compression corner, Coet et al[77] observed a delay in separation due to the introduction of d=2.5 mm and d=5.0 mm hemicylindrical leading edge bluntness. Along with a reduction in the extent of the separation region, these tests showed an order of magnitude decrease in the flap heat transfer due to leading edge bluntness. Pressure measurements conducted upstream of the hingeline by Townsend[78] on blunted flat plate/flap configuration at M_∞=10.0 and Re_∞/cm=5.0x10^4 showed an appreciable reduction in the extent of the separated flow region when leading edge bluntness was introduced. The state of the boundary layer was diagnosed as being laminar.

Measurements on blunt compression corners by Holden et al[79] at M_∞=19 and β=25.7° showed that the extent of the laminar separated region was related to the viscous bluntness interaction parameter, $\chi_{\varepsilon_L} / \kappa_{\varepsilon_L}^{\frac{2}{3}}$, ($\kappa_{\varepsilon L}=M^3 C_d \varepsilon (d_n/x)$ is the bluntness parameter). This effectively accounted for the relative effects of changes in Mach number and Reynolds number on the extent of the interaction. Holden's results indicate that for $\chi_{\varepsilon_L} / \kappa_{\varepsilon_L}^{\frac{2}{3}} \leq 0.1$, the introduction of leading edge bluntness results in a dramatic reduction in the extent of boundary layer separation, Fig. 2.9. This is similar to the "large" bluntness condition discussed above. For $0.1 \leq \chi_{\varepsilon_L} / \kappa_{\varepsilon_L}^{\frac{2}{3}} \leq 0.5$, Holden observed that leading edge bluntness promotes separation, Fig. 2.9. This is typical of the "small" bluntness condition discussed above. Due to the relatively high Mach number and the low freestream unit Reynolds number, it is believed that these tests were entirely laminar. Therefore, bluntness has a dual effect on laminar separation. "Small" bluntness promotes separation of a laminar boundary layer (with respect to equivalent sharp configuration) while "large" bluntness delays separation. The experiments of Holden et al[79] indicate that for small bluntness, the reduction in the local Mach number outweighs the effect of a decrease in the local Reynolds number and thus an increase in the size of the separated region results. At larger bluntnesses, where the changes in local Mach number and Reynolds number for a change in bluntness are small, the effect of the strong favorable pressure gradient is predominant and thus a decrease in the scale of the viscous-inviscid interaction in the corner results[79].

Coleman[38] deduced, from experiments using cone-cylinder-flare and hemisphere-cylinder-flare models, that despite the very different nose sections and hence marked change in flow conditions approaching the flare, the incipient separation angle remained much the same ($\cong 30^\circ$ at $M_\infty=9$). Kuehn[8,9,15], for experiments with cylinder-flare configurations under laminar and turbulent conditions, showed that nose shape had no influence on the variation of Mach number for incipient separation with Reynolds number based upon boundary-layer thickness.

Brinich et al[80], Muir et al[81] and Softley et al[82] have observed promotion of transition by "large" bluntness. In the "small" bluntness tests of Stetson[75], the relatively thin entropy layer meant that the boundary layer edge Mach number remained close to the freestream hypersonic value of $M_\infty=8.0$. Thus the boundary layer remained stable and was only de-stabilised by disturbances from the entropy layer. However, for large bluntness, the entropy layer is an order of magnitude thicker than the boundary layer and thus envelops the boundary layer. Kumar et al[23] have shown that the Mach number across an entropy layer in hypersonic flow is reduced from the hypersonic value at the upper edge of the entropy layer to a supersonic Mach number at the lower limit of the entropy layer. The disturbances in the entropy layer, together with the destabilising influence of the reduced boundary layer edge Mach number results in a promotion of transition by large bluntness, Fig. 2.10. Neal[83] has found that the reduced boundary layer edge Mach number also reduces the length of the transition region for large bluntness.

Fig. 2.10 shows the effect of small and large bluntness on the Reynolds number for the onset of transition of planar and axi-symmetric boundary layers. *For both configurations, small bluntness delays transition and large bluntness promotes transition.* The correlation shows that for "small bluntness" condition with a given leading edge diameter, a planar boundary layer becomes transitional earlier than a conical boundary layer. This effect also appears to hold for the large bluntness condition despite the lack of transition data for planar boundary layers at high $Re_{\infty d}$. From what is discussed in the above sections, it is evident that the unstable nature of the entropy layer is fundamental to the transition of the boundary layer on surfaces submerged either partially or completely within the layer.

2.9 Slender Bodies

The impulsive-flow analogy, first suggested by Allen et al[85] has frequently been applied to qualitatively analyse the flow over a slender body. This assumes that development of the crossflow with distance along an inclined cylindrical body is analogous to development of the flow with time on a circular cylinder starting from rest. To complete this analogy, the cross section is assumed to be expanded with distance along the body in order to simulate the change of body radius. That is, the crossflow plane is moving down with the free-stream axial velocity component, $V_\infty \cos\alpha$, and the flow in the crossflow plane is analogous to the two-dimensional impulsive flow about a cylinder with crossflow velocity $V_\infty \sin\alpha$.

Jorgensen[7] has shown that there are distinct aerodynamic advantages in using elliptic cones rather than circular cones. Reggiori[86] has demonstrated that a cone with anhedral wings can provide good high lift characteristics at high angles of attack in hypersonic speeds and it is worthy of further study as an approach to reducing heat-transfer rates during re-entry. Power-law bodies can be an alternative to the blunted cone configurations because a power-law body has a greater internal volume than a blunted cone of the same fineness ratio and secondly, various theories predict[87,88] that a power-law body represents the minimum drag case at hypersonic speeds.

2.9.1 Slender Circular Bodies

Houwink[89] investigated the leeward flow field of a 7.5° half angle cone at incidences between 14° and 35° in a Mach 3 flow. The qualitative investigation of the leeward flow structure up to 25° incidence indicated a symmetric and approximately conical flow field with vortices and imbedded shockwaves. Above an incidence of about 28° the flow is non-conical and asymmetric. At these large incidences a steady asymmetric system of vortices seems to be present, separating periodically with distance from the cone tip from the leeward cone surface.

Rainbird[90] found that the development of the viscous flow about circular cones, with increasing incidence, is gradual, progressive, steady and essentially a conical process involving the formation of symmetrically disposed lobes of vortical fluid which develop

into vortices and which remain comparatively close to the cone surface on either side of and near, the leeward generator. At high Reynolds numbers there is no general eruption of vortical fluid from the cone surface which would cause sudden changes to the external inviscid flow.

Borovoi et al[91] found that the contribution of lee-side separated flows of a blunt cone to lift and drag is small at high supersonic velocities, but they can have an appreciable effect on moment, tail unit performance and on heat transfer. The analysis has shown that there is a similarity of leeward flows about cones with different semivertex angles ϑ_c and same values of α/ϑ_c. At relatively small angles of attack thickened regions of viscous flow are formed at the leeward side where the gas flows backward (from the leeward generatrix towards the windward one) and the pressure decreases monotonically with distance from the bluntness. As incidence is increasing these regions turn into two vortices detached from the surface. An entropy wake of the nose bluntness lies between vortices. There are weak imbedded shocks from vortex separation points. This system of conical vortices and imbedded shocks generate adverse pressure gradients which are likely to result in closing the separation line. In the regions where the separated boundary layer attaches to the lee-side cone surface a local increase in heat transfer occurs. This flow is similar to a near wake behind a cylinder in a supersonic transverse flow.

Stetson[92] performed experiments in a Mach 14.2 wind tunnel with a 5.6° half-angle cone model with sharp and spherically blunt tips. He found that for both sharp and blunt cones, there is a pair of symmetrical helical vortices with an attachment line on the most leeward ray and resembles Maskell's free vortex layer type separation, Diagram 2.2. For the blunt cone the separation lines appear to originate in the region where the lateral component of skin friction is zero. The origin of separation occurred closer to the nose tip with increasing angle of attack. The vortices are close to the surface (at least up to $\alpha \cong 18°$) and there is no subsonic reverse flow associated with the vortex pattern. Stetson[93] also investigated the transition on cones at angle of attack. He found that transition moves forward on the leeward ray and aft on the windward, which agrees with results from other investigations[94,95].

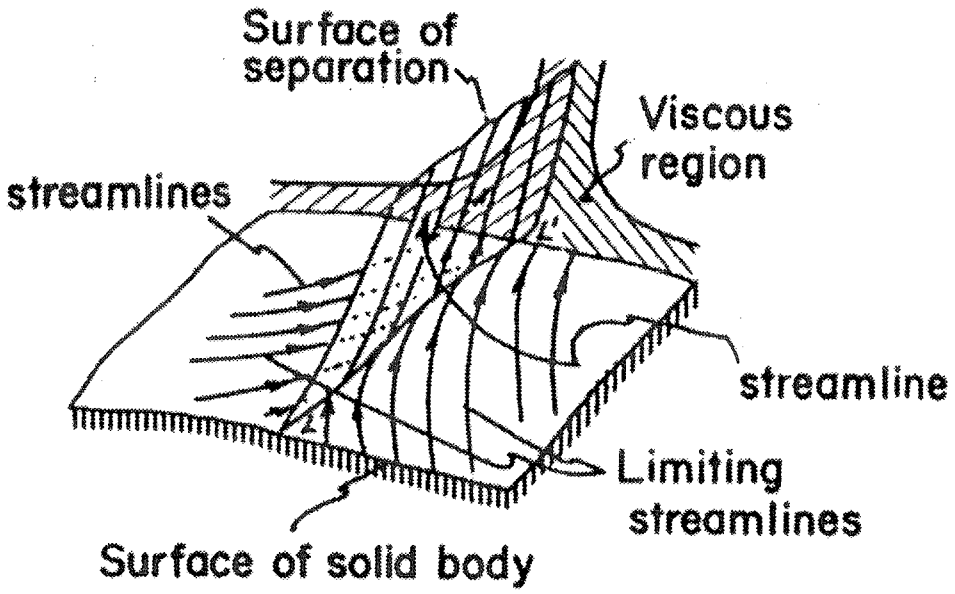

Diagram 2.2 Maskell's free vortex layer type separation[92]

Singh et al[96] conducted a parametric study to determine the effects of nose bluntness on blunted cones and ogives under various hypersonic freestream conditions. The analysis was carried out for air under perfect- and equilibrium-gas assumptions using approximate methods as well as the complete Navier-Stokes and parabolized Navier-Stokes equations. The investigation demonstrated that the effects of nose bluntness and the entropy layer generated by it, persist as far as 260 nose radii downstream depending upon the flow conditions, bluntness and geometry. Tiwari et al[97] determined for hypersonic flows over cones and straight biconic configurations that the flow field variables and surface quantities show significant differences when the angle of attack and nose bluntness are varied and the effect of nose bluntness for slender cones persists as far as 200 nose radii downstream.

Cleary[98] conducted an experimental and theoretical investigation of the pressure distribution and shock-layer properties of a perfect gas over 15° and 30° half-angle spherically blunted cones at hypersonic speeds. The inviscid theoretical solutions demonstrate the unique characteristics of blunted-cone flows. The more pertinent features are an overexpansion of surface pressure below the sharp-cone value and an inflection of the shock. Associated with the shock inflection is a minimum shock angle

which results in a streamline of maximum total pressure and unit Reynolds number within the shock layer. Thinning of the entropy layer at a distance downstream of the nose brings the maximum total-pressure streamline in close proximity to the blunted-cone surface. This effect is accentuated by increasing inclination of windward surfaces. He indicated that the shock inflection may be a factor in the development of turbulent flow by increasing the effective Reynolds number at the edge of the boundary layer. He observed that increasing the angle of attack moved both the inflection of the shock and transition of the flow towards the nose on windward surfaces.

2.9.2 Slender Elliptic Bodies

Palko et al[99] conducted tests on an a/b=1.5 elliptic cone, to determine the pressure distribution, flow streamlines and shock wave shape at an incidence range from 0 to 60 degrees at a Mach number of 10 and a free stream unit Reynolds number of $1.6x10^6$ per foot. The model was oriented both with the major and with the minor axis of the ellipse located in the pitch plane. They found that a pair of symmetrical vortices start at the nose and trace a linear path to the base. These vortices increase in size with travel from the nose to the base. The flow separation lines from which the vortices are fed also trace an essentially linear path along the model surface. When the model was oriented with the major axis of the ellipse located in the pitch plane the vortex core lifted up at approximately 40° incidence. When the model was oriented with the minor axis of the ellipse located in the pitch plane the vortex core lift-up occurred at approximately 50° incidence.

Similar effects were observed by Jorgensen[7] who investigated the aerodynamic advantages of elliptic cones over circular cones at Mach numbers of 1.97 and 2.94 and angle-of-attack range from 0° to 16°. The Reynolds number, based on model length, was $8x10^6$. He also showed that bodies of elliptic cross-section exhibited higher lift to drag ratios than those of circular cross-section of the same fineness ratio and volume. Burk[100] found for tests on elliptic ogives at Mach numbers 5, 6 and 8 that C_L, C_D and C_m decreases in magnitude, the centre of pressure moves forward slightly and the slopes of

the pressure coefficient curves (as the base is approached) decrease as Mach number increases.

Spencer et al[101] found for experiments on a series of 2/3-power low-wave-drag bodies at Mach numbers from 1.50 to 2.86 that increasing the body major-to-minor axis ratio, with the major axis horizontal, resulted in large increases in the lift, drag, and pitching-moment coefficients and lift-drag ratios at positive angles of attack and at all test Mach numbers. The successive increases in major-to-minor axis ratio, with the major axis horizontal, resulted in gains in lift-curve slope for bodies of the same fineness ratio* when the coefficients were based on the respective body projected planform areas. A rearward shift in the body centre-of-pressure location is generally indicated when the horizontal-to-vertical axis ratio is increased from 0.50 to 2.00. Little or no effects of increasing Mach number on the centre-of-pressure location of a given body were shown.

Spencer et al[102] compared experimentally the aerodynamic characteristics of a series of hypersonic minimum zero-lift wave-drag bodies having variation in cross-sectional shape with a series power-law bodies. The power-law bodies are found to exhibit minimum zero-lift-drag as well as maximum lift-drag ratio for n=0.66 for both the circular as well as the elliptical cross-section. However, the zero-lift drag of the theoretical minimum-wave-drag body is slightly lower and the resultant maximum lift-drag ratio is a little higher than that for the n=0.66 power-law body. The increase in the ellipticity ratio for a given power-law or a theoretical minimum wave-drag body results in an almost constant incremental increase in maximum lift-drag ratio, independent of body longitudinal contour. The increase in ellipticity slightly reduces the minimum-drag coefficient, and increases the lift-curve slope for each body. Although the conical bodies (n=1.0) have the highest lift-curve slope and minimum wetted area, the minimum-drag or the n=0.66 power-law-bodies have 25-30% higher lift-drag ratio. The centre of pressure location moves rearward from 53% for n= 0.25 to 67% of body length from the nose for n=1.0.

Fournier et al[103] investigated experimentally the aerodynamic characteristics of a series of elliptic bodies at a Mach number range of 1.5 to 4.63 and an incidence range of -4° to 28° at 0° sideslip. The results indicated that increasing the power-law exponent (i.e.

* The fineness ratio is defined as the ratio of the total body length to the base diameter. For elliptic cones the minor axis length is taken as the "base diameter".

decreasing bluntness and increasing span) for a given value of ellipticity results in increases in the lift-curve slope at low angles of attack and large rearward shifts in the centre of pressure location at all Mach numbers. Increasing the Mach number results in slight effects on the lift characteristics and large reductions in minimum drag. At Mach numbers above 1.5, a maximum value of lift to drag ratio is attained which occurs in the exponent region between 0.5 and 0.66. Increasing the ellipticity for a given body configuration results in large increases in lift and maximum lift to drag ratio with slight effects on the centre of pressure location at all Mach numbers, except for the lowest power law body.

Ashby[104] obtained experimental data for a series of axisymmetric power-law bodies with values of the exponent n of 0.25, 0.5, 0.6, 0.667, 0.75 and 1.0 at Mach 6 and Reynolds numbers, based on model length, from 1.4 million to 9.5 million. These models had a fineness ratio of 6.63 and were tested at incidences from 4° to 16°. It was found that the Reynolds number effects on drag and performance are more significant for power-law bodies from n=0.5 to 1.0. At the higher Reynolds number the variation of boundary layer transition location with nose bluntness causes the drag to be a minimum for the n≈0.6 instead of the n=0.667 body, which has been predicted to have minimum drag in inviscid flow. At the highest Reynolds number, the power-law body for minimum drag is blunter (exponent n lower) than predicted by inviscid theory (n approximately 0.6 instead of n=0.667); however, the peak value of lift-drag ratio occurs at n=0.667.

Graves[105] conducted an experimental investigation to compare the aerodynamic characteristics of a low drag missile concept with a body of circular cross-section, to one with a body of 3:1 elliptical cross-section, (the bodies had identical cross-sectional area distributions). Tests were performed at Mach numbers from 0.5 to 4.63 and at angles of attack from -5° to 28°. The comparison shows that at supersonic speeds the elliptical concept provides increasingly greater normal force up to Mach 2.5 to 3.0, beyond which an incremental increase of about 25% holds through the incidence range. The elliptical concept exhibited lesser longitudinal stability at all test Mach numbers. However, levels of lateral and directional stability are increased, particularly at the higher incidences.

Westby et al[106] conducted an experimental investigation of the longitudinal aerodynamic characteristics of power-law bodies of revolution at Mach 12.8 in a gun-tunnel. The model length and the base diameter were kept constant at 127 mm and 63.5 mm respectively. The Reynolds number based on the body base diameter was $3.5x10^5$ so that the boundary layer was likely to have been laminar along the whole length of the model. Tests were conducted on four models with the power-law exponent, n=0.5, 0.667, 0.75 and 1.0 at incidences from 0° to 20°. The axial force coefficient, C_A, was found to be minimum for the body with n=0.75, however, C_A per unit volume was found to be minimum for the body with n=0.667. The body with n=0.5 exhibited maximum C_A at all the incidences tested. On the other hand the normal force coefficient, C_N, was found to be a minimum for the power-law body with n=0.5 although the values for the other body shapes were found to be very close to each other. Finally the position of the centre of pressure was found to vary with the body shape. The centre of pressure moves further upstream with decreasing values of n from 1.0 to 0.5, as expected because of increased planform area near the nose of the blunter body shapes.

In summary, bodies with elliptic cross-section exhibit higher lift to drag ratios than those of circular cross-section of the same fineness ratio and volume. C_L, C_D and C_m decreases in magnitude as Mach number increases. For bodies with elliptic cross-section, increasing the body major-to-minor axis ratio, with the major axis horizontal, results in large increases in the lift, drag, and pitching-moment coefficients and lift-drag ratios at positive angles of attack. The inviscid calculations for the minimum drag body are of little value.

2.9.3 Slender Bodies with Wings, Fins or Strakes

Reggiori[86] performed an experimental study on a wing-cone configuration, Diagram 2.3, at a freestream Mach number of 5.8 and a range of Reynolds numbers, to obtain surface pressure distributions and lift and drag coefficients for the configuration "wing-up", "wing-down" and "unwinged" (circular cone). The configuration consisted of a 20° right circular cone with wings located at 60° from the plane of symmetry with swept back angle of 75° (with these conditions the leading edge of the wing is subsonic). The same geometry was analysed computationally by Chaudhry et al[107] to examine the flowfield

around the cone. The pressure distribution was not affected by varying the Reynolds number. The cross flow component on the windward side remains very small hence the pressures are nearly constant in this region. The interference effects of the wing on the cone pressure is very strong at positive incidences. On the leeward side, the expansion from the trailing edge of the wing produces a region of low pressure on the cone surface there. The force measurements showed that the lift-drag ratio is increased by both the negative and the positive dihedral wings but the negative dihedral configuration gives much larger increase in comparison to the simple cone.

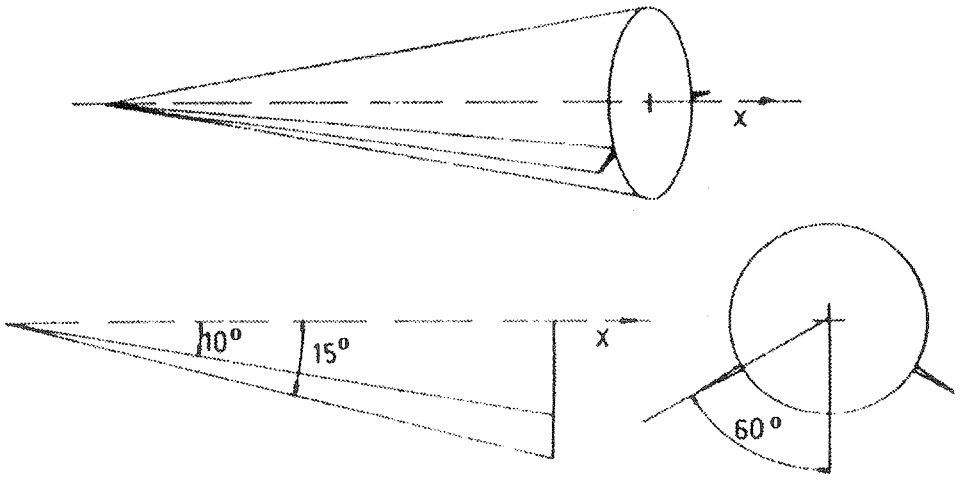

Diagram 2.3 Reggiori's[86] wing-cone configuration

Similar favourable interference effects were studied by Schindel[108] for a Mach 5.9 waverider constructed from a caret wing and a cone, Diagram 2.4. Schindel found an increase in pressure on the waverider and the production of higher lift to drag ratios.

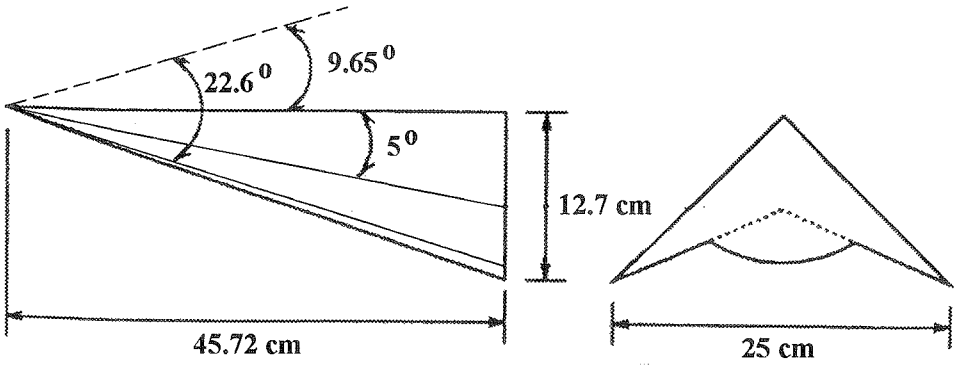

Diagram 2.4 Schindel's[108] waverider configuration

Richards et al[109] and Houwick et al[110] examined the flow over a wing-cone configuration, similar to Reggiori's model, at large angles of attack under simulated re-entry conditions at a Mach number of 15. The behaviour of the flow beneath the wings can be approximated by that around a large angled unpitched cone. They found signs of corner vortex flow at the roots of the wings and outflow around the wing leading edges. The results indicated that increases in lift coefficient of 60% over that obtained on simple cones can be achieved.

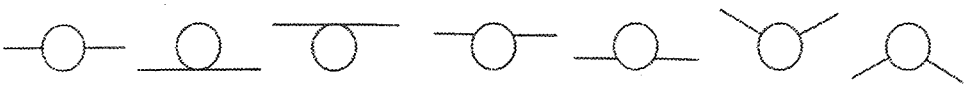

Diagram 2.5 Allen's et al[111] axisymmetric-body delta-wing configurations

Allen el al[111] performed an experimental study at supersonic speeds to measure wing and body spanwise pressure distributions on an axisymmetric-body low aspect ratio delta-wing model, Diagram 2.5, on which the vertical location of the wing on the body was systematically varied from low- to high-mounted positions. In addition, for two of these positions both horizontal and radial wing angular orientations relative to the body were tested. Roll angle effects were investigated for one of the positions. Seven different wing-body configurations and a body-alone configuration were studied. The tests were conducted at Mach numbers from 1.7 to 2.86 at incidences from -4° to 24°.

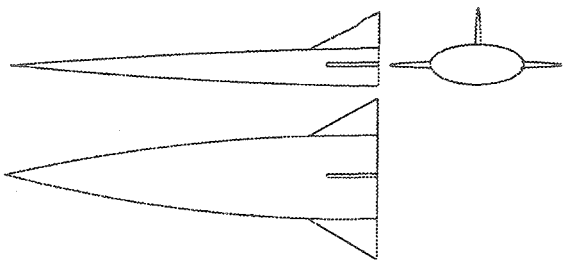

Diagram 2.6 Low-wave-drag elliptical body[112,113]

The important observation was that for a given incidence and at a roll angle of 0°, the pressures were virtually constant in the spanwise direction across the windward surfaces of the wing-body combinations. The vertical location of the wing on the body was found to have a very strong effect on the body surface pressures and the surface pressure on

the lower side of the wing was affected favourably depending upon the vertical location of the wing. Similar effects were found by Spencer et al[112] and Fox et al[113] for experiments on a low-wave-drag elliptical body, Diagram 2.6, in the Mach number range from 1.5 to 10.3.

Jorgensen et al[114] performed an experimental investigation to determine the effects of side strakes on the aerodynamic characteristics of a body of revolution, Diagram 2.7, at Mach numbers 0.6, 0.9, 1.2, 1.5 and 2.0 at incidences from 0° to 58°. The data demonstrated that the aerodynamic characteristics for a body of revolution with side strakes can be significantly affected by changes in nose fineness ratio, nose bluntness, Reynolds number, Mach number and angle of attack. Removing the strakes from the cylindrical aftersection greatly decreased the lift and moved the centre of pressure forward. Levinsky et al[115] showed theoretically and experimentally that relatively large increases in lift with even the smallest strake sizes, i.e. 10% of the body radius, are possible.

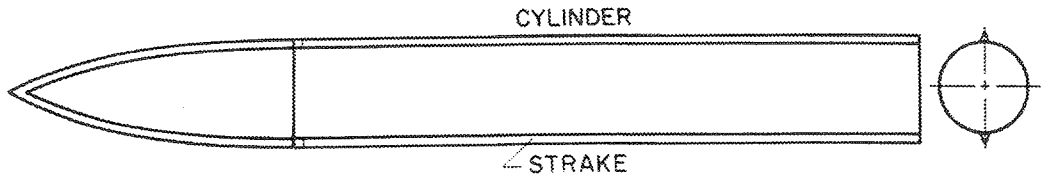

Diagram 2.7 Body of revolution with side strakes[114]

Jorgensen[7] showed that elliptic cones in combination with triangular wings of low aspect ratio, Diagram 2.8, develop higher lift-drag ratios than circular cones with same wings.

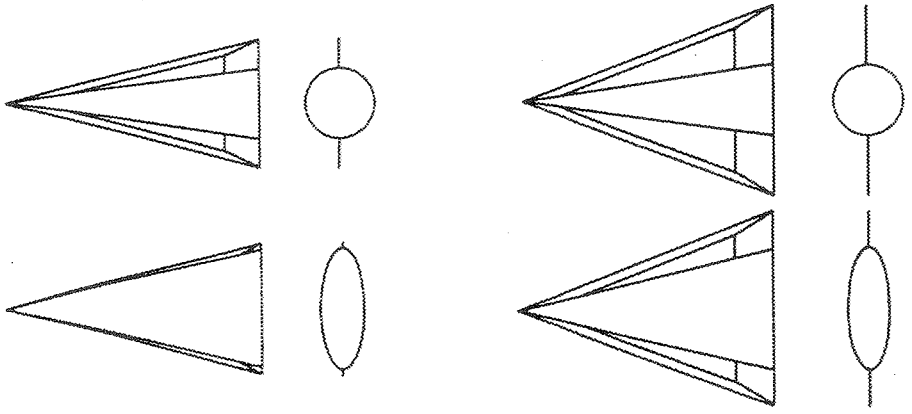

Diagram 2.8 Elliptic cones with triangular wings[7]

By visual-flow studies he demonstrated that the increased lift-drag ratios of the wing-body models is due to the enhanced vortex flow. The difference in lift-drag ratios between circular and elliptical configurations with wings was attributed to the smaller edge radius in the crossflow plane which causes the vortex flow to be enhanced.

2.10 PNS Computations for Slender Body Configurations

In the literature[116,117,118] there are a large number of examples of viscous computations of body vortex flows, obtained using the full and thin-layer forms of the Reynolds Averaged Navier-Stokes (RANS) equations. These computations are generally time consuming and are not practicable for use in a design environment. The Parabolized Navier-Stokes equations (PNS) provide an alternative means to a time-marching full three-dimensional RANS simulation. They are faster but retain the ability to model viscous effects, such as cross flow separation, and allow the use of a space-marching strategy, which reduces both computer execution times and memory requirements. A number of investigators[119,120, 121,122] have successfully applied the PNS approach to a wide range of supersonic and hypersonic flow problems using a number of different solution strategies. A good demonstration of the capabilities of PNS for the prediction of vortex flows around bodies at high incidence is given by the computations of Degani and Schiff[121] who used a modified version of the non-iterative, finite-difference solver developed by Schiff and Steger[119].

Many of the early PNS codes, employed central differencing and, as a result, required user defined damping terms to prevent oscillations when capturing shock waves. Some recent PNS codes[122] are using high resolution upwind schemes for the inviscid fluxes, (these are inherently dissipative and alleviate the need to manually adjust damping terms). The newer codes also use an iterative procedure, where the unsteady term in the governing equations is retained and the steady state solution at each axial step is obtained via local pseudo time-marching. This technique reduces the linearization errors, improves robustness and eases the integration with a time-marching RANS solver. Calculations using a three-dimensional parabolized Navier-Stokes solver are discussed in Chapter 4.

Chapter 3

Methods and Procedures

3.1 Computational Tool

The numerical study employed a three-dimensional, high resolution, iterative, finite volume PNS solver (Cranfield PNS3D) based upon Osher's flux vector difference splitting scheme for the spatial discretisation of the convective flux terms[126,127]. The parabolized Navier-Stokes equations are a reduced form of the three-dimensional RANS equations which can be solved for a range of viscous flow problems using a space-marching procedure. The integral form of the three-dimensional, Reynolds-Averaged Navier-Stokes equations can be expressed as:

$$\frac{\partial}{\partial t}\int_V Q dV + \int_S (H.n) dS = 0 \qquad (3.1)$$

where **S** is the surface of the volume **V**, **n** is the outward unit vector normal to the surface, **Q** is the vector of conserved variables and **H** is the flux tensor.

This approach is computationally more efficient than solving the RANS equations using a time-marching method, and can be used providing the following conditions are satisfied. Firstly, the flow must be steady and supersonic in the streamwise direction outside the viscous boundary layer, and secondly, there should be no streamwise reverse flow. Under these assumptions, the streamwise shear stress and heat transfer terms are neglected and the streamwise flux vector is modified to allow space-marching. The numerical method was developed by Qin and Richards[123] and it was extended to include the effects of turbulence by Birch et al[124]. In the following sections the main features of the method are highlighted.

The region of interest is discretized into small but finite hexahedral cells denoted by **i,j** and **k** (where i, j, k are the cartesian unit vectors). The conservation integral is applied to cell **i,j,k** and it is assumed the tensor **H** remains constant across each face of the cell. The numerical integration procedure produces cell averaged flow properties, which are assigned to the centres of each of the hexahedral cells. The flux vectors are evaluated at the cell interfaces from the two distinct sets of state quantities on either side of the cell interface. Second or third order spatial accuracy is achieved via the MUSCL interpolation with a flux limiter to avoid oscillations at discontinuities such as shock waves. The Baldwin-Lomax[125] algebraic turbulence model with the modification proposed by Degani and Schiff[121] was employed to provide a turbulent contribution to the viscosity.

The inviscid fluxes are computed using the approximate Riemann solver of Osher[126]. This scheme has been demonstrated[127] to be effective in capturing both shock waves and shear layers in compressible viscous flows, and is preferred over the more popular Roe scheme for the following reasons. Firstly, it will not produce non-physical expansion shocks, which require an artificial fix. Secondly, the operator in the Osher scheme is continuously differentiable and offers the potential for smoother and faster convergence for iterative solutions.

After transforming the governing equations from a system of partial differential equations to a system of ordinary differential equations in the streamwise marching co-ordinate, a fully implicit integration method is adopted[128]. The choice of an implicit marching strategy removes the need to consider stability restrictions when determining the size of the streamwise marching step. The viscous fluxes at the cell interfaces are evaluated using Gauss's theorem for the gradient at the cell interfaces. The streamwise fluxes are purely inviscid. The pressure terms in the equations are modified using the approach of Vigneron et al[129], to prevent upstream influence within the subsonic boundary layer and eliminate departure solutions. The streamwise flux is calculated in an upwind fashion using the states at the cell centres upstream.

A pseudo-time term is introduced at each station to solve the resulting non-linear system. The pseudo-time dependent term is discretised using a first order accurate Euler explicit

method. At each streamwise station the discretised equations are marched forward in pseudo-time, using a time step determined from the local CFL (Courant-Friedrichs-Lévy) condition, until a converged steady state solution is obtained.

On the body surface the no-slip and isothermal wall conditions are applied. The values along the singular axis are obtained by averaging the values on the upper and lower symmetry planes, while at the outer boundary, the freestream condition is enforced. At the downstream boundary the values are extrapolated from inside the solution domain. The initial data at the first streamwise station are generated through iteration under the assumption that the flow is locally conical. Basically the method solves a series of two-dimensional problem marching down.

Birch et al[124] assessed the effect of the simplifying assumptions, which are incorporated within the PNS solver, to enable the use of a space-marching strategy, by a computation using a three-dimensional time-marching RANS solver for comparison with the PNS solution. The agreement between the two codes was very good, justifying the use of the PNS approach for missile aerodynamics computational studies. The PNS solver has also been validated[130] to a missile configuration tested experimentally at a Mach number of 8.2.

3.2 Gun Tunnel Facility

3.2.1 Description of the Gun Tunnel Facility

The tunnel consists of a free-piston compression driver feeding an intermittent open-jet blowdown facility. It was originally established at Imperial College. The tunnel is equipped with contoured axisymmetric nozzles for Mach numbers 8.2 and 12.3. A sketch of the tunnel is presented in Fig. 3.1. The fundamental principles of operation of this facility are based on those of free-piston shock tunnels. These principles are discussed in detail by Groth et al[131], Lukasiewicz[132] and Derksen et al[133]. High pressure gas (2015 psia) from a high pressure vessel is used via a double diaphragm set-up to accelerate a piston (mass≈0.1 kg) down a compression tube.

Initially, the barrel is at atmospheric pressure and the vacuum chamber and the test-section are evacuated to pressures less than 0.5 mmHg. The rupturing of the two

aluminium diaphragms applies 2015 psia pressure on the piston placed at the driver end of the barrel. The incident and reflected shock systems associated with the motion of the piston compress and heat up the working gas by a non-isentropic process. The release and subsequent expansion of the working gas through a contoured nozzle produces a high Mach number flow in the working section for a short duration. The test-section and the barrel end are separated by a sellotape diaphragm on the upstream end of the nozzle assembly. The double-diaphragms assembly is made of 12 gauge (0.104 inch thick), commercial grade aluminium alloy (H15), 15 cm square.

A full description of the facility is given by Stollery, Maull and Belcher[134]. Subsequent modifications and calibration of the driver section of the facility are reported by Kumar[76] and Needham[135]. The detailed freestream environment associated with the Mach 8.2 axisymmetric contoured nozzle was studied by Opatowski[136,137] and by Ledford[138] using pitot pressure measurements. Opatowski found the flow to be uniform inside the test section other than along the centreline, where the Mach number varies ±4.5%, Fig. 3.2. The flow was found to be parallel to the floor of the tunnel to within 0.1°. A similar study was conducted for the contoured axisymmetric nozzle of Mach number 12.3 by Mommahadian[139]. The variation of reservoir temperature with the driver to barrel pressure ratio is shown in Fig. 3.3.

During the present study it was required to mount some of the models in the test-section in such a way that part of them lay inside the nozzle. Singh[140] calibrated the flow up to 20 cm inside the 8.2 nozzle. Pitot pressures measured along and 2 cm off the nozzle axis are shown in Fig. 3.4. These measurements had a repeatability of 2.5%. Mach number variations along the nozzle axis and 2 cm off the axis are shown in Fig. 3.5a. The variations in Mach number along the axis of the nozzle are because of the focusing effect of axisymmetric nozzles. These variations are reduced at other points inside the test diamond and the Mach number there can be considered to be uniform within +/-1%. The Mach number variation along a vertical line normal to the axis at 20 cm inside the nozzle is shown in Fig. 3.5b and shows the flow is reasonably uniform in a core of 5 cm radius (except along the nozzle axis).

3.2.2 Flow Establishment Time

In tests performed by Sperinck[193] the run time of tunnel was calibrated. The pressure measurements in the working section revealed that the tunnel provided a useful run time of 25 msec and an overall run time of 35 msec. A typical pressure transducer output signal is shown in Fig. 3.6. For the present study, average readings were taken between 20 and 33 msec.

Because of the complex nature of separated flows, it is important to show that the available running time is sufficient for the flow to become fully established. Needham[135] performed studies in the gun tunnel using a high speed camera to photograph the developing flow. With a film speed of 4500 frames per second, the enlarged photographs over the run time revealed the extent of the separated flow region and indicated that the flow became fully developed after approximately 3-4 msec which is well within the useful running time of the gun tunnel.

3.3 Test Conditions

All the experiments were conducted in the College of Aeronautics hypersonic gun tunnel. Air is used as both driver and test gas. An axisymmetric contoured nozzle provides a flow at M_∞=8.2 with a useful core flow diameter of 15.2 mm, a Reynolds number of 9.3×10^6/m, T_o=1290 K, T_∞=89.3 K, P_o=1580 psia (10.89×10^6 Pa), P_∞=0.137 psi (950.3 Pa), a_∞=189.4 m/sec, ρ_∞=0.0371 kg/m^3, V_∞=1553 m/sec, and μ_∞=6.161 kg/m.sec. The numerical simulations and experiments used an average wall temperature of 296 K. Using the Mach number 8.2 nozzle, by varying the pressure in the driver vessel a variety of Reynolds numbers can be achieved ranging from 4.5×10^6/m to 9.3×10^6/m. This puts most experiments in the laminar or transitional regime and even with very large models it is difficult to investigate a fully turbulent boundary layer in this facility unless some means of boundary layer tripping is employed.

3.4 Models and Supports

3.4.1 Right Elliptic Cone Without Strakes, L_{cone}/d_{minor}=15

The model was a right elliptic cone, a/b=1.6, with a major base axis of 2.96 cm, minor base axis of 1.85 cm, a length of 27.75 cm and total length to minor base axis ratio of 15,

Fig. 3.7a. The model was fabricated of commercial grade aluminium alloy (H15). The model was painted matt black for oil-dot surface flow visualisation. A photograph of the model is shown in Fig. 3.8a.

3.4.2 Half-Power-Law Elliptic Cone With and Without Strakes, $L_{cone}/d_{minor} \approx 11.2$

The models were a pair of half-power-law elliptic cones, a/b=1.6, with and without strakes, Fig. 3.7b, with a major base axis of 2.68 cm, minor base axis of 1.68 cm, a length of 18.75 cm and total length to minor base axis ratio of approximately 11.2. The strakes were approximately 1.67 mm square at base tapered to zero at nose, in height only keeping the width constant. Table 1 presents the power-law body design co-ordinates. The models were made of jelutong wood for lightness. Initial tests showed that the position of the models centre of gravity relative to force balance moment centre (the point at which the model is attached to the force balance), and the mass of the models affected the natural frequency of the balance/models combination. Increasing the mass and/or the distance between the models CG and the balance moment centre decreased the natural frequency, making it impossible to filter the noise without affecting the signal itself. The mass of the model was reduced to the minimum possible by hollowing it from inside and the CG was made to overlap the moment centre by using a dead weight at the base of the model, to get a natural frequency of about 200 Hz. The CG (centre of gravity) position was 2.6 cm from the base independent of strakes and the masses of the models were 56 grams and 33 grams with and without strakes respectively. A photograph of the models is shown in Fig. 3.8a.

3.4.3 Right Elliptic Cone With and Without Strakes, $L_{cone}/d_{minor}=7.5$

The models were a pair of right elliptic cones, a/b=1.6, with and without strakes, Fig. 3.7c, with a major base axis of 4 cm, minor base axis of 2.5 cm, a length of 18.75 cm and total length to minor base axis ratio of 7.5. The strakes were 3 mm square at base.

In experiments designed to validate CFD codes, experimentalists must develop a better understanding of the assumptions made in the numerical simulation so that experiments can be designed that match these assumptions. For example, in choosing a body geometry with which to validate a CFD code, a configuration should be chosen that

eliminates unnecessary numerical difficulties. In the present research, this is achieved by requiring the strakes to extend to the nose of the body by tapering them to zero height at the nose but keeping the width constant up to 1.5 cm from the nose and then conical to zero at nose. It allows a great simplification in body geometry description and outflow boundary conditions in the numerical simulation. It also simplifies manufacture.

The pressure and flow visualisation models were fabricated of commercial grade aluminium alloy (H15). The instrumentation consisted of 10 pressure taps located on the models as shown in Fig. 3.7c. Each orifice diameter was 2 mm, drilled vertical to the body axis and connected to portex plastic tube of 2 mm diameter, which was exited from the base of the models, Fig. 3.8b. During the course of the study, as it will be shown in chapter 4, it was found that the portex tubes exit locations of the first two orifices from the base of the models were interfering with the flow over the bodies. Then the portex tubes of those two orifices were routed to different exit locations marked as *new* in Fig. 3.8b. The models used for oil-dot surface flow visualisation were painted matt black and the pressure orifices were filled with plasticine in order to improve surface smoothness and to prevent gas escaping.

The force models were made of jelutong wood for lightness. The CG position was 5.2 cm from the base, independent of strakes. The model masses were 49 grams with strakes and 33 grams without strakes. The models were carefully fabricated so that dead weights were not needed for any CG position correction. A photograph of the models is shown in Fig. 3.8a.

3.4.4 Axisymmetric Body

The basic configuration was a cylinder to which could be added a choice of two nose geometries, namely a 10° half-angle sharp cone and a hemisphere and four trailing edge flares with angles 10°, 20°, 30° and 45°, Fig. 3.7d. The cylinder had a diameter of 1.7 cm, a length of 15.3 cm and $L_{cyl}/d_{cyl}=9$. The four removable trailing edge flares had a length of 4.25 cm and $L_{flare}/d_{cyl}=2.5$. The schlieren investigation showed that the blockage effects inside the working section dramatically altered the flow structure around the cylinder-flare model with a full length 45° flare for any position within the working section. It was therefore decided to reduce the length of the 45° flare by 1.5 cm. To

ensure that "blocking" did not occur all tests involving the 45° flare were performed by positioning the model 10 cm forward from the position used for all other tests. The model was at all times mounted with the cylinder axis parallel to the freestream.

The selection of the geometrical characteristics of the model was dictated by the requirement of having the same L_{cyl}/d_{cyl}, L_{flare}/d_{cyl} and half-angle sharp cone nose as Kuehn's model[8]. For schlieren, oil-dot and liquid crystal flow visualisation a matt-black painted H15 aluminium alloy uninstrumented model was used. A photograph of the model is shown in Fig. 3.9a. For pressure measurements on the flares, instrumented H15 aluminium alloy flares with pressure tappings were added to the basic cylinder. The flares consisted of 16 pressure orifices placed at equal angular intervals as shown in Fig. 3.9b and their location along the flare is shown in Fig. 3.7d.

For pressure measurements on the cylinder, a second model was fabricated which consisted of a brass instrumented cylinder and H15 aluminium alloy uninstrumented noses and flares. For simplicity the diameter of the cylinder was reduced by 0.05 mm allowing the flares to slide around the cylinder from the nose and to be fixed at the appropriate position. This design left a very small circular step of 0.025 mm thickness (detail A, Fig. 3.7d). This step was so small that it did not affect the quality of the measured flowfield characteristics. The instrumented cylinder consisted of 16 pressure orifices.

The location of all pressure orifices are tabulated in Table 2. Each orifice diameter was 2 mm, drilled vertical to the body axis and connected to steel tubes of 2 mm diameter inserted into the cylinder and flares and rigidly fixed with an adhesive. The 16 steel tubes from the cylinder were taken out through the sting mounting as shown in Fig 3.9c. Two extra pressure orifices were drilled along the cylinder-mounting sting extension to check for interference with no flares present. The 16 steel tubes from the flares, shown in Fig. 3.9b, were taken out through the base of the flares.

Vortex generators were used to trip the boundary layer. They were placed at the nose-cylinder junction circumferentially, as shown in Fig. 3.7d. The vortex generators used were based on the design developed by Coleman[65]. They consisted of a single row of delta shaped vortex generators, 1mm high and 3.5 mm apart. The delta shaped vortex generators were inclined at about 30° to the flow direction as shown Fig. 3.10.

3.4.5 Model Supports

A horizontally rotatable rigid mounting extending from the bottom of the test section, with the model mounted on a 10 mm sting was used to obtain schlieren planar views of the models discussed in sections 3.4.1 and 3.4.3, Fig. 3.11a. A V-shape mounting block extending from the top and bottom of the test section, with the model mounted on a 10 mm diameter sting, was used for the tests with the models discussed in sections 3.4.1 to 3.4.3, Fig. 3.11b. The incidence was adjusted with an accuracy +/- 0.1°. The tests using the models described in sections 3.4.4 used a pedestal support as shown in Fig. 3.11c. The models described in sections 3.4.1 to 3.4.3 were fixed at zero roll angle on to the mounting sting using a setting jig.

3.5 Flow Visualisation

In the present investigation three different flow visualisation methods were used: schlieren, liquid crystals and oil-dot techniques.

3.5.1 Schlieren Technique

The schlieren technique is a well established method for the flow visualisation of the density gradients of the flow field and various flow features can be detected like shock waves, vortices, boundary layer separation and transition. A single pass schlieren system was used. A short duration argon stabilised spark source (1/8 msec) was used as a point light source. A Polaroid camera with Type 667, 3000 ASA black and white film was used for the study. The system was triggered 25 ms after the start of the run. A horizontal knife edge was used to study density gradients normal to the freestream whilst a vertical knife edge was employed for studying density gradients parallel to the freestream. This technique provided essentially a two-dimensional picture of the flowfield. The schlieren pictures obtained using the vertical knife edge did not prove useful since only limited flowfield characteristics were revealed.

Due to the curvature of the compression fans within the boundary layer, there is a lag between the start of the thickening of the sublayer and the deflection of the outer edge of the boundary layer. The lag results in the separation shock emerging some distance downstream of the start of the thickening of the sublayer. In schlieren studies where the

separation streamline cannot be clearly visualised, it was assumed that the axial location of upstream limit of the separation shock at the edge of the boundary layer provided a good approximation for the location of the separation streamline, Fig. 3.12. The upstream limit of the reattachment shock was assumed to provide a good approximation for the reattachment point.

3.5.2 Oil-Dot Flow Technique

The surface oil flow technique is taken as a standard technique for wind-tunnel experimentation. This technique serves for visualising the flow pattern close to the surface of a solid body exposed to an air flow. The surface oil flow technique is not suitable for gun-tunnels because the oil film can not move sufficiently in the short run duration.

A large number of mixtures using a variety of oils and proportions were tried. Discrete dots of a mixture consisting of linseed oil, silicon 4 oil and titanium dioxide powder with a few drops of orleic acid were applied on the matt black painted surface of the models. The following mixture was found to give the optimum results and it is recommended for any future experiments using the present or similar gun tunnel facilities: 23 g of titanium dioxide with 11 ml of linseed oil. The resulting thick mixture was diluted with 7 ml of silicone 4 oil. To improve the dispersion of titanium dioxide in linseed oil, 0.1 ml of orleic acid was added. During the run the oil-dots flow in a direction depending upon the surface shear stress and this is marked by the streaks of each oil-dot. The streaks can be described as being caused by the wake behind coagulations of pigment particles. This would explain the use of orleic acid as an additive, which can control the formation and size of the coagulating blobs.

The size of the oil-dot is important. If the size of the oil-dot is small then they will not move during the run. If the size of the oil-dot is large then they will start speading. The oil dots were applied using an 1mm hypodermic tube. Silicone 4 oil controls the viscosity of the mixture. Since this oil is a low viscosity substance, it makes the mixture thinner. At the same time it decreases the surface tension of the dot causing it to become flat and unable to respond to the air flow. Orleic acid improves the surface tension and the size of the blob. If more orleic acid is added the surface tension is increased considerably,

making the blob unable to respond. A compromise between the amounts of silicone 4 oil and orleic acid is necessary. The ideal dot would be thin enough with limiting surface tension to stop spreading. In the present experiments was found that large changes of surface curvature can cause spreading of the oil-dot.

Due to frictional forces the airstream carries the oil-dot with it, and the remaining streaky deposit of the pigment gives information on the direction of flow. According to Squire[141] the observed pattern can indicate the positions of transition from laminar to turbulent flow in the wall boundary layer, and the positions of flow separation and reattachment. Questions arise concerning the interpretation and the reliability of these observations, because the presence of the oil dots affects the boundary conditions for the air flow near the solid surface. Squire noted that the oil flow pattern must be interpreted with care if the flow separates from the surface.

The question, whether the visible oil flow pattern is in agreement with the direction of the air limiting streamlines can be answered with Squire's analysis. The direction of the oil-dot flow depends on the wall shear stress (skin friction) of the air flow and on the pressure gradient. Generally, the pressure term is small compared with the skin friction, and the oil-dot pattern is a good representation of the actual wall streamlines. Near separation the skin friction is low and the pressure gradient is large so care is needed in interpretation. Because of reduced shear stress in the regions of separated flow the oil dots either do not respond or they show some sign of reverse flow. Downstream of the reattachment flow regions the oil dots are wiped away because of the increase in shear stress there.

Meyer and Vail[142] used the oil-dot flow technique to study the surface flow over the windward side of flat-topped half-cone and delta-wing lifting configuration. A number of dots of high vacuum oil, coloured with lamp black were placed on the surface of the model. Depending upon the magnitude of the shear stress, these dots flow to indicate the direction of the limiting streamlines. The length of the oil streaks formed was found to give a good qualitative indication of the shear stress distribution. Rao[143] used the technique to study the three-dimensional flow over his flapped delta wing in the same gun tunnel facility in which the present tests have been conducted. The method was

found to be useful for locating reattachment boundaries as well as reflected wave impingement over the lower side of the trailing-edge flap.

In the present tests the oil-dot flow pattern was recorded on a 35mm black and white film immediately after the completion of each run.

3.5.3 Liquid-Crystal Technique

Liquid crystals have been used by many researchers as a surface flow visualisation technique. Smith[144] presented an overview of the state of the art of the liquid-crystal technique, including the historical development and a discussion of how it is used. Sample results from several researchers were used to demonstrate the range of flow features that can be illustrated, including laminar boundary layer transition, laminar separation bubbles, shocks, and separation. The technique has been demonstrated in flight and wind-tunnel environments from subsonic to hypersonic speeds. The pressure sensitivity of the liquid crystals is important only if the range of operation is close to the phase change. The liquid crystals are made insensitive to shear stress if they are to be used for temperature measurements. This is done by enclosing the crystals in microcapsules of 5-30 μm diameter. Encapsulated liquid crystals are believed to have a spatial resolution of a fraction of a millimetre and surface temperatures can be measured to within 2°C with a negligible response to shear stress.

Smith and Baxter[145] and Babinsky and Edwards[146,147] demonstrated the use of encapsulated liquid crystals to measure surface heat flux in short duration hypersonic facilities. Haq, Roberts, and East[148] used the technique for qualitative analysis of the surface heat transfer distribution near fin body junctions.

Singh[140] established the technique in the gun-tunnel facility at Cranfield University with very good results. He found the optimum relative locations of the camera and the light source, type of photographic film, camera settings, light source, thickness of the liquid crystal layer to be deposited and the time instant during the tunnel run time for acquiring the image. Singh found that the time response for the liquid crystals is approximately 5 msec and that photographs taken 10, 15, and 25 msec after the flow establishment in the tunnel look very similar to each other.

Encapsulated thermochromic liquid crystals R18C10W have been employed for qualitative analysis of the surface temperature distribution in the present investigation. Their use augments the schlieren and oil-dot flow data. The models used were made out of an aluminium alloy. The crystals reflect a certain component of the incident white light allowing the other components to pass through the crystal layer. The model was, therefore, painted matt black to make the crystal colour change more vivid. The image was recorded on a single shot camera film. The colours perceived depend both upon the orientation of the incident light as well as the viewing angle. It is therefore important to keep the set-up fixed throughout the test schedule to make a meaningful analysis.

The set-up is shown in Fig. 3.13. The SLR camera, equipped with 35/105 mm zoom lens, pointed in a direction normal to the optical window of the test-section. An electronic flash (Vivitar 3500) using extra wide manual mode was used to illuminate the model for about half a millisecond at an incidence of about 45° to the test-section window. The flash was triggered using a delay circuit while the camera was used in 'B setting' mode. A single photograph was taken just before the end of each run, i.e. with a delay setting of 35 msec with respect to the time at which the reservoir end diaphragms are ruptured. Before the gun tunnel run the initial colour of the model is dependent upon test section ambient temperature. During these experiments the initial colour of the model was always bronze red so that regions of high and low temperature can be detected by eye on the photographs. The surface colour distribution was captured using 100 ISO film. The liquid crystal colour variation with temperature is given in Table 3.

3.6 Data Acquisition and Instrumentation

A digital data acquisition was used for acquiring data from a set of 8 pressure transducers and a three component force balance. The system is shown schematically in its pressure and force measurement modes in Fig. 3.14. The system consists of:

1.A +/- 12 V rechargeable DC power source constructed from lead-acid car batteries incorporating a Thevinin transistor circuit to provide a voltage stabilised power source for the diagnostic instrumentation and effectively isolated the instrumentation from the electrical noise associated with the mains system.

2.A data recording system consisted of a low-noise 10-channel Fylde amplifier coupled to an eight channel digital Datalab DL2800 transient recorder. The recorder allowed a maximum sampling rate of 50 kHz and a 10-bit digitisation of the voltage history. A maximum of 4096 points can be recorded on each channel. The digitised output of the transient recorder is proportional to the change in voltage with respect to the level before the run:

$$\Delta V=(V-V_i)=(x-x_i)V_{FS}/1023 \qquad (3.2)$$

where x is the recording reading after the firing of the tunnel, x_i is the initial transient recorder reading before the firing of the tunnel and V_{FS} is the full voltage scale.

The output for each channel was a 12-bit data string. These data strings were transmitted via an RS-232 Kermit interface at a rate of 9600 bits/sec into a data file on the Personal Computer. An SCDUMP.EXE file was used to rearrange the raw digitised data prior to its primary processing in a spreadsheet.

3.The tunnel is equipped with a trigger and delay circuit to capture various events during the operational 35 msec run time of the tunnel. The sound generated by rupturing of the diaphragms is picked up by a microphone. There is a time lag of around 12 msec between the rupturing of the diaphragms and the establishment of the flow inside the test section. The microphone output triggers a 5 volt square wave generator which in turn triggers the relevant measuring and recording equipments. A certain amount of delay is introduced between the firing of the tunnel and the start of the particular event recording. The schlieren pictures are taken about 25 msec after the firing of the tunnel but the liquid crystals are taken 35 msec after the firing of the tunnel (just before the end of the run).

4. Quantitative studies have been made by pressure measurements using Kulite XCS-190 series, absolute pressure transducers (0-15 psia range). The transducers were rigidly fixed at the foot of the model-mounting inside a housing. The pressure tappings of the model were connected to the transducers using 10-15 cm long plastic PORTEX tubes. Prior to each run, the transducers were calibrated linearly by recording the initial atmospheric and final vacuum pressures during the test-section evacuation phase via a vacuum pressure gauge:

$$C=\frac{p_{atm}-p_i}{G_{cal}(V_{atm}-V_i)} \qquad (3.3a)$$

The 10-bit digitised voltage, Eq. 3.2, was processed at the end of the run to obtain the surface pressure by:

$$p = p_{vac} + \frac{\Delta V}{G_{run}} C \qquad (3.3b)$$

where p_{vac} is the initial static pressure before the firing of the tunnel, C is the calibration constant of a particular transducer and G_{run} is the amplifier gain used. The data obtained from Eq. 3.3 was converted to the ratio of local surface pressure to freestream static pressure, p/p_∞.

A number of periodic waves are evident after the run, Fig. 3.6. These are due to reflections from the dump tank. These waves do not affect the core flow through the working section during the run.

3.6.1 Force Measurement System

Direct measurement of the effect of strakes on aerodynamic performance has been made using a 3-component strain guage balance designed by Opatowski[136]. It was originally built for making measurements on thin delta wings. The balance is shown in schematic form in Diagram 3.1.

The most recent use of the balance has been by Kontis el al[149], Kumar[76], Singh[140] and Courtis[150]. Each component uses four semi-conductor strain guages to form a Wheatstone bridge powered by a regulated dc power supply. The balance uses thin tension/compression links as sensing elements to measure lift and drag but the pitching moment is sensed by a cantilever link on which the model is mounted. A photograph of the balance is given in Fig. 3.15.

Due to the short run-time of the tunnel and the relative thermal isolation of the gauges, the components were not temperature compensated. The balance is generally energised with a 5 V dc lead-acid battery power source (described in section 3.6) but in the present tests a 7.5 V dc power source was used to enhance the sensitivity of the balance because the forces and particularly the drag component for the slender bodies of the present research were so small.

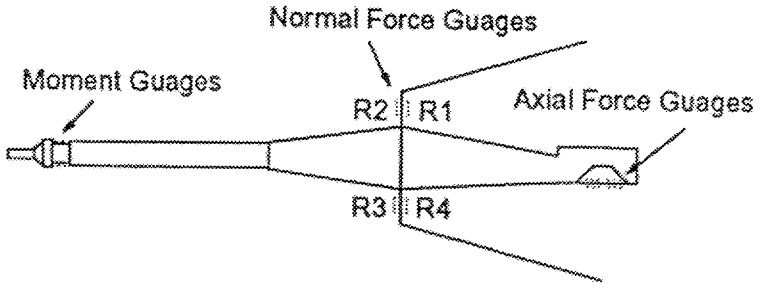

Layout of the Silicon Guages in the Force Balance

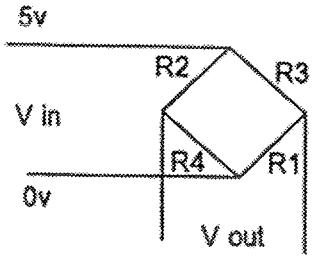

Wheatstone Bridge for Normal Force Component

Diagram 3.1 Schematic form of the balance

During the run, the working section is subjected to some mechanical vibration. Due to the balance and models mass, these vibrations produce damped harmonic oscillations. Kumar[76] determined the natural frequency of these oscillations by a tare calibration in which the tunnel was run with the flow blocked off by means of a 5 cm thick brass disc placed over the nozzle entry plane. He found that the natural frequency oscillations due to mechanical vibrations affected the normal force and pitching moment components at 180 Hz and the axial force component at 2300 Hz. Previous experience suggested that the model should be no heavier than 60 g to keep the natural frequency out of range of the message frequencies. Digital low pass filters were designed, in order to remove the unwanted high frequencies from the test signals using the MSPECT signal processing package developed by Russell and Wyatt[151]. Fig. 3.16a shows a typical unfiltered output

from the normal force channel, which is then transferred to the frequency domain for filtering. Having selected the low pass filter cut off point, the signal is transferred back to the time domain giving a filtered output, Fig. 3.16b. Using the filtered signal, a mean level is selected towards the end of the run, where the signal has reached its most steady state. The output level from each channel, in mV, was then converted to forces and moments using the calibration matrix deduced from the calibration of the balance described in section 3.6.1.1.

3.6.1.1 Calibration of the Force Balance

The balance was calibrated using the set-up shown in Fig. 3.17. This provided a stable platform for the balance allowing calibrated weights to be applied normal and parallel to the axis of the balance sting using a system of pulleys. A non-isotropic force calibration bar was employed to apply forces to the string. The bar was designed so that its CG was coincident with the plane of the bending moment guages, as shown in Fig. 3.18. A pure load (normal, axial or pitching moment: primary components) is applied to the balance and the output from the three channels of the balance is noted. Both increasing and decreasing loads were applied. However, due to coupling effects between the components, an applied primary component, i.e. normal force, also produce a strain in the other two components (secondary components) of the balance, i.e. axial force and pitching moment. The coupling effect changes the voltage response of a given component to its primary load. In order to eliminate this error, the matrix calibration method proposed by Rae and Pope[152] was implemented. The calibration curves are shown in Appendix A.

The complete voltage output from the balance may be written as a matrix equation:

$$\begin{bmatrix} \Delta V_N \\ \Delta V_A \\ \Delta V_M \end{bmatrix} = \begin{bmatrix} \left[dV_N/dN\right]_N & \left[dV_N/dA\right]_A & \left[dV_N/dM\right]_M \\ \left[dV_A/dN\right]_N & \left[dV_A/dA\right]_A & \left[dV_A/dM\right]_M \\ \left[dV_M/dN\right]_N & \left[dV_M/dA\right]_A & \left[dV_M/dM\right]_M \end{bmatrix} \begin{bmatrix} \Delta N \\ \Delta A \\ \Delta M \end{bmatrix} \qquad (3.4)$$

In vector representation the voltage-force response can be written:

$$\Delta\overline{V} = \left[\frac{d\overline{V}}{d\overline{F}}\right] \bullet \overline{F} \tag{3.5}$$

The force-voltage response of the balance may thus be written as:

$$\Delta\overline{F} = \left[\frac{d\overline{V}}{d\overline{F}}\right]^{-1} \bullet \overline{V} \tag{3.6}$$

and hence the relationships for the component outputs can be obtained.

Using this method, the calibrations of the three components were derived:

$$\Delta N = 0.3375\Delta V_N - 0.0039\Delta V_A - 0.03100172\Delta V_M \tag{3.7a}$$

$$\Delta A = 0.0035\Delta V_N - 0.48016\Delta V_A + 0.000496436\Delta V_M \tag{3.7b}$$

$$\Delta M = 0.00005\Delta V_N + 0.0000631\Delta V_A + 0.003231604\Delta V_M \tag{3.7c}$$

The voltage changes in the above equations are in mV. Similar calibration coefficients were derived by Kumar[76], Singh[140] and Courtis[150].

Opatowski[136] showed that the maximum possible errors for the three balance channels are: normal force and pitching moment, ±3% and axial force, ±4%. However, his analysis suffered an overall ±2% error due to trace reading and the oscilloscope. Rao[143] showed that his measurements had an overall accuracy: normal force, ±2%, axial force, ±2.5%, and pitching moment, ±1.25%. In the present investigation an overall repeatability of 97%, over 6 runs, of the force and moment coefficients was achieved. In particular the maximum possible errors are: normal force, ±1.5%, axial force, ±2%, and pitching moment, ±1.5%. Similar maximum possible errors were deduced by Singh[140] and Courtis[150].

Chapter 4

Results and Discussion

Elliptic Cones With and Without Strakes

4.1 Right Elliptic Cone Without Strakes, $L_{cone}/d_{minor}=15$

The investigation started with the schlieren and oil-dot flow visualisation of a right elliptic cone without strakes of fineness ratio, $L_{cone}/d_{minor}=15$, (described in section 3.4.1). The model was oriented in two positions which were designated configurations 1 and 2. For configuration 1 the minor axis of the ellipse was oriented in the pitch plane, and for configuration 2 the major axis was oriented in the pitch plane. Both side and plan schlieren views were taken. The model was tested in the incidence range 0° to 20°. Force measurements using this model were abandoned because past experience[153] has showed that it is difficult to measure axial forces under hypersonic conditions of slender bodies with small cross-section area. The main reasons are: the small axial force to be measured and the high level of noise and natural induced frequencies which make the detection of the actual signal difficult, even if digital filters are used.

4.1.1 Experimental Investigation

Schlieren (both side and plan views) and oil-dot pictures for configurations 1 and 2 are shown in Figs. 4.1 and 4.2 respectively. The Reynolds number based on body's length is $2.6\text{x}10^{6}$. Due to the relatively high Mach number and the low Reynolds number, the boundary layer on the surface of the model is laminar. This deduction is supported by Fig. 2.6.

Fig. 4.1a shows that a shock envelopes the body and the boundary layer is attached for $\alpha=0^{\circ}$. Comparison of the side and plan views of Fig. 4.1a shows that the distance between the shock wave and the body, for 0° incidence, is greater in the meridian plane containing the minor axis than in the meridian containing the major axis. The shock wave is not an ellipse similar to the body, but is 'pushed in' toward the major axis and 'pulled out' from the minor axis. This shape is to be expected on physical grounds, since there is a cross-flow from the high pressure sides at the ends of the major axis to the lower pressure sides at the ends of the minor axis. This cross-flow tends to relieve the pressure somewhat at the high pressure sides and raise the pressure at the low pressure sides, thus causing the corresponding change in shock wave angle. The oil-dot pictures at 0° incidence, Fig. 4.1a, do not give evidence of this crossflow effect. This effect is weakly visible in the oil-dot studies for a right elliptic cone of fineness ratio 7.5 to be discussed later in this chapter. Chapkis[154] has found similar shock-shape geometry in experiments with a right elliptic cone and measured the pressure relieving effects described above.

Fig. 4.1a shows that the oil-dot movement is more pronounced near the nose area, but towards the base this movement becomes weaker. This is because of the low skin friction values on the surface of the elliptic cone which causes that weak response of the oil-dots since the oil-dot technique is skin friction dependant. An indication of the skin friction of an elliptic cone can be obtained by using the concept of the equivalent cone (a right circular cone at zero incidence having the same freestream Mach number and a half angle equal to the angle between the freestream Mach number vector and the ray line on the elliptic cone under examination). The local skin friction coefficient for a flat plate or circular cone with laminar boundary layer is of the form $c_f \sim \frac{1}{\sqrt{Re_x}}$, i.e. $\sim x^{-1/2}$, so it decreases rapidly away from the nose and exhibits high values near the nose region.

For configuration 1, $\alpha=5^{\circ}$, the lee side oil dots are unmoved suggesting flow separation region extends over the whole cone length, Fig. 4.1b. The oil-dot studies show evidence of cross-flow on the windward side, which separates just after the edge of the major axis, Fig. 4.1b. Experimentally, a crossflow shock is often associated with flow separation, however, the schlieren pictures, (side and plan views), do not give evidence of such a shock system (imbedded shocks). Because of the cross-flow separation a pair of

counter-rotating vortices is established over the leeward region of the body. Fig. 4.1b shows that this separated cross-flow reattaches at the top leeward meridian of the cone. Similarly for configuration 2, at $\alpha=5^{\circ}$, the lee-side has separated over the total length of the cone, Fig. 4.2a (side view), and the oil-dot study (depicted in the same figure), reveals similar cross-flow characteristics as configuration 1. However, the oil-dot surface visualisation for configuration 2 does not show evidence of reattachment of the separated cross-flow in the top leeward meridian, this is probably because of the very low levels of skin friction on the lee side. The same observation is true for $\alpha=10^{\circ}$, 15° and 20° for configuration 2 and $\alpha=15^{\circ}$ and 20° for configuration 1. The white line nearer the surface indicates the vortex core[91], Figs. 4.1b and 4.2a.

As incidence increases, the oil-dot studies for both configurations have shown that the cross-flow strength on the windward side increases, Figs. 4.1b,c,d&e and Figs. 4.2a,b,c&d. This is because of the increasing cross-flow velocity component, $V_{\infty}\sin\alpha$, as incidence increases. The schlieren pictures, for both configurations, also show that the position of the vortex core rises as the pair of symmetric vortices grow with incidence. In the cases where the reattachment line on the top leeward generator is visible the reattached flow shows an opposite weak circulation on the sides confined inside a narrow area. The reattached flow does not separate as oil-dot studies show but because of the low levels of skin friction the oil-dots do not respond.

At $\alpha=15^{\circ}$ and 20° the vortex cores are no longer visible in the schlieren pictures for both configurations. This is probably because the large expansion of the flow over the leeward side of the body reduces the local density beyond the sensitivity of the schlieren pictures. All oil-dot pictures show that the flow separation lines which "feed" the vortices trace an essentially linear path along the model surface for both configurations. According to Genxing and Xiao[155] the pair of crossflow vortices is symmetric up to 30° angle of attack for sharp slender bodies with horizontal elliptic sections and 20° for sharp slender bodies with vertical elliptic sections. In the present investigation, by examining the oil-dot and schlieren pictures, it is believed that the pair of crossflow vortices is symmetrical for the whole incidence range ($0^{\circ} \leq \alpha \leq 20^{0}$).

The schlieren study indicates that the windward shock is getting closer to the body surface as incidence is increasing for both configurations. This is because of the increasing crossflow component, $V_\infty \sin\alpha$, of the incident freestream velocity with incidence. The rate of decrease of the distance of the shock from the surface becomes smaller with incidence and it seems to be reaching a limiting shock position. This is depicted in Fig. 4.3. The limiting case is the shock stand-off distance, δ, for the surface vertical. An approximation of the shock stand-off distance is given by Stollery and Maull[156] assuming a circular cylinder or sphere of radius r:

$$\frac{\delta}{r} = 0.77 \cot \vartheta_m \cos \vartheta_m - (1 - \sin \vartheta_m) \qquad (4.1a)$$

For M_∞=8.2, the maximum cone semi-angle for an attached shock wave[157], ϑ_m, is 56.43°, then δ/r is equal to 0.1158. For configuration 1, r=9.25 mm, then δ=1.07 mm. For configuration 2, r=7.4 mm, then δ=0.86 mm. At α=20° the distance of the windward shock from the surface of the elliptic cone at base is, for *configuration 1*, 7.8 mm and for *configuration* 2, 5.2 mm, (see Figs. 4.1e and 4.2d).

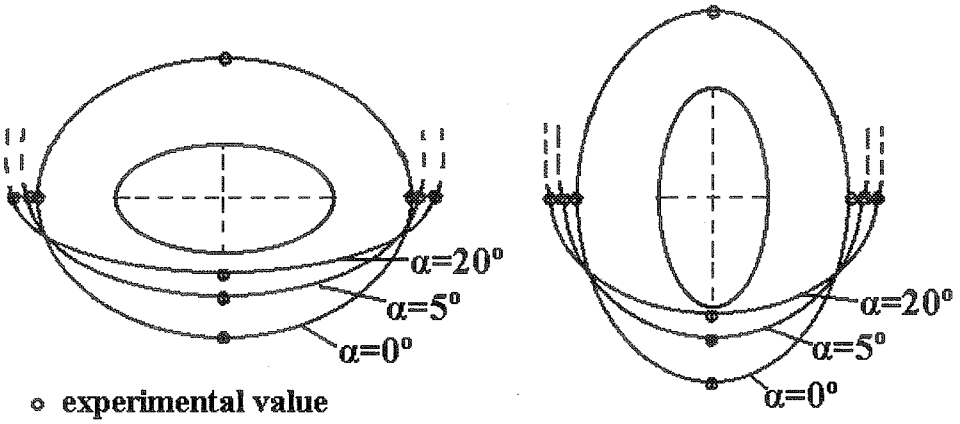

Diagram 4.1 Shock geometry at various incidences

Examining the plan schlieren views of both configurations, it was found that the distance between the elliptic cone surface and the shock envelope is increasing with incidence. This is because that as the windward shock is getting closer to the surface of the elliptic cone and stronger with incidence, the flow pressure after the shock increases and the

Mach number decreases (this is evident from the oblique shock relations[157]). This high pressure flow expands circumferentialy to lower pressures and higher Mach numbers and causes thickening of the shock layer. More crudely, the freestream "sees" a body of greater projected area. Diagram 4.1 shows the shock geometry at various incidences for both configurations.

Using Brower's[158] tables for compressible flow the shock angle of a sharp cone was interpolated at a Mach number of 8.2 for various cone half-angles at 0° incidence. This variation is presented in Fig. 4.4 and shows that as the cone half angle is increasing the shock to cone half angle ratio is decreasing. For cone half angles over 12.5° the variation is very small.

4.1.2 Computational Investigation

The program described in section 3.1 has been used to calculate the flowfield around the right elliptic cone of fineness ratio, $L_{cone}/d_{minor}=15$ without strakes. Results were only obtained for configuration 1, at 10° incidence. This investigation was introductory in order to understand the solver structure and to give a general overview of its capabilities to resolve adequately the flowfield characteristics of elliptic cross-section slender bodies. The freestream conditions were those described in section 3.3. The half circumference grid size was 64x65x65 for discretization of the flow field. A perfect gas and a laminar boundary layer were assumed over the full length of the body. The Navier-Stokes solution converged after about 6000 iterations on a Silicon Graphics workstation Indigo-2. The flow-field results plotted in the form of contour plots using the "Fieldview" software package are shown in Fig. 4.5. All results correspond to station 64 (base of the cone).

The code predicted the complex vortex flowfield surrounding the cone and agreed well with the experimental measurements of the shock and vortex core positions. Because of the structure of the grid the shock definition is quite coarse. Fig. 4.5a shows the velocity vectors. The calculation shows cross-flow separation just after the edge of the major diameter. Because of the cross-flow separation a pair of counter-rotating vortices is established over the leeward region of the body. This separated cross-flow reattaches at the top leeward meridian of the cone.

Fig. 4.5b shows the Mach number contours. Because the high pressure flow of the windward side expands circumferentialy some Mach number contours have values over 8.2. The relative position of the circumferential boundary layer can be seen. The laminar boundary layer is very thin over the windward side. But as the flow expands the shear layer thickens and separates. Fig. 4.5c shows the dimensionless pitot-pressure contours. Fig. 4.5c gives evidence of the existence of an imbedded shock wave within the leeward flow field. Fig. 4.6 gives the probable flow field model for configuration 1 at 10° incidence.

4.2 Half-Power-Law Elliptic Cone With and Without Strakes, $L_{cone}/d_{minor}=11.2$

A half-power-law elliptic cone with and without strakes, described in section 3.4.2, was used to measure lift, drag and pitching moment and take side schlieren views in an incidence range 0° to 15°. The model is oriented with the minor axis of the ellipse in the pitch plane which is designated configuration 3.

The sign convention used for the forces and moment measurements is shown in Fig. 4.7. The balance measures normal and axial forces and pitching moment. An upward lift (normal to the velocity vector), backward drag (parallel to the velocity vector) and a nose-up pitching moment were taken as positive. The calculated forces were non-dimensionalised using the freestream dynamic head and the planform area of the elliptic cones. The pitching moments were measured at the moment reference point located at $x/L_{cone}=-0.14$ and $x/L_{cone}=-0.28$ along the body axis measured from the base for the half-power-law body and the right elliptic cone respectively. The pitching moment values were non-dimensionalised using the freestream dynamic head, the planform area and the total length of the cone. This sign convention and non-dimensionalisation of the aerodynamic coefficients is applicable to all forces and moment measurements of the thesis.

The surface co-ordinates of a power law body are given by $y/r_b=(x/L_{cone})^n$. An explanation of the co-ordinates is given in Diagram 4.2. When n=1 then the body is a sharp cone and when n starts taking values from 1 to 0 then the bluntness of the body increases. The introduction of nose bluntness causes a reduction in the stagnation heating and an increase of the internal volume for a given fineness ratio body.

According to Roper[159] half power law planforms are more amenable to blunting for the avoidance or control of aerothermal ablation than theoretical lower-drag power law bodies. Elliptical section power-law bodies are of interest as they can provide larger amounts of body lift than cylindrical section projectiles and this may be exploited in the design of manoeuvring missiles. Diagram 4.3 shows the theoretical shock shapes for a family of power law bodies (the bodies tested were n=1 and n=0.5).

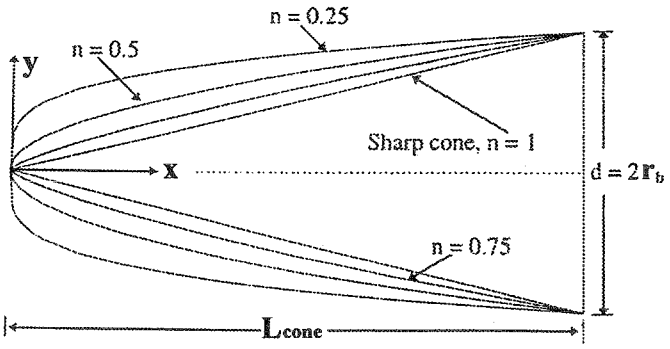

Diagram 4.2 Explanation of a power-law body co-ordinates

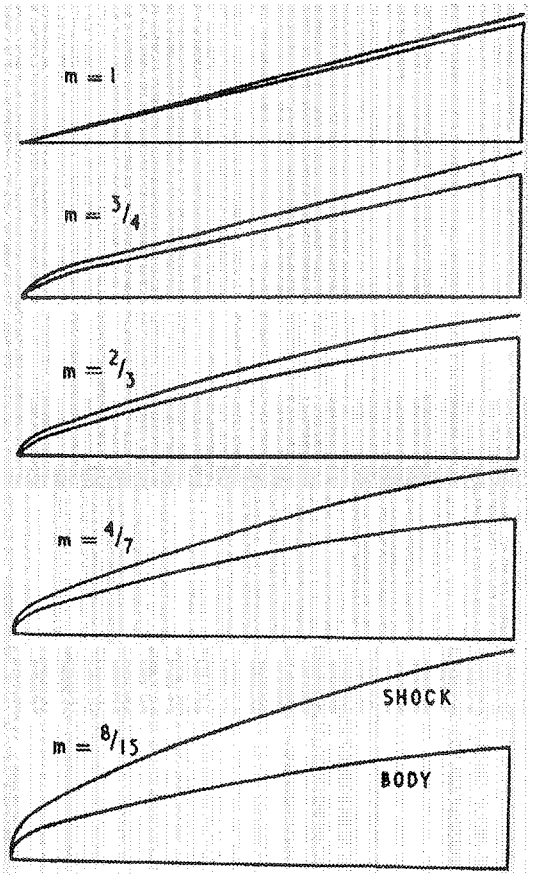

Diagram 4.3 Theoretical shock shapes for a family of power-law bodies[160]

4.2.1 Schlieren and Force Measurements

Fig. 4.8 shows some schlieren pictures of the model (strakes on and off) which show no gross external flow differences due to the addition of strakes. At $\alpha=0^{\circ}$, Fig. 4.9a, the leading nose shock and attached boundary layer are visible. At $\alpha=3^{\circ}$, the leeward flow separates close to the base of the body, probably to form a pair of counter rotating vortices. The incidence at which the cross flow over a power law body separates will probably depend upon the power-law exponent. The white line nearer the surface on the leeward side indicates the vortex core. As the incidence increases the separation point moves forward and by $\alpha=9^{\circ}$ the separation region extends over the whole upper surface. At $\alpha=15^{\circ}$ the vortices are no longer visible. This is probably, as discussed in section 4.1.1, because the large expansion of the flow over the leeward side of the body reduces the local density beyond the sensitivity of the schlieren system.

The effect of the strakes on C_L, C_D, C_m, L/D and x_{cp}/L_{cone} at incidence is presented at Fig. 4.10. The lift and drag measurements for the half-power law elliptic body without strakes at $M_{\infty}=8.2$ are compared with the experimental results obtained by Fournier and Spencer[103] for a half-power-law elliptic body at $M_{\infty}=4.63$, Fig. 4.11, and for a theoretical minimum-wave-drag body at $M_{\infty}=4.63$, Fig. 4.12.

1.Lift coefficient

The effect of the addition of strakes is to increase the C_L-α curve slope, Fig. 4.10a. This increase is due to increased pressure over the lower side of the cone caused by the strakes inhibiting the cross flow. The latter will be discussed further in the section concerning the pressure measurements on a right elliptic cone with and without strakes later in this chapter. Generally speaking, the favourable interference created by the strakes causes an increase in the lift coefficient at all incidences tested. Basically the strakes act as very small wings. Reggiori[86] performed some pressure measurements on a wing-cone configuration which also show this favourable interference.

Fig. 4.11a compares the present lift coefficient measurements (no strakes) with those of Fournier and Spencer[103]. The models used in the present investigation and in the Fournier et al study share only the same power-law exponent (n=0.5). The tests have been conducted at different Mach numbers and ellipticity ratios, a/b. The present results

obtained for a/b=1.6, which are in between those for a/b=1 and 2 obtained by Fournier and Spencer, are following the trend of increasing C_L with increasing a/b. This increase in C_L is primarily due to the increased aspect ratio of the body. The effect of Mach number variation on the C_L-α curve, for the range under consideration, seems to be negligible as concluded by Fournier and Spencer for the Mach number variation of 1.5 to 4.63 which they tested. The lift curve is non-linear and it might be expected to behave in similar fashion to e.g. Eqs. 4.1b and 4.1c (see note below). The separation of lee side flow further increases the slope due to increased suction over the leeward side of the cone.

[Note: Consider a flat plate inclined to an oncoming hypersonic flow at a small angle of attack α. On the upper surface the flow must undergo a Prandtl-Meyer expansion through an angle α, whereas the lower surface appears as a wedge to the oncoming flow:

$$C_{p,lower_surface} = 2\alpha^2\left[\frac{\gamma+1}{4}+\sqrt{\left(\frac{\gamma+1}{4}\right)^2+\frac{1}{K_\alpha^2}}\right] \qquad (4.1b)$$

$$C_{p,upper_surface} = \frac{2\alpha^2}{\gamma K_\alpha^2}\left[\left(1-\frac{\gamma-1}{2}K_\alpha\right)^{2\gamma/(\gamma-1)}-1\right] \qquad (4.1c)$$

$$C_L = C_{p,lower_surface} - C_{p,upper_surface} \qquad (4.1d)$$

$$C_D = C_L \tan\alpha \qquad (4.1e)$$

where K_α, ($=M_\infty\alpha$) is the hypersonic-similarity parameter]

Fig. 4.12a shows the comparison of the present lift measurements for the elliptic cone without strakes with the results for the theoretical minimum-wave-drag body at M_∞=4.63 of Fournier and Spencer[103]. The minimum-wave-drag body (volume and length constraints) had an elliptical cross-section with a/b=2.0 and a power-law longitudinal contour. The minimum-wave-drag body consistently produces more lift than the half power law body of lesser a/b ratio. According to Fournier and Spencer[103] the variation in lift coefficient with angle of attack for the minimum-wave-drag body falls between that of the n=0.50 and n=0.66 bodies for any ellipticity and for all Mach numbers they tested.

2.Drag coefficient

Fig. 4.10b shows that adding strakes increases the drag coefficient of the configuration, as expected. The addition of strakes does not change the nose shape and hence the nose shock and any increase in the drag coefficient due to comparatively small strakes is therefore expected to be small.

Fournier and Spencer[103] tests show that the drag coefficient does not vary significantly with a variation of a/b from 1 to 2, Fig. 4.11b. However comparison of their results with the present investigation show a large reduction in C_D values close to $\alpha=0^\circ$ as the Mach number varies from 4.63 to 8.2, Fig. 4.11b. This reduction in the minimum drag coefficient is believed to be due to the reduction in the base drag as the Mach number is increased from 4.63 to 8.2. The worst base drag case is when $p_b=0$ and the maximum base-drag coefficient is given as a function of Mach number as: (C_{DB} is based on base area)

$$C_{D_{B_{max}}} = \frac{2}{\gamma M_\infty^2} = \frac{1.4286}{M_\infty^2} \qquad (4.2)$$

Hence, for $M_\infty=4.63$ then $C_{D_{B_{max}}} = 0.067$ and for $M_\infty=8.2$ then $C_{D_{B_{max}}} = 0.021$.

Fig. 4.12b shows that the present power-law body without strakes and the theoretical minimum-wave-drag body at $M_\infty=4.63$ of Fournier and Spencer[103] have close zero-lift drag values but at higher incidences the half power-law body has higher drag than the minimum wave-drag-body (as theory[161] predicts).

3.Pitching moment

Fig. 4.10c shows that adding strakes increases the curve slope of the pitching moment coefficients about the balance moment-centre. As incidence increases, there is an increase in the pitching moment coefficient because the increase in the lift coefficient for the cone with strakes over that without the strakes continues to increase with α.

4.L/D ratio

The L/D ratio determines the overall aerodynamic efficiency of a lifting configuration. Adding strakes increases both the lift and the drag coefficients. Fig. 4.10d shows there is an overall increase in L/D of approximately 17% with the addition of strakes.

Fig. 4.11c shows that the L/D ratio increases with an increase in a/b ratio at a given Mach number e.g. 4.63. Increase in a/b increases the lift coefficient without any

significant change in the drag coefficient so that L/D values for the a/b=1.6 configuration should lie in between the values for the a/b=1 and a/b=2.0 configurations. However, because of the Mach number effect which reduces the drag coefficient, the L/D ratio for the a/b=1.6 configuration at M_∞=8.2 is in fact more than that of the a/b=2.0 configuration tested at M_∞=4.63.

5.Centre of pressure

The centre of pressure is located at approximately 64% of total cone length from nose tip, for the cone with strakes and approximately 60% of total length from nose to tip, for the cone without strakes, Fig. 4.10e. The following equation was used for the calculation of the centre of pressure:

$$x_{cp} / L_{cone} = 1 - (L_{cone} \frac{C_m}{C_N} + x_{moment_centre}) / L_{cone} \qquad (4.3)$$

The distance of the moment reference point from the base, x_{moment_centre}, is added in order to estimate the x_{cp} location relative to the base. The latter value is subtracted from the total length of the cone to calculate the x_{cp} position relative to the tip of the cone. This procedure is used for the calculation of the centre of pressures of the thesis.

Fig. 4.13 shows the level of scattering in the location of the centre of pressure for the elliptic cone with and without strakes. The difference is well covered by the scatter so that there is no noticeable shift in the centre of pressure due to the addition of the strakes.

4.3 Right Elliptic Cone With and Without Strakes, L_{cone}/d_{minor}=7.5

A right elliptic cone with and without strakes of fineness ratio, L_{cone}/d_{minor}=7.5, (described in section 3.4.3) was tested at a Mach number of 8.2 in the incidence range 0° to 20°. The model was oriented in two positions which were designated configurations 4 and 5. For configuration 4 the minor axis of the ellipse was oriented in the pitch plane, and for configuration 5 the major axis was oriented in the pitch plane. Experiments were conducted to obtain lift, drag and pitching moment coefficients. Both side and plan schlieren views were taken to examine the flowfield around the cone and an oil-dot technique was employed to investigate the surface flow patterns. The pressure

distribution along the windward and leeward meridians was measured for configuration 4 only.

4.3.1 Theoretical Estimation of Pressure Distribution

4.3.1.1 Cone Theory of Leung and Emanuel[163]

Hypersonic small-disturbance theory is combined with a laminar boundary-layer analysis though this is not needed for the pressure calculations which follow. The analysis assumes a non-reacting perfect gas with no radiative heat transfer. The Mach number M_∞ and cone half angle ϑ_c satisfy the hypersonic small disturbance requirement that K_ϑ is of order unity.

The theory was applied to predict the inviscid surface values of pressure along the windward meridian of configuration 4 assuming the concept of the equivalent cone, (a right circular cone at zero incidence having the same freestream Mach number and a half cone angle equal to the angle between the freestream Mach number and the ray line on the cone under examination). δ_e was calculated by:

$$\delta_e=\sin^{-1}(\sin\vartheta_c\cos\alpha+\cos\vartheta_c\sin\alpha\cos\Phi) \qquad (4.4a)$$

with $\Phi=0^\circ$ along the bottom generator and 180° along the top generator. In the present case, the comparison is only made for $\Phi=0^\circ$.

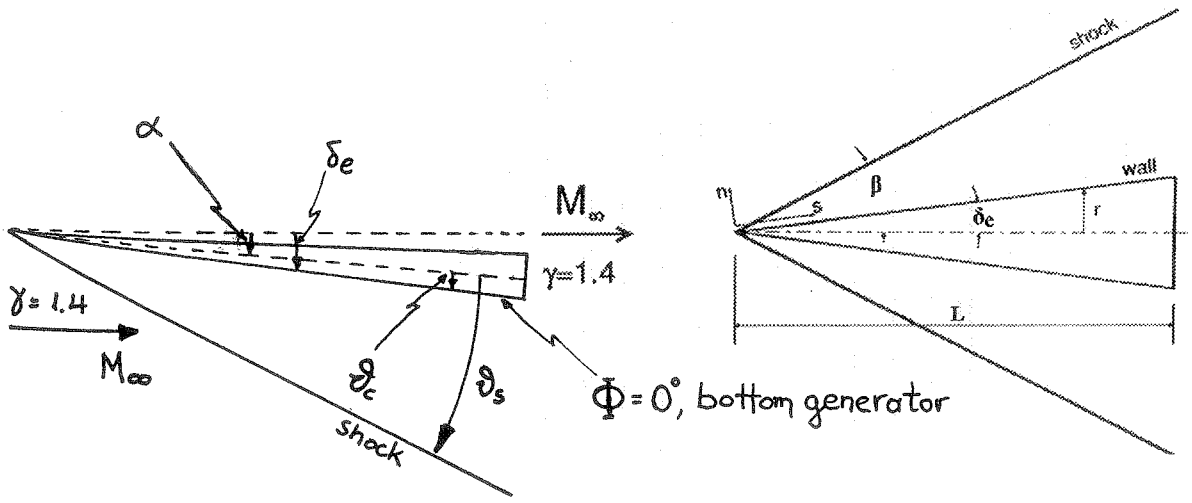

Diagram 4.4 Schematic for flow over the equivalent cone

Diagram 4.4 shows the flow over the equivalent cone. The theory predicts that:

$$\frac{p}{p_\infty} = 1 + \gamma K_{\delta_e}^2 \left\{ \frac{1}{2} + \frac{1 + [(\gamma+1)/2] K_{\delta_e}^2}{1 + [(\gamma-1)/2] K_{\delta_e}^2} \ln\left(\frac{K_{\beta c}}{K_{\delta_e}}\right) \right\} \qquad (4.4b)$$

where $K_{\beta c}=\{1+[(\gamma+1)/2]\ K_{\delta e}^2\}^{1/2}$ (this is an approximation[164]) and $K_{\delta e}=M_\infty \delta_e$.

4.3.1.2 Newtonian Theory

Newtonian theory has been found to offer a relatively simple means of determining the pressure distribution and force and moment characteristics of most arbitrary bodies of revolution at high hypersonic Mach numbers. Generalised expressions for applying Newtonian theory to a given body of revolution were developed by Wells and Armstrong[165]. These expressions may be applied to a variety of body shapes defined in a suitable co-ordinate system to develop closed-form expressions for determination of the force and moment characteristics throughout any range of incidence and sideslip.

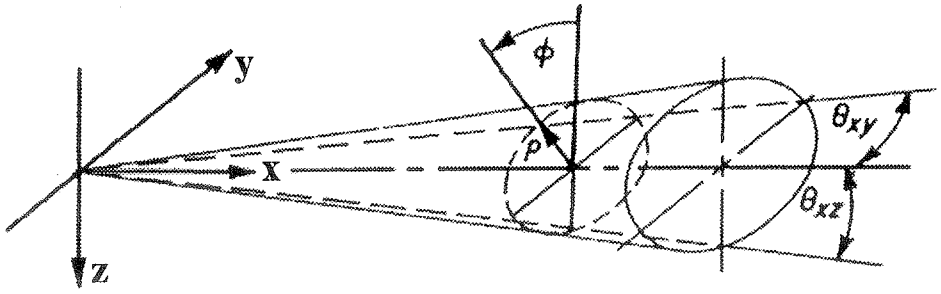

Diagram 4.5 Elliptic cone co-ordinate system

For any body the Newtonian expression for the pressure coefficient, based on a momentum exchange between air particles and the body gives the relation $C_p=2\cos^2\eta$. The angle η is defined as the angle between the unit vector normal to the surface and the unit wind vector. Diagram 4.5 shows the co-ordinate system and explains the notation used. According to Wells and Armstrong[165] the Newtonian pressure coefficient for a right elliptic cone is (for $\Phi=0^o$):

$$C_p=2(\sin\theta_{xz}\cos\alpha-\cos\theta_{xz}\sin\alpha)^2 \qquad (4.5a)$$

or

$$\frac{p}{p_\infty} = 1 + \sin^2(\theta_{xz} - \alpha)\gamma M_\infty^2 \qquad (4.5b)$$

which predicts the pressure distribution along the windward meridian of a right elliptic cone at incidence.

4.3.2 Estimation Model of Aerodynamic Forces and Moments

1.Right Elliptic Cone Without Strakes

The aerodynamic force and moment coefficients, for configurations 4 and 5 were estimated using the closed-form expressions from Wells and Armstrong[165].

2.Right Elliptic Cone With Strakes

A theoretical prediction model was derived, based on the standard Newtonian theory. The strakes were assumed to be "square cones" of half-angle 0.7° and total length of 188 mm, Diagram 4.6.

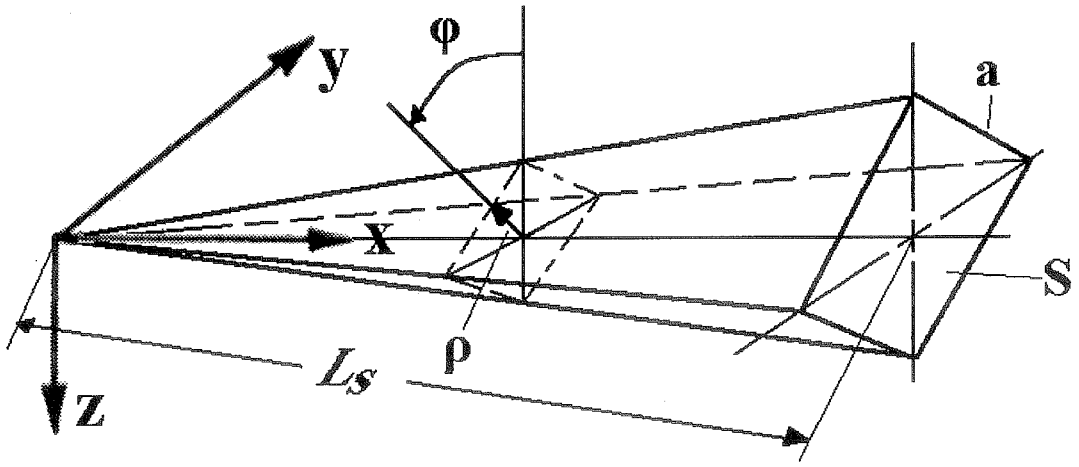

Diagram 4.6 Strake co-ordinate system

Any vortices caused by boundary layer separation and regions of trapped flow, such as at the strake-body junction were neglected. The contribution of the strakes to the aerodynamic forces and moments was neglected if they are located inside the shadow region of the elliptic cone. The contribution of areas of the main body to the aerodynamic forces and moments, occupied by strakes or located inside the strakes shadow region, was subtracted from the total values. With the basic cone at 0° incidence, each strake was assumed to be at an incidence of 4.27° and a sideslip angle of 4.19° with

respect to the velocity vector, Diagram 4.7. The derivation started from the Newtonian relation $C_p=2\cos^2\eta$

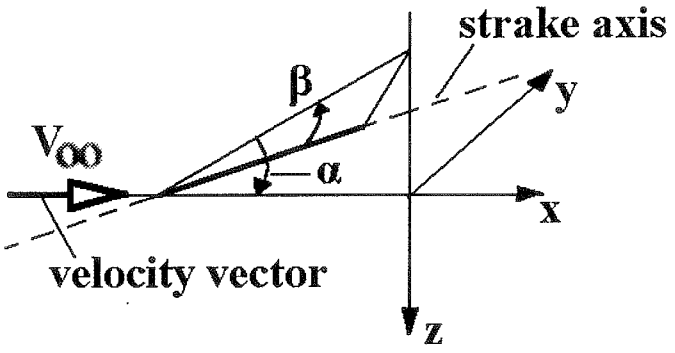

Diagram 4.7 Wind diagram

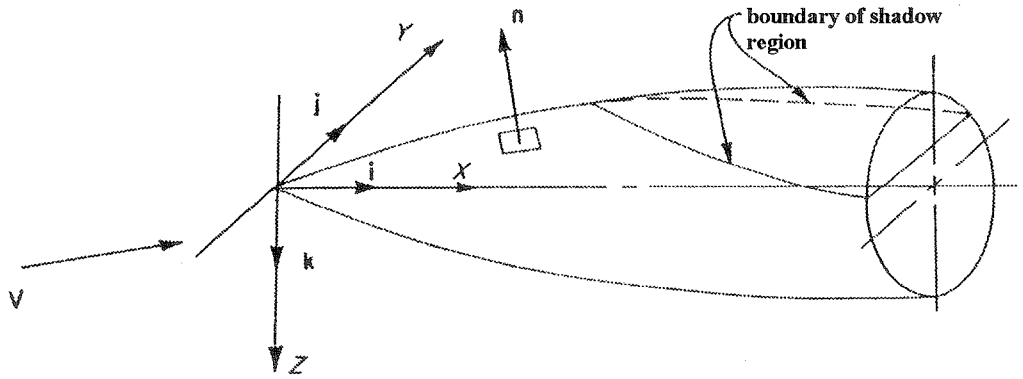

Diagram 4.8 General body of revolution

In order to determine the unit normal vector, the equation of the body surface must be derived in a suitable co-ordinate system, that is, f=g(x,y,z). The unit normal vector n was expressed as the gradient of the surface divided by its magnitude:

$$n=\frac{\nabla f}{|\nabla f|}=\frac{\frac{\partial f}{\partial x}i+\frac{\partial f}{\partial y}j+\frac{\partial f}{\partial z}k}{\sqrt{(\frac{\partial f}{\partial x})^2+(\frac{\partial f}{\partial y})^2+(\frac{\partial f}{\partial z})^2}} \qquad (4.6a)$$

The unit wind vector V was expressed in terms of the body axis, Diagram 4.7:

$$V=-\cos\alpha\cos\beta i-\sin\beta j-\sin\alpha\cos\beta k \qquad (4.6b)$$

The value of $\cos\eta$ is then determined by taking the dot product of the unit normal and wind vectors. In this analysis, the co-ordinate axis system was chosen with positive

directions x,y and z as forward, to the right, and downward, respectively, when viewed from the rear of the body, Diagram 4.8.

The equation for the surface of a conic body whose cross section is a square may be expressed as follows (see Diagram 4.6):

$$f = -x^2 + \frac{4\sin^2(135-\varphi)}{a^2} L_S^2 (y^2 + z^2) \tag{4.6c}$$

For purposes of integration, some convenient means is needed to identify the limits of the body in terms of the variables of the analysis. For this purpose cylindrical co-ordinates were used, (see Diagram 4.6):

$$x = x \tag{4.6d}$$

$$y = -\rho\sin\varphi \tag{4.6e}$$

$$z = -\rho\cos\varphi \tag{4.6f}$$

where φ is the angle measured from the vertical axis positive in a counterclockwise direction and ρ is the distance from the origin to a point on the surface of the square:

$$\rho = \frac{a}{2\sin(135-\varphi)} \tag{4.6g}$$

The equation of the body written in terms of this new co-ordinate system is expressed as:

$$x = -\frac{2\sin(135-\varphi)}{a} L_S \rho \tag{4.6i}$$

By substituting equations 4.6d, 4.6e, 4.6f and 4.6g into equation 4.6c and taking the dot product of the unit normal vector, determined by equation 4.6a, and the unit wind vector, determined by equation 4.6b, the Newtonian pressure coefficient for the right rhombic cone was derived, (Appendix B gives the formula of the Newtonian pressure coefficient for the right rhombic cone).

The force and moment coefficients were obtained by performing numerical integration using the pressure coefficient as determined by Newtonian theory:

$$C_N = -\frac{L_S}{S} \int_0^{-L_S} \int_{\varphi_i}^{\varphi_f} \frac{C_p a x \sin(135-2\varphi)}{2L_S \sin^2(135-\varphi)} d\varphi dx \tag{4.6j}$$

$$C_A = \frac{L_S}{S} \int_0^{\rho_b} \int_{\varphi_i}^{\varphi_f} \frac{C_p \rho(\cos^2\varphi - \sin^2\varphi)}{2} d\varphi d\rho \tag{4.6k}$$

$$C_m = \frac{1}{L_S S}\left[\int_0^{\rho_b}\int_{\varphi_i}^{\varphi_f}\frac{C_p\rho^2\cos\varphi(\cos^2\varphi-\sin^2\varphi)}{2}d\varphi d\rho + \int_0^{-L_S}\int_{\varphi_i}^{\varphi_f}-\frac{C_p(L_S+x)ax\sin(135-2\varphi)}{2L_S\sin^2(135-\varphi)}d\varphi dx\right] \quad (4.6l)$$

Lift and drag coefficients were calculated from:

$$C_L = C_N\cos\alpha - C_A\sin\alpha \quad (4.7a)$$

$$C_D = C_N\sin\alpha - C_A\cos\alpha \quad (4.7b)$$

Newtonian theory is restricted to those regions of the body which are inclined toward the free-stream direction or which may be thought of as being exposed to the flow. The flow is tangent to the surface at points on the surface which satisfy the relation that $\cos\eta=0$. The shadow-region boundary determined by this relationship, forms the boundary behind which the surface is shielded from the flow. Since this shadowed region does not contribute to the forces, the integration was restricted to the regions which see the flow, that is regions where $\cos\eta\geq 0$. Therefore, the limits of integration φ_i and φ_f were determined as the points where shadow begins and are given by setting $C_p=0$. The two values of φ obtained from this expression give the points on the base of the strake which are used as the values φ_i and φ_f in the integration. If the surface of the strake is in contact with the main elliptic cone at these points then the body limit forms the limits of integration.

The force and moment coefficients generated by the basic cone and each strake were estimated. The total force and moment coefficients, for each incidence, e.g. lift coefficient, were predicted according to:

$$C_{Ltotal} = \sum_{strakes} C_{Lstrake} + C_{Lbasic_cone} \quad (4.7c)$$

This method for deriving the individual forces and moments fundamentally assumes that the forces and moments generated in the presence of strakes are equal to the sum of the individual components i.e. the algebraic sum of the forces and moments generated by the cone and the strakes. This method can not take into account of the real vortex flows existing but it allows for the shadow on the body caused by the strake.

4.3.3 Results and Discussion for Configuration 4

4.3.3.1 Navier-Stokes Study

The flowfield of the lifting elliptic cone with and without strakes was simulated, assuming a perfect gas and a laminar boundary layer over the full length of the body for incidences 10°, 15° and 20°. A 65x65x165 half circumference grid was used for discretization of the flowfield of the elliptic cone with strakes, see Figs. 4.14a, b, c and d, and a 64x65x65 half circumference grid was used for discretization of the flowfield of the elliptic cone alone, see Fig. 4.14e. Basically the code solves a series of two-dimensional problems marching down.

The Navier-Stokes solution converged after about 6000 iterations on a Silicon Graphics workstation Indigo-2. The convergence to the steady state solution was checked by monitoring the flowfield parameters residuals. The important parameters are the pressure coefficient $Cp=(p-p_\infty)/(1/2\rho_\infty V^2_\infty)$ and the rate of heat transfer to the body $q=k\,\partial T/\partial n$ along the top, leeward and windward meridians. From the convergence histories, it was found that the inviscid parameters such as the pressure coefficient have achieved steady state before the viscous parameters such as the rate of heat transfer to the body. The solution was considered to be converged when $\|R(Q)\| \leq \varepsilon$ where $\varepsilon=10^{-4}$ or the maximum number of iterations is satisfied. The monitoring of the residuals of forces and moment is not reliable[166], because there are cases where the residuals of these parameters have achieved a steady state and the solution is still converging. The flowfield results were visualised using the *Flowfield* software package. All the numerical results are presented as an integral part to the discussion of the experimental measurements later in the chapter.

The computational grids were generated using a three-dimensional transfinite interpolation technique[167,168]. For complicated geometries like the elliptic cone with strakes multi-block gridding is normally used but in the present study all the grids were single block. The grid was generated in the following order:

1. Generation of the one-dimensional line grids at all junctions of the domain surfaces with the appropriate stretching according to the curve length;

2. Generation of the two-dimensional surface grids for all the domain boundary surfaces using the one-dimensional line grids as the interpolation boundaries and applying any geometric constraints where necessary, (see Appendix C);
3. Generation of the three-dimensional field grid by interpolation of the surface grids and ensuring the orthogonality of the grid at the wall by specifying the derivative information at the wall. The cluster of the grid at the wall was controlled by either the magnitude of the derivative or the stretch factor in the interpolation (ref. 196);
4. A 3D elliptic smoother was used to smooth the grid in regions where this is critical, i.e. around the sharp corners of the strake (ref. 196).

By the above procedure the grid points generated are the vertices of the hexahedral cells in the finite volume formulation. During the solver execution the flow properties are stored at the centres of the cells and a secondary grid is created by these central points for the presentation of the results from the finite volume solution.

There are a number of factors which can influence the quality of vortex flow predictions. In this study, the sensitivity of the numerical solution to the computational grid of the cone with strakes was examined. Since the forces and moment coefficients are the main parameters that are compared with experimental data, they are used as the representative factors for the grid sensitivity study. Smoothing and stabilising parameters were kept to a minimum during the grid sensitivity studies. The grid is refined in each direction of the three dimensions while holding the other two dimensions fixed.

Computations were made using a number of grids ranging from a coarse grid, consisting of 40 axial, 40 radial and 100 circumferential points, to a fine grid with 100 points in axial and radial direction and 200 in circumferential direction. Intermediate grids have been studied, along with the effect of changing the degree of radial clustering. Fig. 4.15 presents the study of the sensitivity of numerical results to grid density in each of the three co-ordinate directions. A better resolution of the vortical flowfield is obtained with the finer grid. However, the finer grid requires higher computer memory and more computing time leading to higher computing costs. The study showed considerable sensitivity of the calculated forces and moment coefficients in the streamwise direction. This is attributed to the integration routines which have been used to evaluate the forces and moments. This is a conjecture and needs further investigation.

The results of this study suggested that 165 grid points placed in the circumferential direction (**k**) and 65 grid points in each of the other directions (**i** and **j**) might be sufficient to resolve the flow features of interest for the elliptic cone with strakes, see Figs. 4.14a and 4.15. This grid is highly clustered in the radial direction towards the wall and yields a typical value of y+<l for the first cell off the body surface for better resolution of the viscous layer. In the circumferential direction a uniform grid spacing was employed for the regions between the strakes. The grid on the strakes was stretched towards the strake's corner intersections with the elliptic surface. The grid is required to be orthogonal at the wall for easy treatment of the boundary conditions.

4.3.3.2 Schlieren and Oil-Dot Visualisation Studies

The Reynolds number based on body's length is 1.75×10^6 and due to the relatively high Mach number and the low Reynolds number, the boundary layer on the surface of the model is laminar (see Fig. 2.6). Fig. 4.16 shows some schlieren pictures of the model (strakes on and off) which show no gross external flow differences due to the addition of strakes which agrees with the deduction for the half-power-law body described in section 4.2.1. The CFD investigation predicted approximately similar shock and vortex core positions for configuration 4 with and without strakes (the difference in the shock angles, strakes on and off, is approximately 0.5°). This is evident in Fig. 4.17a, which presents side by side the base Mach number contours at α=15° for the elliptic cone with and without strakes. The 10° and 20° incidence cases, run by the solver, again showed only small differences between the strakes on and off. Hence only the representative case of 15° incidence with and without strakes is presented.

The oil-dot surface visualisation technique successfully captured the cross-flow characteristics on the windward side, and some details of the flow phenomena on the leeward side can also be seen in Fig. 4.18. The strakes altered the surface flow characteristics and tended to inhibit the cross-flow on the windward side at all incidences tested (see for example Fig. 4.18c, α=10°).

Fig. 4.19a shows that a shock envelopes the body and the boundary layer is attached for α=0°. Comparison of the side and plan view of Fig. 4.19a shows that the distance between the shock wave and body is greater in the meridian plane containing the minor

axis than in the meridian plane containing the major axis. Exactly the same was observed for the elliptic cone of fineness ratio of 15, described in section 4.1.1, and the physical explanation of the phenomenon can be found there. The oil-dot pictures without strakes, Fig. 4.18a, show a weak cross-flow from the ends of the major axis to the ends of the minor axis. The oil-dot pictures with strakes, Fig. 4.18a, show evidence of a similar type of cross-flow. It seems that the strakes do little to inhibit the cross-flow on the body at 0^{o} incidence. This is supported by the pressure measurements, to be discussed in the next section, which show identical pressure distributions at 0^{o} incidence with and without strakes.

For the cone without strakes, at $\alpha=5^{o}$, the axial flow velocity is dominant and the flow is attached, (see Figs. 4.19c and 4.18b). The oil-dot pictures without strakes, Fig. 4.18b, show that the oil-dots motion is weak over the leeward side of the cone. The oil-dot pictures with strakes, Fig. 4.18b, show that the strakes inhibit the cross-flow on the windward side. The left side oil-dot picture shows that the escaping flow from the windward side must separate somewhere near the top surface of the bottom strake, *point B*, Fig. 4.20, (this is not very clear) and reattaches very close to the corner of the same strake, *point C*, Fig. 4.20, (the same applies for the right side). The left side oil-dot picture shows that the flow remains attached up to the top strake. The leeward side oil-dot picture shows evidence of reattachment and vortex formation. It is believed that the flow may separate just after the inner tip line of the leeward strakes, *point F*, Fig. 4.20.

As incidence increases, the schlieren study, Figs. 4.19d, e and f, shows that the separation point moves forward, from the base to the tip of the body, and by $\alpha=10^{\circ}$ the separation region extends over the whole upper surface of the model, Fig. 4.19g. The white line nearer the surface on the leeward side indicates the vortex core.

The oil-dot pictures without strakes, Fig. 4.18c, ($\alpha=10^{\circ}$) show that the flow separates after the end of the major axis and reattaches at the top leeward meridian and after the flow diverges. There is no evidence of secondary separation on the leeward side. The flow separation lines from which the vortices are fed also trace an essentially linear path along the model surface. The oil-dot pictures with strakes, Fig. 4.18c, ($\alpha=10^{\circ}$) show that the strakes inhibit the cross-flow even further on the windward side. The left side oil-dot picture also shows more clearly that the escaped flow from the windward side separates

just at the tip line of the bottom strake, *point B*, Fig. 4.20, and reattaches near the corner of the same strake, *point C*, Fig. 4.20. The flow there diverges in two parts: the first part towards the windward side and the second part towards the leeward side, Figs. 4.20 and 4.18c. The first part looks to separate again at the bottom strake corner and possibly to form a strake vortex. This suggestion is supported a few paragraphs later by the computational results (see page 73). The second part of the flow converges to an essentially straight line before the top strake and separates, *point D*, Fig. 4.20. This flow reattaches again at the top strake, *point E*, Fig. 4.20. The leeward side oil-dot picture shows that flow again separates at the inner tip line of the leeward strakes, *point F*, Fig. 4.20 and reattaches at the top leeward meridian, *point G*, Fig. 4.20, where it flows in the opposite direction.

Very similar flowfield characteristics were found for incidences 15° and 20° with and without strakes with those described above. The oil-dot pictures with and without strakes at α=15°, exhibit very similar flowfield characteristics to those for the 10° case, Fig. 4.18d. The oil-dot pictures with strakes, Fig. 4.18d, show that the strakes greatly inhibit the cross-flow on the windward side.

As incidence increases further, e.g. α=20°, the strakes inhibit the flow dramatically, Fig. 4.18e. The oil-dot pictures without strakes, Fig. 4.18e, do not show evidence of cross-flow reattachment on the leeward side. This because of the very low levels of skin-friction on the lee-side surface of the cone which causes the no response of the oil-dots. The pressure distribution on the top leeward meridian, (to be presented in the next section), supports this argument since they do not show evidence of vortex lift-off. The oil-dot pictures with strakes, Fig. 4.18e, show only weak evidence of cross-flow reattachment on the leeward side because again of the low levels of skin friction there.

By comparing the oil-dot pictures with and without strakes, Fig. 4.18, it can be seen that the oil-dot motion along the leeward side is slightly more pronounced for the case of the elliptic cone with strakes. Because the oil-dot method is skin-friction dependant, the latter is an indication that the presence of strakes causes an increase of the levels of local skin-friction along the leeward side.

Fig. 4.20 shows models of the flow characteristics in the crossflow plane of the elliptic cone with and without strakes as deduced from the experimental results only. Fig. 4.21

shows a comparison of the schlieren pictures (side and plan views) with the numerical results for incidences 10°, 15° and 20°. The numerical pictures exhibit the density of the flow. The computational plane which is shown in the numerical "schlieren" pictures corresponds to the plane which contains the minor axis. The experimental schlieren pictures are focussed on the same plane but do respond to some extent to all density gradients in the beam path. The computational study predicts satisfactorily the experimental shock shapes for all incidences under consideration and the fact that the *windward shock* is getting closer to the body surface as incidence is increasing.

The experimental schlieren *plan views* do not reveal any detailed flow characteristics. However, they show that the distance between the cone surface and the shocks envelope is increasing with incidence. This is supported by the numerical "schlieren" pictures of Fig. 4.21. The same was found for the elliptic cone of fineness ratio of 15 described in section 4.1.1. Combined examination of the schlieren and oil-dot pictures without strakes revealed that the cross-flow strength on the windward side increases as incidence increases from 5° to 20°. This is because of the increasing cross-flow velocity component with incidence. This was observed, as well, by other researchers on experiments on a tangent ogive-cylinder configuration[169] and on a cone with side-jet model[149].

The typical flowfield characteristics as predicted by the PNS solver at an incidence of 15° with and without strakes are shown in Fig. 4.17 (the results are presented side by side for the cone with and without strakes). The numerical code predicted the complex vortex flowfield surrounding the cone, gave better understanding of the complicated nature of the flow and good indications of the shock shape and vortex core positions. The Mach number contours, Fig. 4.17a, show the relative position of the circumferential boundary layer which is thin over the windward side and thickens as the flow expands. As it can be seen in Figs. 4.17a, b and c, the code predicts flow-separation after the end of the major axis which is in agreement with the experimental results. For the cone without strakes, Figs. 4.17d and 4.23 give evidence of secondary separation over leeward side. The velocity vectors in Fig. 4.17c represent the resultant velocity directions associated with the elevational and circumferential velocity components of the spherical co-ordinate system centred at the apex of the cone. Figs. 4.22 and 4.17c exhibit the very complicated flow around the strakes and show regions of vortical flow.

The oil surface flow visualisation and numerical surface streamline results are compared for the cone with and without strakes at 15° incidence in Fig. 4.23. The PNS calculation of the windward side flowfield captures successfully the inhibiting effect of strakes to the cross-flow. Because strakes inhibit the crossflow then the shock envelope should be closer. This is evident in Fig. 4.17a. The numerical predictions of the position of the main separation and reattachment lines agree quite well with the oil-dot study. However, the computation reveals a very complicated flow which in some regions, especially for the cone with strakes, the separation and reattachment lines occur very close to each other and the oil-dot technique is not able to capture all the flow phenomena in such a detail as the numerical study, Fig. 4.22. The numerical streamline results reveal that the flow after reattaching at the top leeward meridian, it flows in the opposite direction and separates. The position of this separation line is in agreement with the experimental one. The numerical study shows that this separated flow reattaches almost immediately on the leeward side.

In the region of the separation line, an interaction is established between the flow that has separated and the approaching inviscid flow. If the resultant Mach number associated with the elevational and circumferential velocity components exceeds one, there will be an imbedded shock wave system on the leeward side of the cone. The examination of the predicted flowfield for the cone without strakes, Figs. 4.17a and b, suggests the existence of an imbedded shock wave on the leeward side, above the vortex. A "near field" analogy with a blunt body in supersonic flow is shown in Fig 4.24. For the cone with strakes, Figs. 4.17a and b show that there may be a system of imbedded shock waves. The main imbedded shock wave occurs above the leeward side vortex in a position close to that predicted for the cone without strakes. This is a conjecture and requires further investigation of the crossflow plane using experimental techniques such as vapour screen, Rayleigh scattering and LIF.

4.3.3.3 Pressure Measurements

Initial pressure measurements on the elliptic cone without strakes showed a sudden increase in the pressure distribution along the top leeward meridian for incidences 0° to 20°, Fig. 4.25. Examination of Fig. 4.25 (see arrows) reveals that the starting point of

this increase in pressure along the leeward meridian moves slowly upstream as incidence increases. The measurements were repeated after re-routing the portex tubes exit locations of the first two orifices from the base of the model to different positions (see Fig. 3.8b). The relocation of those two tubes removed the sudden increase in the pressure distributions, Fig. 4.26.

It is believed that those two portex tubes, because they were placed very near the circumference of the base of the elliptic cone, were interfering with the leeward side flow by increasing the effective sting-support diameter. This effective increase in diameter caused an increase in the base pressure which allowed disturbances due to the portex tubes to be fed upstream through the subsonic part of the leeward boundary layer. The effect of these disturbances is more pronounced as incidence is increasing because the pressure along the leeward side is decreasing with incidence.

Fig. 4.26 displays the effect of strakes on the pressure distributions along the windward and leeward sides. The pressure distributions show a repeatability of ±5%. The experimental results show that the pressure along the windward meridian is increasing with incidence while the pressure along the leeward meridian is decreasing with incidence. Fig. 4.26 shows that the addition of strakes causes an increase in pressure on the windward side and a reduction of pressure on the leeward side. The increase of pressure on the windward side is caused by increased amount of air entrapped by the strakes over the lower side of the cone. As was displayed in the oil-dot pictures, Fig. 4.18, strakes inhibit the crossflow and promote more streamwise flow.

The CFD investigation predicted (see section 4.3.3.2, Fig. 4.17a) that adding strakes to an elliptic cone at $\alpha=15^{\circ}$ causes an increase in the windward shock angle of about 0.5° (4%). The equivalent sharp cone half-angle, for the elliptic cone without strakes at $\alpha=15^{\circ}$, is 18.8°. From Ames tables[157], this cone semivertex angle corresponds to a surface pressure ratio of $p/p_{\infty}=11.4$ and a shock angle of about 21.9°. Hence the shock angle of the equivalent sharp cone, for the elliptic cone with strakes at $\alpha=15^{\circ}$, is 22.4°. From the tables[157], this shock angle corresponds to an equivalent sharp cone semivertex angle of 19.5° and a surface pressure ratio of $p/p_{\infty}=12.2$. This simple method predicts an

increase of pressure of about 7% due to strakes for the elliptic cone at $\alpha=15^{\circ}$. The experimental measurements show a 10% increase due to strakes at $\alpha=15^{\circ}$, Fig. 4.26.

Expansion of the flow over the leeward surfaces of the other two strakes having positive dihedral reduces the pressure on the leeward side of the body in comparison with the pressure there for the body alone configuration. Reggiori[86] found similar effects on the pressure distributions along the windward and leeward sides of a circular cone configuration, due to the presence of positive and negative dihedral wings.

As expected, Fig. 4.26 shows that the strakes do not alter the pressure distribution along the top windward meridian for $\alpha=0^{\circ}$. However, on the windward side, the percentage of increase in pressure due to the strakes addition increases with incidence. The effectiveness of the strakes increases with incidence because of the increasing cross-flow component on the windward side they can "block". Conversely on the leeward side, the percentage of reduction in pressure due to the strakes addition decreases with incidence. This is because the top strakes act on a separated region and as the separation point moves round with incidence, their effect is getting smaller.

Along the windward meridian the computational study predicted successfully all the experimental trends described in the previous paragraphs, Fig. 4.27. The numerical results show good agreement with the experimental pressure distributions along the windward meridian both with and without strakes, Fig. 4.27. The CFD results predict a slight gradual decrease of the pressure distribution towards the tip of the cone. The rate of this decrease is getting higher with incidence. Palko et al[99] also found this effect in their experiments. Because of the lack of extra pressure tappings near the nose, it is not possible to confirm this in the present investigation.

Along the leeward meridian the numerical results seem to overpredict the experimental pressure distributions for the cone with and without strakes, Fig. 4.27. This difference is attributed to the inability of the code to capture accurately the complicated viscous phenomena on the leeward side of the cone with and without strakes.

The pressure results without strakes on the windward side have been compared with the standard Newtonian theory predictions and with the cone theory of Leung and Emanuel, (sections 4.3.1.2 and 4.3.1.1 respectively), Fig. 4.28. Both theories predicted the

experimental trend of increasing windward pressure with incidence. For $\alpha=0^{\circ}$, the Newtonian theory predicts surface pressures which are about 50 percent too low. This is because $M_{\infty}\alpha$ is really too low for the theory to hold. As α increases, the Newtonian theory becomes more and more accurate. This result is also expected, since at higher angles of attack the component of Mach number normal to the surface is larger, and the shock wave on the high pressure side is closer to the surface of the body. The Leung and Emanuel[163] cone theory is more accurate at low incidences, while at incidences 10° to 20° it overpredicts the pressure considerably. This is probably due to the crossflow being inaccurately modelled in the theory.

4.3.3.4 Forces and Moment Measurements

The effect of strakes on C_L, C_D, C_m, L/D and x_{cp}/L_{cone} at incidence is presented in Fig. 4.29. Fig. 4.29 also compares the experimental results for the elliptic cone with and without strakes with estimates using the theoretical models discussed in section 4.3.2 and with the PNS computations. The computational solver does not take into account the effects of the base drag coefficient into the calculations. The theoretical models do not include the effects of the base drag and the skin friction drag.

An indication of the value of the base drag coefficient is given from Eq. 4.2 (section 4.2.1). Its contribution at each incidence to the lift and drag coefficients predicted by the PNS solver and the theory with and without strakes is calculated by:

$$C_L = -C_{D_B}\frac{A_b}{A_p}\sin\alpha \tag{4.8a}$$

$$C_D = C_{D_B}\frac{A_b}{A_p}\cos\alpha \tag{4.8b}$$

For example, at 20° incidence, the addition of the base drag component causes the predicted lift coefficients by computation and theory to decrease by 0.004 (this is the maximum contribution to the lift coefficients for the incidences under consideration). Therefore, the addition of the base drag coefficient contribution causes a very small increase of the disagreement in magnitude of the predicted lift coefficients with experiment and an improvement of the agreement of the predicted drag coefficients with the experimental results.

By following the numerical "shooting" technique described by Anderson[170], the total laminar skin-friction drag coefficient on a flat plate with length equal to the length of the elliptic cone is approximately 0.0004. The total skin-friction drag for the "equivalent plate", D_p, is:

$$\frac{D_p}{q_\infty} = \bar{c}_f A_{wetted} \tag{4.8c}$$

$$A_{wetted} = \left\{ \frac{\pi k L_{cone}}{\cos \vartheta_c} \left[1 - \frac{1}{4} e^2 - \frac{3}{64} e^4 - \ldots \right] + \xi \sum_1^4 A_{strake_i} \right\} \tag{4.8d}$$

where k=a, if the major axis is placed horizontally and k=b, if the minor axis is placed horizontally, $e=(a^2-b^2)^{1/2}/a$, ϑ_c is the angle enclosed by the top meridian and the horizontal plane of symmetry, $\xi=0$ for the elliptic cone without strakes and $\xi=1$ for the elliptic cone with strakes. For the elliptic cone without strakes, when the major axis is horizontal $C_{D_f}=0.0006$, when the minor axis is horizontal $C_{D_f}=0.0009$. For the elliptic cone with strakes, when the major axis is horizontal $C_{D_f}=0.0007$, when the minor axis is horizontal $C_{D_f}=0.0014$. The above results show that the contribution of the skin-friction drag coefficient to the theoretical lift and drag coefficients is very small. As was expected the skin-friction drag coefficient is higher for the elliptic cone with strakes and the minor axis horizontal. It should be noted that the above method is a crude approximation.

1.Lift coefficient

The effect of strakes is to increase the C_L-α curve slope, Fig. 4.29a. This increase is due to increased pressure over the lower side of the cone caused by increased amount of air "entrapped" by the strakes. The two strakes having negative dihedral create strong interference with the flow over the windward side of the body. The lift curve is non-linear with its slope increasing with α (see note in section 4.2.1, Eqs. 4.1b to e). The separation of the leeside flow further increases the slope due to increased suction over the leeward side of the cone. This is supported by the pressure measurements, see Fig. 4.26.

Both theory and computation successfully predicted the experimental trends, Fig. 4.29a. The estimation models underpredict the magnitude of the experimental results and forecast a higher increase in the lift coefficient due to the strakes. The computation also

underpredicts the experimental results but it is in a better agreement with them and predicts a similar increase in the lift coefficient due to the strakes. For angles of attack beyond the cone half-angle (this is the angle enclosed by the top leeward or windward meridian with the horizontal plane of symmetry), vortical flow develops on the leeward side of the cone (as it was discussed in section 4.3.3.2). The increasing importance of vortical flow, and the resulting non-linearity, as incidence is increasing further, causes a deterioration in the comparison of both calculation and the theoretical models with experiment.

The lack of ability of the PNS code to capture accurately the complicated viscous phenomena on the leeward side of the cone especially beyond the cone half-angle (see above) leads to poorer predictions at higher incidences. The differences can probably be reduced, for example, inputting more detailed knowledge of the boundary layer state over the cone.

2.Drag coefficient

Fig. 4.29b shows that adding strakes increases the C_D values at all incidences tested. This increase is small particularly at the lower incidences. This is because the addition of strakes does not change the nose shape and hence the nose shock (see Fig. 4.16) and any increase in the drag coefficient due to comparatively small strakes is therefore expected to be small.

Both theory and computation predicted successfully the experimental *trends*, Fig. 4.29b. The increasing importance of the complicated viscous phenomena on the leeward side of the cone as incidence increases, causes a deterioration in the comparison of both calculation and the theoretical models with experiment. The theory does not take into account these viscous characteristics of the flow and the solver does not resolve accurately the complicated viscous phenomena which leads to poorer predictions at higher incidences.

3.Pitching moment coefficient

Fig. 4.29c shows that adding strakes increases the curve slope of the pitching moment coefficients about the balance moment-centre. As incidence increases, there is an increase in the pitching moment coefficient because the increase in the lift coefficient for the cone with strakes over that without the strakes continues to increase with α.

Both theory and computation predicted successfully the experimental trends, Fig. 4.29c. The estimation models overpredict the magnitude of the experimental results and forecast a higher increase in the pitching moment coefficient due to the strakes. The computation exhibits better agreement with the experimental results than theory.

4.Centre of pressure

Because of the data scattering in Fig. 4.29d, the centre of pressure is located between 67.5% and 66.0% of the total length from nose tip, for the cone with strakes, and between 69.5% and 67.5% of the total length for the cone without strakes, Fig. 4.29d. Both theory and computation predicted the experimental *trend* that adding strakes causes the forward movement of the centre of pressure. The theory predicts a movement of the centre of pressure from 62.5% without strakes to 62.4% with strakes. The computation predicts a movement of the centre of pressure from 65.5% without strakes to 64.5% with strakes. According to slender body theory[162] the location of the centre of pressure is given by $x_{cp}/L_{cone}=2n/(2n+1)$. Substituting n=1, then $x_{cp}/L_{cone}=0.67$.

5.L/D ratio

Fig. 4.29e shows that adding strakes causes an overall decrease in L/D. This is because the percentage of increase in lift due to strakes is smaller than the percentage of increase in drag. For the cone without strakes $L/D_{max}=4.6$ and occurs at $\alpha=5^{\circ}$. For the cone with strakes, $L/D_{max}=3.8$ and occurs at the same incidence.

Both theory (over the whole incidence range) and computation (over the latter half of the incidence range) predicted successfully the experimental trends, 4.29e. The estimation models overpredict the magnitude of the experimental results and forecast a smaller decrease in L/D due to strakes. The computation underpredicts the experimental values but it is in a better agreement with them than theory. As it was discussed in the previous paragraphs the increasing importance of vortical flow and viscous phenomena as incidence is increasining, causes the lack of agreement in the comparison of both calculation and the theoretical models with experiment. The theory does not take into account these viscous characteristics of the flow and the solver does not resolve accurately the complicated viscous phenomena.

4.3.3.5 Comparison of Forces and Moment Measurements with Other Data

1.Lift coefficient

Fig. 4.30a compares the present lift coefficient measurements (no strakes) with those reported by Fournier and Spencer[103]. Fournier and Spencer's model is a right elliptic cone at M_∞=4.63. The present results obtained for a/b=1.6 are following the trend of increasing C_L-α slope with increasing a/b.

Fig. 4.31a compares the present lift coefficient measurements (strakes on and off) with those discussed in section 4.2.1 (half-power-law body). The comparison shows that as the body exponent n increases from 0.5 to 1.0 (decreasing bluntness and increasing span) the lift-curve slope increases. A similar trend was found by Fournier and Spencer[103] on experiments with bodies of increasing exponent from 0.25 to 1.00. The effect of strakes on lift is more pronounced for the power-law body. This is probably because adding strakes produces a stronger favourable interference with the power-law body.

2.Drag coefficient

Fig. 4.30b compares the present drag coefficient measurements (no strakes) with those reported by Fournier and Spencer[103]. The comparison of their results with the present investigation shows a reduction in C_D values close to α=0° as the Mach number increases from 4.63 to 8.2. This is probably because of the reduction of base drag with increasing Mach number (see section 4.2.1, Eq. 4.2).

Fig. 4.31b shows that as the body exponent n increases from 0.5 to 1.0 the zero-lift drag coefficient increases. A similar trend was found by Fournier and Spencer[103]. The effect of strakes on drag is more pronounced for the right elliptic cone. The strake size for the right elliptic cone is 3mm square at the base while the strake size for the power-law body is 1.67mm square at the base. Therefore the strakes of the right elliptic cone should contribute more drag than the strakes of the power-law body.

3.Pitching moment coefficient

Fig. 4.31c shows that as the body exponent n increases from 0.5 to 1.0 the pitching moment curve slope decreases. A similar trend was found by Fournier and Spencer[103]. This is because the effect of increased lift, as the body exponent n increases from 0.5 to 1.0, is accompanied by a rearward shift of the centre of pressure, Fig. 4.31d. The effect

of strakes on pitching moment is more pronounced for the power-law body. This is because adding strakes to the power-law body causes a larger percentage of increase in the lift curve slope.

4.3.4 Results and Discussion for Configuration 5 (elliptic cone with the major axis vertical)

4.3.4.1 Schlieren and Oil-Dot Visualisation Studies

Fig. 4.32 shows some schlieren pictures of the model (strakes on and off). No detectable differences in the schlieren pictures (side and plan views) were found due to the presence of the strakes which agrees with the deduction for the half-power-law body described in section 4.2.1 and for the elliptic cone, configuration 4, described in section 4.3.3.2.

The oil-dot technique successfully captured the cross-flow characteristics on the windward side, and some details of the flow phenomena on the leeward side can also be seen in Fig. 4.33. The oil-dot pictures with and without strakes of the present configuration, Fig. 4.33, revealed similar flow characteristics with those of configuration 4 (see section 4.3.3.2). The strakes altered the surface flow characteristics and tended to inhibit the cross-flow on the windward side at all incidences tested. A summary of the effect of strakes on the flow field of configuration 5 (as deduced from the oil-dot pictures) is shown in Fig. 4.35.

Fig. 4.34a shows the side and plan schlieren photos for $\alpha=0^{\circ}$. These photos are the same as those displayed in Fig, 4.19a. The picture labelled as *side view* in Fig. 4.34a, corresponds to the picture labelled as *plan view* in Fig. 4.19a. The picture labelled as *plan view* in Fig. 4.34a, corresponds to the picture labelled as *side view* in Fig. 4.19a.

At low incidences, the axial flow velocity is dominant and the flow is attached (see Figs. 4.34a, b and c). The oil-dot pictures without strakes, $\alpha=5^{\circ}$, Fig. 4.33a, show that the flow is attached around the cone and the oil-dots converge to a single line along the top leeward meridian. The comparison of Figs. 4.34a, b and c shows that the boundary layer over the leeward side thickens with incidence. The flow on the windward side of the cone is dominated by the inviscid flowfield between the shock wave and the thin viscous boundary layer. In this region, the pressure gradient in the circumferential direction is favourable. On the leeward side of the cone, this pressure gradient becomes adverse.

Tracy[171] has showed, on experiments with a circular cone at a Mach number of 7.95, that as crossflow increases the boundary layer thickens over the leeward side.

With increasing incidence, e.g. $\alpha=7^{\circ}$, there is the establishment of a disturbed flow region over the leeward side close to the rear of the cone, Fig 4.34d. The pressure gradient becomes adverse. The crossflow separates, resulting in the establishment of a pair of counter-rotating vortices over the leeside of the body. At $\alpha=10^{\circ}$, the separation point moves forward, towards the tip of the body, Fig. 4.34e. For this incidence, the separation region extends approximately over the 4/5 of the length of the cone, (Figs. 4.34e and 4.33b), and the cross-flow separates in an essentially straight line. The separation line is located well after the ends of the minor axis. The oil-dot pictures without strakes, $\alpha=10^{\circ}$, (Fig. 4.33b), show that the flow reattaches at the top leeward meridian, where it flows in the opposite direction. The white line nearer the surface on the leeward side indicates the vortex core, Fig. 4.34e. The oil-dot pictures without strakes, $\alpha=15^{\circ}$, Fig. 4.33c, show that the separation region extends over the whole upper surface of the model. At $\alpha=15^{\circ}$ and 20°, the vortex core is no longer visible, Figs. 4.34f and g. The oil-dot pictures without strakes, $\alpha=20^{\circ}$, Fig. 4.33d, show a weaker movement of the oil-dots over the leeward side. This is because of the low levels of skin friction there.

The schlieren *plan views* do not reveal any detailed flow characteristics. However, they show that the distance between the cone surface and shocks envelope is increasing with incidence. The same was found for configurations 1, 2 and 4 (see sections 4.1.1 and 4.3.3.2). Combined examination of the schlieren and oil-dot pictures without strakes revealed that the cross-flow strength on the windward side increases as incidence increases from 5° to 20°. This is because of the increasing cross-flow velocity component with incidence.

4.3.4.2 Forces and Moment Measurements

The effect of strakes on C_L, C_D, C_m, L/D and x_{cp}/L_{cone} at incidence is presented in Fig. 4.36. Fig. 4.36 also compares the experimental results for the elliptic cone with and without strakes with estimates using the theoretical models discussed in section 4.3.2. The present measurements are compared with the experimental results for the elliptic cone with its major axis horizontal (configuration 4, section 4.3.3.4), see Fig. 4.37.

1.Lift coefficient

The effect of strakes is to increase the C_L-α curve slope, Fig. 4.36a. This increase is due to increased pressure over the lower side of the cone caused by increased amount of air "entrapped" by the strakes. The lift curve is non-linear with its slope increasing with α (see section 4.2.1, Eqs. 4.1b to 4.1e).

The theory predicted the experimental trends, Fig. 4.36a. The estimation models underpredict the magnitude of the experimental results and forecast a higher increase in the lift coefficient due to the strakes. For angles of attack beyond the cone half-angle, vortical flow develops on the leeward side of the cone (see section 4.3.4.1). The increasing importance of vortical flow, and the resulting non-linearity, as incidence is increasing further, causes a deterioration in the comparison of the theoretical models with experiment.

Fig. 4.37a compares the present lift measurements with those for configuration 4. Both models have the same a/b=1.6 but the present model is rotated by 90°. For the elliptic cones of Fig. 4.37a, the lengths and base areas are constant but the planform area is smaller for the elliptic cone with its major axis vertical. In view of this fact, it is not surprising that the configuration 4 without strakes exhibits higher lift coefficients than configuration 5. This can be understood better by taking the limiting cases for configurations 4 and 5 ($a/b\rightarrow\infty$ and $a/b\rightarrow 0$). The limiting case for configuration 4 is a flat delta wing placed horizontally and the limiting case for configuration 5 is a flat delta wing placed vertically under the same freestream conditions. Adding strakes produces a more favourable interference with configuration 5 than configuration 4 which causes a higher increase in the lift curve slope for configuration 5. This can be understood further by taking the limiting cases for configurations 4 and 5, see Diagram 4.9.

2.Drag coefficient

Fig. 4.36b shows that adding strakes increases the C_D values at all incidences tested. This increase is smaller at the lower incidences. This is because the addition of strakes does not change the nose shape and hence the nose shock (see Fig. 4.32) and any increase in the drag coefficient due to comparatively small strakes is therefore expected to be small.

The theory predicted the experimental trends, Fig. 4.36b. The increasing importance of the complicated viscous phenomena on the leeward side of the cone as incidence

increases, causes a deterioration in the comparison of the theoretical models with experiment. The theory does not take into account these viscous characteristics of the flow.

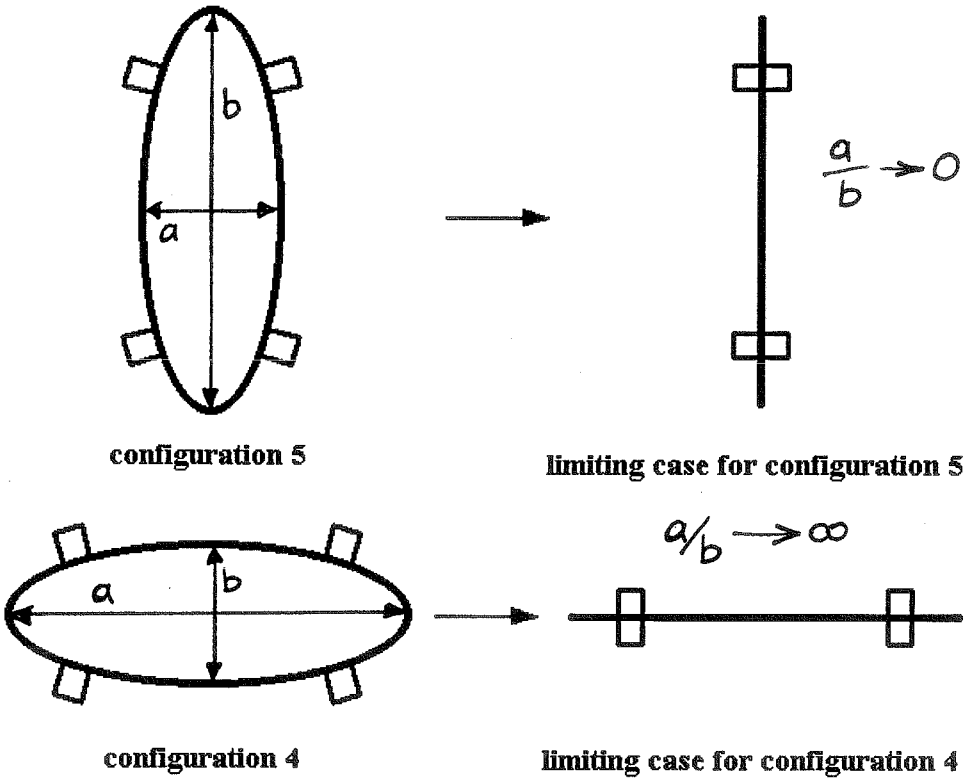

Diagram 4.9 Limiting cases of configurations 4 and 5

Fig. 4.37b compares the present drag measurements with those for configuration 4. Configuration 5 without strakes exhibits lower drag coefficient values than configuration 4 without strakes. This is possibly because configuration 5 develops less drag due to lift. It is believed that the lower drag due to lift can be attributed to less vortex drag associated with the formation of vortices in the bodies without strakes at angle of attack. Because of the better streamlining in the crossflow plane, the formation of vortices is inhibited more for the elliptic cone with its major axis vertical and the drag due to lift is reduced. This can be understood better by taking the limiting cases for configurations 4 and 5 i.e. a flat delta wing placed horizontally and vertically respectively.

Adding strakes produces a larger percentage of increase in drag for configuration 5 than for configuration 4, Fig. 4.37b. The difference can be explained by taking into account the limiting cases shown in Diagram 4.9. Both configurations have the same size of

strakes. Adding strakes in configuration 4 produces less drag due to lift. This lower drag due to lift can be attributed to less vortex drag associated with the formation of vortices due to strakes around the elliptic cone with its major axis horizontal, (see oil-dot pictures with strakes for configurations 4 and 5, Figs. 4.18 and 4.33 respectively).

3.Pitching moment coefficient

Fig. 4.36c shows that adding strakes increases the pitching moment coefficients about the balance moment-centre. As incidence increases, there is an increase in the pitching moment coefficient because the increase in the lift coefficient for the cone with strakes over that without the strakes continues to increase with α.

The theory predicted successfully the experimental *trends*, Fig. 4.36c. The estimation models overpredict the *magnitude* of the experimental results and forecast a higher increase in the pitching moment coefficient due to the strakes.

Fig. 4.37c compares the present pitching moment measurements with those for configuration 4. Configuration 5 without strakes exhibits lower values of pitching moment coefficients than configuration 4 without strakes. This is because configuration 4 without strakes produces higher lift values than configuration 5. Adding strakes produces a larger percentage of increase in pitching moment for configuration 5 than configuration 4. This is because adding strakes in configuration 5 produces a larger percentage of increase in lift than configuration 4 with strakes.

4.Centre of pressure

The centre of pressure is located between 65.8% to 64.8% of the total length from nose tip, for the cone with strakes, and between 66.7% to 65.6% of the total length for the cone without strakes, Fig. 4.36d. The theory predicted the experimental trend that adding strakes causes the forward movement of the centre of pressure. The theory predicts a movement of the centre of pressure from 66.0% without strakes to 65.8% with strakes.

Fig. 4.37d shows that the centre of pressure for configuration 5 without strakes is slightly forward from the centre of pressure for configuration 4. In both cases adding strakes causes a forward movement of x_{cp} and this movement is small.

5.L/D ratio

Fig. 4.36e shows that adding strakes causes an overall increase in L/D of 4%. This is because the percentage of increase in lift is slightly larger than the percentage of increase in drag. For the cone without strakes $L/D_{max}=2.44$ and occurs at $\alpha=7^{o}$. For the cone with strakes, $L/D_{max}=2.54$ and occurs at the same incidence.

The theory predicted the experimental trends, 4.36e. The estimation models overpredict the magnitude of the experimental results and forecast a larger increase in L/D due to strakes.

Fig. 4.37e compares the present L/D ratios with those for configuration 4. Configuration 4 without strakes exhibits higher L/D ratios than configuration 5. This is because configuration 4 without strakes produces larger lift coefficients. Adding strakes causes a decrease in L/D for configuration 4 and an increase in L/D for configuration 5. This can be understood by taking into account Diagram 4.9. The strakes of configuration 5 act like small "wings", whereas the strakes of configuration 4 are hidden by the cone.

Chapter 5

Results and Discussion

Flare Control Effectiveness

5.1 Cylinder-Flare Body

A cylinder flare body was tested at a Mach number of 8.2 at zero incidence under laminar and turbulent boundary layer conditions (described in section 3.4.4). Two nose geometries, namely a 10^{o} half-angle sharp cone and a hemisphere, were used. Experiments were conducted to measure the pressure distribution along the cylinder body and the flares. Schlieren pictures were taken to examine the flowfield around the model and an oil-dot technique and liquid crystals were employed to investigate the surface flowfield.

5.2 Hemisphere-Cylinder, Theoretical Correlations

5.2.1 Blast Wave Theory

The blast wave theory is a variation of the hypersonic equivalence principle. This states that the steady hypersonic flow over a slender body is equivalent to an unsteady flow in one less space dimension. The steady physical effects of a blunt nose are analogous to unsteady effects in the y-t plane associated with the propagation of a cylindrical blast wave, Diagram 5.1.

The first and second approximations of the blast wave theory, as obtained by Lukasiewicz[172], were used to compare with the experimental schlieren bow shock wave

co-ordinates and the pressure measurements for the hemisphere nose cylinder body, Figs. 5.1a and b. The first approximation of the shock geometry and pressure distribution is:

$$\frac{r}{d} = 0.795 C_{D_n}^{\frac{1}{4}} \sqrt{\frac{x}{d}} \tag{5.1a}$$

$$\frac{p}{p_\infty} = 0.067 M_\infty^2 \frac{\sqrt{C_{D_n}}}{(x/d)} \tag{5.1b}$$

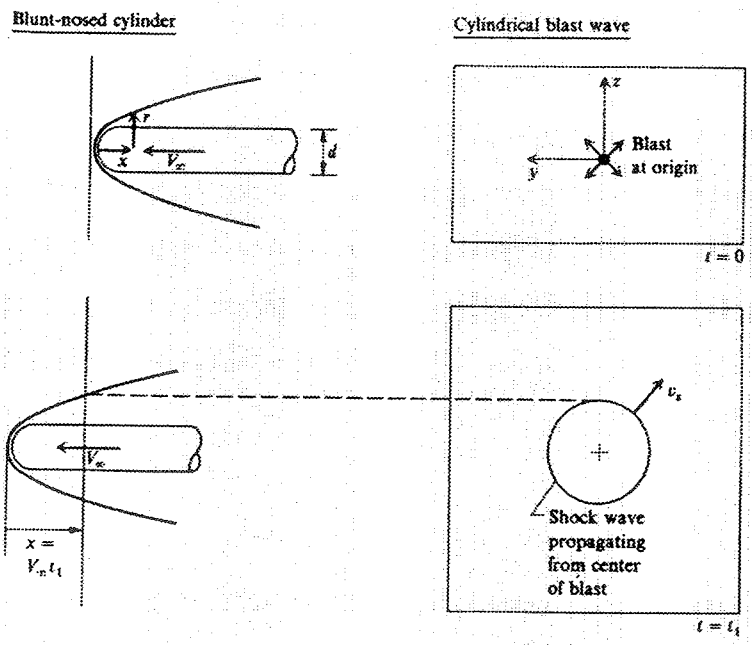

Diagram 5.1 Blast wave analogy for a blunt-nosed cylinder[170]

The second approximation of the shock geometry and pressure distribution is:

$$\frac{r/d}{M_\infty C_{D_n}^{1/2}} = 0.795 \sqrt{\frac{(x/d)}{M_\infty^2 C_{D_n}^{1/2}} \left[1 + 3.15 \frac{(x/d)}{M_\infty^2 C_{D_n}^{1/2}} \right]} \tag{5.1c}$$

$$\frac{p}{p_\infty} = 0.067 M_\infty^2 \frac{\sqrt{C_{D_n}}}{(x/d)} + 0.44 \tag{5.1d}$$

where x is the distance measured from the nose, in the flow direction, d is the cylinder diameter, r is the local distance between the body axis and the shock wave in the lateral direction and C_{D_n} is the nose drag coefficient. By integrating the modified Newtonian flow pressure distribution over the hemispherical nose, the nose drag coefficient is equal to 0.964. Both the first and second approximations become invalid at x=0 where they

predict an infinite pressure ratio. In the actual flow, the pressure ratio at x=0 is the normal shock value (p/p_∞=78.28 see ref. 157).

Fig. 5.1a shows that the best agreement with the experimental pressure distribution is obtained with the first approximation but the theory is a crude one and is primarily useful in indicating trends. Fig. 5.1a contains the experimental pressure distributions along the cylinder body under laminar (without vortex generators) and turbulent (with vortex generators) boundary layer conditions. The shock wave shape for the hemisphere cylinder is given in Fig. 5.1b. The shock location predicted by the first and second blast wave theory is not very accurate because it takes no account of stand-off distance and the hemisphere nose cylinder body does not add energy to the flow instantaneously, nor is this energy addition precisely at a point (the assumption of the blast wave solutions). This is why better agreement is obtained by shifting the predicted shock shape by an amount of $\Delta r/d$=0.35, as indicated in Fig. 5.1b.

5.2.2 Alpha Code

Alpha code was developed by Wells and Thornley[173]. It predicts the inviscid pressures only. Viscous effects, such as induced pressures owing to the presence of a boundary layer, are not included. The pressure correlation equation for spherical noses for angles $0\leq\theta\leq90^\circ$ is:

$$C_p = C_{p_{max}}\left[1-\eta\sin^2\theta+\nu\sin^4\theta-\kappa\sin^6\theta-\varphi\left(\frac{\theta}{90}\right)^{10}+\Delta\right] \tag{5.1e}$$

which is an improved version of the modified Newtonian method and:

$$\eta=1.25,\ \nu=0.310,\ \varphi=0.0259 \tag{5.1f}$$

$$\kappa = 10.81e^{-3.015M_\infty} \tag{5.1g}$$

$$\Delta=\begin{cases}\varepsilon\sin\left(\dfrac{\theta}{32.5}90\right) & \theta<65^\circ\\ -\rho\left(\dfrac{\theta-65}{25}\right) & \theta\geq65^\circ\end{cases} \tag{5.1h}$$

$$\varepsilon = 0.0034+\frac{0.15}{M_\infty^{2.1}} \quad M_\infty\geq3.5 \tag{5.1i}$$

$$\rho = 0.29e^{-0.6579M_\infty}+0.015e^{-0.1535M_\infty} \tag{5.1j}$$

$C_{p_{max}}$ is computed from the Rayleigh pitot equation for a perfect gas[157], which is:

$$\frac{p_{o1}}{p_\infty} = \left[\frac{(\gamma+1)M_\infty^2}{2}\right]^{\frac{\gamma}{\gamma-1}} \left[\frac{\gamma+1}{2\gamma M_\infty^2 - (\gamma-1)}\right]^{\frac{1}{\gamma-1}} \tag{5.1k}$$

(at M_∞=8.2, p_{o1}/p_∞=87.037)

then:

$$C_{p_{max}} = \frac{\frac{p_{o1}}{p_\infty} - 1}{\frac{1}{2}\gamma M_\infty^2} \tag{5.1l}$$

(at M_∞=8.2, $C_{p_{max}} = 1.828$)

On the cylinder, the improved version of the hypersonic blast-wave correlation of Kuehn[174] is used:

$$C_p = \begin{cases} C_{p_{tp}} e^{-\mu\left(\frac{x}{r_n}-1\right)} & \frac{x_{tp}}{r_n} \le \frac{x}{r_n} < 5 \\ \frac{1.4283}{M_\infty^2}\left(\frac{p_{blast_wave}}{p_\infty} - 1\right) & \frac{x}{r_n} \ge 5 \end{cases} \tag{5.1m}$$

and

$$\frac{p}{p_\infty} = \frac{1}{2}\gamma M_\infty^2 C_p + 1 \tag{5.1n}$$

where the suffix *tp* corresponds to the tangent point (between hemisphere and cylinder) and:

$$\frac{p_{blast_wave}}{p_\infty} = \frac{0.85}{\chi} + 0.55 + \Omega \tag{5.1o}$$

$$\chi = \frac{x / r_n}{0.1285 M_\infty^2} \tag{5.1p}$$

$$\Omega = \begin{cases} 0 & \chi \le 2 \\ 0.45\left[1 - e^{-0.145(\chi-2)}\right] & \chi > 2 \end{cases} \tag{5.1q}$$

$$\mu = -\frac{1}{4}\ln\left(\frac{C_{p_{ref}}}{C_{p_{tp}}}\right) \tag{5.1r}$$

where $C_{p_{ref}} = C_p$ at x/r_n=5.

Fig. 5.2 shows the predicted pressure distribution along the hemisphere nose and cylinder body using the above relations. The pressure falls around the spherical nose to a value of a few times the freestream, pressure aft of the hemisphere nose junction through an expansion. The strong interaction between the bow shock and the expansion causes a high shock curvature for some distance downstream of the nose, Fig. 5.3a.

Fig. 5.3b compares the experimental pressure distributions along the cylinder body, under laminar (without vortex generators) and turbulent (with vortex generators) boundary layer conditions, with the prediction from Eqs. 5.1m and n. The experiments show $p/p_\infty<1$ so it would appear that the overexpansion around the shoulder is greater than the correlations suggest.

5.2.3 Flowfield around a Hemisphere-Cylinder Body

Fig. 5.4 shows the flow structure over a hemisphere-cylinder body and Fig. 5.5 shows the streamline pattern. The streamlines close to the body axis require large deflections. This is achieved by the formation of a strong near normal shock ahead of the nose which decelerates the flow to subsonic speeds. Following this, the flow accelerates back to supersonic speeds. Away from the body axis, the deflection angles required are small and the stream lines in this region of the flowfield are processed by weaker oblique shockwaves.

The shock detachment distance, δ, is approximately 1.36 mm (measured from the schlieren photograph, Fig. 5.3a). An estimation can be made using the following relation[175]:

$$\delta \cong \frac{\varepsilon r_n}{1+\sqrt{2\varepsilon}} \qquad (5.1s)$$

The above equation gives a value of stand-off distance of 1.38 mm which agrees very well with the experimental result. An approximation of the shock stand-off distance is also given by Stollery and Maull[156] assuming a circular cylinder or sphere of radius r:

$$\frac{\delta}{r} = 0.77 \cot \vartheta_m \cos \vartheta_m - (1 - \sin \vartheta_m) \qquad (5.1t)$$

For M_∞=8.2, the maximum cone semi-angle for an attached shock wave[157], ϑ_m, is 56.43°, then δ/r is equal to 0.1158. For r=8.5 mm, $\delta \cong 0.99$ mm.

The shock curvature causes variation in the strength of the nose shock which produces a gradient in reservoir pressure normal to the surface. The boundary layer edge streamlines, having passed through the strong normal shock at the leading nose are subject to the greatest reservoir pressure loss. Away from the body axis, the loss of reservoir pressure is lower due a decrease in the local shock strength. These variations are confined to a region called the entropy layer.

The thickness of the entropy layer is a function of the curvature of the nose shock and hence of the nose radius. The effects of bluntness are limited to the point at which the entropy layer is swallowed by the boundary layer. Fig. 5.4 shows the effect of nose bluntness creating a thick entropy layer such that $\delta_{entropy} >> \delta$. This results in the boundary edge conditions being characterised by the low supersonic Mach number conditions in the lower portion of the entropy layer. The large thickness of the entropy layer means that the boundary layer is unable to swallow any significant portion of the entropy layer, which causes the boundary layer edge Mach number along the cylinder body to be well below the freestream value.

5.2.4 Boundary Layer Edge Mach Number

Figs. 5.4 and 5.5 show that the boundary layer edge streamtube is processed by the strong near normal section of the nose shockwave. This reduces the reservoir pressure at the edge of the boundary layer to values that are close to that downstream of a normal shock. The boundary layer grows with x so the edge Mach number will change. Assuming the flow at the edge of the boundary layer to be isentropic, the boundary layer edge Mach number is given approximately by:

$$M_e = \sqrt{\left(\frac{2}{\gamma - 1}\right)\left[\left(\frac{p_{o1}}{p_\infty}\frac{p_\infty}{p_2}\right)^{\frac{\gamma-1}{\gamma}} - 1\right]} \qquad (5.1u)$$

The predicted pressure ratio distribution along the nose-cylinder body (given by combination of Eqs. 5.1e, l, m and n) and the reservoir pressure relationship given by Eq. 5.1k are substituted into Eq. 5.1u. Fig. 5.6a shows the predicted local boundary layer edge Mach number distributions for the present hemisphere-cylinder body at Mach numbers of 5, 7, 8.2, 10 and 20.

In Fig. 5.6b, the experimental boundary layer edge Mach number distribution (from pitot pressure measurements) deduced by Crawford et al[176] at a freestream Mach number of 6.8 is compared with the prediction from Eqs. 5.1e, l, m, n, k and u. The agreement between the experimental results and the theoretical prediction is good. This supports the conclusion that the reservoir pressure at the edge of the boundary layer in bluntness dominated flows is approximately equal to the reservoir pressure downstream of a normal shock.

Fig. 5.6b also shows the predicted M_e distribution along the body in the present investigation deduced by substituting the experimental pressure ratios of the hemisphere-cylinder body (laminar and turbulent boundary layer conditions) into Eq. 5.1u. The predicted distribution is compared with the theoretical results from Eqs. 5.1e, l, m, n, k and u. The analytical model predicts the experimental results in trend but it underpredicts them in value.

5.2.5 Entropy-Layer Mach Profile Prediction

The local streamline curvature in the entropy layer is assumed to be small and therefore the static pressure gradient in the entropy layer is negligible. But as a result of the highly curved nose shock, a normal gradient in reservoir pressure is produced. The nose shock is approximated by a series of straight line segments. This model is depicted in Diagram 5.2.

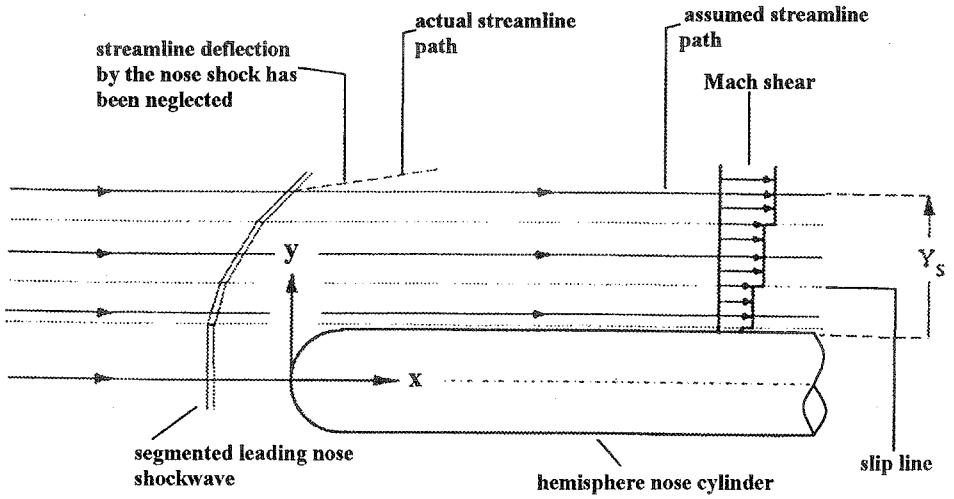

Diagram 5.2 Model for entropy-layer mach profile prediction

The shock shape on a hemisphere-cylinder body is given by Eq. 5.1a. By differentiating this equation, the shock angle may be calculated from:

$$\tan \vartheta_s = \frac{dr}{dx} = 0.3975 C_{D_n}^{1/4} \left(\frac{d}{x}\right)^{1/2} \tag{5.1v}$$

The reservoir pressure downstream of an oblique shock for γ=1.4 is[157]:

$$\left[\frac{p_{01}}{p_\infty}\right]_{y=r} = \left(\frac{6}{7M_\infty^2 \sin^2 \vartheta_s - 1}\right)^{\frac{5}{2}} \left(\frac{6M_\infty^2 \sin^2 \vartheta_s (M_\infty^2 + 5)}{5(M_\infty^2 \sin^2 \vartheta_s + 5)}\right)^{\frac{7}{2}} \tag{5.1w}$$

The conditions along a streamline downstream of the nose shock are isentropic and hence the reservoir pressure along a streamline passing the shock facet is constant. Therefore, Eq. 5.1w gives the reservoir pressure distribution within the entropy layer. The local Mach number is a function of the local reservoir and static pressure. The experimental local static pressure ratio, i.e. $p/p_\infty \cong 0.66$. Fig. 5.7 shows the predicted entropy-layer Mach profile at a location along the cylinder body which corresponds to the hingeline of the hemisphere-cylinder-flare body.

5.3 Sharp Cone-Cylinder Correlations

5.3.1 Flowfield about a Sharp Cone-Cylinder Body

Fig. 5.8a shows the flow structure over a sharp cone-cylinder body and the streamline pattern. A streamline past the sharp cone nose undergoes an outward deflection when it crosses the shock and then a further gradual deflection as it becomes asymptotic to the body. Because of the presence of the conical nose shock the flow will be homentropic upstream of the shock at the free-stream value and it will be homentropic between the shock and the body with a larger value of entropy because the flow undergoes an entropy jump across the shock. Therefore every streamline undergoes the same entropy jump across the nose shock.

The flow is expanded around the cone-cylinder junction through an expansion fan there. The schlieren study, Fig. 5.8b, shows that the expansion fan at the cone-cylinder junction interacts with the nose shock. The point at which influence is felt can be identified as the position at which the straight conical shock begins to curve. The nose shock angle,

measured from the schlieren photographs is about 13°, which agrees well with the tabulated theoretical value from Brower[158] of 12.93°.

5.3.2 Pressure Distribution Estimation

For convenience the pressure along the sharp cone nose has been predicted using Schwartz[177] equation:

$$C_{p_c} = 2\exp(z)\sin^2 \vartheta_c \tag{5.2a}$$

where:

$$z=0.18145-0.20923y+0.09092y^2+0.006876y^3-0.0062225y^4-0.000971y^5 \tag{5.2b}$$

$$y=\ln(\beta\sin\vartheta_c) \tag{5.2c}$$

$$\beta = \sqrt{M_\infty^2 - 1} \tag{5.2d}$$

Schwartz's correlation offers an excellent agreement with the exact numerical solutions of Sims[178]. The average error of this method is 0.38%. Eq. 5.2a predicts a pressure ratio, $p_c/p_\infty=4.201$ or $C_{pc}\cong0.068$ along the 10° half-angle sharp cone nose. The cone Mach number, M_c, is 6.43 and it was calculated by interpolation using Brower's tables for compressible flow[158]. NACA 1135[157] gives $M_c=6.37$.

A local Prandtl-Meyer expansion was assumed to take place at the cone-cylinder junction through an angle equal to the cone half angle. The assumption is made that the pressure thus obtained will remain constant along the entire length of the cylindrical body. This assumes that the reflected waves from the shock are weak, Fig. 5.8a. The analysis shows that the flow expands isentropicaly to a Mach number, $M_2=8.55$ and a pressure ratio, $p_2/p_\infty=0.68$ (this result gives a negative pressure coefficient). The flow overexpands around the junction and the shoulder pressure is less than the free-stream. This is also evident from the experimental pressure measurements, Fig. 5.9. However, the experimental study displays pressure ratios after the junction, along the cylinder, lower than the predicted value. The pressure ratio along the cylinder body increases gradually with distance. Downstream, ahead of the hingeline location, the pressure ratios acquire values similar with the predicted value.

This discrepancy between theory and experiment is attributed to the boundary layer, which, in effect, changes the geometric shape of the body. Thus instead of experiencing the theoretical *instantaneous* expansion at the corner, the flow undergoes a comparatively gradual expansion which originates slightly ahead of the geometric corner and is completed at a point considerably downstream from it. If the cylinder was very long the pressure would have approached the free-stream pressure asymptotically. Rasmussen[161] quotes that for values of K_{ϑ_s} ($=M_\infty \vartheta_s$, ϑ_s in radians) less than 3.6 for a cone cylinder combination, the pressure coefficient (as predicted by the Prandtl-Meyer expansion) at the shoulder is negative. For the present investigation, K_{ϑ_s} is equal to 1.43 which agrees with the above discussion. Computational studies by Hughson et al[178] on a cone cylinder body of 10° half-angle at a freestream Mach number of 6.86 predicted the phenomenon of pressure drop ($p/p_\infty<1$) across the Pradtl-Meyer expansion at the nose-cylinder juncture. They used the code EAGLE[180] (a viscous calculation) which predicted pressure ratio values as low as 0.4 near the junction.

5.4 Boundary-Layer Thickness Estimation Methods

The pressure distributions along the cylinder-flare body (to be presented later in the chapter) were found to exhibit qualitative similarities with the two dimensional results of Kumar[76] and Elfstrom[37]. To get a rough estimate of the boundary-layer thickness along the cylinder-flare body under laminar and turbulent conditions, the correlations which are applicable to flat plates are used.

Method A

Bertram et al[181] give the displacement thickness for a compressible laminar boundary layer over a sharp leading edge flat plate, in a region of varying pressure gradient, as:

$$\frac{\delta^*}{x}\sqrt{Re_{\infty x}} \approx 0.865\left[\frac{T_w}{T_r}+0.38\right](\gamma-1)M_\infty^2\sqrt{\frac{p_\infty}{p}} \qquad (5.2e)$$

Stollery[182] gives the ratio of the displacement to boundary layer thickness as:

$$\frac{\delta^*}{\delta} = 1-\frac{n+2}{(1+n)+\left[1+\frac{\gamma-1}{2}M_\infty^2\right]\left[\frac{T_r}{T_o}+\left(\frac{n+2}{n}\right)\frac{T_w}{T_o}\right]} \qquad (5.2f)$$

$$\frac{T_r}{T_\infty} = 1 + r_f \frac{\gamma - 1}{2} M_\infty^2 \qquad (5.2g)$$

where $r_f=P_r^{1/2}$ for laminar boundary layers and $r_f=P_r^{1/3}$ for turbulent boundary layers (P_r=0.72 for air), p/p_∞ is the experimental local pressure ratio, n is the index in the velocity profile, $u/u_\infty=(y/\delta)^n$. n=1/2 for laminar boundary layers and n=1/5 for turbulent boundary layers.

By inputting the appropriate values for laminar conditions into the above equations, the estimated boundary layer thickness at the hingeline of the sharp cone-cylinder-flare body is 2.92 mm. The schlieren pictures give a value of about 3 mm. Pitot pressure traverses by Needham[34] have shown that the outer edge of dark line in the schlieren pictures is very close to the outer edge of the boundary layer such that it can be taken as a measure of the boundary layer thickness. Eq. 5.2e shows that the increase in pressure on the flare compresses and thus reduces the local boundary layer thickness. This decrease is mainly because of the compression of the streamtubes in the outer supersonic portion of the boundary layer.

Method B

Popinski and Ehrlich[18] suggest the following equations for estimation of laminar boundary layer thickness:

1.For blunt leading edge:

$$\delta = \frac{5.2}{\sqrt{\frac{p}{p_\infty}}} \sqrt{\frac{d_n x}{Re^*_{\infty d_n}}} \qquad (5.2h)$$

2.For sharp leading edge:

$$\delta = \frac{5.2x}{\sqrt{\frac{p}{p_\infty} Re^*_{\infty x}}} \qquad (5.2i)$$

where

$$\frac{Re^*_\infty}{x} \approx \frac{Re_\infty}{x} \left[\frac{T_\infty}{T^*}\right]^{1.76} \qquad (5.2j)$$

(Eckert[183] reference temperature ratio) $$\frac{T^*}{T_\infty} = 0.28 + 0.5\frac{T_w}{T_\infty} + 0.22\frac{T_{aw}}{T_\infty} \qquad (5.2k)$$

$$\frac{T_{aw}}{T_\infty} = 1 + \frac{\gamma - 1}{2} M_\infty^2 r_f \tag{5.2l}$$

By inputting the appropriate values for laminar conditions into the above equations, the estimated laminar boundary layer thicknesses at the hingeline of the sharp cone and hemisphere-cylinder-flare body are 3.35 mm and 3.53 mm respectively. The boundary layer thickness for turbulent flow is given by[18]:

$$\delta = \frac{0.154x}{\left[Re_{\infty x} \left(\frac{T_\infty}{T^*} \right)^{1.67} \right]^{1/7}} \tag{5.2m}$$

By inputting the appropriate values for turbulent conditions into the above equation, the estimated turbulent boundary layer thickness at the hingeline of the sharp cone-cylinder-flare body is 5.71 mm. The schlieren pictures give a mean value of about 5 mm.

Method C

Creager[184] suggests the following equation for estimation of laminar boundary thickness on flat plate with blunt leading edge:

$$\frac{\delta}{d} \sqrt{Re_{\infty d}} = \left[\frac{1.73}{M_\infty^2} \left(\frac{T_w}{T_\infty} \right) + 0.332(\gamma - 1) + \frac{4.27}{M_\infty^2} \right] M_\infty^2 \sqrt{C} \sqrt{\frac{x}{d}} \tag{5.2n}$$

By substituting the appropriate values (corresponding to the hemisphere-cylinder body) and assuming C≅1 the estimated laminar boundary layer thickness at the hingeline is 2.49 mm.

Method D

Stollery[182] give the displacement thickness for a compressible turbulent boundary layer over a flat plate as:

$$\frac{M_\infty \delta^*}{x} = 0.051 \frac{\left(1 + 1.3 \frac{T_w}{T_0} \right)}{\left(1 + 2.5 \frac{T_w}{T_0} \right)^{3/5}} \left\{ \frac{M_\infty^9}{Re_{\infty x}} \right\} \tag{5.2o}$$

By inputting the appropriate values into Eqs. 5.2o and f and assuming C≅1 and a velocity profile index, n=1/5, the estimated turbulent boundary layer thickness at the hingeline of the sharp cone-cylinder body is 3.44 mm.

It is impossible to measure the boundary-layer thickness for the hemisphere-cylinder body under laminar and turbulent conditions from the schlieren pictures. This is because the highly curved shock wave produces strong density gradients throughout the entire flowfield that obscure the density gradients in the boundary layer, thus making the identification of the boundary layer edge very difficult. For the same reason it is impossible to clearly identify the flow separation regions near the cylinder-flare junction from schlieren pictures (as will be shown later).

Generally, the methods quoted for boundary layer thickness estimation overpredict the experimental deduced thicknesses (for the cases it was possible to measure the boundary layer thickness). The main reason is that they are applicable to two dimensional configurations. The differences between flows past an axisymmetric and two-dimensional configuration, i.e. a cylinder body and a flat plate are because the cylinder body demonstrates a three-dimensional relief effect. It presents less of an overall disturbance to the flow because the flow can pass around the cylinder body on all sides, whereas the flow is restricted to only upward and downward directions for the flat plate. The experimental and estimated boundary layer thickness values are tabulated below:

	Experiment	*Method A*	*Method B*	*Method C*	*Method D*
sharp-cone-cylinder body (laminar case)	**3 mm**	**2.92 mm**	**3.35 mm**		
sharp-cone-cylinder body (turbulent case)	**5 mm**		**5.71 mm**		**3.44 mm**
hemisphere-cylinder body (laminar case)			**3.53 mm**	**2.49 mm**	
hemisphere-cylinder body (turbulent case)					

5.5 The Effect of Mach-Shear and Area-Change on Flare Pressure

The inviscid flow structure over a hemisphere-cylinder-flare combination is shown in Fig. 5.10. The hemisphere nose generates a thick entropy layer which modifies the flow associated with the flare "submerged" within it.

According to Hayes and Probstein[185], the presence of Mach shear and its interaction with an incident compression wave or shock causes a series of reflected waves. This is

sketched in Fig. 5.11a. The ratio of the pressure rise across a reflected wave to that across the incident wave is:

$$\Re_v = \frac{\Gamma_2 - \Gamma_1}{\Gamma_2 + \Gamma_1} = \frac{p_c - p_b}{p_b - p_a} \tag{5.2p}$$

where the quantity Γ is defined as:

$$\Gamma = \frac{\gamma M^2}{\sqrt{M^2 - 1}} \tag{5.2q}$$

Hayes and Probstein used the method of characteristics, with the condition that the pressure and flow deflection on both sides of the slip line to be constant, to derive the above result. When the shear layer is very weak, $M_2 \rightarrow M_1$ and $\Gamma_2 \rightarrow \Gamma_1$, with the result that the strength of the reflected wave tends to zero. For a strong shear layer, $M_2 >> M_1$ and $\Gamma_2 >> \Gamma_1$, then $\Re \cong 1$. In such a case, the change in pressure across the reflected wave is equal to the change in pressure across the incident wave, so that the wave reflects from the shear layer as if from a solid wall. Fig. 5.11b shows the variation of the reflected coefficient with the strength of the Mach shear.

In the case of the body with a hemisphere nose, reflected and transmitted waves may be produced, when a flare-generated-shock crosses the entropy gradient from the curved bow shock, Diagram 5.3a.

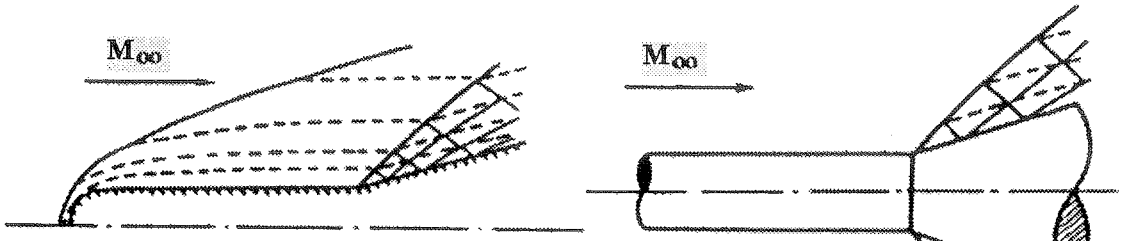

a) shock interaction with entropy gradient

b) "area-change" interaction

Diagram 5.3 Some types of wave interaction

The reflected waves will increase the pressure above the level immediately downstream of the flare shock. The examination of the entropy-layer Mach profile of Kuehn[9] shown in Fig. 5.12a reveals that the edge of the boundary layer has a value of $M_2/M_1=1.08$. Thus, the strength of reflection of any compression waves propagated through this

section of the entropy layer are negligible. From Fig. 5.12a at $y/\delta=1.8$, $M_2/M_1=1.13$. From Fig. 5.11b, this value of M_2/M_1 gives a reflection coefficient of 0.06 so that the reflected waves in the present experiments can be neglected. No further rise in pressure on the flare is visible in Fig. 5.12b.

Now considering the "area change" interaction shown in Diagram 5.3b, the pressure at the beginning of the flare (right in the corner) corresponds to the two-dimensional value appropriate to the angle of the flare. Moving downstream, away from the corner, the pressure will tend asymptotically to the appropriate conical value. This pressure change is due to reflected waves. These waves are generated from the shock interaction with the increase in flow area with distance from the axis[186].

5.6 Flare Pressure Distribution Estimation Methods

The method of Schwartz[177] discussed in section 5.3.2 is used to calculate the inviscid conical pressure ratio values on the flares. The locally two-dimensional values in the cylinder-flare junction have been estimated from wedge tables[157]. However, these techniques do not predict the premature rise of pressure ahead of the hingeline due to upstream viscous effects and the non-instantaneous pressure rise to the inviscid value due to the Mach number profile in the boundary layer.

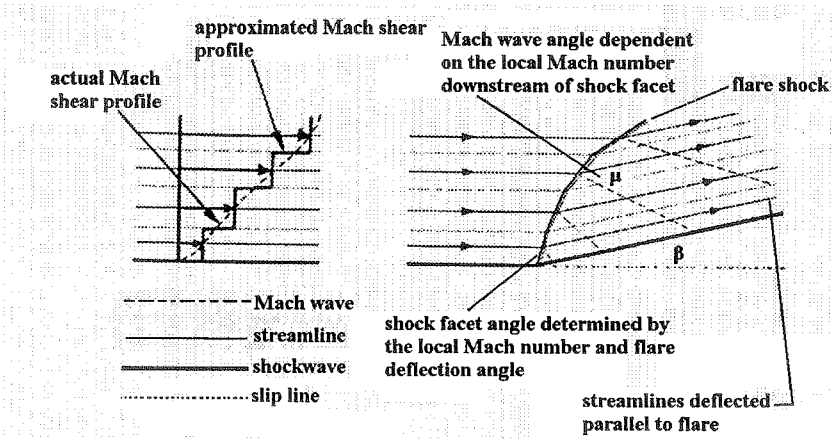

Diagram 5.4 Elfstrom's[37] model for viscous attached flow over the flare for both sharp and blunt nosed bodies

The method of characteristics could be used to calculate the effects of Mach shear interaction on the flare pressure distribution. However, this approach is very complex and numerically demanding, therefore it is necessary to devise another procedure. Diagram 5.4 shows Elfstrom's[37] model. The method is applicable to prediction of attached flow pressure distribution along the flare. The model assumes the flare shock at the juncture to be segmented in accordance to a Mach number profile and the flow to be two-dimensional at the corner. The facet angle at a particular height above the surface is determined by the requirement to turn the streamlines parallel to the flare to satisfy the no flow boundary conditions on the surface and the local upstream Mach number. The pressure disturbance is assumed to propagate down to the surface, downstream of the shock facet, along Mach lines. The Mach angle is determined by the local Mach number immediately downstream of the shock segment. There are no reflections from the wall. The resulting triangle defines a small region in which all properties are constant. The resulting wall static pressure distribution is then a series of step jumps, through which an average line is faired to give the final pressure distribution. This technique ignores the presence of the viscous region at the wall and assumes that the boundary layer acts like an inviscid rotational stream.

The analysis starts with an approximate boundary layer profile. Kuehn's[8,9] experimental Mach profiles, at a Mach number of 4.92, are assumed to represent the hingeline flowfield for the corresponding laminar body configurations of the present investigation. Kuehn's Mach profiles are shown in Fig. 5.12a.

For turbulent flow, a seventh power law velocity profile is also used. The corresponding Mach number profile is calculated from the linear Crocco relationship for the temperature distribution:

$$\frac{T}{T_\infty} = \frac{T_w}{T_\infty} + \left(\frac{T_r - T_w}{T_\infty}\right)\left(\frac{u}{u_\infty}\right) - \left(\frac{T_r - T_\infty}{T_\infty}\right)\left(\frac{u}{u_\infty}\right)^2 \qquad (5.2r)$$

where T_r/T_∞ is given by Eq. 5.2g then:

$$\frac{M}{M_e} = \frac{M}{M_\infty}\frac{M_\infty}{M_e} = \frac{u}{u_\infty}\sqrt{\frac{T_\infty}{T}}\frac{M_\infty}{M_e} \qquad (5.2s)$$

The resulting computed Mach number profile is shown in Fig. 5.13a. Fig. 5.13b shows the flow field construction. The above profiles are used as the input Mach number profiles for the technique. The input flow is stratified into layers as explained in Diagram 5.4. In hypersonic flow, the results should not be particularly sensitive to step size because the curvature of the M/M_e profile is generally low. The results are discussed later in the chapter together with the experimental measurements.

5.7 Sharp Cone-Cylinder-Flare Laminar Boundary Layer Studies

5.7.1 Sharp Cone-Cylinder Body

The oil-dot picture, Fig. 5.14, shows that the surface streamlines follow linear paths along the body starting from the apex of the cone. It is evident that the oil-dot response is decreasing towards the base of the cylinder. This is because the skin-friction along the surface is decreasing and the oil-dot technique is skin-friction dependent.

The liquid crystal measurements are shown in Fig. 5.15. The liquid crystal picture for the sharp cone-cylinder body under laminar conditions shows that the colour of the surface starts from a vivid green near the nose region (higher temperature) and progresses to a lighter green with tones of red (lower temperature). The liquid crystal picture for the body under turbulent conditions shows that the colour of the cylinder surface is everywhere vivid green.

The total length of the cone-cylinder body is approximately 24.4 cm which gives a Reynolds number based on the model length of 2.27×10^6. Due to the relatively high Mach number and the modest Reynolds number, the boundary layer on the surface of the body is laminar. This is supported by the liquid crystal pictures. The value for the onset of transition from the correlation shown in Fig. 2.6 is 3.75×10^6.

5.7.2 The Effect of Flare Deflection (Attached Flows)

An adverse pressure gradient is created due to the presence of a flare or any other compressive deflection of the inviscid flowfield. This pressure rise feeds upstream via a relatively thin subsonic portion of the boundary layer, referred to as the sublayer. The adverse pressure gradient causes a loss of momentum and a subsequent thickening of the sublayer some distance upstream of the agency responsible for the pressure rise. Within

the supersonic portion of the boundary layer, compression fans are generated. These fans deflect the local streamlines past the thickening sublayer. The fans induce a pressure rise which thickens the sublayer further. This mutual interaction process between the pressure rise and the thickening boundary layer continues until equilibrium is reached.

Compression fans also cause an increase in the local temperature and hence in the sound speed. Shockwave boundary layer interaction studies of Chapman et al[19] at a Mach number of 1.5 show evidence that the compression waves coalescing well *outside* the boundary layer to form an oblique shock wave. This is because, for supersonic flows, there is only a small increase in sound speed but the local Mach angles are relatively large. At hypersonic speeds, the compression waves coalesce rapidly and ultimately, within the boundary layer. This is shown schematically in Fig. 5.16. This is because at hypersonic speeds, the Mach number increases the temperature ratio (temperature thickens the boundary layer) and hence the sound speed across a compression fan and the Mach angle is relatively small (because of the high Mach number).

The experimental study did not encounter attached flow type interaction over the sharp cone-cylinder-flare body under laminar boundary layer conditions. As will be shown in the next sections, for all flare angles tested the flow over the sharp cone-cylinder-flare body under laminar boundary layer conditions showed evidence of separation ahead of the flare.

5.7.3 The Effect of Flare Deflection (Separated Flows)

An increase in the flare deflection angle increases the strength of the flare shockwave and this causes an increase in the local adverse pressure gradient. This increases the loss of momentum in the upstream interaction region. At a certain flare deflection angle the adverse pressure gradient reduces the wall velocity gradient and hence the wall skin friction to zero at the cylinder flare junction. This flare deflection is called the incipient separation flare deflection angle. The discussion of the condition is given in section 2.4. Increasing the flare deflection angle beyond the incipient separation angle causes the flow to separate with separation and reattachment points upstream and downstream of the junction. Holden's[79] skin friction measurements on flat plates, Fig. 5.17, show that in

well-separated flows, the skin friction is negative in a region between locations upstream and downstream of the hingeline.

Katzer[31] has shown computationally that in a well-separated interaction region, there is a significant increase in displacement thickness but little change in the associated momentum thickness. The recirculating fluid within the separation bubble moves slowly and possesses negligible momentum which causes the magnitude of the wall skin-friction in the separation region to be small. In entirely laminar interactions, the thickening of the boundary layer in the separated flow interaction region reduces the wall temperature gradient. This reduces the heat transfer within the separation region below the local sharp cone-cylinder level.

Both the separation and reattachment points are characterised by local shockwaves. This dual shock interaction structure differentiates separated flows from the single shock structure of attached flows. In the reattachment point region, the shear layer is turned parallel to the flare by the strong reattachment shockwave. The strength of this shock causes a large increase in the local pressure, with reattachment occurring near the point of maximum pressure gradient. On the flare, the compression from the reattachment shock regenerates the local velocity profile. In these regions, the flare skin friction and heat transfer distributions also increase even beyond their equivalent sharp cone-cylinder distributions[22].

Under the present test conditions, the flap deflection for incipient separation of a 2D flow, as deduced by the Needham and Stollery[25] criterion (section 2.4, Eq. 2.1) assuming $C \cong 1$, is 6.2°. Kumar[76] on experiments with flat plates under the same test conditions predicted an incipient separation angle of 6.6°. Fig. 5.18 shows that flare deflection causes a dual-shock structure which is characteristic of separated flow. It is difficult to see the 10° flare separation, because the separation region is very small and the flare angle is close to incipient separation angle. Promotion of separation is expected between 0° and 10° flare angles. Fig. 5.19a shows the cross-plot of Kuehn's[9] laminar incipient separation data. The lines have been extended to the right to include the higher range of Mach numbers. For a freestream Mach number of 8.2 and a Reynolds number based on

the laminar boundary layer thickness at the hingeline of 28000, Fig. 5.19a indicates a incipient separation angle of approximately 10.5°.

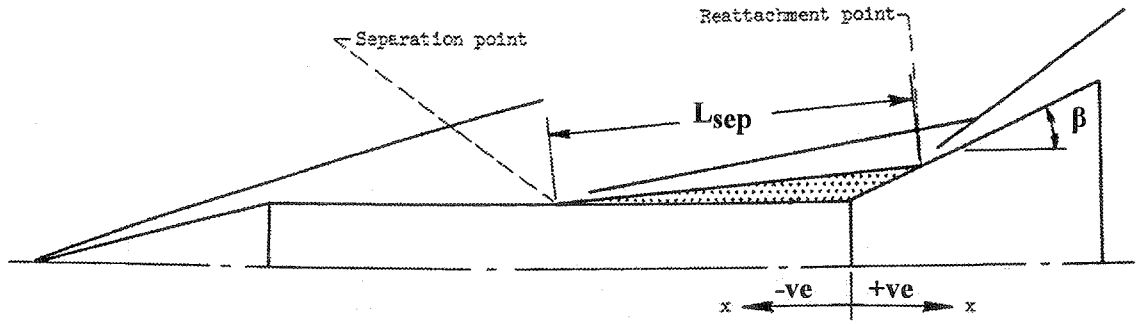

Diagram 5.5 Definition of geometry of the separated region

In the present tests longitudinal pressure distributions provided the primary evidence for the existence of separated flow. Separation of the boundary layer was associated with the presence a two-inflection points pressure distribution curve. This method was used throughout the present investigation both under laminar and turbulent boundary layer conditions. The oil-dot technique was used mainly to support the deductions from the pressure distributions. The first occurrence of separation detected by the oil-dot technique agrees with that determined from the longitudinal pressure distributions.

Schlieren pictures were also used to indicate the presence of separated regions but by themselves they are not conclusive. The variables defining the geometry of the separated region are shown in Diagram 5.5. The point of separation was taken as the point at which the boundary layer began to thicken because of separation. The reattachment point was taken as the intersection of the extension of the line that delineated the edge of the separation region.

The separation lengths, as deduced by the various experimental techniques of the present investigation, versus the flare angles are plotted in Fig. 5.19b. A best fit line is drawn which is extended to the left until it met the x-axis. This method indicates a value of incipient separation for the sharp cone-cylinder flare body of approximately 9.0°. It is evident that the incipient separation angle for the flared body is higher than the predicted two-dimensional value of 6.2° and experimental value of 6.6°. This is because of the three-dimensional relief effect associated with axisymmetric bodies (discussed in section 5.4) which causes the thickness of the boundary layer along the cylinder body to be

smaller than the equivalent flat plate boundary layer. The incipient separation angle as predicted by Kuehn[9] overpredicts the incipient separation angle of the present investigation. However, Kuehn's work also shows the trend that the axisymmetric flared body exhibits a higher incipient separation angle than the corresponding two-dimensional case.

The effect of flare deflection on the separation of laminar and transitional boundary layers was studied by Gray[16] at a Mach number of 7 over a range of Reynolds numbers. The tests performed under *transitional conditions* showed an *upstream movement* of reattachment point with increasing flare angle. The tests performed under *fully laminar conditions* showed a *downstream movement* of the reattachment point. In the present study the increased pressure rise associated with flare deflection causes a progressive upstream movement in the location of separation, as shown in Figs. 5.18 and 5.20, and a small *downstream movement* in reattachment. This behaviour of reattachment suggests the boundary layer over the flares at all deflection angles is laminar.

Fig. 5.18 shows a significant thinning of the boundary layer over the flare as the deflection angle increases. This is because the impingement of the shear layer on the flare and the subsequent formation of a reattachment shock causes the pressure to increase over the flare and this pressure rise compresses the boundary layer, Fig. 5.20. The figure also shows that for separated flow a pressure plateau develops upstream of the cylinder flare junction.

The close examination of the liquid crystal photos, Fig. 5.20b, shows that the colour of the surface is vivid green (higher temperature) around the cone-cylinder shoulder and is getting lighter (lower temperature) towards the cylinder-flare junction. Just before the junction the surface colour starts to become vivid green again. This effect suggests that the heat transfer rates drop below the sharp cone cylinder values towards the cylinder-flare corner and then rise again just before the corner is reached. This effect is due to the laminar nature of the boundary layer. However, the liquid crystal pictures do not give clear evidence of separation along the cylinder body but they indicate the level of heat transfer along the model. After the corner the liquid crystals change colour rapidly from vivid green to dark blue and eventually they become colourless. This is an indication of

high heat transfer rates along the flare body. The increase in heat transfer rates on the flare is a direct consequence of the increased local compression of the boundary layer.

Close examination of all experimental results of the present case do not give any conclusive evidence about transition on the flare. It is believed that due to the unstable nature of the separated shear layer, transition is occurring well downstream of the interaction region for flare angles up to 30°. It is conjectured that the 45° flare exhibits transition somewhere between the separation and reattachment points. This is deduced by examining the flowfield structure of the 45° flare, Fig. 5.18, which resembles the transitional flowfield structure observed by Ferguson et al[22] on experiments with a 15° half-angle cone-cylinder with a 56° flare under laminar initial conditions.

Fig. 5.20 also shows the results of the oil-dot studies. The oil-dot technique manage to successfully capture the surface flow patterns and lines of separation and reattachment. Fig. 5.19b shows that the separation lengths deduced by the pressure measurements and oil-dot and schlieren techniques agree reasonably well with each other within a variation range ±1.5%. This variation reinforces the argument that the accurate detection of incipient separation depends on the method of detection used. For the case of the 45° flare, Fig. 5.20d, the oil-dot technique manages to capture the reverse flow region at the corner. Diagram 5.6 shows the typical schematic streamline pattern along the surface of the model with separated flow at the cylinder flare junction.

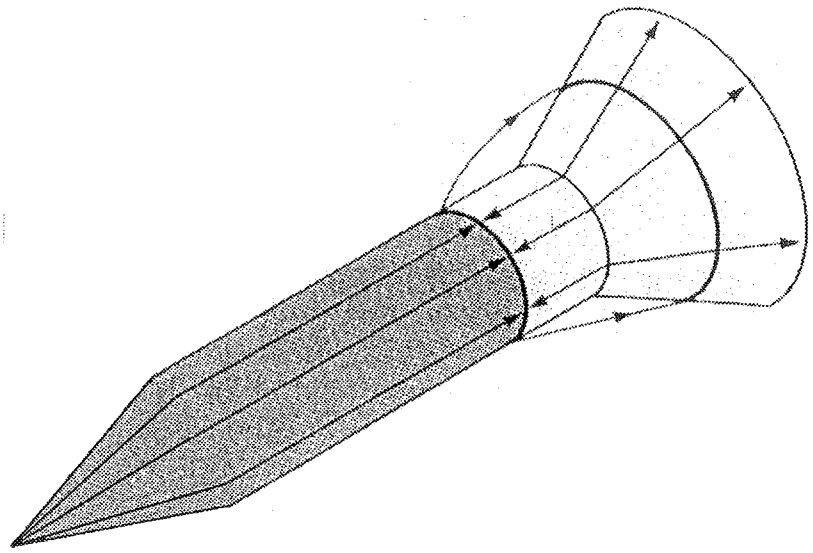

Diagram 5.6 Schematic streamline pattern of separated flow

5.8 Hemisphere-Cylinder-Flare Laminar Boundary Layer Studies

5.8.1 Hemisphere-Cone-Cylinder Body

Fig. 5.21 makes a direct comparison of the pressure distributions along the cylinder body with sharp cone and hemisphere noses under laminar and turbulent boundary layer conditions. The strong bow shock ahead the hemisphere nose (discussed in section 5.2.3) creates higher pressure levels along the cylinder body than the sharp cone nose. Eventually all pressure distributions acquire the same level of value ahead the cylinder-flare corner location.

The oil-dot picture, Fig. 5.22 shows that the surface streamlines follow linear paths along the body starting from the nose. It is evident that the oil-dot response is decreasing towards the base of the cylinder. This is because the skin-friction along the surface is decreasing (see section 5.7.1) and the oil-dot technique is skin-friction dependent. The liquid crystal pictures, see Fig. 5.23, show that the hemisphere nose body exhibits higher heat transfer coefficients near the nose region than the sharp cone nose body.

The total length of the hemisphere-cylinder body is 20.4 cm which gives a Reynolds number based on the model length of 1.9×10^6. Due to the relatively high Mach number and the moderate Reynolds number, the boundary layer on the surface of the body is laminar. This is consistent with the data correlated in Fig. 2.6.

5.8.2 The Effect of Bluntness (Attached Flows)

As was discussed in sections 5.2.3 and 5.2.5 the nose bluntness significantly alters the Mach number profile over the cylinder body. Fig. 5.24 shows the effects of bluntness on the flare shock structure. For supersonic flows over sharp cone-cylinder bodies the small Mach number gradient between the sublayer and the edge of the boundary layer results in a small curvature of the compression wave within the boundary layer. Due to the absence of Mach number gradients outside the boundary layer, the compression waves become straight. Because of the low freestream Mach number in supersonic flows ("high" Mach angle), a well spread out compression region is produced. This can be seen in Kuehn's[8] experimental pictures at Mach numbers 2 to 4. At hypersonic speeds, the compression waves generated by the flare interaction process become highly swept (due to the lower Mach angles) and lie close to the edge of the boundary layer. The absence of any Mach

number gradients outside the boundary layer produces a straight flare shock in the inviscid flow outside the boundary layer.

For flows over cylindrical bodies with nose bluntness, the boundary layer edge Mach number is reduced from the hypersonic freestream value to supersonic values. This effect was discussed in section 5.2.4. The reduced local Mach number causes a reduction in the Mach number gradients in the outer portion of the boundary layer and thus it reduces the sweep of the compression fans within the boundary layer. This causes the boundary layer edge shock structure to look similar to that of a supersonic rather than a hypersonic flow. Furthermore, the Mach number gradients in the entropy layer cause a curvature of the compression fans within the entropy layer. Eventually, the compression waves coalesce to form a shockwave well away from the surface.

The effect of the hemisphere nose on the flare shock structure for the 10^{o} flare is shown in Fig. 5.25. The angle of the flare shock increases above that on the sharp cone nose configuration. The increase in the shock angle is due to the reduced Mach number within the entropy layer.

The pressure distribution in the flare interaction region for the 10^{o} flare configuration with a hemisphere nose is shown in Fig. 5.26. The important observation is that the sharp cone nose configuration (see Fig. 5.20a) shows evidence of separation upstream of the cylinder-flare junction, while the pressure distribution of the hemisphere-nose body upstream of the interaction region does not (evidence of attached flow along the hemisphere nose body is also shown in the oil-dot pictures, Fig. 5.27). The pressure distribution for the hemisphere nose body shows an increase in pressure upstream of the hingeline. The increase is due to the pressure rise associated with the thickening of the sublayer. This sublayer is much thicker due to the reduced Mach numbers in the entropy layer.

From Schwartz's[177] equation (Eq. 5.2a, section 5.3.2) the pressure ratio across the flare shock is calculated using the local Mach number at the hingeline boundary layer. It was shown in section 5.2.4 that the loss of reservoir pressure across the normal nose shock reduces the hingeline Mach number on the hemisphere configuration to around M_{eHL}~4. Assuming the flare on the blunt configuration to be submerged in an "effective" supersonic freestream at the hingeline Mach number, the flare shock p_3/p_2 is 1.87. From

blast wave theory given in section 5.2.1, the hingeline pressure ratio on the hemisphere nose configuration is p_2/p_∞=0.91. Thus the flare pressure ratio for the hemisphere nose body is 1.7 (see Fig. 5.26). The reduction in the flare pressure ratio p_3/p_2 due to bluntness (from 4.2, sharp cone nose, to 1.87, hemisphere nose) occurs due to the reduced hingeline Mach number resulting from loss of reservoir pressure across the bow shock wave. This decreases the pressure ratio p_3/p_2 across the flare shock and thus decreases the overall pressure realised on the flare. Towards the back of the flare the pressure is constant. This means for this configuration the effects of the entropy layer Mach shear interaction (see section 5.6) on the flare pressure distribution are negligible. This is due to the relative weakness of the flare shock.

The liquid crystal comparison, shown in Fig. 5.28, shows that for both blunt and sharp configurations, there is a reduction in heat transfer levels in the upstream interaction region. This is due to the laminar state of their respective cylinder body boundary layers. The comparison of liquid crystal pictures in Fig. 5.28 shows that the compression associated with the flare shock increases the heat transfer for the flare on both configurations. However, the heat transfer levels along the flare on the hemisphere nose configuration are well below those on the sharp cone nose configuration. The flare heat transfer rate is proportional to the local pressure ratio[36]. The reduction in the flare pressure ratio for the hemisphere configuration (due to the lower hingeline Mach number) is responsible for the observed reduction in flare heat transfer levels for the blunt nosed configuration.

5.8.3 The Effect of Bluntness (Separated Flows)

The pressure distributions, oil-dot and liquid crystal pictures for the 20°, 30° and 45° flare configuration are shown in Fig. 5.29. The corresponding pressure distributions comparisons with the sharp-cone case are shown in Fig. 5.30. The comparison shows that the final pressure realised on the flare is significantly decreased by nose bluntness and is well below those for the sharp cone configuration. The similarity in Fig. 5.29a between the predicted conical values (based on the model shown in Fig. 5.10, see also section 5.6) and the measured flare pressure ratios immediately downstream of reattachment suggests that the decrease in the flare pressure ratio due to bluntness is due

to the reduction in cylinder-flare corner Mach number. This reduction is because of the loss of reservoir pressure across the bow shock. The pressure distributions on the hemisphere nose configuration show a secondary increase in pressure following reattachment. This is due to the Mach shear interaction effect which is discussed later in the chapter.

The schlieren, oil-dot and liquid crystal pictures for the 20°, 30° and 45° flare cases for the two nose configurations are shown in Figs. 5.31, 5.32 and 5.33 respectively. The dual shock structure of the sharp nose configurations indicates the flow to be well separated, Fig. 5.31. Separation is confirmed by the presence of a plateau in the pressure between the separation and reattachment points (see Fig. 5.30). For the same flare deflection angles, the schlieren pictures for the hemisphere nose body are inconclusive because the strong entropy layer obscures the boundary layer and hence it makes it difficult to see where separation occurs.

The liquid crystal pictures, shown in Fig. 5.33, show that the laminar structure of the corresponding cylinder boundary layers results in a decrease in heat transfer in the upstream interaction region. The flare boundary layer is fully laminar. This is because the reattachment line is moving downstream with increasing flare angle, which is a characteristic of fully laminar interactions (see Figs. 5.29, 5.30 and 5.32). The significant decrease in flare heat transfer due to bluntness (see liquid crystal pictures) is due to the reduction in the flare pressure ratio (due to the lower hingeline Mach number).

The pressure distributions and oil-dot pictures for the 10°, 20°, 30° and 45° flare cases for the two nose configurations, Figs. 5.26, 5.27, 5.30 and 5.32, show that the hemisphere nose delays separation ahead of the hingeline and for the 10° blunt nose case the flow is completely attached. The suppression of separation is characterised by the presence of a single shock at the hingeline which is evident in the schlieren photographs for the case of 10° flare, see Fig. 5.25, and it is confirmed by the absence of a pressure plateau in the corresponding pressure distribution, (Fig. 5.26), and the pattern of the oil-dots, Fig. 5.27. The flare pressure ratio is critical to boundary separation on bluntness dominated configurations. For the 10° flare case, the reduction in the flare pressure ratio by increasing nose bluntness is responsible for the suppression of separation.

The pressure distributions, oil-dot pictures for the 20°, 30° and 45° flare cases for the two nose configurations, Figs. 5.30 and 5.32, show that the hemisphere nose causes later reattachment. In other words, nose bluntness "pushes" the reattachment line to the back of the flare with increasing deflection angles. The downstream movement of the reattachment line is slightly less than the downstream movement of the separation line due to bluntness. The combined effect of nose bluntness is a very small decrease of the overall extent of the separated flow region.

5.8.4 The Effect of Hemisphere Nose on Incipient Separation

Figs. 5.26, 5.27, 5.30 and 5.32 show that the effect of the hemisphere nose is a small reduction of the length of separated flow and suppression of separation for the 10° flare case. Therefore, bluntness must influence the incipient separation behaviour of control surfaces submerged within the entropy layer flow field. The separated flow lengths for the sharp cone and hemisphere noses are plotted in Fig. 5.34. The incipient separation flare angle is defined as the greatest flare deflection angle for which the separated flow length is zero. This is derived from the separated flow length curves by extrapolation to the x-axis, as shown in Fig. 5.34. The separation lengths for every flare case are the experimental lengths deduced by different experimental methods. The extrapolation shows that the hemisphere nose configuration causes a small increase of the incipient separation flare angle from 9° to 10.8°.

5.8.5 Mach Shear Interaction Effect

Fig. 5.29 shows that for the hemisphere nose body, the reattachment pressure rise on the flare is followed by a secondary compression. This effect is more pronounced for the 20°, 30° and 45° flares. A similar effect was observed in the large bluntness measurements of Kumar[76]. According to the discussion in section 5.5, this secondary rise is associated with the interaction of the flare shock with the Mach number gradient associated with the entropy layer. Fig. 5.35b shows the comparison of the predicted pressure distribution from the Mach shear interaction model described in section 5.6 with the experimental data from the 20° flare case. The Mach shear profile at the hingeline has been estimated by using the predicted entropy-layer Mach profile (M_∞=8.2), see Fig. 5.7. This model is

unable to predict separation but the calculated growth of pressure over the flare is similar to the measured pressure distribution. Similarly, Figs. 5.35a and c show the comparisons for the 10°, 30° flares. The overall agreement confirms the Mach shear interaction effect as the cause of the secondary pressure rise on the flare.

5.9 Sharp Cone-Cylinder-Flare Turbulent Boundary Layer Studies

5.9.1 Sharp Cone-Cylinder Body

The general flowfield characteristics are the same as those discussed in section 5.3. The effect of utilising vortex generators to force the incoming boundary layer into transition was investigated by Coleman[65]. He found that vortex generators are an effective means of forcing transition. Gentry and Jacobi[187] have shown that there are two important parameters influencing heat transfer behaviour using vortex generators: the strength of the vortex and its location relative to the boundary layer. The desired situation is a strong vortex located near the edge of the boundary layer. In the present investigation this was achieved by measuring first the laminar boundary layer thickness along the cylinder from the schlieren pictures (where it was possible) and placing them in a location along the cylinder where the vortex generator edges are protuding several millimeters beyond the boundary layer edge.

A schlieren picture of the sharp cone-cylinder body with vortex generators is shown in Fig. 5.36. The comparison with Fig. 5.8b shows that the thickness of the boundary layer is greater with the vortex generators. The oil-dot and liquid crystal pictures with and without vortex generators are shown in Figs. 5.37 and 5.38. It is evident that the vortex generators produce strong vortices which travel downstream on the cylinder. These vortex filaments can be seen up to approximately 30% of the cylinder length.

The disappearance of these vortices is due to the combination of two effects. The breakdown of these vortices is promoted by surface skin friction and as the vortex element travels downstream its core diameter is increased and its strength is reduced by the phenomena of turbulent dissipation of kinetic energy[187]. Fig. 5.39 shows the process of vortex development and final breakdown. It is conjectured, that the vortices may still exist up to the cylinder flare junction and influence the boundary layer characteristics in

the interaction region and the liquid crystals and oil-dot technique are not sensitive enough to capture them.

Certainly, the development of the turbulent boundary layer due to forced transition is not the same as that which would be expected if the transition was natural. A naturally turbulent boundary layer does not develop strong vortices. Coleman[65] performed tests on flat plates with forced and natural boundary layers at a freestream Mach number of 9. He found that the boundary layer thickness is smaller in the natural developed turbulent boundary layer.

The liquid crystal pictures with and without vortex generators, shown in Fig. 5.38, show that the liquid crystal colour for the body with vortex generators is vivid green over the entire cylinder length. The liquid crystal colour for the body without vortex generators is becoming less vivid and near the flare junction is light green. The latter observation confirms the fact that in laminar flow the heat transfer rate is lower than for turbulent flow.

5.9.2 Effect of Flare Angle Variation (Cone-Cylinder-Flare with Vortex Generators)

All the experimental results of the sharp nosed configuration with flares are shown in Fig. 5.40. Fig. 5.41 is a composite of all pressure distributions. From these figures is obvious that for attached flow (flare angles 10° and 20°) the upstream influence is limited to less than one boundary layer thickness. The flare shock for the attached flow cases, is seen to originate just in front of the junction. This is due to thickening of the subsonic portion of the boundary layer. The final pressure on the flare is very close to the conical value.

For flare angles 30° and 45°, the upstream influence increases with deflection angle and develops a plateau of increasing length, indicative of separated flow. This is because of the increasing adverse pressure gradient due to the increase of the flare deflection angle. An estimation of separation and reattachment points was obtained by examining schlieren and oil-dot pictures and the pressure distributions when the boundary layer was separated. These points were chosen at the positions where the boundary layer physically appeared to separate and reattach. The liquid crystals offer inconclusive results but they give qualitative information so far as the heat transfer is concerned. There is no clear

evidence from the schlieren pictures, shown in Fig. 5.40, until the 45° flare case when two shockwaves can be seen near the flare junction. Close examination of the schlieren photograph of a flare angle of 30° shows a very small separation shock in the junction region. This observation is supported by the oil-dot pictures and pressure measurements, which confirm that the flow has separated at 30° deflection angle.

The liquid crystal pictures, shown in Fig. 5.40, show that the heat transfer levels along the cylinder body up to the 30° flare case is the same as that of the cylinder alone. For the 45° flare case, there is an increase in heat transfer upstream of the cylinder-flare junction, because of the separation region. It is known that in contrast to laminar flow, the heat transfer in the separated region for turbulent flows increases. The same behaviour in heat transfer rates in the separation region was found by Elfstrom[37] in experiments with flat plates with compression corners. For all deflection angle cases, the heat transfer on the flare is much higher than that on the cylinder body. This is due to compression from the flare shock which envelops the flare body.

A pressure overshoot of increasing magnitude forms on the flare. This overshoot in pressure appears after reattachment. This feature usually characterises separated flow and Elfstrom[37] used it as a criterion of incipient separation in his experiments with compression corners on a flat plate. However, in the present pressure distributions this overshoot also appears in the attached 20° flare case and to a very small extent in the 10° flare case, Fig. 5.40 and 5.41. This makes it unreliable as a tool for incipient separation detection. This overshoot is attributed to the locally two-dimensional pressure rise at the corner followed by a gradual decay to the cone value further downstream on the flare. The same overshoot can be seen in the laminar pressure distributions of the present configuration shown in Figs. 5.20. For separated flow this overshoot is due to the intersection of the separation and reattachment shocks and this results in a single shock together with a reflected expansion fan[188], which brings the high pressure back towards the inviscid conical pressure value.

Fig. 5.42 shows a suggested model for the separated region of the hypersonic turbulent boundary layer at the flare junction.

5.9.3 The Effect of Boundary Layer Turbulence on Incipient Separation

The first most important observation from the comparison of the experimental results for the sharp cone-cylinder-flare with and without vortex generators, shown in Figs. 5.18, 5.20 and 5.40, is that boundary layer turbulence delays separation. This is evident from the schlieren and oil-dot pictures and the pressure distributions. The turbulent boundary layer suppresses separation along the cylinder body in the 10° and 20° flare cases. In the extreme case of the 45° flare, the presence of turbulent boundary layer causes separation to occur at approximately 2.4 cylinder diameters from the junction while in the laminar boundary layer case separation occurs just after the sharp cone-cylinder junction. The delay in separation is because turbulent boundary layers are more energetic and hence more resistant to adverse pressure gradients. The liquid crystal pictures, shown in Figs. 5.20, 5.40, show that heat transfer levels are higher along the flares for the turbulent boundary layer and the whole flare body exhibits high heat transfer from the junction to the trailing edge. Incipient separation was determined by looking for a "plateau" in the pressure distributions and by plotting the separation length as measured from the schlieren and oil-dot pictures against flare angle and extrapolating to zero separation length, Fig. 5.43. The agreement between the incipient separation methods used for detection is of the order of a degree. Fig. 5.43 also shows the comparison with results from the sharp cone-cylinder-flare body under laminar conditions. The incipient separation angle for the turbulent boundary layer configuration is approximately 28°, while the incipient separation angle for the laminar boundary layer configuration is approximately 9°. Hence from the above discussion it is evident that the most important difference between the laminar and turbulent boundary layer interaction is that the turbulent boundary layer can withstand much greater flare angles than the laminar case before separation occurs.

The comparison of the present turbulent incipient separation angle with Elfstrom's[37] results, who performed experiments under similar test conditions with compression corners, indicates a lower incipient angle of approximately 3°. This contradicts the findings of Kuehn[8,9] and Coleman[65] who found that axisymmetric bodies exhibit higher incipient separation angles than the two-dimensional cases. However, the conclusion of

the present investigation, as far as the incipient angle, is in agreement with the results of Rose et al[40] who found that separation occurs in axially symmetric flows at lower pressure rises than would be expected for planar two-dimensional flows. It is believed that the contradiction with the findings of Kuehn[8,9] and Coleman[65] is because the determination of incipient separation is very sensitive to the detection method employed, as found by Spaid and Frishett[42]. The initial state of the turbulent boundary layer is also important. Kuehn and Coleman had forced transition in their experiments while Rose et al had free transition.

The oil-dot picture for the 20° flare case, (Fig. 5.40), shows that the oil-dots very near the junction of the cylinder-flare have not moved. If only the oil-dot technique was available for incipient angle detection the conclusion would have been that the 20° flare case shows some evidence of flow separation. However, the pressure measurements and schlieren pictures do not support this deduction. A possible explanation of the non-movement of the oil-dots near the juncture of the 20° flare case is that the oil-dot technique is skin-friction dependent and its response is insensitive to very small skin-friction values. This means that in reality the oil-dots stop responding just before the skin-friction drops to zero.

Another explanation of the no-motion of the oil-dots just before the junction of the cylinder-flare is the suggestion that before the unseparated flow develops to a fully steady separation, it acquires an intermittent separation state. Therefore this no-motion region detected by the oil-dot technique could correspond to the existence of a very small separation bubble at the junction. Such small scale separations were observed by Babinsky et al[44] from experiments using a cylinder-flare configuration and were predicted computationally by Edwards et al[45]. Kuehn[35] mentioned that these small separated regions do not perceptibly affect the wall pressure distribution.

The accuracy of each method used for incipient separation depends on the smallest size of separated region that can be detected. Observations of Appels and Richards[39] and Spaid and Frishett[42] have proved the existence of small separation bubbles at very low corner deflection angles. The important criterion for design purposes is when does

separation make significant changes to the pressure and heat transfer distributions. That is the definition of "incipient" used here.

5.9.4 Flare Pressure Prediction (Attached Flows)

The method described in section 5.6, based on Elfstrom's[37] model, is used to predict the pressure distributions along the flare for the 10° and 20° cases. For the turbulent boundary layer a seventh power law velocity profile was converted to Mach number profile, shown in Fig. 5.13a, using the linear Crocco relationship. This Mach number profile was used as the input for the technique. The numerical results are shown together with the experimental measurements in Figs. 5.44 and 5.45. The agreement is good near the junction region but the error is increasing towards the end of the flares. This is because the present method is based on the oblique shock relations which are applicable to two-dimensional flows or flows which exhibit locally two-dimensional characteristics. As was discussed earlier the flow at the junction region and up to the reattachment is locally two-dimensional. However, after reattachment the pressure ratio values drop towards the inviscid conical values.

For the case of the seventh power law, the computed "wall" or "slip" Mach number is 2.42, see Fig. 5.13a. The corresponding turning angle which produces a detached shock is approximately 29°. This value was calculated using the Ames tables[157]. This predicted incipient separation angle agrees very well with the experimental value of 27.9°.

5.10 Hemisphere-Cylinder-Flare Turbulent Boundary Layer Studies

5.10.1 Hemisphere-Cylinder Body

The flowfield around the hemisphere-cylinder body is discussed in section 5.2.3. Sections 5.2.1 and 5.2.2 discuss the pressure distribution characteristics and comparisons are made with various theoretical models. Further discussion is given in section 5.8.1. However, the present model utilises vortex generators to force the incoming boundary layer into transition (see discussion in section 5.9.1). The liquid crystal and oil-dot pictures for the hemisphere-nosed model with and without vortex generators are shown in Fig. 5.46. It is evident that the vortex generators produce strong vortices which travel

downstream along the cylinder. These vortex filaments, for the present model with vortex generators, can be traced to approximately 50% of the cylinder length.

Comparison of the liquid crystal pictures for the sharp cone and hemisphere nose configurations, both with vortex generators, are shown in Fig. 5.46. This shows that the vortex traces on the surface can be traced further downstream for the hemisphere nose configuration. It is conjectured that the process of vortex development and final breakdown is slower for the hemisphere nose body (because the boundary layer edge Mach number is lower).

The liquid crystal pictures with and without vortex generators, shown in Fig. 5.46, show that the liquid crystal colour on the cylinder with vortex generators is darker green over the entire cylinder length than for the hemisphere nosed body without vortex generators. Fig. 5.46 also shows that the blunt nose body with vortex generators exhibit higher heat transfer levels along the cylinder length than the sharp nose body with vortex generators.

5.10.2 The Effect of Bluntness

All the experimental results of the present configuration with flares are shown in Fig. 5.47. Fig. 5.48 is a composite of all pressure distributions. An explanation of the flare shock structure for attached flows of the present configuration is based on a combination of the effects of bluntness and turbulence. The discussion of the effects of bluntness in section 5.8.2 is valid here. Bluntness causes the boundary layer edge shock structure to look similar to that of a supersonic rather than a hypersonic flow and the Mach number gradients in the entropy layer cause a curvature of the compression fans within the entropy layer. The compression waves coalesce to form a shock wave. Fig. 5.47a shows that for the attached flow case of 10° flare, the angle of the flare shock increases above that on the sharp nose configuration with vortex generators, Fig. 5.40a. The increase in the shock angle is due to the reduced Mach number within the entropy layer. The Mach number variation within the entropy layer results in the flare shock becoming more "upright".

Figs. 5.47a and 5.48 show that for attached flow (flare angle 10°) the upstream influence is limited to less than one boundary layer thickness. Because the strong entropy layer obscures the boundary layer it makes it difficult to observe clearly the flowfield

characteristics. However, the flare shock is visible and by extending it to the left, it bisects the surface of body just in front of the junction. The same was observed for the sharp cone-cylinder flare body with vortex generators.

The comparison of liquid crystal pictures of the bodies with vortex generators with sharp cone and hemisphere noses, Figs. 5.40 and 5.47, shows that the compression associated with the flare shock increases the heat transfer on the flare. However, the heat transfer levels along the flare of the hemisphere nose configuration is well below that of the sharp cone nose configuration. Since the heat transfer rate is directly proportional to the local pressure ratio[36], the reduction in the flare pressure ratio for the hemisphere configuration (due to the lower Mach number) is responsible for the observed reduction in flare heat transfer levels.

The comparison of Figs. 5.47 and 5.40 shows that the final pressure realised on the flare is significantly decreased by nose bluntness and well below those for the sharp cone configuration. The magnitudes of pressure rise on the flare is reduced to by 30-40%, indicating the large effect of the detached bow shock and associated entropy layer. The predicted flare pressure level shown for the hemisphere configuration is based on the model shown in Fig. 5.10 and described in section 5.6. The agreement between the theoretical prediction and the measured flare pressure ratios immediately downstream of reattachment suggests that the decrease in the flare pressure ratio due to bluntness is due to the reduction in cylinder-flare corner Mach number. This reduction is because of the loss of reservoir pressure across the bow shock. The pressure distributions on the hemisphere nose configuration show a secondary increase in pressure following reattachment. This is due to the Mach shear interaction effect. The secondary increase in pressure following reattachment is similar to that for the hemisphere-cylinder-flare without vortex generators

For flare angles 20°, 30° and 45°, Figs. 5.47 and 5.48, the upstream influence increases with deflection angle and develops a plateau of increasing length, indicative of separated flow. This is because of the increasing adverse pressure gradient due to the increase of the flare deflection angle. An estimation of separation and reattachment points was obtained by examining schlieren and oil-dot pictures and the pressure distributions when the boundary layer was separated. These points were chosen at the positions where the

boundary layer physically appeared to separate and reattach. The liquid crystals offer inconclusive results but they give qualitative information as far as the heat transfer is concerned. The oil-dot pictures and pressure measurements confirm that the flow has separated at an angle of 20°.

The liquid crystal pictures, shown in Fig. 5.47, show that the heat transfer along the cylinder body up to the 30° flare case is the same with that of the cylinder alone. For the 45° flare case, there is an increase in heat transfer upstream of the cylinder-flare juncture, because of the increased separation region. It is know, in contrast to laminar flow, the heat transfer in the separated region for turbulent flows increases. On the flare, for all deflection angle cases, the heat transfer is much higher than that on the cylinder body. This is due to compression from the flare shock which envelops the flare body.

The comparison of the pressure distributions for the sharp cone and hemisphere nose bodies with vortex generators, Figs. 5.40 and 5.47, shows that the hemispherical-nosed model has larger separated regions. This is attributed to the possibility that the turbulent boundary layer profile of the hemisphere nosed model is not as full as the turbulent boundary layer profile of the sharp nose body. The boundary layer on the hemisphere nosed model is enveloped by a layer of air at a Mach number and Reynolds number much lower than the freestream values. Consequently, the Mach number and Reynolds number at the boundary layer edge are less than for the sharp cone nose model. A proper answer whether the boundary layer is fully developed can only be given experimentally by boundary-layer surveys. Unfortunately it was impossible due to time constraints to conduct such an investigation. Therefore, the experimental results for the blunt nosed configuration with vortex generators are considered inconclusive.

Kuehn[8] performed pitot pressure surveys on sharp and blunted nose cylinder-flare bodies with a boundary layer trip. From these surveys, he obtained the boundary-layer Mach number profiles and he converted them to velocity profiles using the linear Crocco relation (Eq. 5.2r) with Eq. 5.2s (see section 5.6). The velocity-profile parameter, n, was determined from the plots of u/u_∞ versus y/δ. He used the velocity-profile parameter to determine whether the turbulent boundary layers on the blunt models and the sharp models were fully developed. He found that the boundary layers on the hemispherical-nosed models were not as full as the boundary layers on the sharp and moderate

bluntness nosed models. He observed that a turbulent boundary layer which is not fully developed will be more prone to separation than a fully developed boundary layer i.e. a higher n, fuller profile (with a stronger, well-developed wake component) results in a more energetic boundary layer which is more resistant to separation.

The comparison of pressure distributions and oil-dot pictures for the hemisphere-cylinder-flare with and without vortex generators, shown in Figs. 5.47, 5.26, 5.27 and 5.29, shows that turbulence delays separation. In the extreme case of the 45^{o} flare, the presence of a turbulent boundary layer causes separation to occur at approximately 4.2 cylinder diameters from the cylinder-flare junction while in the laminar boundary layer case separation occurs at approximately 7.5 cylinder diameters from the cylinder-flare junction.

The incipient separation was determined using the same methods described in section 5.9.3. Fig. 5.49 shows the separation length, as measured from the pressure distributions and oil-dot pictures against flare angle, extrapolated to zero separation length. The agreement between the incipient separation methods used for detection is of the order of one degree. Fig. 5.49 also shows the comparison with results from the hemisphere-cylinder-flare under laminar conditions. The incipient separation angle for the turbulent boundary layer configuration is approximately 17^{o}, while the incipient separation angle for the laminar boundary layer configuration is approximately 11^{o}. Therefore the effect of turbulent boundary layer for the hemisphere model is an increase of about 55% in the incipient separation angle. The effect of turbulence for the sharp nosed model is an increase of 214%. This difference of the effectiveness of turbulence is attributed to the Mach number and Reynolds number effects. The results from the four configurations are tabulated below:

incipient separation angle	**sharp cone nose**	**hemisphere nose**
laminar boundary-layer	**9^{o}**	**11^{o}**
turbulent boundary-layer	**28^{o}**	**17^{o}**

5.11 Correlations

a.Laminar correlations

Experimental studies by Needham and Stollery[25] of laminar incipient separation in hypersonic flow have shown that for a sharp leading edge flat plate of length L with a trailing edge flap at angle β:

$$M_\infty \beta_{incip} = 80 \overline{\chi}_{\infty L}^{1/2} \tag{5.3a}$$

where $\overline{\chi}_{\infty L} \equiv M_\infty^3 \sqrt{C} / \sqrt{Re_L}$. The laminar incipient separation data of the present study is correlated with laminar axisymmetric incipient separation data of other investigators, see Fig. 5.50. The data is plotted as $M\beta_{incip}$ vs $\overline{\chi}_L$, together with the 2-D correlation of Needham and Stollery. The data point of ref. 21 in Fig. 5.50 does not correlate and according to Becker et al[21] their data is transitional incipient interaction. The laminar axisymmetric data of Fig. 5.50 is tabulated in Table 4. For the sharp cone nose and hollow cylinder flare cases the freestream conditions are used.

For the blunted nose cylinder flare cases the local conditions ahead the cylinder flare junction are used. For the flow between the freestream region and the nose, the normal shock relations are used[157] (note $T_{o\infty}=T_{o2}$). The flow is assumed to expand isentropically downstream of the nose shock to $p_e=p_\infty$. Hence:

$$M_e = \sqrt{\left(\frac{2}{\gamma-1}\right)\left[\left(\frac{p_{o2}}{p_\infty}\right)^{\frac{\gamma-1}{\gamma}} - 1\right]} \tag{5.3b}$$

where p_{o2} is given by the Rayleigh pitot equation for a perfect gas[157], Eq. 5.1k. The ratio of local to freestream unit Reynolds number is:

$$\frac{Re_e}{Re_\infty} = \frac{\rho_e U_e \mu_\infty}{\rho_\infty U_\infty \mu_e} = \frac{\rho_e M_e \mu_\infty}{\rho_\infty M_\infty \mu_e}\sqrt{\frac{T_e}{T_\infty}} \tag{5.3c}$$

Assuming $C \cong 1$ and $\mu_e/\mu_\infty = \left(T_e/T_\infty\right)^{0.7}$ then:

$$\frac{Re_e}{Re_\infty} = \frac{\rho_e M_e}{\rho_\infty M_\infty}\left(\frac{T_\infty}{T_e}\right)^{0.2} \tag{5.3d}$$

b.Turbulent correlations

A collection of turbulent 2-D incipient separation data is shown in Fig. 2.5. The correlation and explanation of all the data presented is impossible because of the difficulty in defining the incipient separation condition in turbulent flow. The same figure shows the trend reversal of β_{incip} with $Re_{\delta L}$ at high values of Reynolds number. Elfstrom[37] indicates that this reversal closely follows the wake component development in the velocity profile and hence the power law exponent n in the relation $u/u_\infty=(y/\delta)^{1/n}$. Johnson et al[190], with experiments in turbulent boundary layers on flat plates, have shown that close to transition n decreases with increasing Reynolds number. They further showed that at high Reynolds number, when the boundary layer is fully developed, n increases with Reynolds number.

Stollery and Bates[53] have shown that the strong viscous interaction parameter for turbulent flow is:

$$\overline{\chi}_S \equiv \left\{\frac{M_\infty^9 C}{Re_x}\right\}^{\frac{2}{7}} \tag{5.3e}$$

and they have suggested that by analogy to the laminar case:

$$M_\infty \beta_{incip} \sim \overline{\chi}_S^{1/2} \tag{5.3f}$$

The turbulent incipient separation data of the present study is correlated with turbulent axisymmetric incipient separation data of other investigators, see Fig. 5.51. The data is plotted as $M\beta_{incip}$ vs $\overline{\chi}_S$. The data point marked as "x" in Fig. 5.51 is the hemisphere nose cylinder flare with vortex generators of the present study. This data point is below the correlation trendline of the other values, suggesting that the turbulent boundary layer along the cylinder of the model is not fully developed (see discussion of section 5.10.2). The turbulent axisymmetric data of Fig. 5.51 is tabulated in Table 5. For the sharp cone nose and hollow cylinder flare cases the freestream conditions are used. For the blunted nose cylinder flare cases the local conditions ahead the cylinder flare junction are used (this local conditions were calculated using the method described above).

Fig. 5.52 shows the angle of turbulent incipient separation as a function of Reynolds number, $Re_{\delta L}$, with Mach number as parameter. In this figure the result for the sharp

cone cylinder-flare model of the present study is compared with the wedge compression corner experiments of Kuehn[35], Coleman[65] and Appels[39] and the axisymmetric results of Kuehn[8], Coleman[65] and Rose et al[40]. The data of Coleman[65] and Kuehn[35,8] exhibit the trend of decreasing β_{incip} with increasing $Re_{\delta L}$, where δ_L is the undisturbed boundary layer thickness at the junction. Whereas the data of Appels[39] and Rose et al[40] exhibit the opposite trend. This difference is due to the different upstream histories of the turbulent boundary layer development and the method of detecting incipient separation.

Chapter 6

Concluding Remarks

6.1 Elliptic Cones With and Without Strakes

1. No gross external flow differences were detected from the schlieren pictures for models tested due to the addition of strakes.
2. The flow separates on the leeward side of the body to form a pair of counter rotating vortices at a low incidence for all models tested. The vortices grow with incidence.
3. Oil-dot visualisation demonstrates that the strakes alter the surface flow characteristics by inhibiting the cross-flow.
4. The addition of strakes caused a reduction of pressure on the leeward side and an increase of pressure on the windward side. The strakes produced a significant increase in the lift and drag coefficients, in the incidence range of 0° to 20°.
5. Adding strakes produces a stronger favourable interference with the power-law body. Increasing the body exponent, n, increases the lift-curve slope and the zero-lift drag coefficient.
6. The right elliptic cone without strakes with its major axis horizontal exhibits higher lift coefficients than the cone with its major axis vertical. The addition of strakes produces a stronger favourable interference on the elliptic cone with its major axis vertical than on the elliptic cone with its major axis horizontal.
7. An estimation model of the aerodynamic forces and moments for the right elliptic cone with and without strakes was developed based on the standard Newtonian theory. The model successfully predicted the experimental trends in the aerodynamic

coefficients. It is suggested that the model may also be used as an engineering tool to estimate the effectiveness of strakes on slender bodies.

8. The numerical study employed an iterative, three-dimensional, finite volume PNS solver, based on Osher's flux difference splitting scheme. The code predicted the complex flowfield surrounding the right elliptic cone with its major axis horizontal, gave a better understanding of the complicated nature of the flow, good indications of the shock shape and vortex core positions and captured all the main experimental trends. But the actual predicted values were in poor agreement with experiment.
9. In the experimental design stage, CFD can be used to identify important areas and important flow conditions before the model is cut, which can save unnecessary waste in the experimental tests. After data collection from the experiments, detailed numerical simulation can be conducted for the experimental conditions. In the present study, the simulation was able to provide flowfield information to enhance the understanding of the experimental results.

6.2 Flare Control Effectiveness

1. Turbulent boundary layers inhibit separation. Flare deflection promotes separation of both laminar and turbulent boundary layers. The increasing flare deflection angle causes a significant thinning of the boundary layer over the flare.
2. Bluntness promotes turbulent boundary layer separation but has a small beneficial effect on laminar separation.
3. Bluntness greatly reduces the surface pressure and heat transfer loading on the flare of a cylinder-flare body. This would significantly reduce the stability and control effectiveness of flares on blunt nosed bodies.
4. The entropy-layer Mach number profile has been estimated theoretically. This result has been used as an input to a method (based on oblique shock theory and wave interactions) to calculate the effect of Mach shear on the flare pressures distribution. The model predicted the experimental results satisfactorily.
5. The most important difference between the laminar and turbulent boundary layer interaction is that the turbulent boundary layer can withstand much greater flare angles than the laminar case before separation occurs. The determination of incipient

separation is very sensitive to the detection method employed. The existence of a very small scale separation bubble can explain the differences in the determination of incipient separation angles if different experimental methods are used.

6.3 Suggestions for Further Work

1. Further studies are necessary in order to measure the pressure distribution circumferentialy and to examine in more detail the effects of strakes on the local flowfield (e.g. by altering the strakes thickness). More advanced flow visualisation planar techniques may be needed for these studies.
2. The CFD solutions can be improved further by using a multi-block solver with grid adaptation. A numerical simulation of the flare control effectiveness is suggested to understand better the flowfield interaction.
3. The effect of bluntness on axisymmetric bodies (in particular under turbulent conditions) needs further study and boundary-layer surveys are required to give a proper answer whether the boundary layer is fully developed for the hemisphere nose-cylinder flare body with vortex generators.

Tables

Table 1 Power-law body design co-ordinates

x/L_{cone}	a/L_{cone}	b/L_{cone}	x/L_{cone}	a/L_{cone}	b/L_{cone}
0.0000	0.0000	0.0000	**0.3600**	0.0429	0.0268
0.0050	0.0051	0.0032	**0.4400**	0.0475	0.0297
0.0100	0.0072	0.0045	**0.5200**	0.0516	0.0322
0.0200	0.0101	0.0063	**0.6000**	0.0554	0.0346
0.0400	0.0143	0.0089	**0.6800**	0.0590	0.0369
0.0600	0.0175	0.0110	**0.7600**	0.0624	0.0390
0.1200	0.0248	0.0155	**0.8400**	0.0656	0.0410
0.2000	0.0320	0.0200	**0.9200**	0.0686	0.0429
0.2800	0.0379	0.0237	**1.0000**	0.0716	0.0447

Table 2 The location of the pressure orifices on the cylinder-flare body

	Orifice No.	x/d_{cyl}		Orifice No.	x/d_{cyl}
cylinder body ↓	**1**	-0.0588	flare body ↓	**19**	0.29412
	2	-0.1177		**20**	0.41176
	3	-0.2353		**21**	0.52941
	4	-0.2941		**22**	0.58824
	5	-0.4118		**23**	0.76471
	6	-0.5882		**24**	0.88235
	7	-0.7647		**25**	1.05882
	8	-0.8824		**26**	1.17647
	9	-1.0588		**27**	1.35294
	10	-1.4706		**28**	1.41177
	11	-2.0588		**29**	1.47059
	12	-2.3529		**30**	1.52941
	13	-2.9412		**31**	1.58824
	14	-4.1176		**32**	1.64706
	15	-6.4706		**33**	1.76471
↓	**16**	-8.2353		**34**	1.94118
flare body	**17**	0.11765	↓	**35**	2.05882
↓	**18**	0.17647		**36**	2.35294

Note: a) orifice numbers 28, 30, 31 and 32 are only available on the 45° flare
b) orifice numbers 29, 33, 34, 35 and 36 are only available on the 10°, 20° and 30° flares

An explanation diagram of the geometrical characteristics of the model is given below:

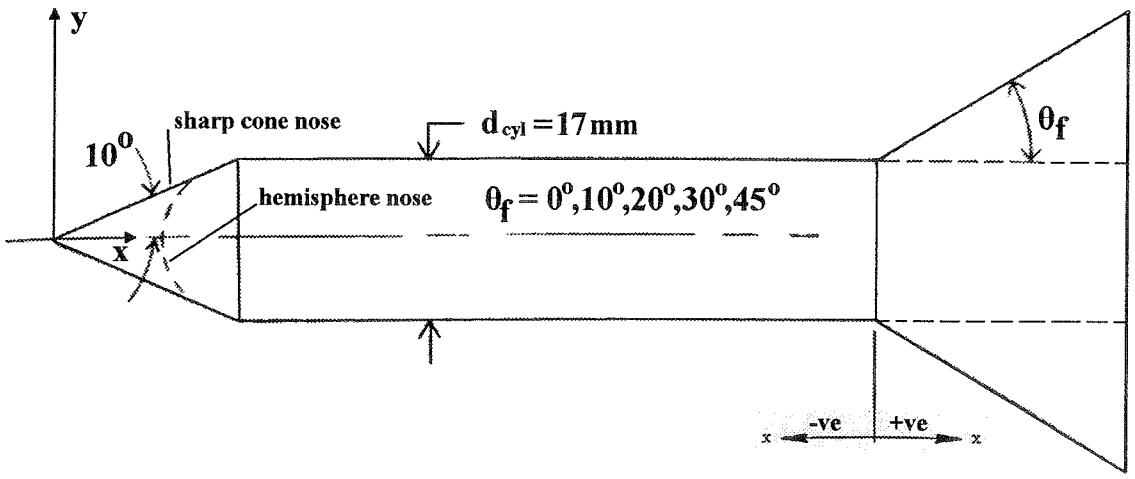

Table 3 Temperature profile of the liquid crystal (ref. 195)

temperature /°C	**colour emitted**
17.9	visible start
18.3	red start
21.3	green start
24.0	bright green
29.9	blue start
39.9	colourless

Table 4 Laminar supersonic and hypersonic axisymmetric incipient separation data

source	M_∞	M_e	β_{incip}	Re_∞/cm	Re_e/cm	L (cm)	T_w/T_o	model description
present study	8.20	$M_e=M_\infty$	9	93500	Re_e/cm=Re_∞/cm	20.12	0.23	sharp cone nose cylinder-flare (a)
ref. 9	3.10		5	58500		12.18		
	3.70		5	81900		12.18		
	4.25		5	133000		12.18		
	4.94		7.5	139300		12.18		
	4.25		7.5	89400		12.18		
	3.85		7.5	63300		12.18		
	3.20		7.5	40400		12.18		
	5.00		10	92600		12.18		
	4.10		10	55900		12.18		
	3.75		10	45750		12.18		
	4.75		5	175600		17.18		
	4.20		5	122400		17.18		
	3.55		5	71300		17.18		
	2.75		5	39400		17.18		
ref. 21	6.80		10	144400		38.67	0.50	sharp ogive nose cylinder-flare (b)
ref. 22	4.98		5	175500		28.78		sharp cone nose cylinder-flare (a)
present study	8.20	3.59	11	93500	7700	16.15	0.23	hemisphere nose cylinder-flare (c)
ref. 9	3.70	2.55	5	35800	12300	4.76		
	3.13	2.38	5	23900	10900	4.76		
	2.83	2.25	5	15500	8350	4.76		
	2.40	2.05	5	10300	6350	4.76		
	4.40	2.65	7.5	40200	10350	4.76		
	3.35	2.45	7.5	17500	6950	4.76		

Table 4 Continue

source	M_∞	M_e	β_{incip}	Re_∞/cm	Re_e/cm	L (cm)	T_w/T_o	model description
ref. 9	3.00	2.28	7.5	11150	5370	4.76		hemisphere nose cylinder-flare (c)
↓	5.20	2.95	10	45700	8550	4.76		↓
	4.60	2.50	10	28650	5250	4.76		
	3.70	2.80	5	38800	17500	9.84		
	3.30	2.55	5	29430	13500	9.84		
	4.90	2.85	5	97430	21500	14.92		
	3.85	2.58	5	47700	13500	14.92		
ref. 191	2.21	$M_e=M_\infty$	5	12000	Re_e/cm=Re_∞/cm	6		hollow cylinder-flare (d)
ref. 15*	14.40	4.44	36	3900		4.45	0.15	blunt 45° conical nose cylinder-flare (e)
↓	14.40	4.44	37.5	3900		3.97	0.15	hemisphere nose cylinder-flare (c)
	14.40	4.44	37	3900		4.45	0.15	flat nose cylinder flare (f)

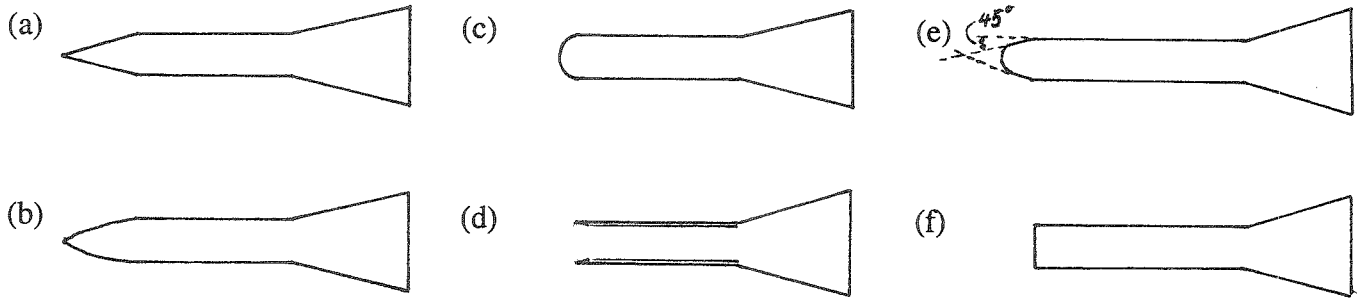

Note: *Not enough flowfield parameters are provided in ref. 15 to calculate Re_e/cm. The correlation in Fig. 5.50 does not include ref. 15 incipient separation data.

Table 5 Turbulent supersonic and hypersonic axisymmetric incipient separation data

source	M_∞	M_e	β_{incip}	Re_∞/cm	Re_e/cm	L (cm)	T_w/T_o	model description
present study	8.20	$M_e=M_\infty$	28	93500	Re_e/cm=Re_∞/cm	20.12	0.23	sharp cone nose cylinder-flare (a)
ref. 21	6.8		30	2150000		38.67	0.50	sharp ogive nose cylinder-flare (b)
ref. 65	8.96		33	120000		45.70	0.28	hollow cylinder-flare (d)
	9.22		32	470000		45.70	0.28	
ref. 38	9.22		32	470000		63.85	0.28	sharp cone nose cylinder-flare (a)
ref. 8	3.72		25	282000		37.60		
	3.25		25	183000		37.60		
	2.30		25	83300		37.60		
	2.05		25	66500		37.60		
	4.20		30	266500		37.60		
	3.11		30	106000		37.60		
	3.31		30	133000		15.03		
	2.51		30	63500		15.03		
present study	8.2	3.59	17	93500	7700	16.15	0.23	hemisphere cylinder-flare (c)
ref. 38	9.22	3.76	32	470000	31400	48.90	0.28	
ref. 8	4.05	3.45	30	191000	117000	31.30		blunt 45° conical nose cylinder-flare (e)
	3.5	2.95	30	114500	67000	31.30		
ref. 192*	3	$M_e=M_\infty$	20	98500	Re_e/cm=Re_∞/cm	103.76		hollow cylinder-flare (d)
	4		20	220500		103.76		
	5		20	216500		79.63		
	3		20	157500		53.34		sharp cone nose cylinder-flare (a)
	4		20	220500		53.34		
	5		20	216500		29.21		

Note: *It is conjectured by Gray[192] that this incipient separation data is under turbulent boundary layer conditions ahead the hingeline.

References

1. Bertin, J.J., "Hypersonic aerothermodynamics", AIAA Education Series, 1995.
2. Babinsky, H., "A study of roughness in turbulent hypersonic boundary layers", PhD thesis, Cranfield University, Department of Aerospace Sciences, 1993.
3. Van Dyke, M.D., "The elliptic cone as a model for non-linear supersonic flow theory", J. Fluid Mech., Vol. 1, Part 1, pp. 1-15, 1956.
4. Ferri, A., Ness, N., Kaplita, T., "Supersonic flow over conical bodies without axial symmetry", Journal of the Aeronautical Sciences, Vol. 20, pp. 563-571, 1953.
5. Seaman, D., Dore, F., "Force and pressure coefficients of elliptic cones and cylinders in newtonian flow", Consolidated-Vultee Report XA-7-004, 1952.
6. Fraenkel, L.E., "Supersonic flow past slender bodies of elliptic cross-section", ARC R&M 2954, 1955.
7. Jorgensen, L., "Elliptic cones alone and with wings at supersonic speeds", NACA TN-4045, 1957.
8. Kuehn, D.M., "Turbulent boundary-layer separation induced by flares on cylinders at zero angle of attack", NASA TR-R-117, 1961.
9. Kuehn, D.M., "Laminar boundary-layer separation induced by flares on cylinders at zero angle of attack", NASA TR-R-146, 1962.
10. Stetson, K.F., "On non-linear aspects of hypersonic boundary layer stability", AIAA J., Vol. 26, No. 7, pp 883-885, 1988.
11. Stetson, K.F., Thompson, E.R., Donaldson, J.C., Siler, L.G., "Laminar boundary layer stability experiments on a cone at Mach 8, part 1: sharp cone", AIAA 83-1761, 1983.
12. White, F.M., "Viscous fluid flow", McGraw Hill, 1974.
13. Malik, M.R., Zang, T.A., Bushnell, D.M., "Boundary layer transition in hypersonic flows", AIAA 90-5232, 1990.
14. Coleman, G.T., Stollery, J.L., "Incipient separation of axially symmetric hypersonic turbulent boundary layers", AIAA J., Vol. 12, No. 1, pp. 119-120, 1974.

15.Kuehn, D.M., "Laminar boundary-layer separation induced by flares on cylinders with highly cooled boundary layers at a Mach number of 15", NASA TN D-2610, 1965.

16.Gray, J., "Investigation of the effect of flare and ramp angle on the upstream influence of laminar and transitional reattaching flows from Mach 3 to 7", AEDC TR-66-190, 1967.

17.Ginoux, J.J., "On some properties of reattaching laminar and transitional high speed flows", VKI TN-53, 1969.

18.Popinski, Z., Ehrlich, C.F., "Development design methods for predicting hypersonic aerodynamic control characteristics", AFFDL-TR-66-85, 1966.

19.Chapman, D.R., Kuehn, D.M., Larson H.K., "Investigation of separated flows in supersonic and subsonic streams with emphasis on the effect of transition", NACA TN 1356, 1958.

20.Delery, J., Marvin, J.G., "Shockwave boundary layer interactions", AGARD AG 280, 1986.

21.Becker, J.V., Korycinski, P.F., "Heat transfer and pressure distribution at a Mach number of 6.8 on bodies with conical flares and extensive flow separation", NASA TN D-1260, 1956.

22.Ferguson, H., Schaefer, J.W., "Heat transfer and pressure distribution on cone-cylinder-flare configuration with boundary-layer separation", NASA TN D-1436, 1962.

23.Kumar, D., Stollery, J.L., "Hypersonic control flap effectiveness", The Aeronautical Journal, Vol. 100, No. 996, pp. 197-208, 1996.

24.Bloy, A.W., "Hypersonic laminar boundary layer flow over sharp compression and expansion corners", PhD Thesis, University of London, 1973.

25.Needham, D.A., Stollery, J.L., "Boundary layer separation in hypersonic flow", AIAA 66-455, 1966.

26.Holden, M.S., "A study of flow separation in regions of laminar shockwave boundary layer interactions in hypersonic flow", AIAA 78-1169, 1978.

27.Hankey, W.L., Holden, M.S., "Experimental studies of shockwave/boundary layer interactions", AGARD AG-203, 1975.

28.Inger, G.R., "Scaling of incipient separation in high speed laminar flows", AIAA 93-3435, 1993.

29.Needham, D.A., Stollery, J.L., "Hypersonic studies of incipient separation and separated flows", ARC 27752, 1966.

30.Simeonides, G., "Hypersonic shockwave boundary layer interactions over compression corners", PhD thesis, VKI/University of Bristol, 1992.

31.Katzer, E., "On length-scales of laminar shockwave boundary layer interactions", Joumal of Fluid Mechanics, Vol. 206, pp 477-496, 1989.

32.Potter, J.L., Whitfield, J.D., "Effects of unit Reynolds number, nose bluntness and roughness on boundary layer transition", AEDC TR-60-5, 1960.

33.Coles, D., "Measurements in the boundary layer on a smooth flat plate in supersonic flow", ORDCIT Report, No. 20-71, 1953.

34.Needham, D.A., "Laminar separation in hypersonic flows", PhD thesis, University of London, 1965.

35.Kuehn, D.M., "Experimental investigation of the pressure rise required for the incipient separation of turbulent boundary in two-dimentional supersonic flow", NACA Memorandum 1-21-59A, 1958.

36.Coleman, G.T., Stollery, J.L., "Heat transfer from hypersonic turbulent flow at a wedge compression corner", J. of Fluid Mech., Vol. 56, part 4, pp. 741-752, 1972.

37.Elfstrom, G.M., "Turbulent separation in hypersonic flow", I.C. Aero Report 71-16, 1971.

38.Coleman, G.T., "A study of hypersonic boundary layers over a family of axisymmetric bodies at zero incidence", I.C. Aero Report 73-06, 1973.

39.Appels, C., Richards, B.E., "Incipient separation of a compression turbulent boundary layer", AGARD CP-168, 1975.

40.Rose, W.C., Page, R.J., Childs, M.E., "Incipient separation pressure rise for a Mach 3.8 turbulent boundary layer", AIAA Journal, Vol. 11, No. 5, pp. 761-764, 1973.

41.Zheltovodov, A.A., "Shock waves/turbulent boundary-layer interactions: Foundamental studies and applications", AIAA 96-1977, 1996.

42.Spaid, F.W., Frishett, J.L., "Incipient separation of a supersonic, turbulent boundary layer, including effect of heat transfer", AIAA Journal, Vol. 10, No. 7, pp. 915-922, 1972.

43.Settles, G.S., Bogdonoff, S.M., Vas., I.E., "Incipient separation of a supersonic turbulent boundary layer at high reynolds number", AIAA Journal, Vol. 14, No. 1, pp. 50-56, 1976.

44.Babinsky, H., Edwards, J.A., "On the incipient separation of a turbulent hypersonic boundary layer", The Aeronautical Journal, Vol. 100, No. 996, pp. 209-214, 1996.

45.Edwards, J.A., Roper, J.J., "A computational investigation of the incipient separation of a hypersonic turbulent boundary layer", Report No. DRA/DWS/WX7/TR951003, 24 of 32, 1995.

46.Korkegi, R.H., "A lower bound for three-dimentional turbulent separation in supersonic flow", AIAA Journal, Vol. 23, No. 3, pp. 475-476, 1985.

47.Dolling, D.S., Murphy, M.T., "Unsteadiness of the separation shock wave in a supersonic compression ramp flowfield", AIAA Journal, Vol. 21, No. 12, 1983. See also AIAA 90-0377 and 90-0380.

48.Drugge, G., "An experimental investigation of the influence of strong adverse pressure gradients on turbulent boundary layers at supersonic speeds", FFA Report 47, 1953.

49.Holden, M.S., "Experimental studies of shock wave boundary layer interaction", VKI LS62, January 1974.

50.Kessler, W.C., Reilly, J.F., Mockapetris, L.J., "Supersonic turbulent boundary layer interaction with an expansion ramp and compression corner", Mc Donnell Douglas Report, MDC E0264, 1970.

51.Law, H.C., "Supersonic turbulent boundary layer separation measurements at Reynolds numbers of 10^7 to 10^8", AIAA paper 73-665, July 1973.

52.Sterrett, J.R., Emery, J.C., "Experimental separation studies for two-dimensional wedges and curved surfaces at Mach numbers of 4.8 to 6.2", NASA TN D-1014, 1962.

53.Stollery, J.L., Bates, L., "Turbulent hypersonic viscous interaction", J. Fluid Mech., Vol. 63, part 1, pp. 145-156, 1974.

54.Kilburg, R.F., Kotansky, D.R., "Experimental investigation of the interaction of a plane oblique incident-reflecting shock witha turbulent boundary layer on a cooled surface", NASA CR-66-841, 1969.

55.Back, L.H., Cuffel, R.F., "Shock-wave/turbulent boundary-layer interactions with and without surface cooling", AIAA Journal, Vol. 14, No. 4, pp. 526-532, 1976.

56.Delery, J., "Etude experimentale de la reflexion d'une onde de choc sur une paroi chauffee en presence d'une couche limite turbulente", La Recherche Aerospatiale, No. 1992-1, pp. 1-23, 1992.

57.Zheltovodov, A.A., Kharitonov, A.M., "About the analogy of 2-D and 3-D separated flows", Physical Gas Dynamics, ITAM, USSR, Academy of Science, Novosibirsk, Vol. 6, pp. 130-133, 1976.

58.Roshko, A. and Thomke, G.J., "Flare-induced interaction lengths in supersonic, turbulent boundary layers", AIAA Journal, Vol. 14, No. 7, pp. 873-879, 1974.

59.Miller, D.S., Hijman, R., Childs, M.E., "Mach 8 to 22 studies of flow separation due to deflected control surfaces", AIAA Journal, Vol. 2, No. 2, pp 312-321, 1964.

60.Smith, A.J.D., "The dynamic response of a wedge separated hypersonic flow and its effects on heat transfer", PhD thesis, Univ. of Southampton, 1993.

61.Appels, C., "Turbulent boundary layer separation at Mach 12", VKI TN-90, 1973.

62.Inouye, M., Sisk, J.B., "Wind-tunnel measurements at Mach numbers from 3 to 5 of pressure and turbulent heat transfer on a blunt cone-cylinder with flared afterbody", NASA TM X-654, 1962.

63.Kauffman, L.G., Meckler, L., Hartofilis, S.A., "An investigation of flow separation and aerodynamic controls at hypersonic speeds", Joumal of Aircraft, Vol. 3, No. 6, pp. 555-561, 1966.

64.Korkegi, R.H., "Transition studies and skin-friction measurements on an insulated flat plate at a Mach number of 5.8", J. of the Aero. Sci., Vol. 23, No. 2, 1956.

65.Coleman, G.T., "Hypersonic boundary layer studies", PhD thesis, Univ. of London, 1973.

66.Nagamatsu, H.T., Sheer, R.E., Graber, B.C., "Hypersonic laminar boundary layer transition on 8-foot long 10° cone, at M_1=9.1-16", AIAA Joumal, Vol. 5, No. 7, pp. 1245-1252, 1967.

67.Spall, R.E., Malik, M.R., "Görtler vortices in supersonic and hypersonic boundary layers", Physics of Fluids A 1, Vol. 11, pp. 1822-1835, 1989.

68.Mack, L.M., "Linear stability theory and the problem of supersonic boundary layer transition", AIAA Journal, Vol. 13, No. 3, pp. 278-289, 1975.

69.Simeonides, G., Hasse, W., Manna, M., "Experimental, analytical and computational methods applied to hypersonic compression ramp flows" AIAA Journal, Vol. 32, No. 2, 1994.

70.Stollery, J.L., Coleman, G.T., "A correlation between pressure and heat transfer distributions at supersonic and hypersonic speeds", Aeronautical Quarterly, November, 1975.

71.Edwards, C.L.W., Anders, J.B., "Low density, leading edge bluntness and ablation effects on wedge induced laminar boundary layer separation at moderate enthalpies in hypersonic flows", NASA TN D-4829, 1968.

72.Brinich, P.F., "Effect of leading edge geometry on boundary layer transition at M_∞=3.1", NACA TN-3659, 1956.

73.Deem, R.E., Murphy, J.S., "Flat plate boundary layer transition at hypersonic speeds", AIAA 65-0128, 1965.

74.Richards, B.E., "Film cooling in hypersonic flows", PhD Thesis, University of London, 1967.

75.Stetson, K., Thompson, E.R., Donaldson, J.C., Siler, L., "Laminar boundary layer stability experiments on a cone at Mach 8, part 2: blunt cone", AIAA 84-0006, 1984.

76.Kumar, D., "Hypersonic control effectiveness", PhD Thesis, Cranfield University, 1995.

77.Coet, M.C., Delery, J., Chanetz, B., "Experiments on shock wave-boundary layer interaction at high mach number with entropy layer effect", IUTAM Symposium, Marseille, France, 1992.

78.Townsend, J.C., "The effects of leading edge bluntness and ramp deflection angle on laminar boundary layer separation in hypersonic flow", NASA TN D 3290, 1966.

79.Holden, M.S., Moselle, J.R., "A database of aerothermal measurements in hypersonic flow for CFD validation", AIAA 92-4023, 1992.

80.Brinich, P.F., Sands, N., "Effects of bluntness on transition for a cone and a hollow cylinder at Mach 3.1", NACA TN 3979, 1957.

81.Muir, J.F., Trujillo, A.A., "Experimental investigation of the effects of nose bluntness, freestream unit, Reynolds number and angle of attack on cone boundary layer transition at Mach 6", AIAA 72-0216, 1972.

82.Softley, E.J., Graber, B.C., Zempel, R.C., "Experimental observation of transition of the hypersonic boundary layer", AIAA Journal, Vol. 7, pp. 257-263, 1969.

83.Neal, L., "A study of pressure, heat transfer and skin friction on sharp and blunt flat plates at Mach 6.8", NASA TN D 3312, 1966.

84.Ericsson, L.E., "Effects of nose bluntness and cone angle on slender vehicle transition", AIAA Journal, Vol. 26, No. 10, pp 1168-1174, October 1988.

85.Allen, J.H., Perkins, E.W., "Characteristics of flow over inclined bodies of revolution", NACA RM A50L07, 1971.

86.Reggiori, A., "Lift and drag of wing-cone configuration in hypersonic flow", AIAA Journal, Vol. 9, No. 4, pp. 744-745, 1971.

87.Eggers, A.J., Resnikoff, M.M., Dennis, D.H., "Bodies of revolution having minimum drag at high supersonic speeds", NACA Report 1306, 1957.

88.Cole, J.D., "Newtonian flow theory for slender bodies", Journal of Aeronautical Sciences, Vol. 24, No. 6, pp. 448-455, 1957.

89.Houwink, R., "Measurements at the leeward side of a cone at large incidences in supersonic flow", Delft University of Technology, Report VTH-186, 1974.

90.Rainbird, W.J., "The external flowfield about yawed circular cones", AGARD CP-30. 1968.

91.Borovoi, V.Ya., Brazhko, V.N., Maikapar, G.I., "Leeward separated supersonic flows", Moscow: Mashinostroyeniye, 1983.

92.Stetson, K.F., "Boundary-layer separation on slender cones at angle of attack", AIAA Journal, Vol. 10, No. 5, pp. 642-648, 1972.

93.Stetson, K.F., Rushton, G.H., "Shock tunnel investigation of boundary-layer transition at M=5.5", AIAA Journal, Vol. 5, pp. 899-906, 1967.

94.DiCristina, V., "Three-dimentional laminar boundary-layer transition on a sharp 8° cone at Mach 10", AIAA Journal, Vol. 5, No. 5, pp. 852-856, 1970.

95.Julius, J.D., "Measurements of pressure and local heat transfer on a 20° cone at angles of attack up to 20° for a Mach number 4.95", NASA TN D-179, 1959.

96.Singh, D.J., Kumar, A., Tiwari, S.N., "Effect of nose bluntness on flowfield over slender bodies in hypersonic flows", Journal of Thermophysics, Vol. 5, No. 2, 1991.

97.Tiwari, S.N., Singh, D.J., Sehgal, A.K., "Combined effect of nose bluntness and angle of attack on slender bodies in viscous hypersonic flow", AIAA 92-0755, 1992.

98.Cleary, J.W., "An experimental and theoretical investigation of the pressure distribution and flow fields of blunted cones at hypersonic Mach numbers", NASA TN D-2969, 1965.

99.Palko, R.L., Ray, A.D., "Pressure distribution and flow visulaization tests of a 1.5 elliptic cone at Mach 10", AEDC TDR-63-163, 1963.

100.Burk, J.L., "Force and pressure tests of two elliptic ogive body shapes at Mach number 5,6 and 8", AEDC TN-61-49, 1961.

101.Spencer, B., Phillips, W.P., "Supersonic aerodynamics characteristics of a series of bodies having variations in fineness ratio and cross-section ellipticity", NASA TN D-2389, 1964.

102.Spencer, B., Fox, C.H., "Hypersonic aerodynamic performance of minimum wave-drag bodies", NASA TR R-250, 1966.

103.Fournier, R.H., Spencer, B.Jr., "Supersonic aerodynamic characteristics of a series of related bodies with cross-sectional ellipticity", NASA TN D-3539, 1966.

104.Ashby, G.C., Jr., "Longitudinal aerodynamic performance of a series of power-law and minimum-wave-drag bodies at Mach 6 and several Reynolds numbers", NASA TM X-2713, 1974.

105.Graves, E.B., "Aerodynamic characteristics of a monoplanar missile concept with bodies of circular and elliptical cross sections", NASA TM 74079, 1977.

106.Westby, M.F., Regan, J.D., "The aerodynamic characteristics of power-law bodies in continuum and transitional hypersonic flow", RAE TM Aero 2164, 1989.

107.Chaudhry, S.R., Qin, N., Richards, B.E., "Hypersonic viscous flows around waverider configurations", Proceedings of the First Innternational Waverider Symposium, University of Maryland, 1990.

108.Schindel, L.H., "High lift/drag ratio hypersonic missiles", NATO P253759, 1983.

109.Richards, B.E., Houwink, R., "An experimental study of space vehicle configurations with high lift during reentry", VKI TN-117, 1976.

110.Houwink, R., Richards, B.E., "Experimental study of a high lift reentry vehicle configuration", AIAA Journal, Vol. 11, No. 5, pp.749-751, 1973.

111.Allen, J.M., Watson, C.B., "Experimental effects of wing location on wingbody pressures at supersonic speeds", NASA TM-4434, 1993.

112.Spencer, B.Jr., Fournier, R.H., "Supersonic aerodynamics characterisitcs of hypersonic low-wave-drag elliptical body-tail combinations as affected by changes in stabilizer configuration", NASA TM X-2747, 1973.

113.Fox, C.H., Spencer, B.Jr., "Hypersonic aerodynamics characterisitcs of hypersonic low-wave-drag elliptical body-tail combinations as affected by changes in stabilizer configuration", NASA TM X-1620, 1968.

114.Jorgensen, L.H., Nelson, E.R., "Experimental aerodynamics characterisitcs for a cylindrical body of revolution with side strakes and various noses at angles of attack from 0° to 58° and Mach numbers from 0.6 to 2.0", NASA TM X-3130, 1975.

115.Levinsky, E.S., Wei, M.H.Y., "Non-linear lift and pressure distribution of slender conical bodies with strakes at low speeds", NASA CR-1202, 1968.

116.Baysal, O., Fouladi, K., Miller, D.S., "Computations of supersonic flows over a body at high angles of attack", AIAA Journal, Vol. 27, No. 4, 1989.

117.Borrel, M., d'Espiney, P., Jouet, C., "Three-dimensional thin-layer and space marching Navier-Stokes computations using an implicit MUSCL approach: Comparisons with experiments and Euler computations", 9th GAMM Conference on Numerical Methods in Fluid Dynamics, 1991.

118.Graham, J.E., Hankey, W.L., "Computation of the Asymmetric Vortex Pattern for Bodies of Revolution", AIAA 82-0023, 1982.

119.Schiff, L.B., Steger, I.L., "Numerical simulation of steady supersonic viscous flow", AIAA Journal, Vol. 18, No. 12, 1980.

120.Jettmar, R.U., Kordulla W., "Computation of aerodynamic forces on bodies with non-circular cross-section in supersonic viscous flow", AIAA 83-2077, 1983.

121.Degani, D., Schiff L.B., "Computation of turbulent supersonic flows around pointed bodies having crossflow separation", Journal of Computational Physics, Vol. 66, 1986.

122.Greene, F.A., "An upwind-biased space marching algorithm for supersonic viscous flow", NASA TP-3068, 1991.

123.Qin, N., Richards, B.E., "Finite volume 3DNS and PNS solutions of hypersonic viscous flows around a delta wing using Osher's flux-difference splitting", Proceedings of a Workshop on Hypersonic Flows for Re-entry Problems, Vol. 2, 1990.

124.Birch, T.J., Qin, N., Jin, X., "Computation of supersonic viscous flows around a slender body at incidence", AIAA 94-1938, 1994.

125.Baldwin, B.S., Lomax, H., "Thin-layel approximation and algebraic turbulence model for separated turbulent flows", AIAA 78-257, 1978.

126.Osher, S., Chakravathy, S.R., "Upwind schemes and boundary conditions with applications to Euler equations in general co-ordinates", Journal of Computational Physics, Vol. 50, 1983.

127.Qin, N., Scriba, K.W., Richards, B.E., "Shock-shock, shock-vortex interaction and aerodynamic heating in hypersonic corner flow", The Aeronautical Journal, Vol. 95, No. 945, 1991.

128.Qin, N., Ludlow, D., Shaw, S., "Calculation of pitch damping coefficients using the PNS equations in a non-inertial framework. Cranfield University, COA/9601, 1996.

129.Vigneron, Y.C., Rakich, J.V., Tannehill, J.C., "Calculation of supersonic viscous flow over delta wings with sharp leading edges. AIAA 78-1137, 1978.

130.Edwards, J.A., Roper, J.J., "A computational assessment of static and dynamic coefficients for the H3 hypervelocity projectile", AIAA 97-0640.

131.Groth, C.P.T., Gottlieb, J.J., Sullivan, P.A., "Numerical investigation of high-temperature effects in the UTIAS-RPI hypersonic impulse tunnel", Canadian Journal of Physics, Vol. 69, No. 7, pp. 897-918, 1969.

132.Lukasiewiez, J., "Experimental methods in hypersonics", Marcel Dekker, New York, 1973.

133.Derksen, W.B.G., Veldman, J., "Measurements on model pistons for gun tunnel applications", 42nd Annual Meeting of the Supersonic Tunnel Association, Calspan, 1973.

134.Stollery, J.L., Maull, D.J., Belcher, D.A., "The Imperial College hypersonic gun tunnel", J. of Royal Aero. Soc., Vol. 64, No. 589, 1960.

135.Needham, D.A., "Progress report on the Imperial College hypersonic gun tunnel", Imperial College of Science and Technology, Aero TN-118, 1963.

136.Opatowski, T., "A three component gun tunnel balance designed for testing thin delta wings", ARC 31278, 1969.

137.Opatowski, T., "An experimental study of the flow around and the forces developed by hypersonic lifting vehicles", PhD Thesis, University of London, 1967.

138.Ledford, O.C., "Hypersonic film cooling", PhD Thesis, University of London, 1973.

139.Mohammadian, S., "Calibration of the Mach 12 contoured nozzle", ICST Report 70-02, 1968.

140.Singh, A., "Experimental study of slender vehicles at hypersonic speeds", PhD Thesis, Cranfield University, 1996.

141.Squire, L.C., "The motion of a thin oil sheet under the boundary layer on a body", AGARDograph, AGARD AG-70, 1962.

142.Meyer, R.F., Vail, C.F., "An experimental study of the hypersonic flow about a particular half-cone and dealta-wing lifting configuration", NRC, NAE Aero LR-475, 1967.

143.Rao, D.M., "Hypersonic control effectiveness studies on delata wings with trailing edge flaps", PhD Thesis, University of London, 1970.

144.Smith, S.C., "Use of shear-sensitive liquid crystals for surface flow visualisation", Journal of Aircraft, Vol. 29, No. 2, pp. 289-293, 1992.

145.Smith, A.J.D., Baxter, D.R.J., "Liquid crystal thermography for aerodynamic heating measurements in short duration hypersonic facilities", IEEE 1989.

146.Babinsky, H., Edwards, J.A., "Quantitative heat transfer measurement using liquid crystal thermography in a hypersonic gun tunnel", IUTAM Symposium, Aerothermochemistry of Spacecraft and Associated Hypersonic Flows, 1992.

147.Babinsky, H., Edwards, J.A., "The application and analysis of liquid crystal thermographs in short duration hypersonic flow", AIAA 93-0182, 1993.

148.Haq, Z.U., Roberts, G.T., East, R.A., "Interference heating near fin body junctions on hypersonic vehicles", 1st European symposium on hypersonic flow, ESTEC, 1991.

149.Kontis, K., Stollery, J.L., "Control effectiveness of a jet-slender body combination at hypersonic speeds", AIAA 96-2470, 1996. Also to appear in the Journal of Spacecraft and Rockets.

150.Courtis, N.C., "Hypersonic lifting shapes for manoeuvring projectiles", Mphil Thesis, Cranfield University, 1996.

151.Russell, D., Wyatt, J., "MSPECT signal processing package", private communication, Cranfield University, 1994.

152.Rae, W.H.Jr., Pope, A., "Low-speed wind tunnel testing", 2nd edition, A Wiley Interscience Publication, 1984.

153.Singh, A., "Private communication", 1995.

154.Chapkis, R.L., "Hypersonic flow over an elliptic cone: theory and experiment", Journal of the Aerospace Sciences, Vol. 28, No. 11, November, 1961.

155.Genxing, W., Ming, X., "Vortex patterns on slender bodies", Encyclopedia of Fluid Mechanics, Vol. 8, Aerodynamics and Compressible Flows, Ch. 9.

156.Stollery, J.L., Maull, D.J., "A note on shock detachment distance", Journal of the Royal Aeronautical Society, Vol. 64, June, 1960.

157.Ames research staff., "Equations, tables and charts for compressible flows", NACA Report 1135, 1952.

158.Brower, W., "Theory, tables and data for compressible flow", New York: Hemisphere, 1990.

159.Roper, J.J., "Literature survey of hypersonic lifting body shapes", DERA, DRA, R-DRA/WS/WX7/TR94510, UK, October. 1994.

160.Cox, R.N., Crabtree, L.F., "Elements of hypersonic aerodynamics", Academic Press, New-York, 1965.

161.Rasmussen, M., "Hypersonic flow", A Wiley-Interscience Publication, New York, 1994.

162.Sigal, A., "Noncircular fuselage analysis", Tactical Missile Aerodynamics: Prediction Methodology, Progress in Astronautics and Aeronautics, AIAA series, 1991.

163.Leung, K.K., Emanuel G., "Hypersonic inviscid and viscous flow over a wedge and cone", Journal of Aircraft, Vol. 32, No. 2, 1995.

164.Kim, B.S., Rasmussen, M.L., Jischke, M.C., "Optimisation of waverider configurations generated from axisymmetric conical flows", Journal of Spacecraft and Rockets, Vol. 20, No. 5, pp-461-469, 1983.

165.Wells, W., Armstrong, W., "Tables of aerodynamic coefficients obtained from developed Newtonian expressions for complete and partial conic and spherical bodies at combined angles of attack and sideslip with some comparisons with hypersonic experimental data. NASA TR R-127, 1961.

166.Kokkalis, A., "Private communication", Westland Helicopters, UK, 1997.

167.Eiseman, P.R., "Ann. Rev. Fluid Mechanics", Vol. 17, pp 487-522. 1985.

168.Eriksson, L.E., "SIAM", J. Sci. St. Comput., Vol. 6, pp 712-741, 1985.

169.Pagan, D., Molton, P., Delery, J., "Basic experiments on a supersonic vortex flow around a missile body", Journal of Spacecraft and Rockets, Vol. 29, 1992.

170.Anderson, J.D., Jr., "Hypersonic and high temperature gas dynamics", McGraw-Hill Editions, 1989.

171.Tracy, R.R., "Hypersonic flow over a yawed circular cone", Graduate Aeronautical Labs, CIT, HRP Memo. No. 69, August, 1963.

172.Lukasiewicz, J., "Blast-hypersonic flow analogy - Theory and application", American Rocket Society Journal, Vol. 32, No. 9, September 1962, pp. 1341 -1346.

173.Wells, P.B., Thornley, P.D., "Blunt cone pressure correlations for supersonic and hypersonic flow", AIAA 96-2447 CP, 1996.

174.Kuehn, D.M., "Experimental and theoretical pressures on blunt cylinders for equilibrium and nonequilibrium air at hypersonic speeds", NASA TN D-1979, 1963.

175.Hayes, W.D., "Some aspects of hypersonic flow", The Ramo-Wooldridge Corp. Rep, California, USA, 1955.

176.Crawford, D.H., McCauley, W.D., "Investigation of the laminar aerodynamic heat-transfer characteristics of a hemisphere-cylinder in the Langley 11-inch hypersonic tunnel at a Mach number of 6.8", NACA 1323, 1957.

177.Schwartz, L.W., "Comment on an empirical expression for drag coefficients of cones at supersonic speeds", AIAA J., Vol. 7, No. 3, 1969.

178.Sims, J.L., "Tables for supersonic flow around right circular cones at zero angle of attack", NASA SP-3004,1964.

179.Hughson, M.C., Cottrell, C.J., "Hypersonic prediction comparisons with experimental data for a cone-cylinder at Mach 6.86", AIAA 89-0524.

180.Lijewski, L.E., Cipolla, J.R., Thompson, J.F., Gatlin, B., "Program EAGLE User's Manual", AFATL-TR-88-117, Vols. 1, 2, 3, 4, 1988.

181.Bertram, M.H., Blackstock, T.A., "Some simple solutions to the problem of predicting boundary-layer self-induced pressures", NASA TN D-798.

182.Stollery, J.L., "Private communication", Cranfield, UK, 1997.

183.Eckert, E.R.G., "Survey of boundary layer heat transfer at high velocities and high temperatures", WADC TR 59-624, 1960.

184.Hayes, W.D., Probstein, R.F., "Hypersonic flow theory", Academic press, London, 1959, pp 265-277.

185.Creager, M.O., "The effects of leading edge bluntness on the local heat transfer and pressure distributions", NACA TN 4142, 1957.

186.Bird, G.A., "Effect of wave interactions on pressure distributions in supersonic and hypersonic flows", AIAA Journal, Vol. 1, No. 3, pp. 634 - 638, 1963.

187.Gentry, M.C., Jacobi, A.M., "Heat transfer enhancement by delta-wing vortex generators on a flat plate: Vortex interactions with the boundary layer", Experimental Thermal and Fluid Science, Vol. 14, No. 3, pp 231-242, 1997.

188.Sullivan, P.A., "Hypersonic flow over slender double wedges", AIAA Journal, Vol. 1, No. 8, 1963, pp 1927.

189.Wilby, P.G., "The flow field about a hemisphere-cylinder body at a Mach number of 7.3", FFA report 92, 1962.

190.Johnson, C.B., Bushnell, D.M., "Power law velocity profile exponent variations with Reynolds number, wall cooling, and Mach number in a turbulent boundary layer", NASA TN D-5753, 1970.

191.Horton, H.P., "The calculation of adiabatic laminar boundary layer shock wave interactions in axi-symmetric flow: Part I - Hollow cylinder-flare bodies with zero spin", VKI TN-63, 1970.

192.Gray, Don, J., "Laminar boundary-layer separation on flared bodies at supersonic and hypersonic speeds", AEDC-TDR-64-277, 1965.

193.Sperinck, N.P.B., "The simulation of rocket plume effects on a blunted conical body", COA MSc thesis, CIT, UK, 1989.

194.Vermeulen, J.P., Simeonides, G., "Parametric studies of shockwave boundary layer interactions in two dimensional compression corners at Mach 6", VKI TN-181, 1992.

195.Hallcrest Ltd., "Private communication", Dorset, UK, 1996.

196.Qin, N., "Private communication", Cranfield, UK, 1996.

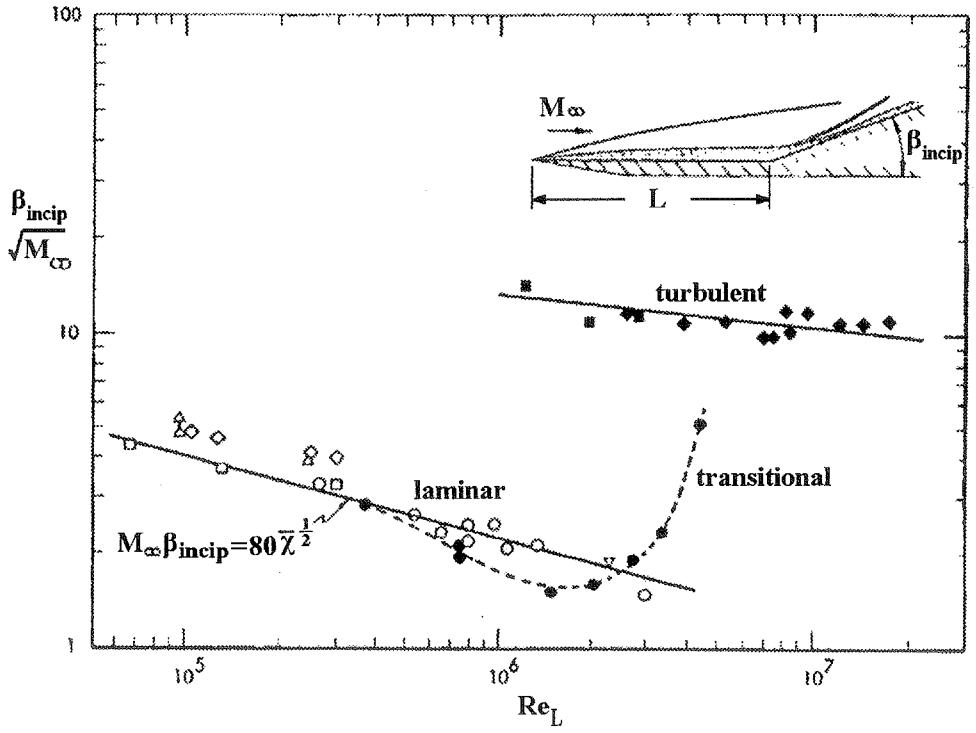

Fig. 2.1 Incipient separation angles for laminar and turbulent separation (ref. 29)

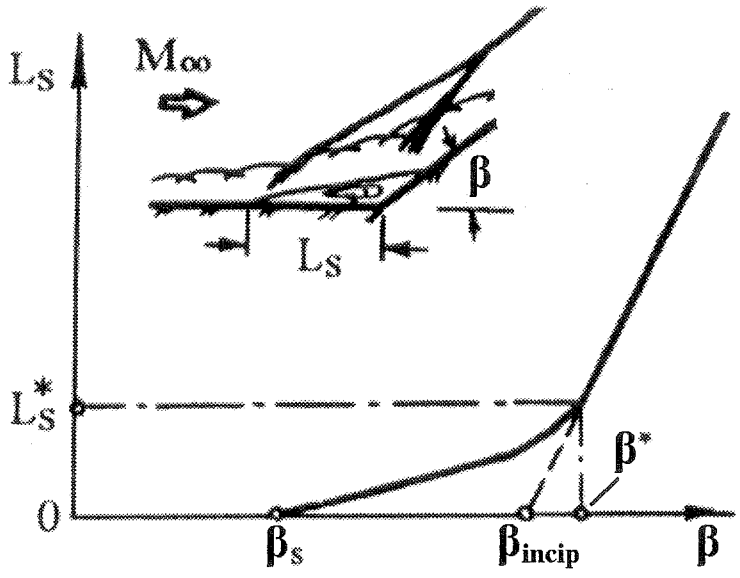

Fig. 2.2 Variation of separation length in vicinity of 2-D compression corner (ref. 41)

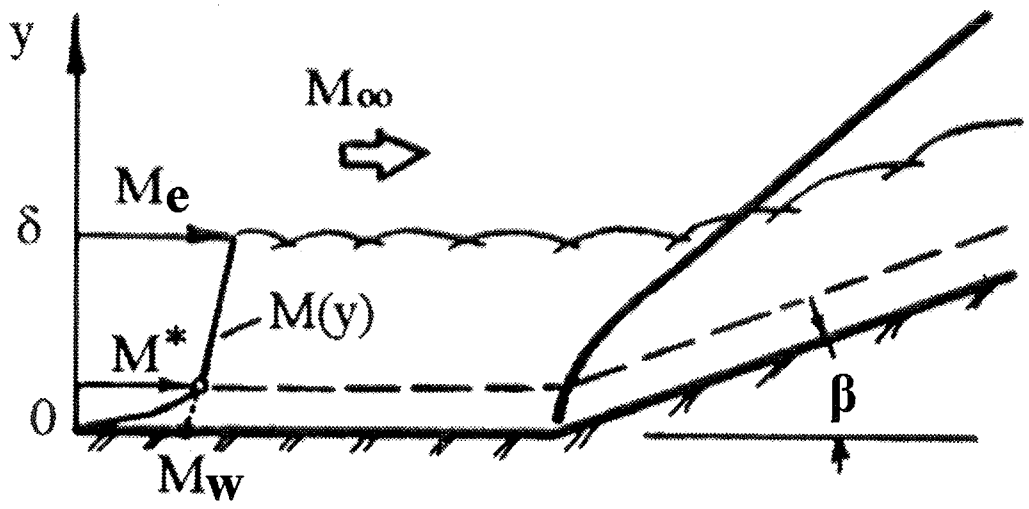

Fig. 2.3 Model of Elfstrom (ref. 37)

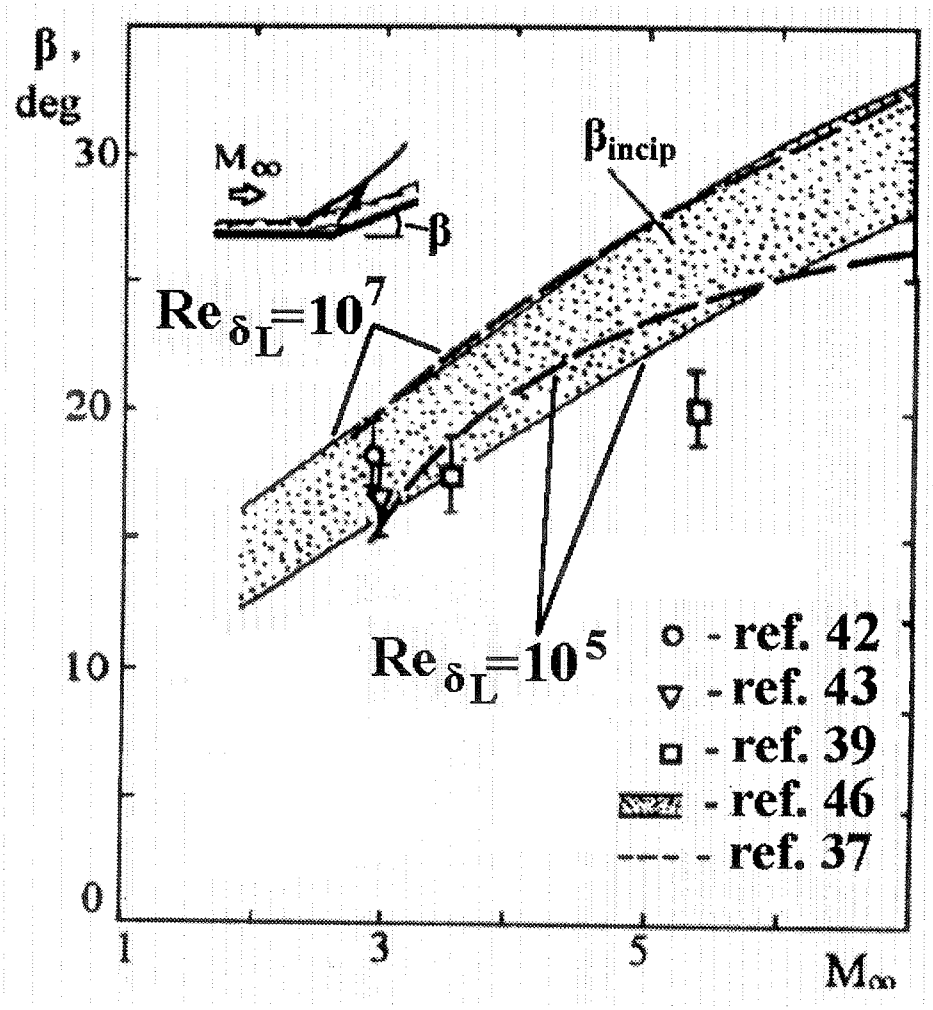

Fig. 2.4 2-D compression corner incipient separation data

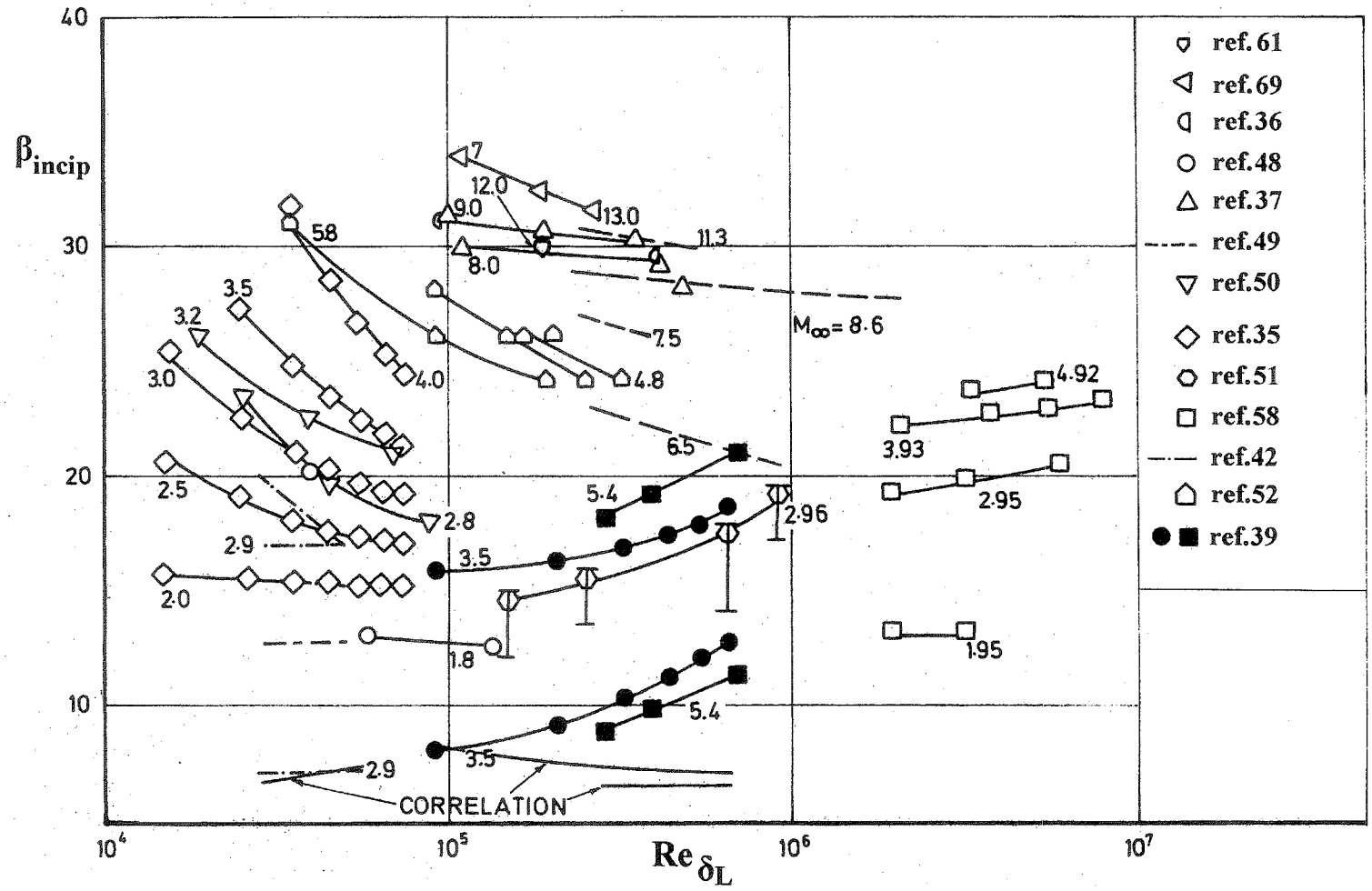

Fig. 2.5 Incipient separation at a wedge compression corner

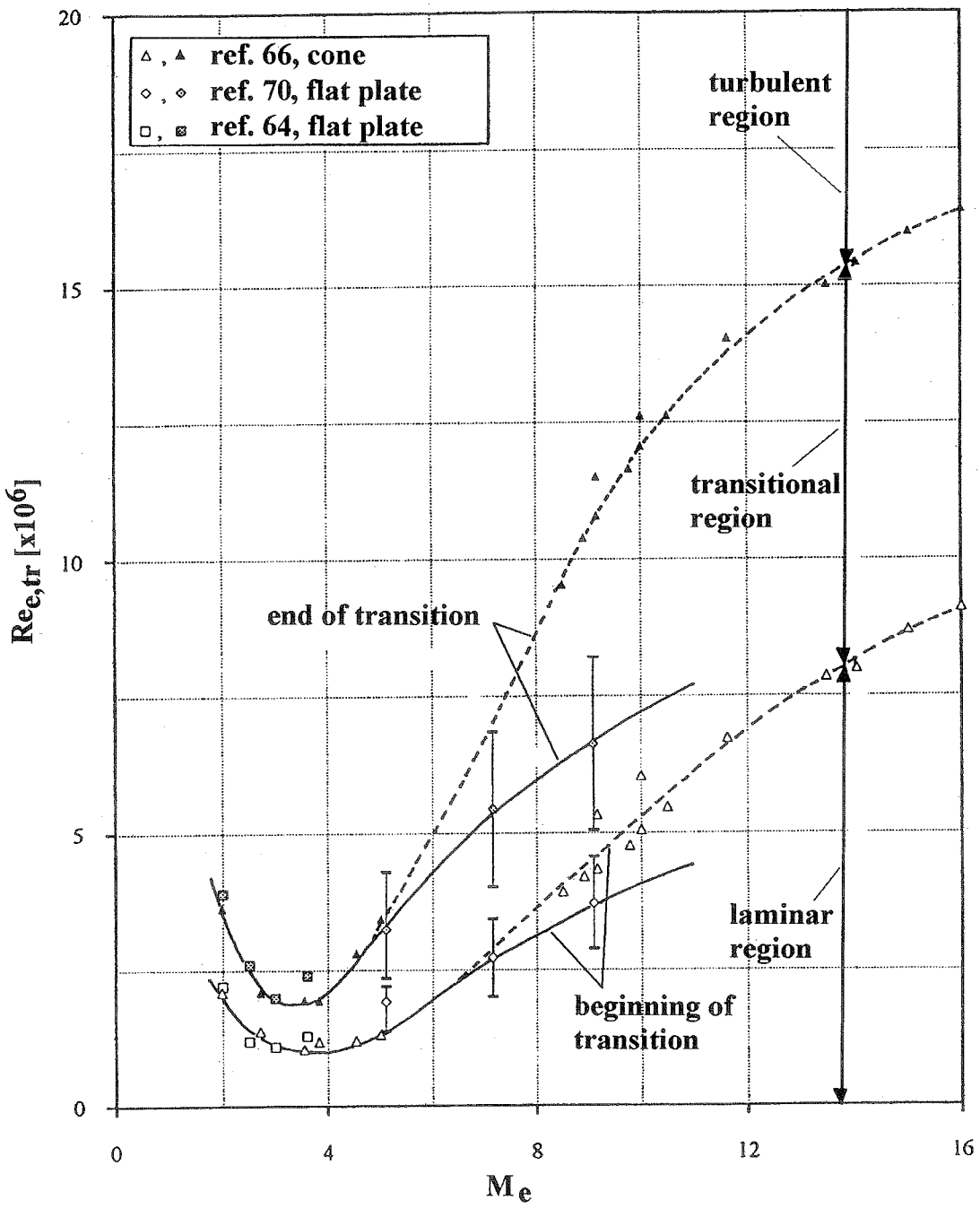

Fig. 2.6 The effect of Mach number on the transition of conical and quasi two-dimensional boundary layers

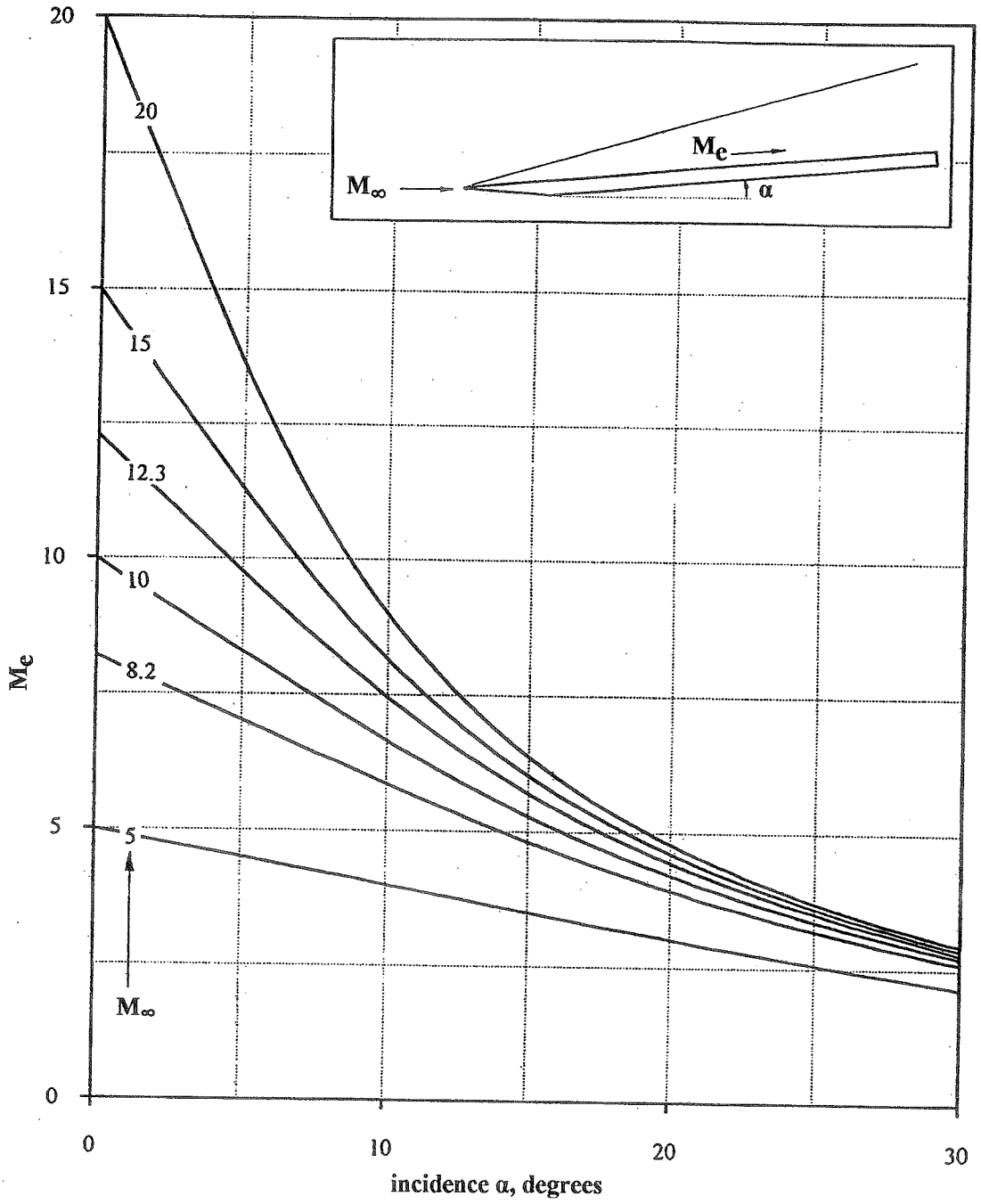

Fig. 2.7 The effect of incidence on the local Mach number over a flat plate

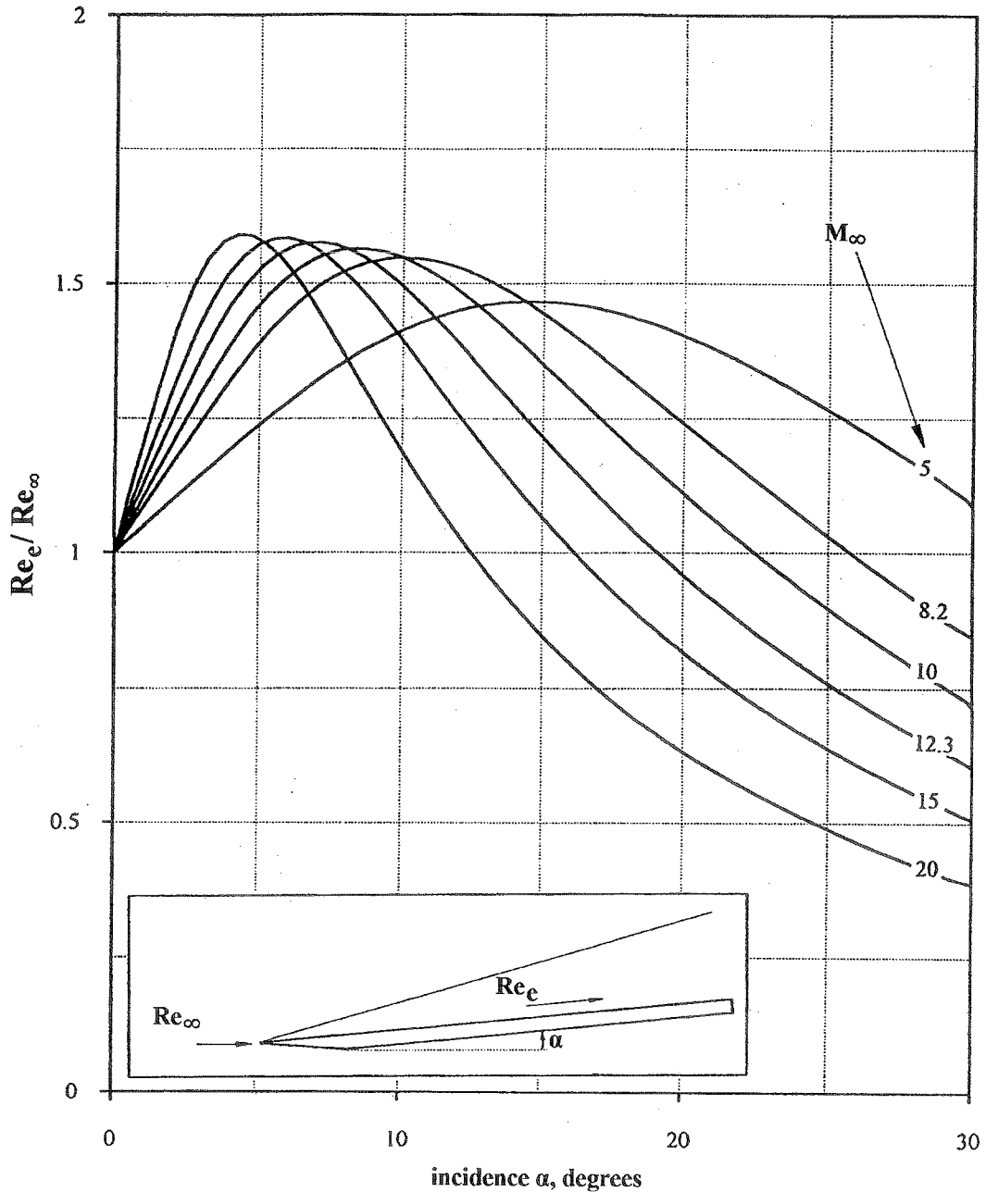

Fig. 2.8 The effect of incidence on the local unit Reynolds number over a flat plate

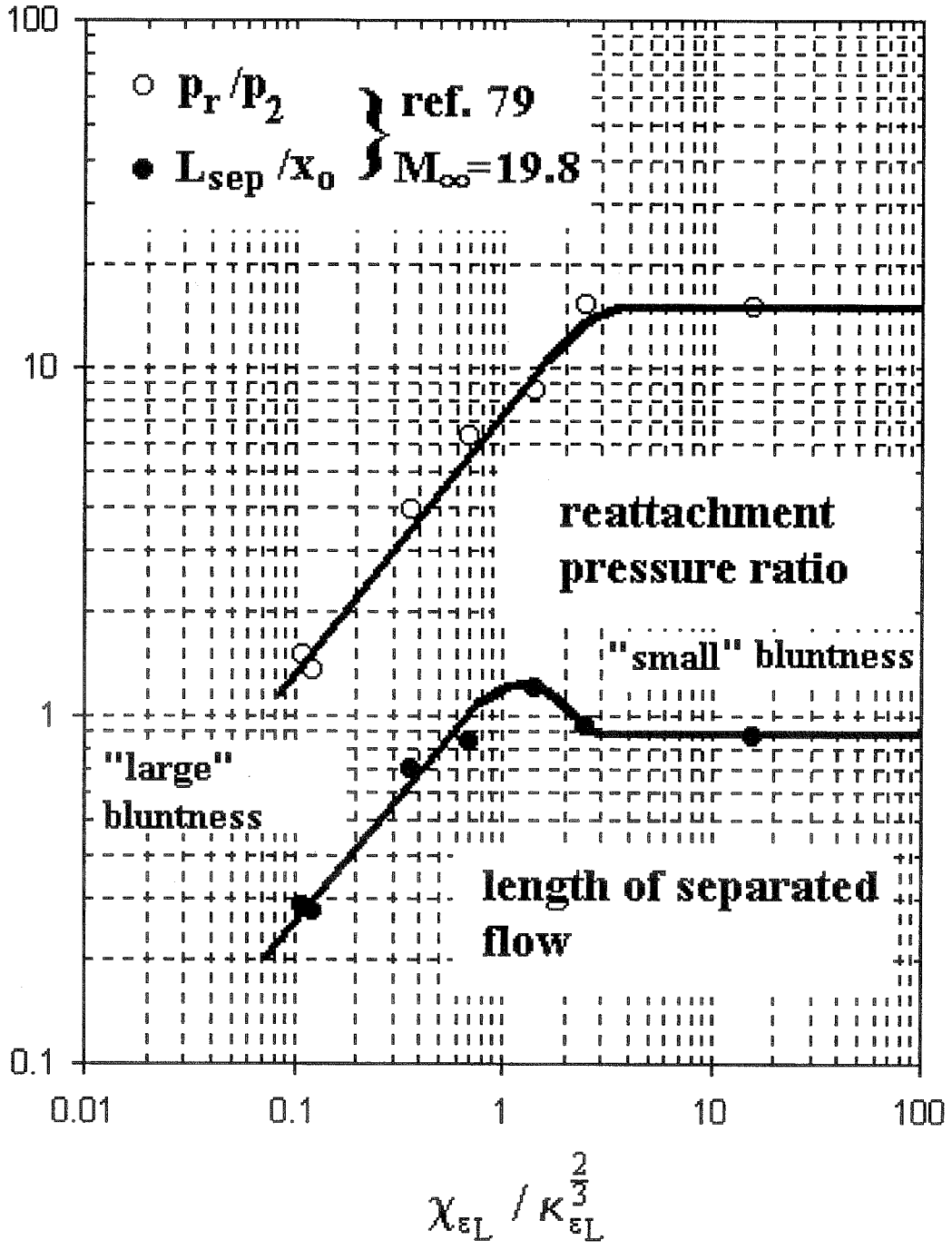

Fig. 2.9 Correlation between the effect of leading edge bluntness on the length of separated flow and on the reattachment pressure ratio (ref. 79, α=0°, β=25°)

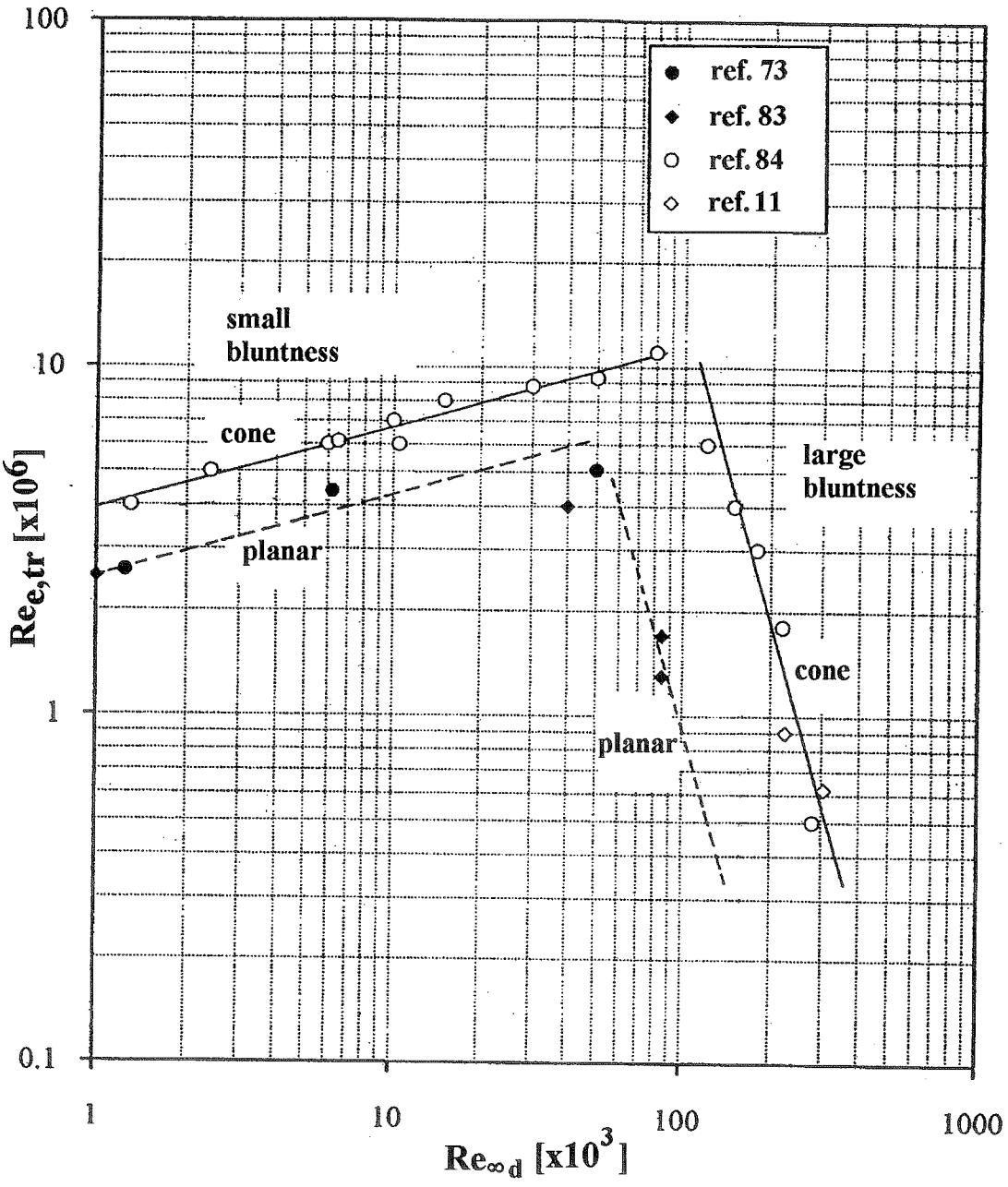

Fig. 2.10 The effect of "small" and "large" bluntness on the onset of transition in planar and conical boundary layers

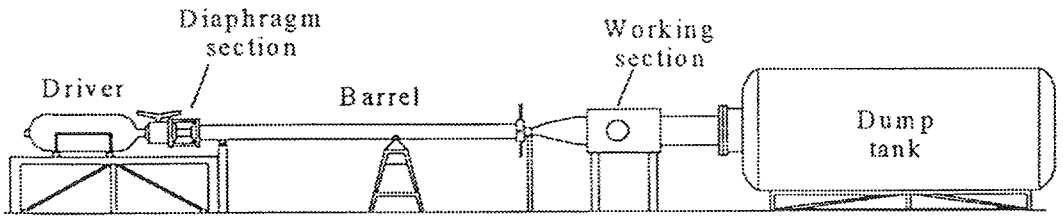

Fig. 3.1 A sketch of the gun-tunnel

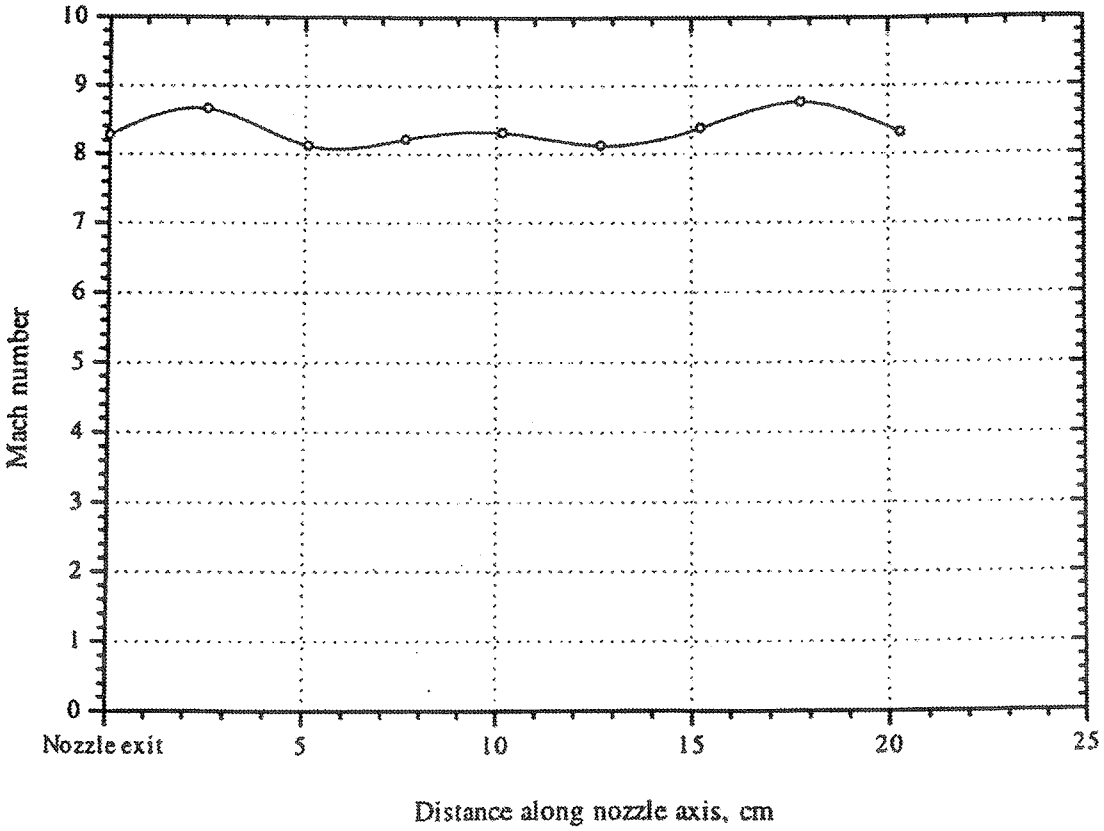

Fig. 3.2 Variation of Mach number along the axis of the nozzle (ref. 137)

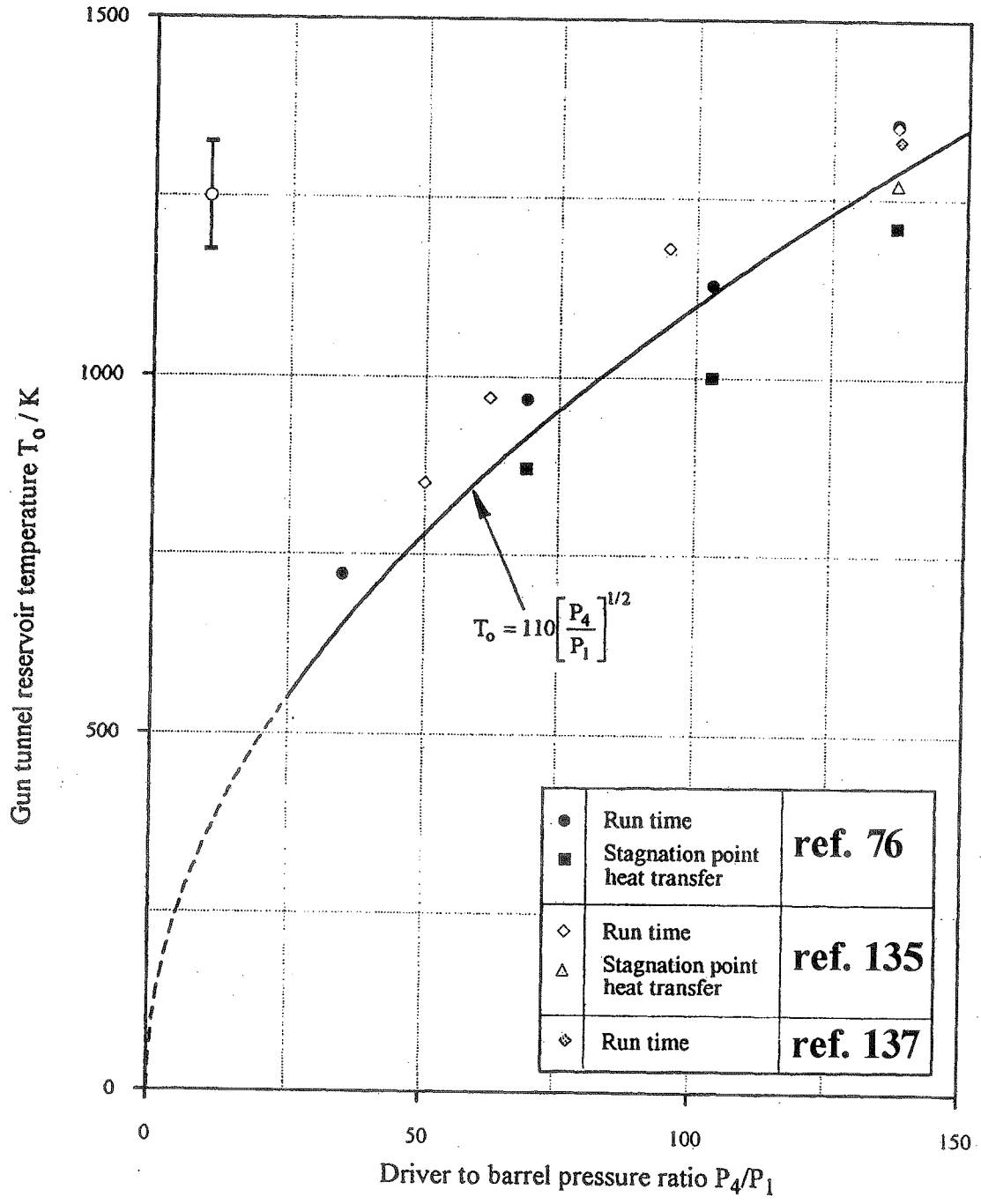

Fig. 3.3 Variation of reservoir temperature with the driver to barrel pressure ratio (ref. 76)

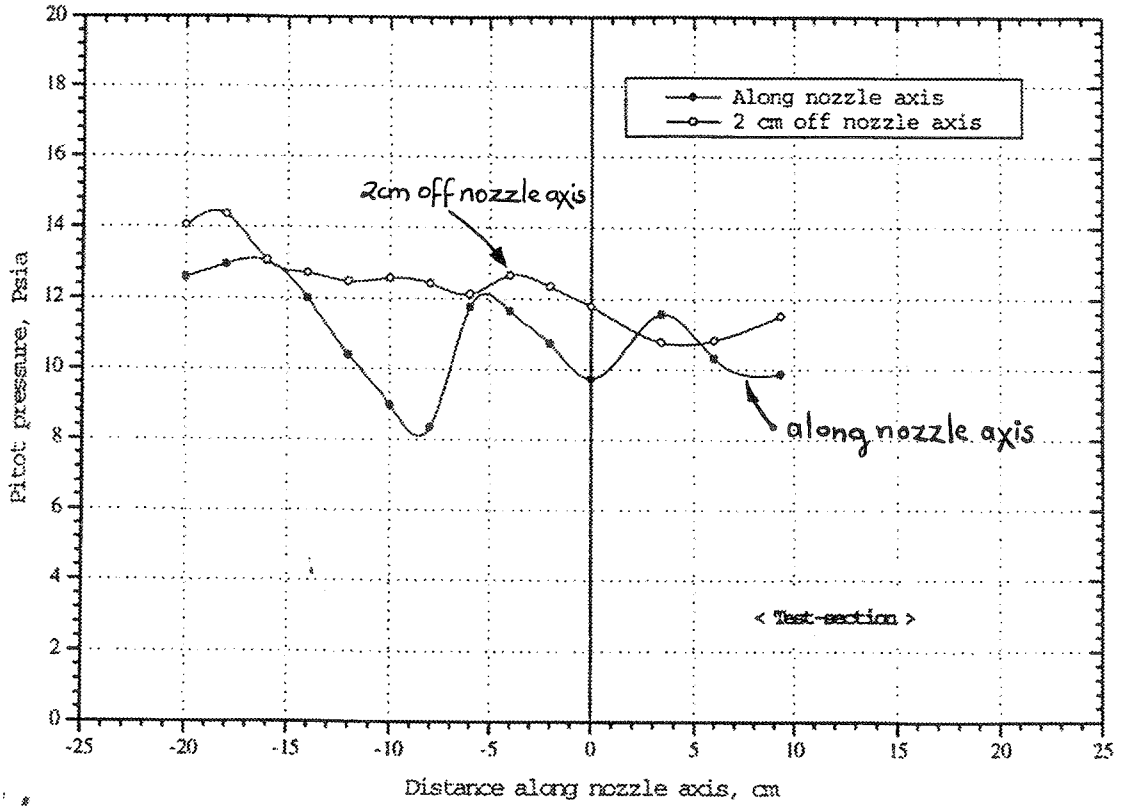

Fig. 3.4 Pitot pressure measurements along and off the axis of Mach 8.2 nozzle (ref. 140)

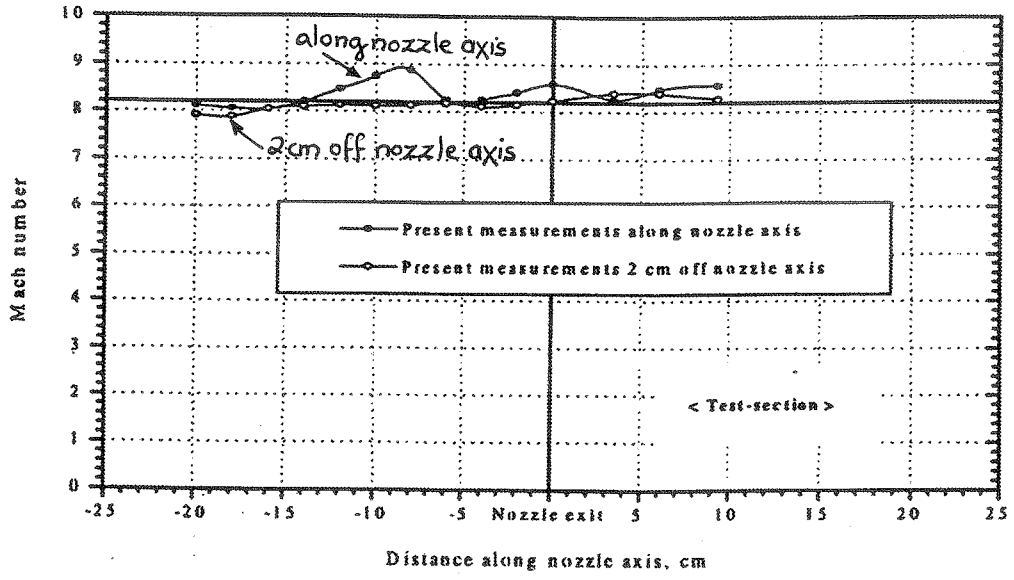

Fig. 3.5a Mach number survey along and off the axis of Mach 8.2 nozzle (ref. 140)

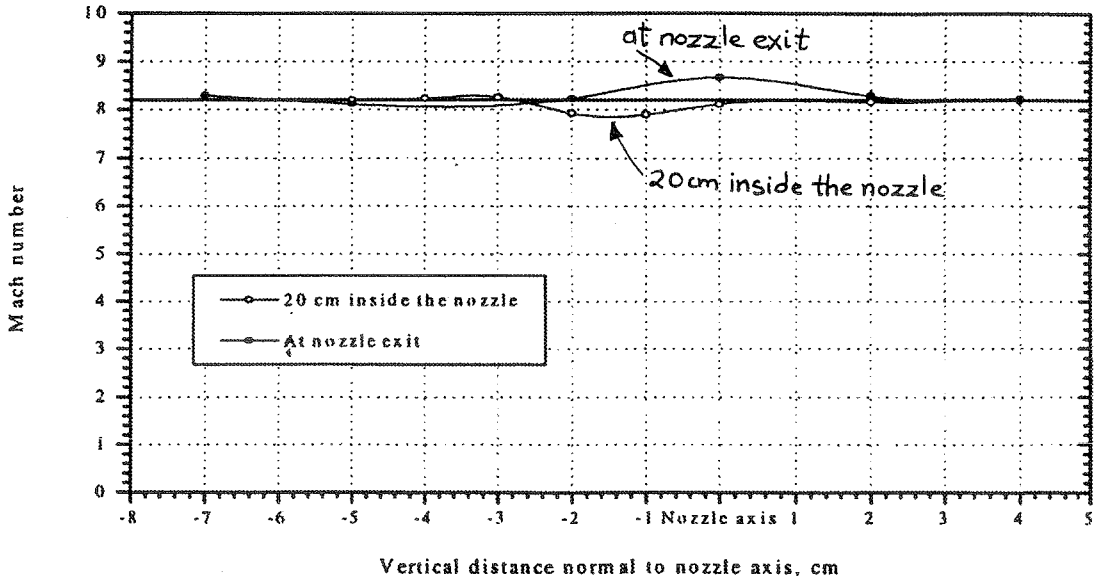

Fig. 3.5b Mach number survey along a vertical line normal to the axis of the Mach 8.2 nozzle (ref. 140)

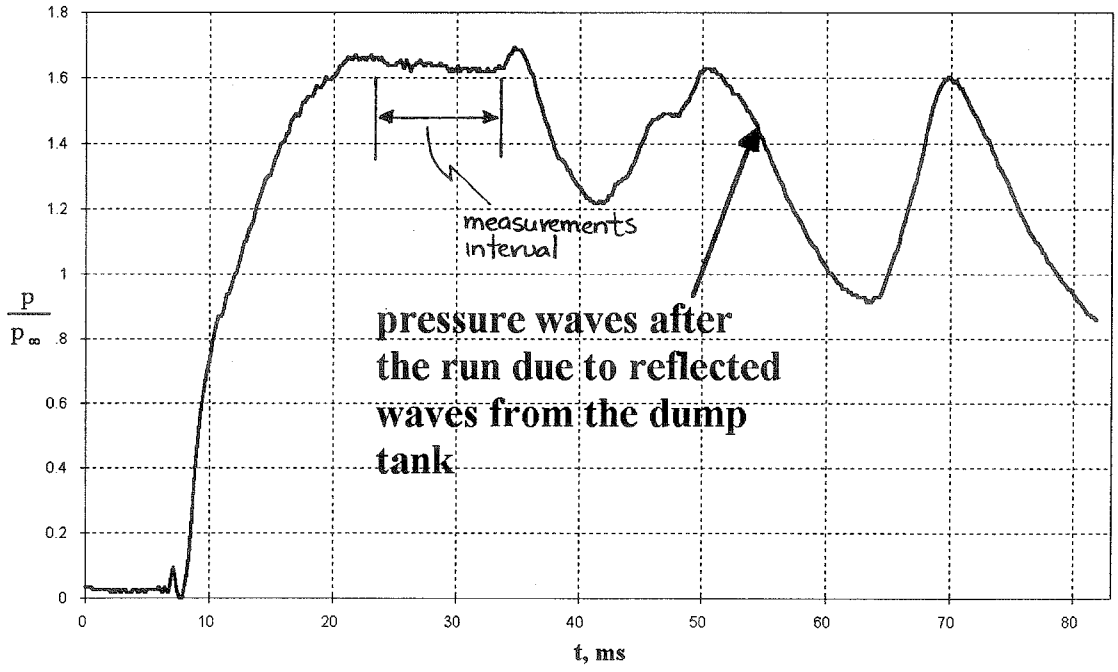

Fig. 3.6 A typical pressure transducer output signal

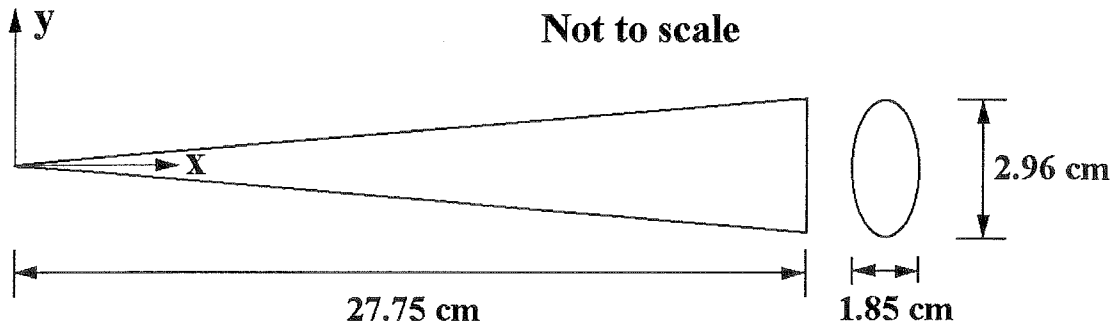

Fig. 3.7a A sketch of the elliptic cone without strakes, $L_{cone}/d_{minor}=15$

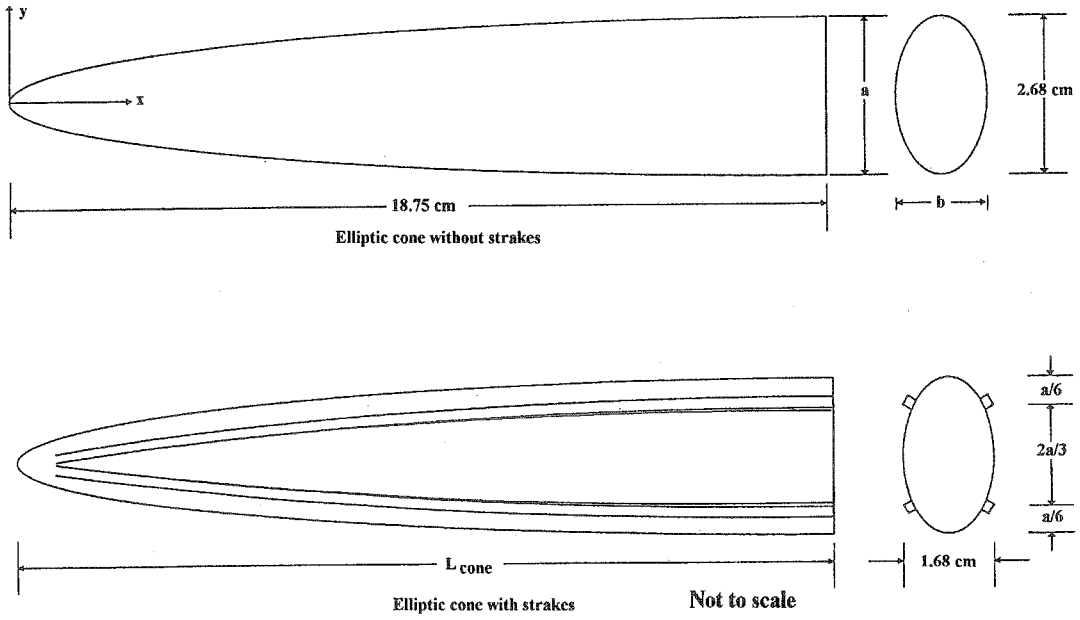

Fig. 3.7b A sketch of the power-law elliptic cone with and without strakes

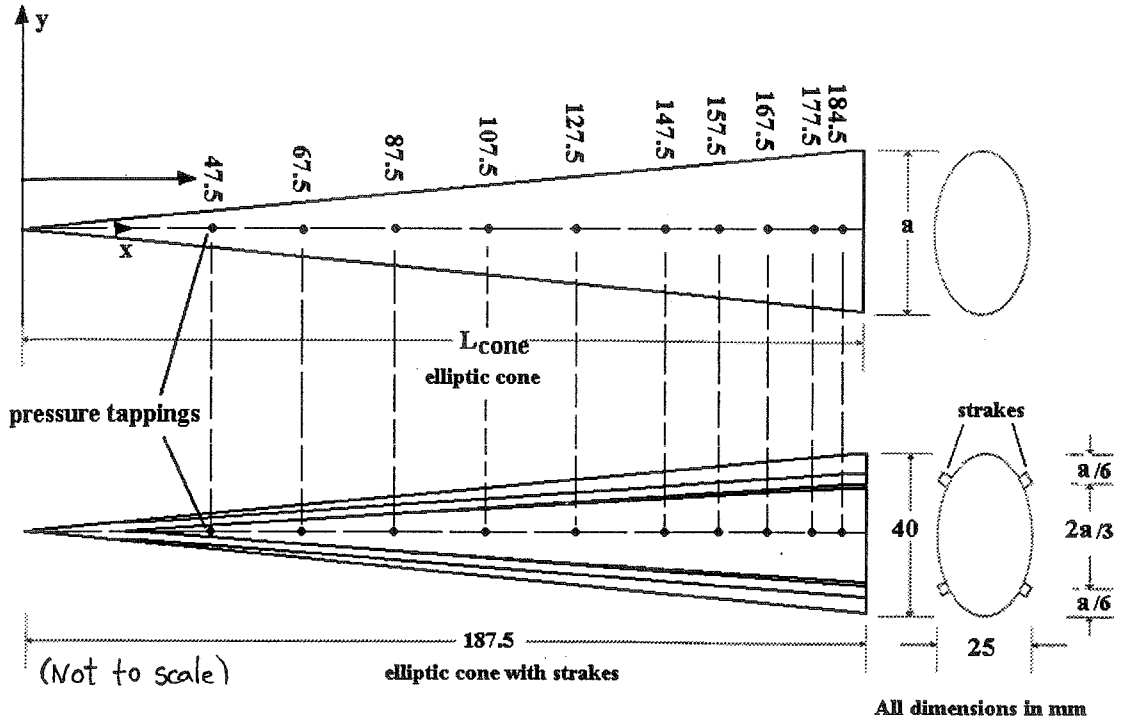

Fig. 3.7c A sketch of the elliptic cone with and without strakes, L_{cone}/d_{minor}=7.5

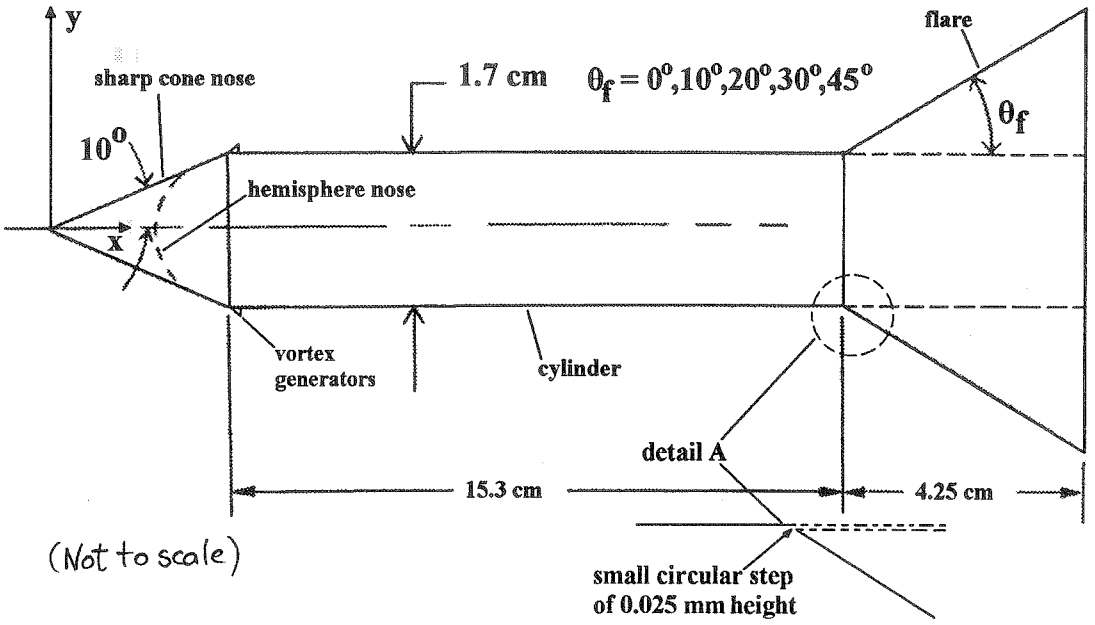

Fig. 3.7d A sketch of the cylinder-flare body

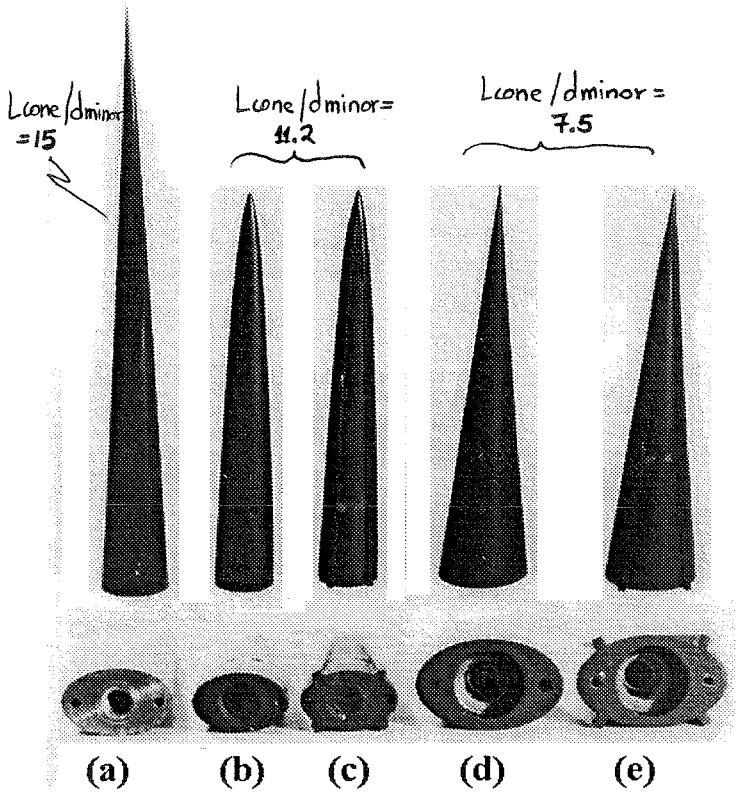

Fig. 3.8a Photographs of the elliptic cone models

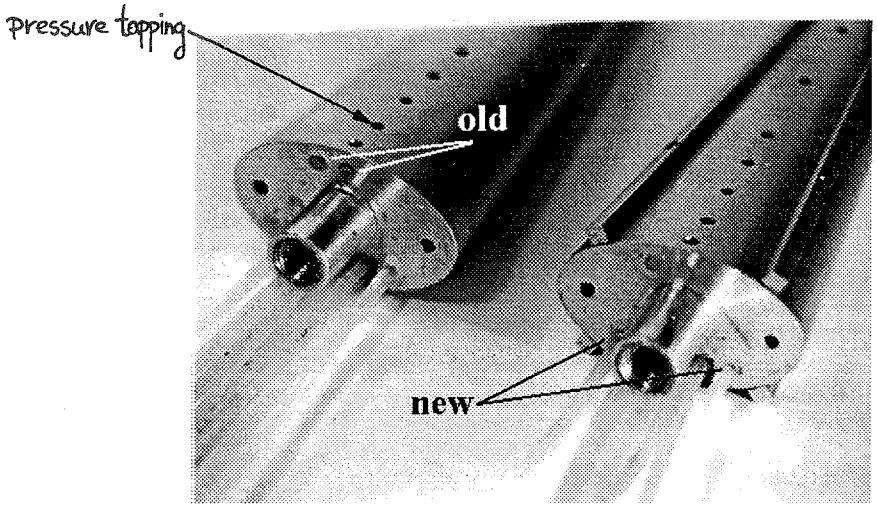

Fig. 3.8b Photographic detail of the base region of the pressure model, (elliptic cone with and without strakes, $L_{cone}/d_{minor}=7.5$)

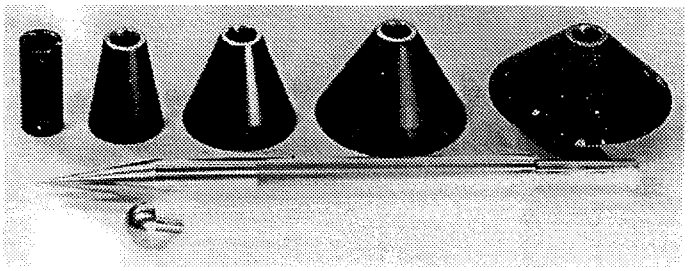

Fig. 3.9a Photograph of the cylinder-flare model

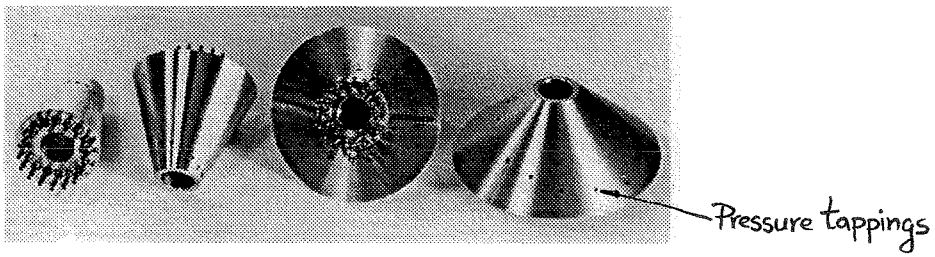

Fig. 3.9b Photograph of the instrumented flares with pressure tappings

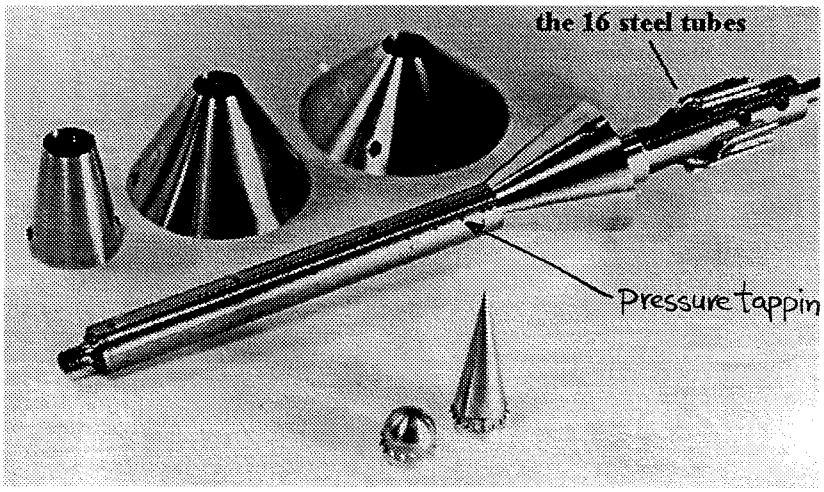

Fig. 3.9c Photograph of the instrumented cylinder-flare model with pressure tappings

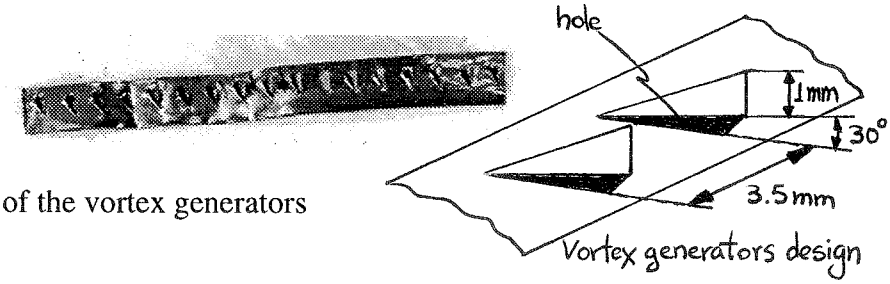

Fig. 3.10 Photograph of the vortex generators

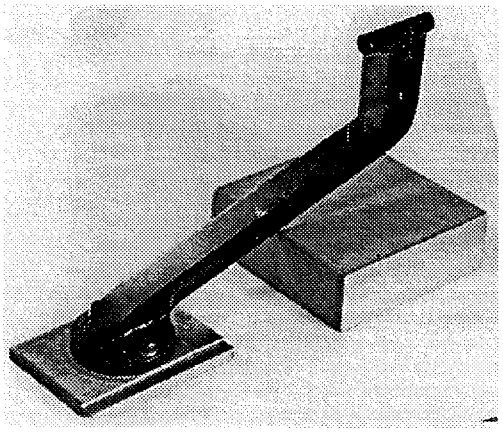

Fig. 3.11a Photograph of the horizontally rotatable rigid mounting

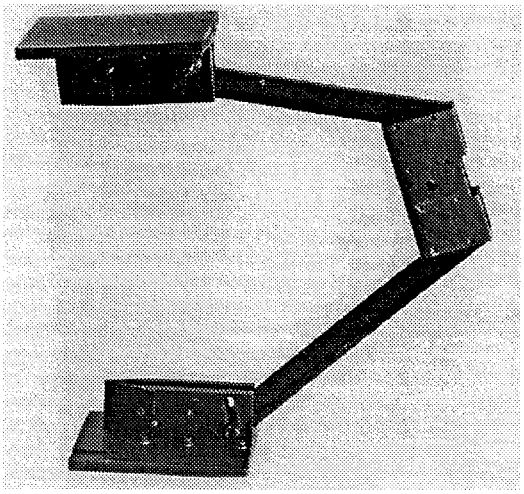

Fig. 3.11b Photograph of the V-shape mounting block

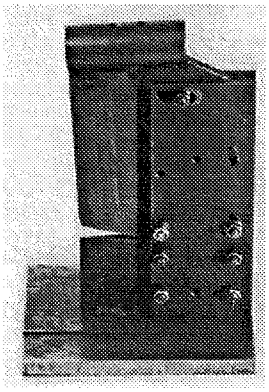

Fig. 3.11c Photograph of the pedestal support

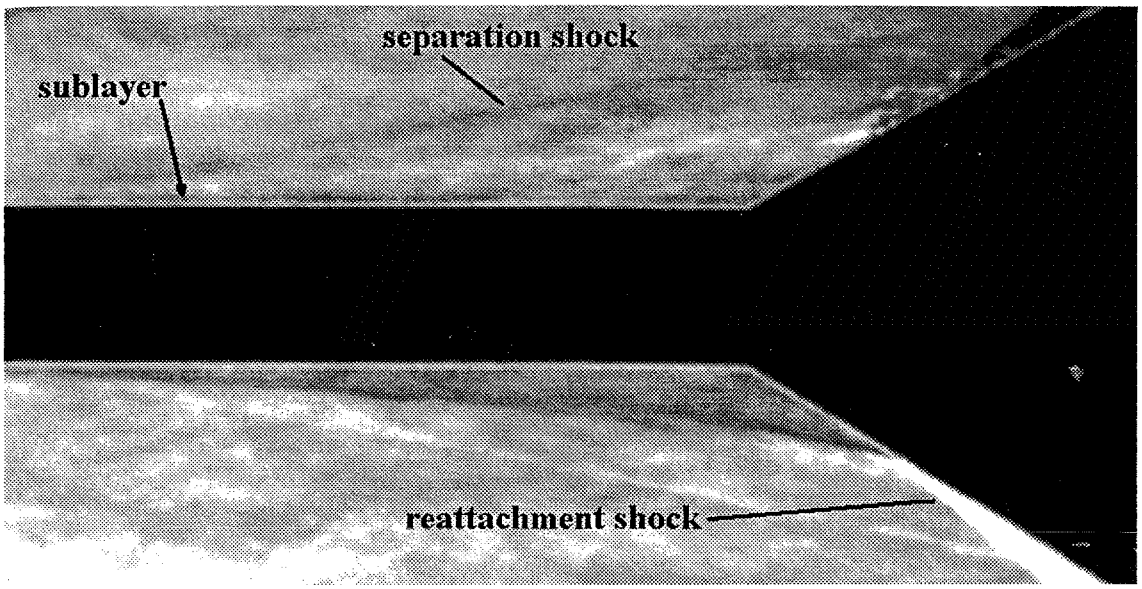

Fig. 3.12 Typical schlieren picture of flow separation and reattachment (sharp cone-cylinder-30°-flare body without vortex generators)

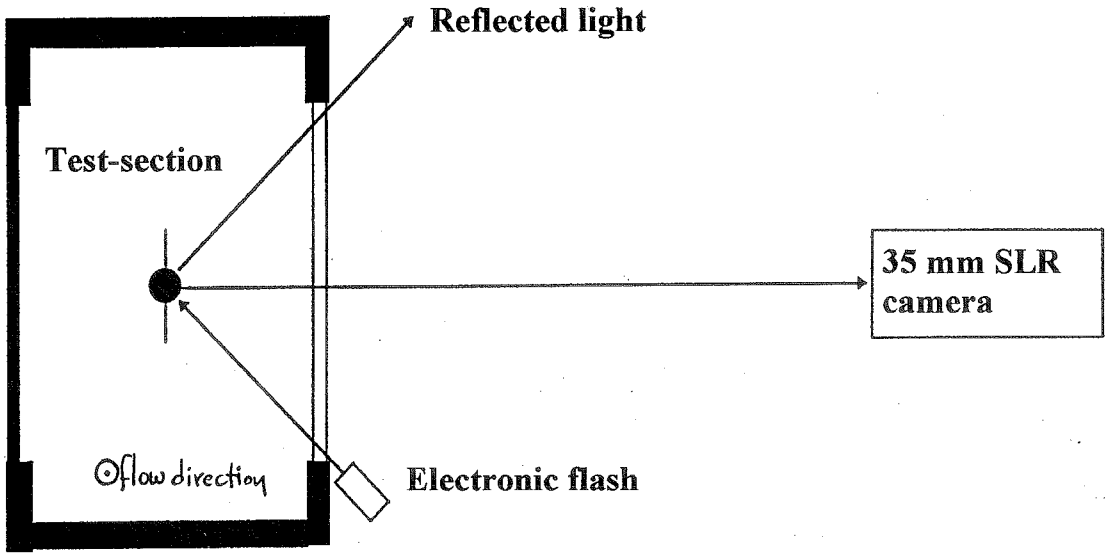

Fig. 3.13 Schematic of the set-up for the liquid crystal technique as viewed along the direction of the flow

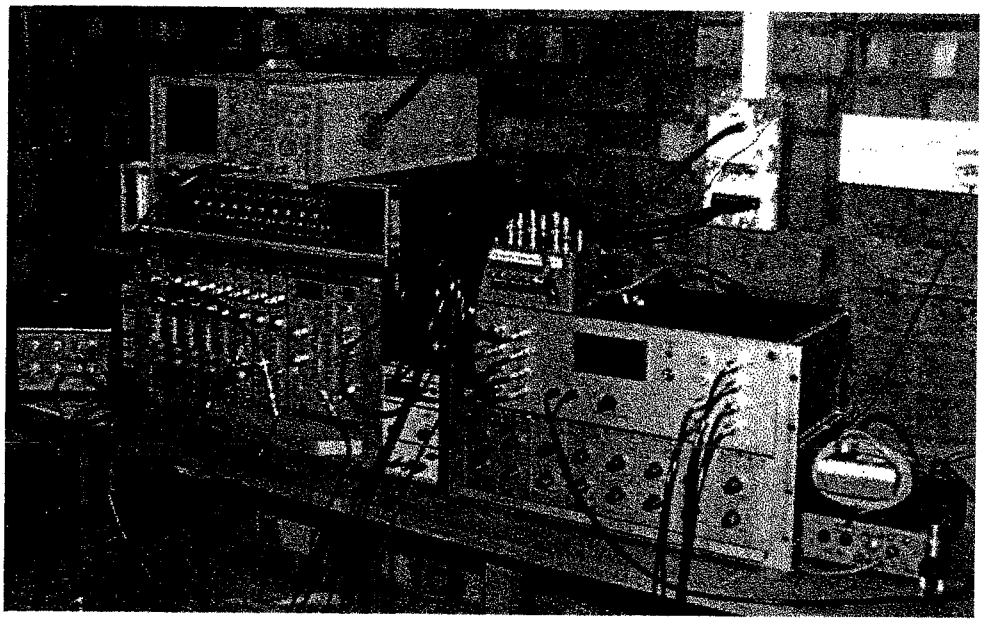

Fig. 3.14 Photograph of the system used for pressure and force data acquisition

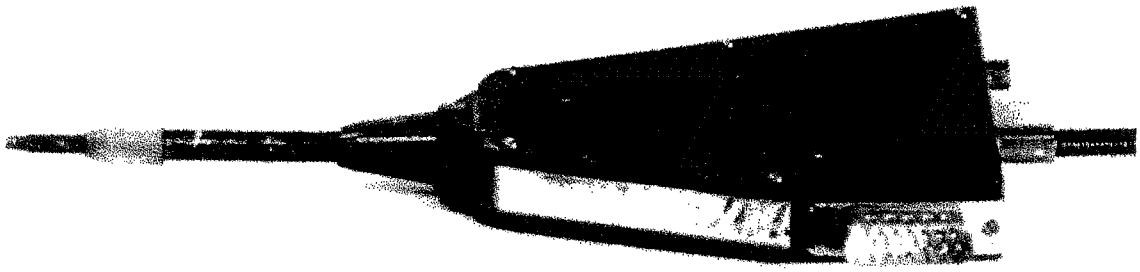

Fig. 3.15 Photograph of the force balance

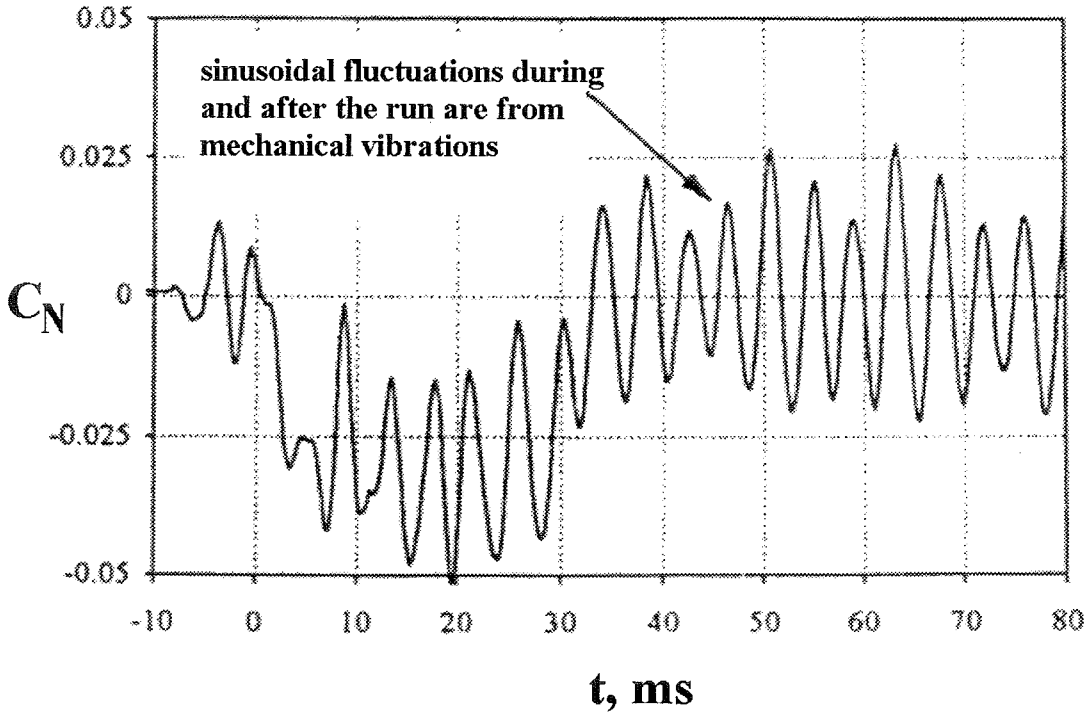

Fig. 3.16a Typical unfiltered signal trace of the strain gauge balance (normal force component)

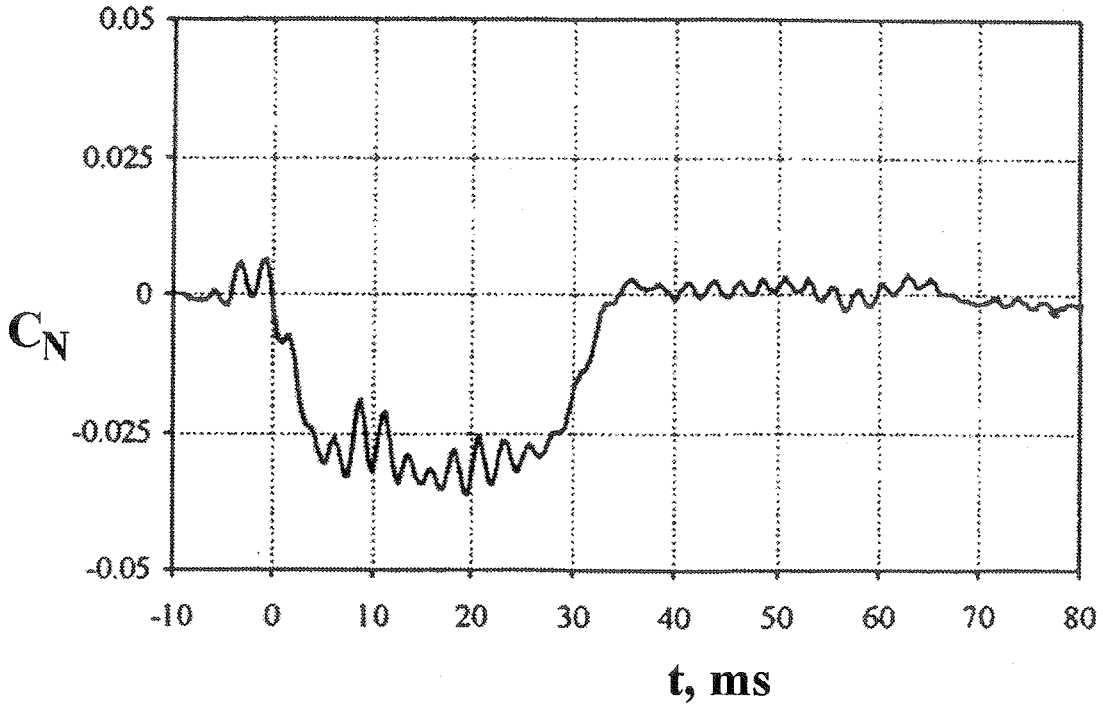

Fig. 3.16b Typical filtered signal trace of the strain gauge balance (normal force component)

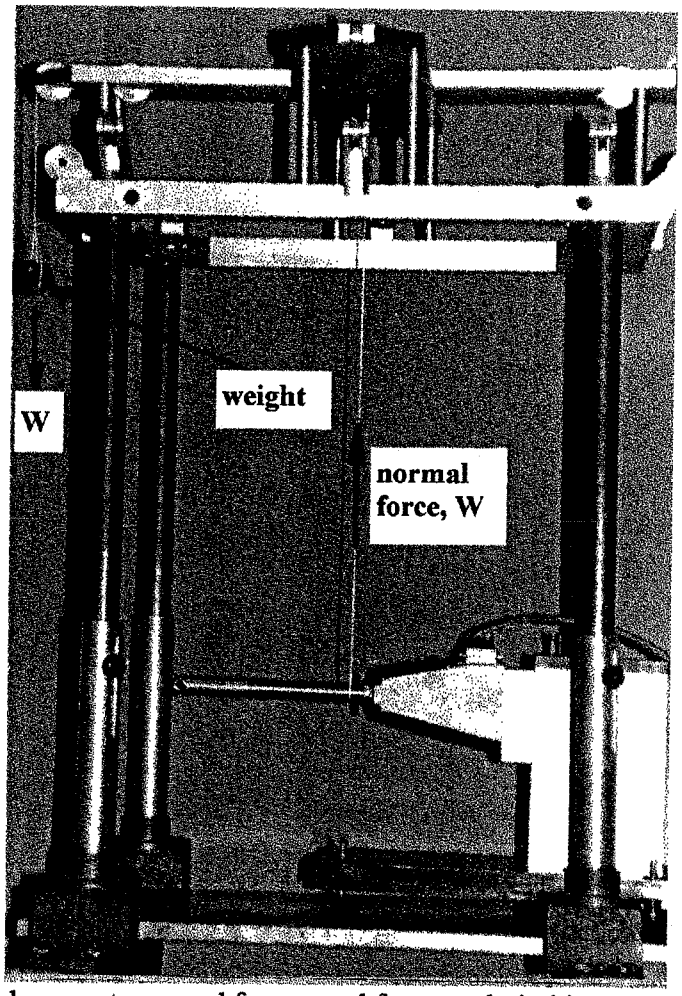

a) horizontal balance set-up used for normal force and pitching moment calibration

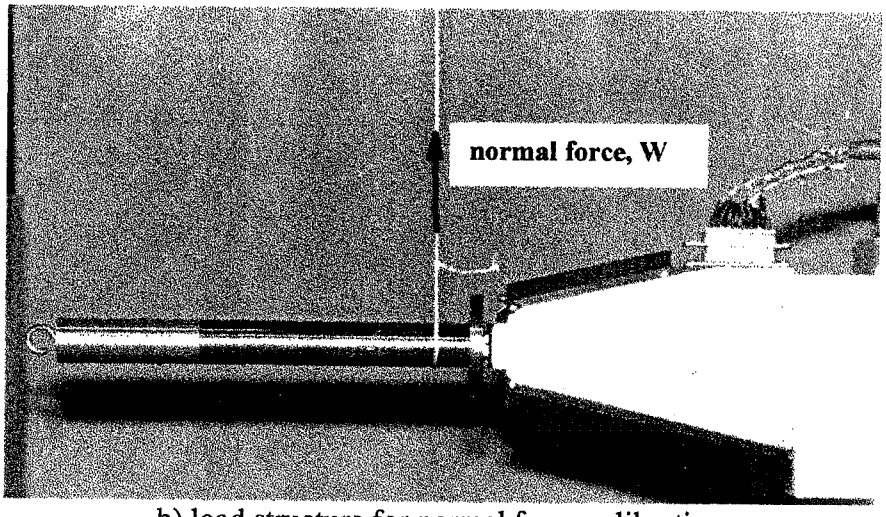

b) load structure for normal force calibration

Fig. 3.17 Set-up used for calibration of gun-tunnel 3-component force balance

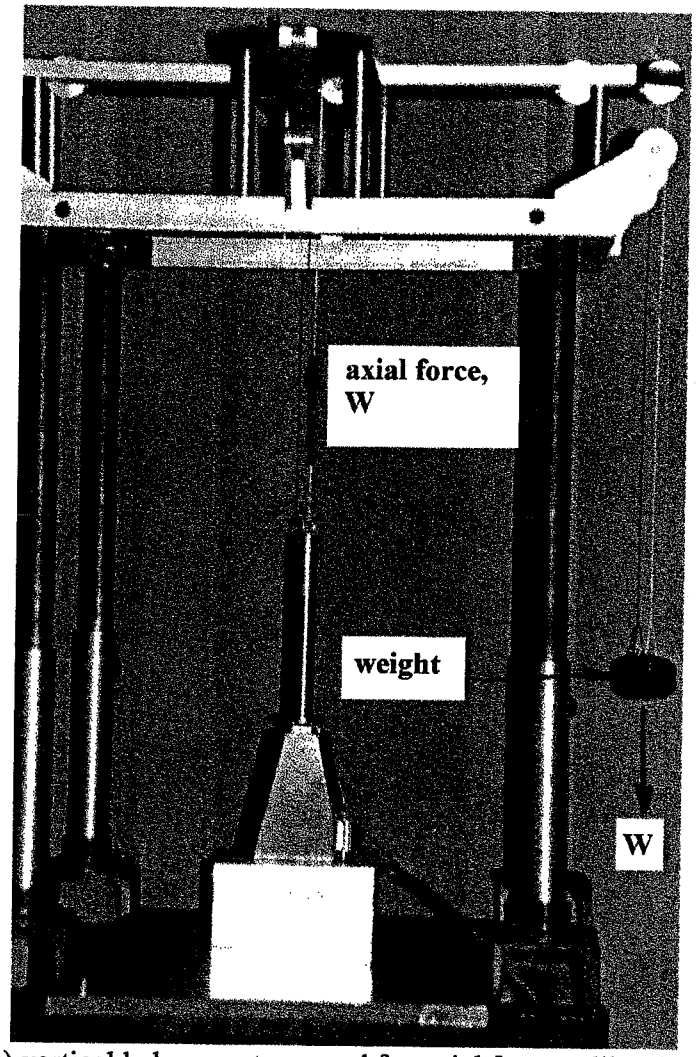

c) vertical balance set-up used for axial force calibration

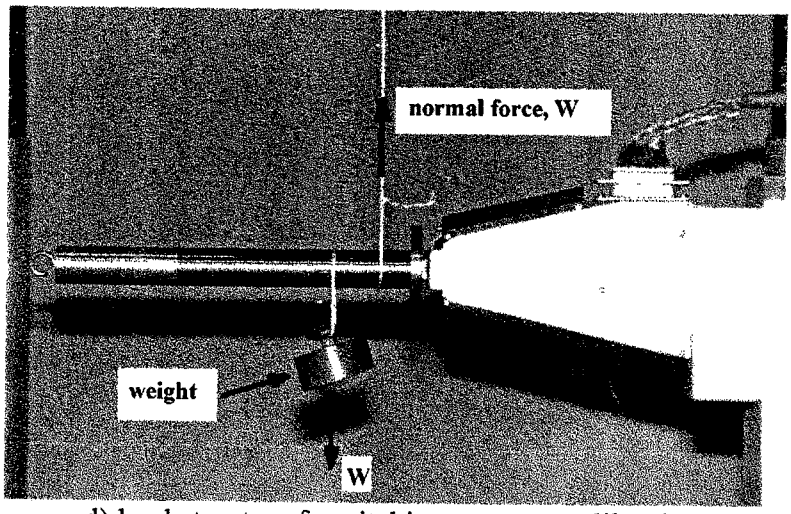

d) load structure for pitching moment calibration

Fig. 3.17 Concluded

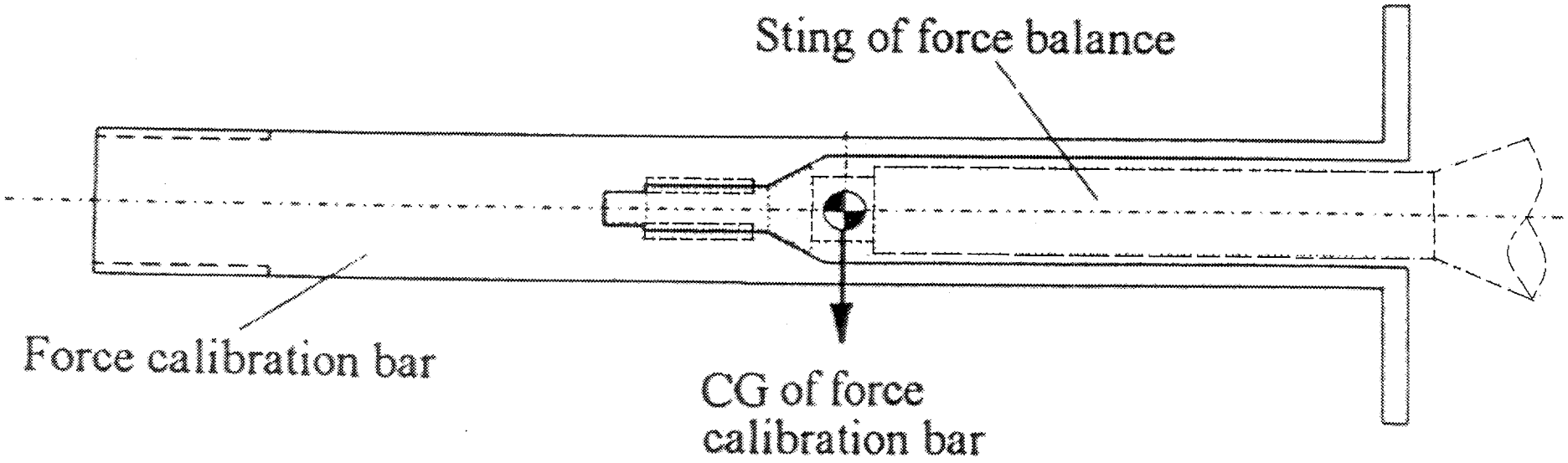

Fig. 3.18 Calibration bar

side view

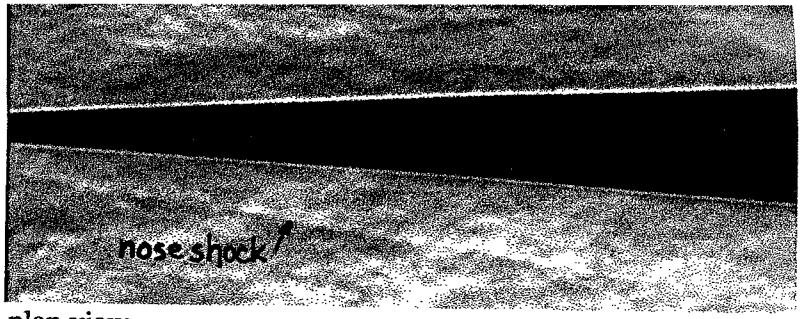

plan view

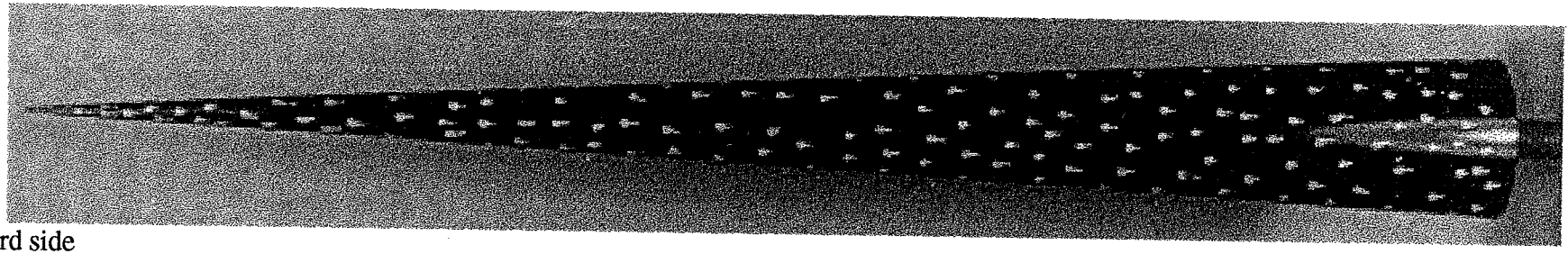

windward side

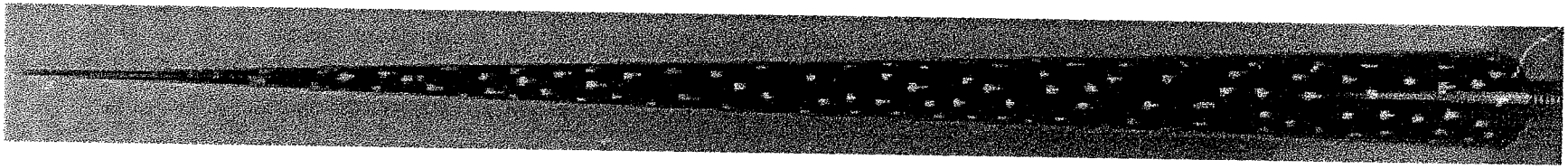

left side

a) $\alpha=0°$

Fig. 4.1 Schlieren and oil-dot pictures for configuration 1

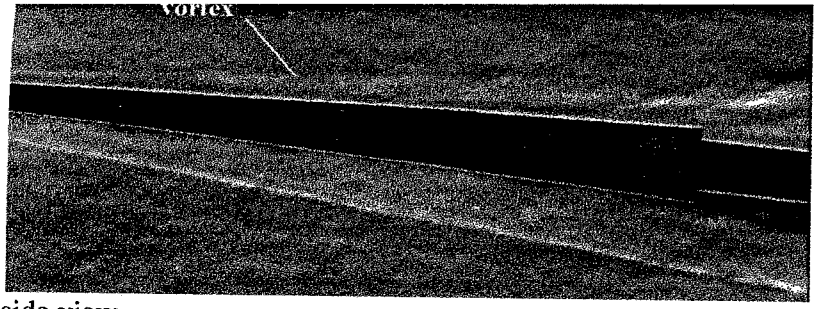

side view

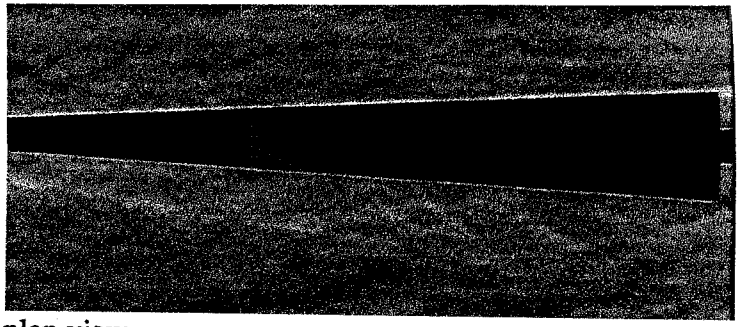

plan view

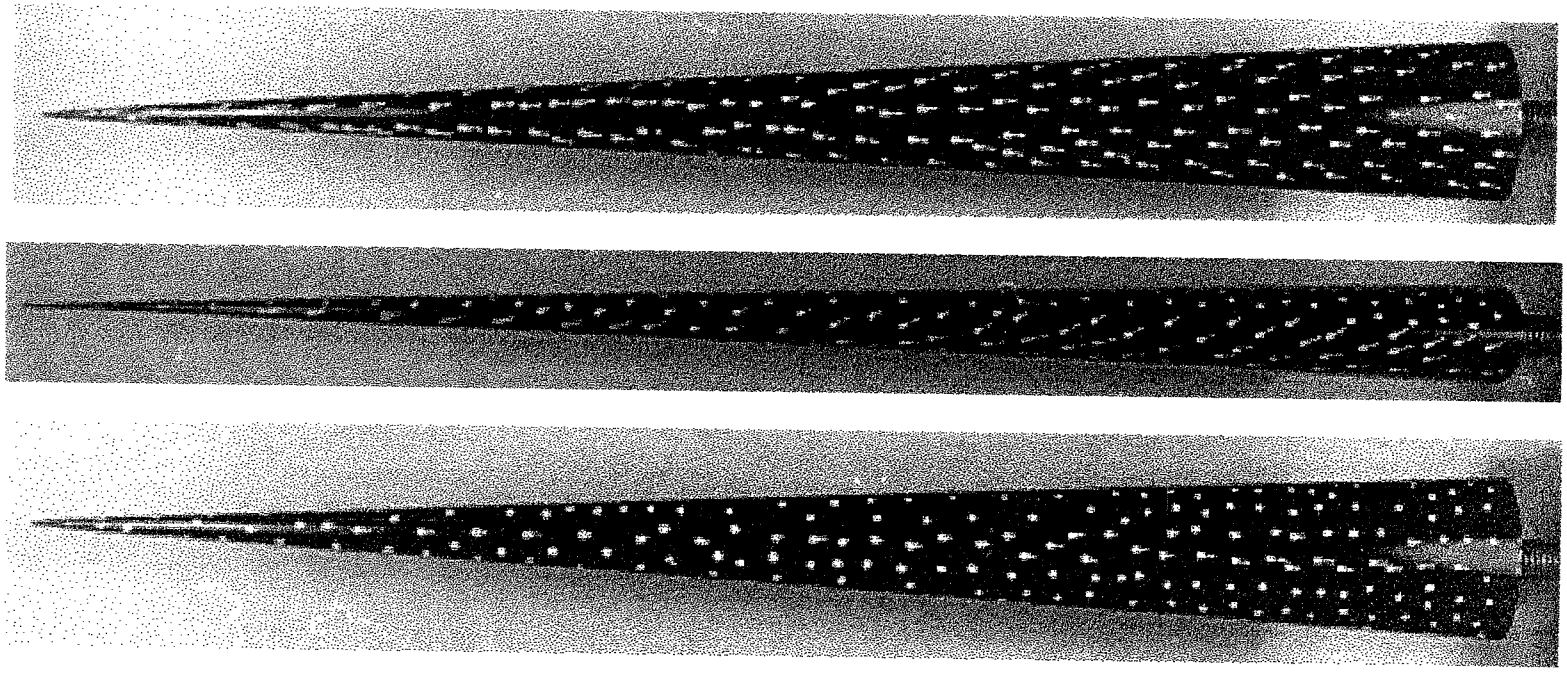

windward side

left side

leeward side

b) α=5°

Fig. 4.1 Continue

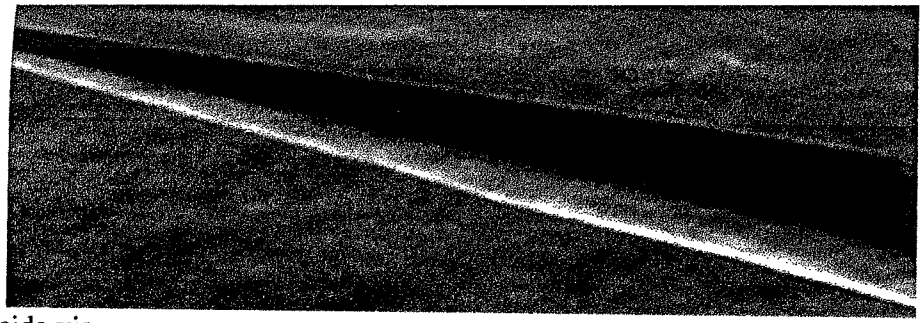

side view

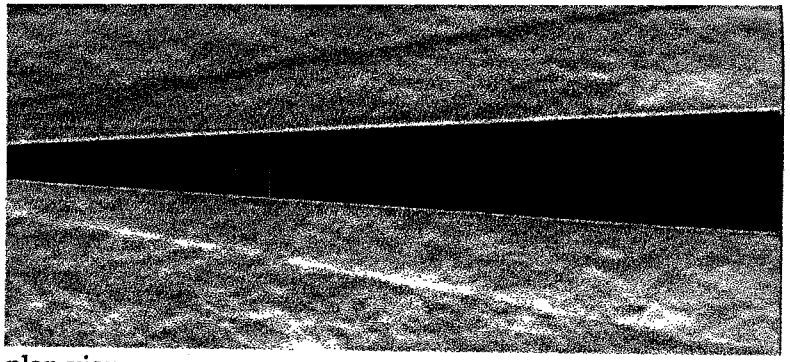

plan view

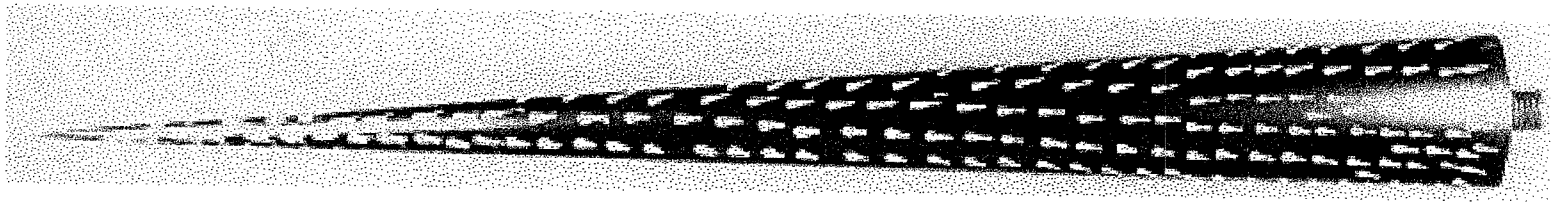

windward side

left side

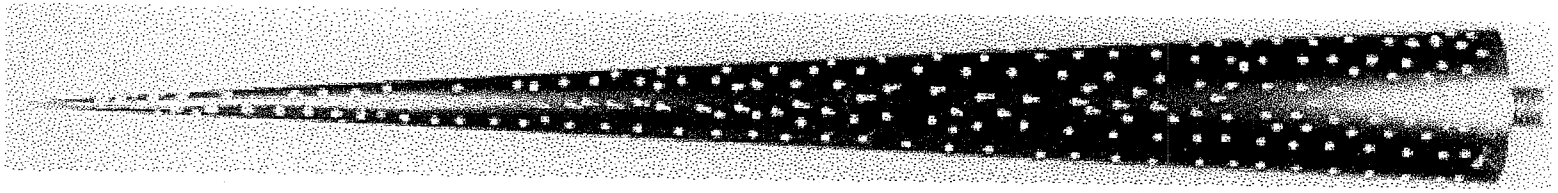

leeward side

c) α=10°

Fig. 4.1 Continue

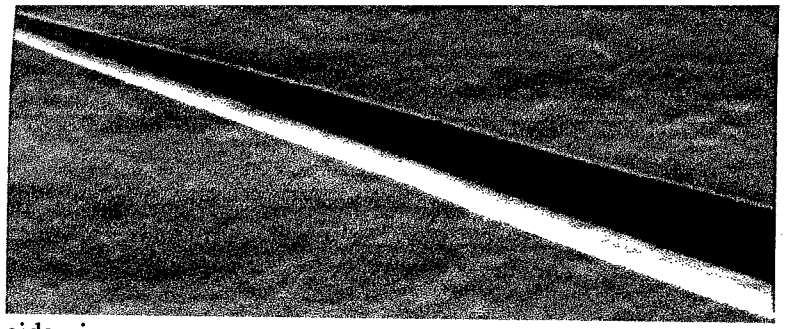

side view

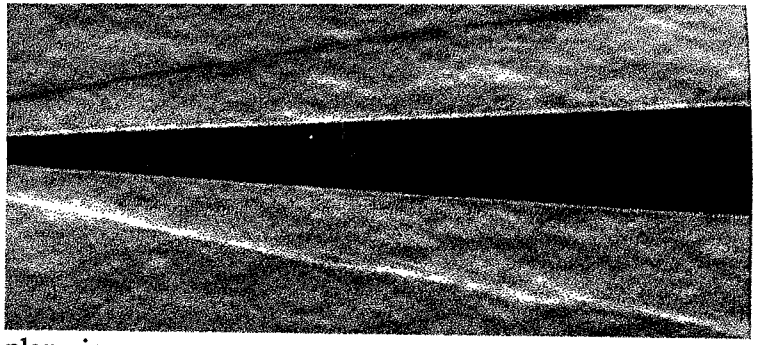

plan view

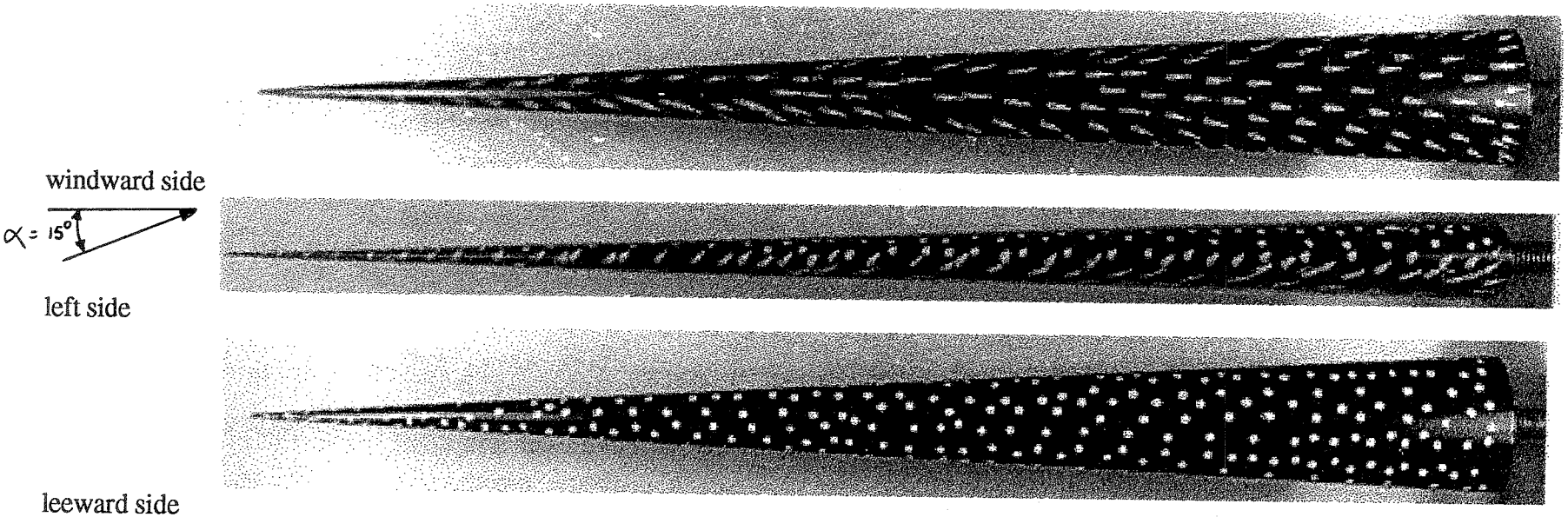

d) α=15°

Fig. 4.1 Continue

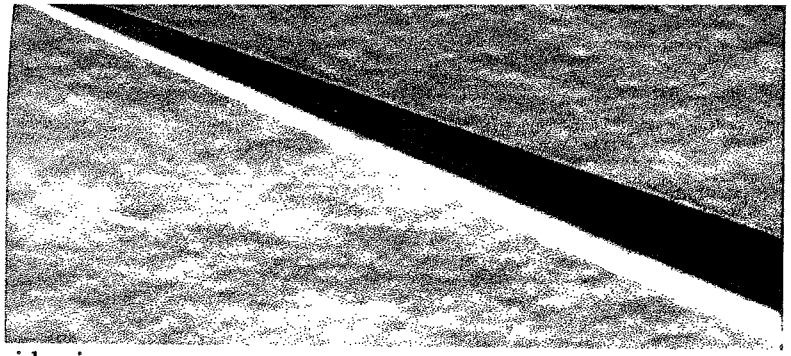

side view

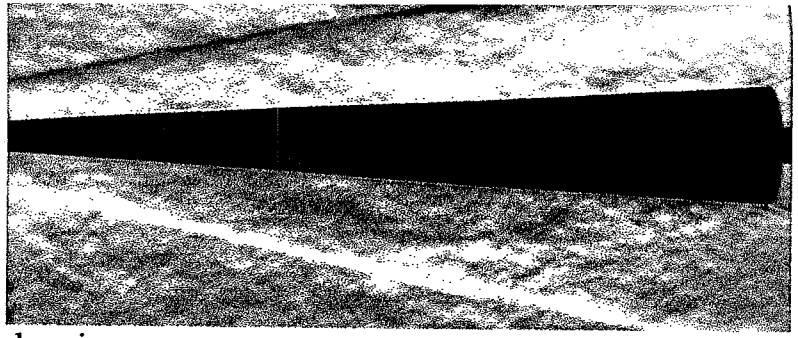

plan view

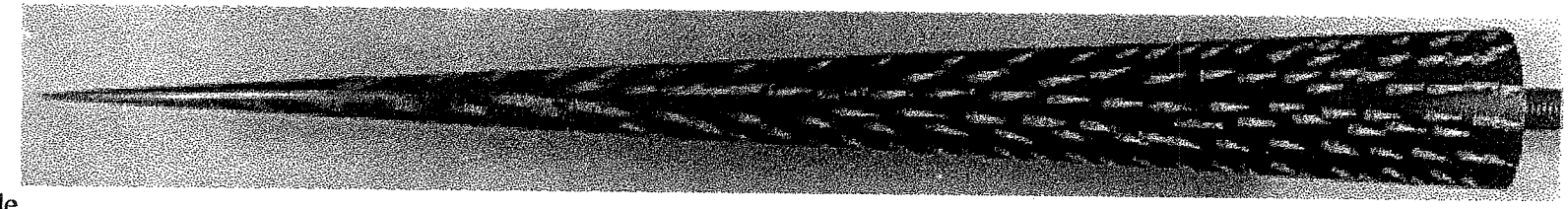

windward side

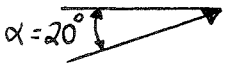

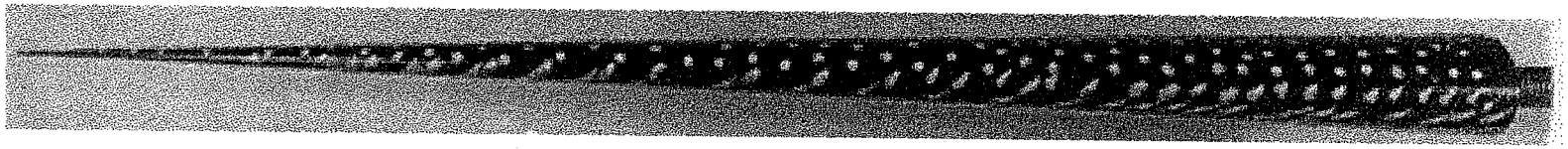

left side

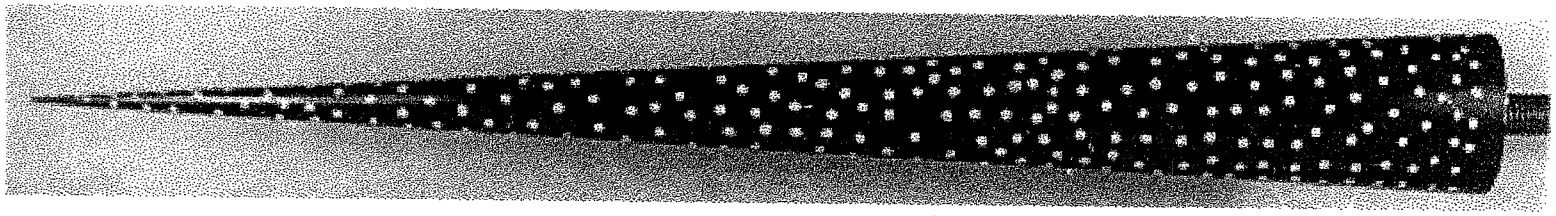

leeward side

e) α=20°

Fig. 4.1 Concluded

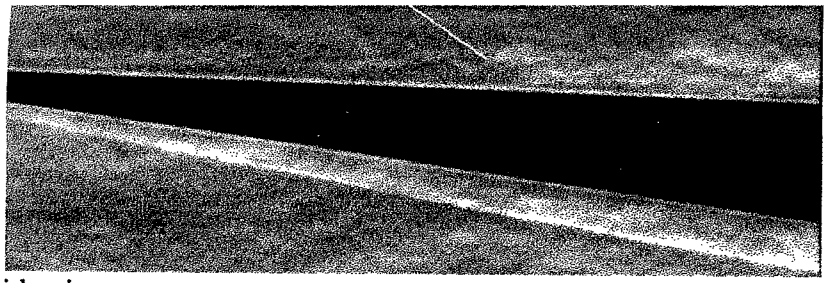

side view

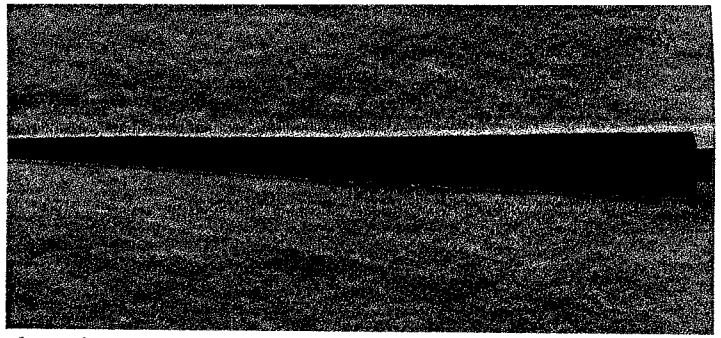

plan view

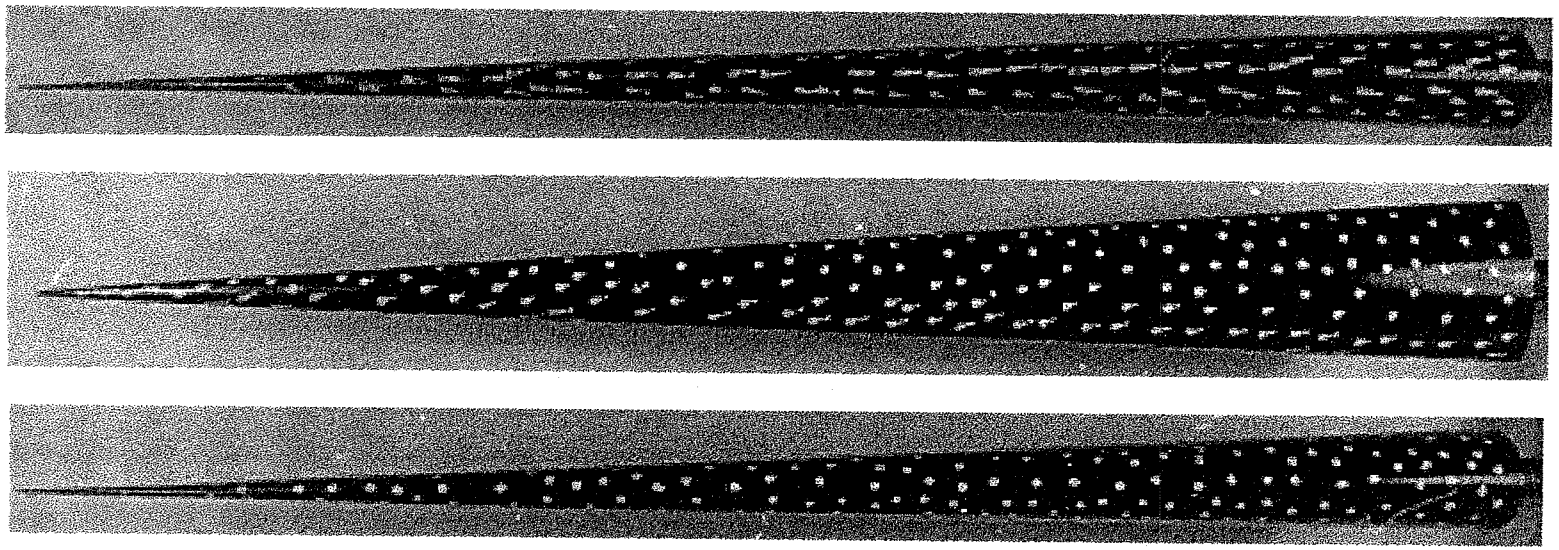

a) α=5°

Fig. 4.2 Schlieren and oil-dot pictures for configuration 5

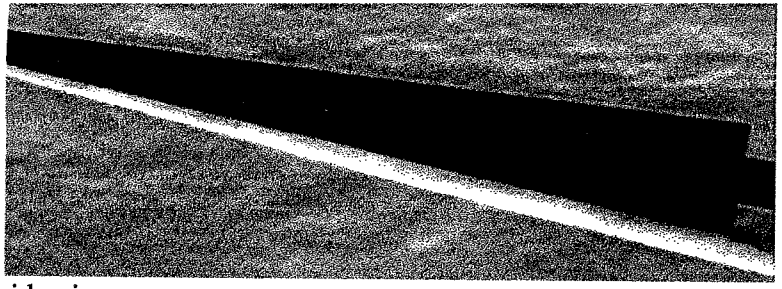

side view

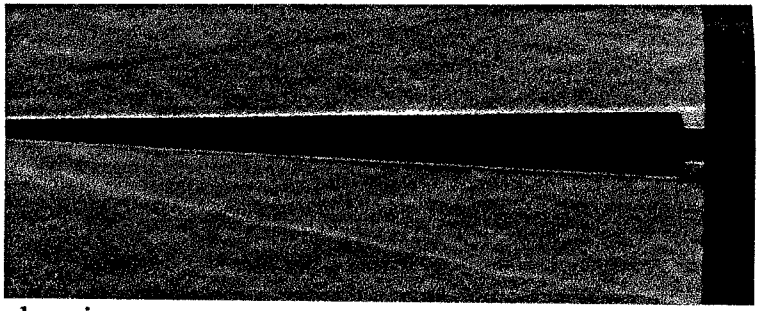

plan view

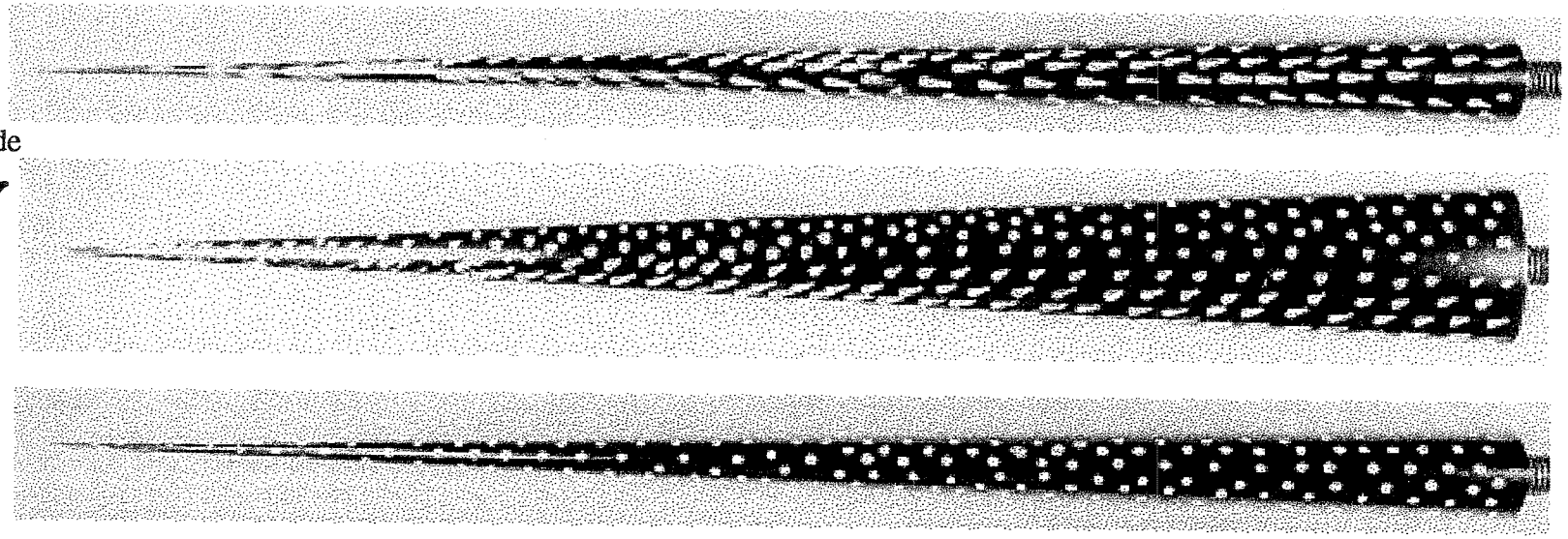

b) α=10°

Fig. 4.2 Continue

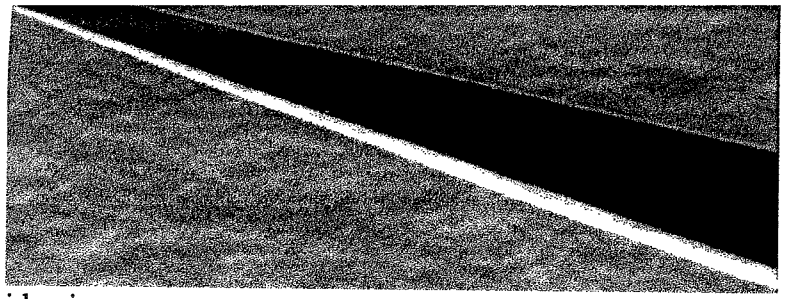

side view

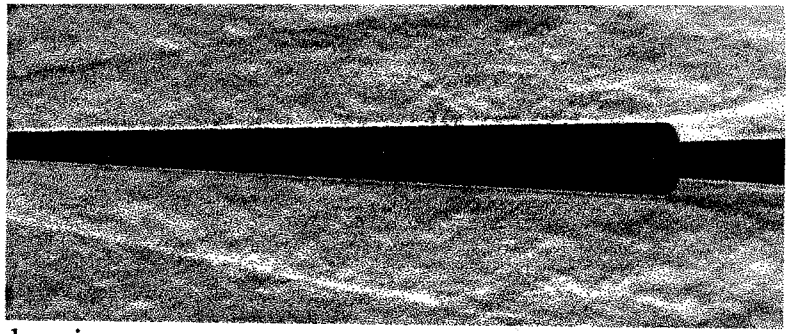

plan view

windward side

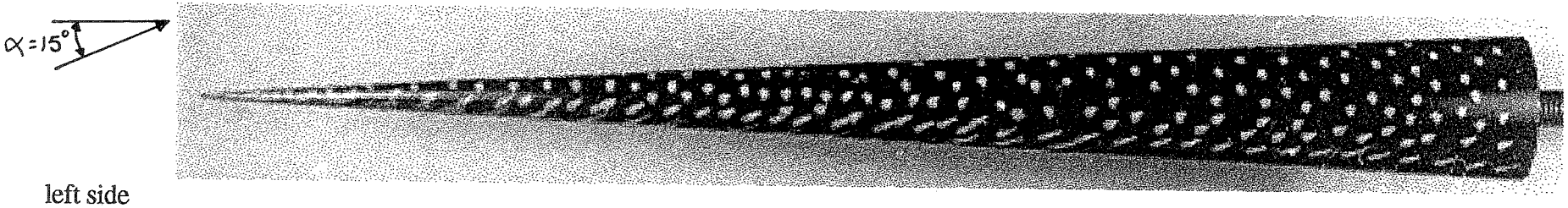

left side

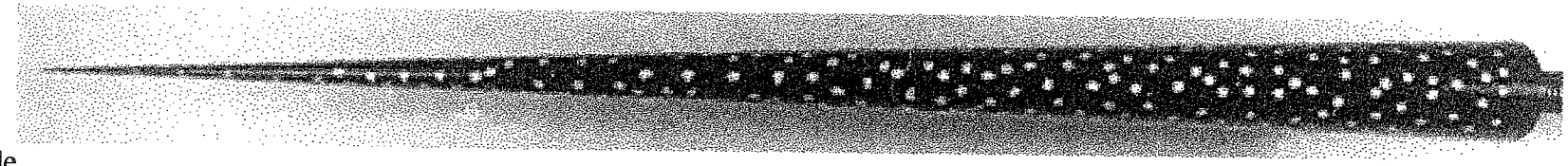

leeward side

c) α=15°

Fig. 4.2 Continue

side view

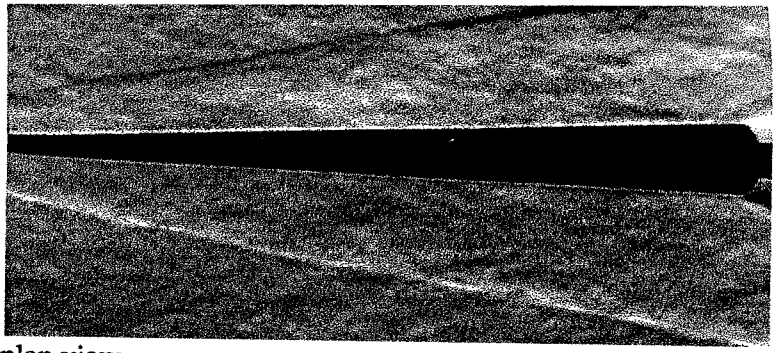

plan view

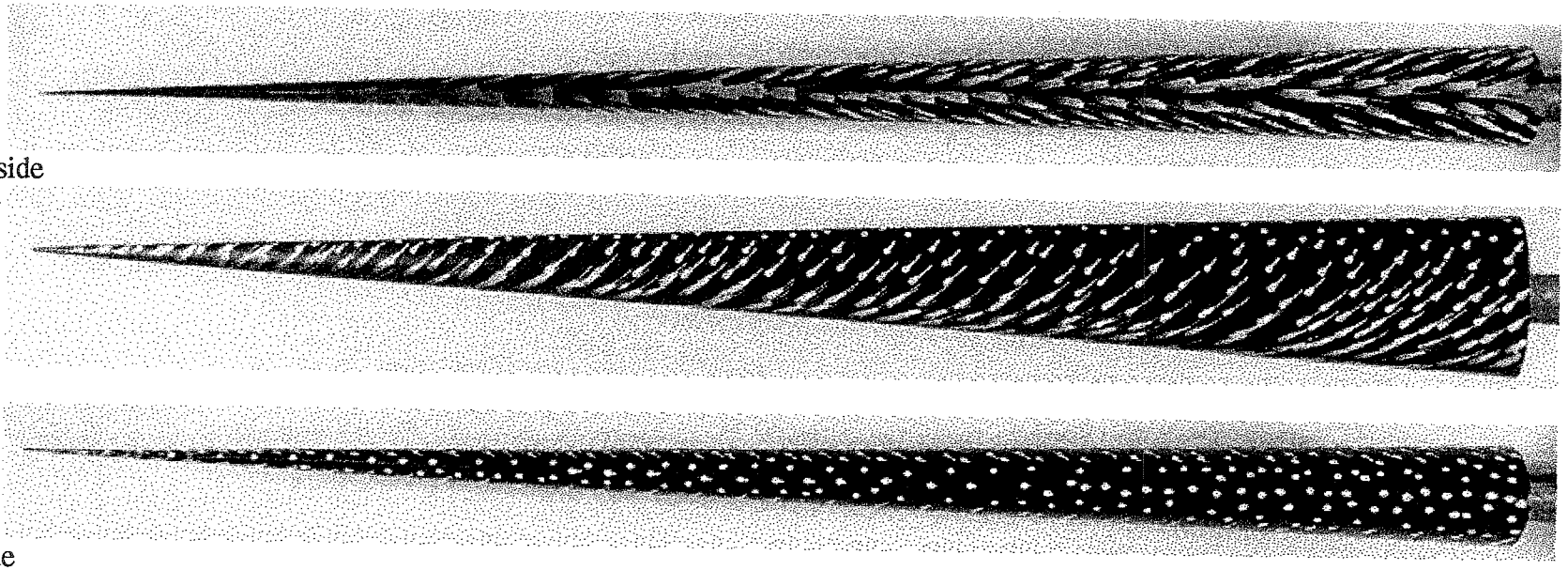

d) $\alpha=20°$

Fig. 4.2 Concluded

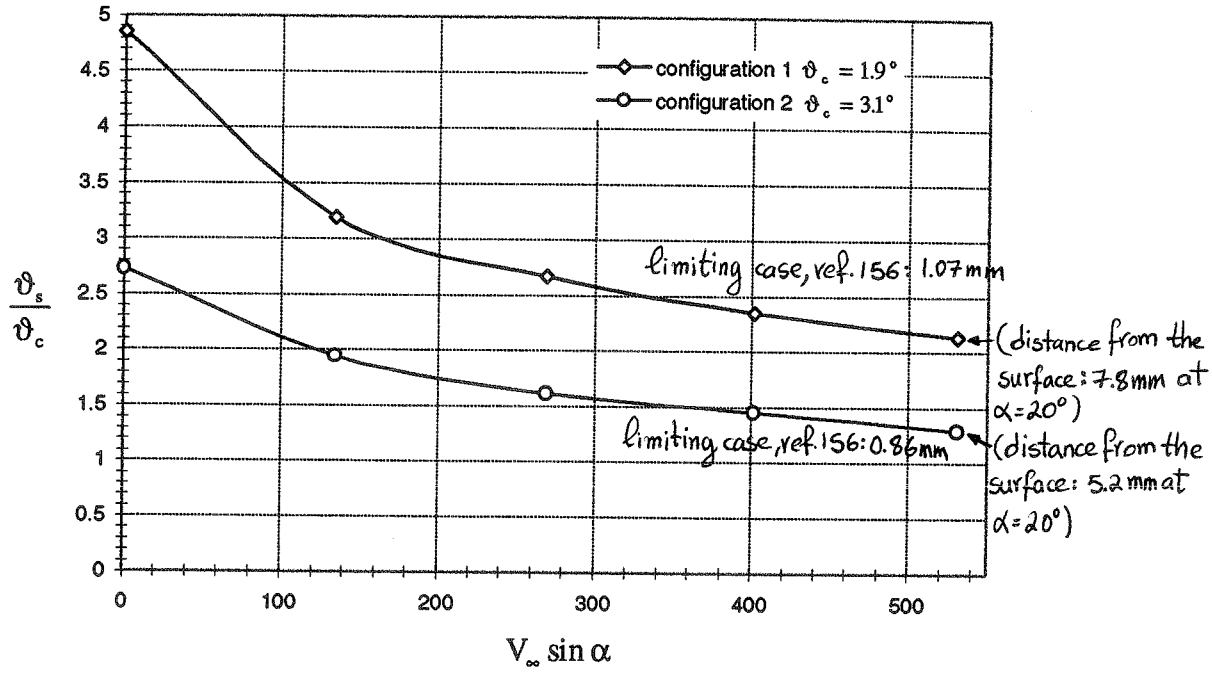

Fig. 4.3 Effect of incidence to the windward shock angle (angle was determined from the schlieren pictures and was measured from the body centre axis)

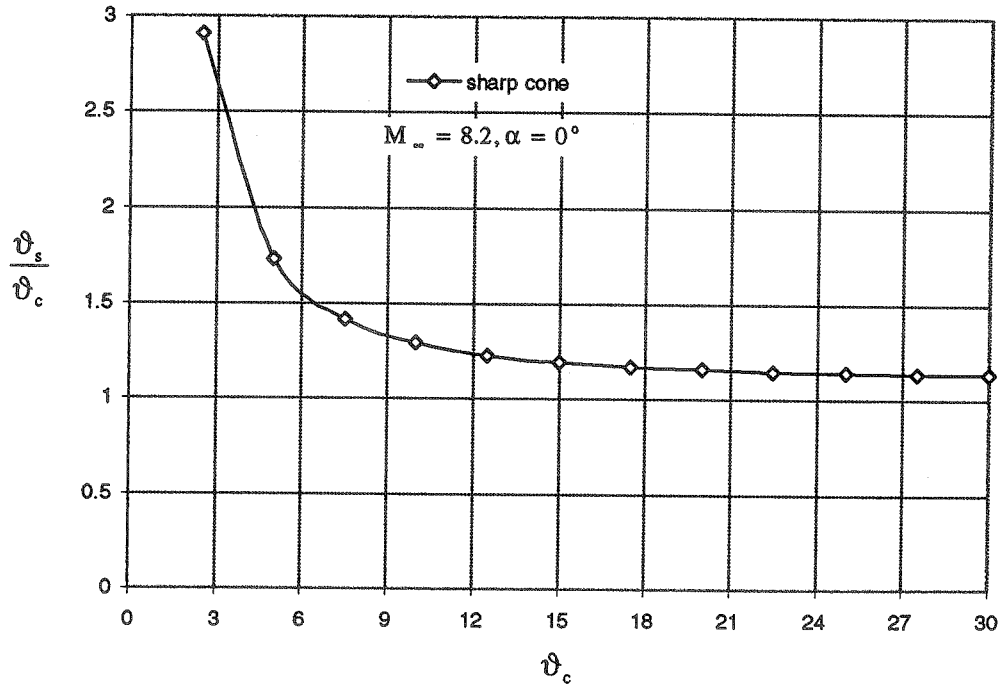

Fig. 4.4 Effect of sharp-cone half-angle to the shock angle (α=0°, M_∞=8.2)

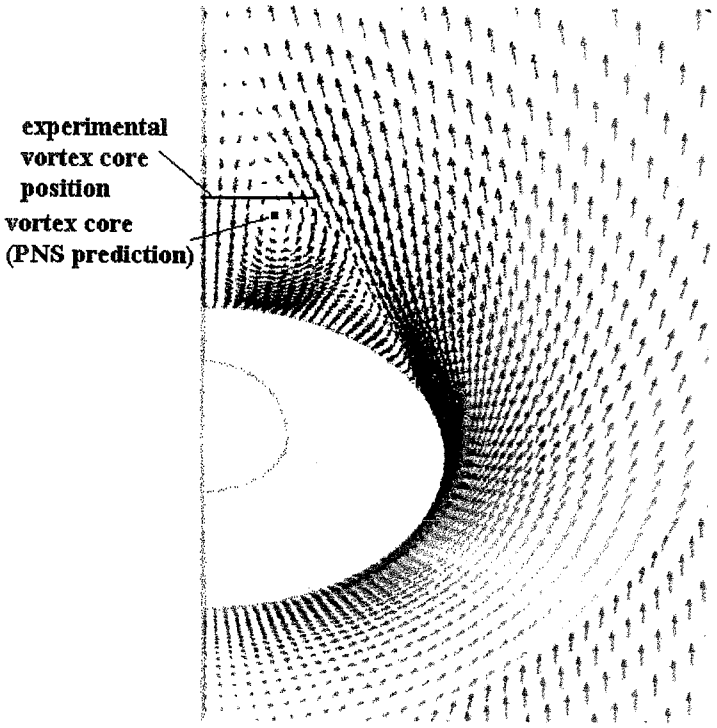

a) base velocity contours

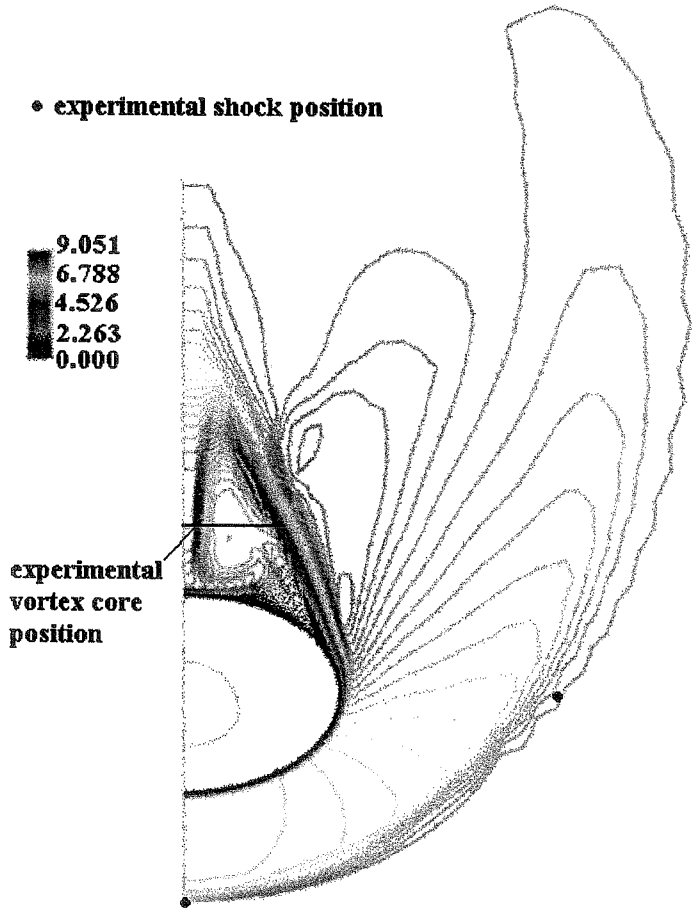

b) base Mach number contours

$L_{cone}/d_{minor}=15$

4.5 Base flowfield computational results for configuration 1 at $\alpha=10°$

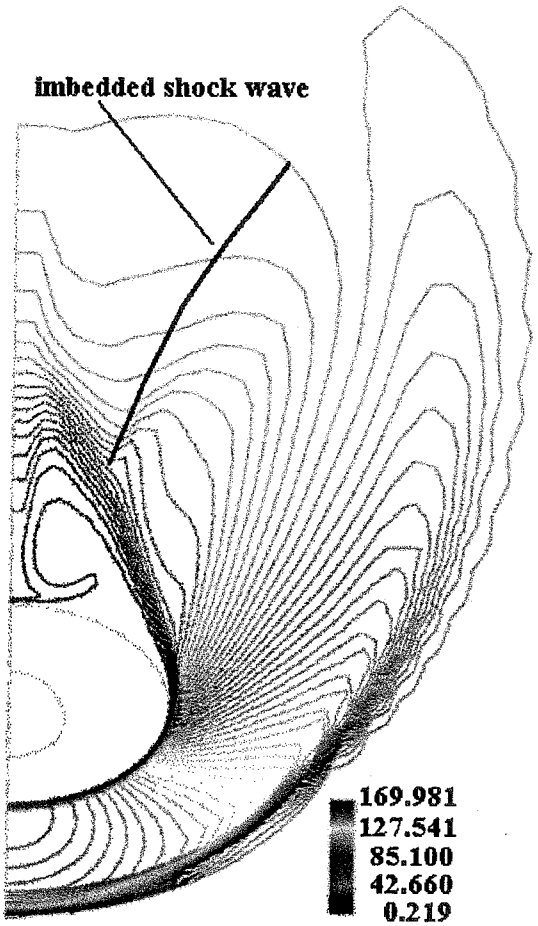

c) base pitot-pressure contours

Fig. 4.5 Concluded

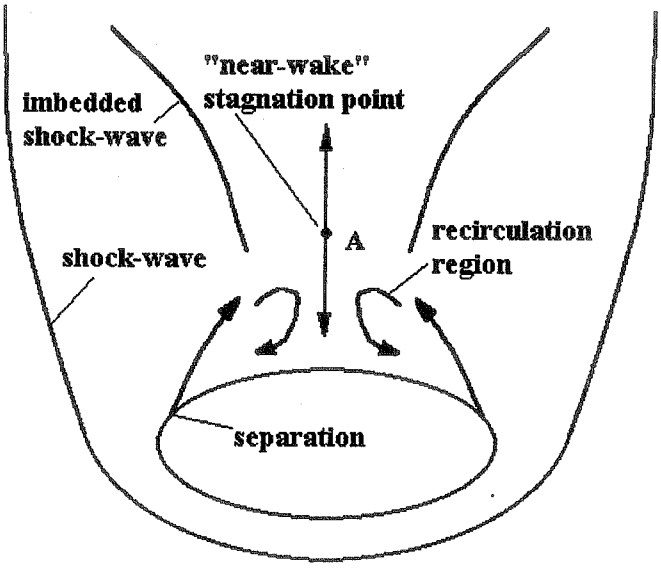

Fig. 4.6 Proposed flow field model for configuration 1 at $\alpha=10°$

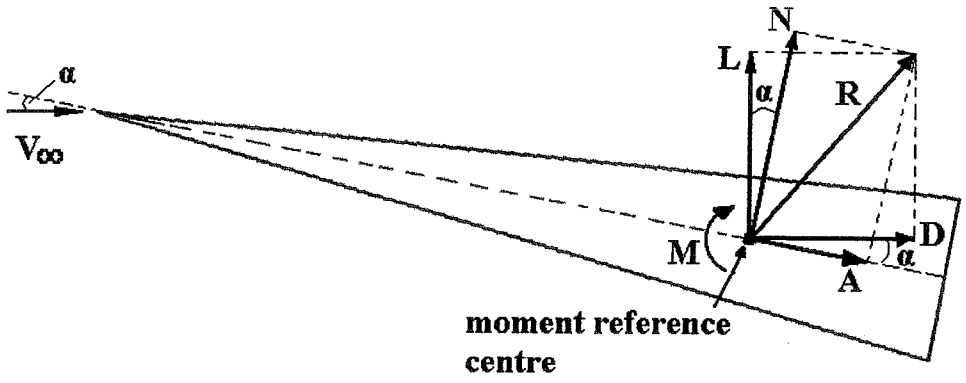

Fig. 4.7 Forces and pitching moment sign convention

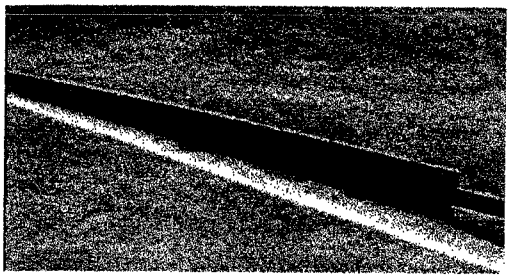

strakes-off

strakes-on

Fig. 4.8 Comparison of the schlieren pictures (strakes on and off) for the power-law body at α=12°

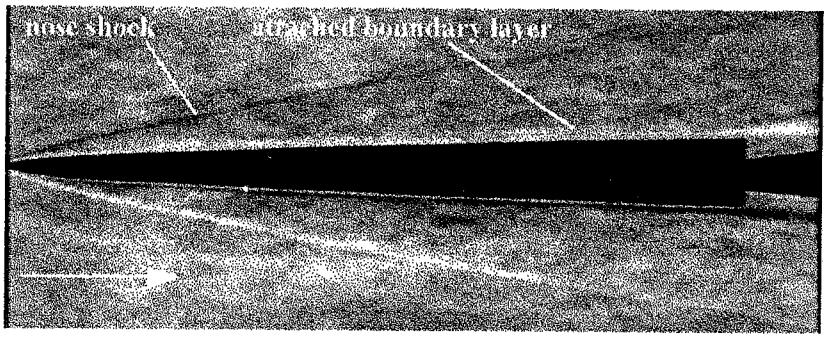

α=0°

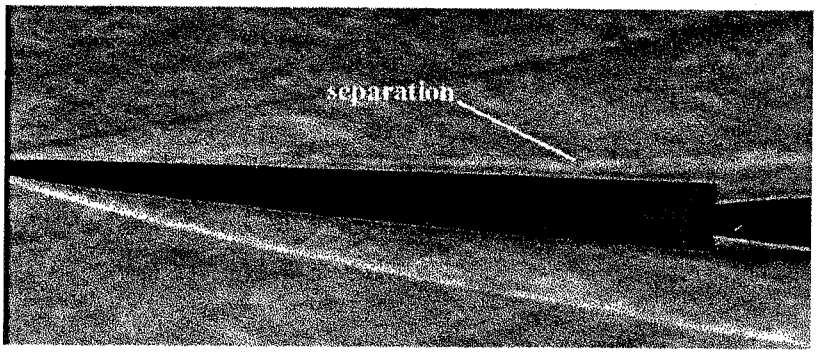

α=3°

Fig. 4.9 Schlieren photographs of power-law body (strakes off)

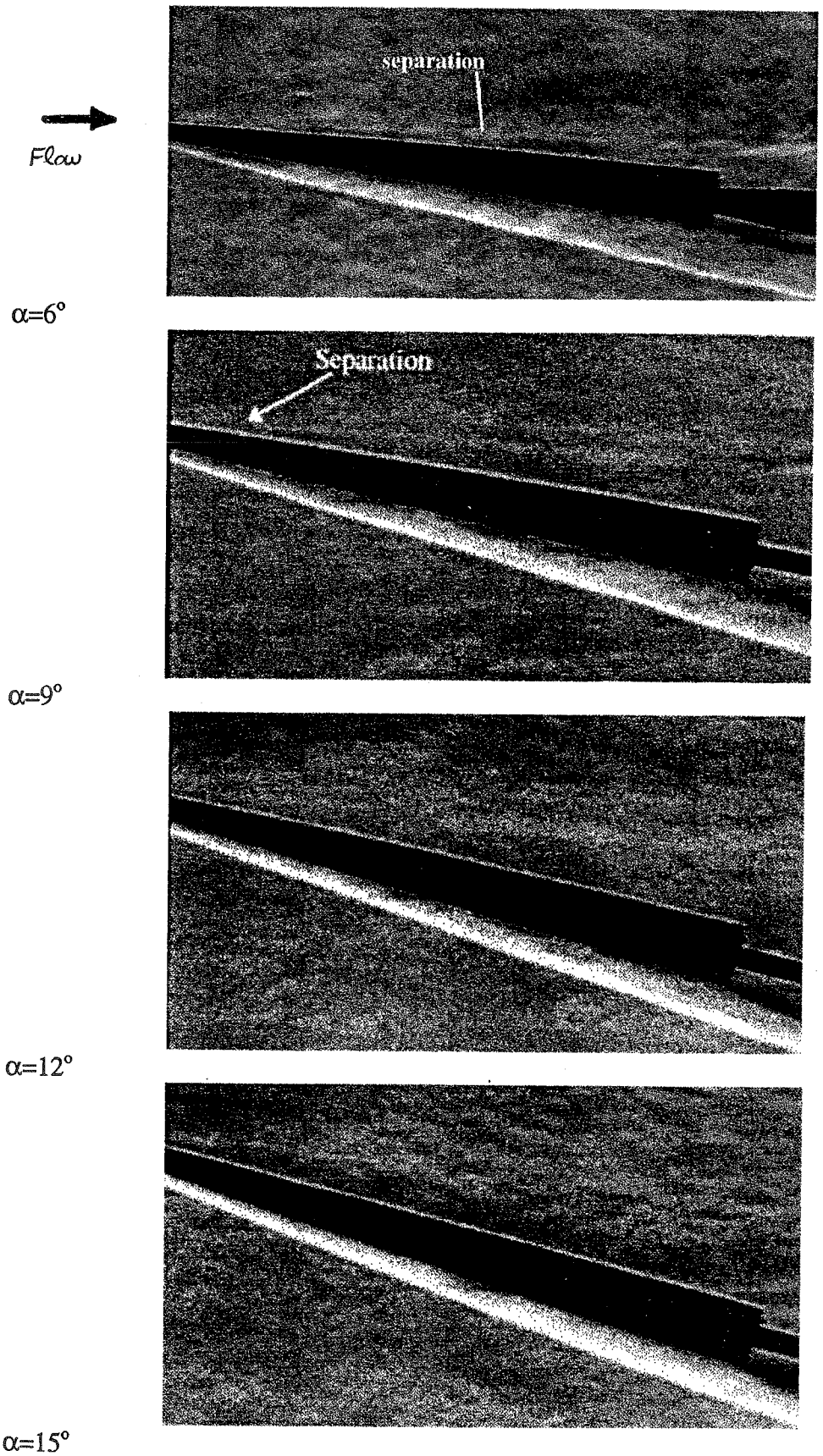

Fig. 4.9 Concluded

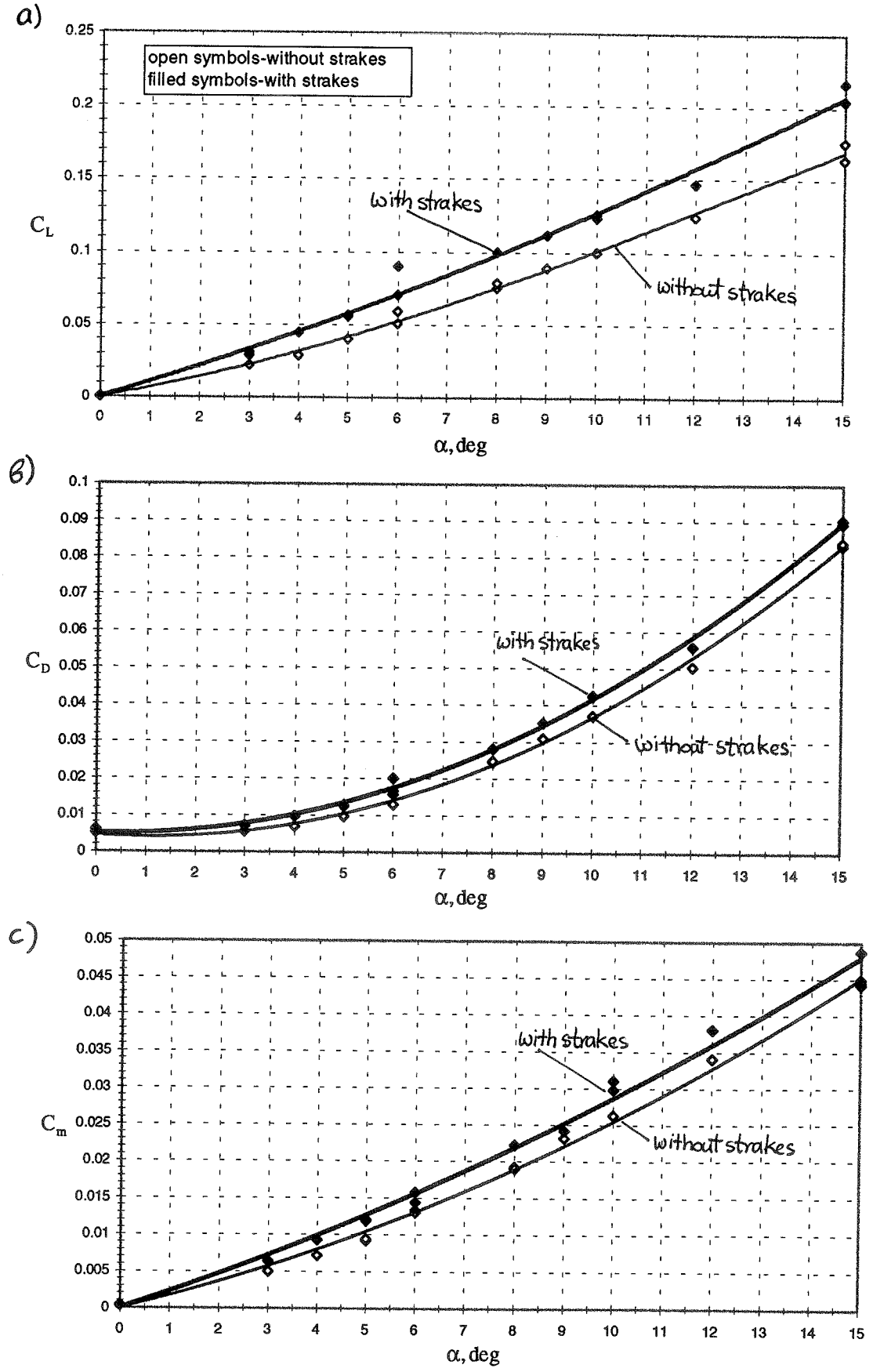

Fig. 4.10 Effect of strakes on the aerodynamic characteristics of the power-law body

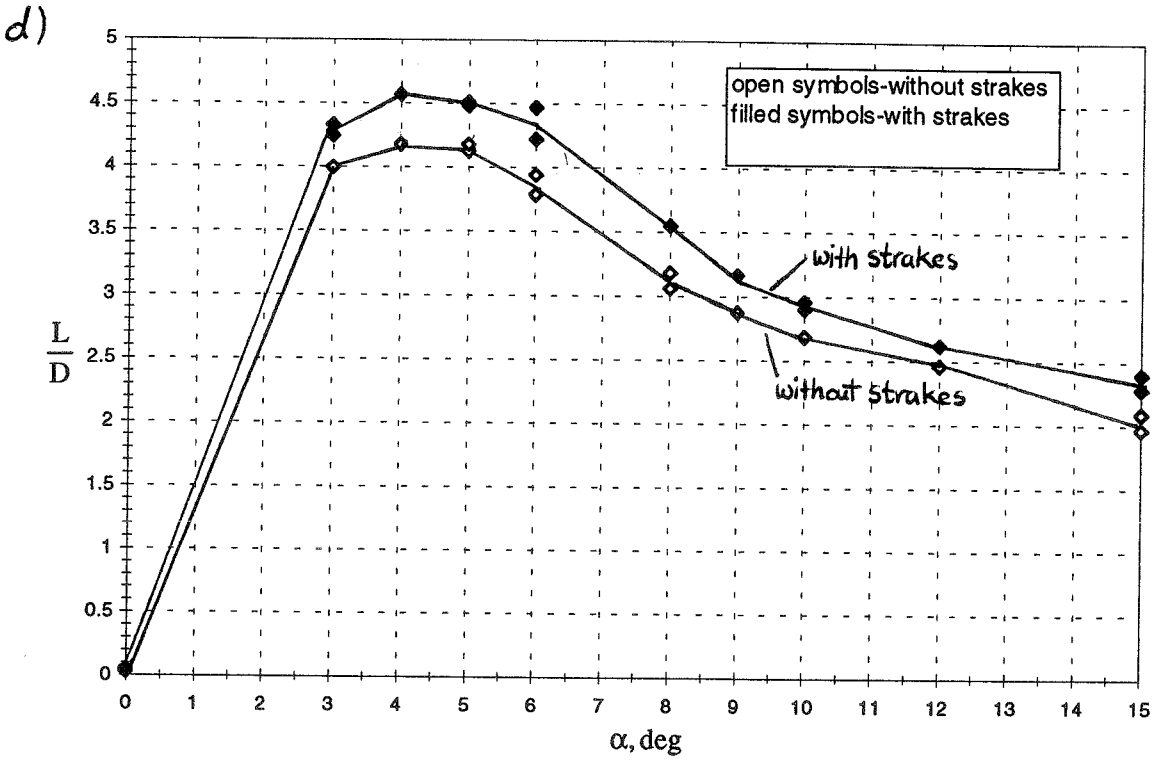

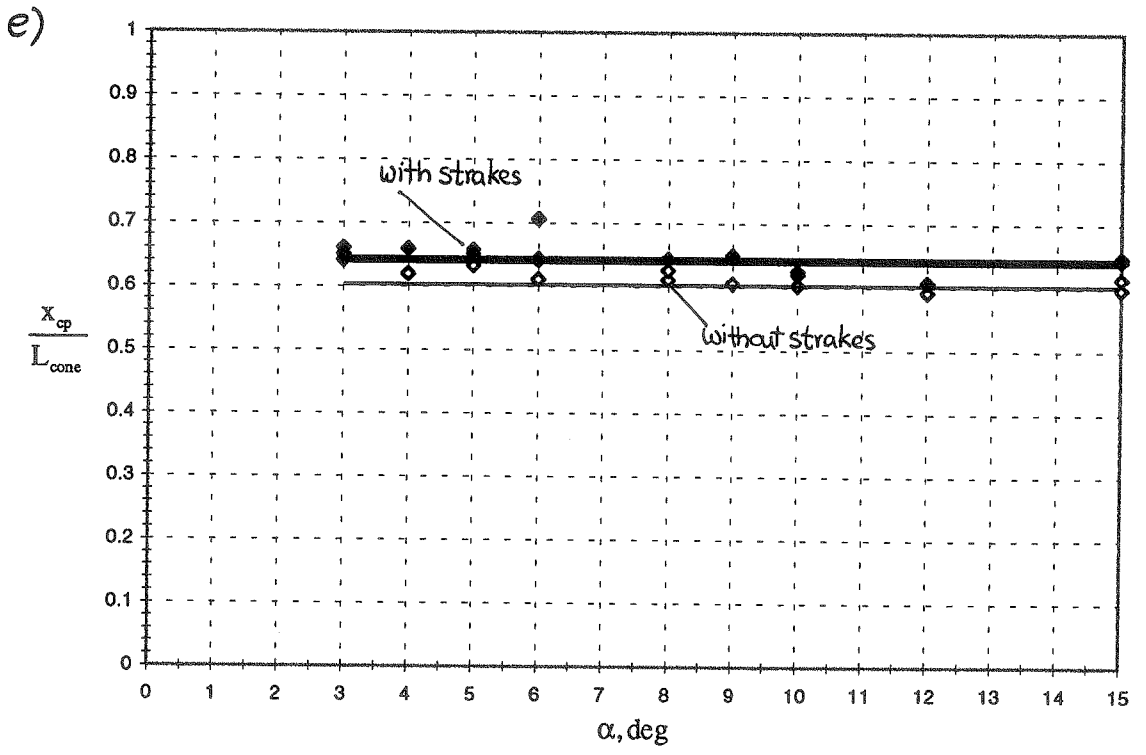

Fig. 4.10 Concluded

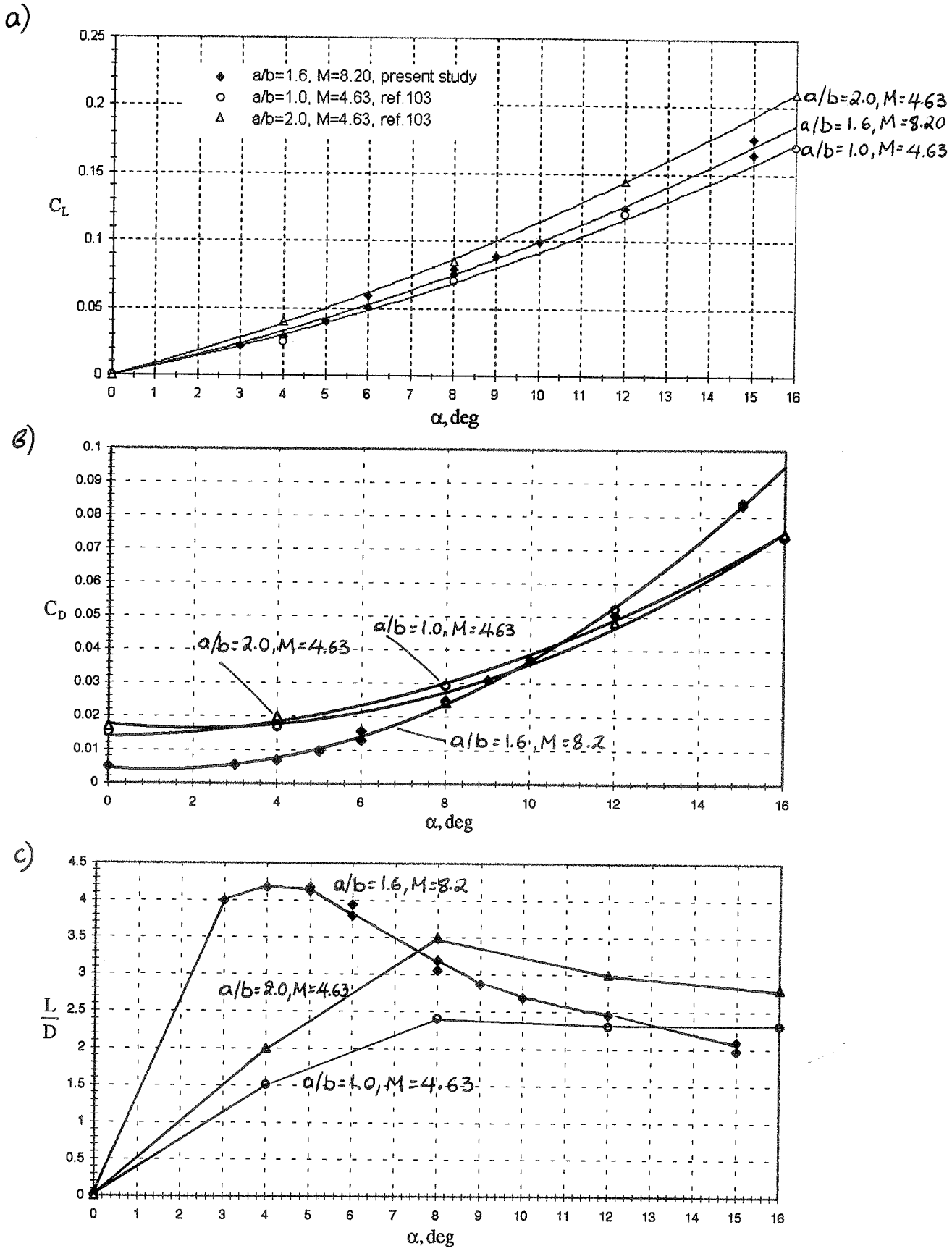

Fig. 4.11 Comparison of present force data (strakes off) with other experimental results (of ref. 103)

a)

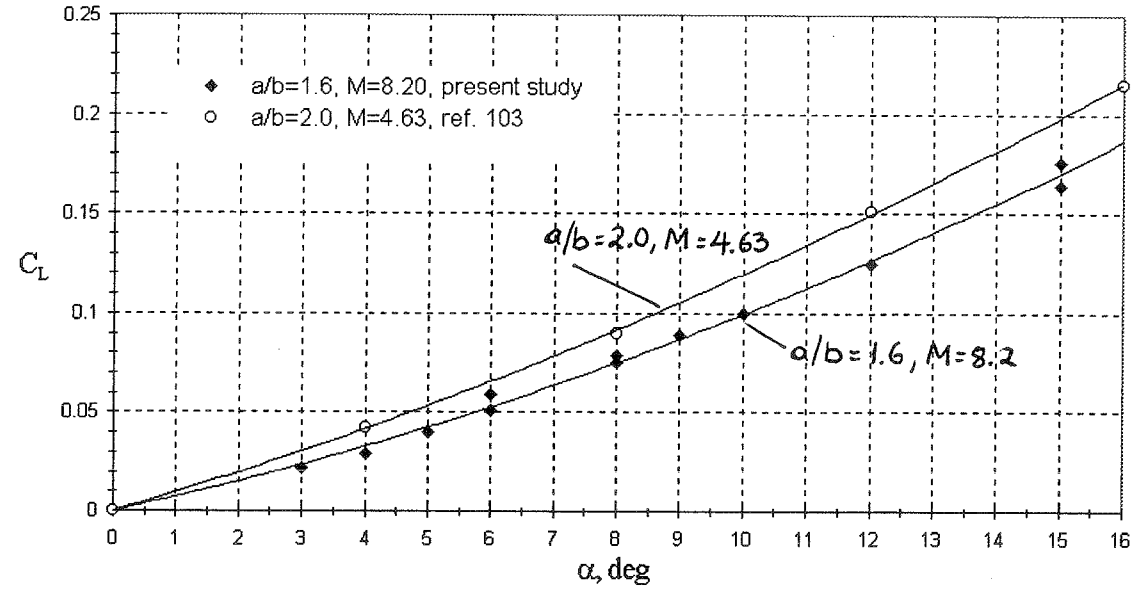

b)

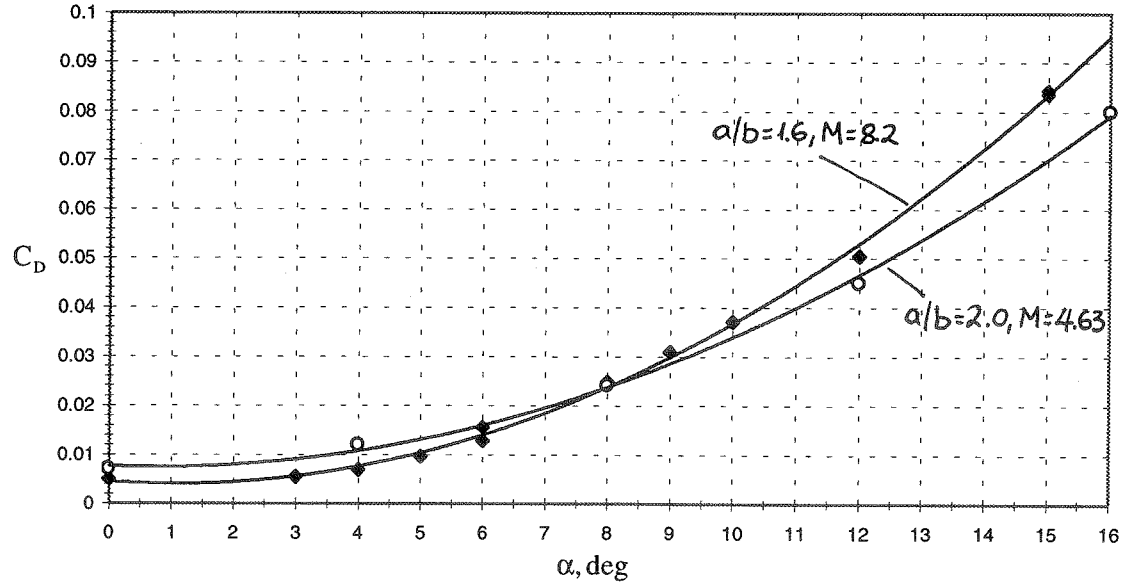

Fig. 4.12 Comparison of present force data (strakes off) with a theoretical minimum-wave-drag body (of ref. 103)

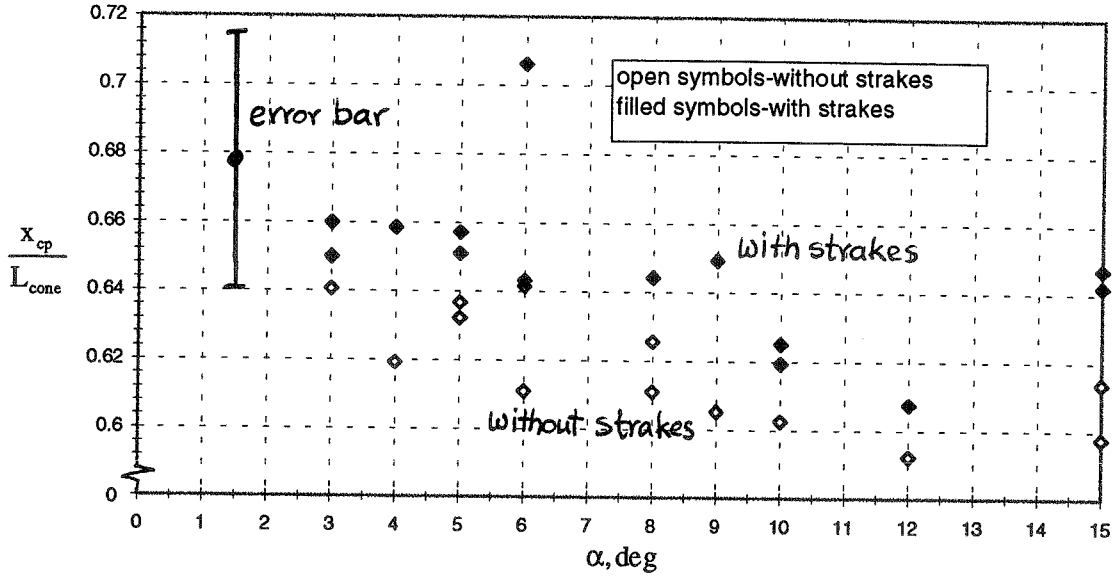

Fig. 4.13 Experimental level of scattering in the location of the centre of pressure

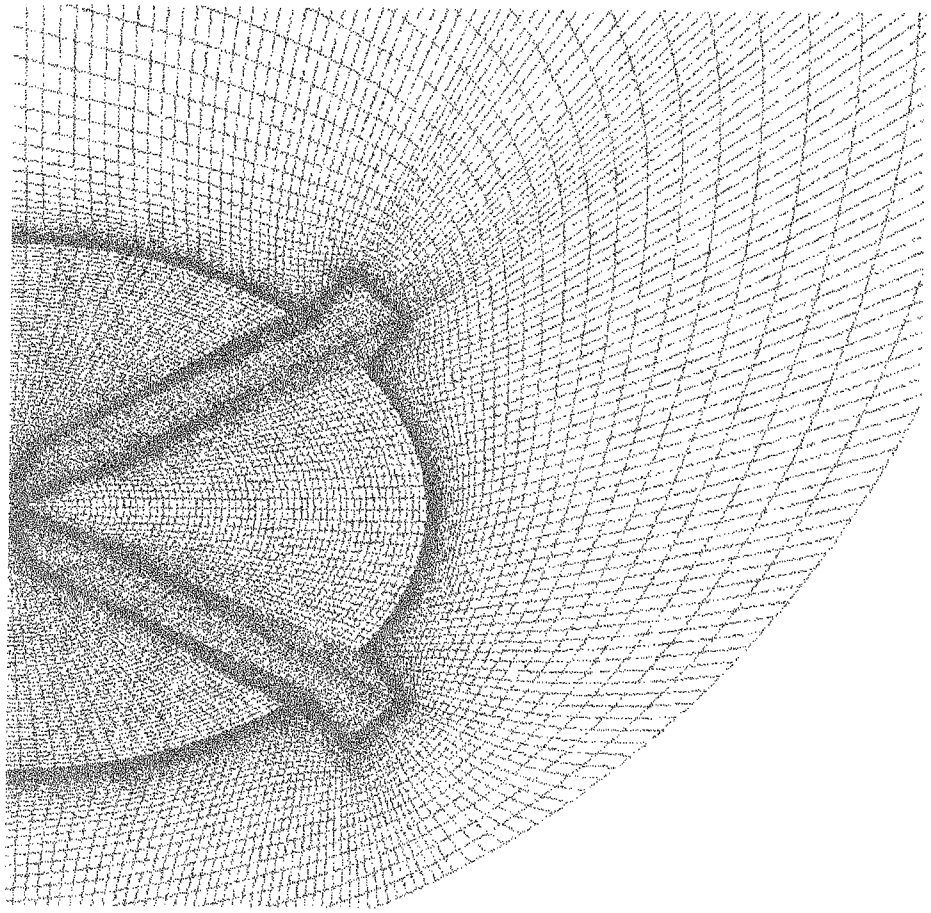

a) elliptic cone with strakes

Fig. 4.14 Grid used for the discretization of the flowfield of the elliptic cone (strakes on and off)

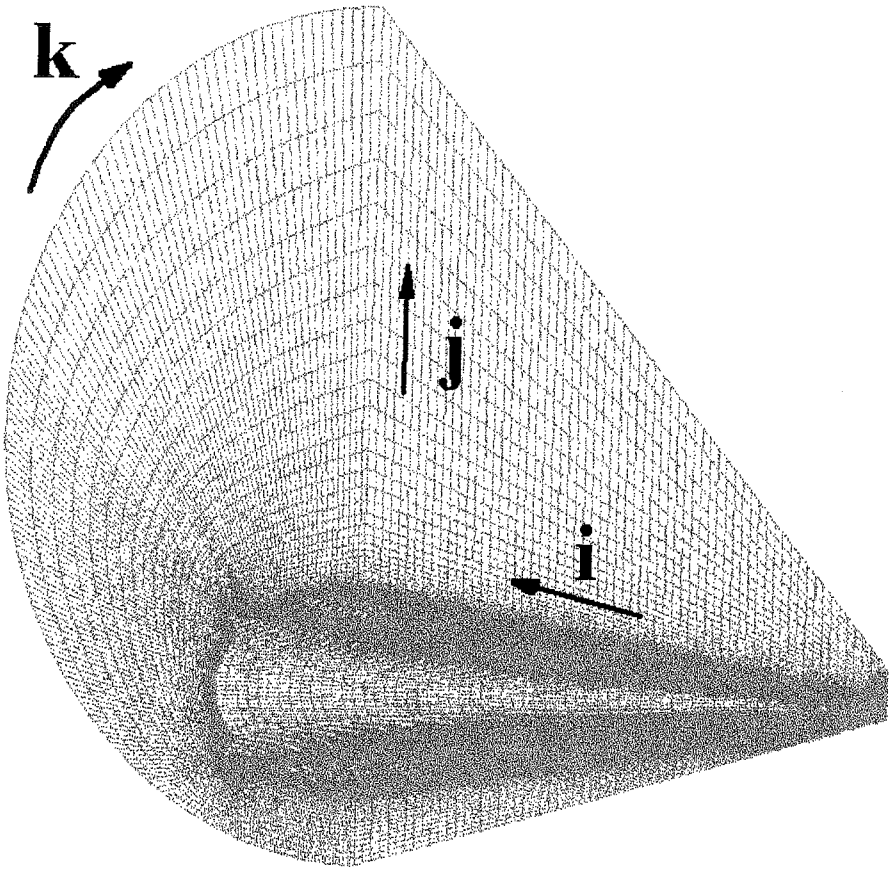

b) elliptic cone with strakes

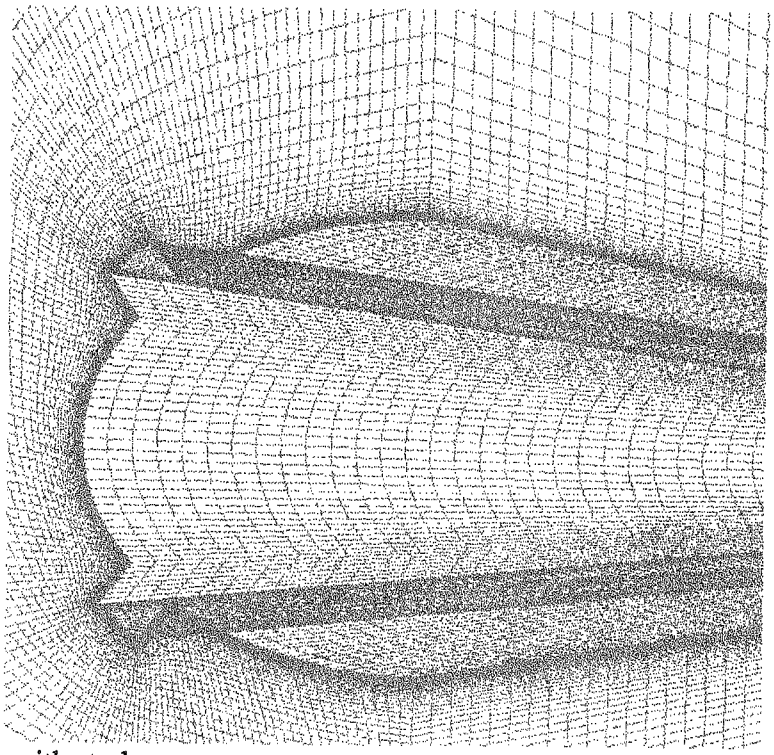

c) elliptic cone with strakes

Fig. 4.14 Continue

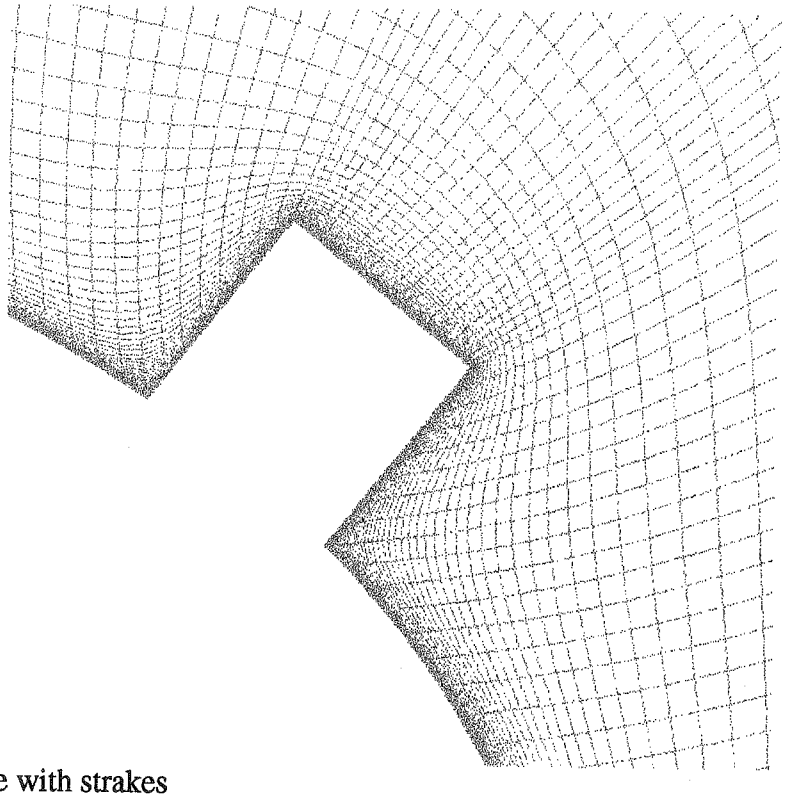

d) elliptic cone with strakes

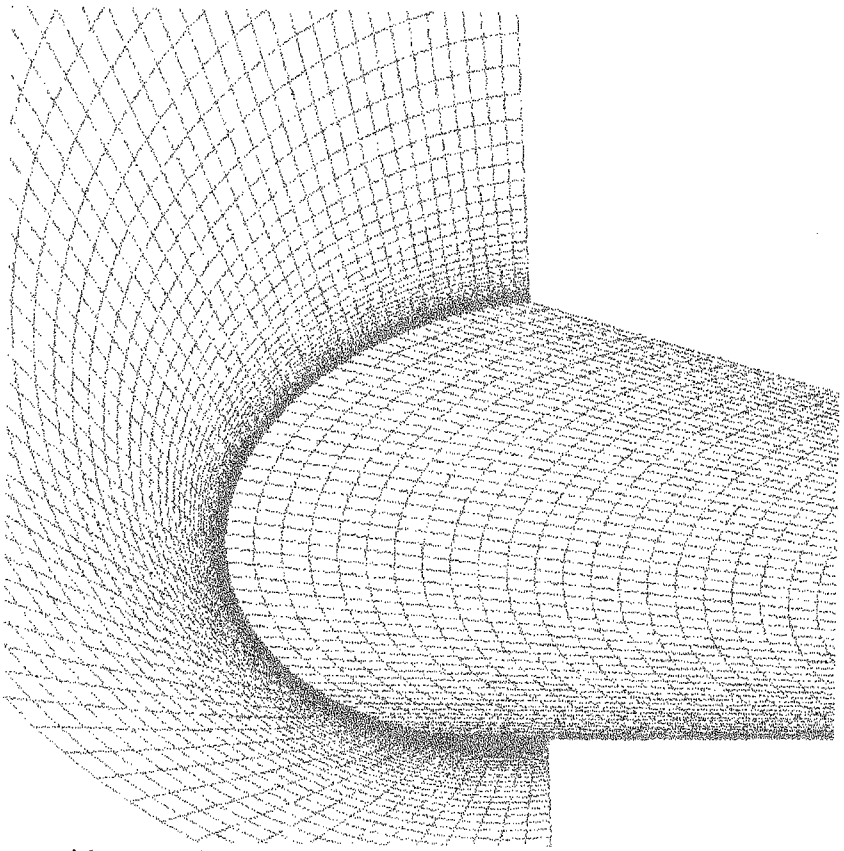

e) elliptic cone without strakes

Fig. 4.14 Concluded

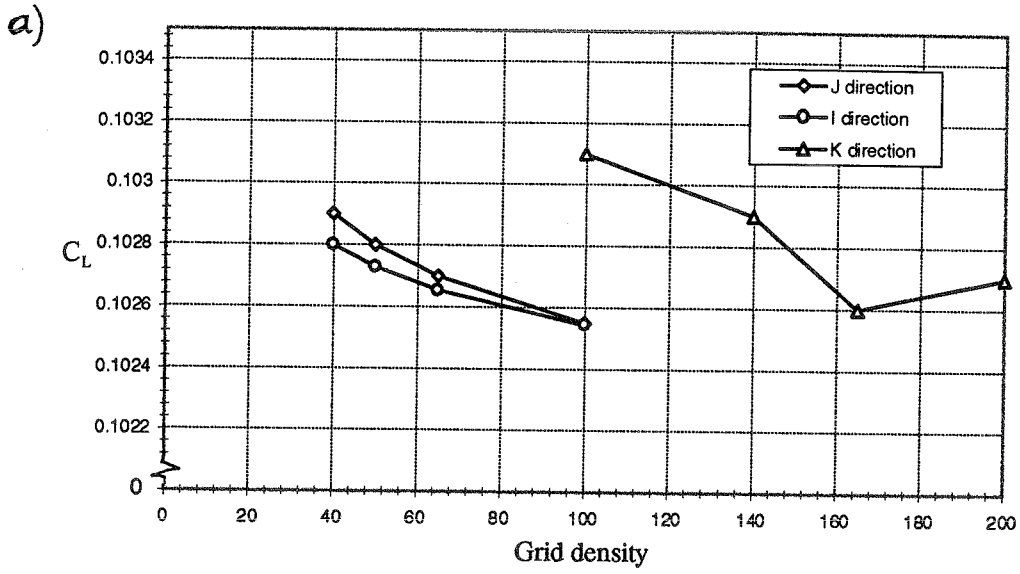

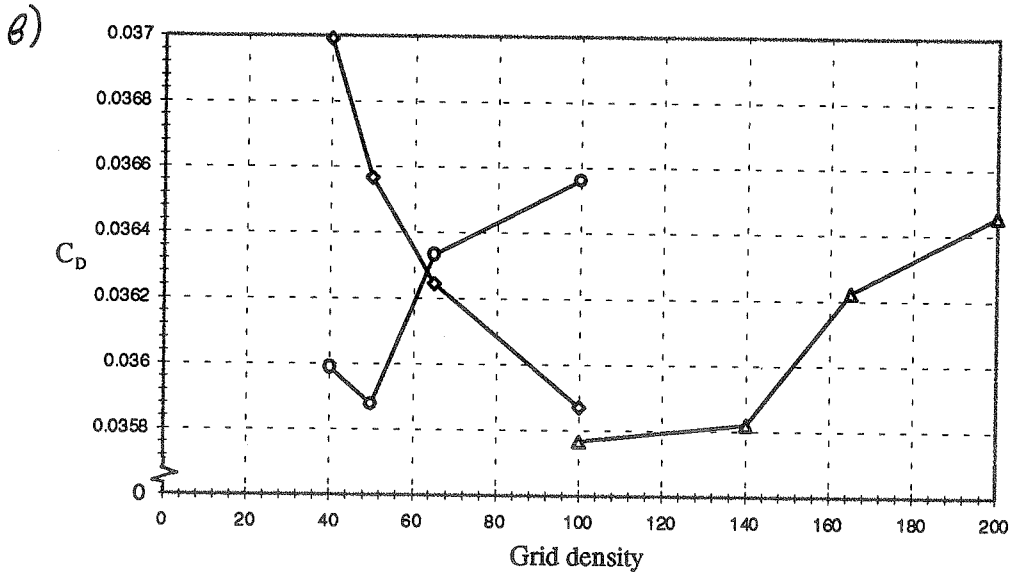

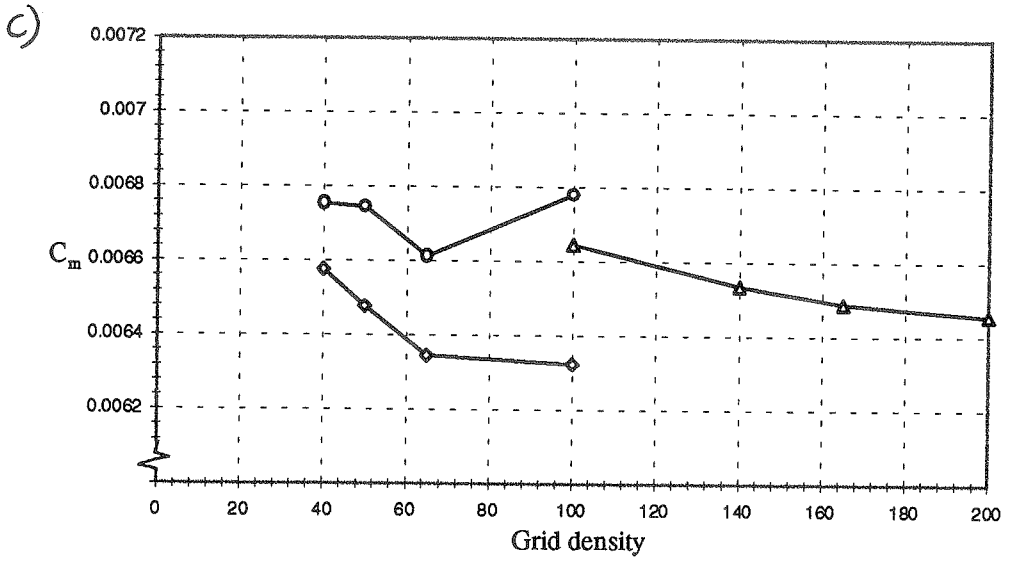

Fig. 4.15 Sensitivity of numerical results to grid density

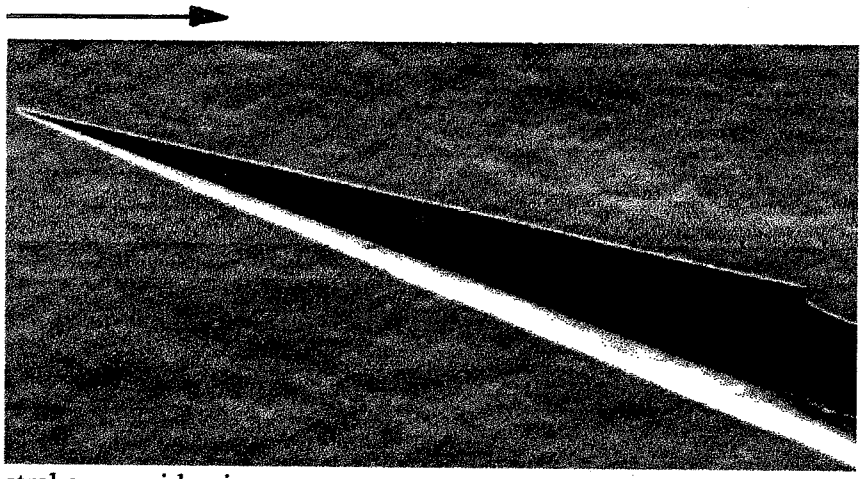

strakes on, side view

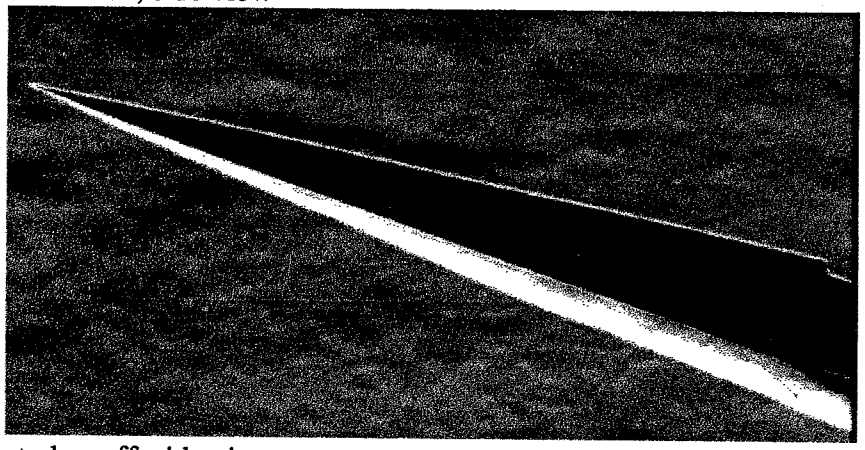

strakes off, side view

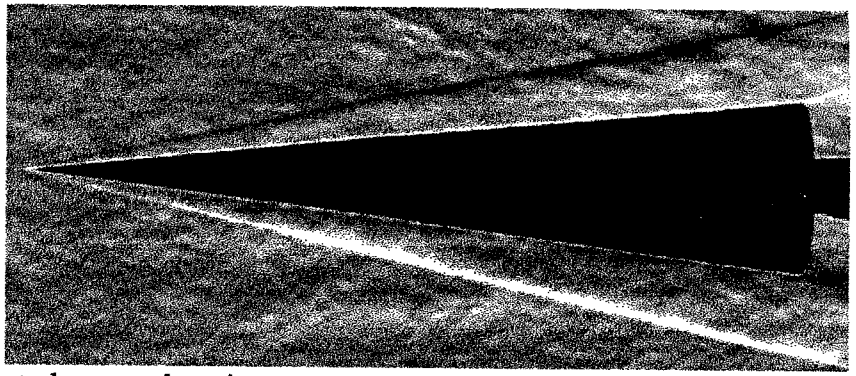

strakes on, plan view

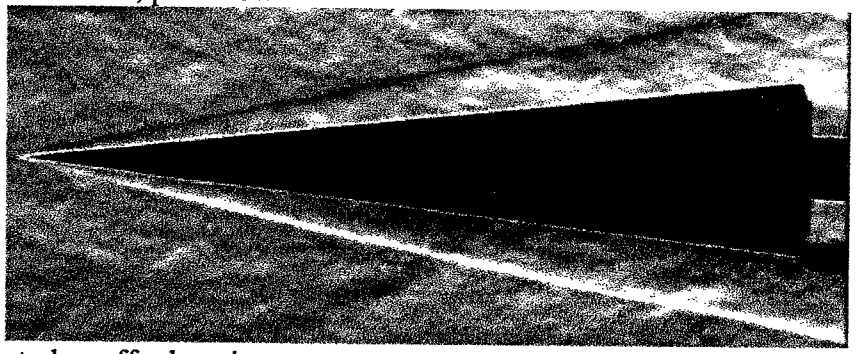

strakes off, plan view

Fig. 4.16 Comparison of the schlieren pictures (strakes on and off) of configuration 4 at α=15°

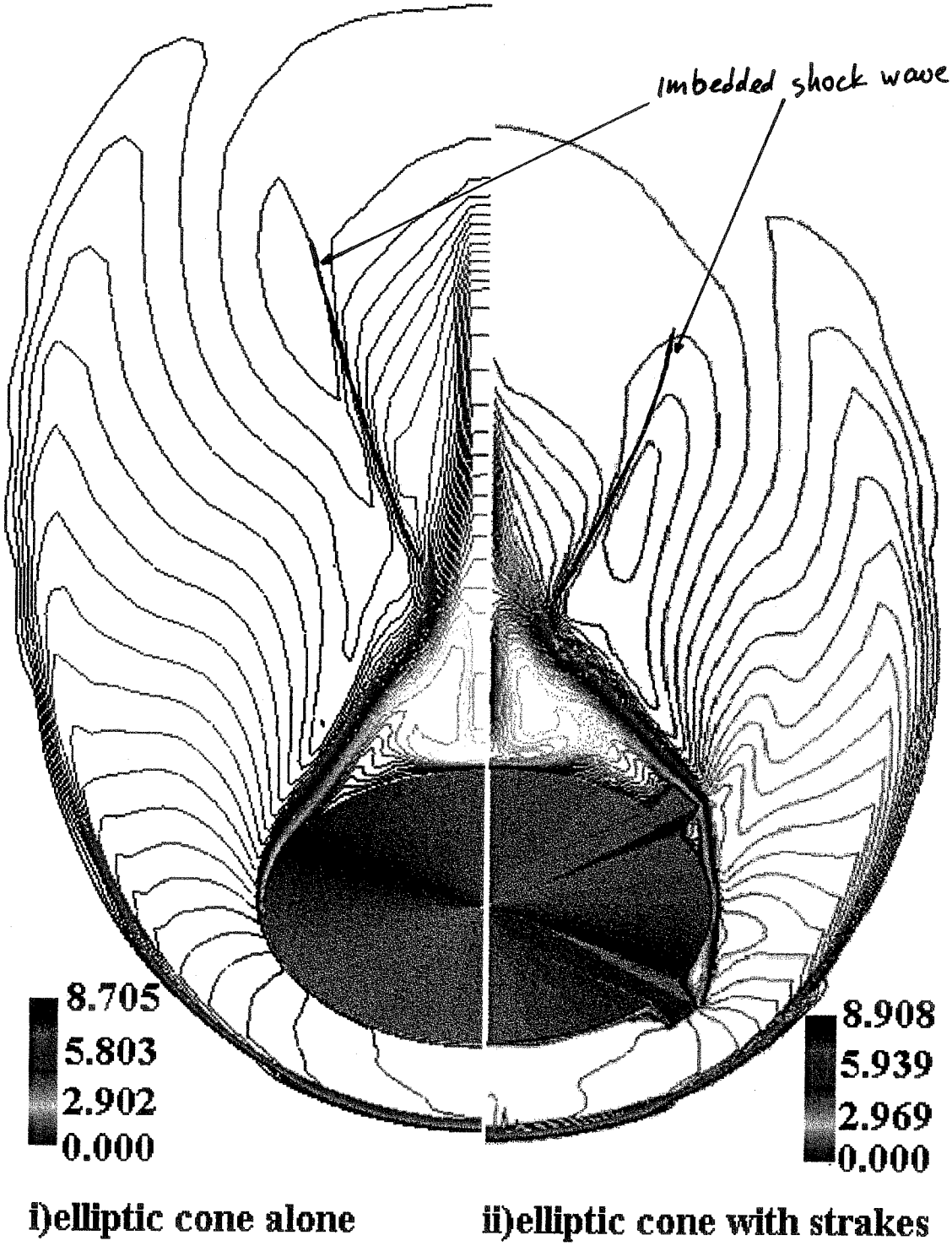

a) base Mach number contours

Fig. 4.17 Comparison of the base flowfield computational results of configuration 4 ($\alpha = 15°$)

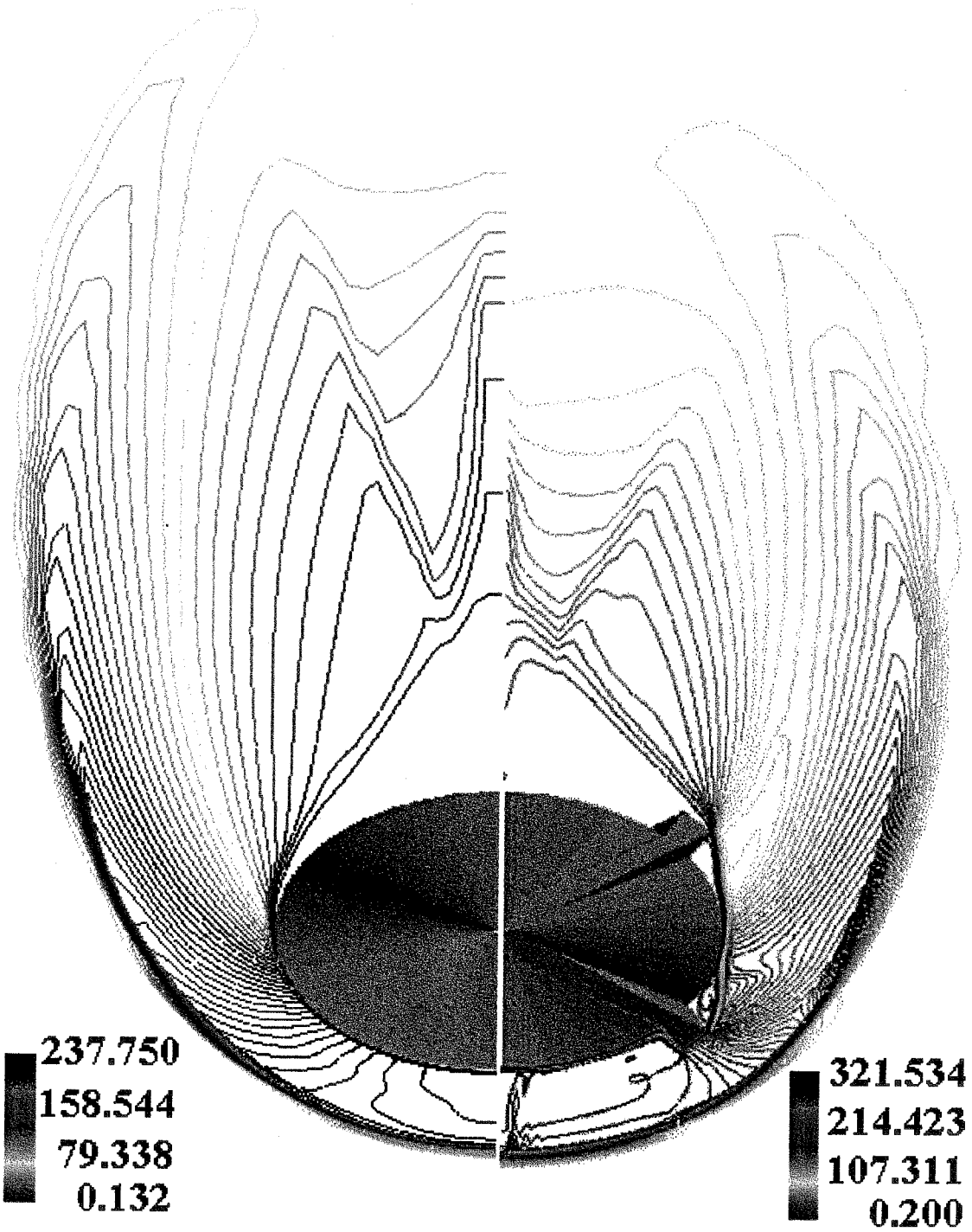

b) base pitot-pressure contours

Fig. 4.17 Continue

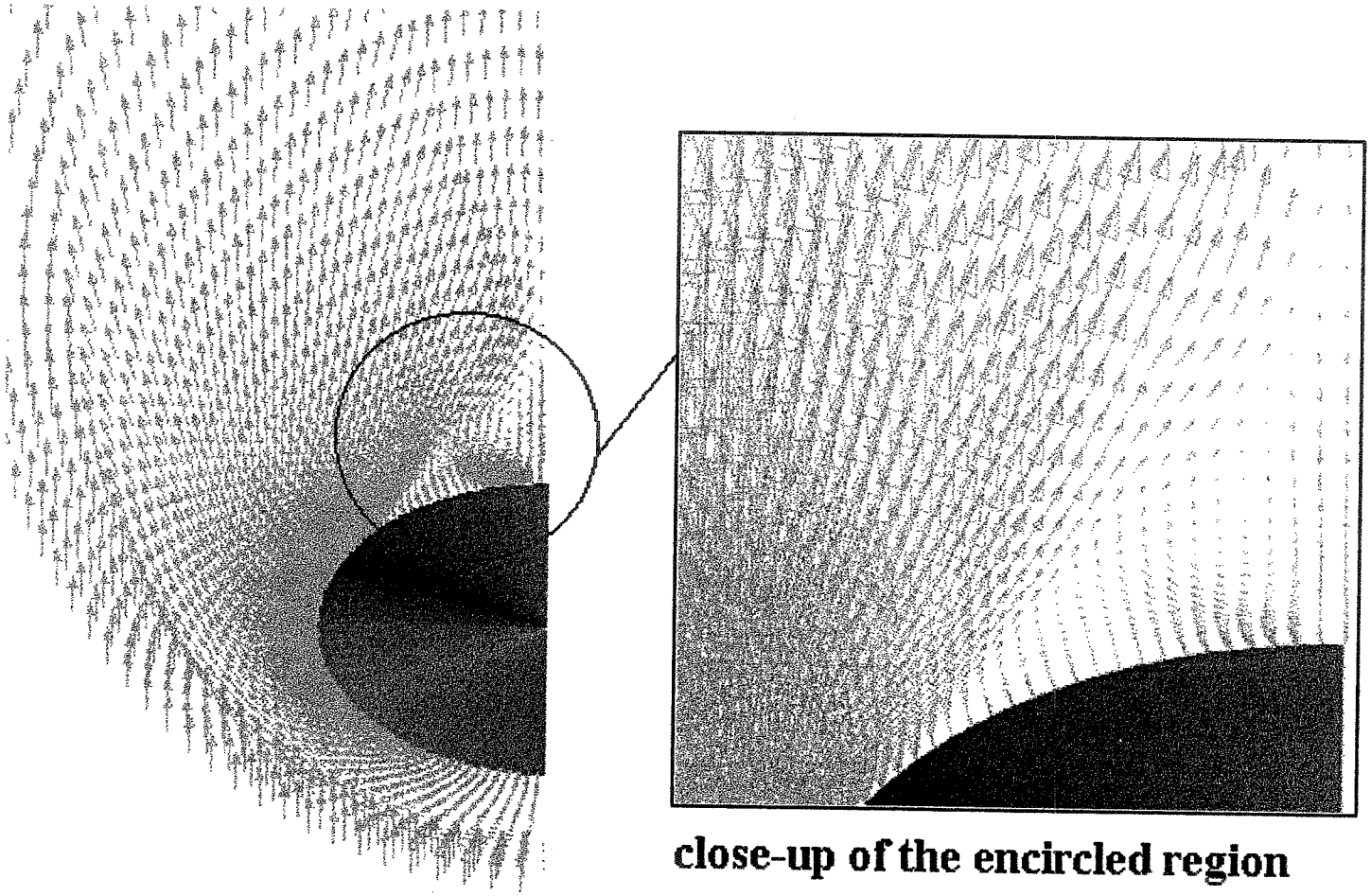

c) base velocity vectors, strakes off
Fig. 4.17 Continue

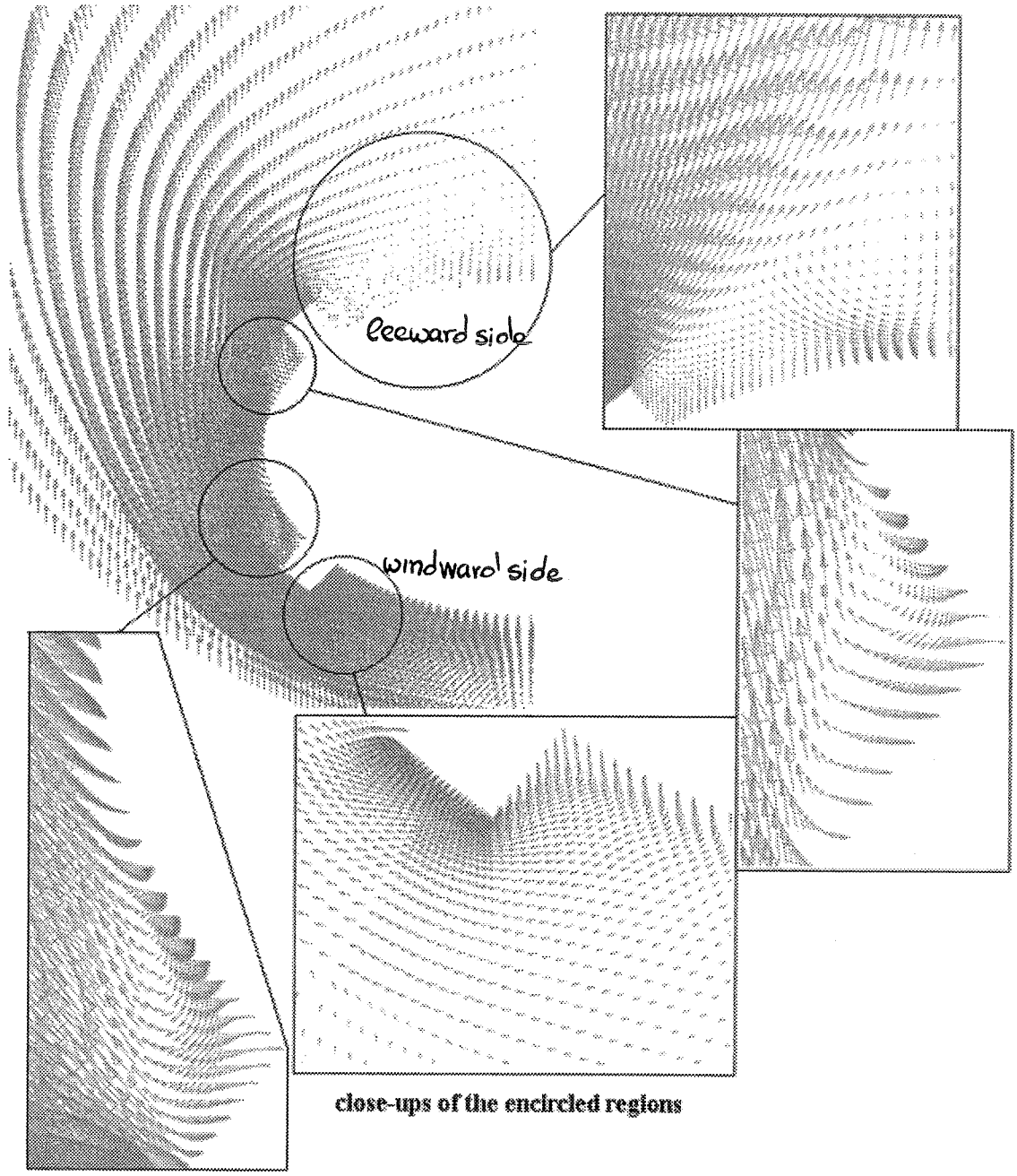

c) base velocity vectors, strakes on

Fig. 4.17 Continue

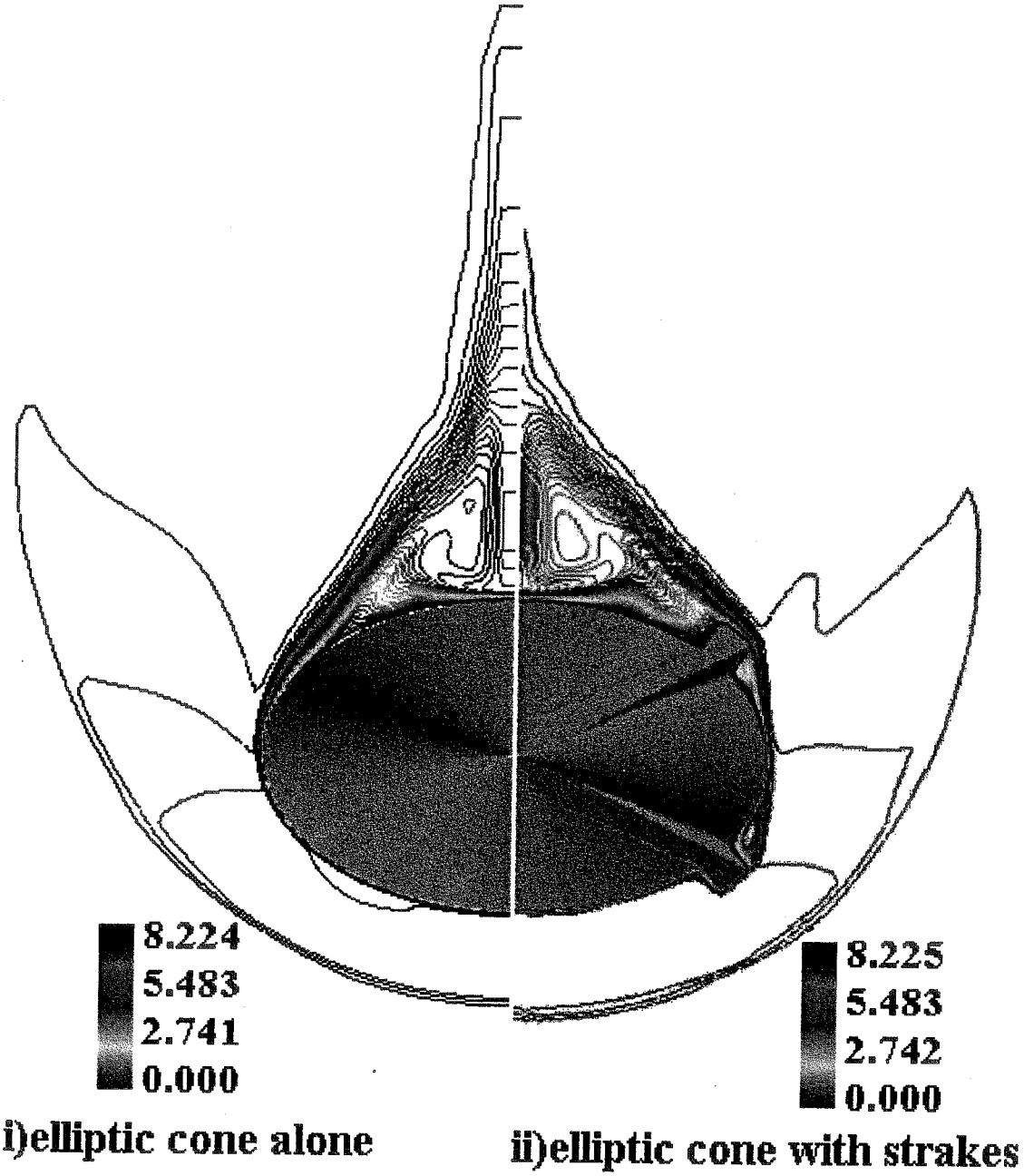

d) base circumferential Mach number contours

Fig. 4.17 Concluded

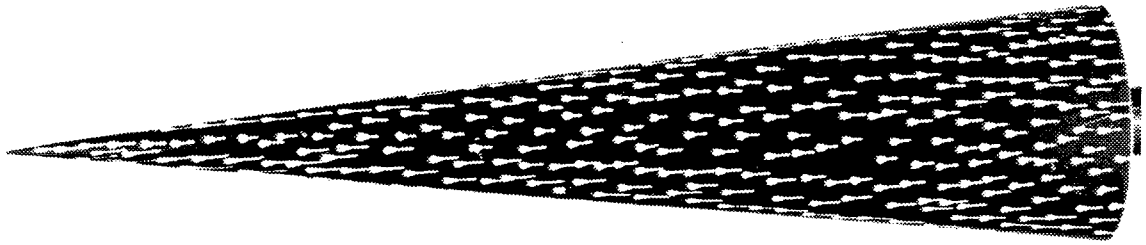

windward side

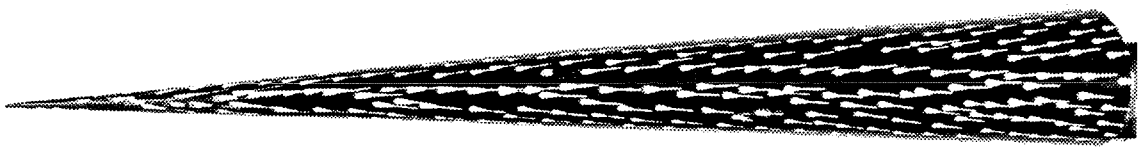

left side

a) strakes off, $\alpha=0^{\circ}$

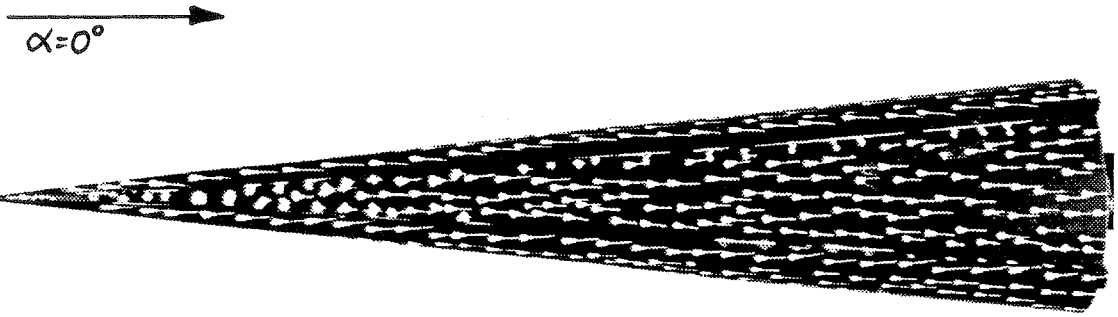

windward side

left side

a) strakes on, $\alpha=0^{\circ}$

Fig. 4.18 Oil-dot pictures of configuration 4 (strakes off and on)

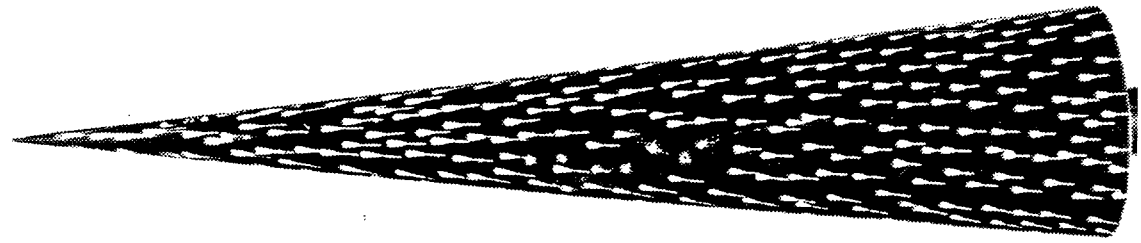

windward side

left side

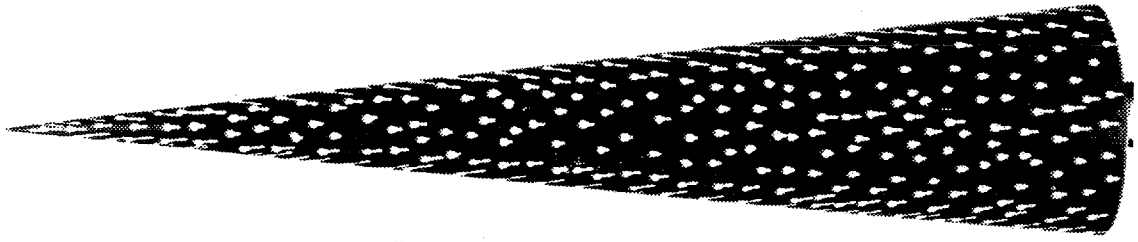

leeward side
b) strakes off, $\alpha=5^{\circ}$

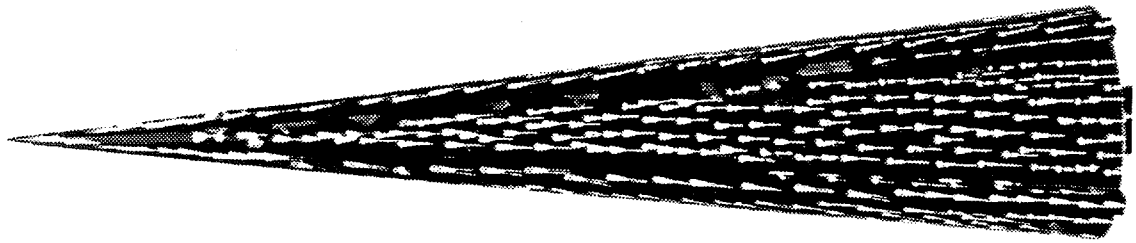

windward side

left side

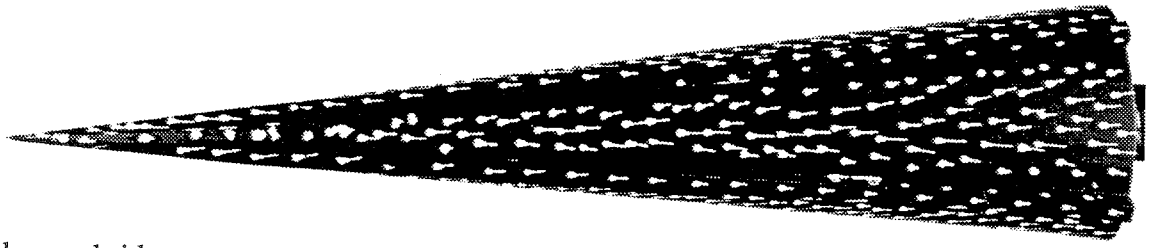

leeward side
b) strakes on, $\alpha=5^{\circ}$

Fig. 4.18 Continue

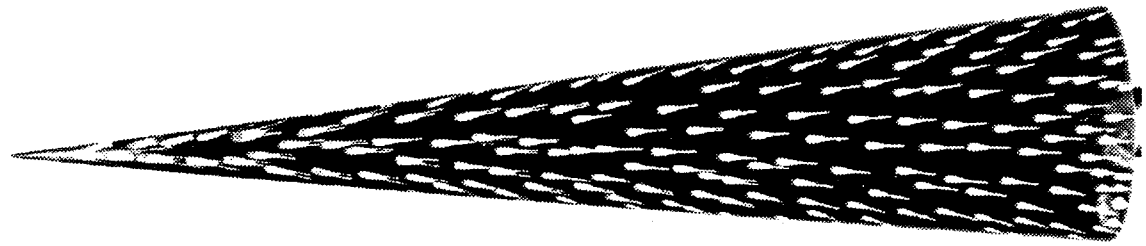

windward side

left side

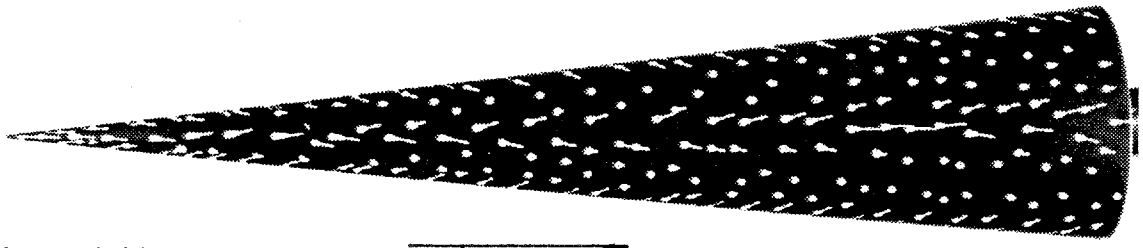

leeward side
c) strakes off, $\alpha=10^{o}$

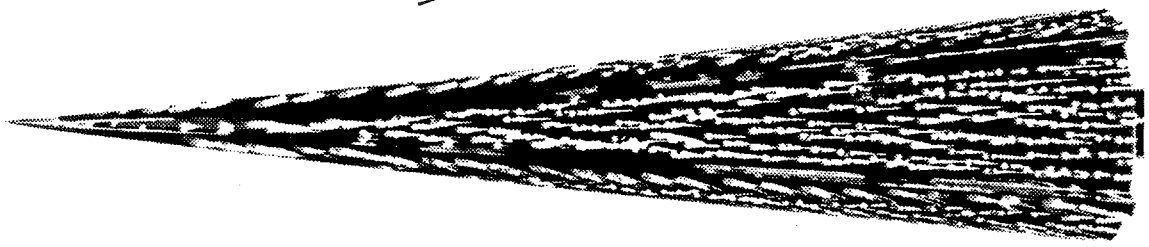

windward side

left side

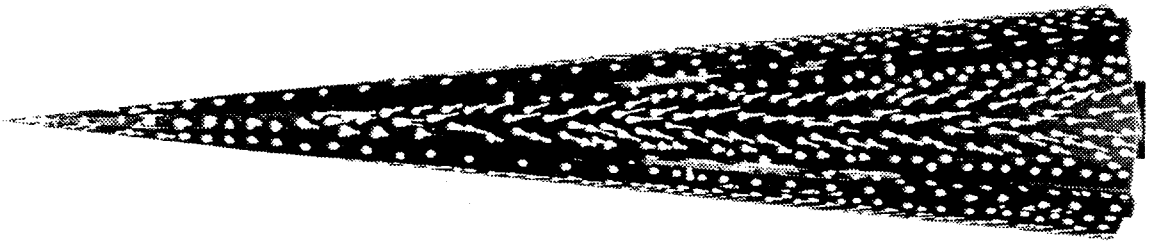

leeward side
c) strakes on, $\alpha=10^{o}$

Fig. 4.18 Continue

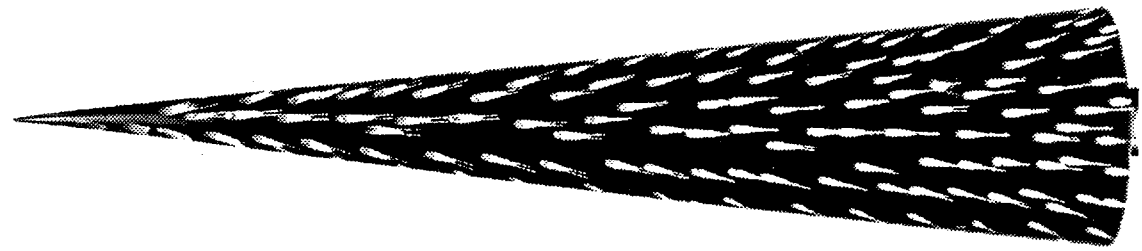

windward side

left side

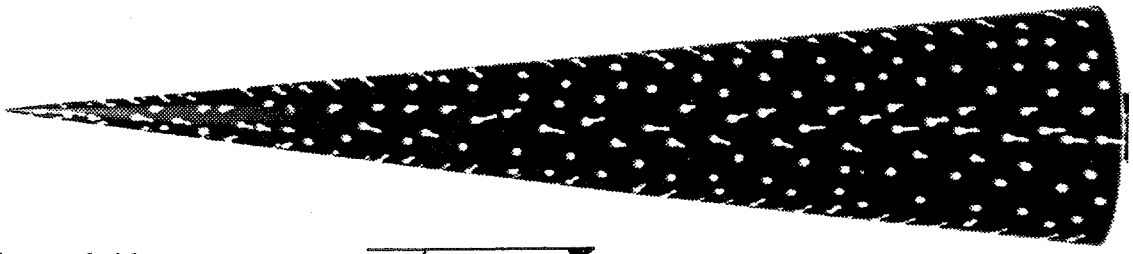

leeward side
d) strakes off, α=15°

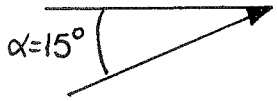

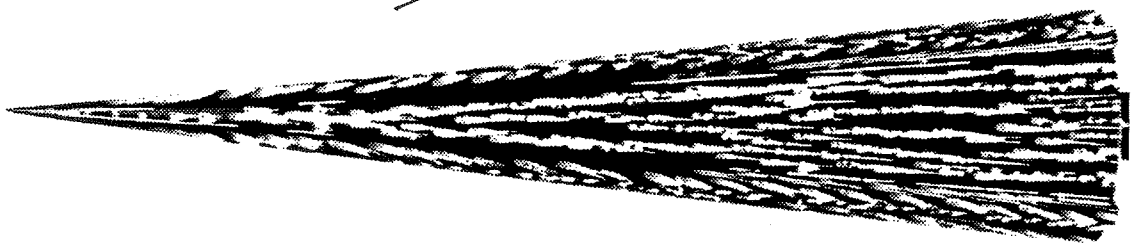

windward side

left side

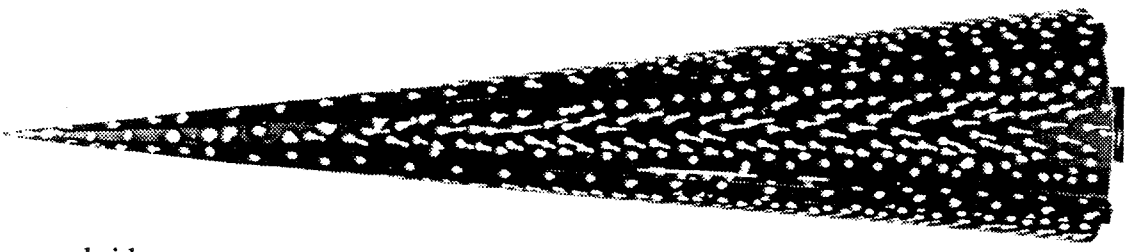

leeward side
d) strakes on, α=15°

Fig. 4.18 Continue

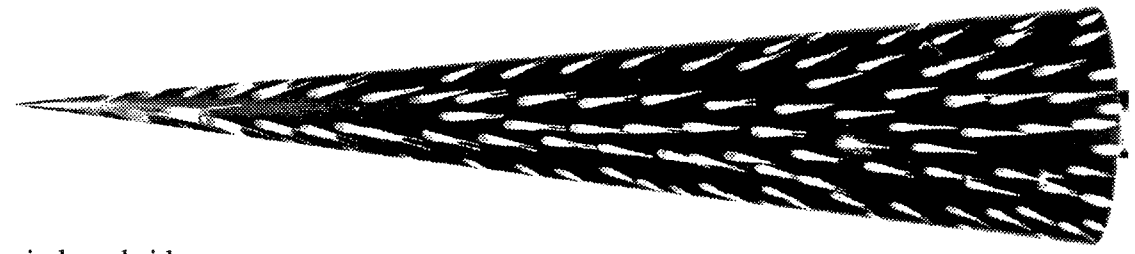

windward side

left side

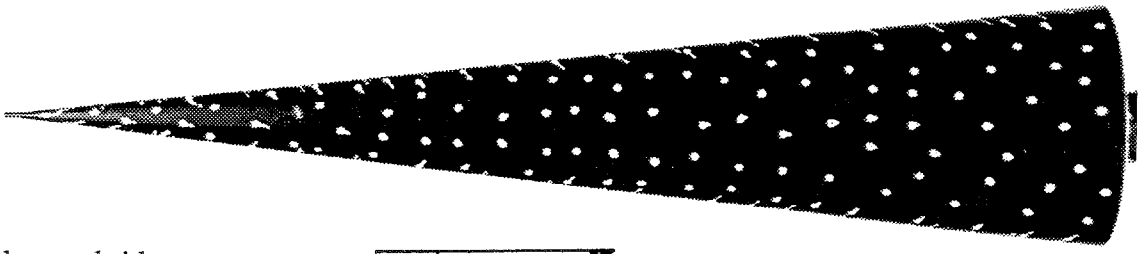

leeward side
e) strakes off, α=20°

windward side

left side

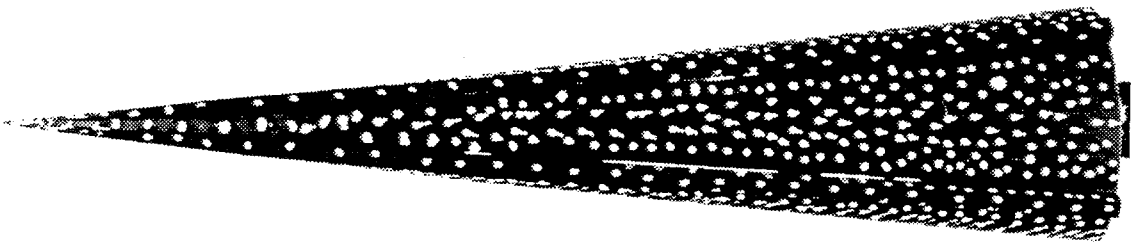

leeward side
e) strakes on, α=20°

Fig. 4.18 Concluded

a) α=0°

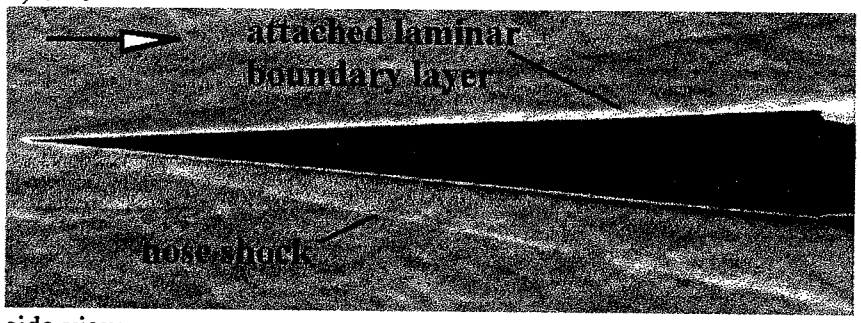

side view

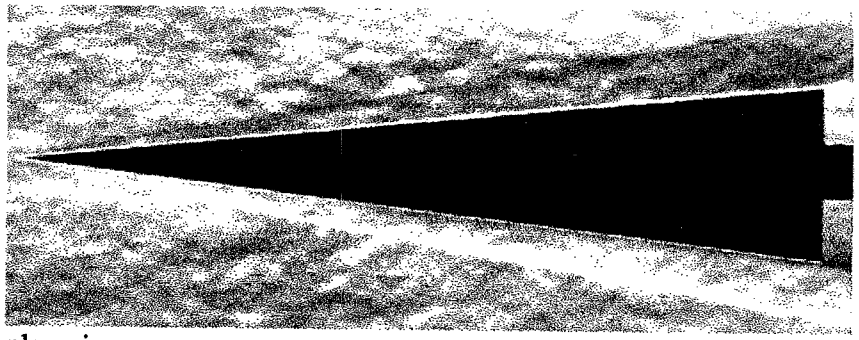

plan view

b) α=4°

side view

c) α=5°

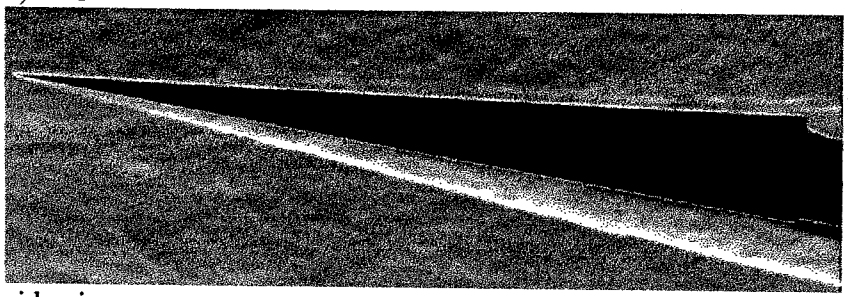

side view

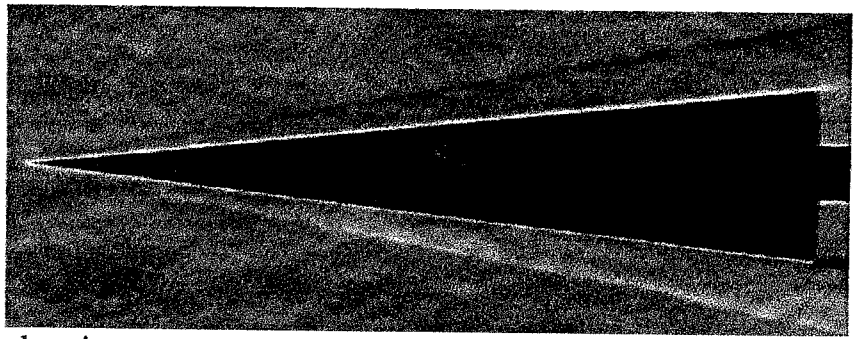

plan view

Fig. 4.19 Schlieren photographs of configuration 4 (strakes on)

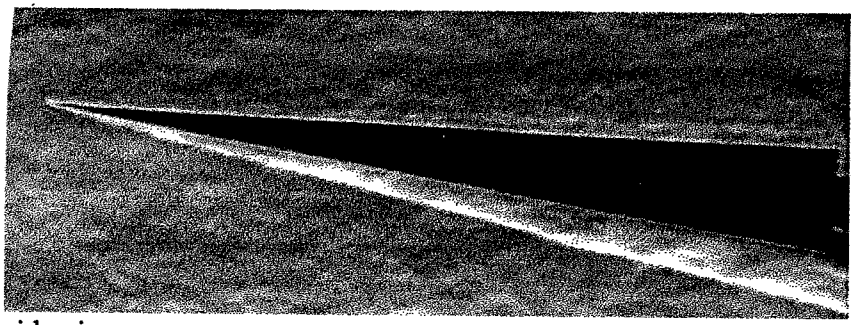

side view

e) $\alpha=7°$

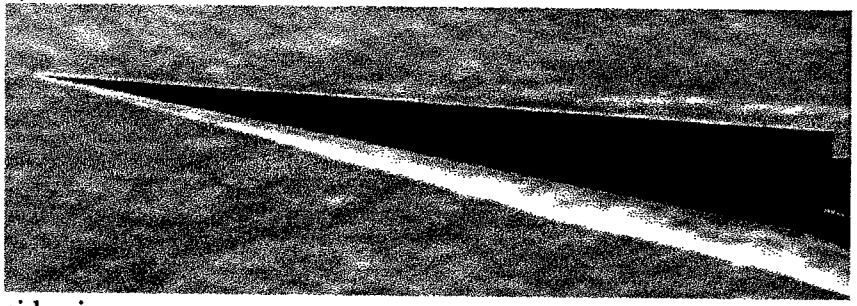

side view

f) $\alpha=8°$

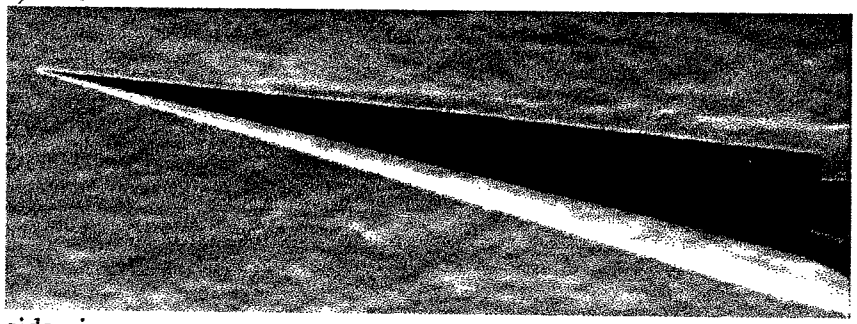

side view

Fig. 4.19 Continue

g) α=10°

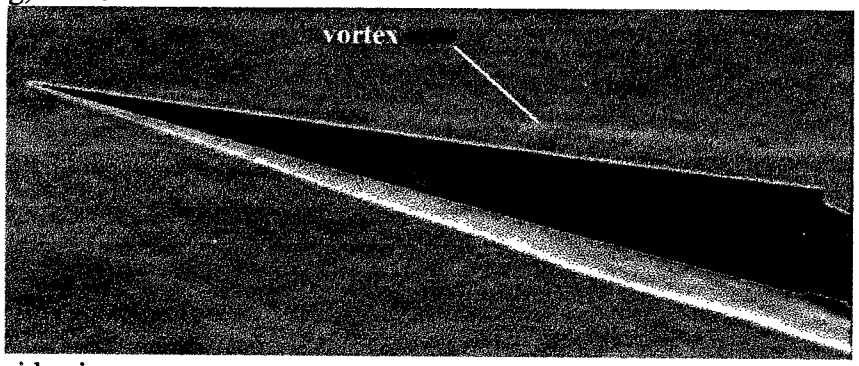

side view

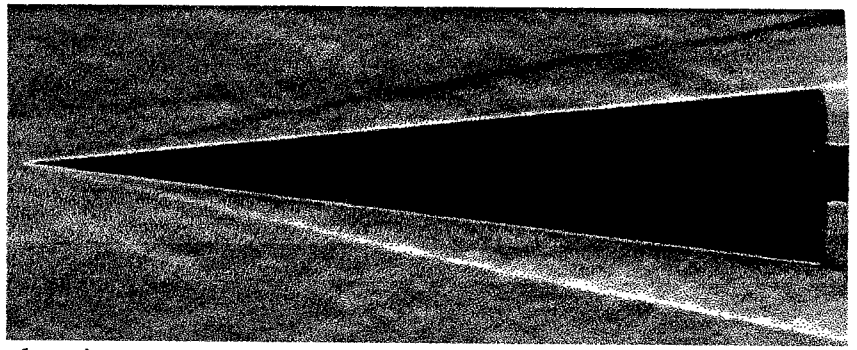

plan view

h) α=15°

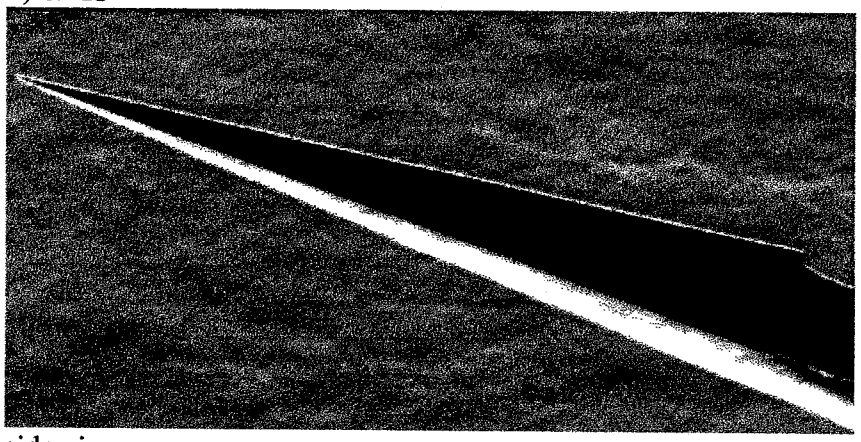

side view

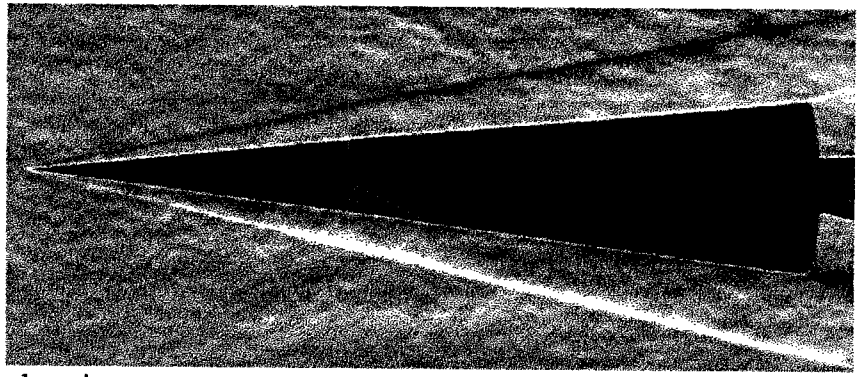

plan view

Fig. 4.19 Continue

i) α=20°

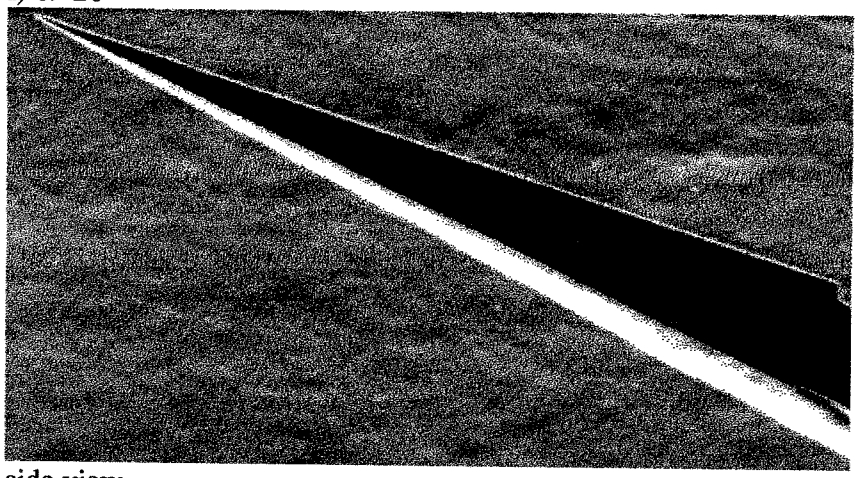

side view

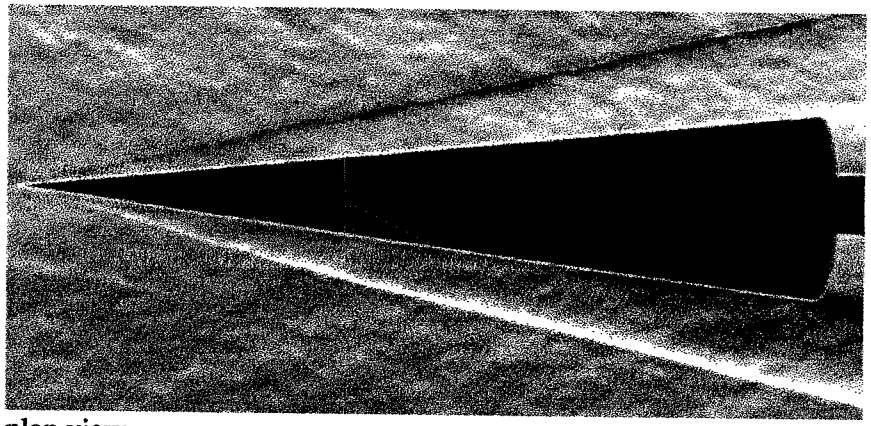

plan view

Fig. 4.19 Concluded

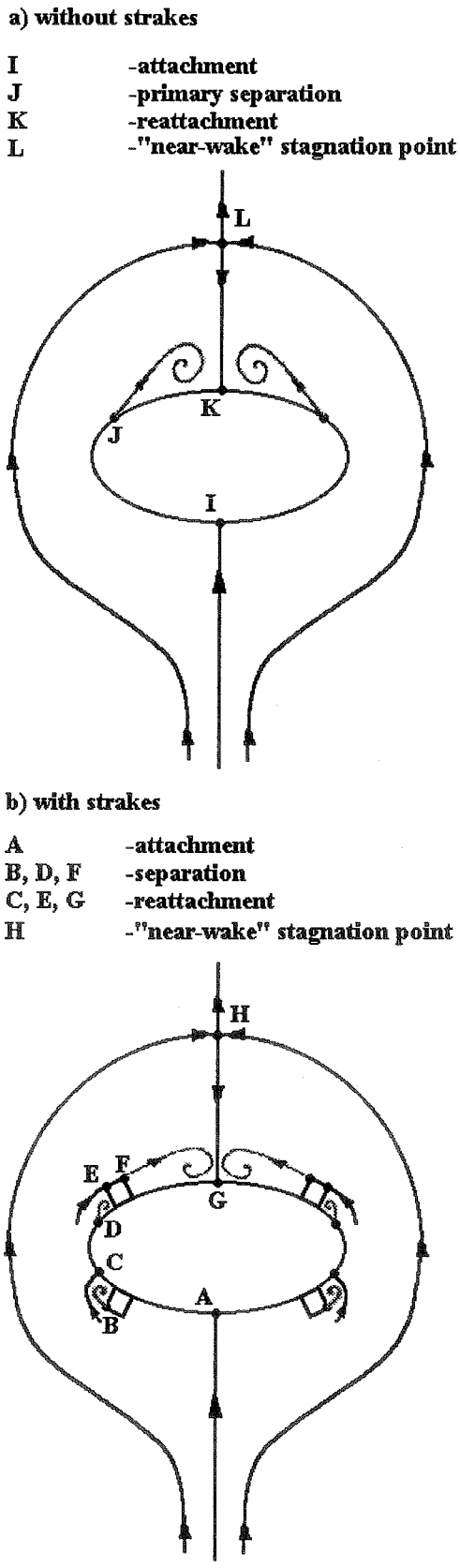

Fig. 4.20 Proposed flow field models for configuration 4 (strakes off and on)

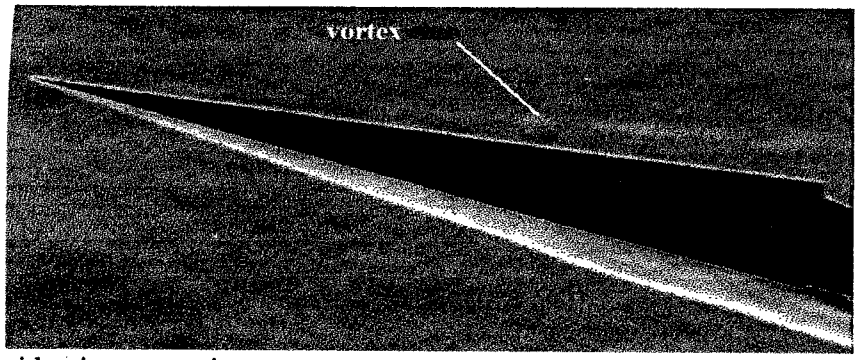

side view, experiment

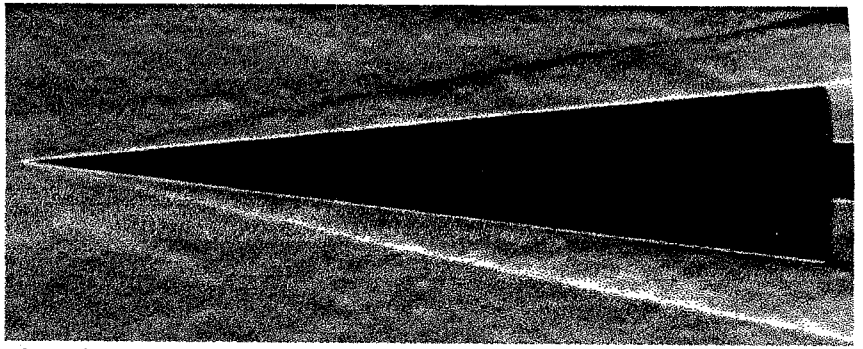

plan view, experiment

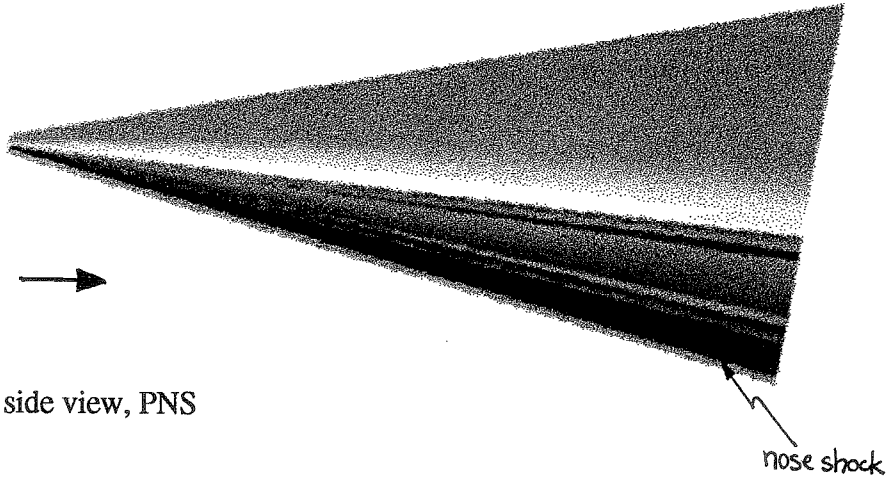

side view, PNS

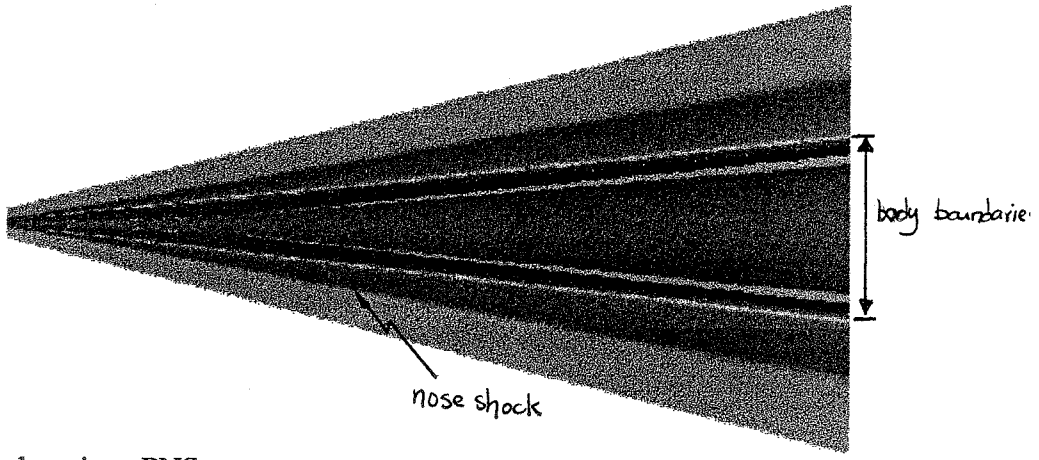

plan view, PNS

a) α=10°

Fig. 4.21 Comparison of the schlieren pictures (α=10°, 15° and 20°) with the numerical results (strakes -on)

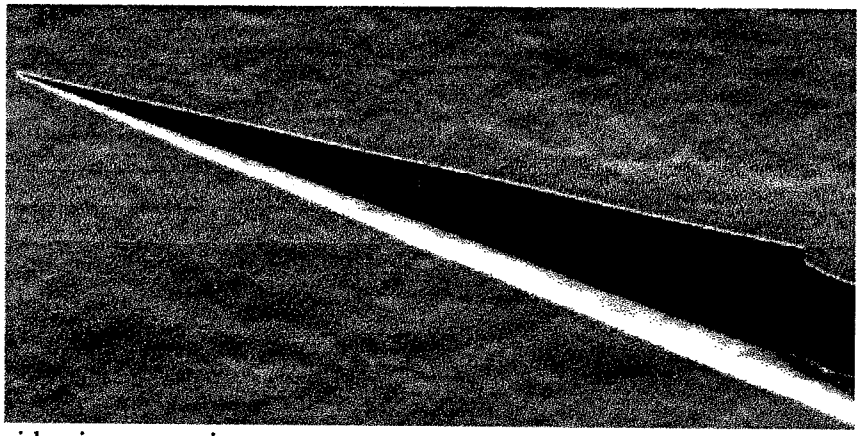

side view, experiment

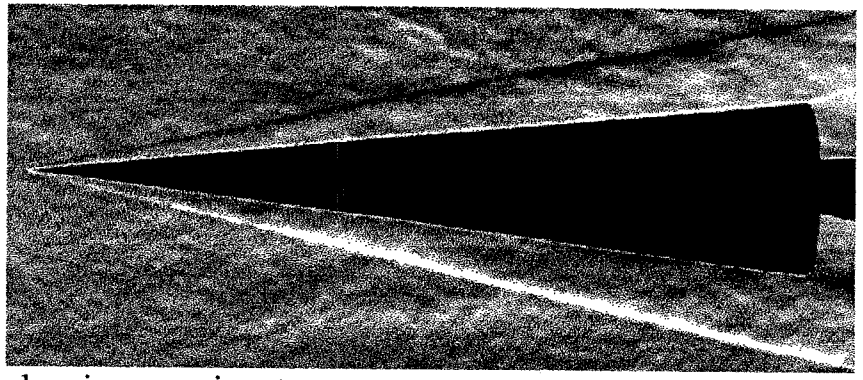

plan view, experiment

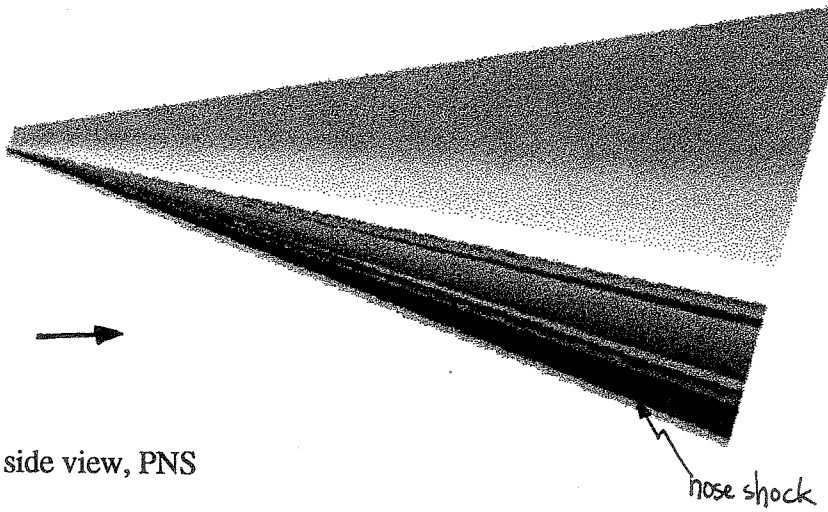

side view, PNS

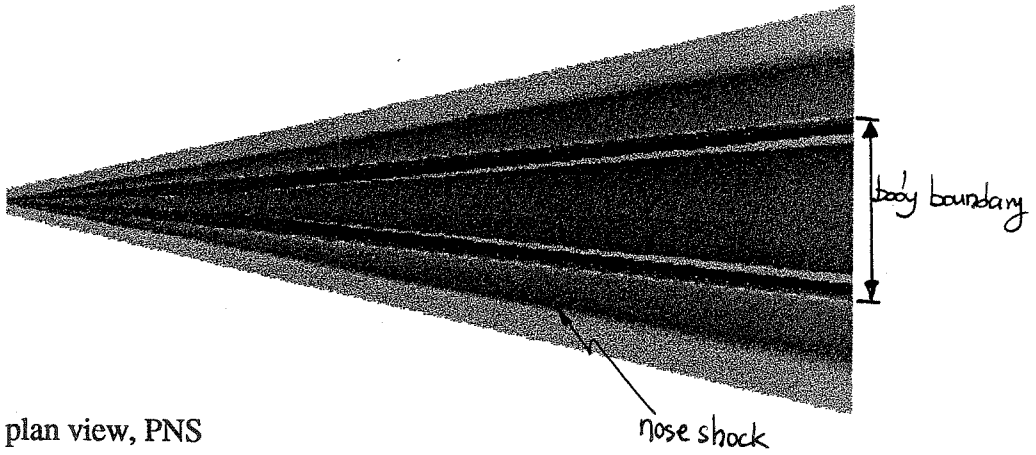

plan view, PNS

b) α=15°

Fig. 4.21 Continue

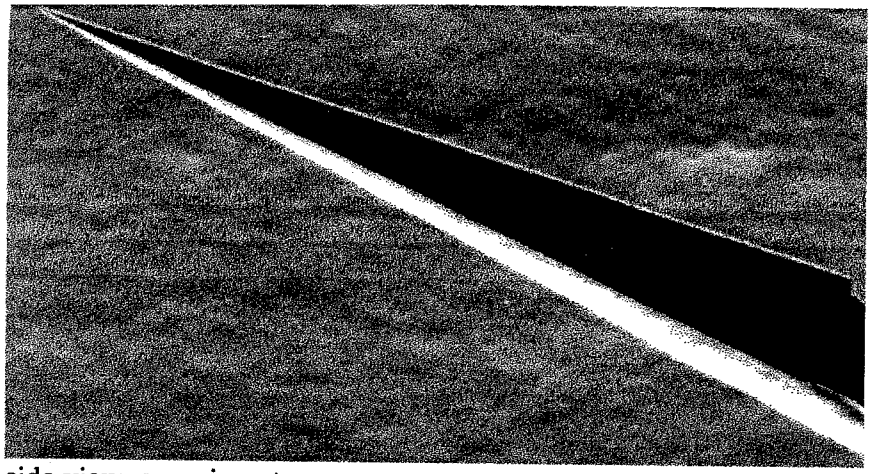

side view, experiment

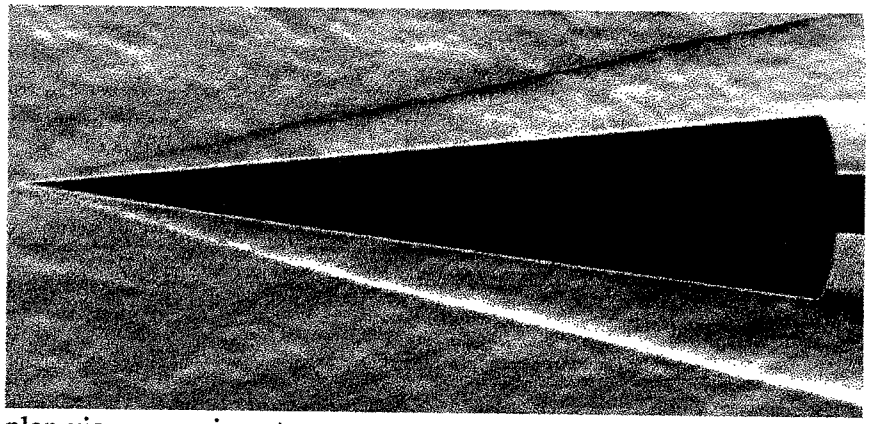

plan view, experiment

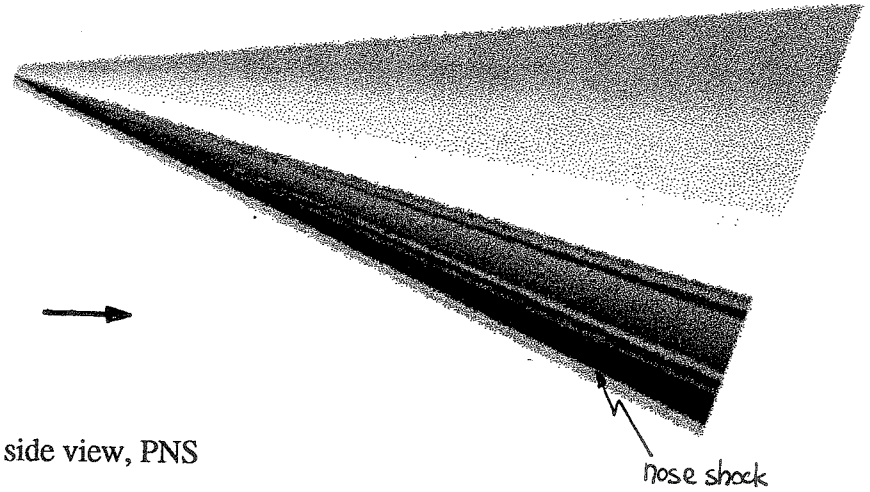

side view, PNS

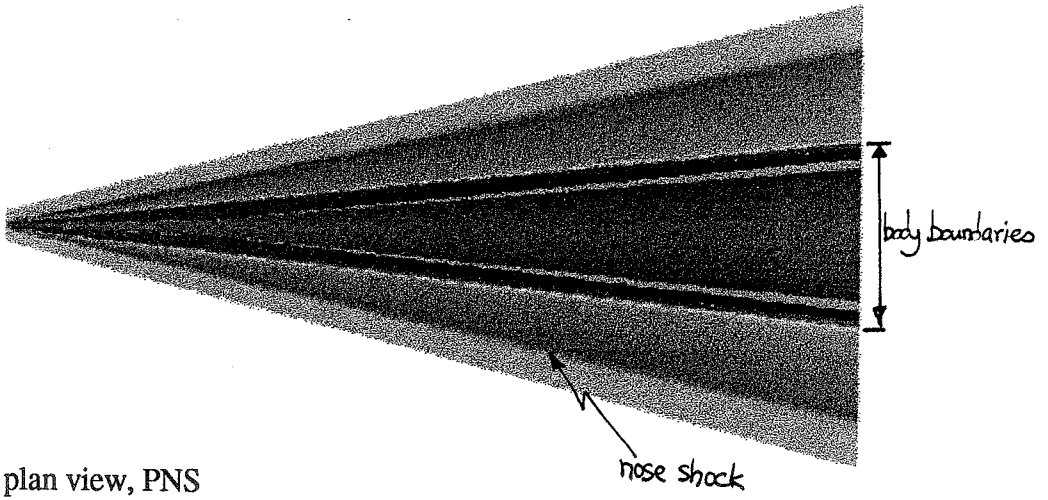

plan view, PNS

c) $\alpha=20°$

Fig. 4.21 Concluded

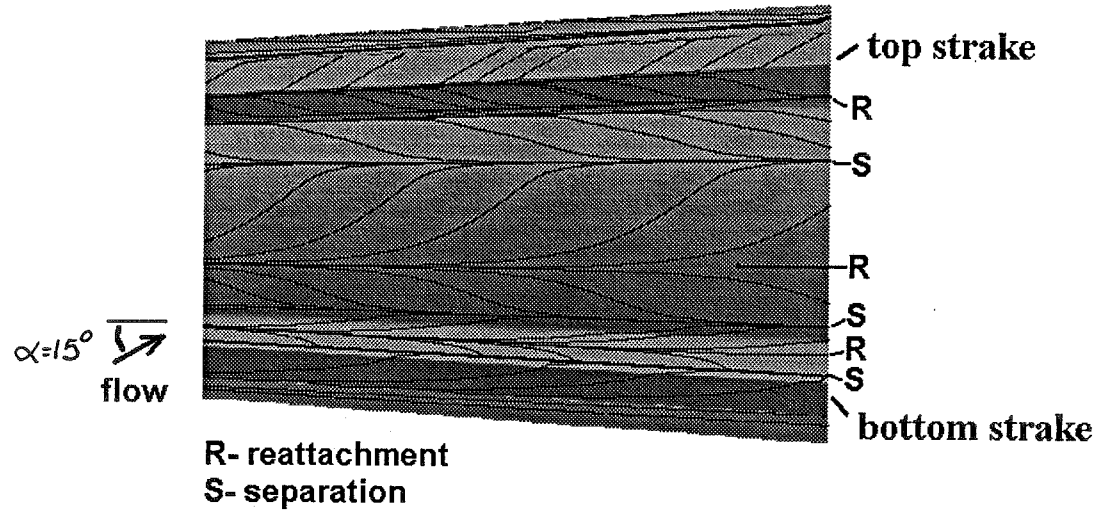

Fig. 4.22 Detail of the flow field near the strakes region (PNS)

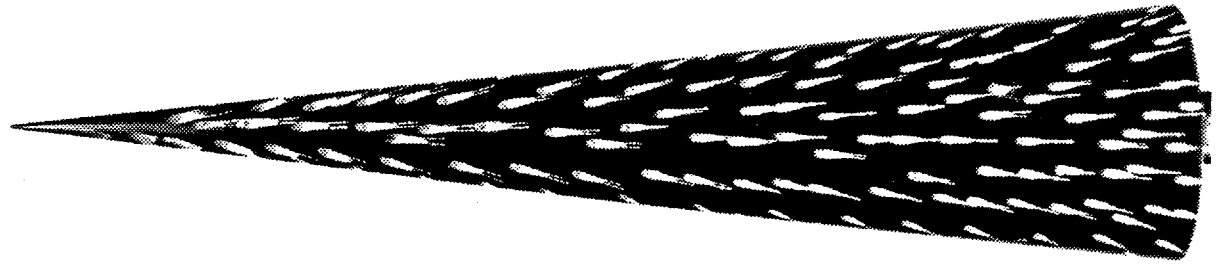

experiment

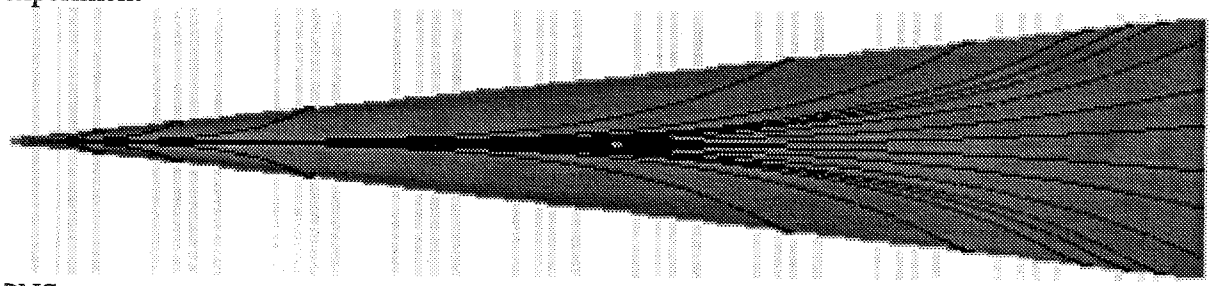

PNS

a) windward side, strakes off

experiment

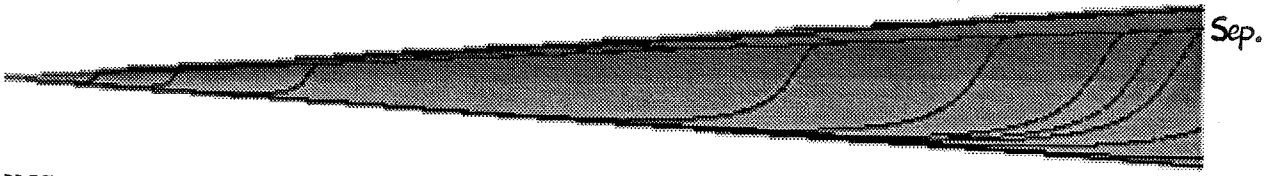

PNS

) left side, strakes off

Fig. 4.23 Comparison of the oil-dot flow visualisation and numerical streamline results for the cone with and without strakes at $\alpha=15^{\circ}$

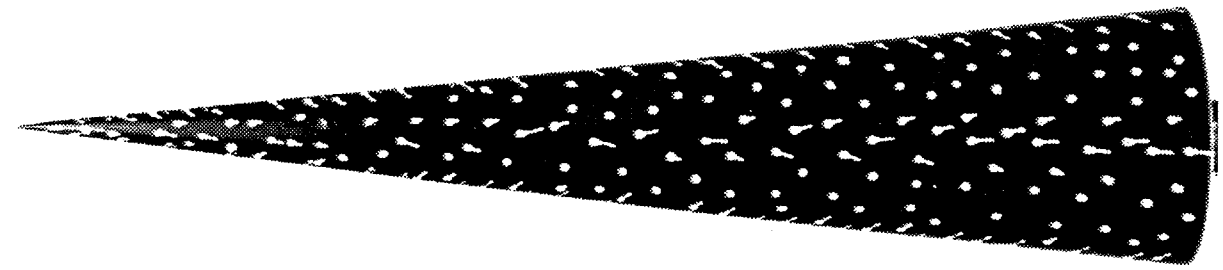

experiment

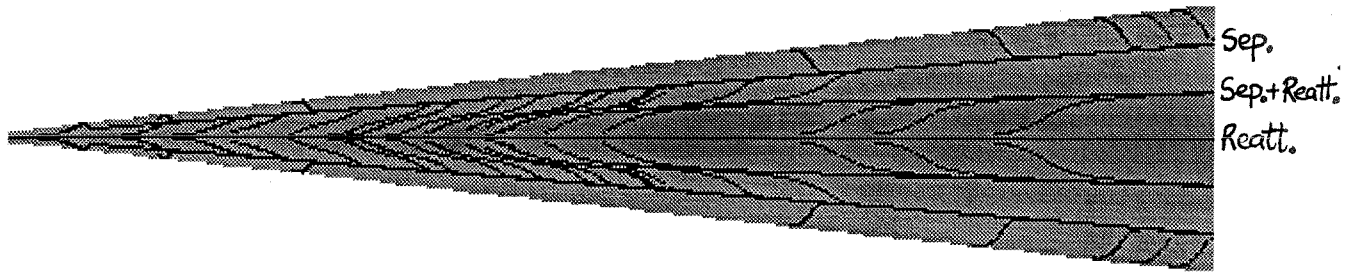

PNS

c) leeward side, strakes off

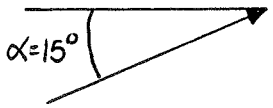

* Seperation and Reattachment lines very close to each other

experiment

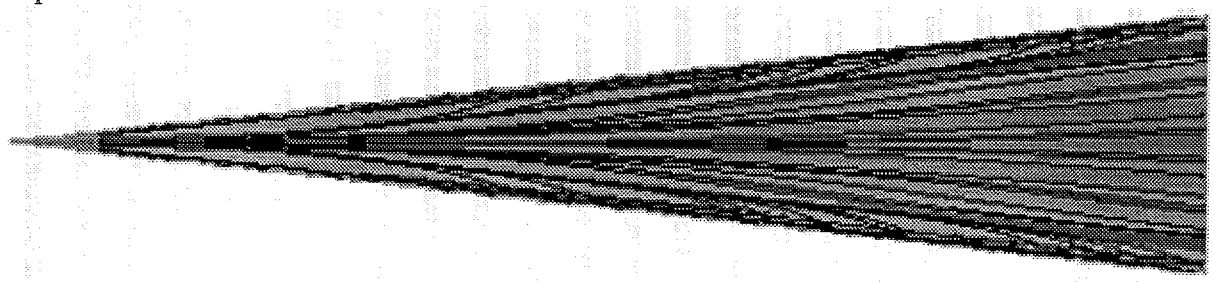

PNS

d) windward side, strakes on

Fig. 4.23 Continue

experiment

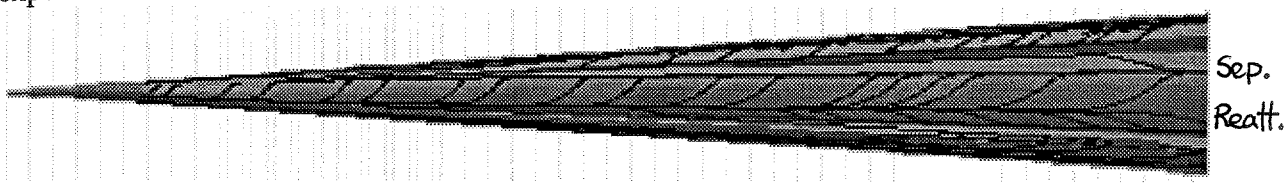

PNS

e) left side, strakes on

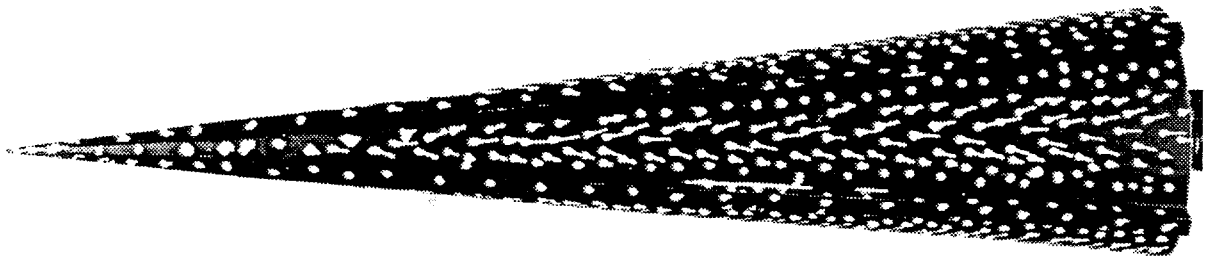

experiment

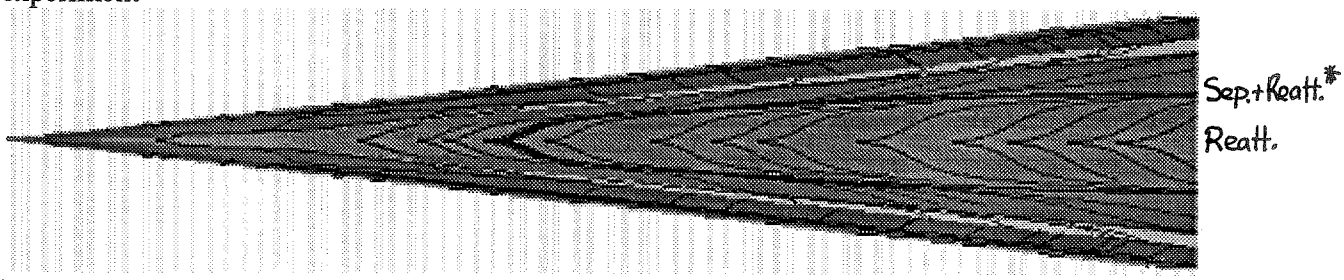

PNS

f) leeward side, strakes on

* Separation and Reattachment lines close to each other

Fig. 4.23 Concluded

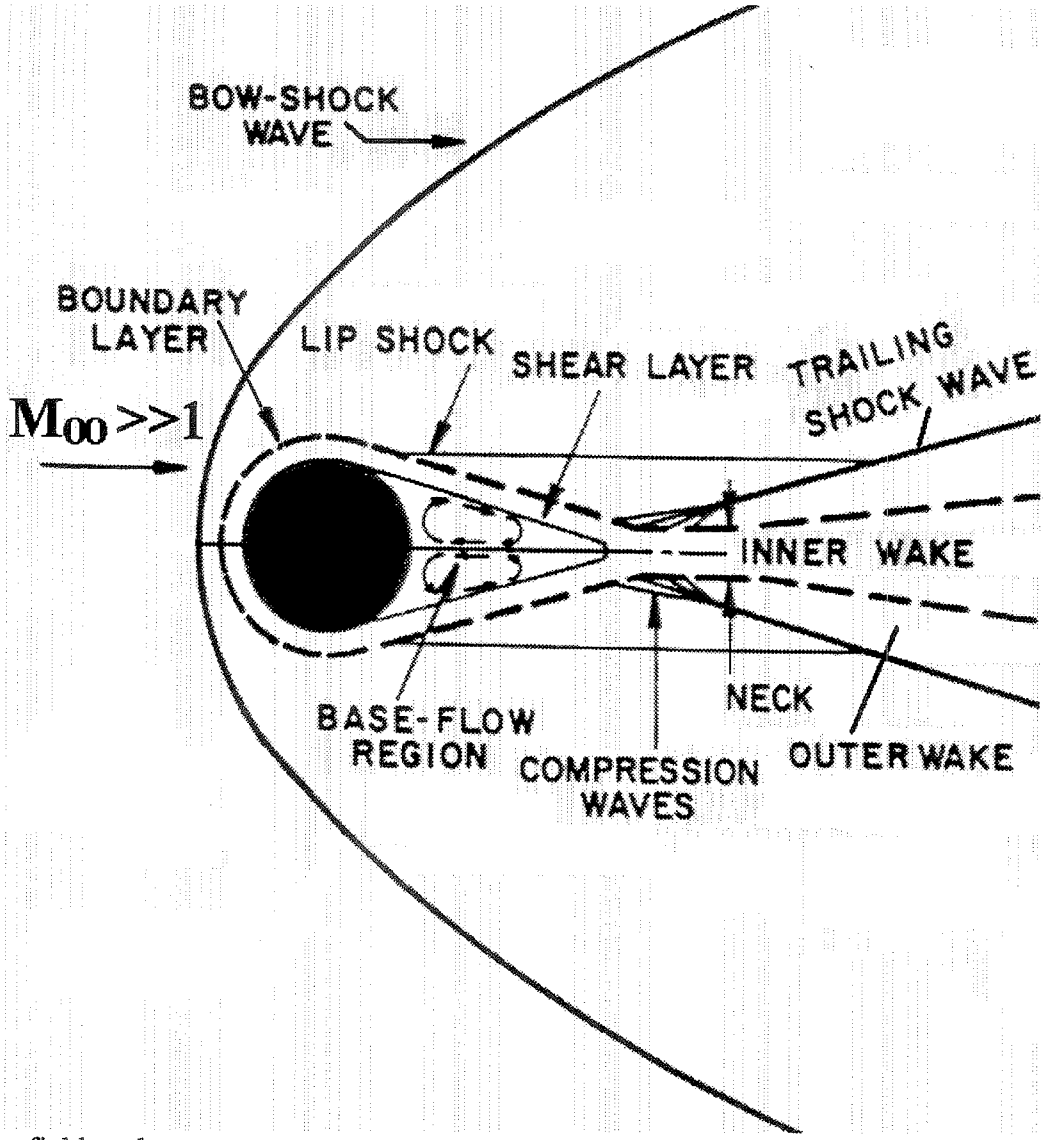

Fig. 4.24 Proposed near flow field analogy

a) windward side

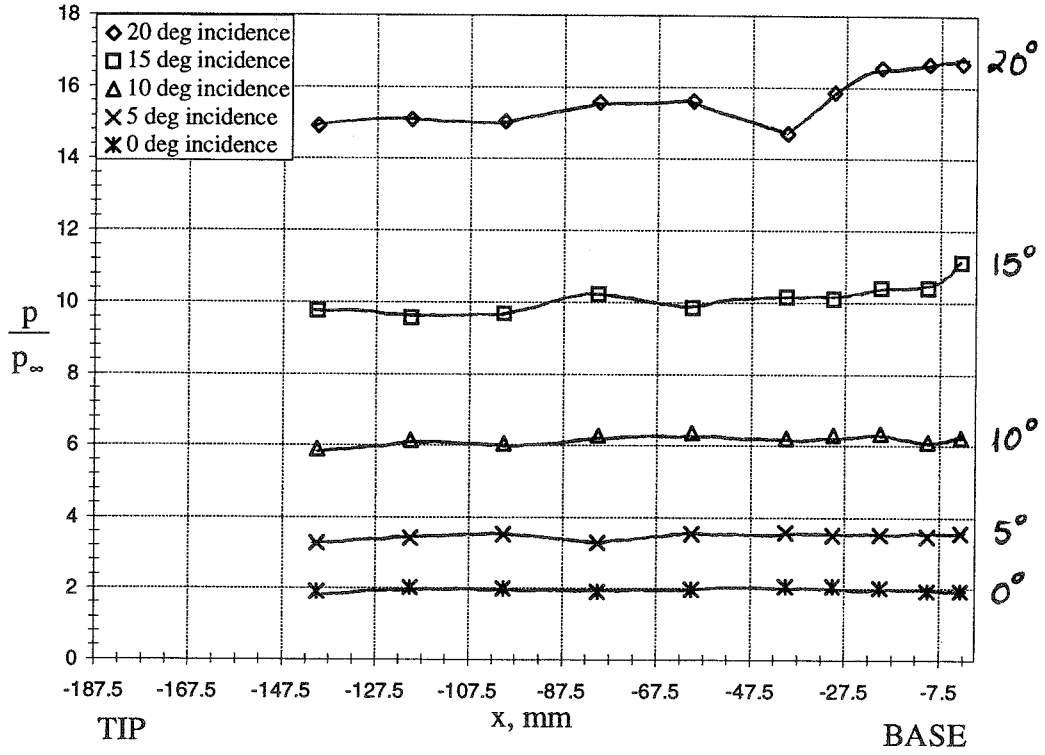

b) leeward side

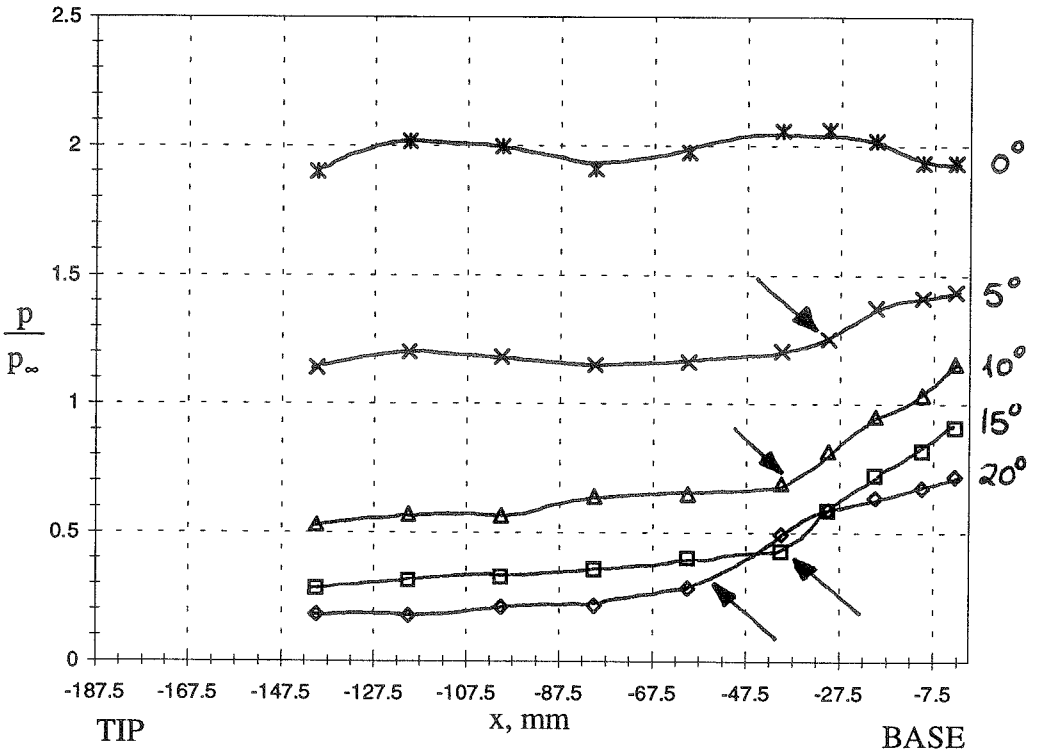

Fig. 4.25 Initial pressure measurements on the elliptic cone without strakes

a) windward side

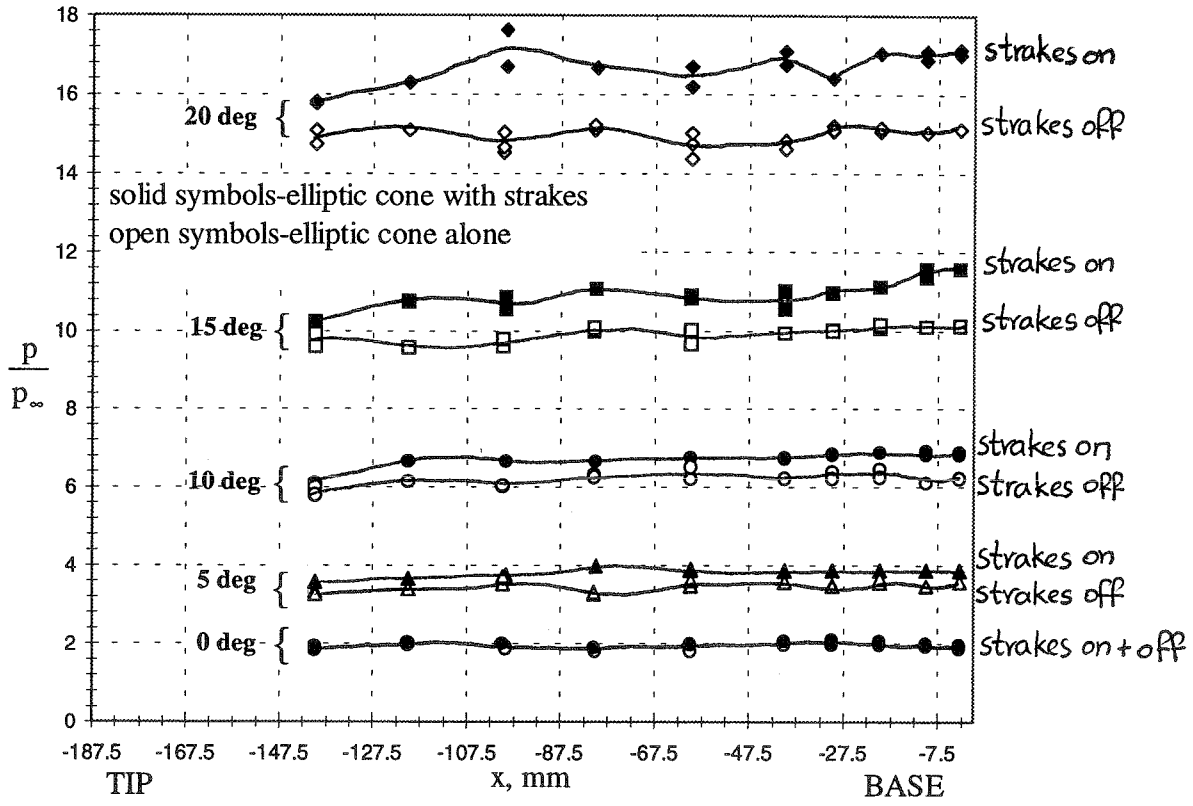

b) leeward side

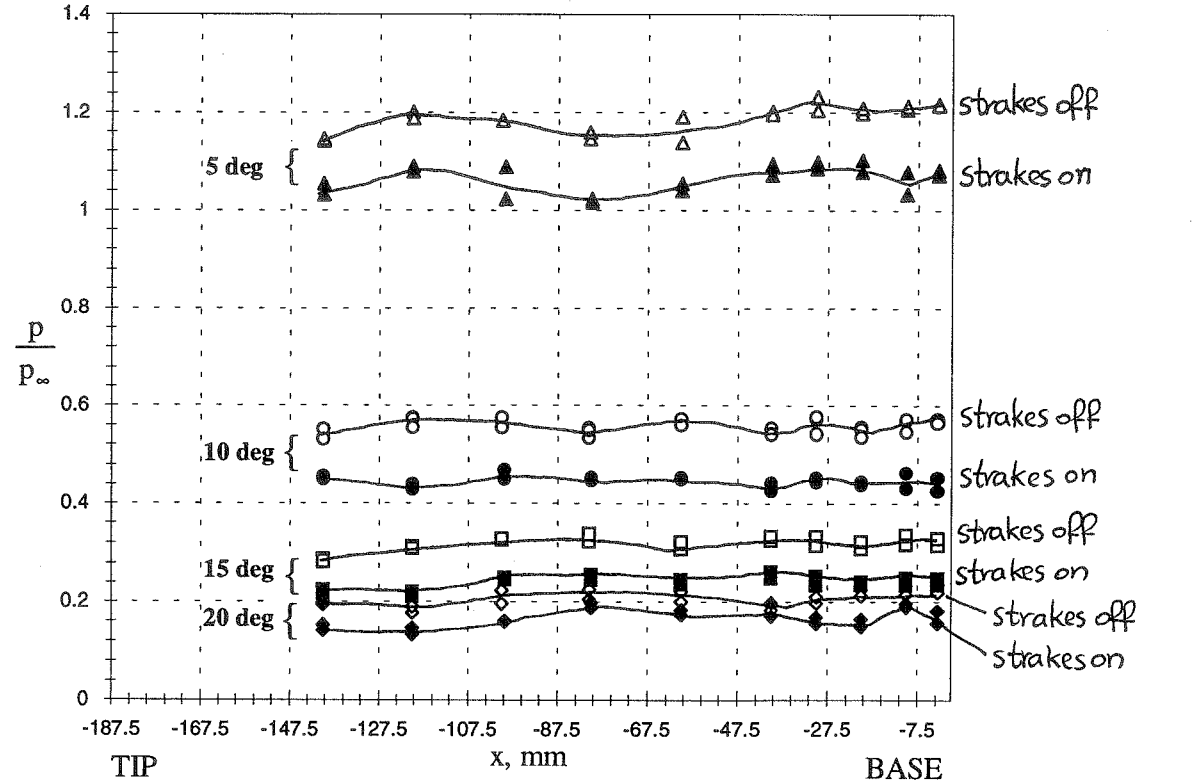

Fig. 4.26 Effect of strakes on the pressure distributions along the windward and leeward sides

a) windward side

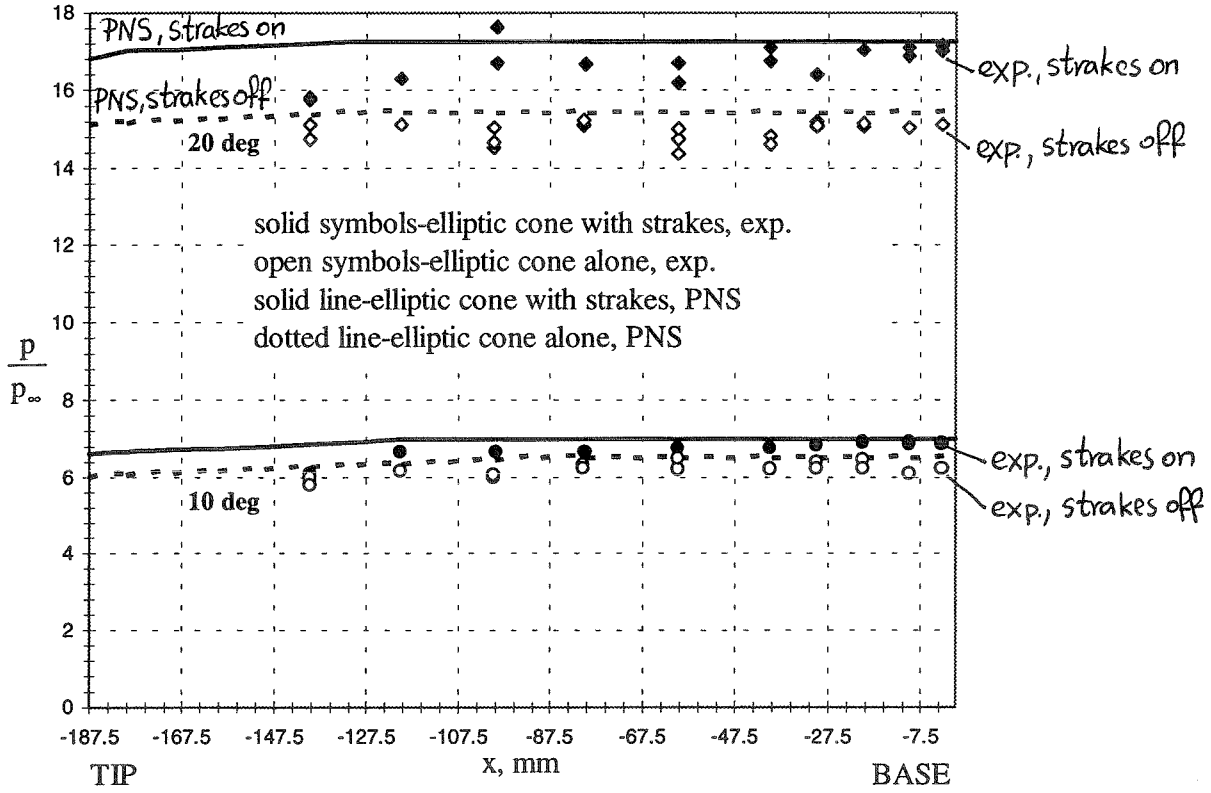

b) leeward side

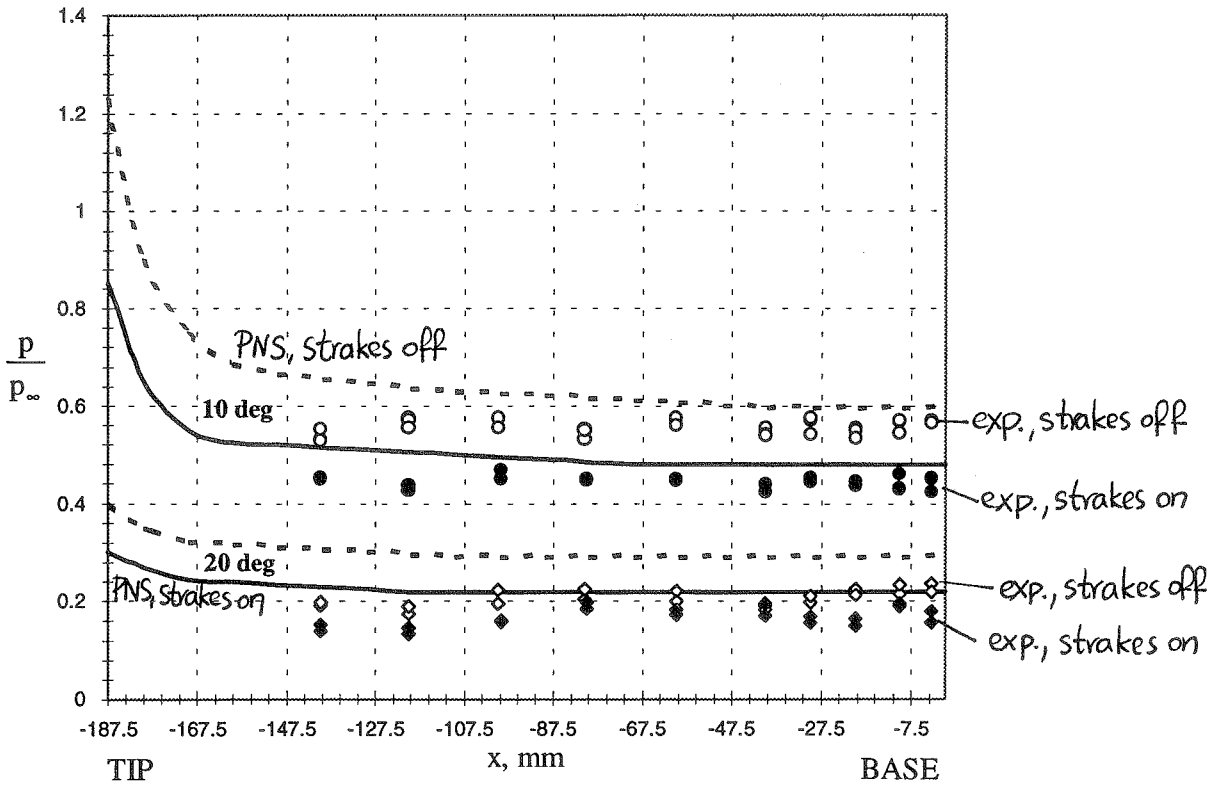

Fig. 4.27 Comparison of numerical results with experimental pressure measurements (strakes on and off, windward and leeward sides)

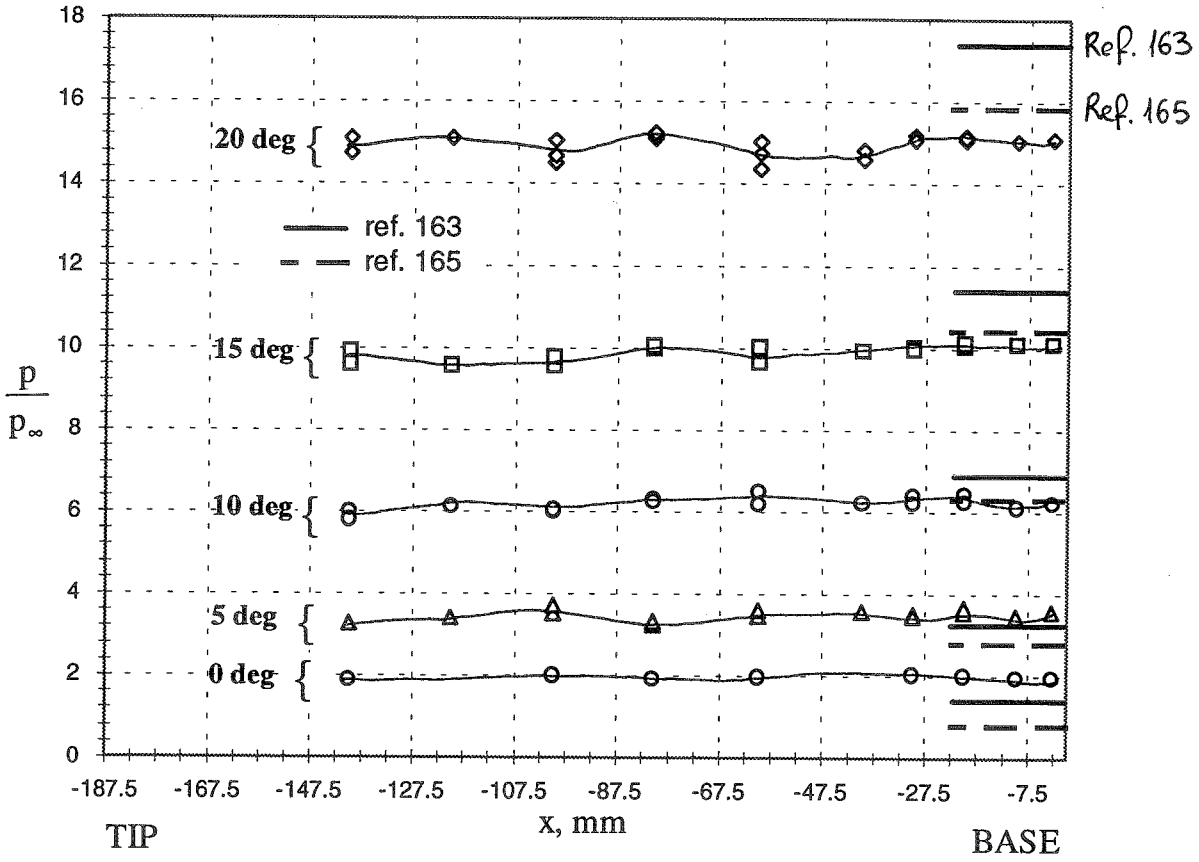

Fig. 4.28 Comparison of theoretical results with experimental pressure measurements (strakes off, windward side)

a)

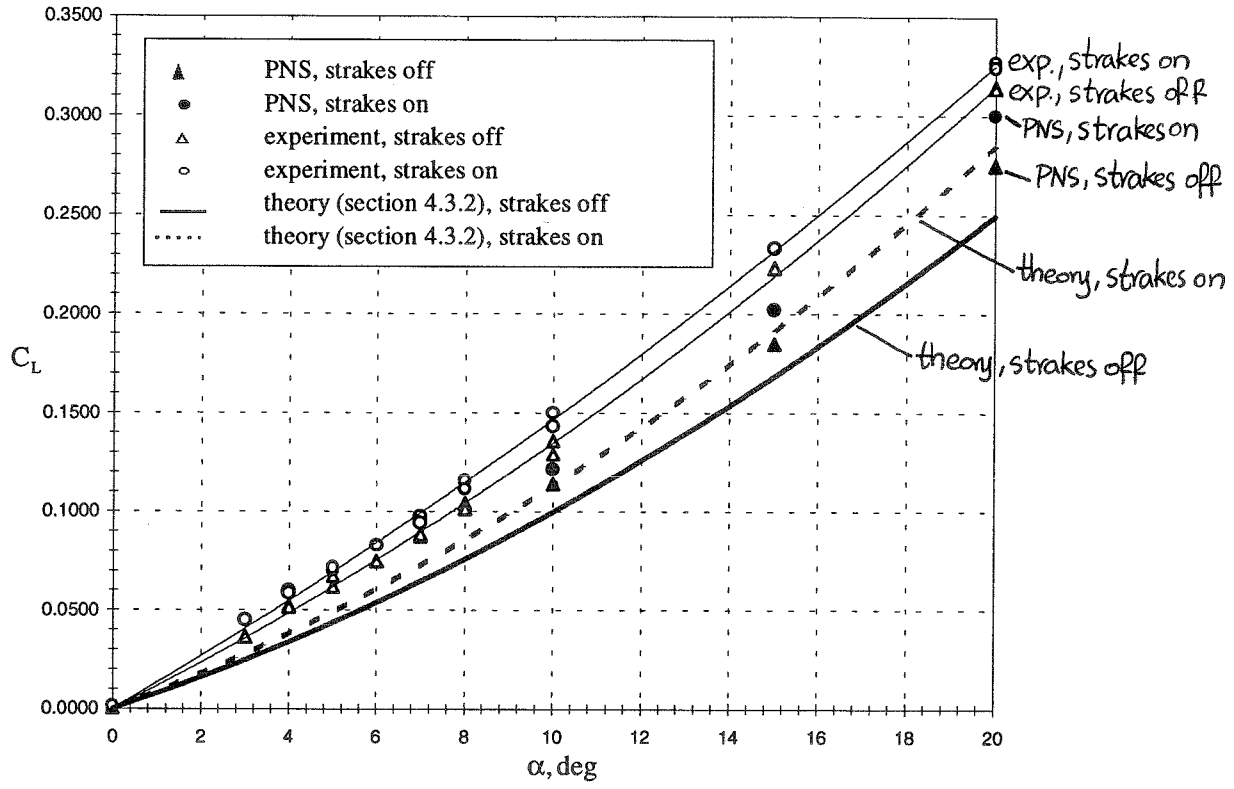

b)

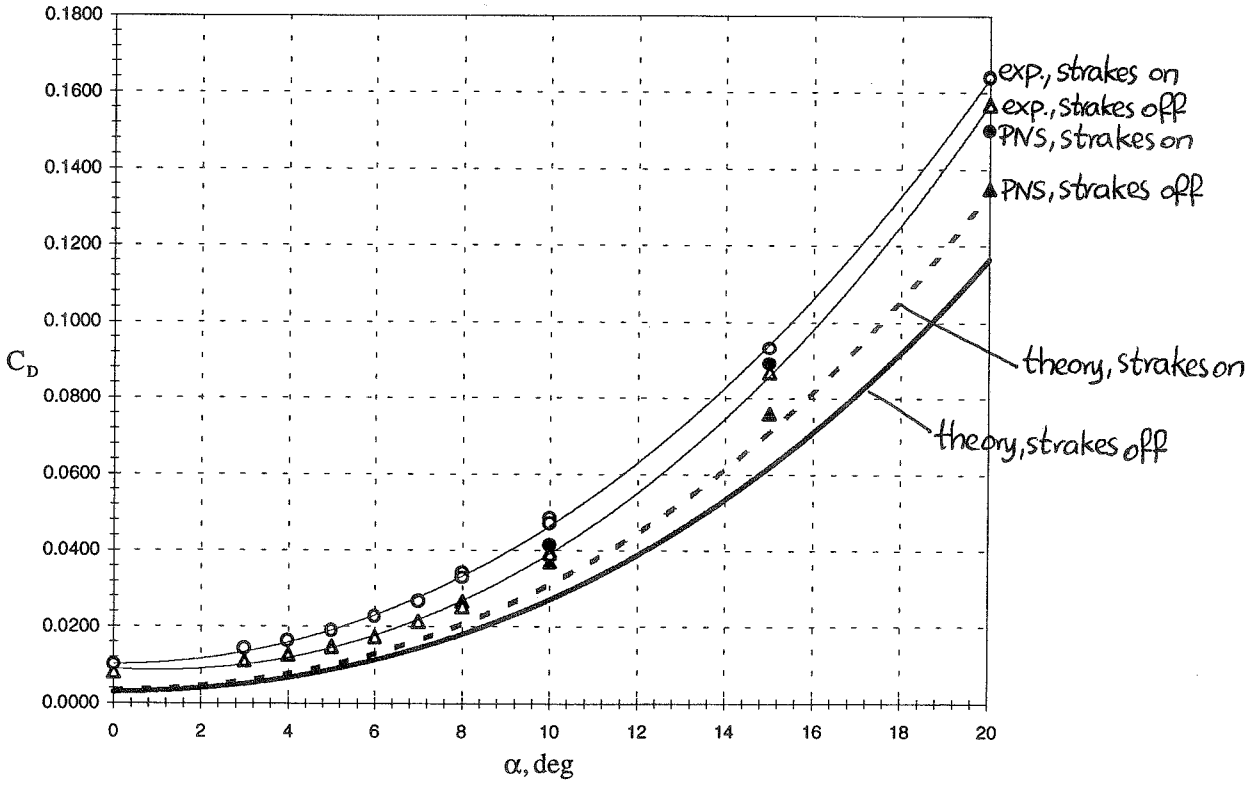

Fig. 4.29 Effect of strakes on the aerodynamic characteristics of configuration 4

. c)

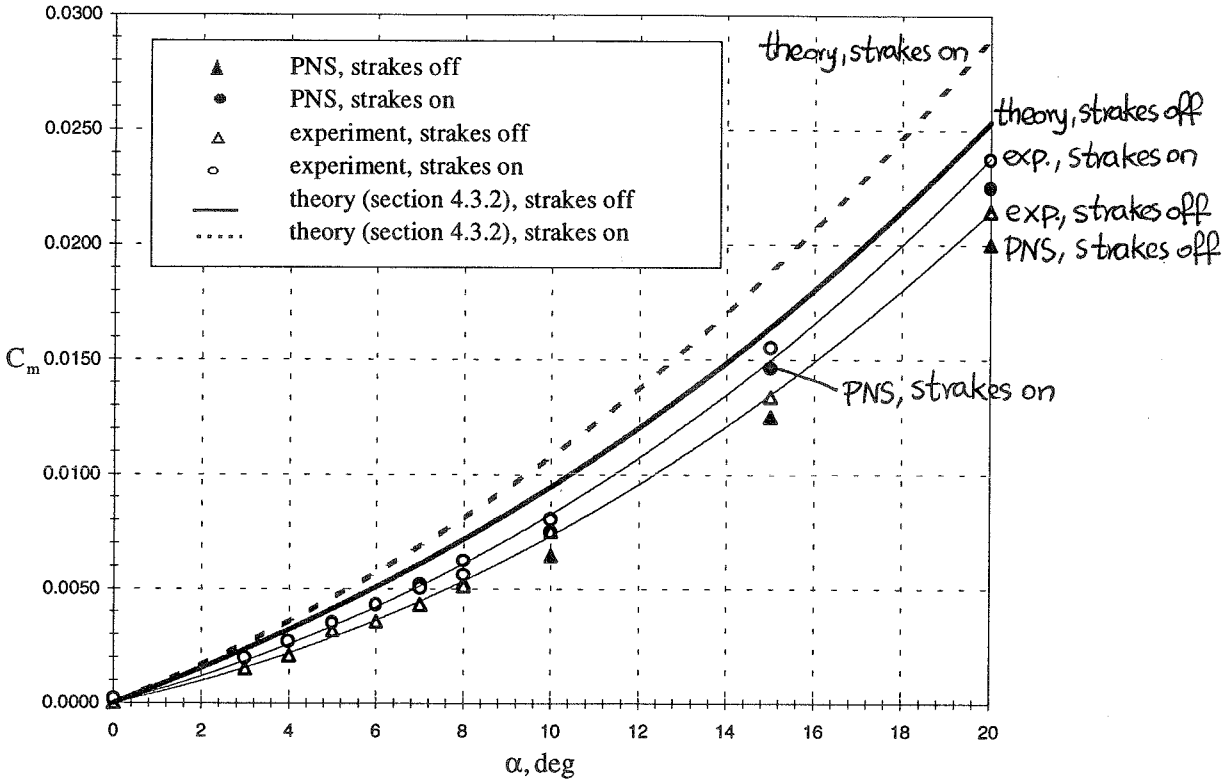

d)

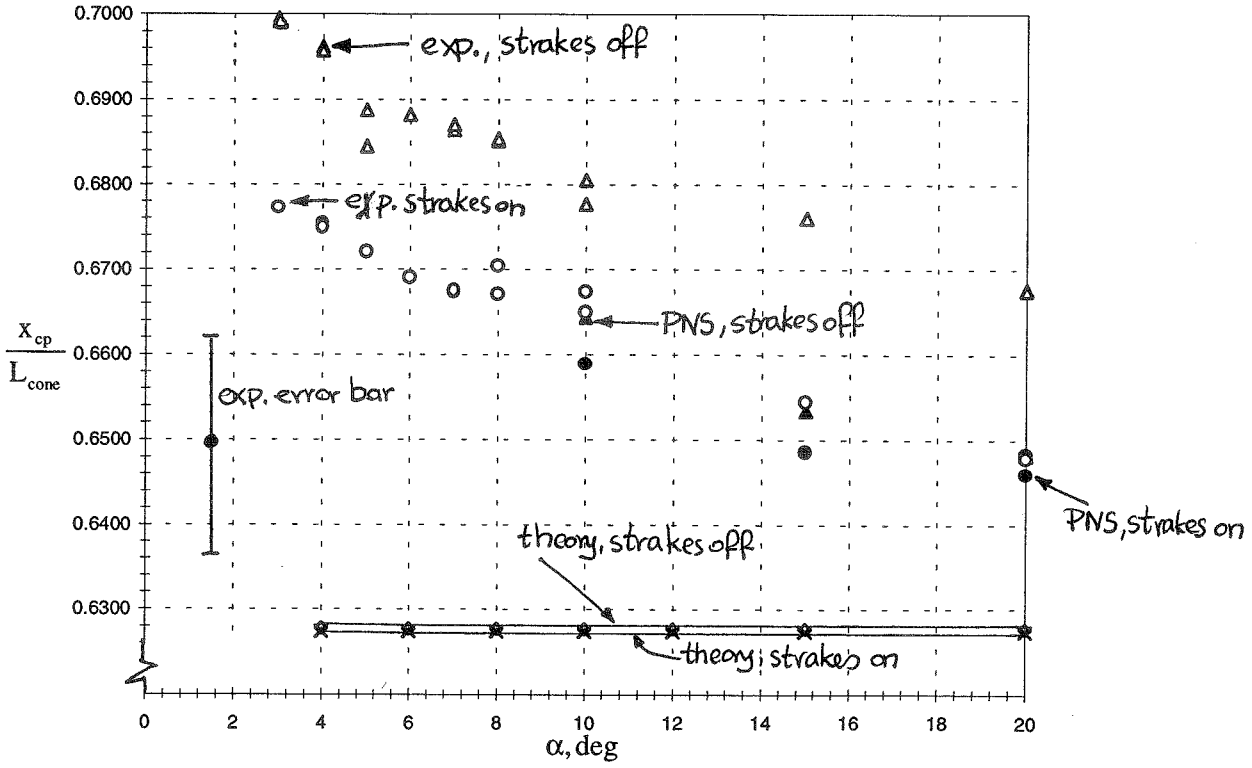

Fig. 4.29 Continue

e)

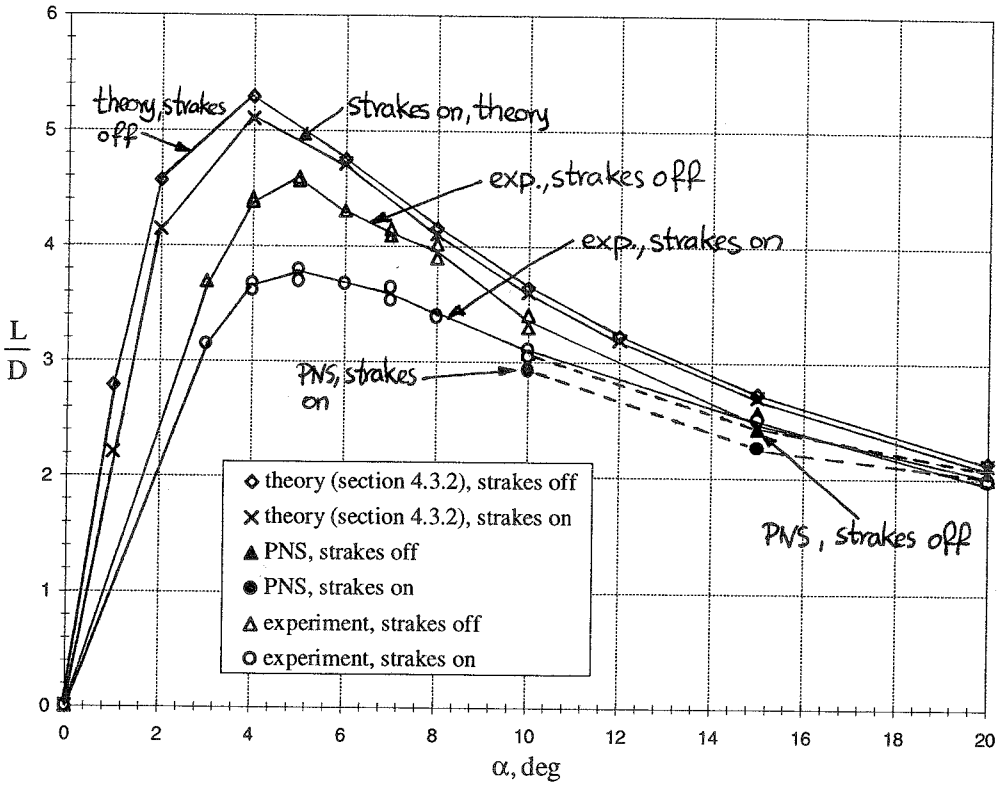

Fig. 4.29 Concluded

a)

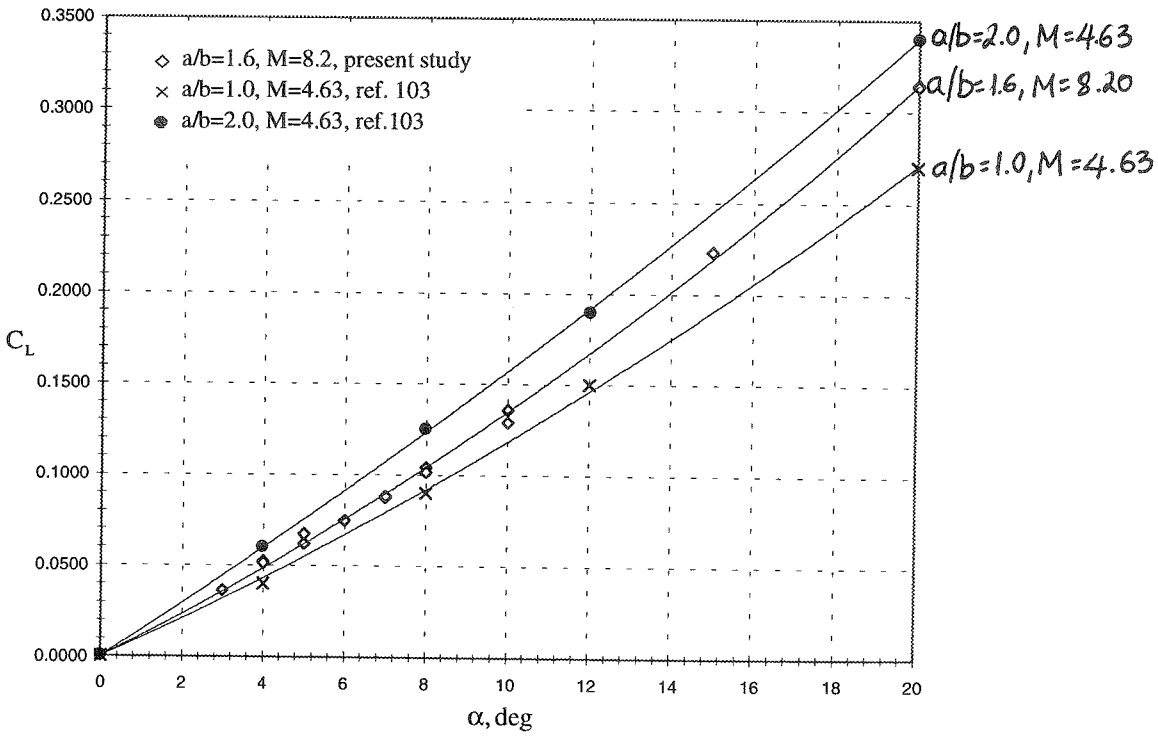

Fig. 4.30 Comparison of present force data (strakes off) with other experimental results (of ref. 103)

b)

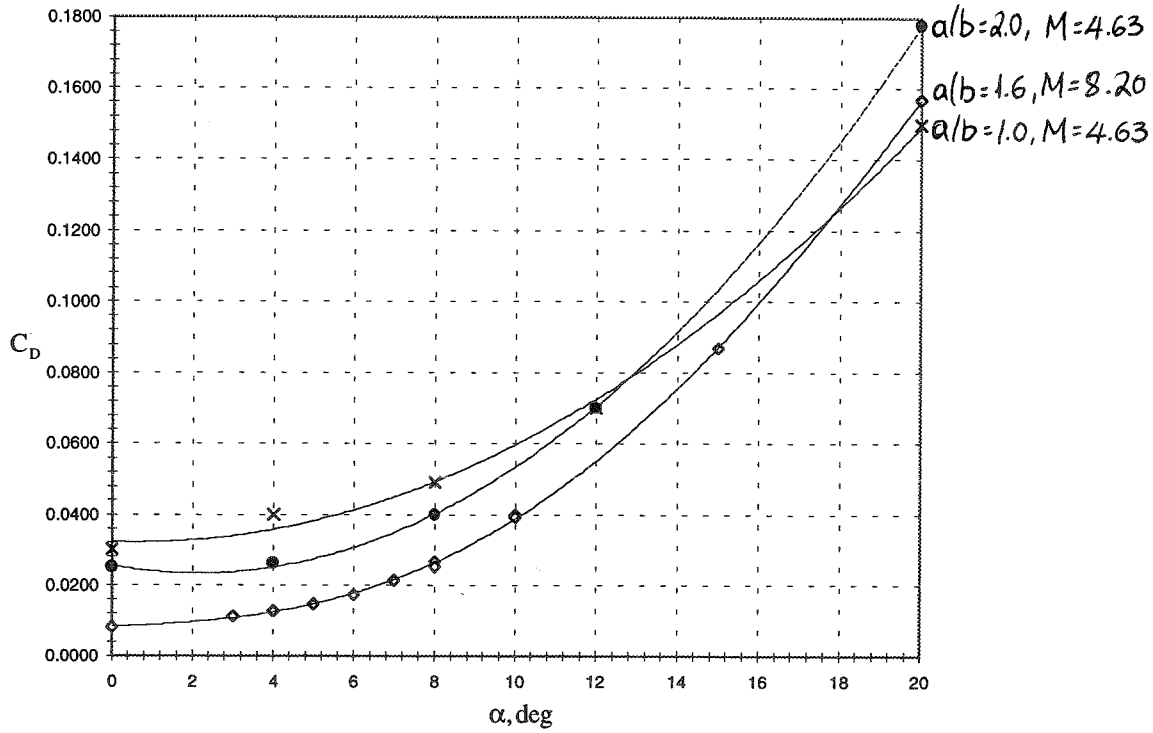

c)

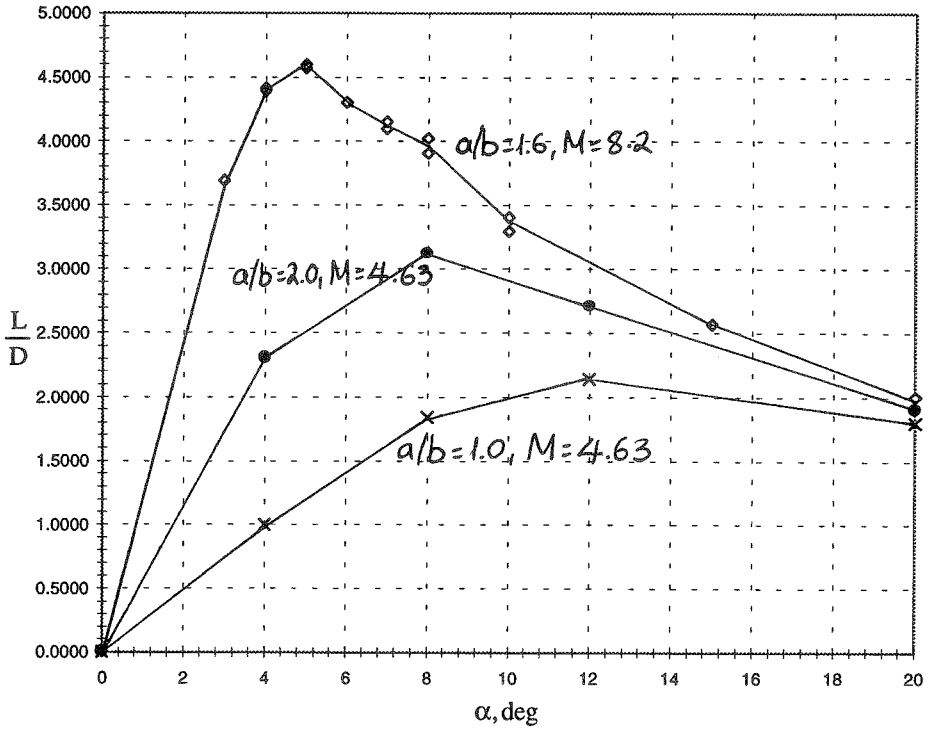

Fig. 4.30 Concluded

a)

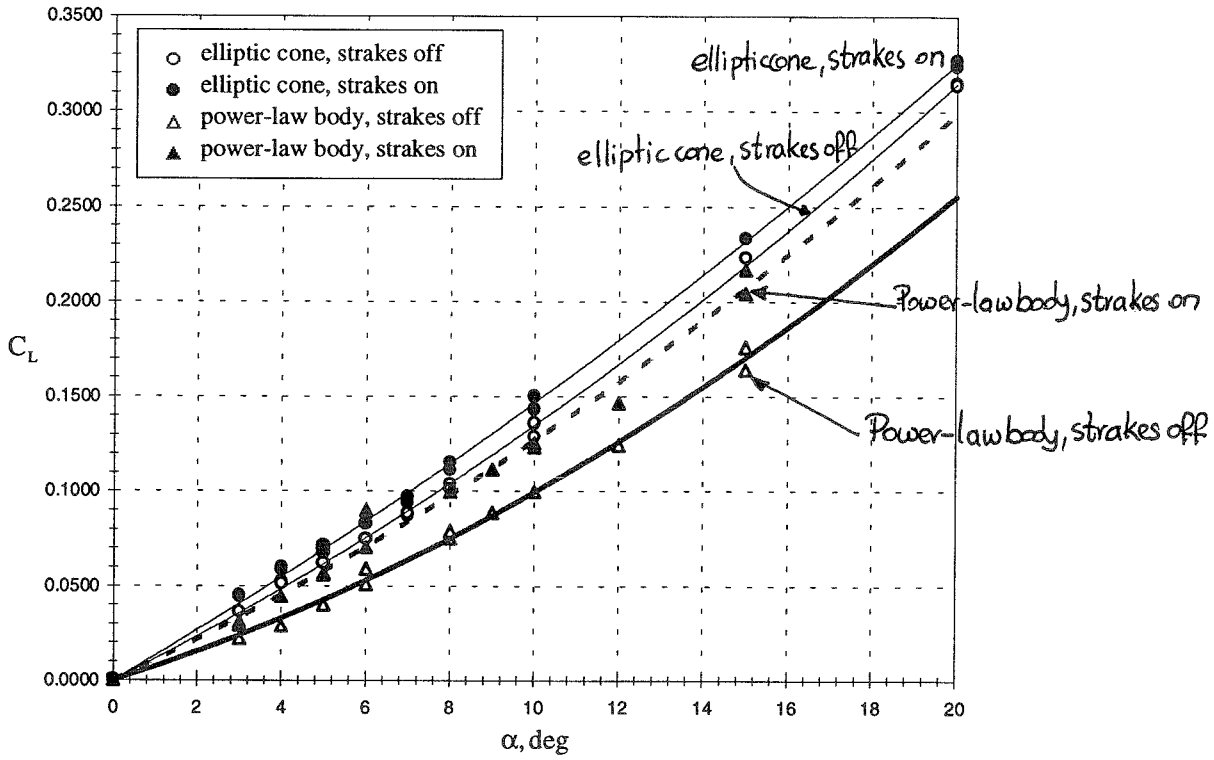

b)

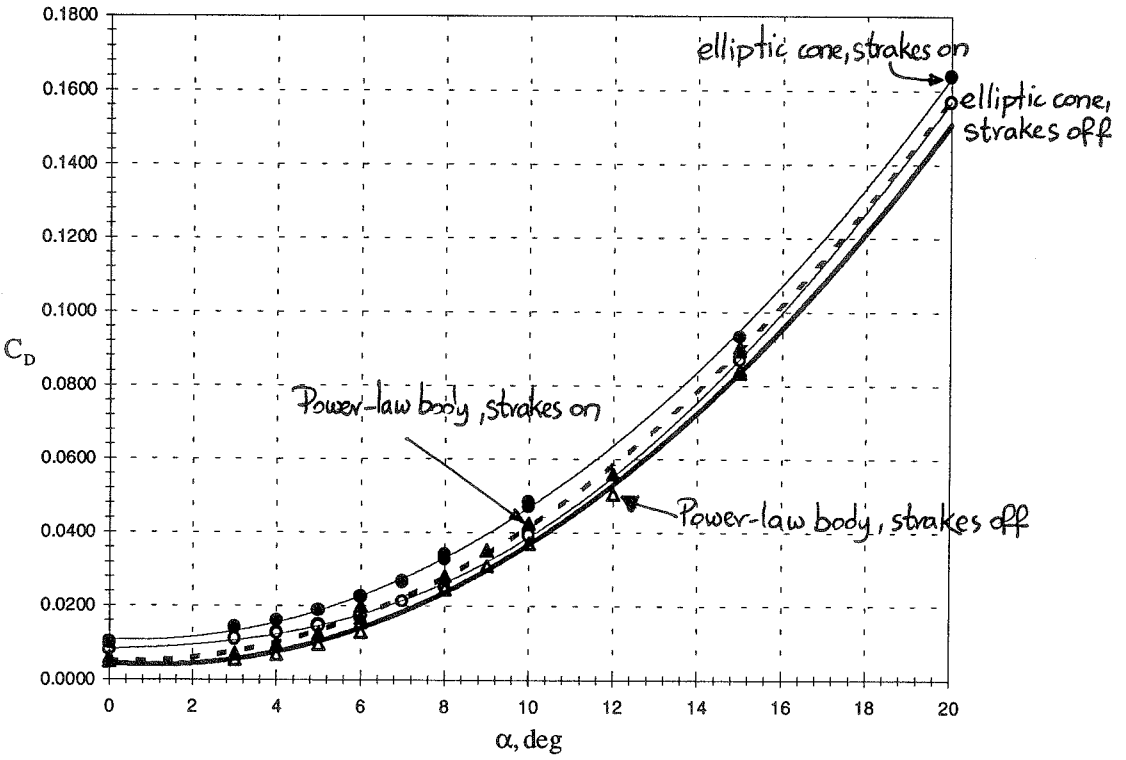

Fig. 4.31 Comparison of present aerodynamic characteristics with those of the power-law body (see section 4.2.1)

c)

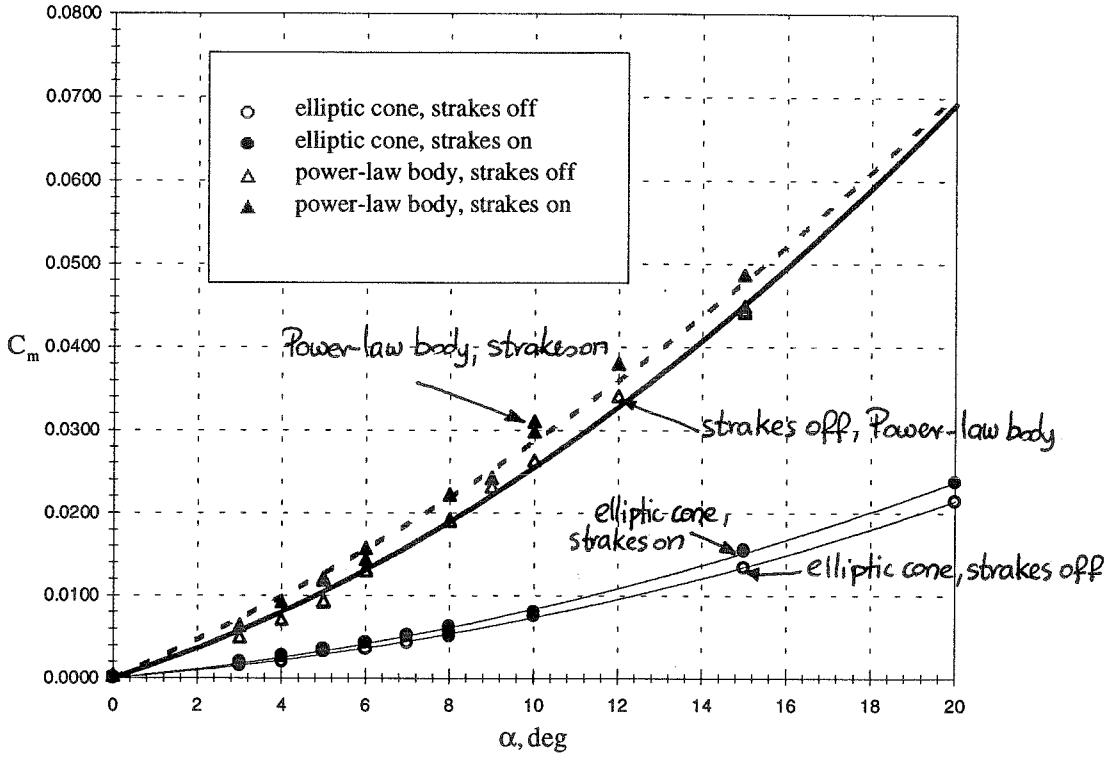

d)

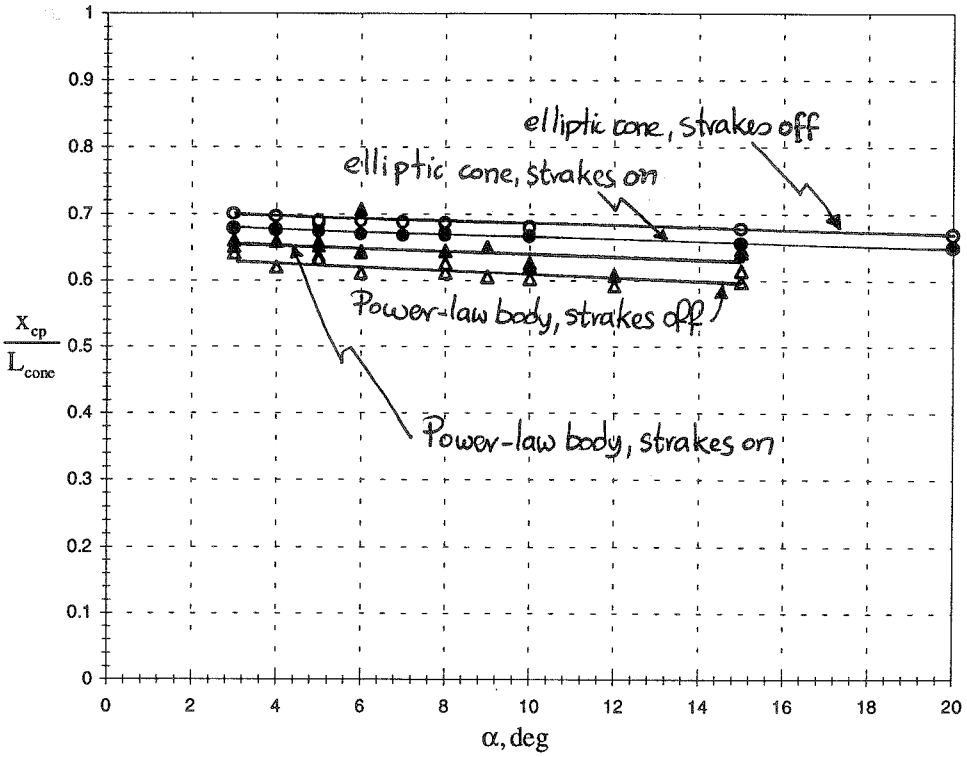

Fig. 4.31 Continue

e)

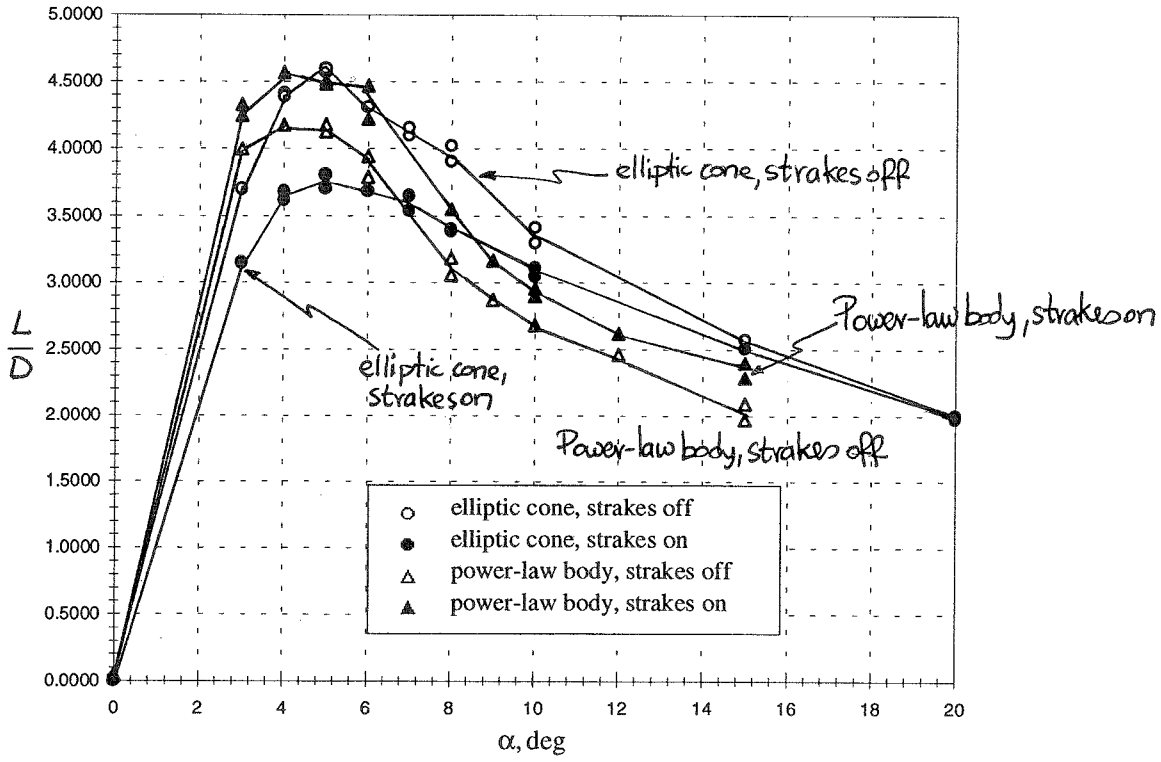

Fig. 4.31 Concluded

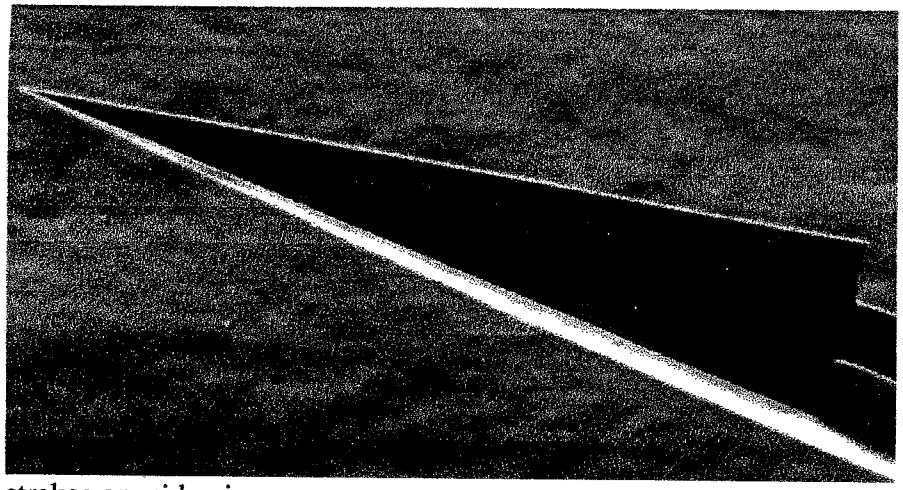

strakes on, side view

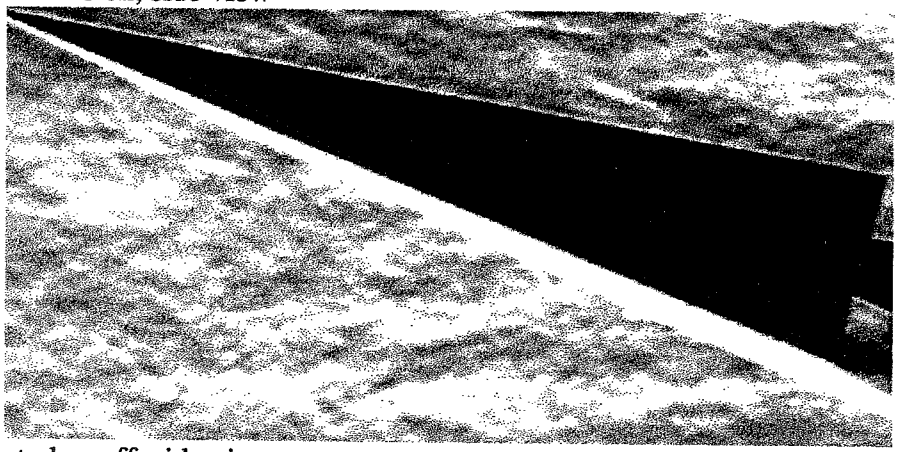

strakes off, side view

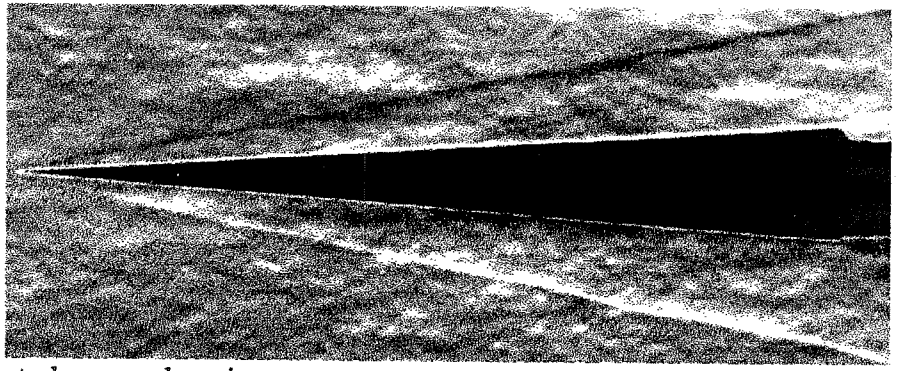

strakes on, plan view

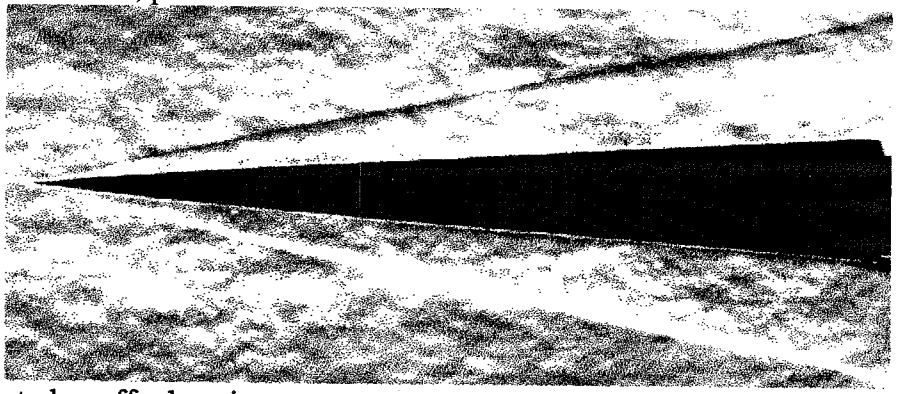

strakes off, plan view

Fig. 4.32 Comparison of the schlieren pictures (strakes on and off) of configuration 5 at α=15°

windward side

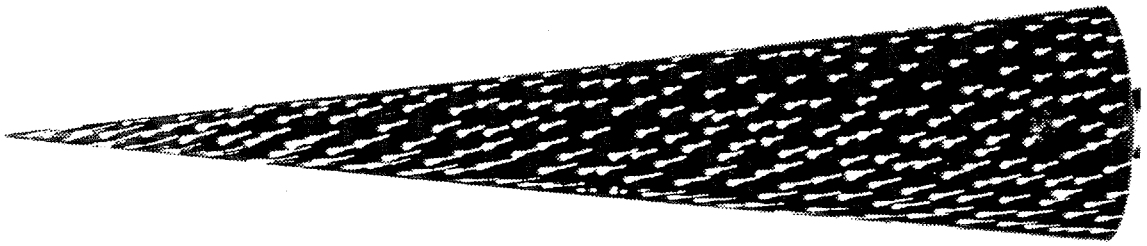

left side

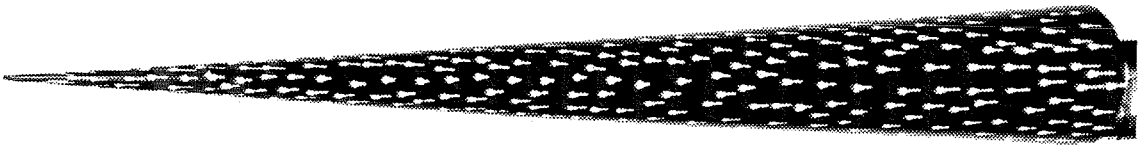

leeward side
a) strakes off, $\alpha=5^{o}$

windward side

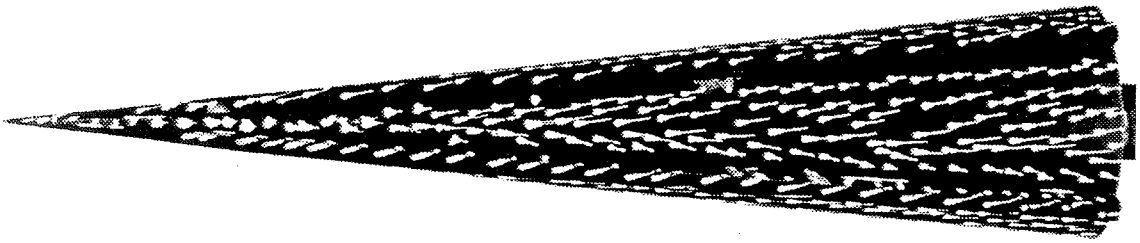

left side

leeward side
a) strakes on, $\alpha=5^{o}$

Fig. 4.33 Oil-dot pictures of configuration 5 (strakes off and on)

windward side

left side

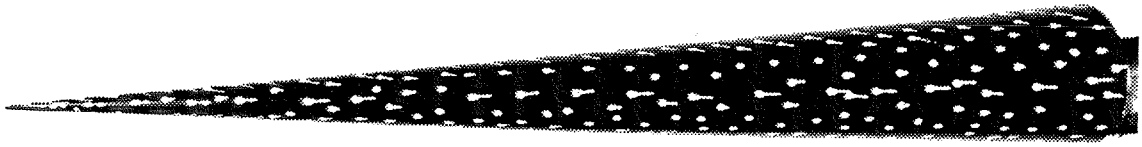

leeward side

b) strakes off, $\alpha=10^{\circ}$

windward side

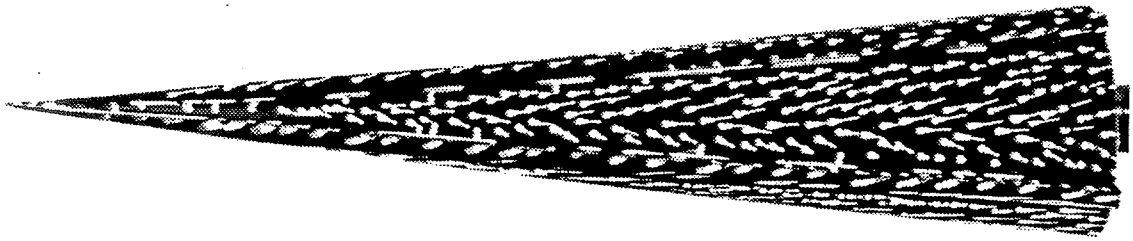

left side

leeward side

b) strakes on, $\alpha=10^{\circ}$

Fig. 4.33 Continue

windward side

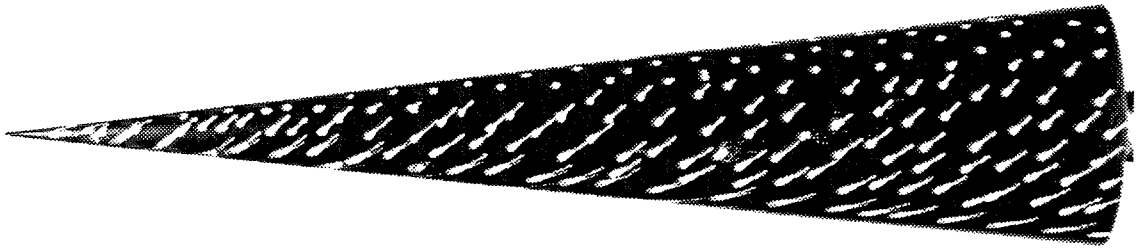

left side

leeward side
c) strakes off, α=15°

windward side

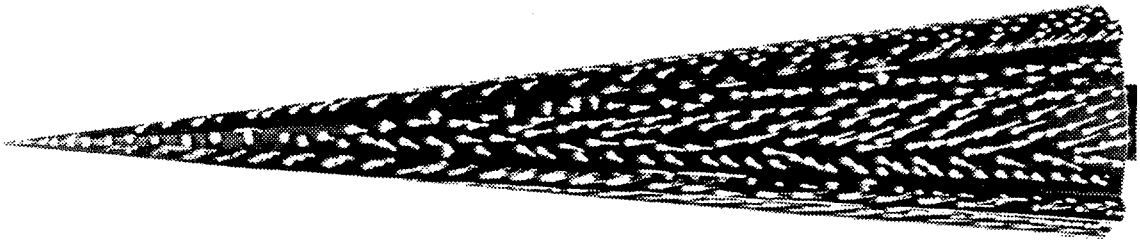

left side

leeward side
c) strakes on, α=15°

Fig. 4.33 Continue

windward side

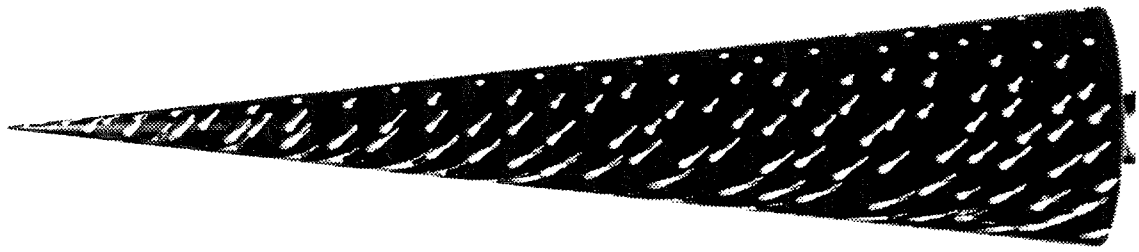

left side

leeward side

d) strakes off, α=20°

windward side

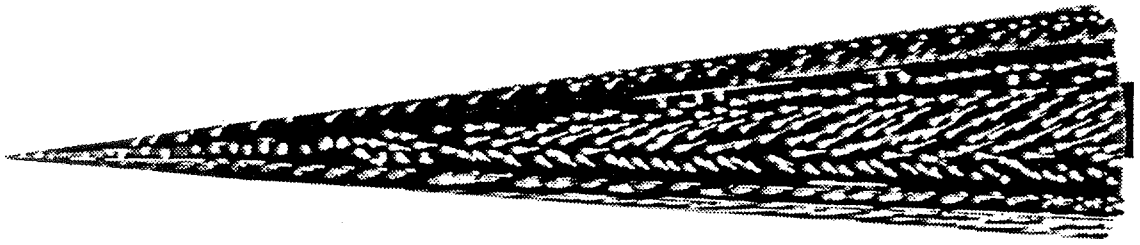

left side

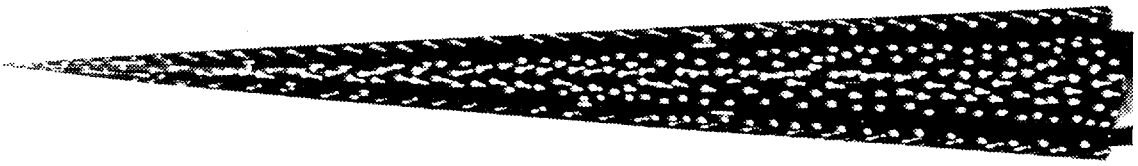

leeward side

d) strakes on, α=20°

Fig. 4.33 Concluded

a) α=0°

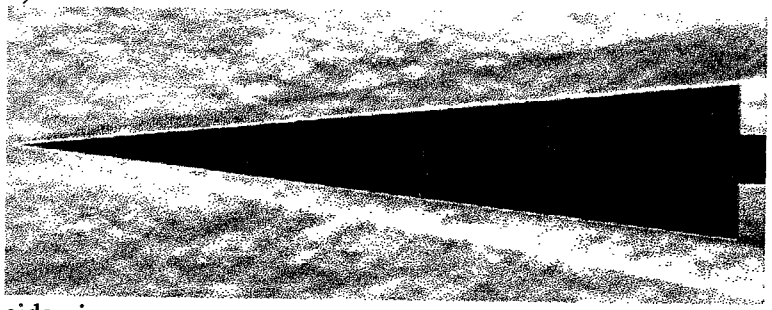

side view

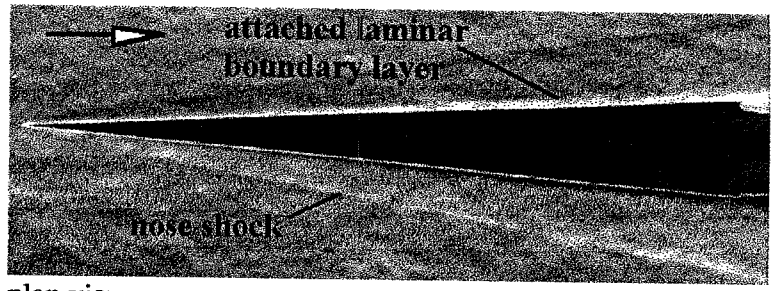

plan view

b) α=3°

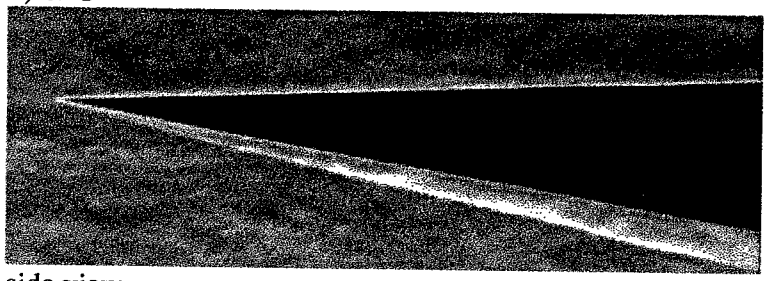

side view

c) α=5°

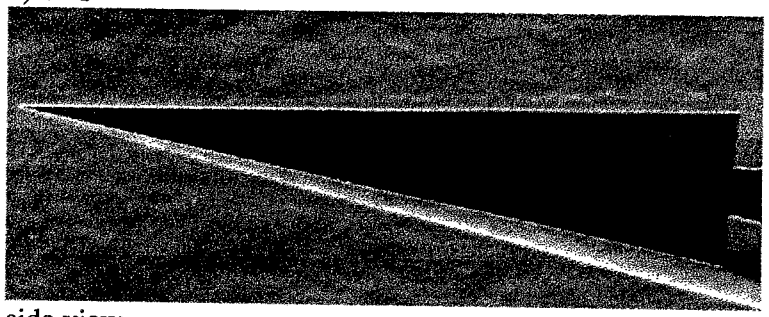

side view

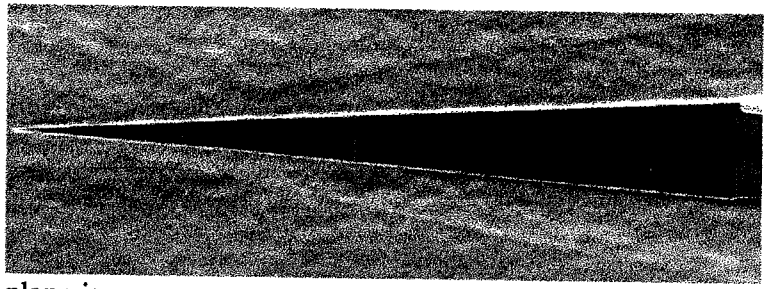

plan view

Fig. 4.34 Schlieren photographs of configuration 5 (strakes on)

d) α=7°

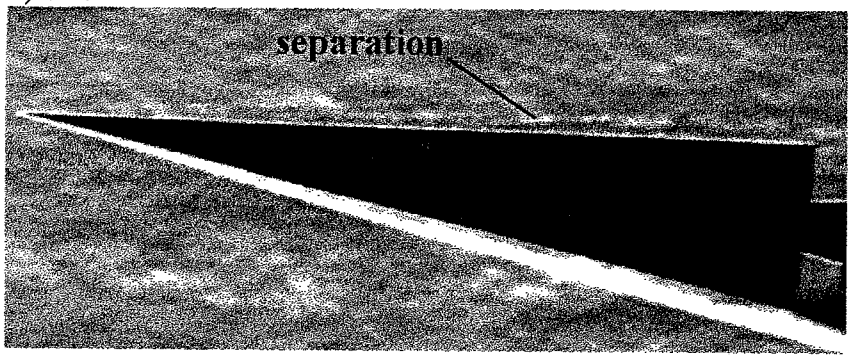

e) α=10°

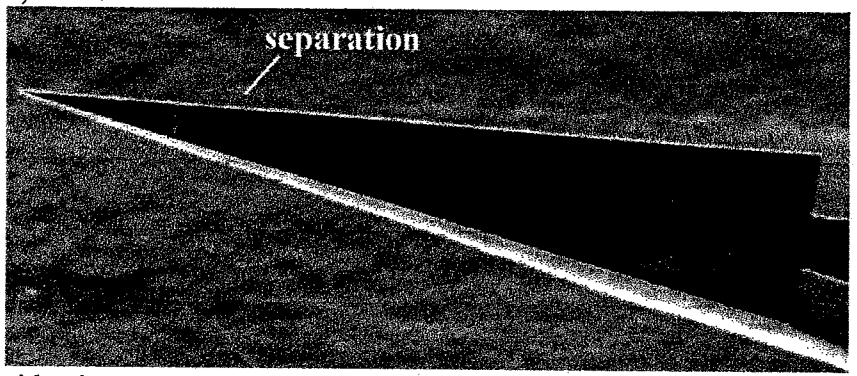

side view

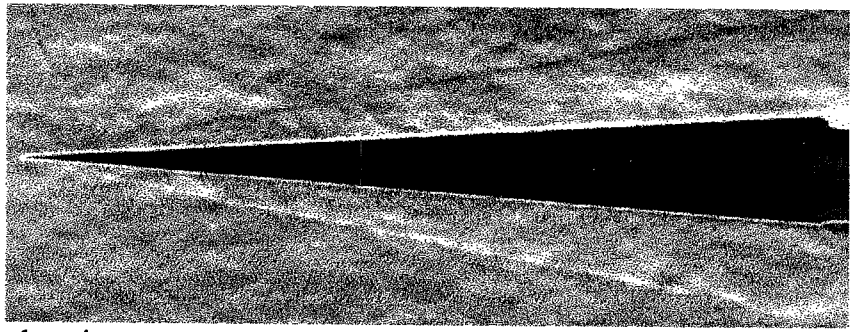

plan view

Fig. 4.34 Continue

f) α=15°

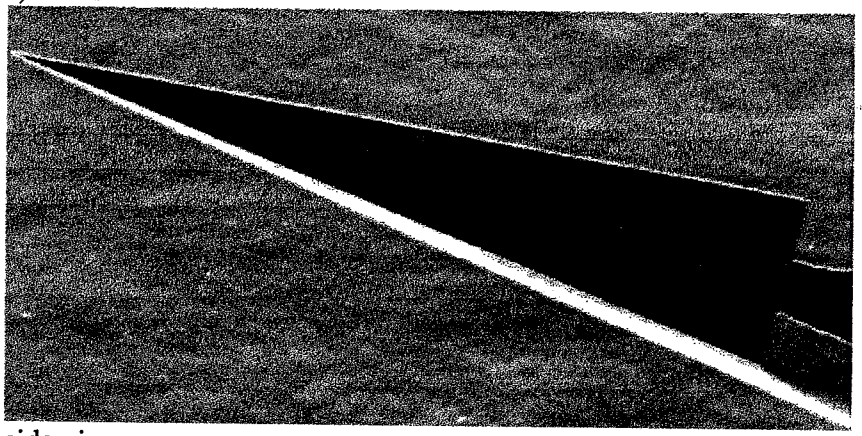

side view

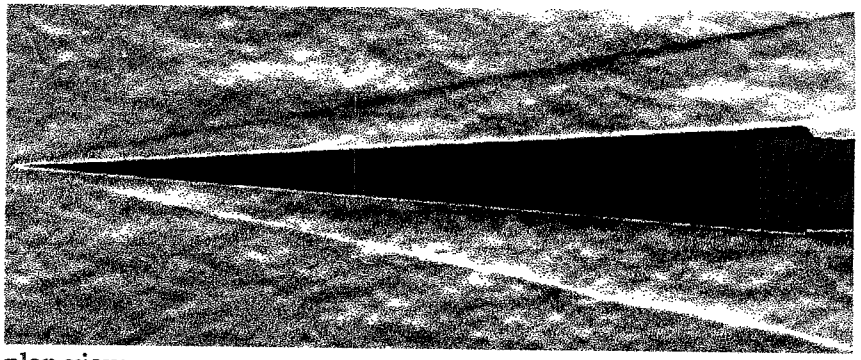

plan view

g) α=20°

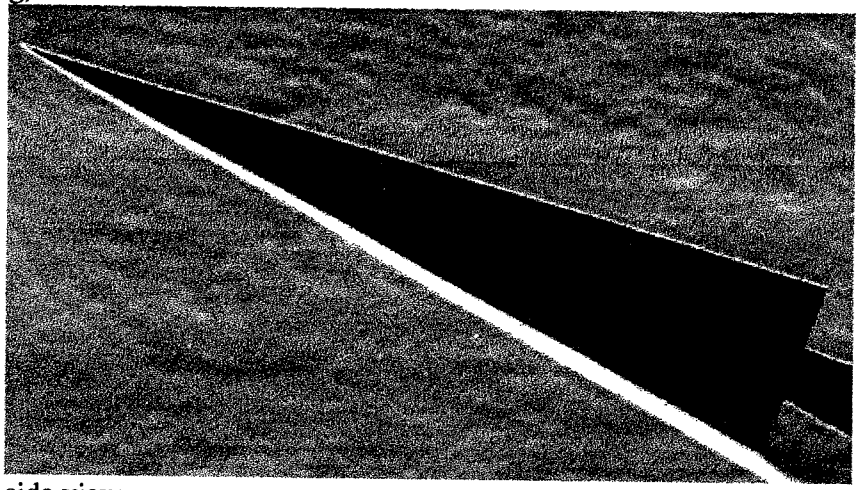

side view

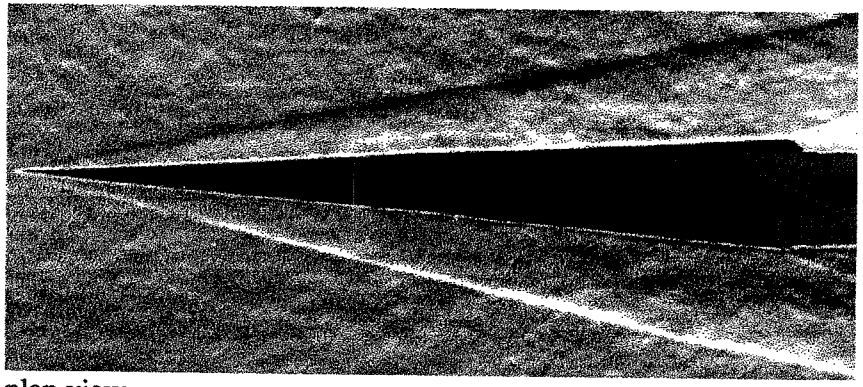

plan view

Fig. 4.34 Concluded

a) without strakes

I	**-attachment**
J	**-primary separation**
K	**-reattachment**
L	**-"near-wake" stagnation point**

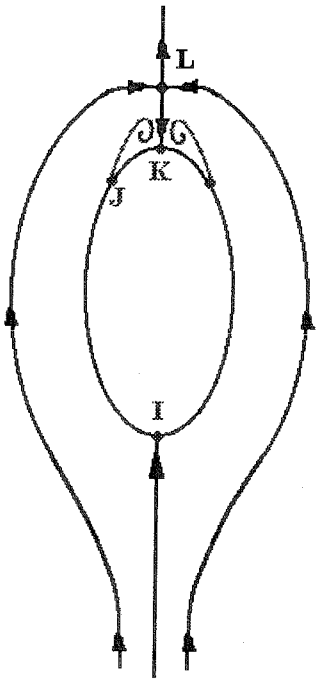

b) with strakes

A	**-attachment**
B, D, F	**-separation**
C, E, G	**-reattachment**
H	**-"near-wake" stagnation point**

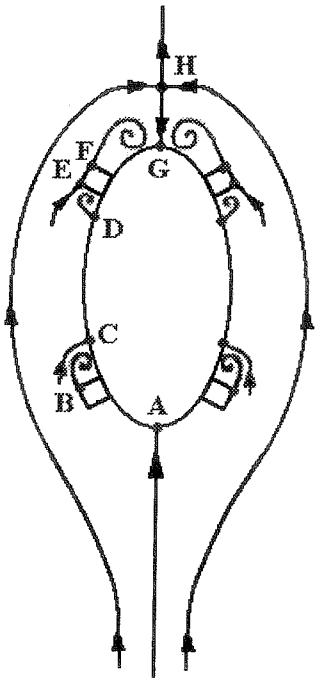

Fig. 4.35 Proposed flow field for configuration 5 (strakes off and on)

a)

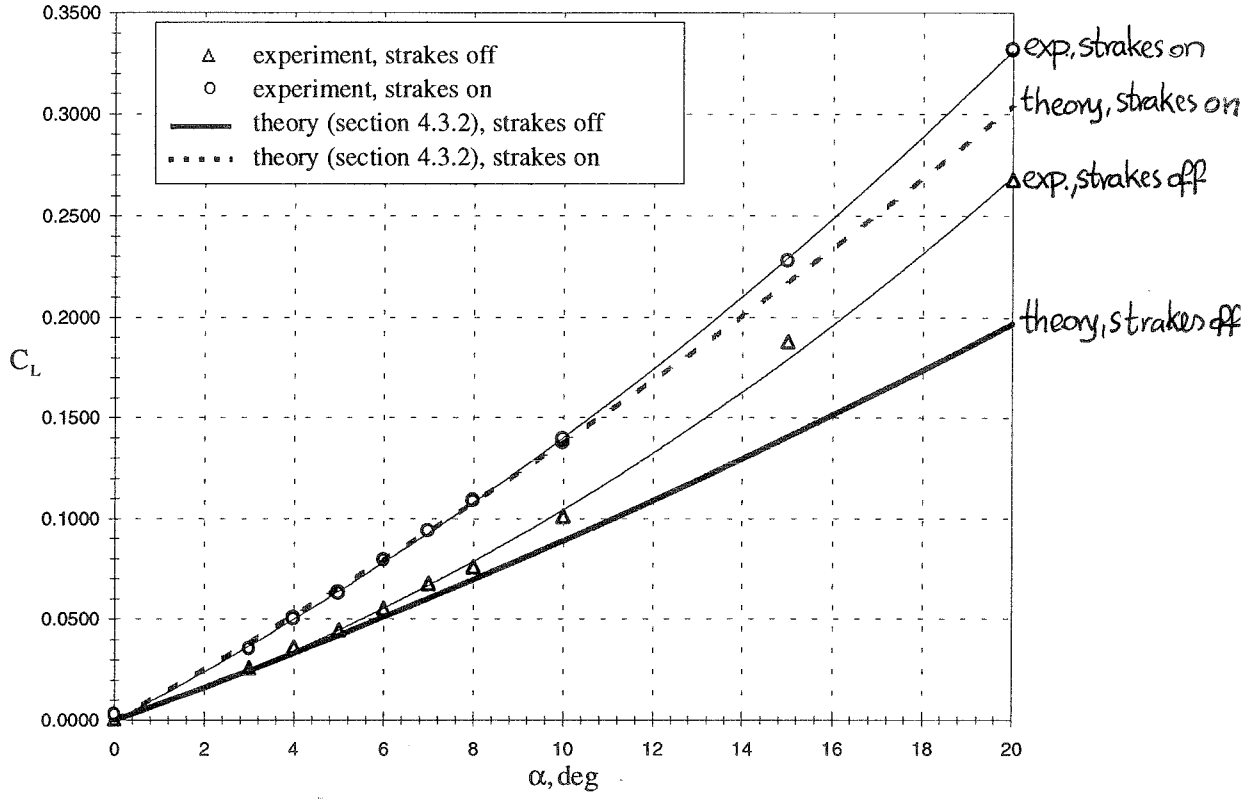

b)

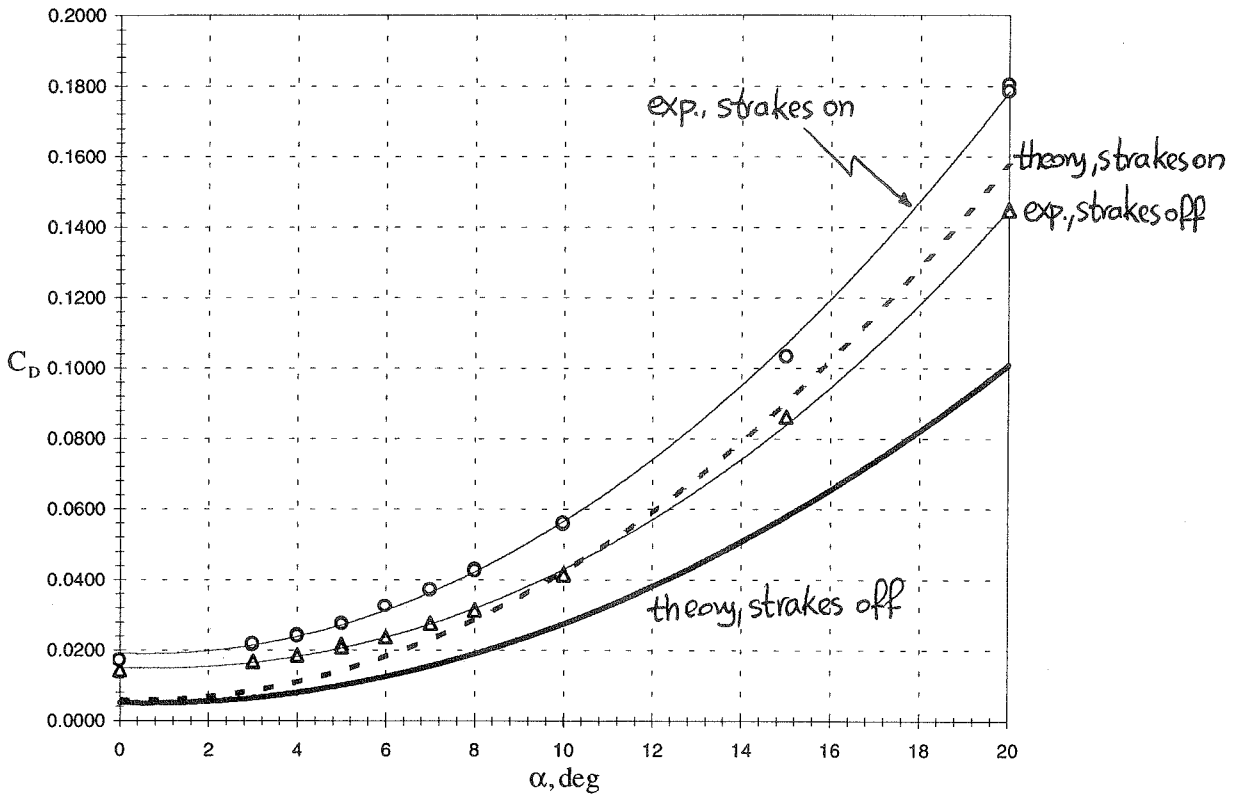

Fig. 4.36 Effect of strakes on the aerodynamic characteristics of configuration 5

c)

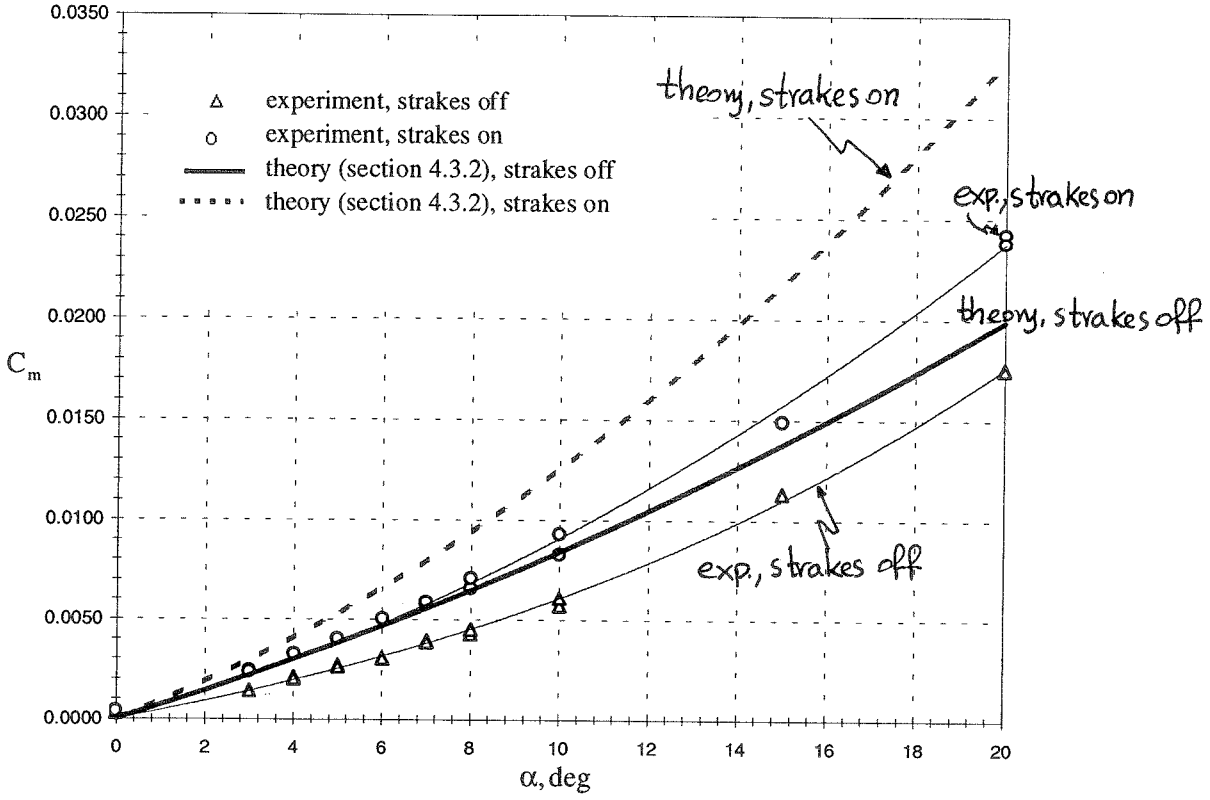

d)

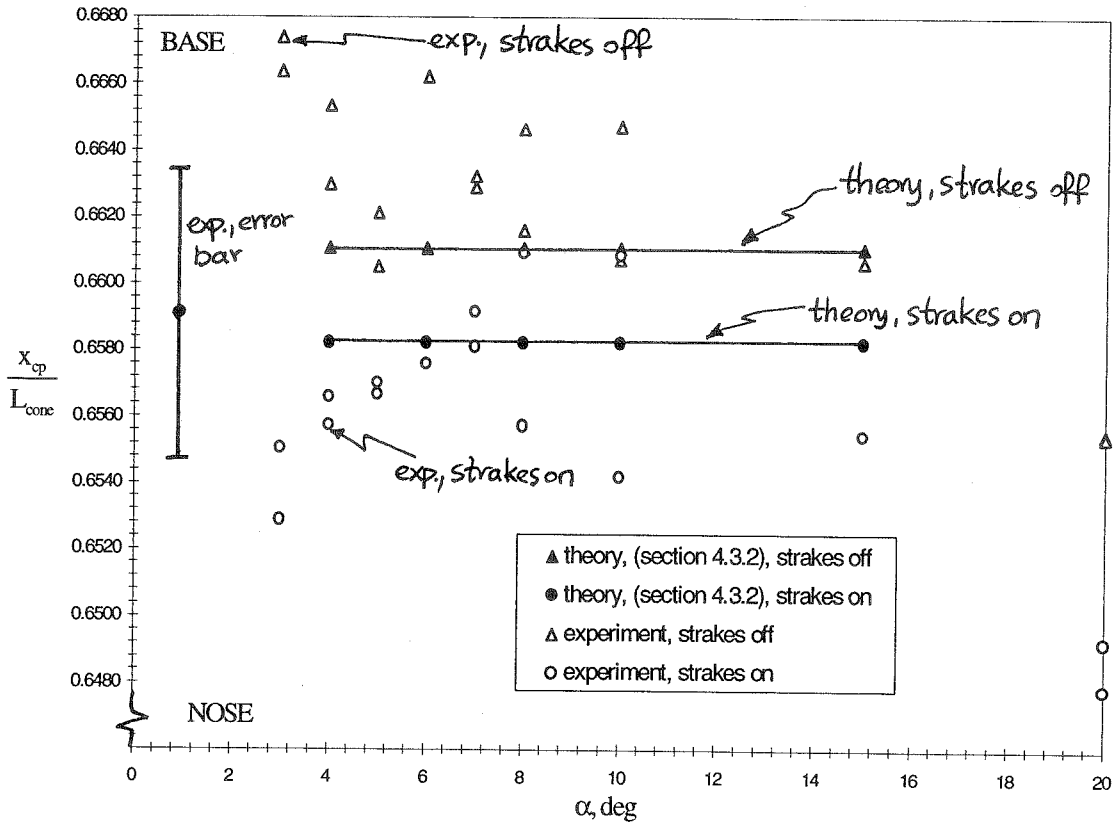

Fig. 4.36 Continue

e)

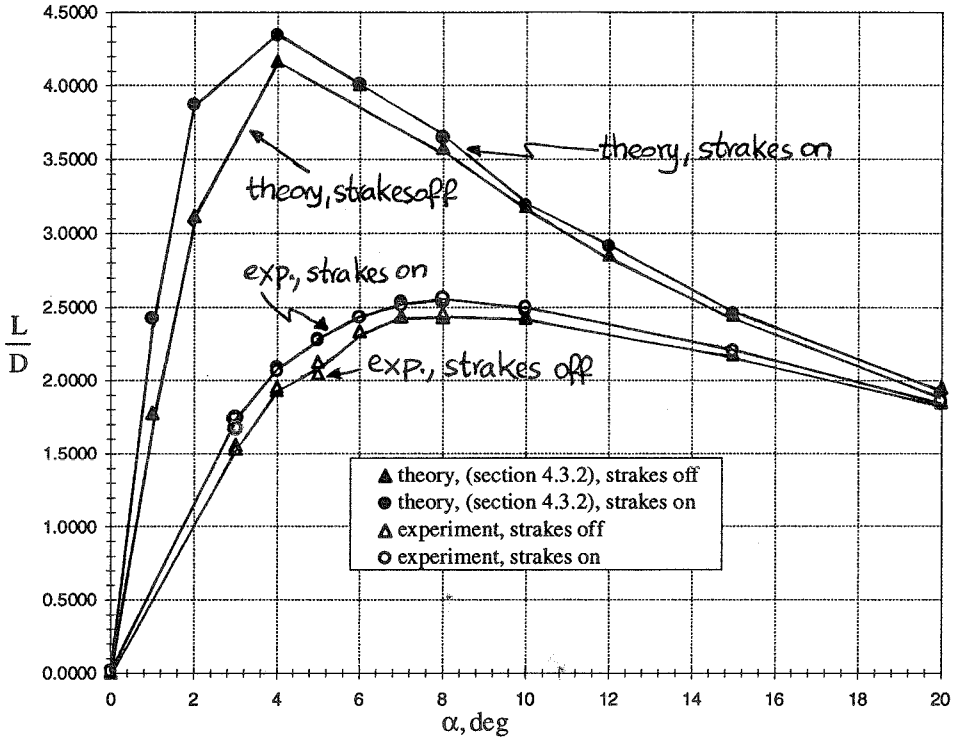

Fig. 4.36 Concluded

a)

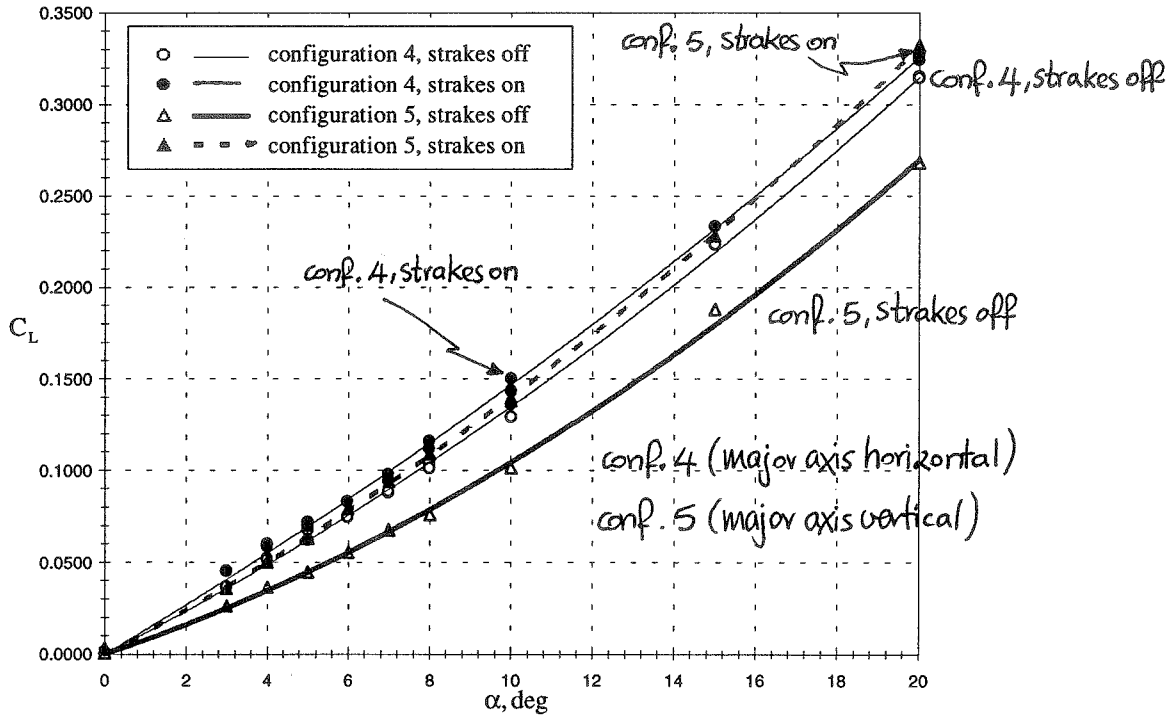

Fig. 4.37 Comparison of present measurements with those of configuration 4 (see section 4.3.3.4)

b)

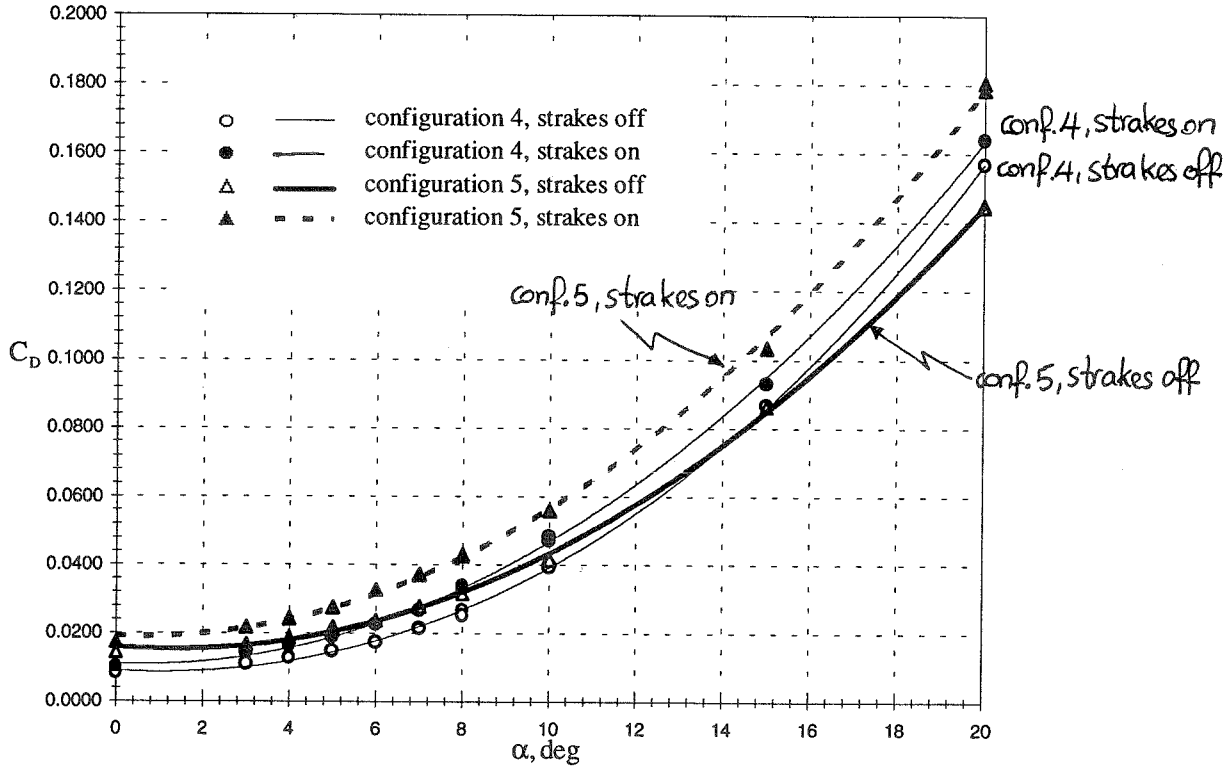

c)

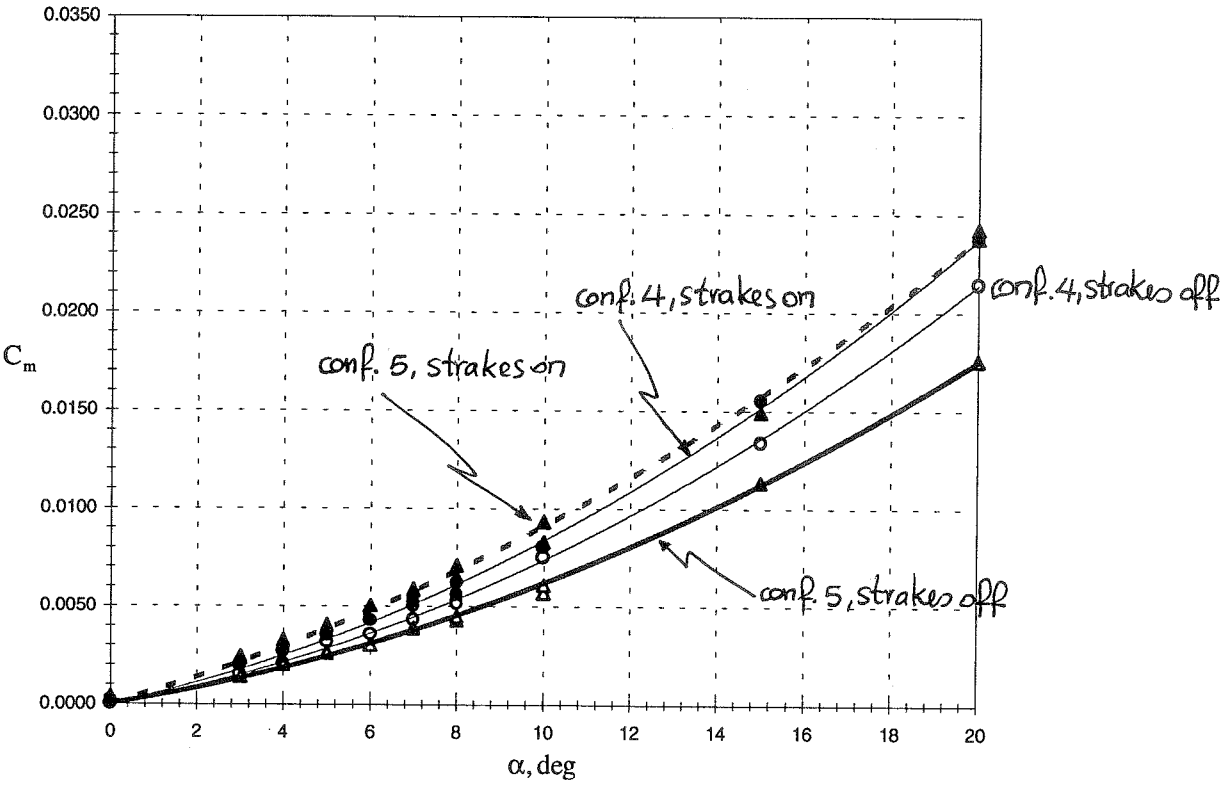

Fig. 4.37 Continue

d)

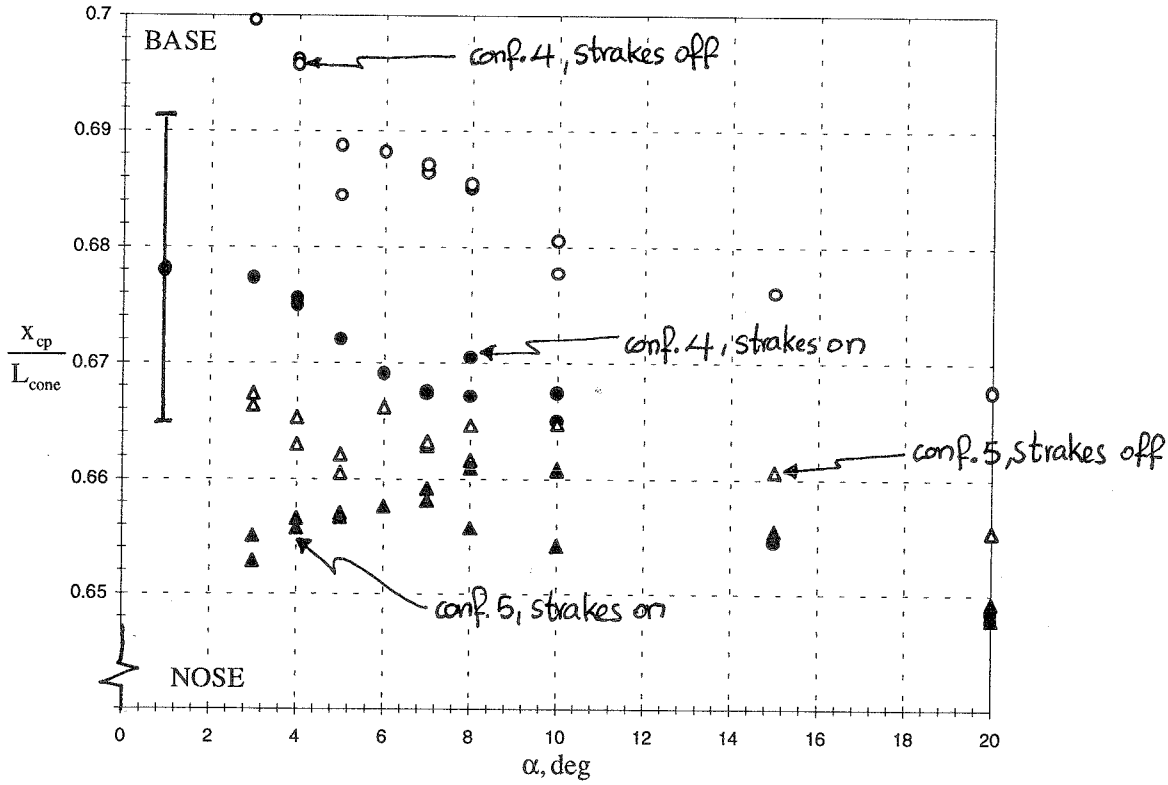

e)

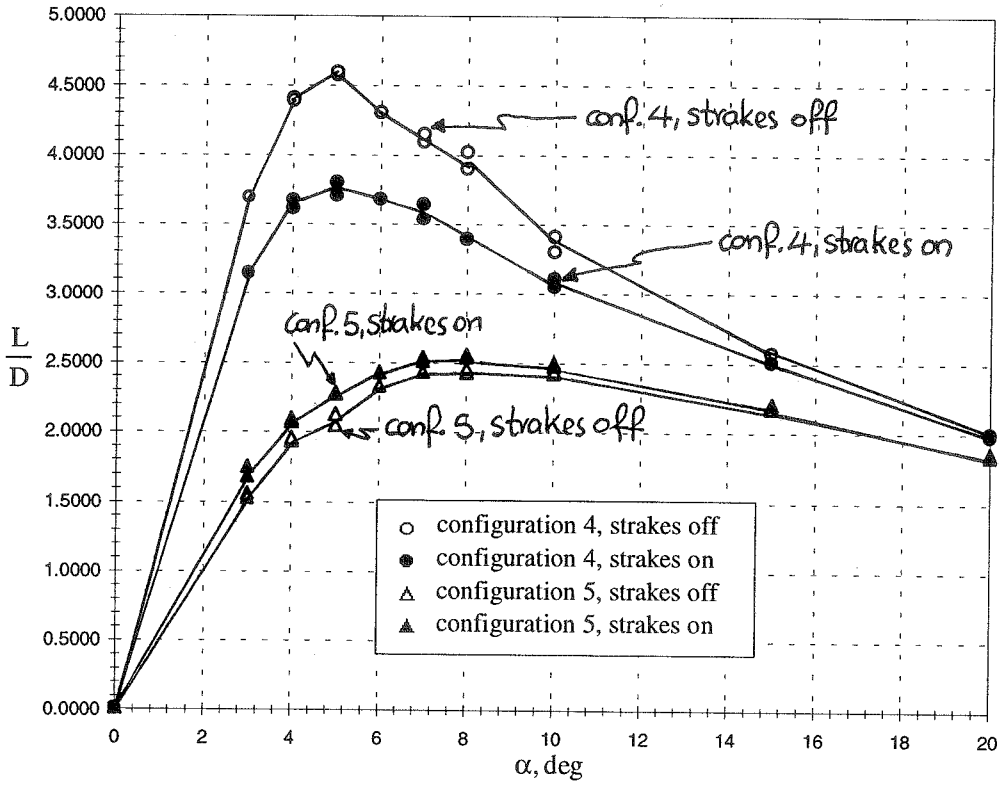

Fig. 4.37 Concluded

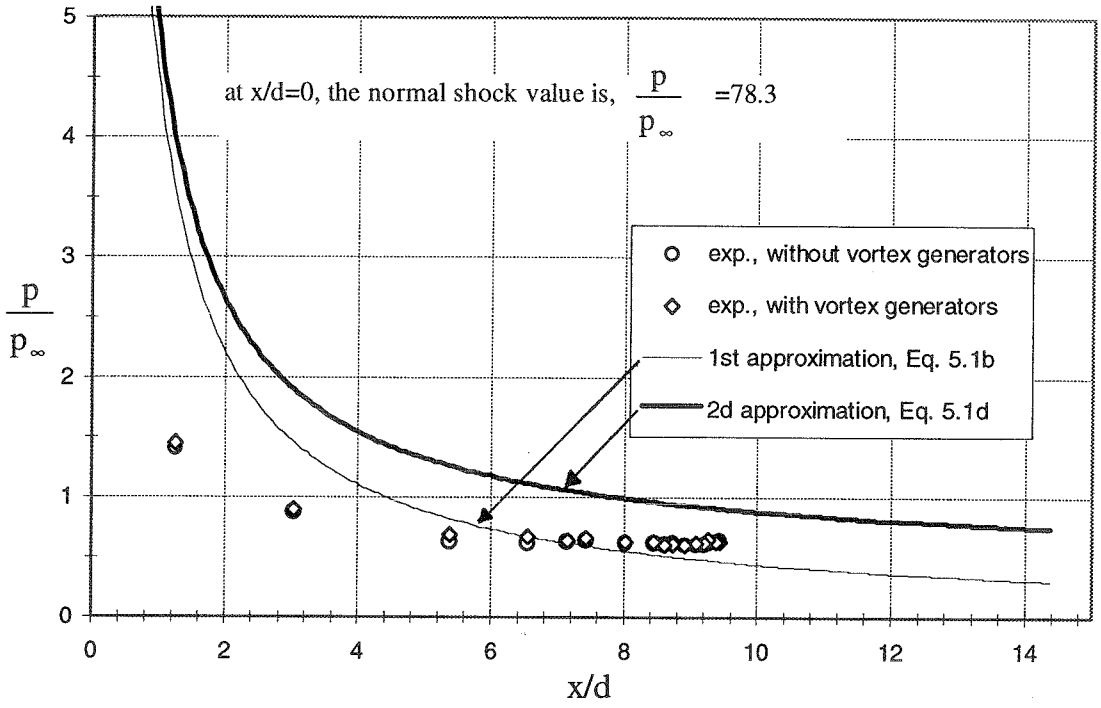

Fig. 5.1a Pressure distributions on the hemisphere cylinder (M_∞=8.2)

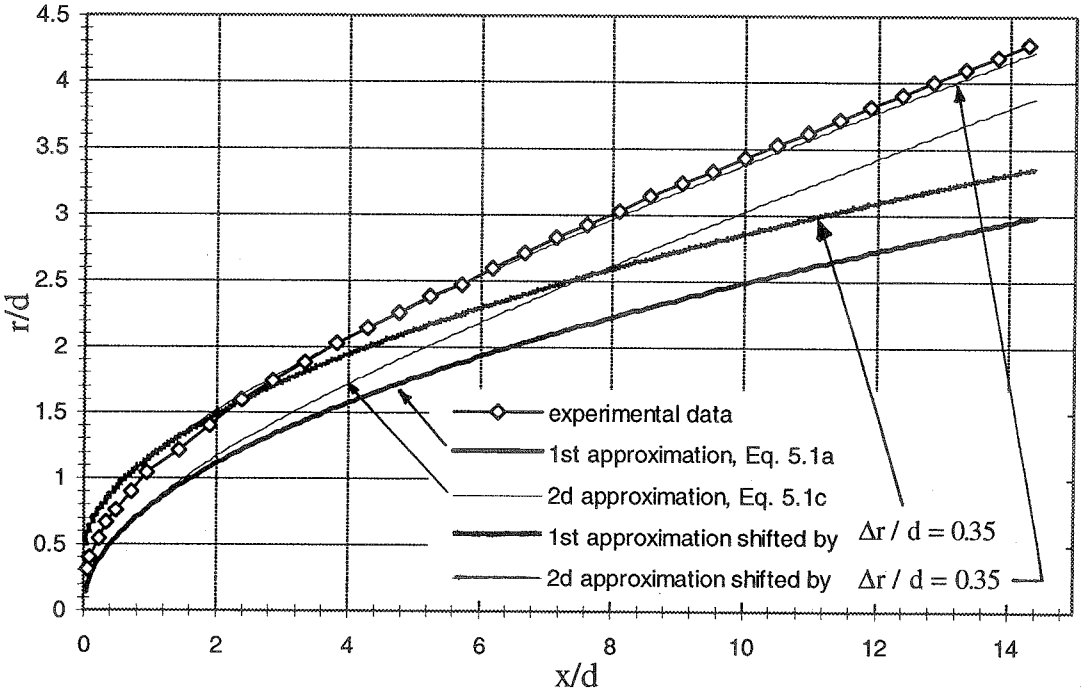

Fig. 5.1b Shock-wave shape around the hemisphere cylinder

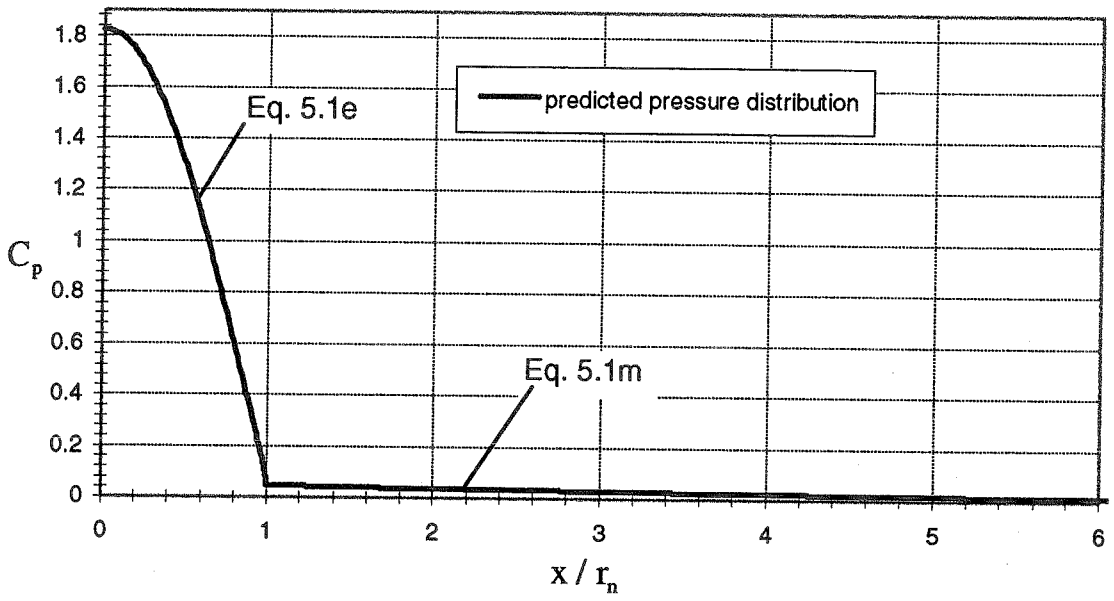

Fig. 5.2 Predicted pressure distribution along the hemisphere nose and cylinder body (M_∞=8.2, r_n= 8.5 mm)

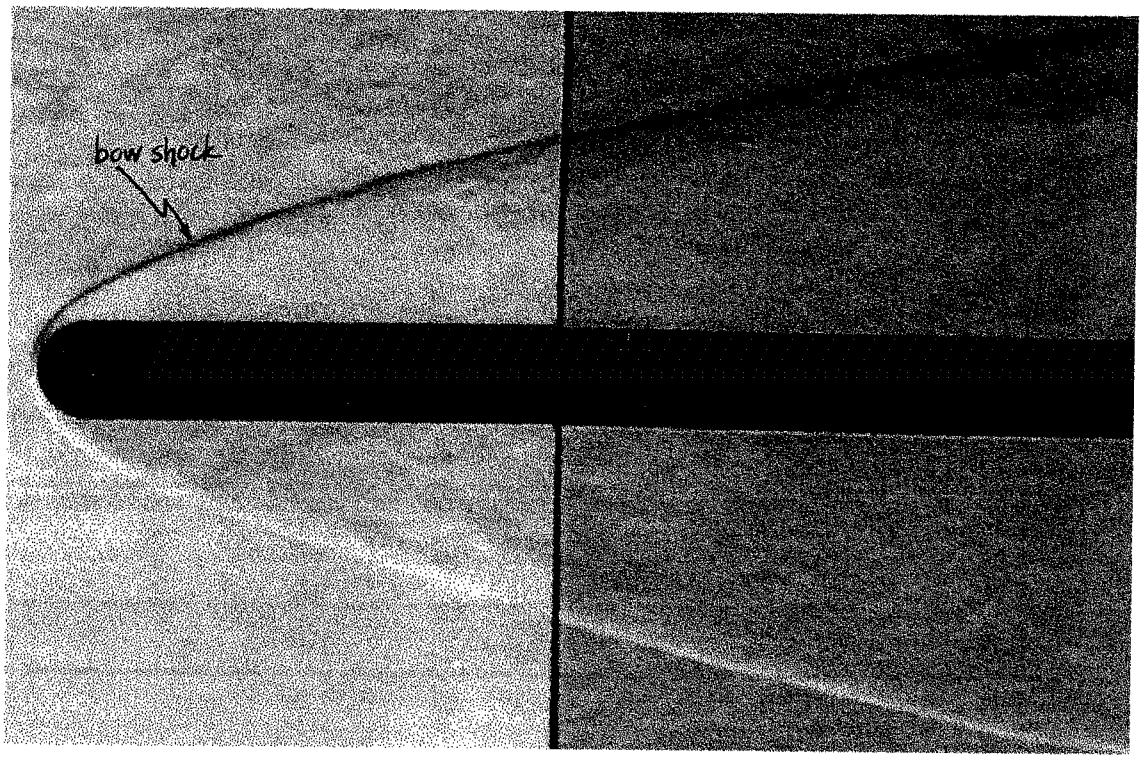

Fig. 5.3a Schlieren photo of the hemisphere cylinder (M_∞=8.2, Re_∞/cm=93000, laminar boundary layer)

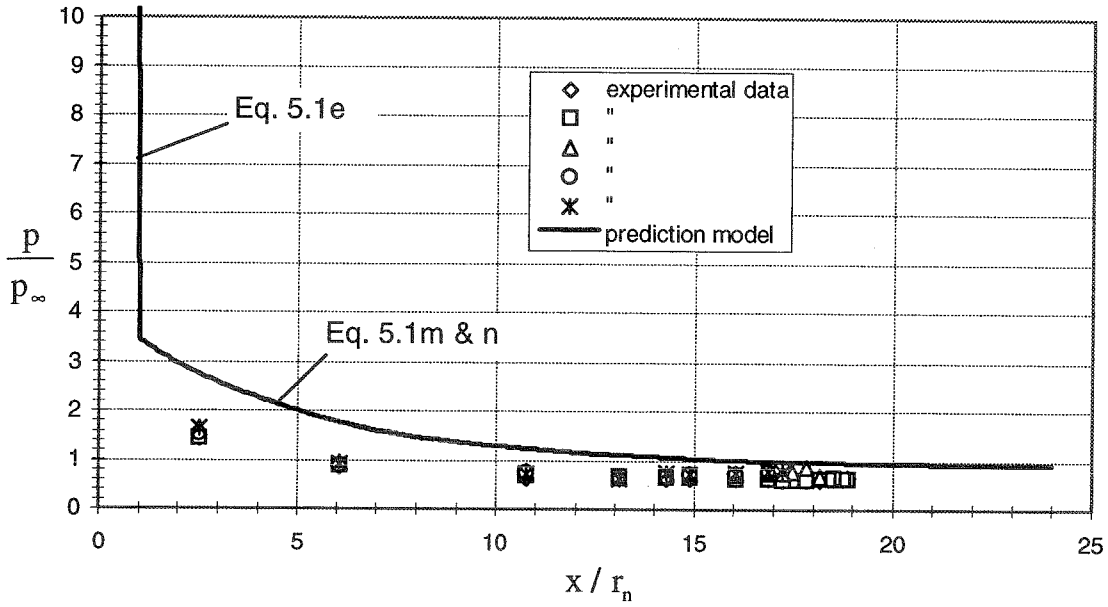

Fig. 5.3b Comparison of the experimental pressure distribution along the cylinder body with a prediction model (M_∞=8.2, r_n= 8.5 mm)

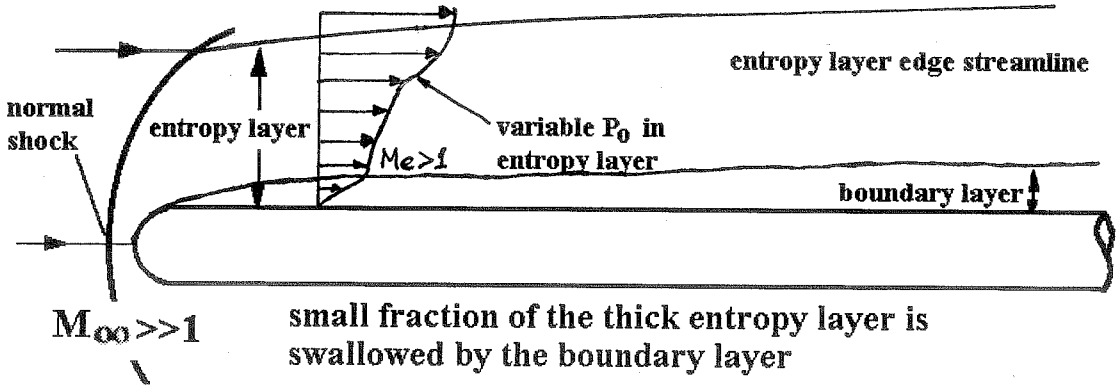

Fig. 5.4 Flow structure over a hemisphere cylinder

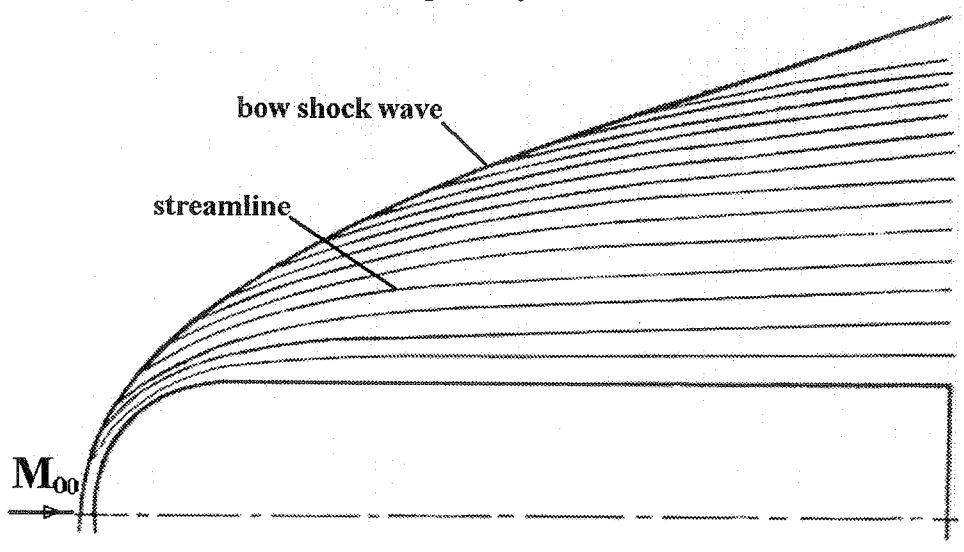

Fig. 5.5 Predicted streamline pattern around a hemisphere cylinder (ref. 189)

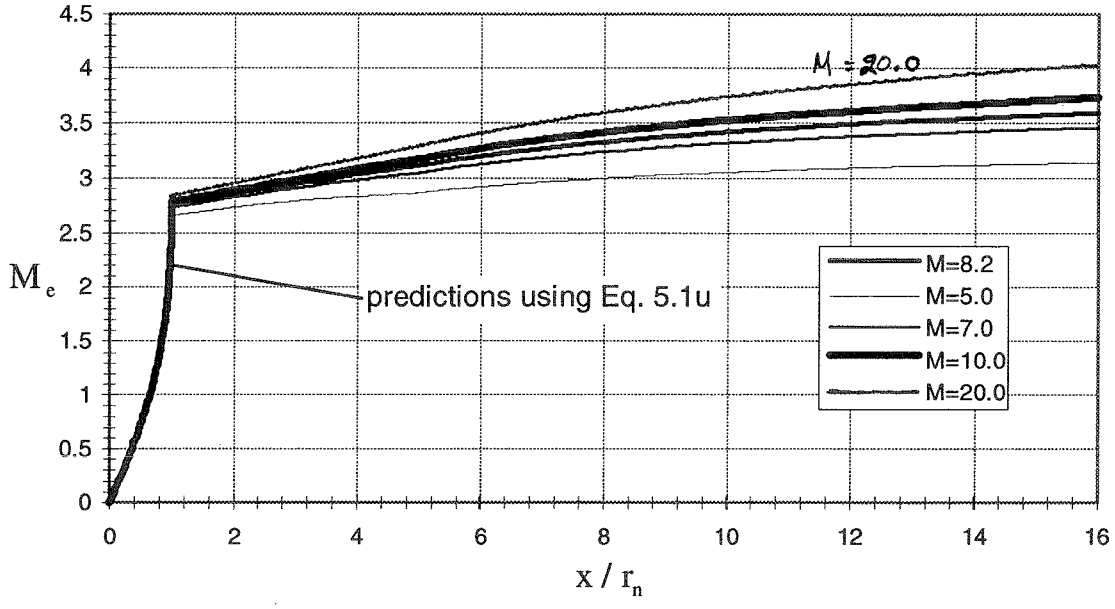

Fig. 5.6a Predicted local boundary layer edge Mach number distribution of the present hemisphere cylinder at various Mach numbers

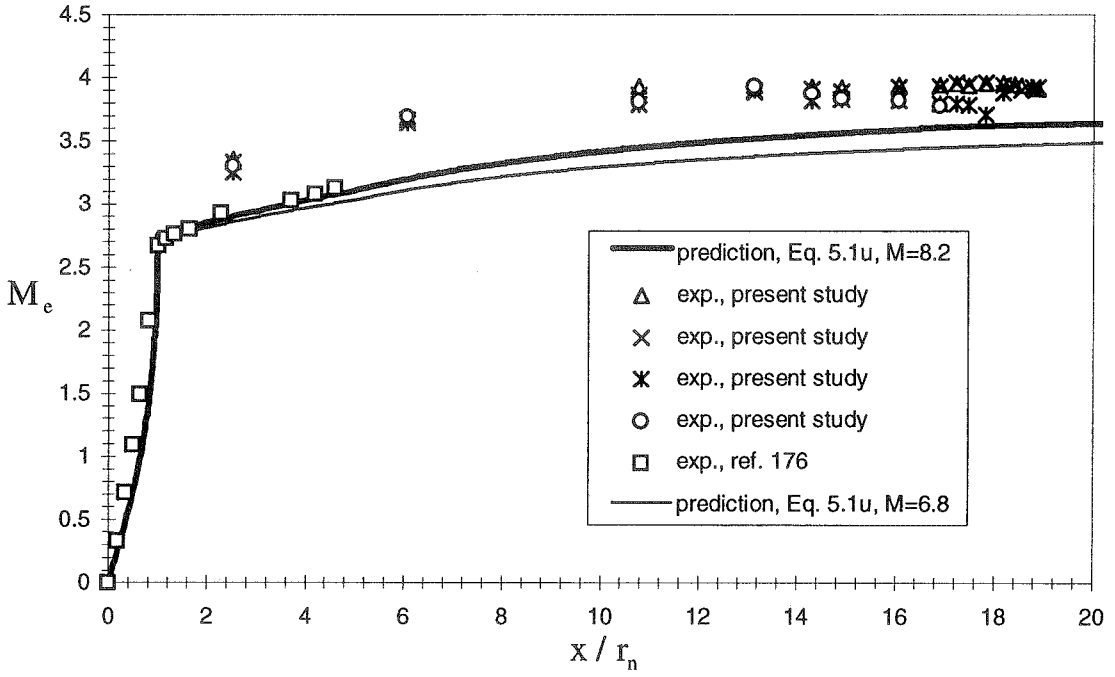

Fig. 5.6b Comparison of experimentally predicted local boundary layer edge Mach number distribution with theory

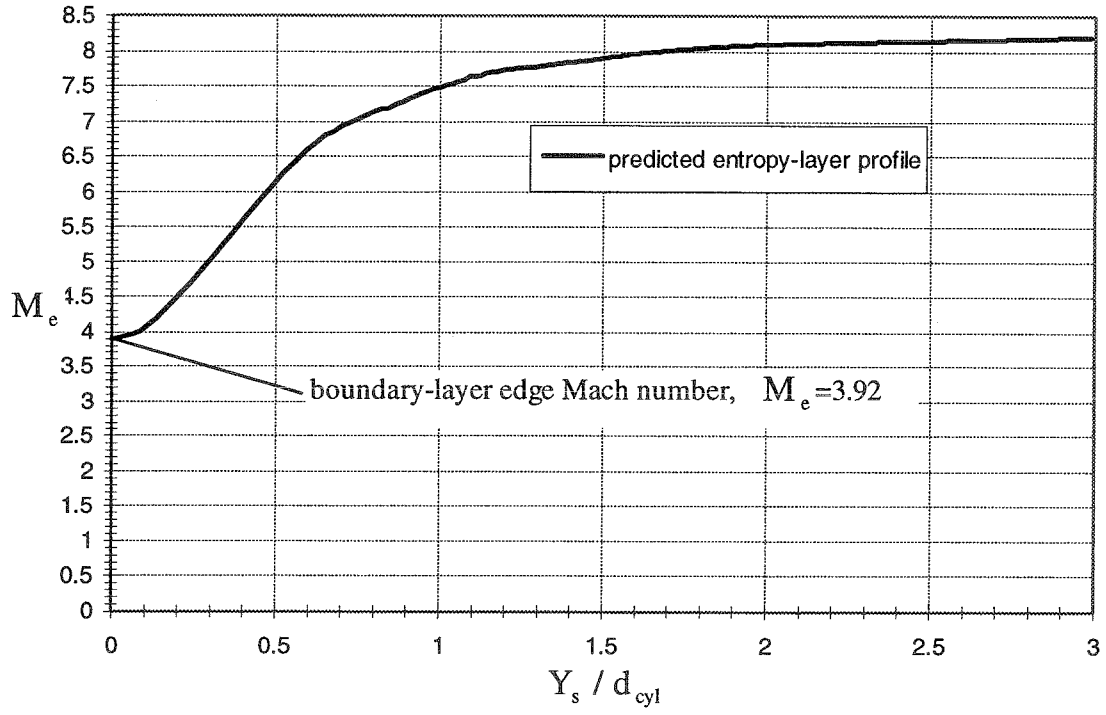

Fig. 5.7 Predicted entropy-layer Mach profile (M_∞=8.2, Re_∞/cm=93000, d_{cyl}=1.7 cm)

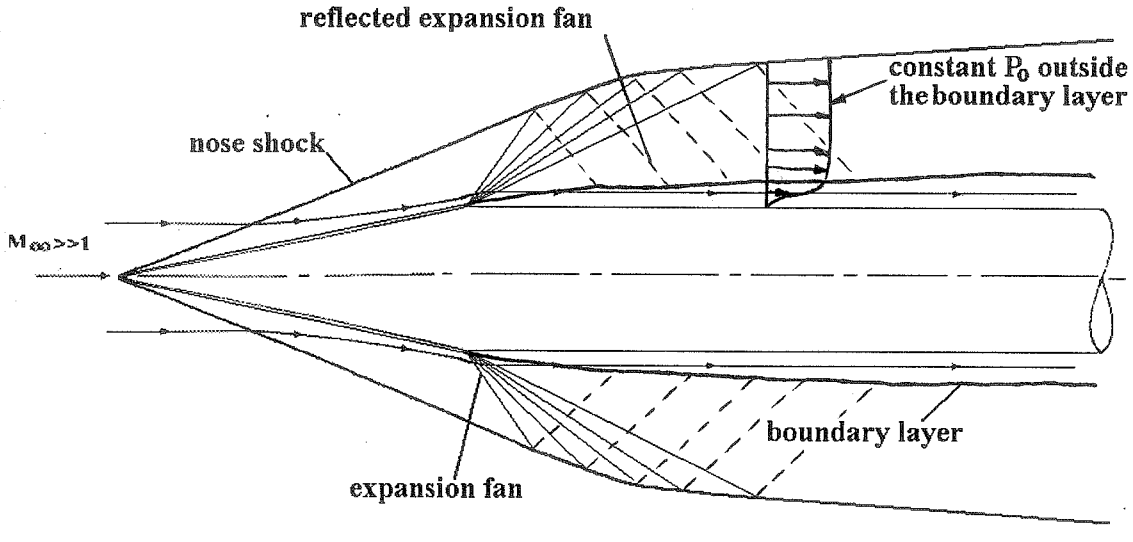

Fig. 5.8a Flow structure over a sharp cone-cylinder body and streamline pattern

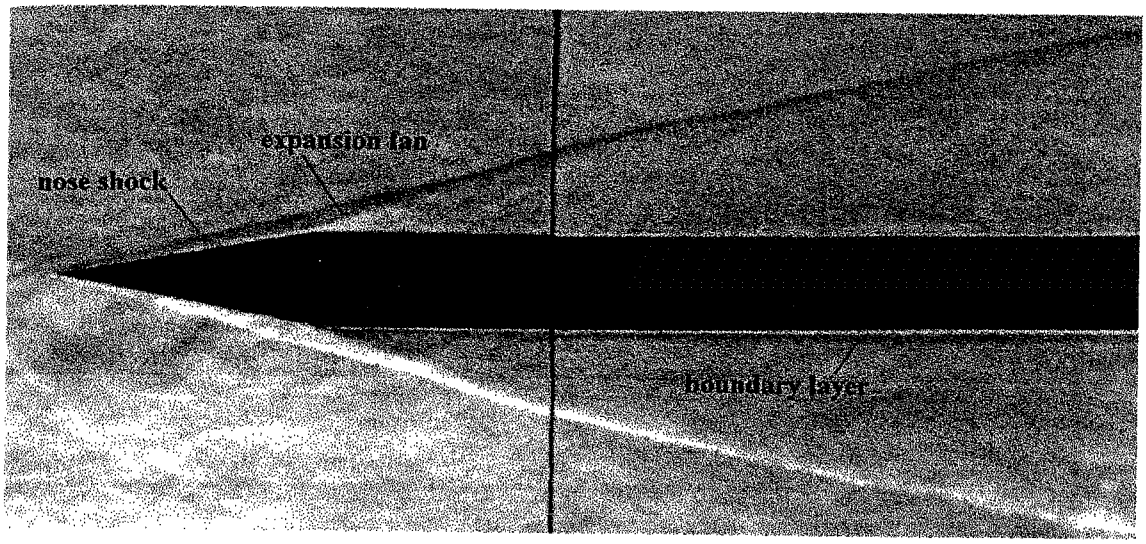

Fig. 5.8b Schlieren photo of the sharp cone cylinder (M_∞=8.2, Re_∞/cm=93000, laminar boundary layer)

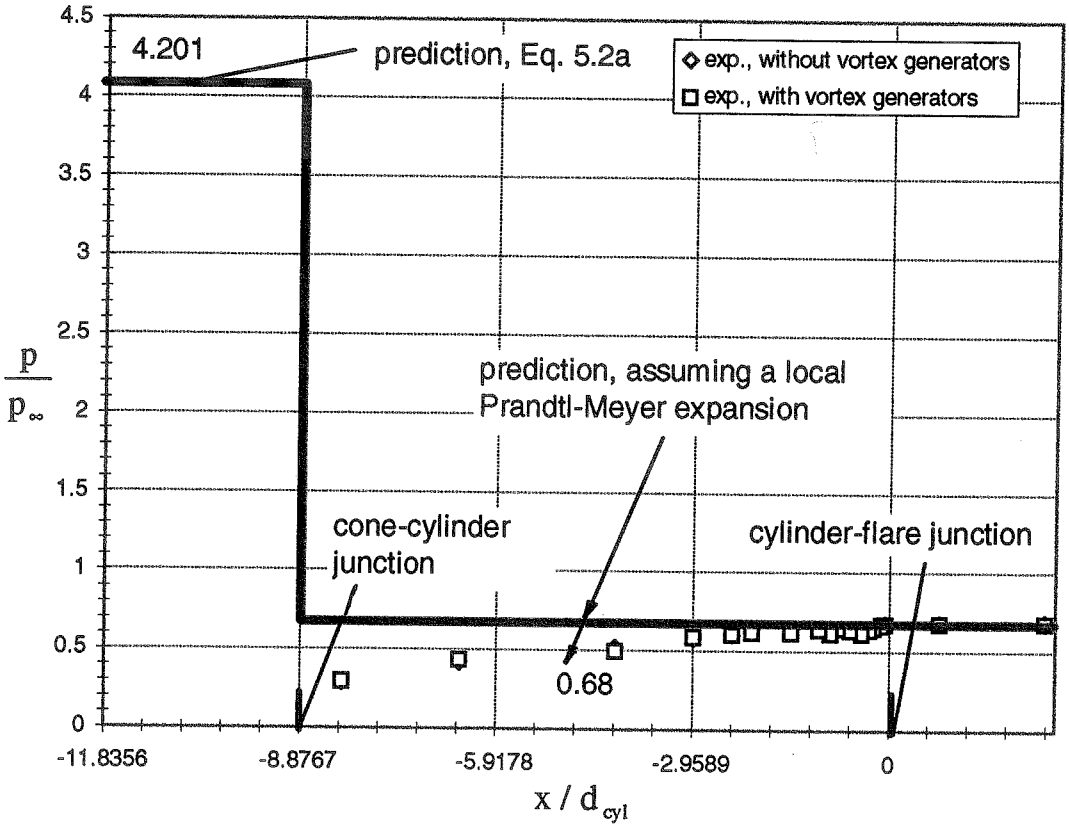

Fig. 5.9 Pressure distributions on the sharp cone cylinder (M_∞=8.2, Re_∞/cm=93000)

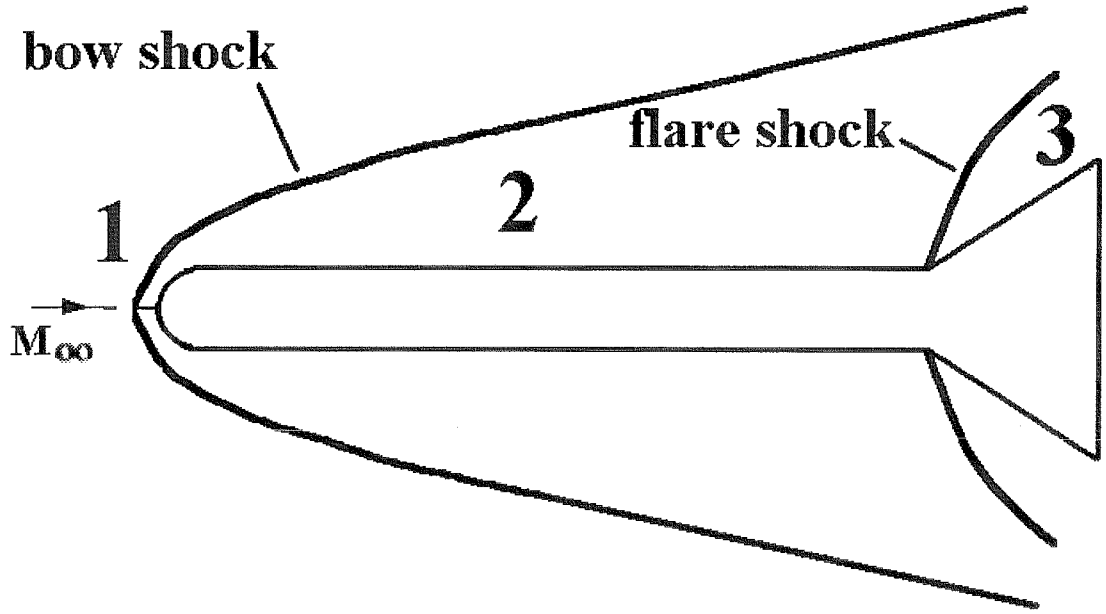

Fig. 5.10 Inviscid flow structure over a hemisphere-cylinder-flare body

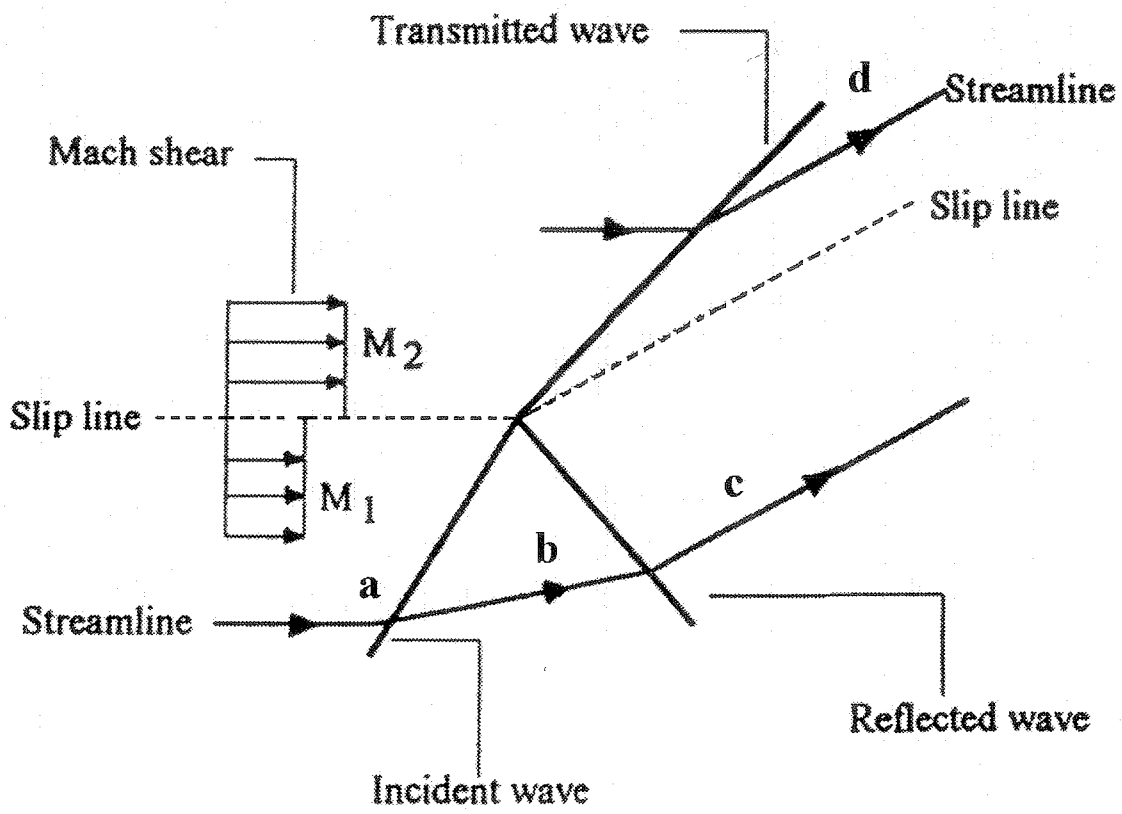

Fig. 5.11a Wave reflection from a shock wave

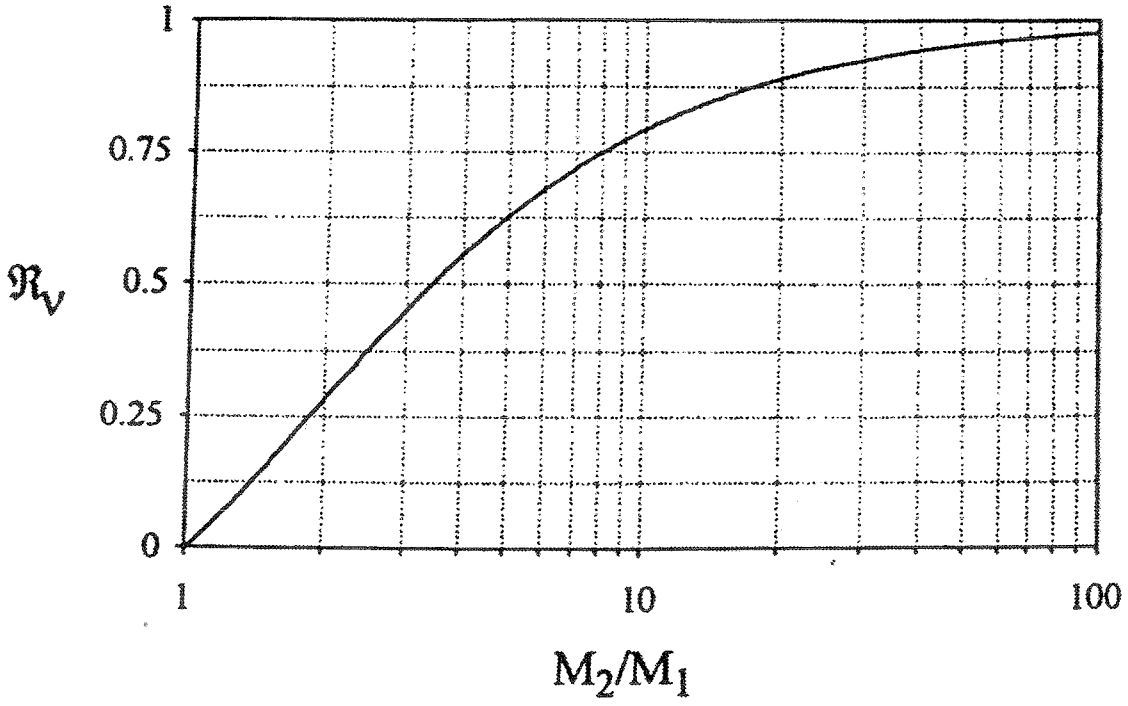

Fig. 5.11b Variation of the reflected coefficient with the strength of the Mach shear

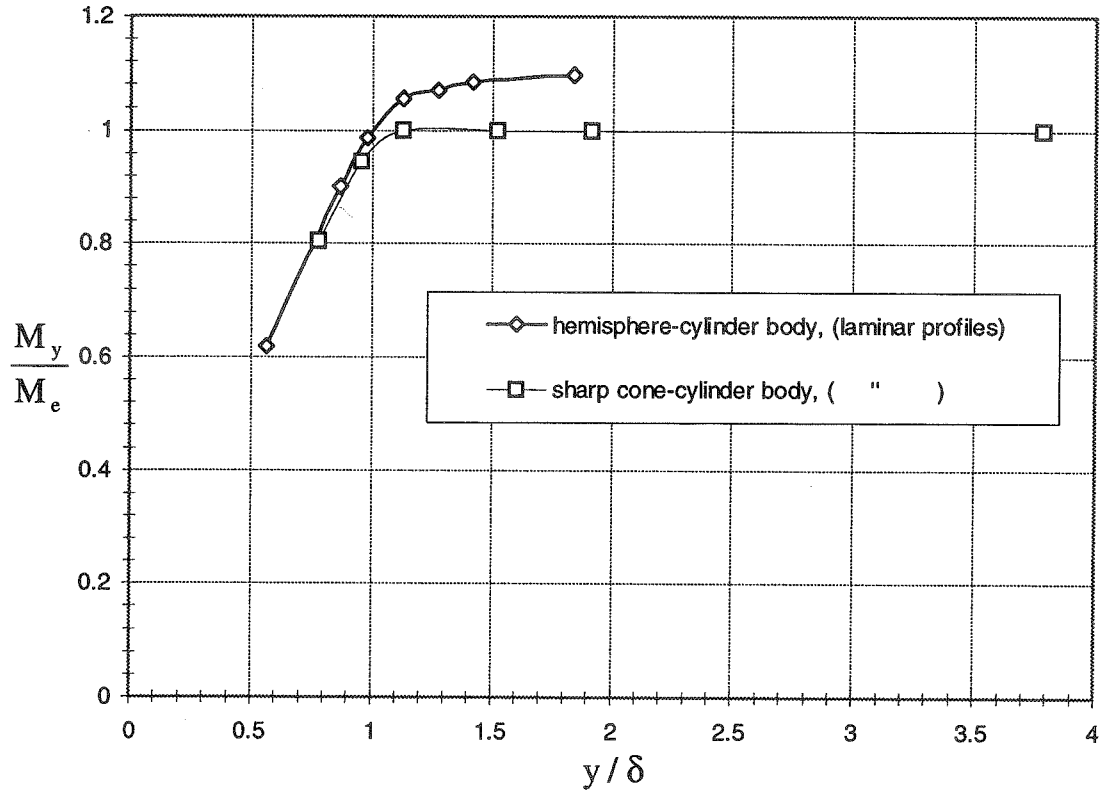

Fig. 5.12a Kuehn's[9] laminar Mach profiles (10° semi-vertex sharp cone and hemisphere noses, M_∞=4.76, Re_∞/cm=40000)

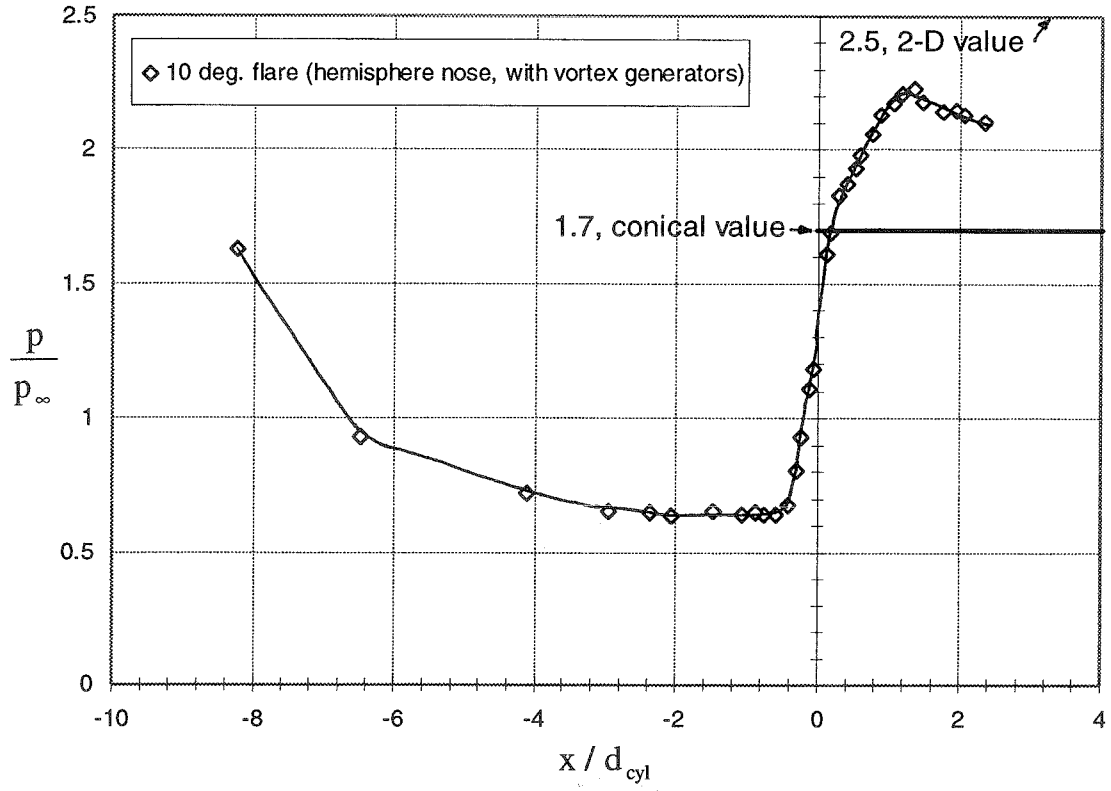

Fig. 5.12b Attached flow pressure distribution over the hemisphere-cylinder-flare body (M_∞=8.2, Re_∞/cm=93000, turbulent boundary layer, $\beta=10^o$)

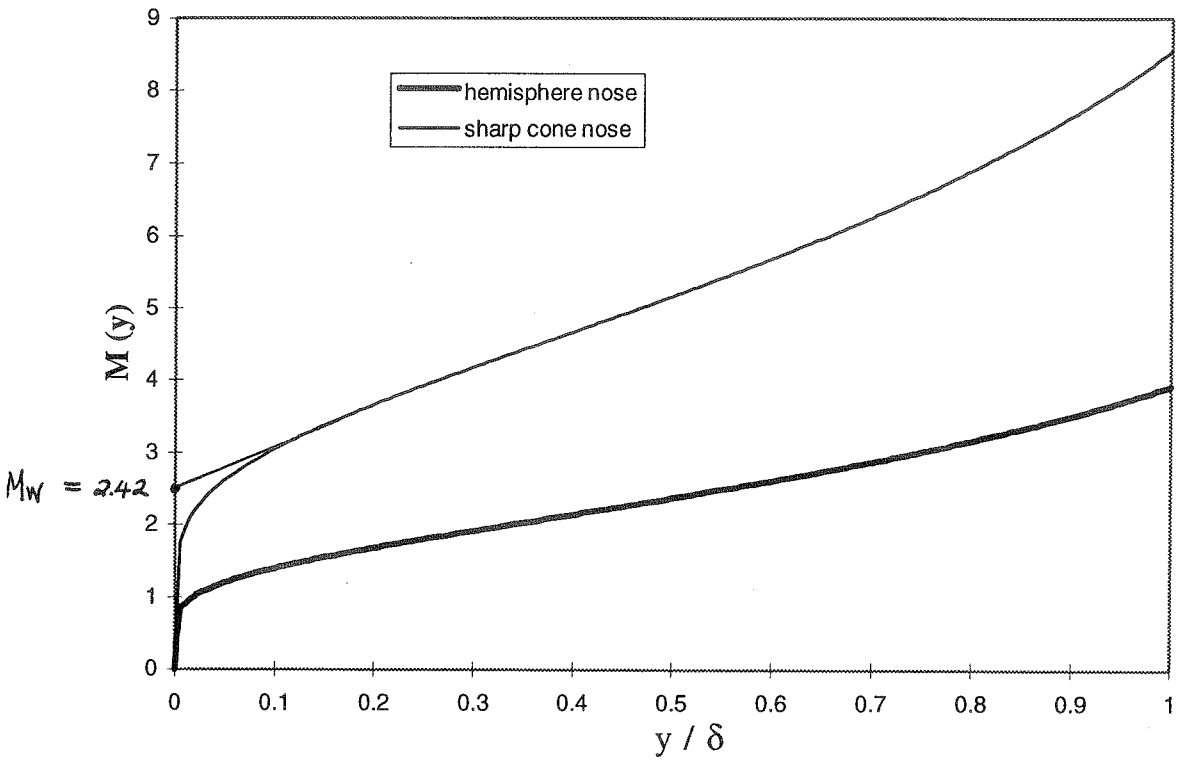

Fig. 5.13a Predicted inviscid Mach profile (derived from a seventh power law profile)

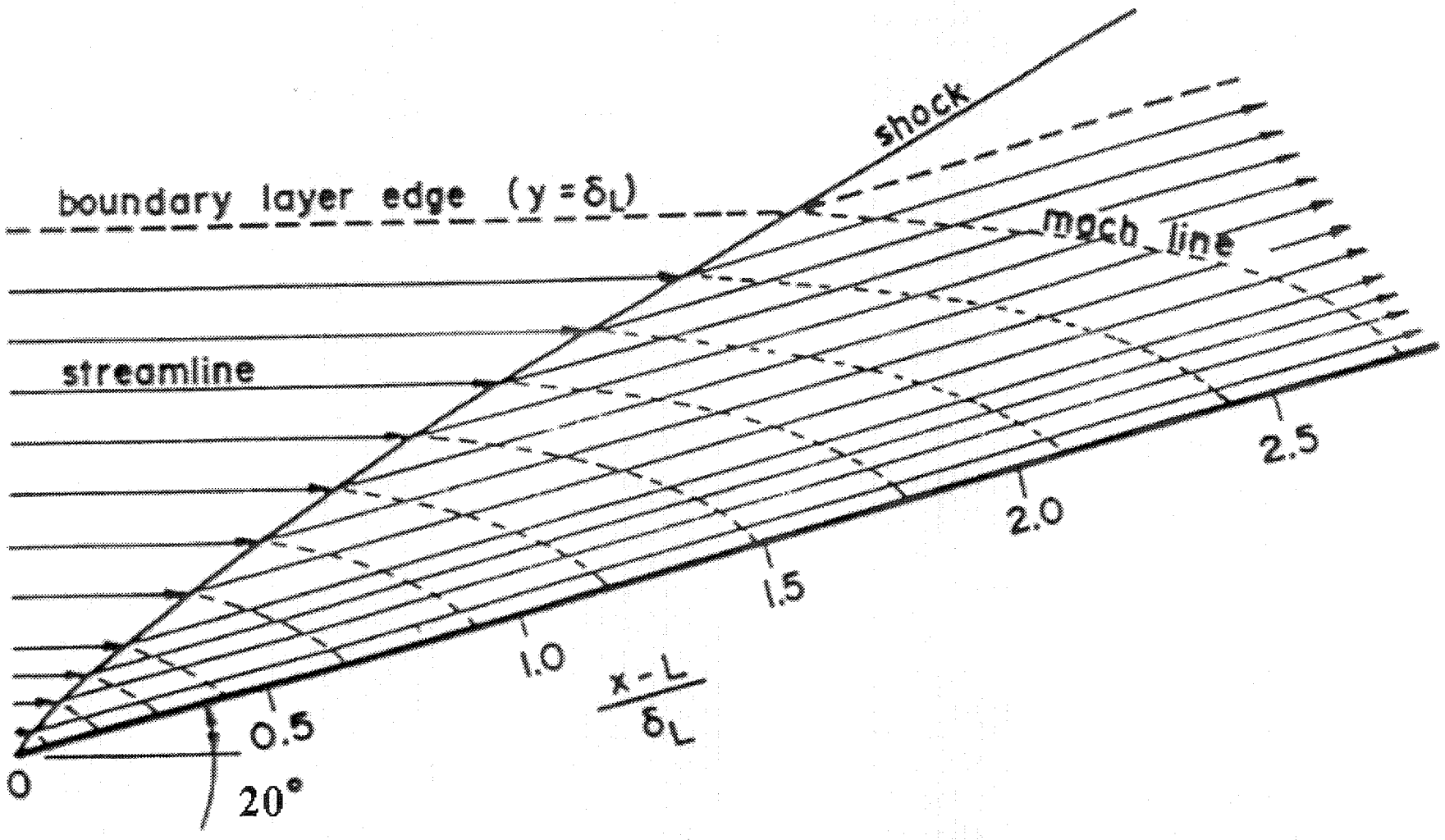

Fig. 5.13b Elfstrom's[37] flow field construction

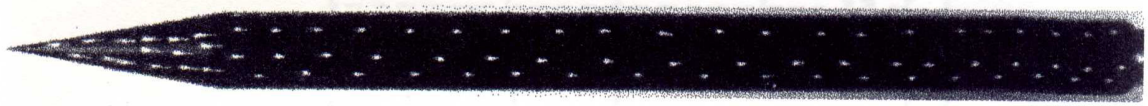

Fig. 5.14 Oil-dot photo of the sharp cone cylinder (M_∞=8.2, Re_∞/cm=93000, laminar boundary layer)

a) without vortex generators

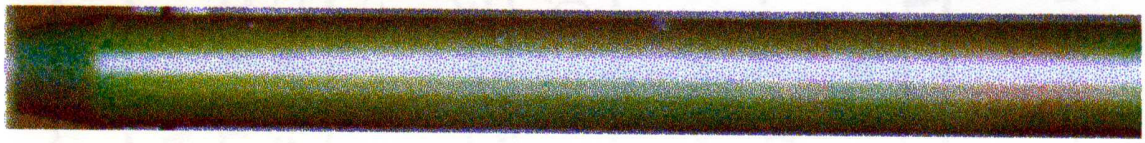

b) with vortex generators

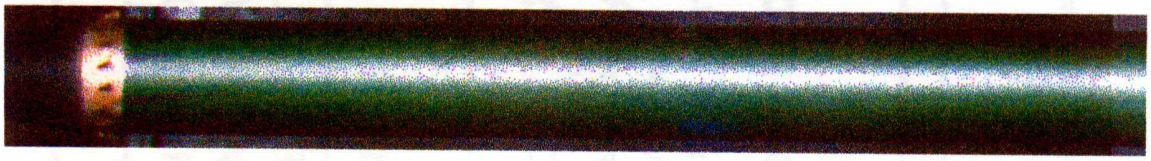

Fig. 5.15 Liquid-crystal photos of the sharp cone cylinder (M_∞=8.2, Re_∞/cm=93000, laminar and turbulent boundary layers)

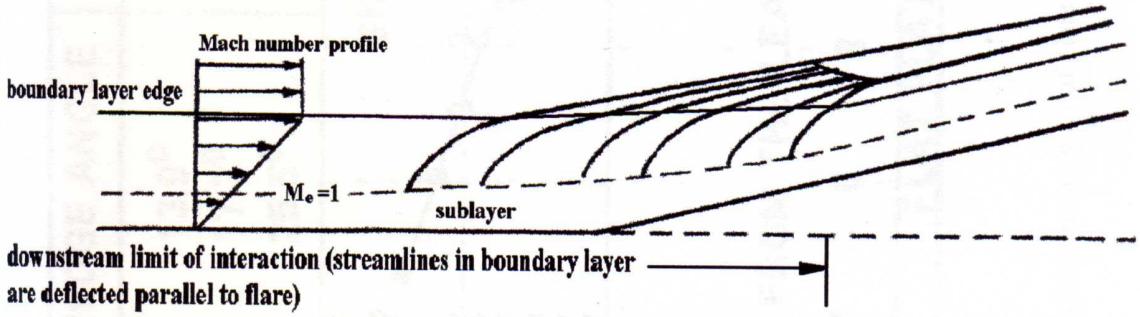

Fig. 5.16 Schematic diagram of the effect of flare deflection on local flowfield in laminar unseparated flow

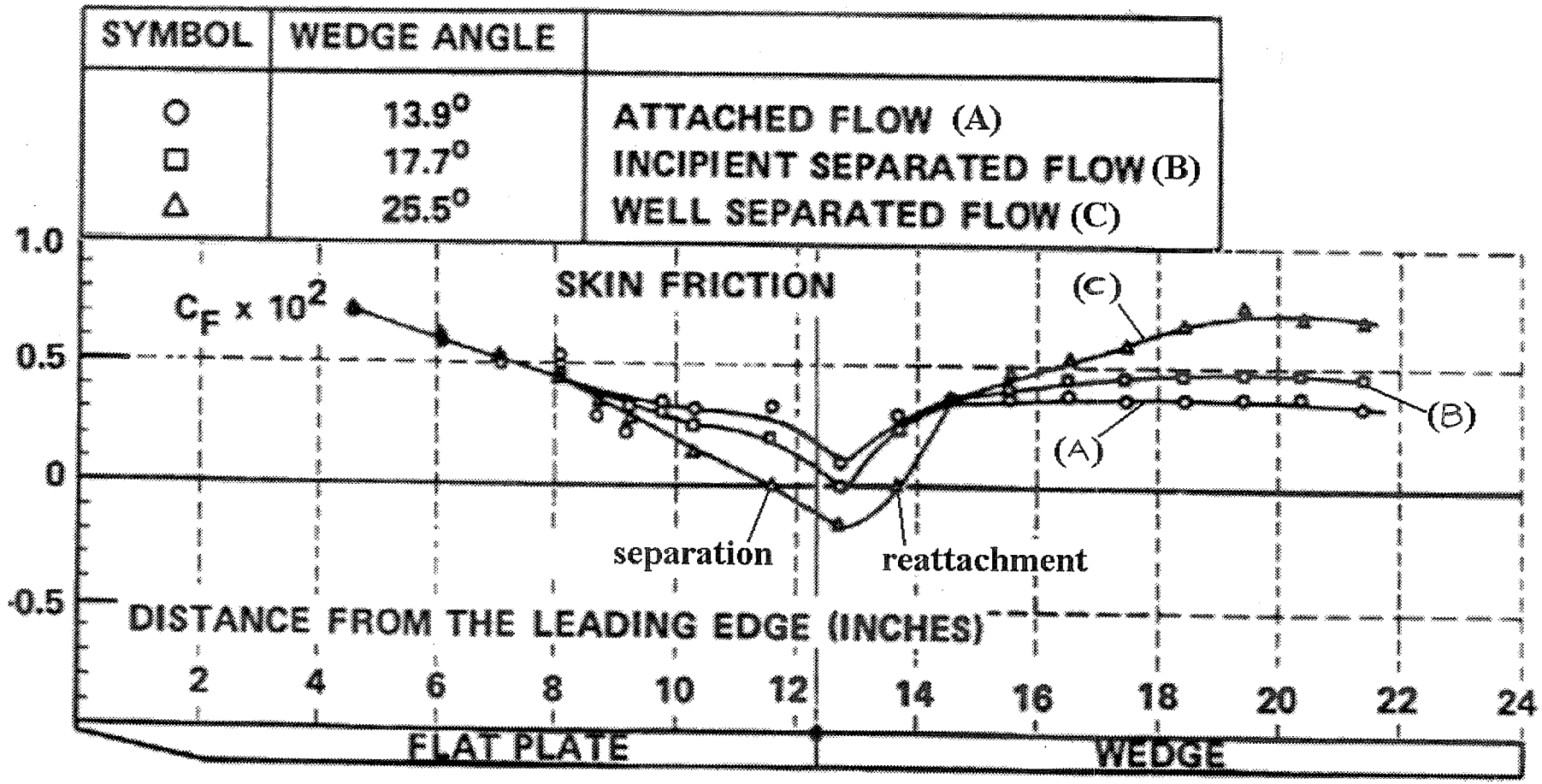

Fig. 5.17 Skin friction distribution along a flat plate-wedge model (ref. 27, M_∞=19.8, Re_∞/in=8.7x10^3)

a) $\beta=10^{\circ}$

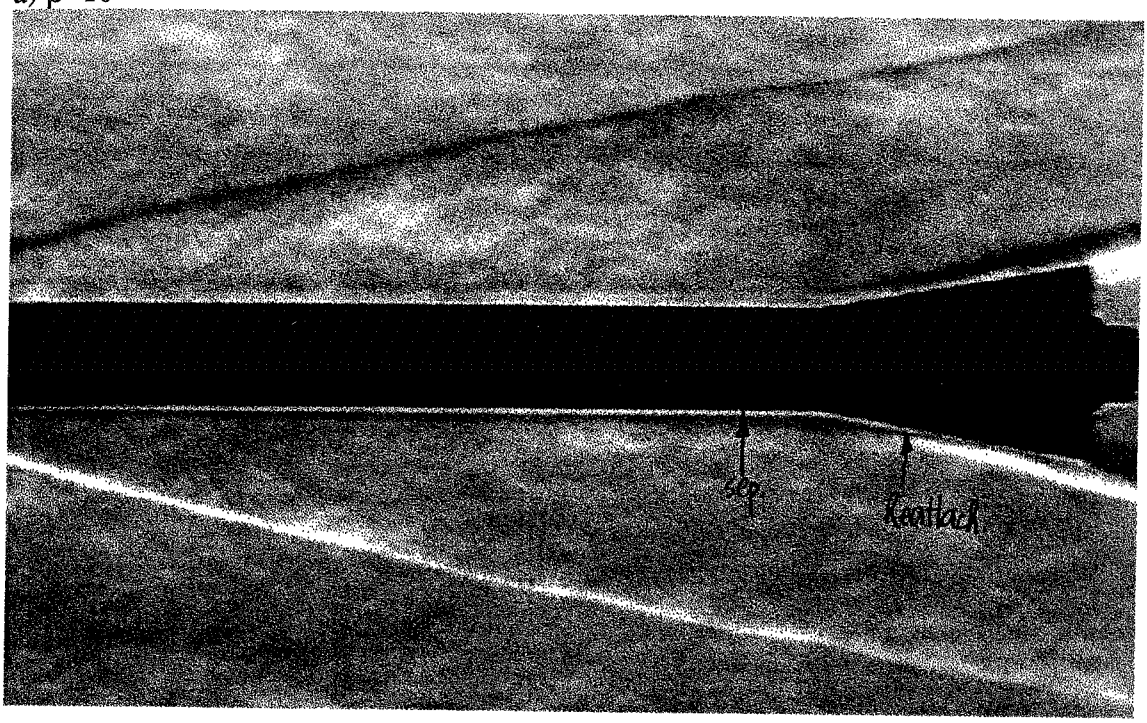

close-up of the cylinder-flare junction

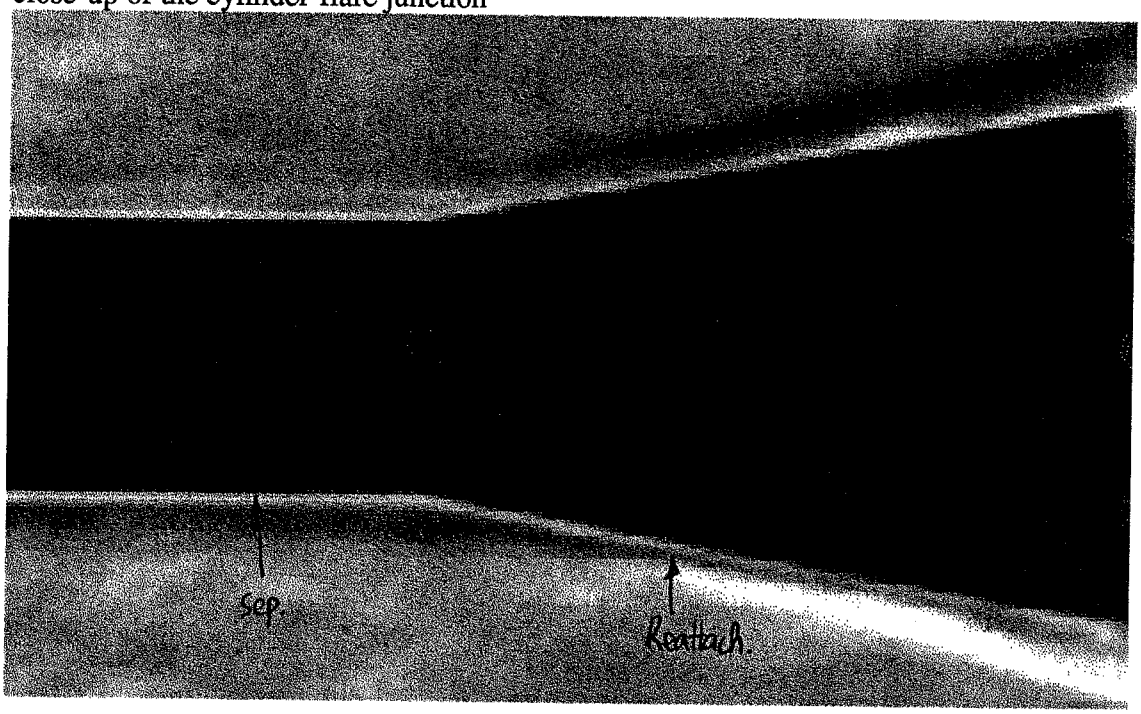

Fig. 5.18 The effect of flare deflection on the location of separation and reattachment in laminar flows ($M_{\infty}=8.2$, $Re_{\infty}/cm=93000$, $L_{cyl}=15.3$ cm, sharp cone nose)

b) β=20°

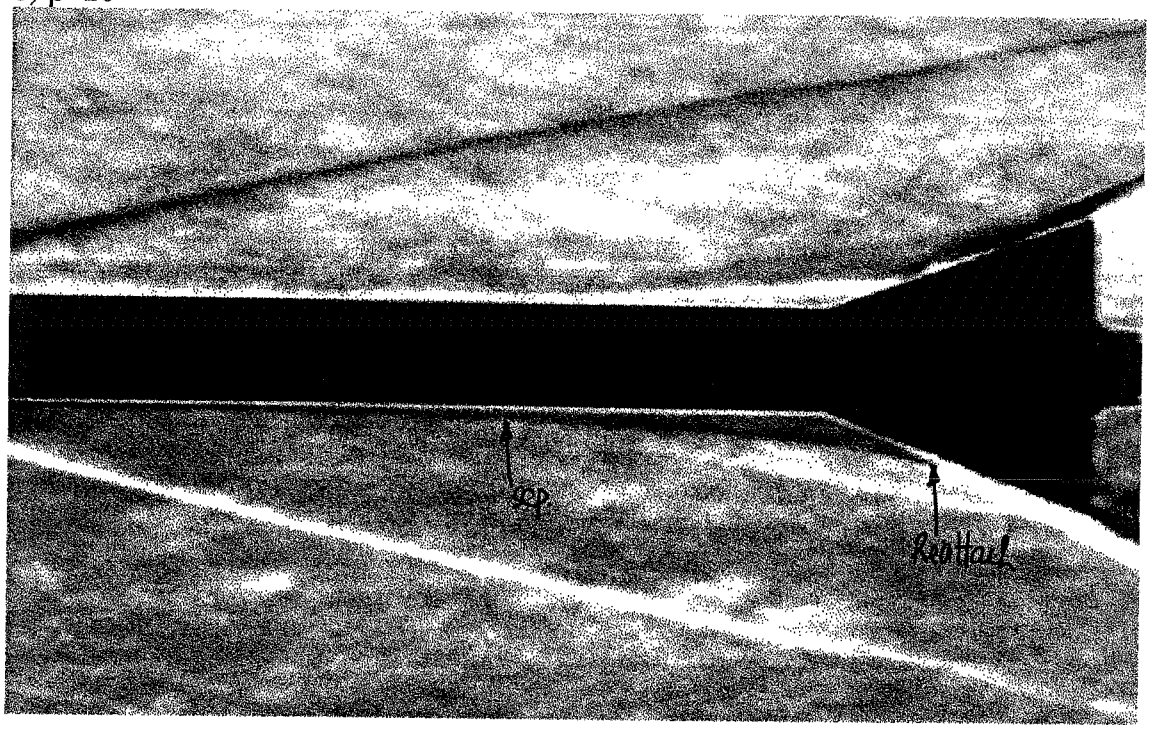

c) β=30°

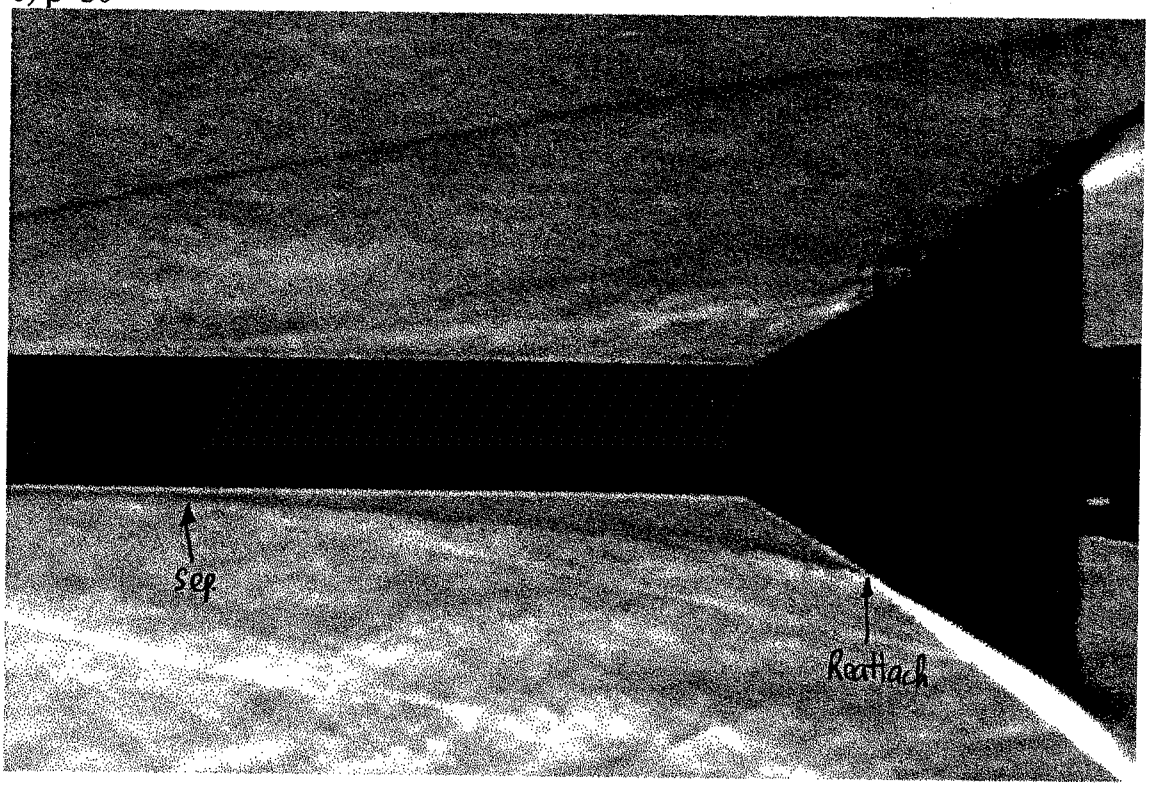

Fig. 5.18 Continue

d) β=45°

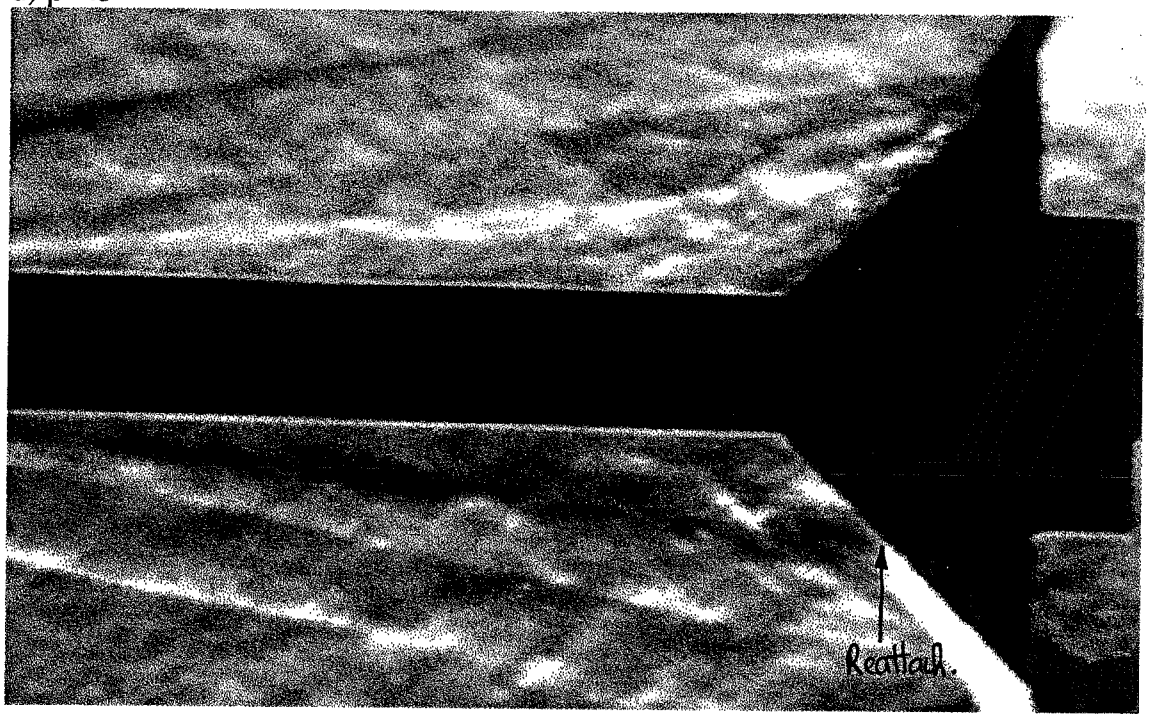

Fig. 5.18 Concluded

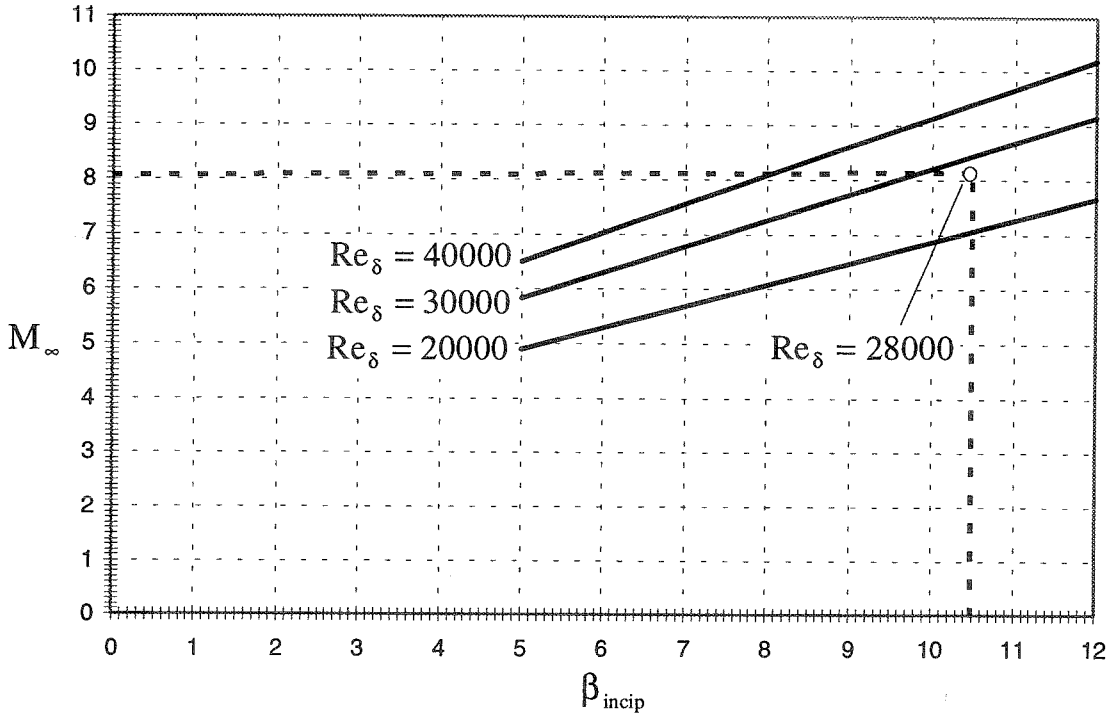

Fig. 5.19a Cross-plot of Kuehn's[9] laminar incipient separation data

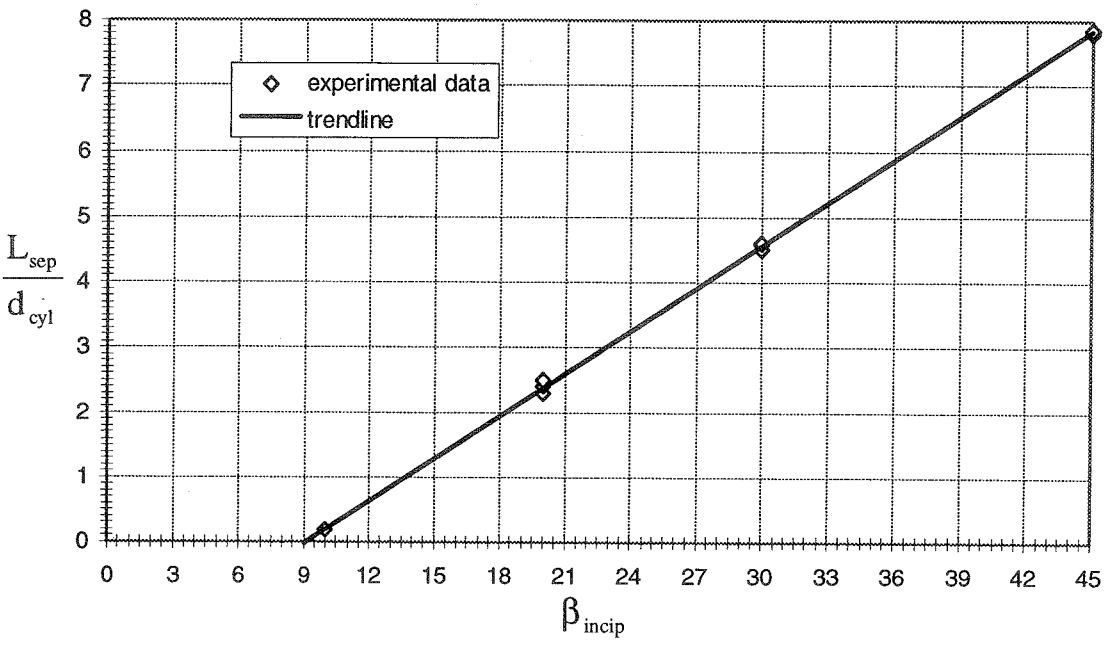

Fig. 5.19b Determination of incipient separation angle (laminar boundary layer, sharp cone nose)

i) liquid-crystal picture

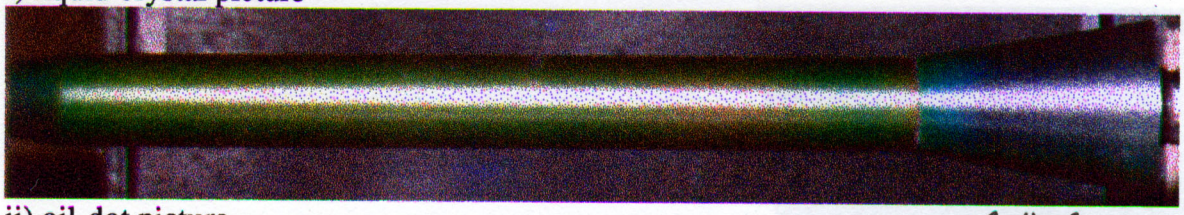

ii) oil-dot picture

iii) pressure distribution

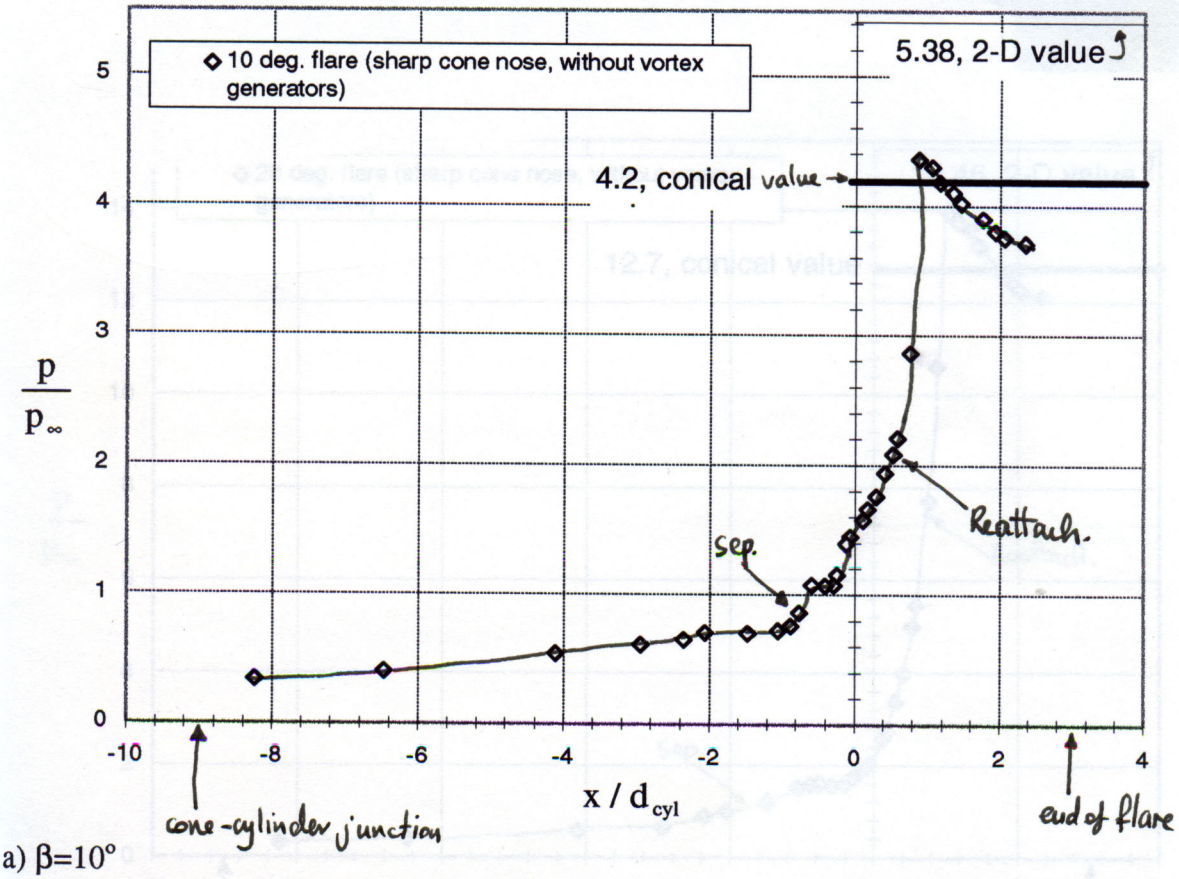

a) $\beta=10°$

Fig. 5.20 Liquid-crystal and oil-dot flow visualisation and pressure measurements on control flare configurations ($M_\infty=8.2$, $Re_\infty/cm=93000$, $L_{cyl}=15.3$ cm, $d_{cyl}=1.7$ cm, sharp cone nose, laminar boundary layer)

i) liquid-crystal picture

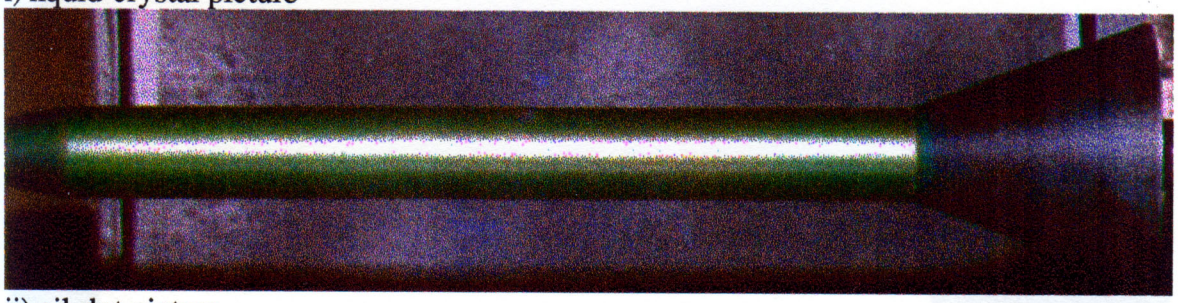

ii) oil-dot picture

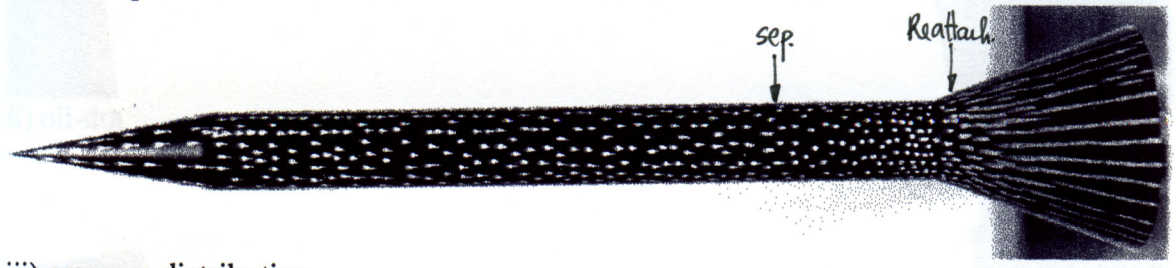

iii) pressure distribution

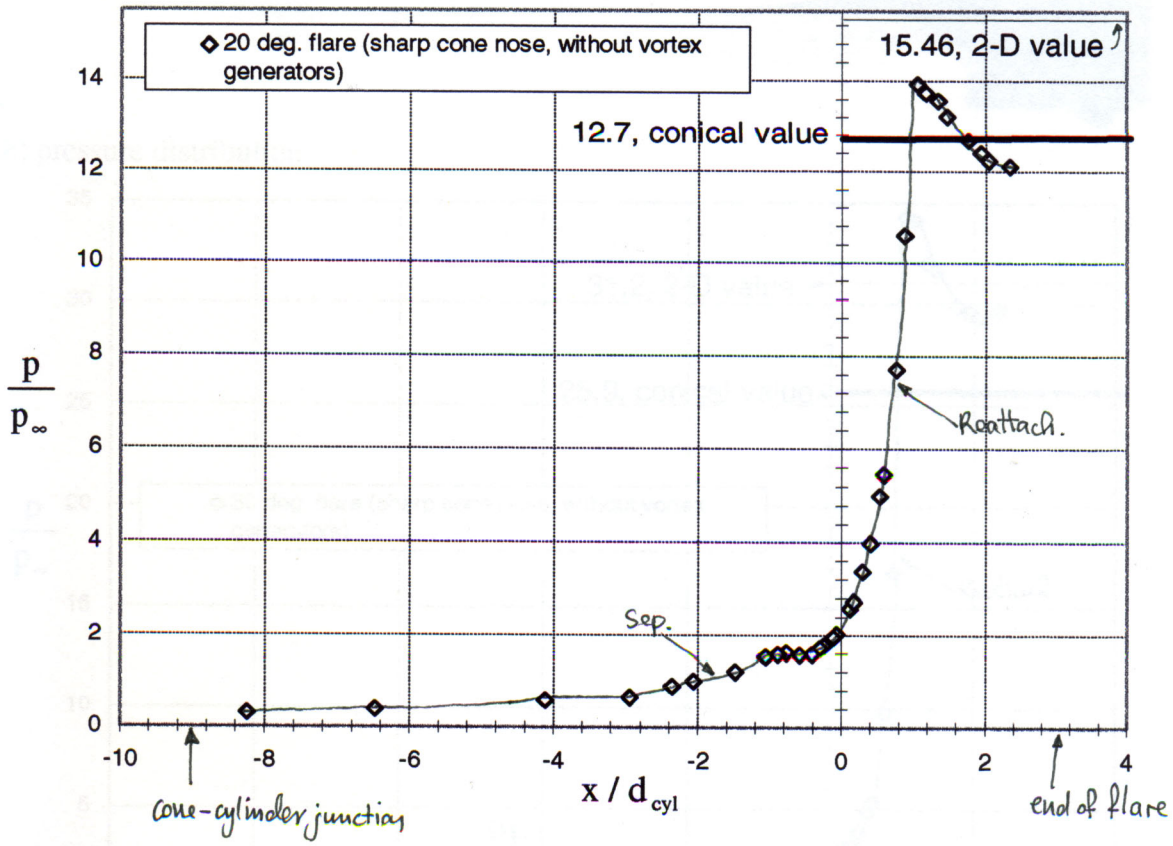

b) β=20°

Fig. 5.20 Continue

i) liquid-crystal picture

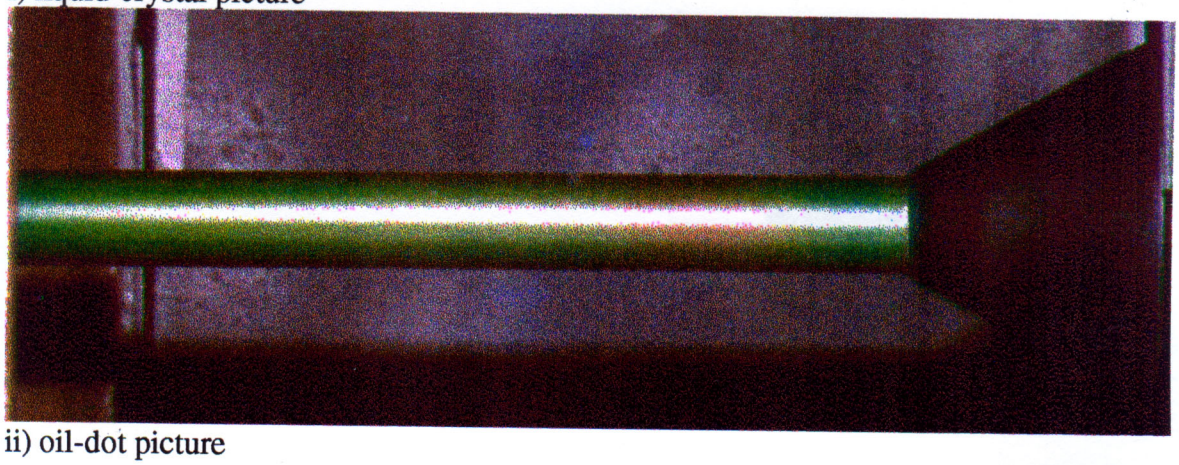

ii) oil-dot picture

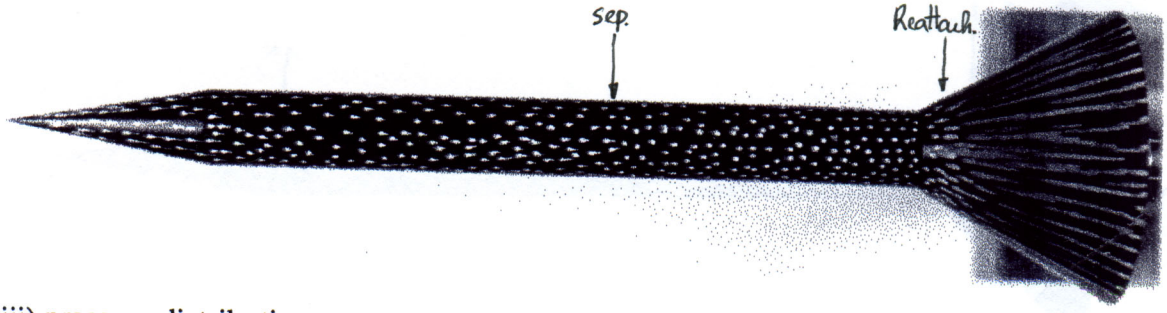

iii) pressure distribution

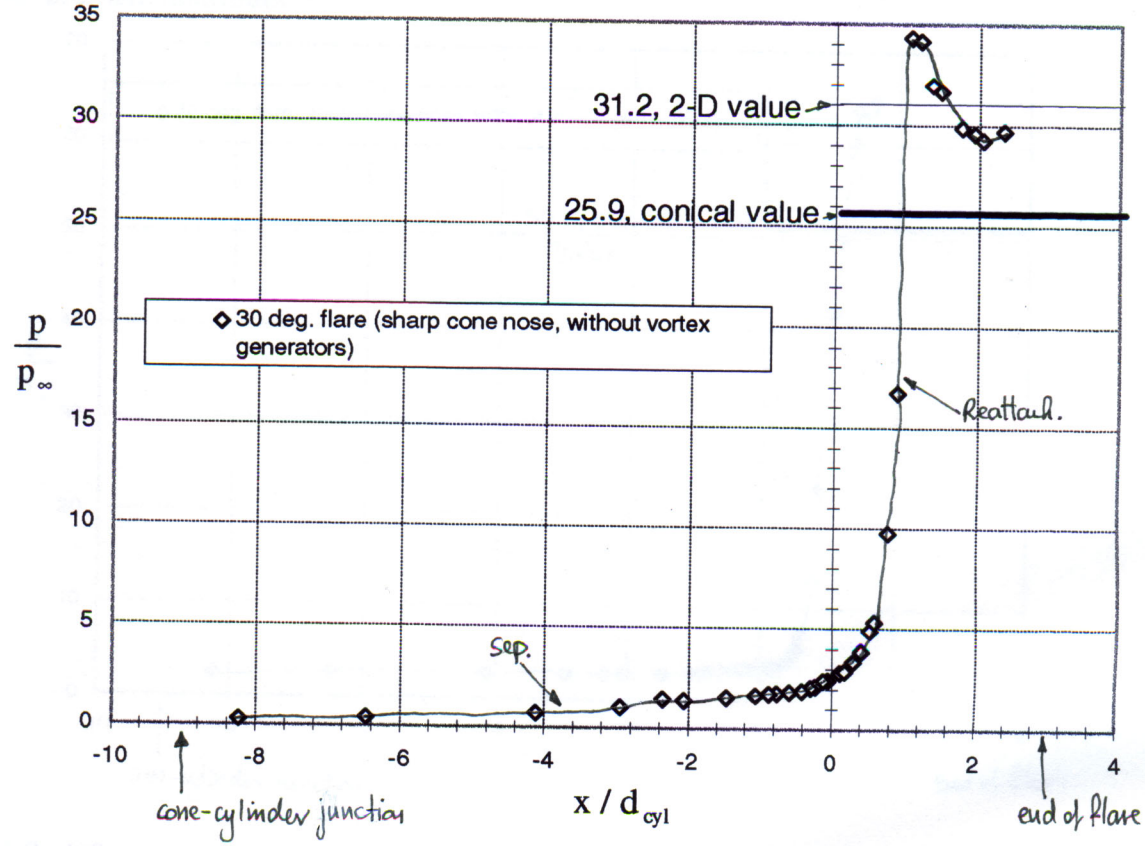

c) β=30°

Fig. 5.20 Continue

i) liquid-crystal picture

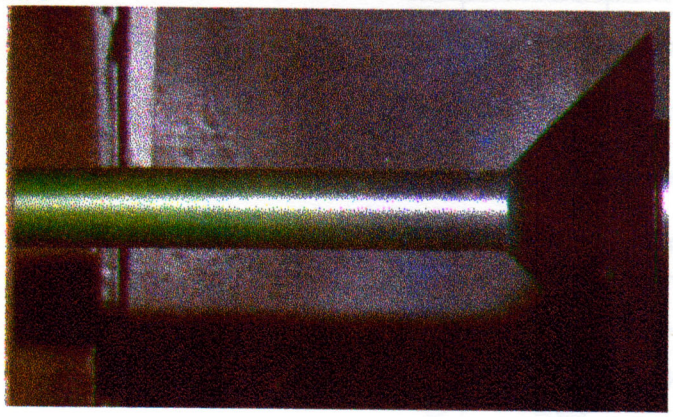

ii) oil-dot picture

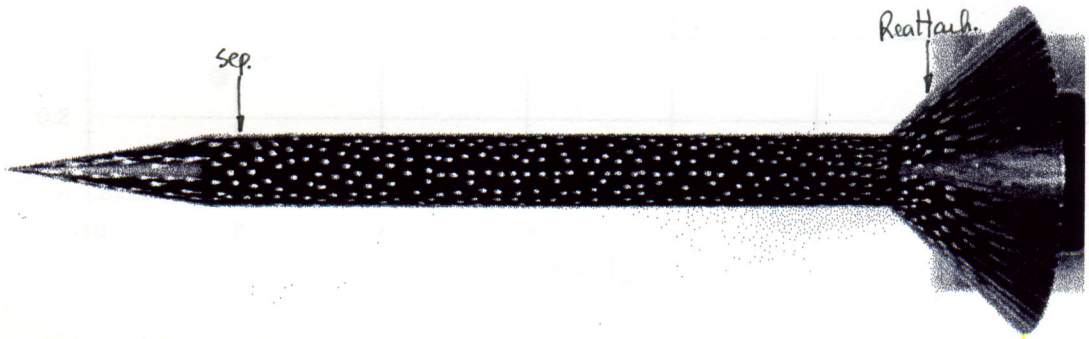

iii) pressure distribution

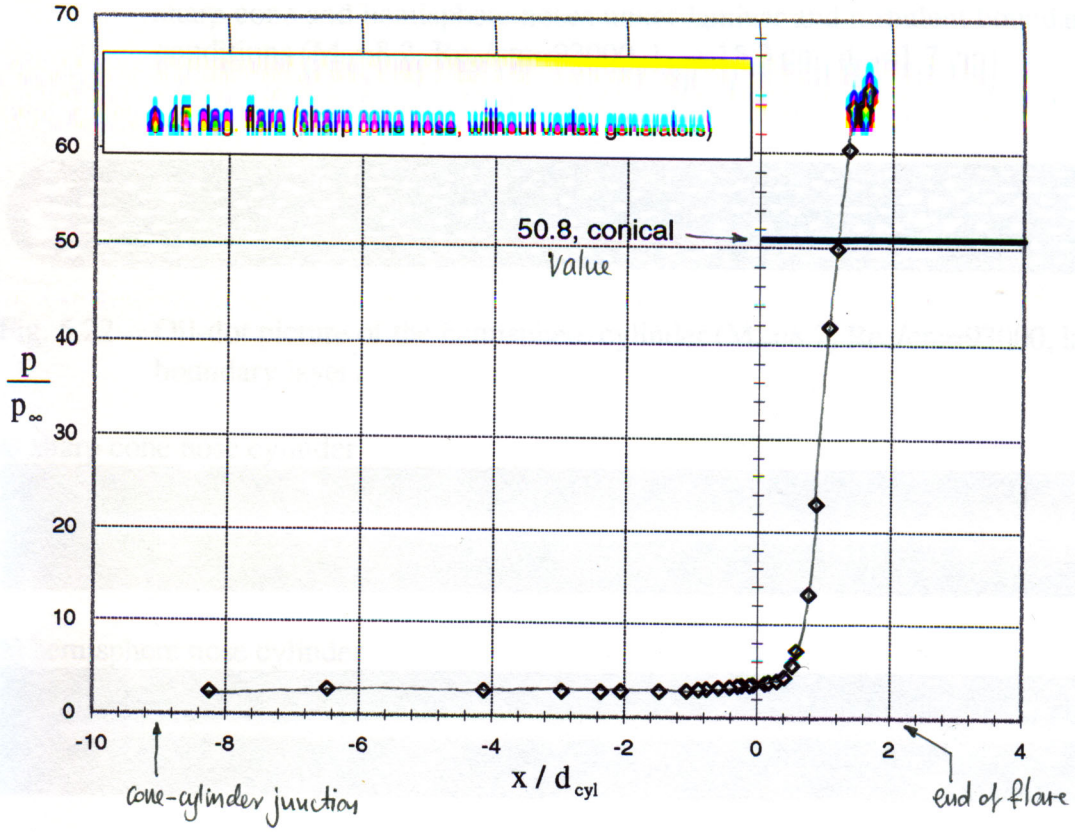

d) β=45°

Fig. 5.20 Concluded

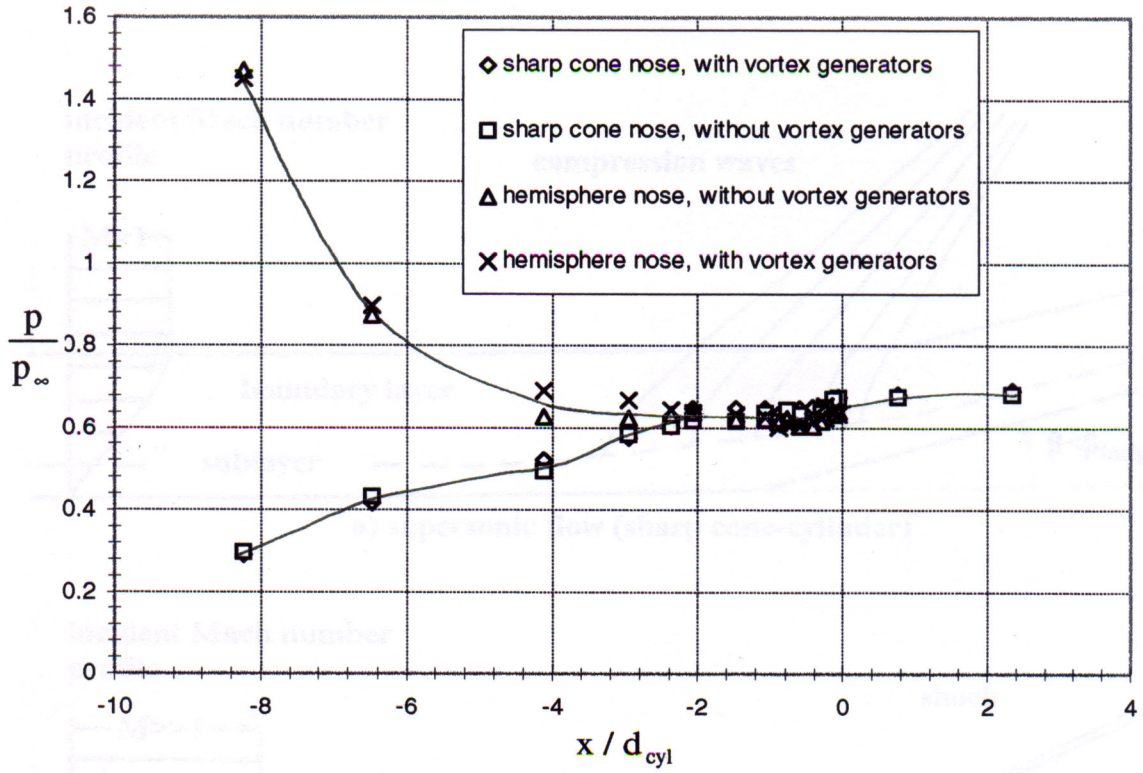

Fig. 5.21 Direct comparison of the pressure distributions along the cylinder body with sharp cone and hemisphere noses under laminar and turbulent boundary layer conditions (M_∞=8.2, Re_∞/cm=93000, L_{cyl}=15.3 cm, d_{cyl}=1.7 cm)

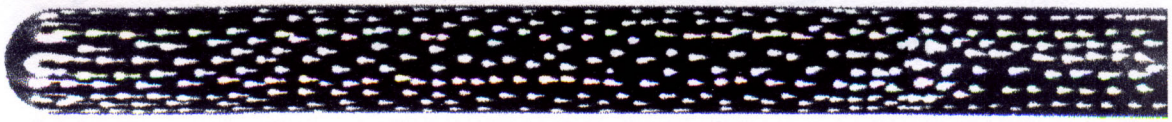

Fig. 5.22 Oil-dot picture of the hemisphere cylinder (M_∞=8.2, Re_∞/cm=93000, laminar boundary layer)

a) sharp cone nose cylinder

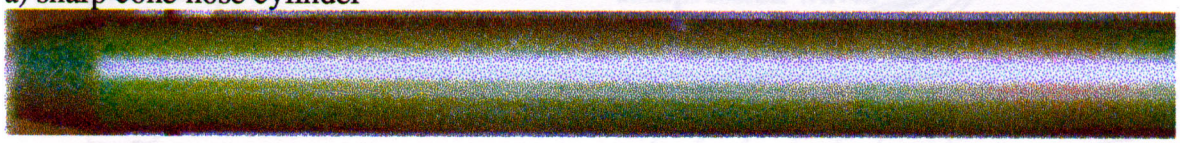

b) hemisphere nose cylinder

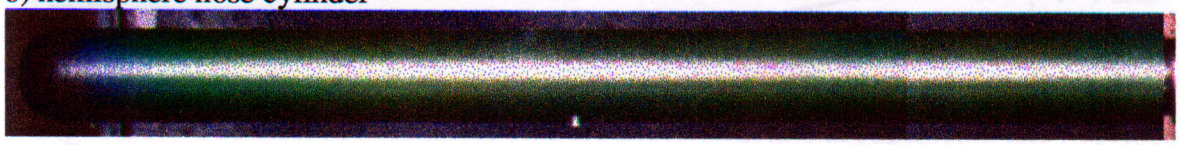

Fig. 5.23 Comparison of liquid crystal pictures of the sharp cone and hemisphere cylinder bodies (M_∞=8.2, Re_∞/cm=93000, laminar boundary layer)

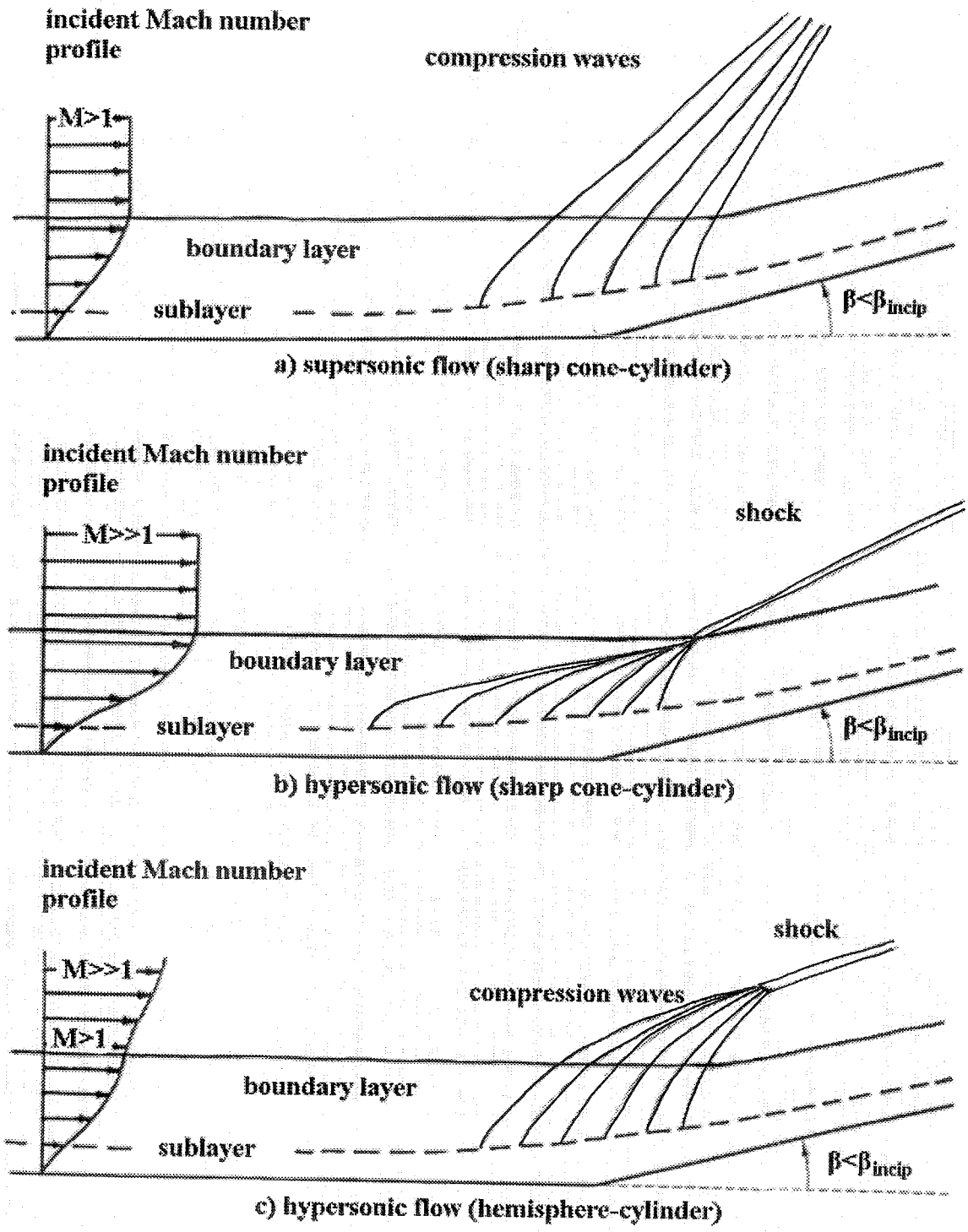

Fig. 5.24 The effect of bluntness on flare shock structure at supersonic and hypersonic speeds

a) sharp cone nose cylinder-flare

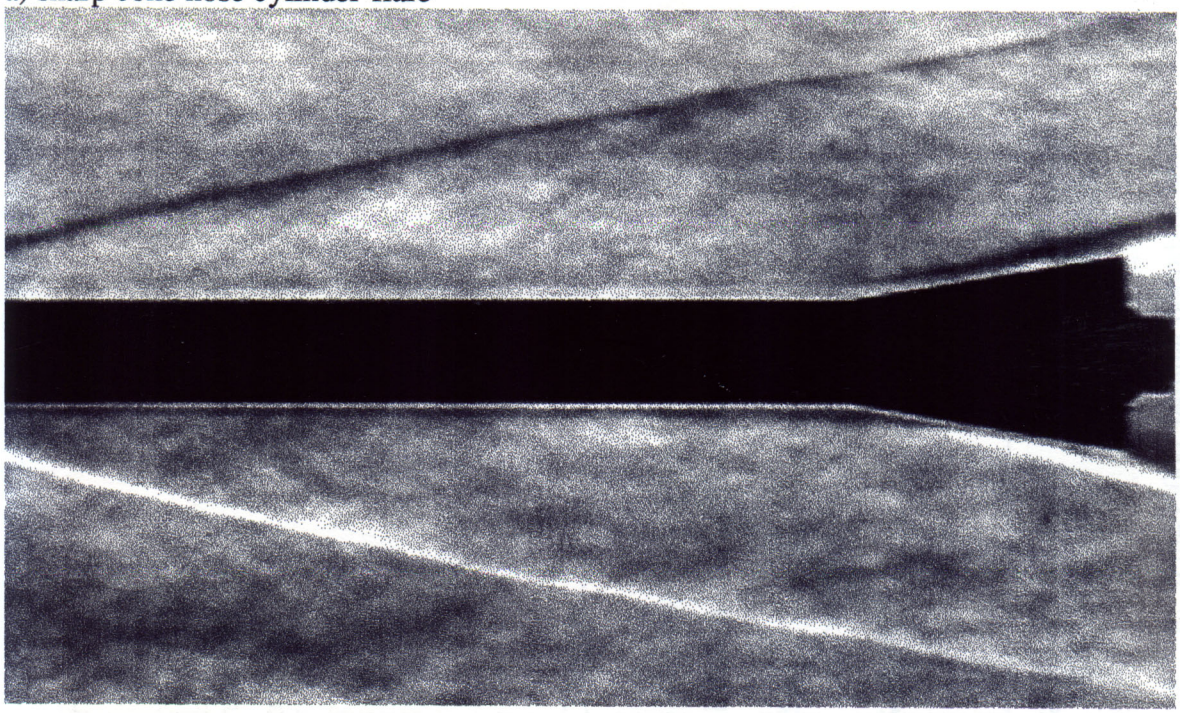

b) hemisphere nose cylinder-flare

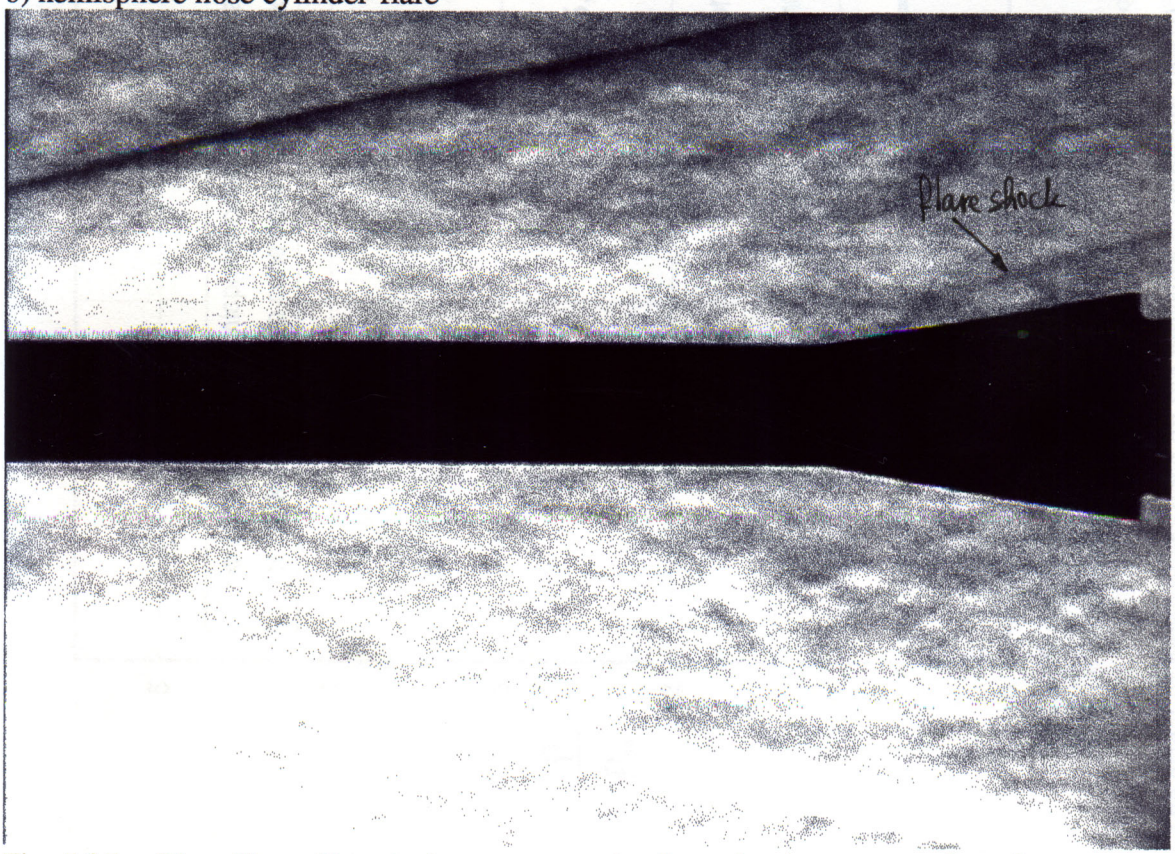

Fig. 5.25 The effect of hemisphere nose on the flare shock structure (β=10°, M_∞=8.2, Re_∞/cm=93000, laminar boundary layer)

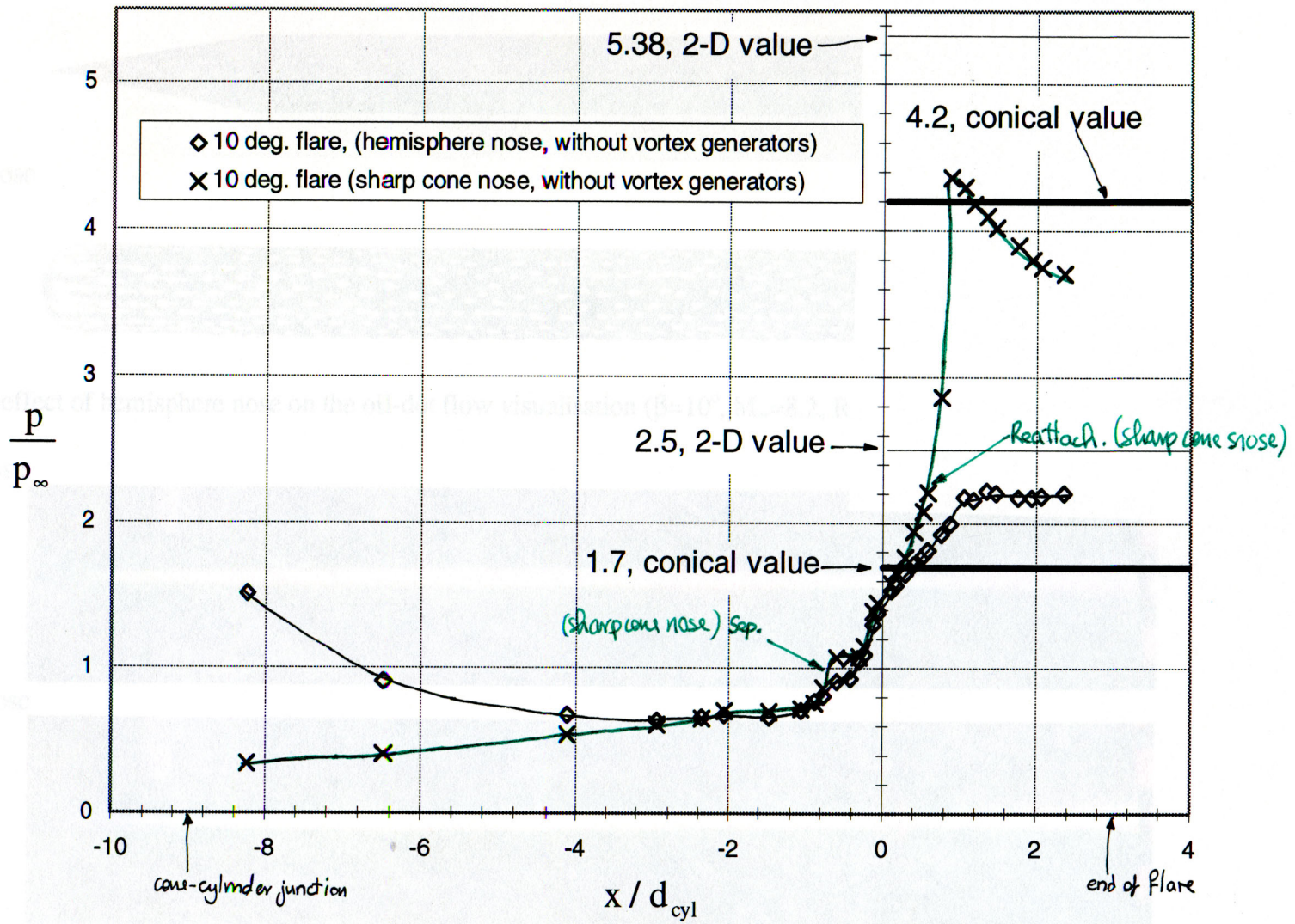

Fig. 5.26 The effect of hemisphere nose on the pressure distribution ($\beta=10^{o}$, $M_{\infty}=8.2$, $Re_{\infty}/cm=93000$, laminar boundary layer)

a) sharp cone nose

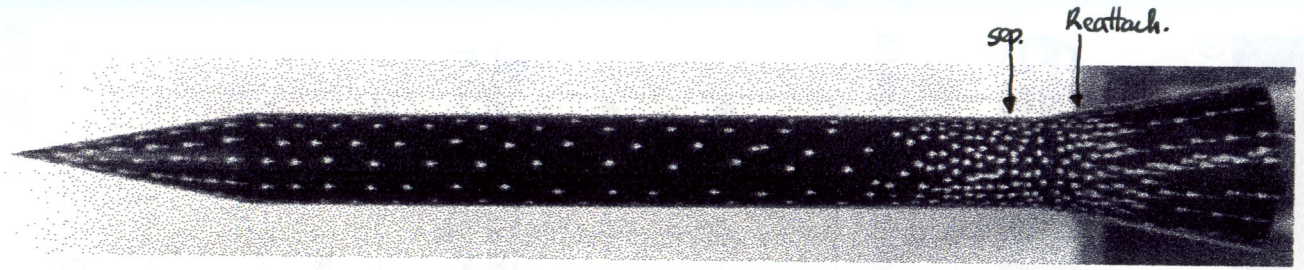

b) hemisphere nose

Fig. 5.27 The effect of hemisphere nose on the oil-dot flow visualisation (β=10°, M_∞=8.2, Re_∞/cm=93000, laminar boundary layer)

a) sharp cone nose

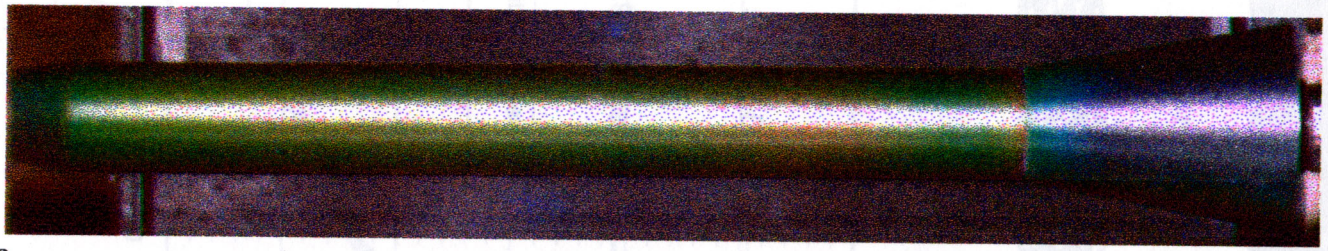

b) hemisphere nose

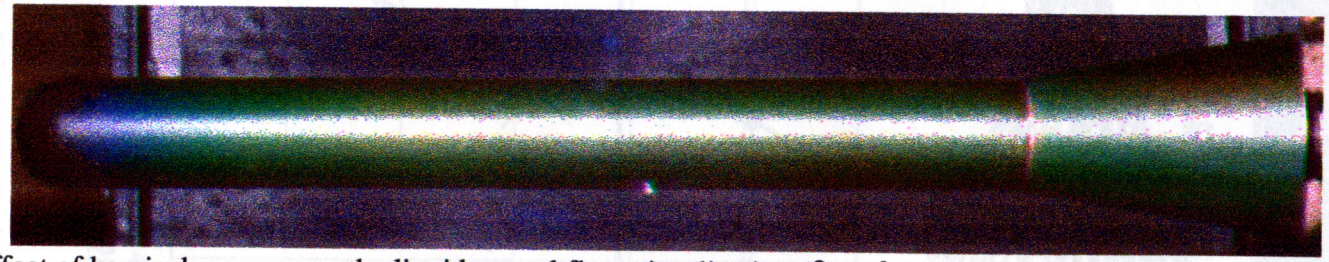

Fig. 5.28 The effect of hemisphere nose on the liquid crystal flow visualisation (β=10°, M_∞=8.2, Re_∞/cm=93000, laminar boundary layer)

i) liquid crystal picture

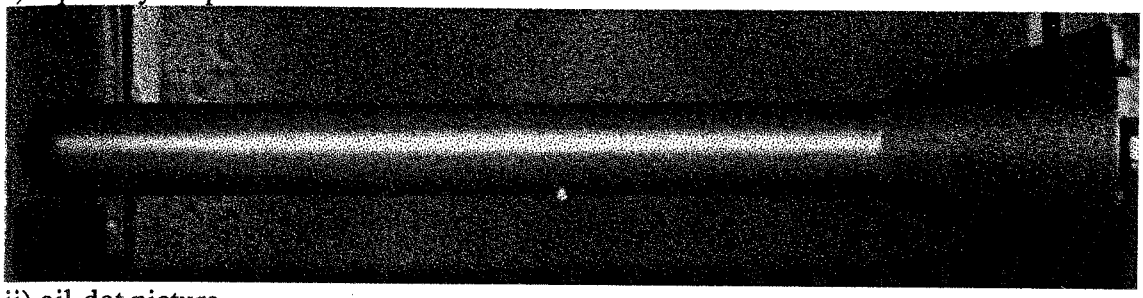

ii) oil-dot picture

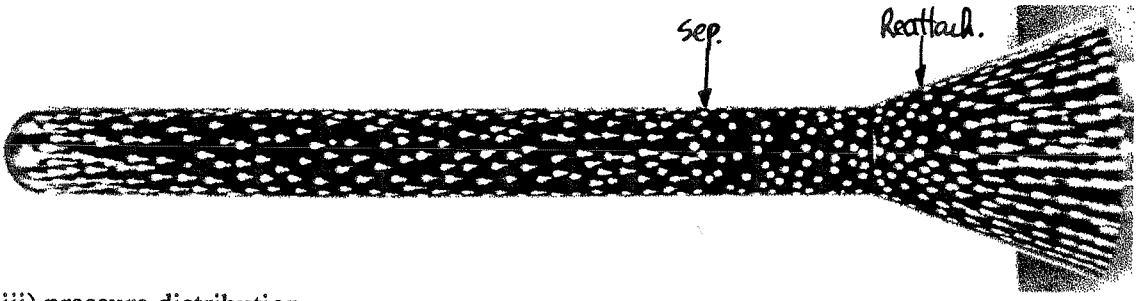

iii) pressure distribution

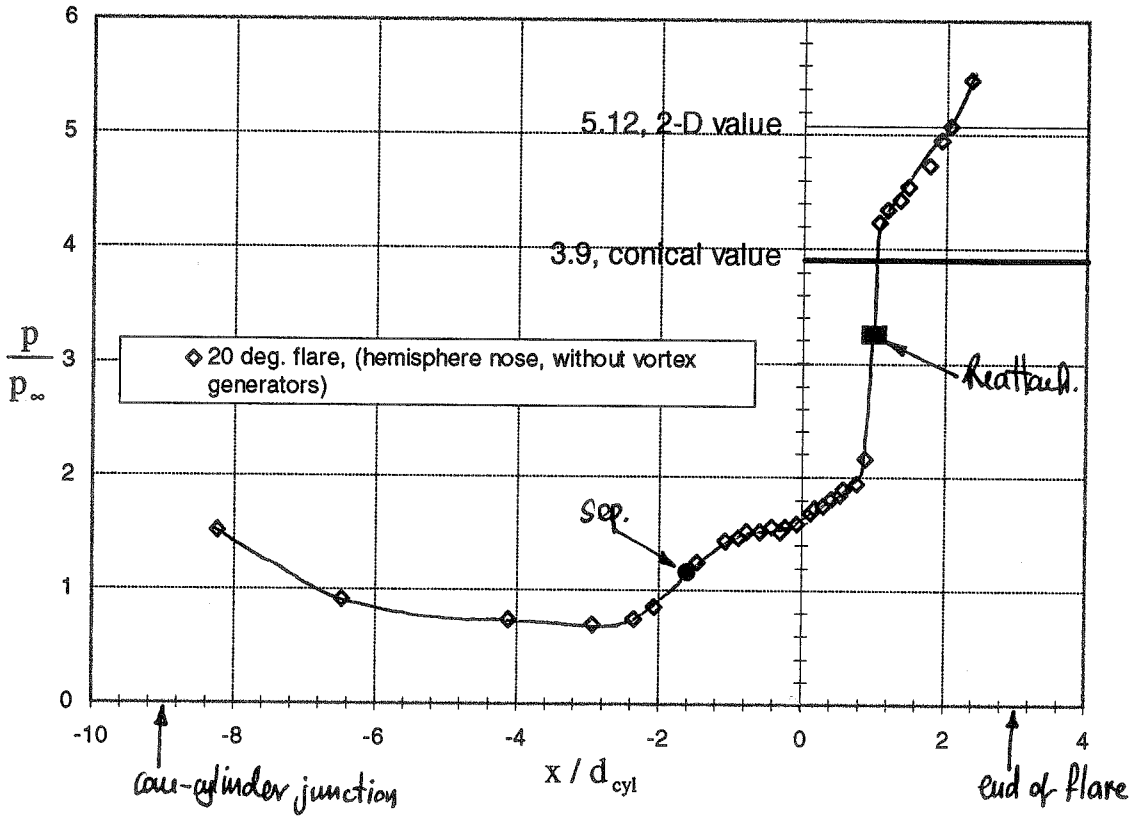

a) β=20°

Fig. 5.29 Liquid-crystal and oil-dot flow visualisation and pressure measurements on hemisphere nose control flare configurations (M_∞=8.2, Re_∞/cm=93000, laminar boundary layer)

i) liquid crystal picture

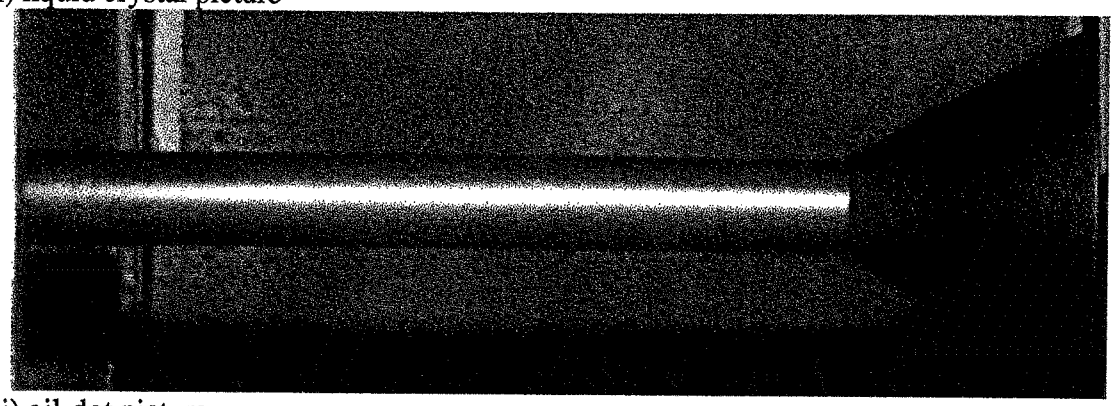

ii) oil-dot picture

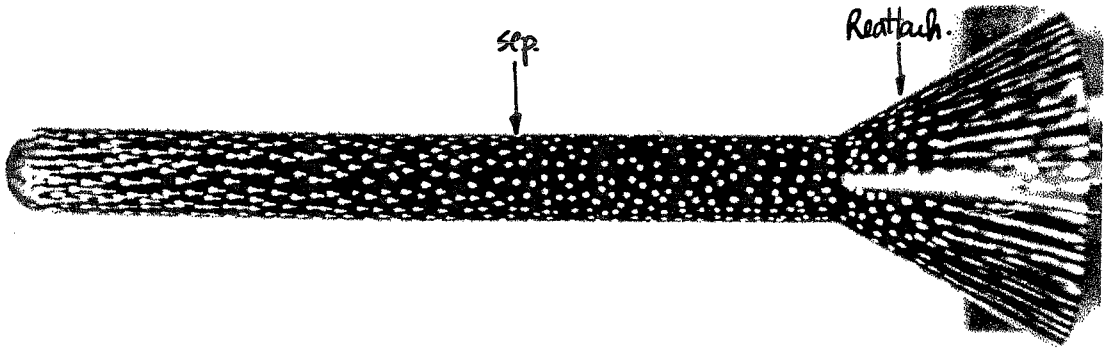

iii) pressure distribution

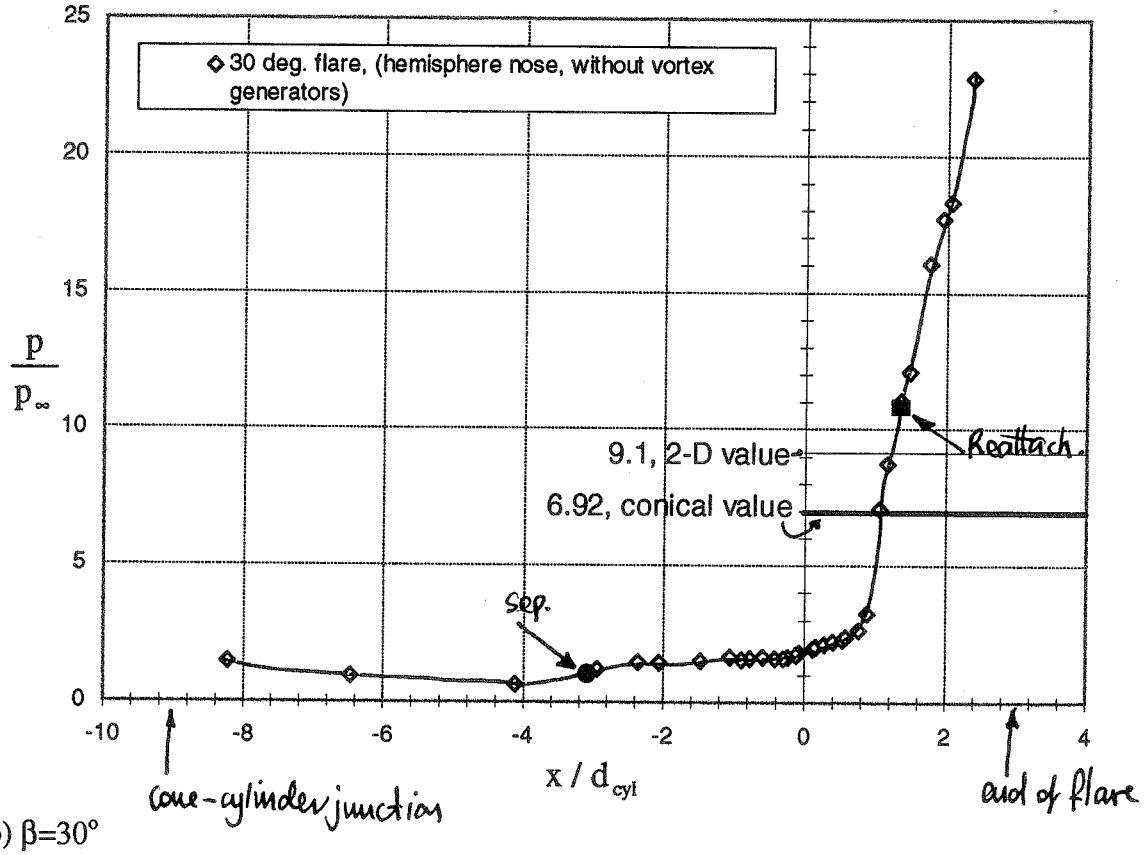

b) β=30°

Fig. 5.29 Continue

i) liquid crystal picture

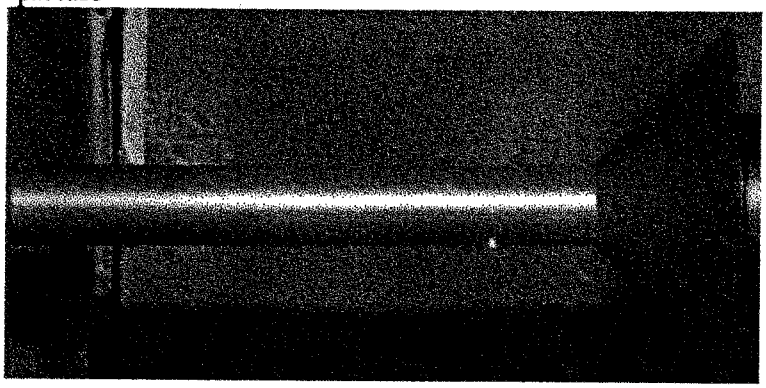

ii) oil-dot picture

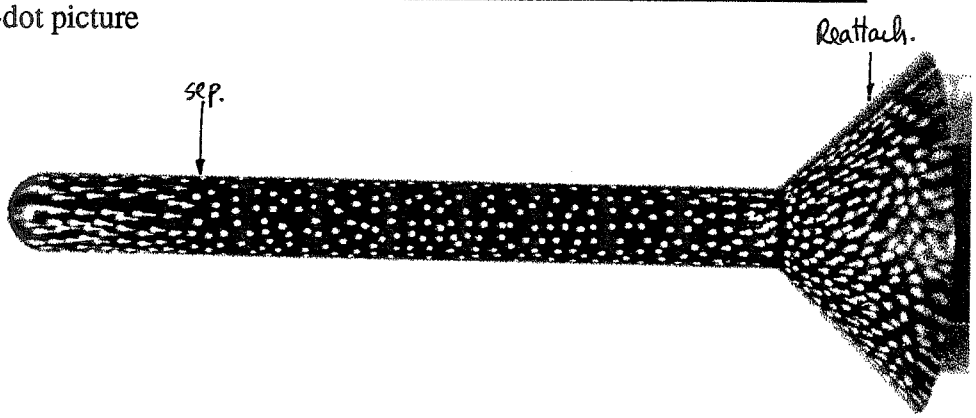

iii) pressure distribution

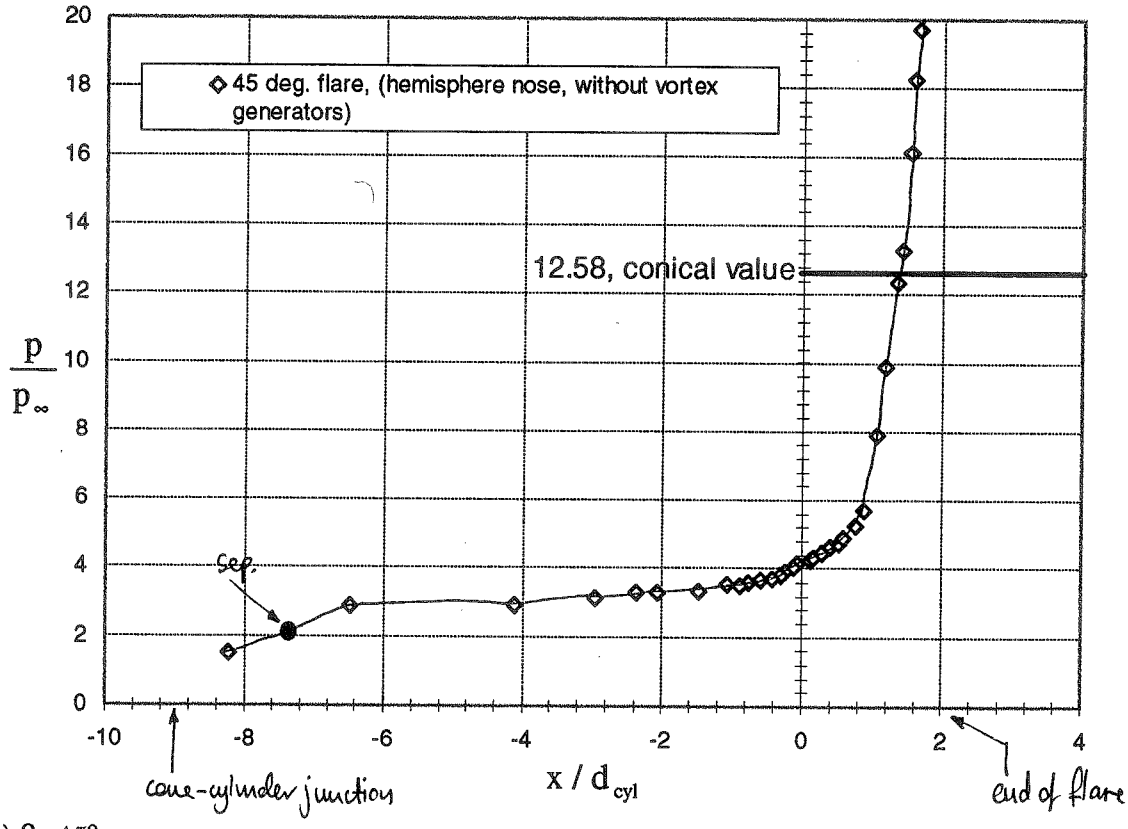

c) β=45°

Fig. 5.29 Concluded

a) $\beta=20^{o}$

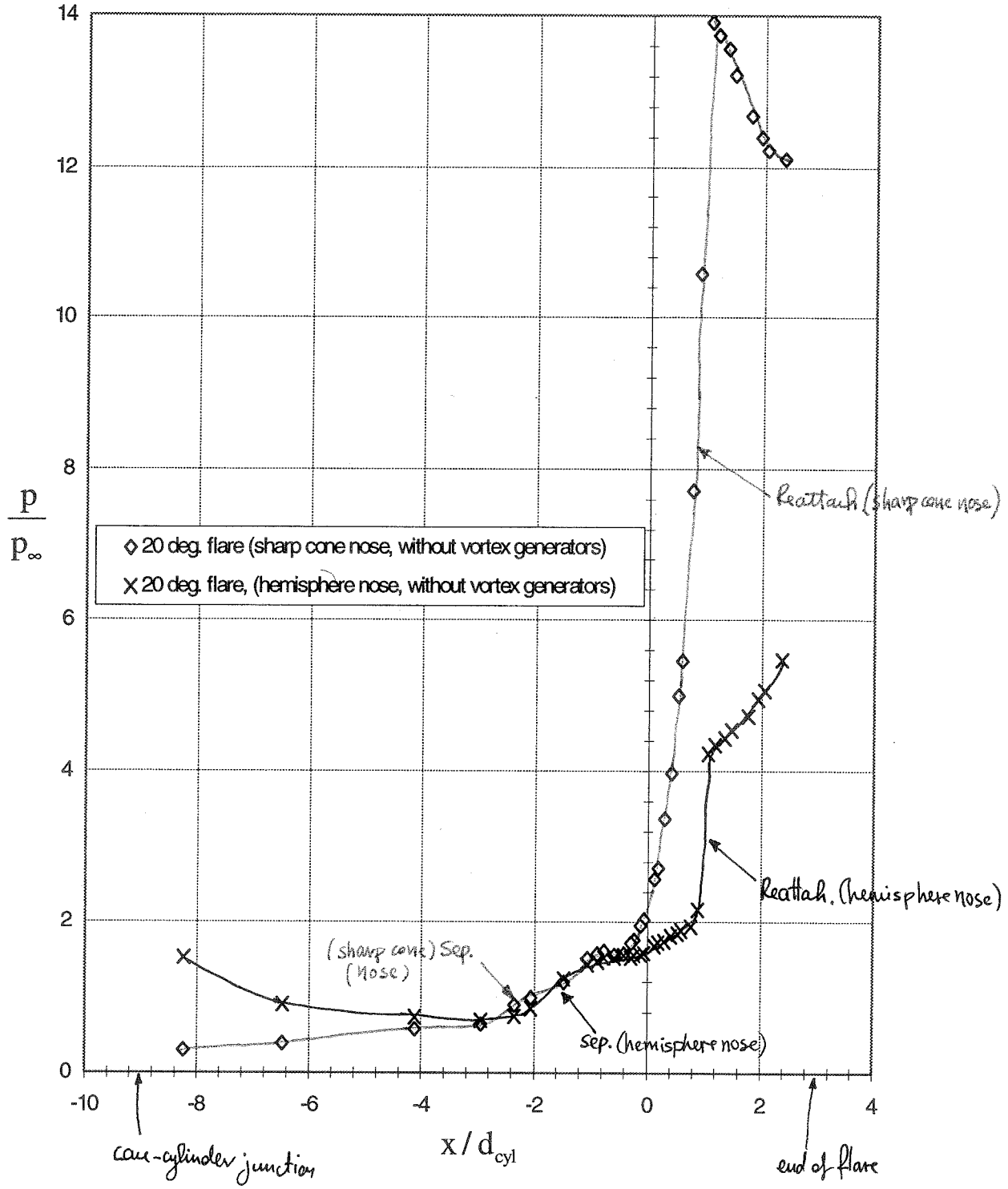

Fig. 5.30 The effect of hemisphere nose on the pressure distributions of control flare configurations (M_{∞}=8.2, Re_{∞}/cm=93000, laminar boundary layer)

b) $\beta=30^{\circ}$

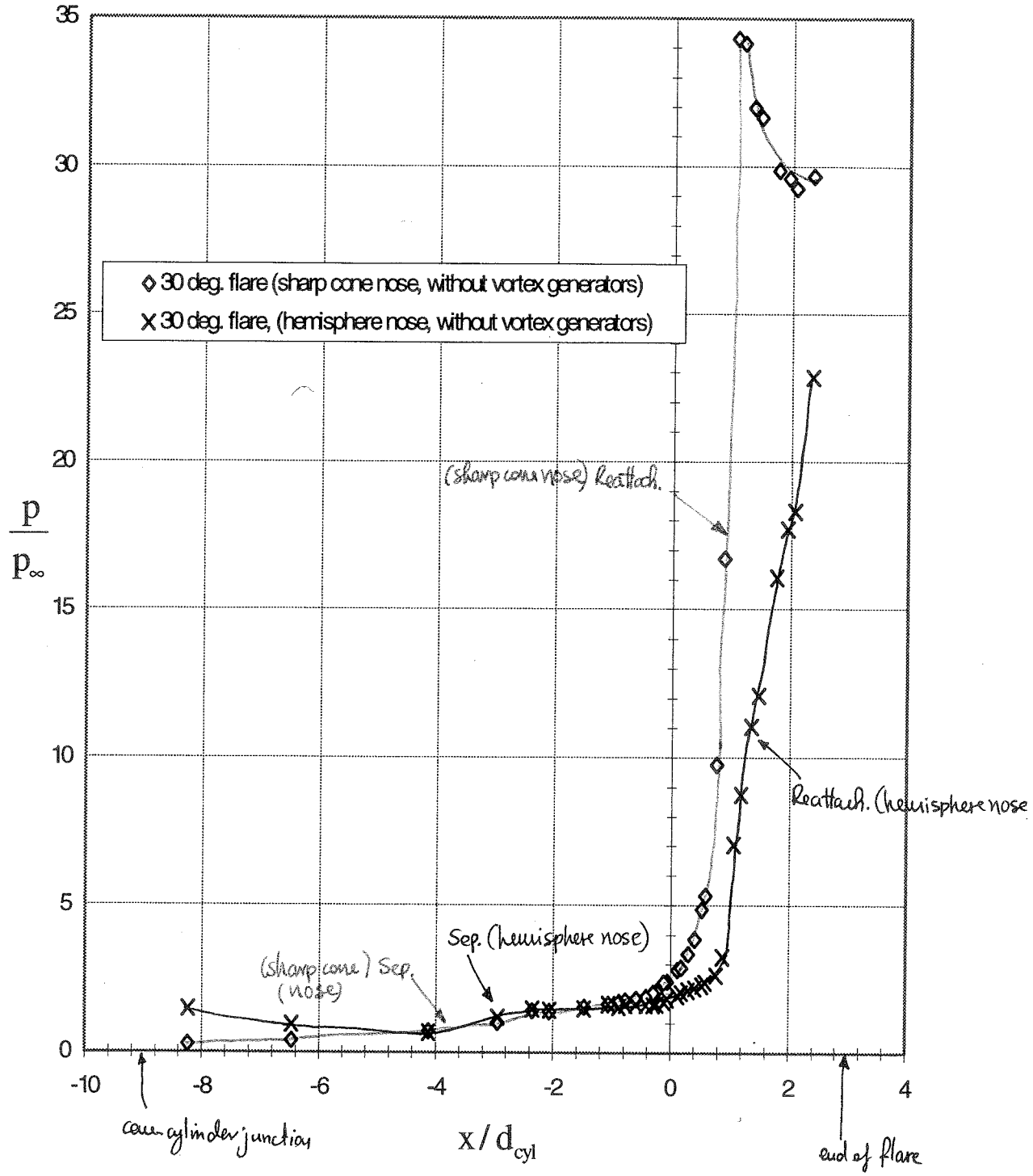

Fig. 5.30 Continue

c) β=45°

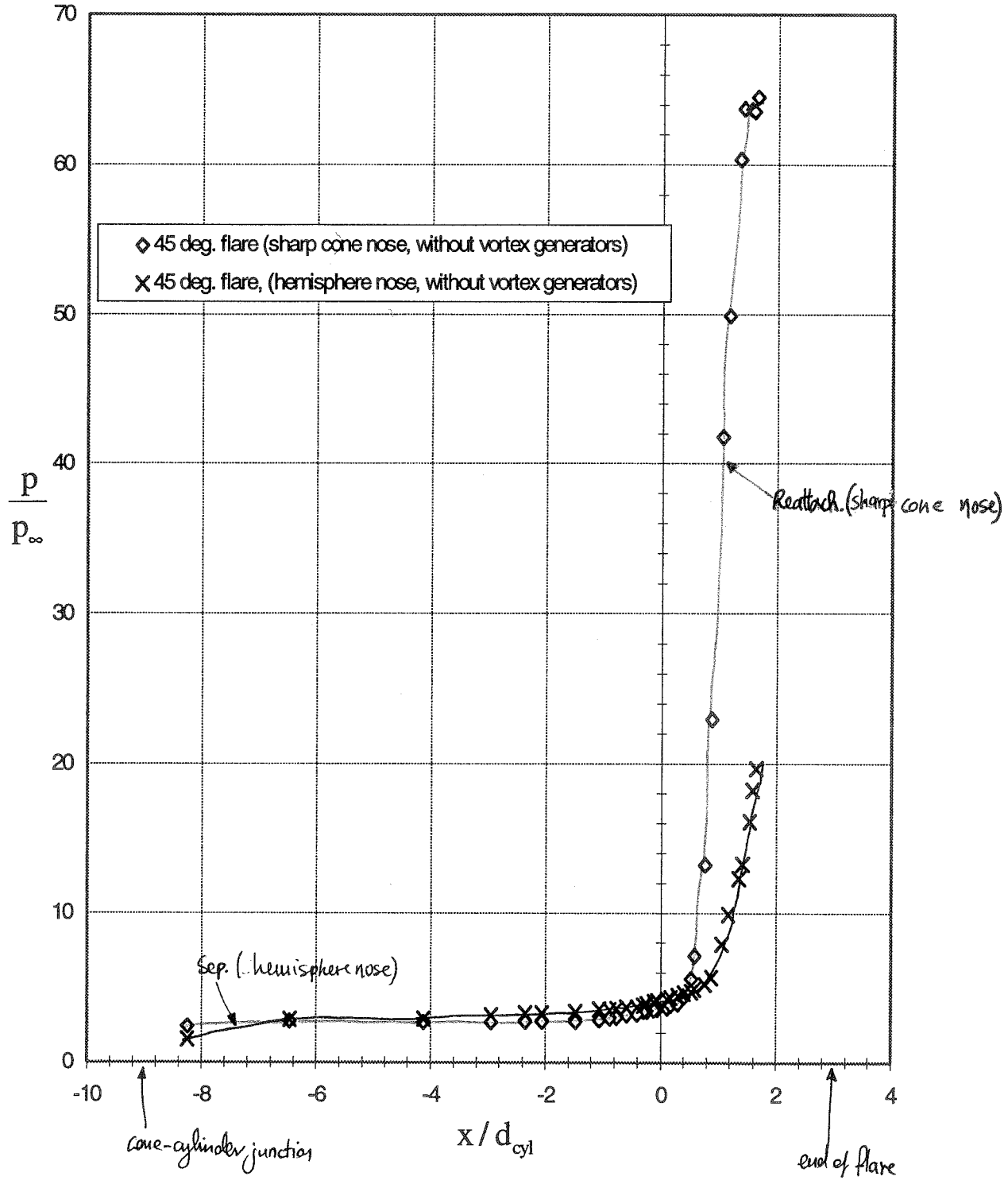

Fig. 5.30 Concluded

i) sharp cone nose cylinder

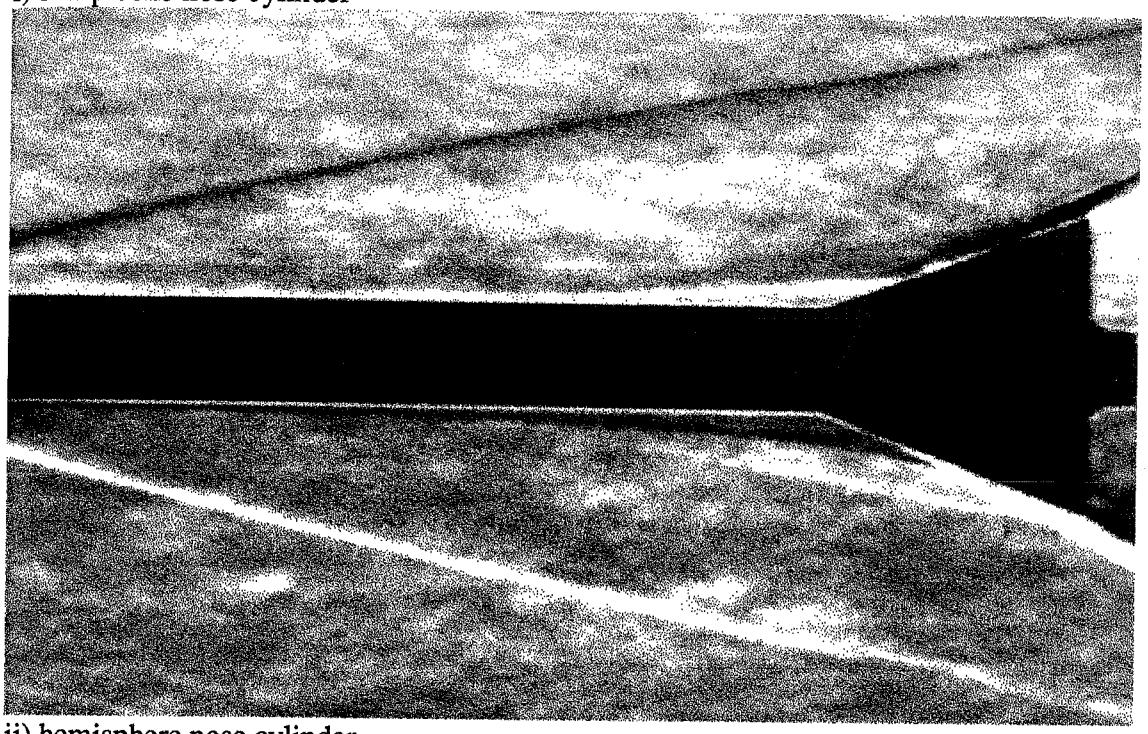

ii) hemisphere nose cylinder

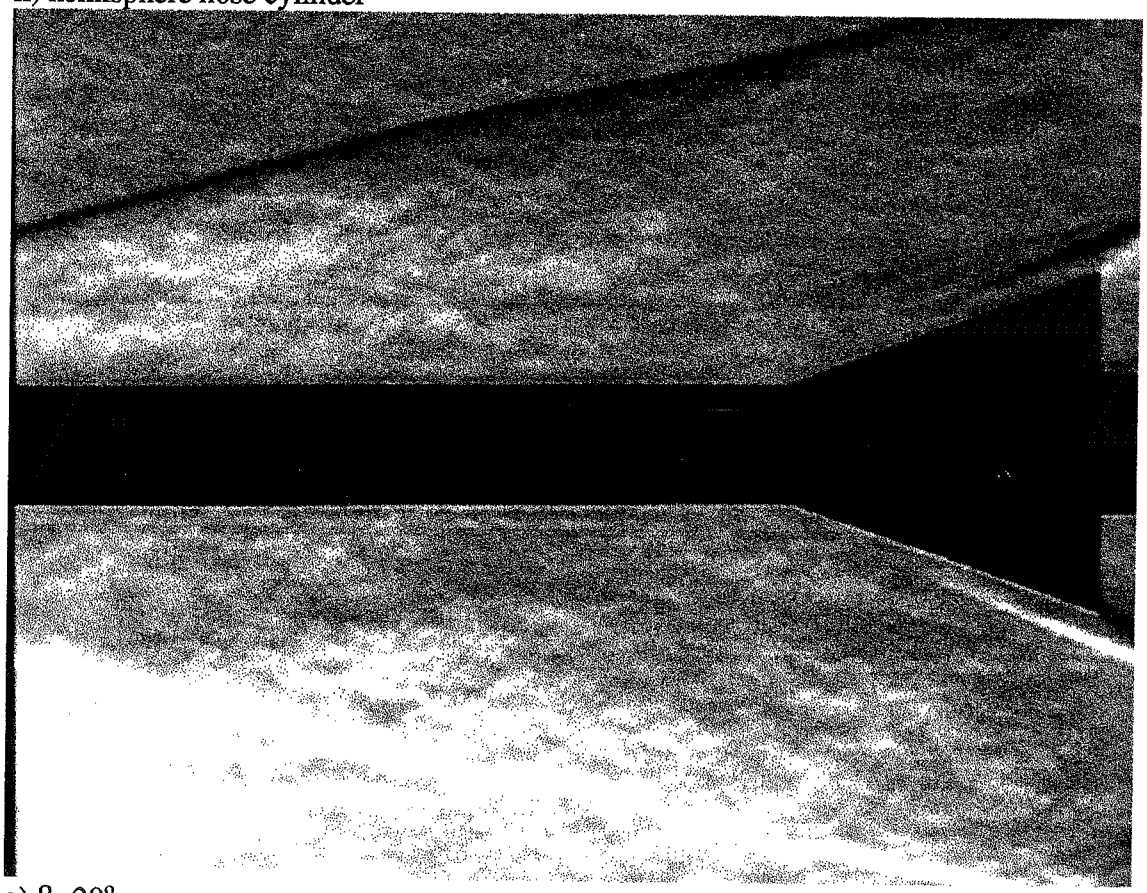

a) $\beta=20^{\circ}$

Fig. 5.31 The effect of hemisphere nose on the schlieren flow visualisation of control flare configurations ($M_{\infty}=8.2$, $Re_{\infty}/cm=93000$, laminar boundary layer)

i) sharp cone nose cylinder

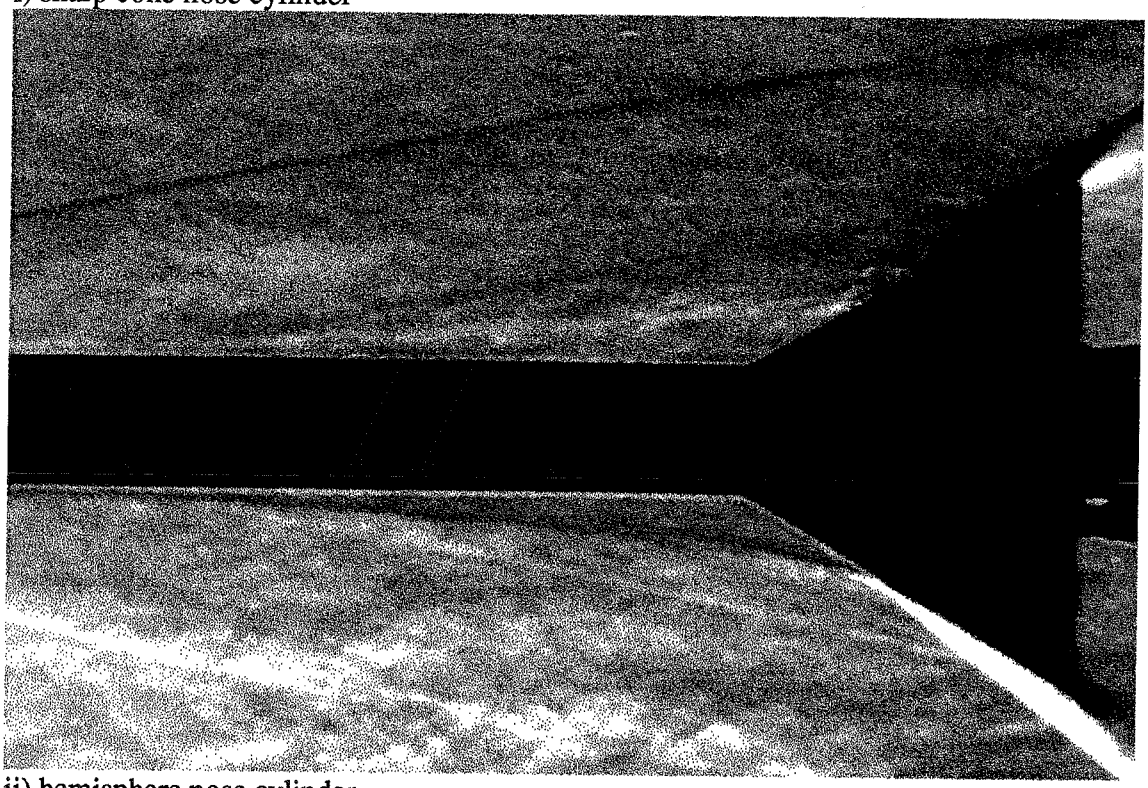

ii) hemisphere nose cylinder

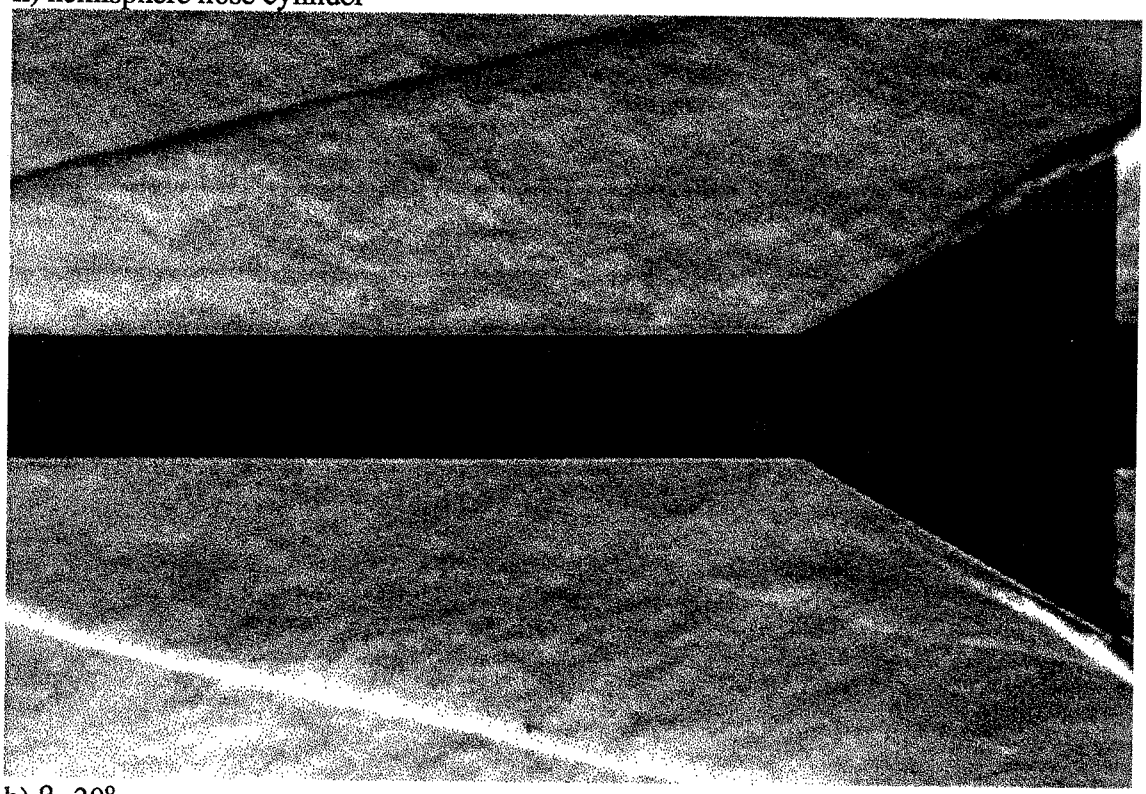

b) $\beta=30^{\circ}$

Fig. 5.31 Continue

i) sharp cone nose cylinder

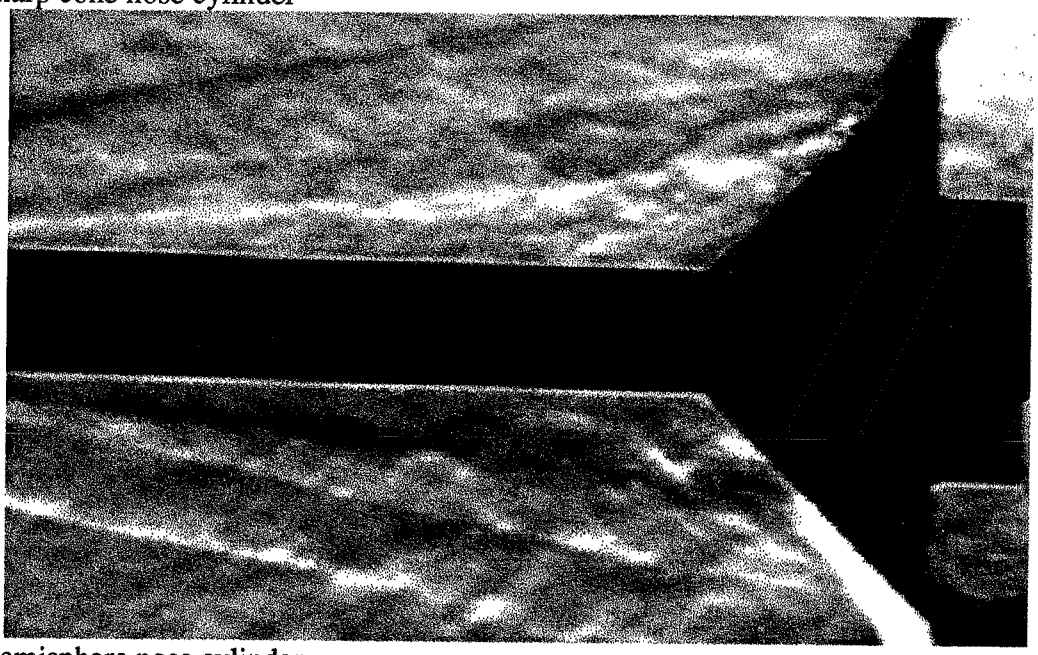

ii) hemisphere nose cylinder

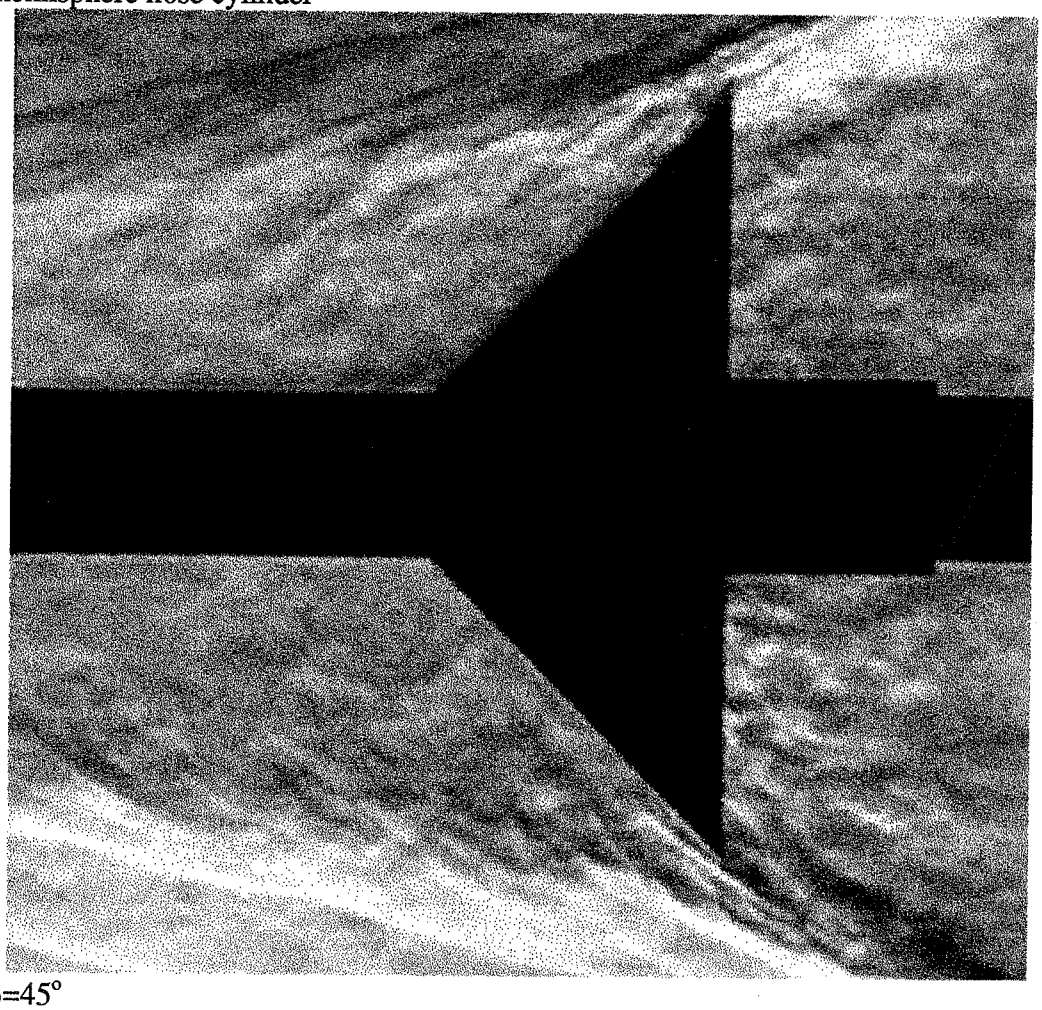

c) β=45°

Fig. 5.31 Concluded

i) sharp cone nose cylinder

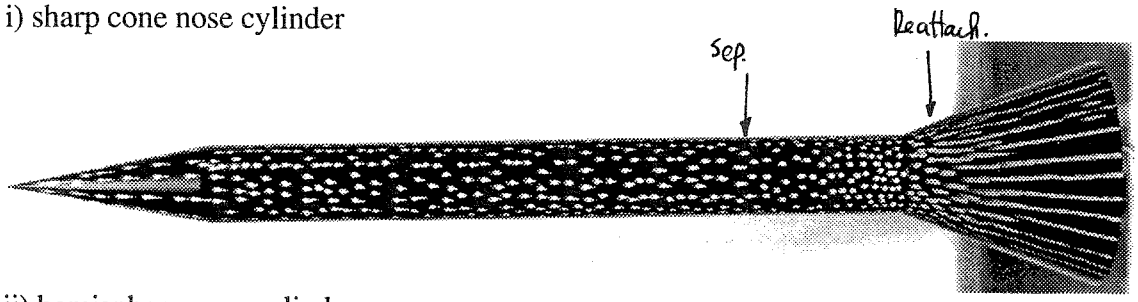

ii) hemisphere nose cylinder

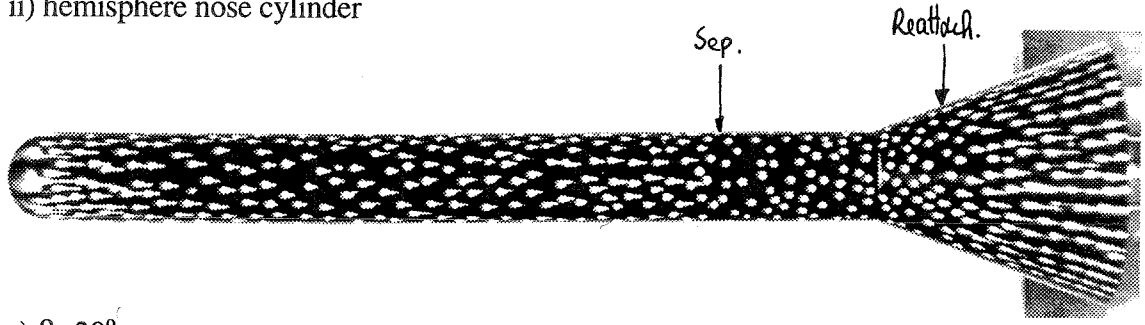

a) $\beta=20^{o}$

i) sharp cone nose cylinder

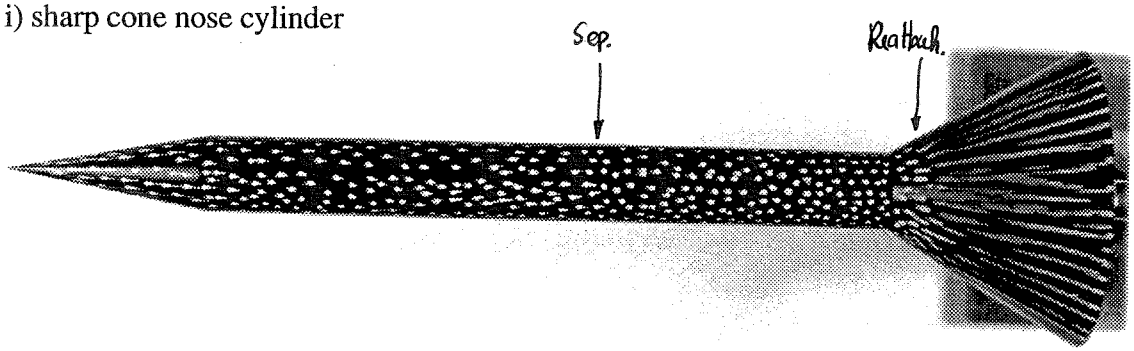

ii) hemisphere nose cylinder

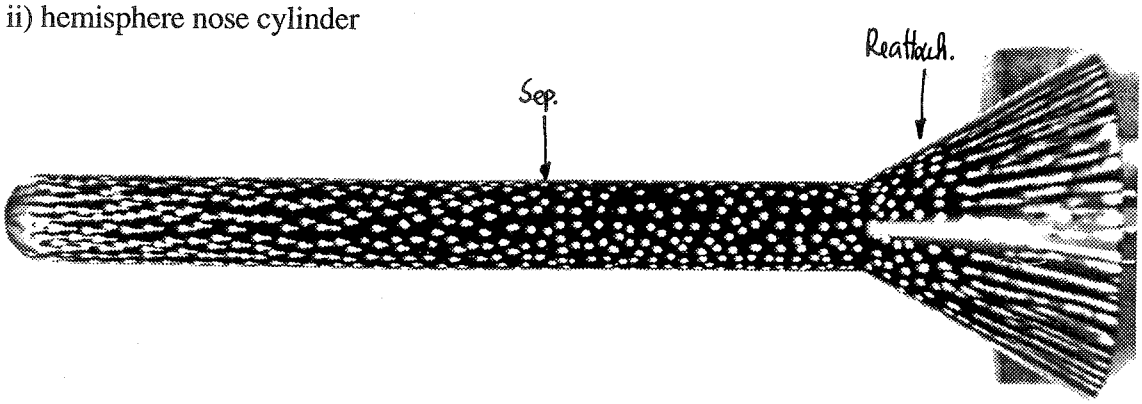

b) $\beta=30^{o}$

Note: not same scale

Fig. 5.32 The effect of hemisphere nose on the oil-dot flow visualisation of control flare configurations ($M_{\infty}=8.2$, $Re_{\infty}/cm=93000$, laminar boundary layer)

i) sharp cone nose cylinder

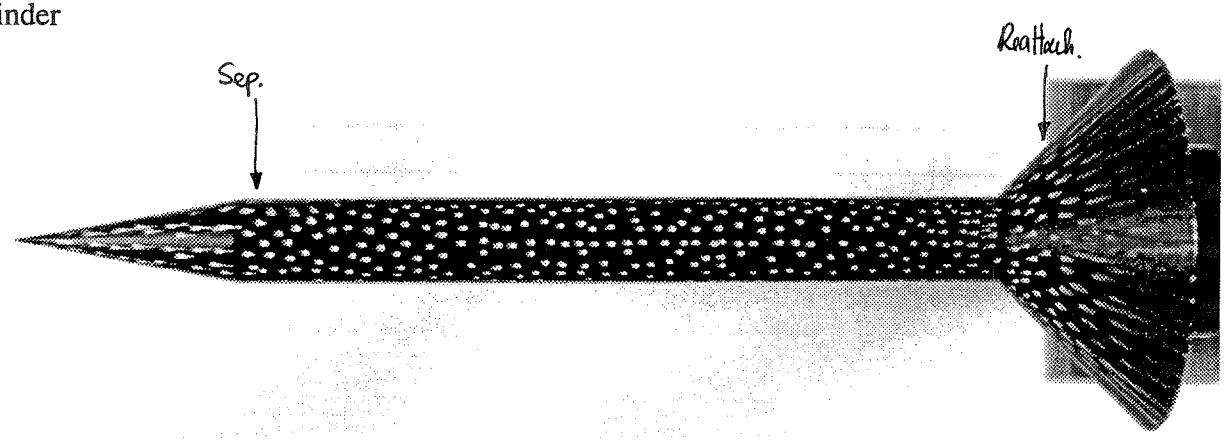

ii) hemisphere nose cylinder

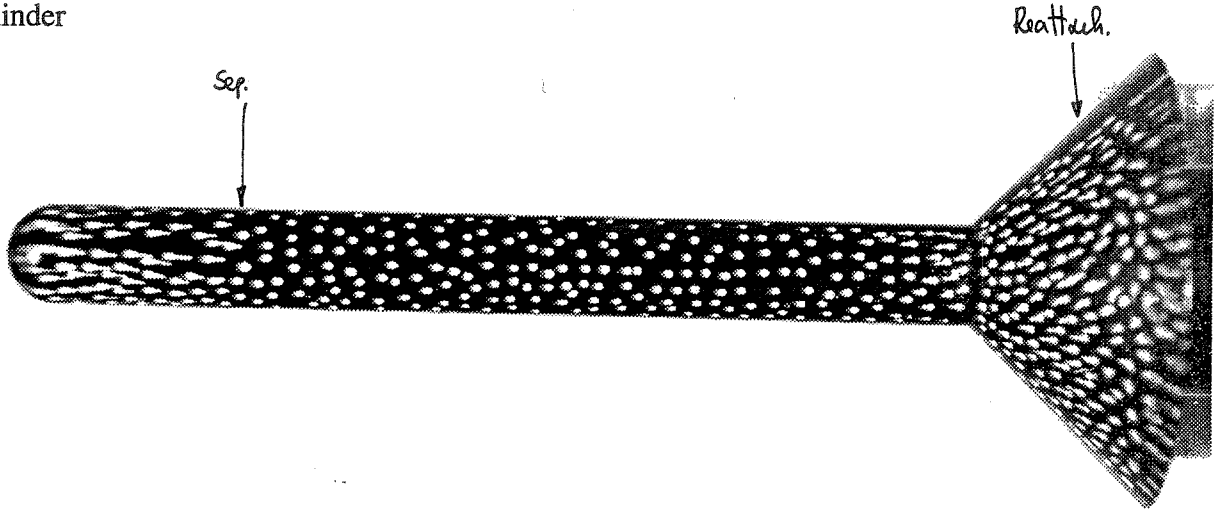

c) $\beta=45^{\circ}$

Fig. 5.32 Concluded

i) sharp cone nose cylinder

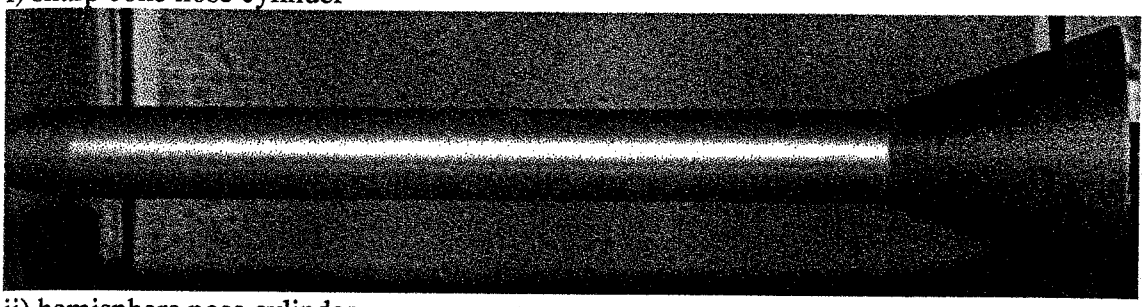

ii) hemisphere nose cylinder

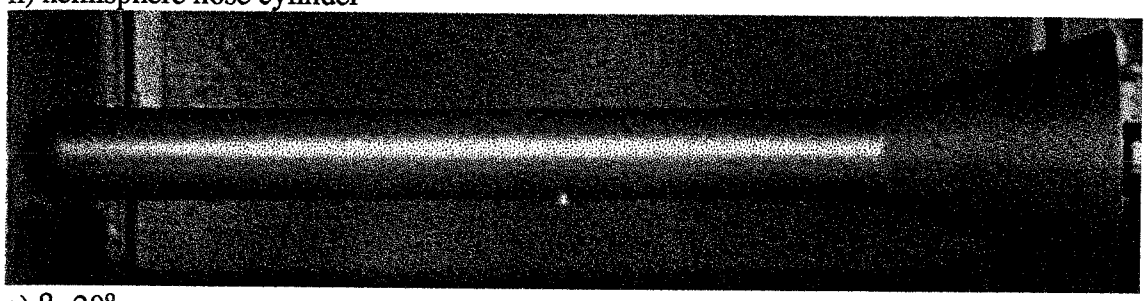

a) β=20°

i) sharp cone nose cylinder

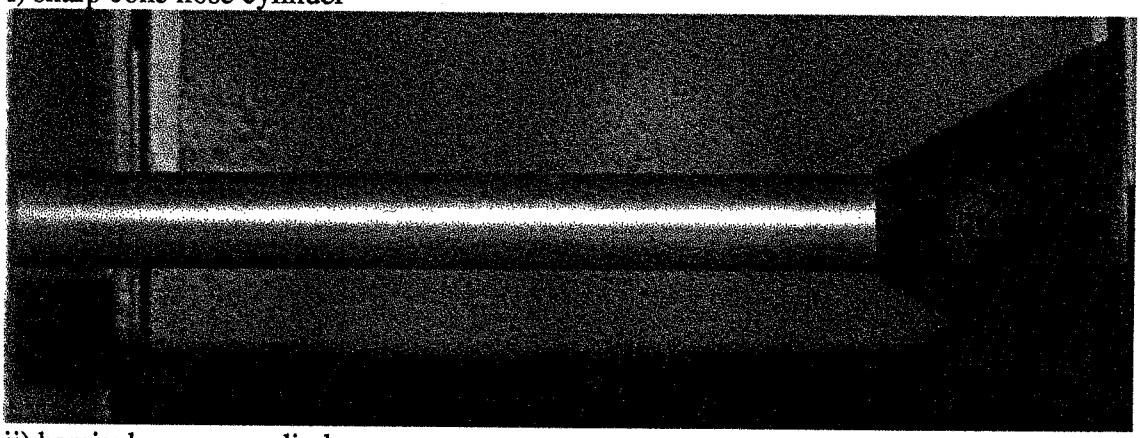

ii) hemisphere nose cylinder

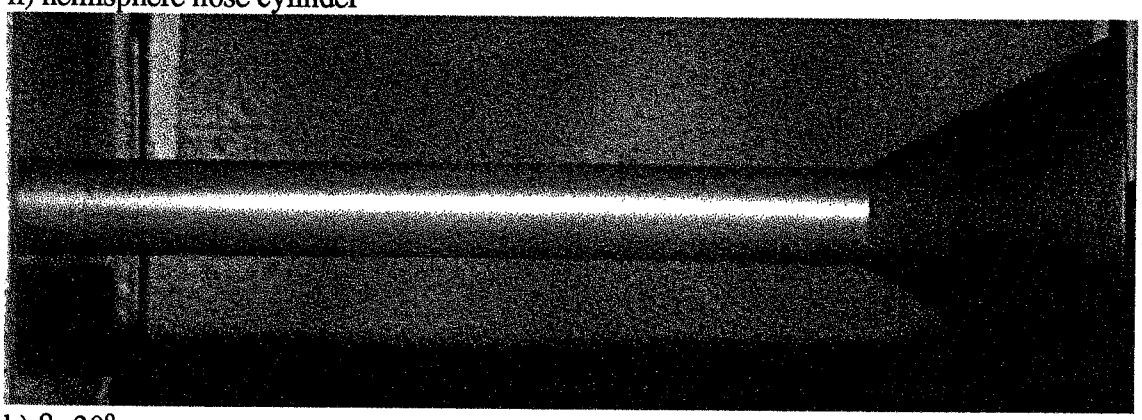

b) β=30°

Fig. 5.33 The effect of hemisphere nose on the liquid-crystal flow visualisation of control flare configurations (M_∞=8.2, Re_∞/cm=93000, laminar boundary layer)

i) sharp cone nose cylinder

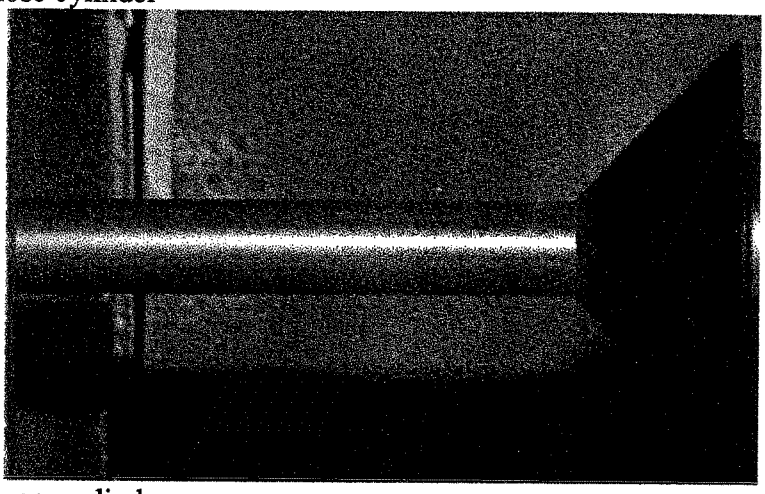

ii) hemisphere nose cylinder

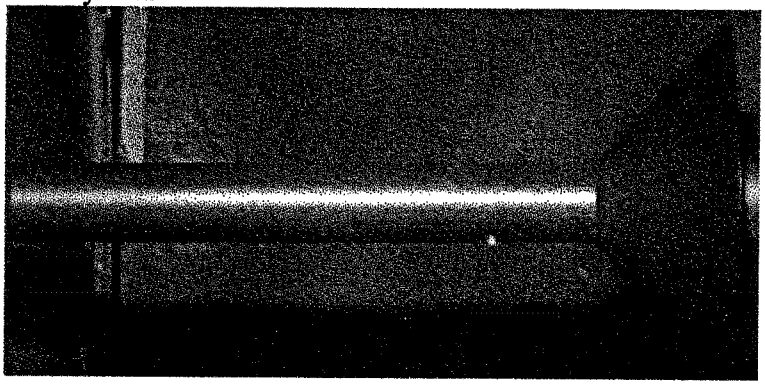

c) β=45°

Fig. 5.33 Concluded

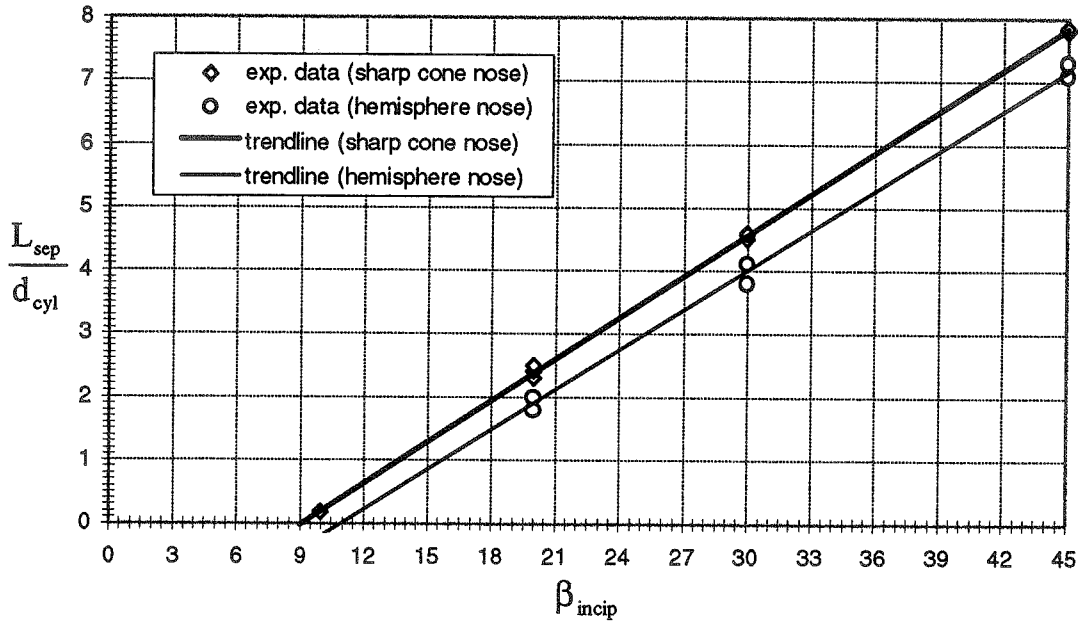

Fig. 5.34 Determination of incipient separation angle (laminar boundary layer, hemisphere nose)

a)

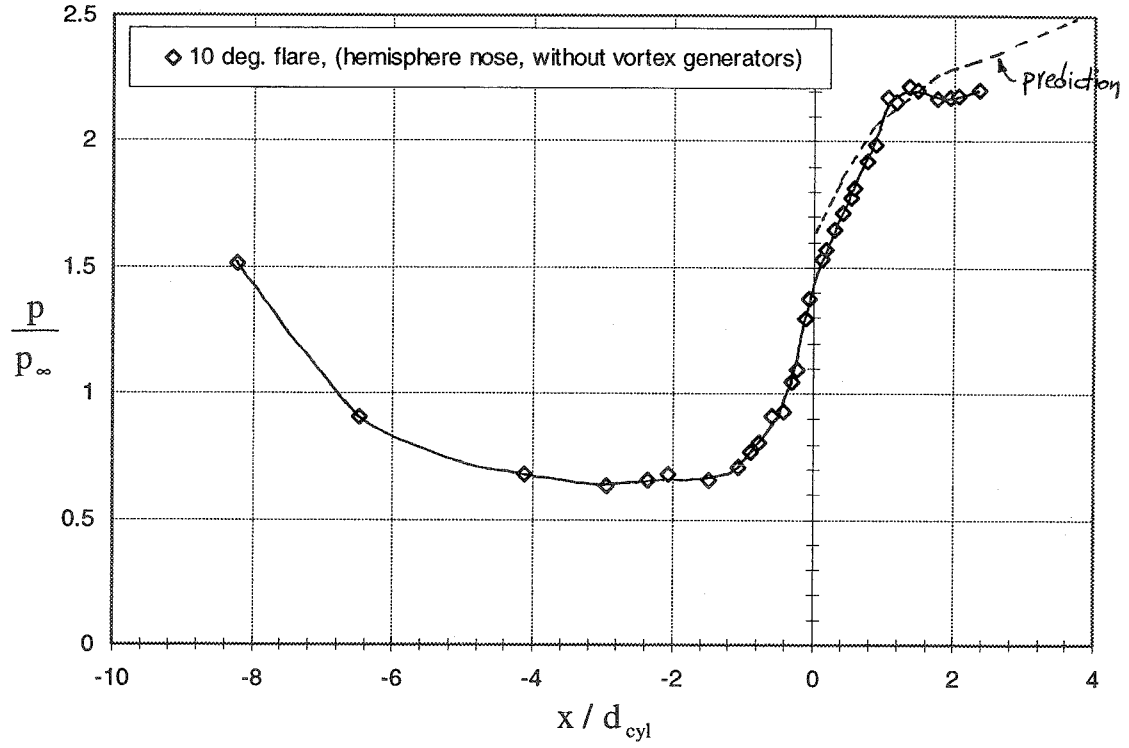

b)

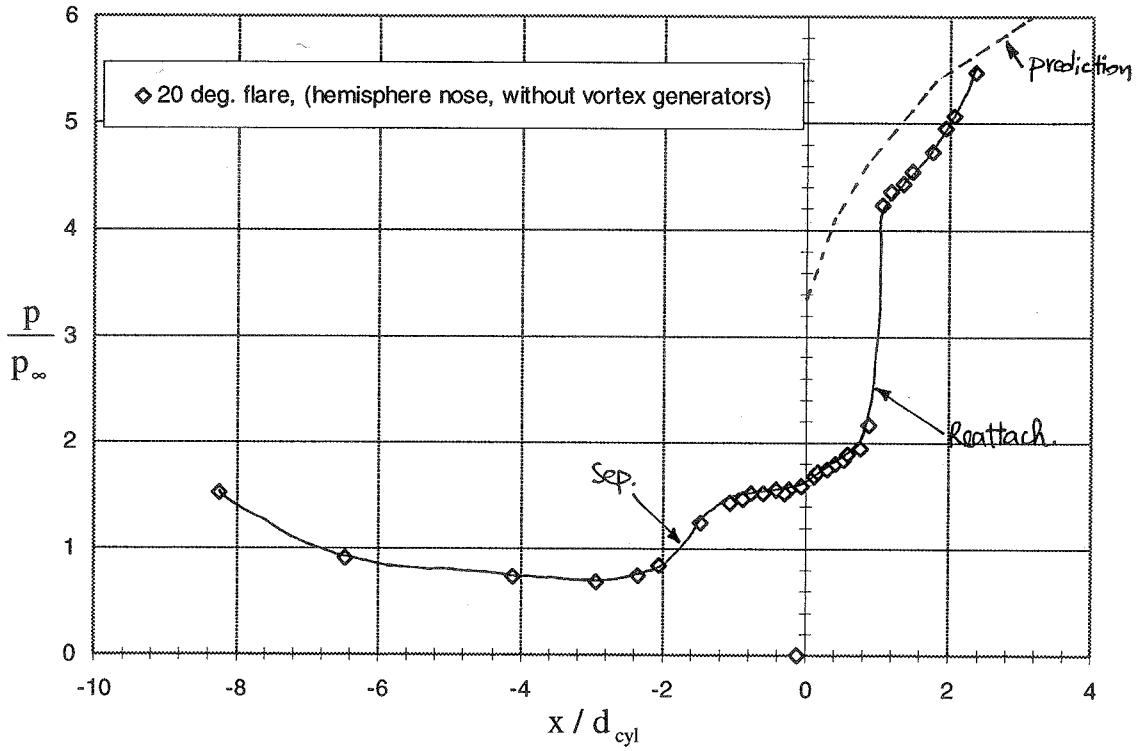

Fig. 5.35 The effect of entropy layer Mach shear interaction on the flare pressure distribution (M_∞=8.2, Re_∞/cm=93000, laminar boundary layer, hemisphere nose)

c)

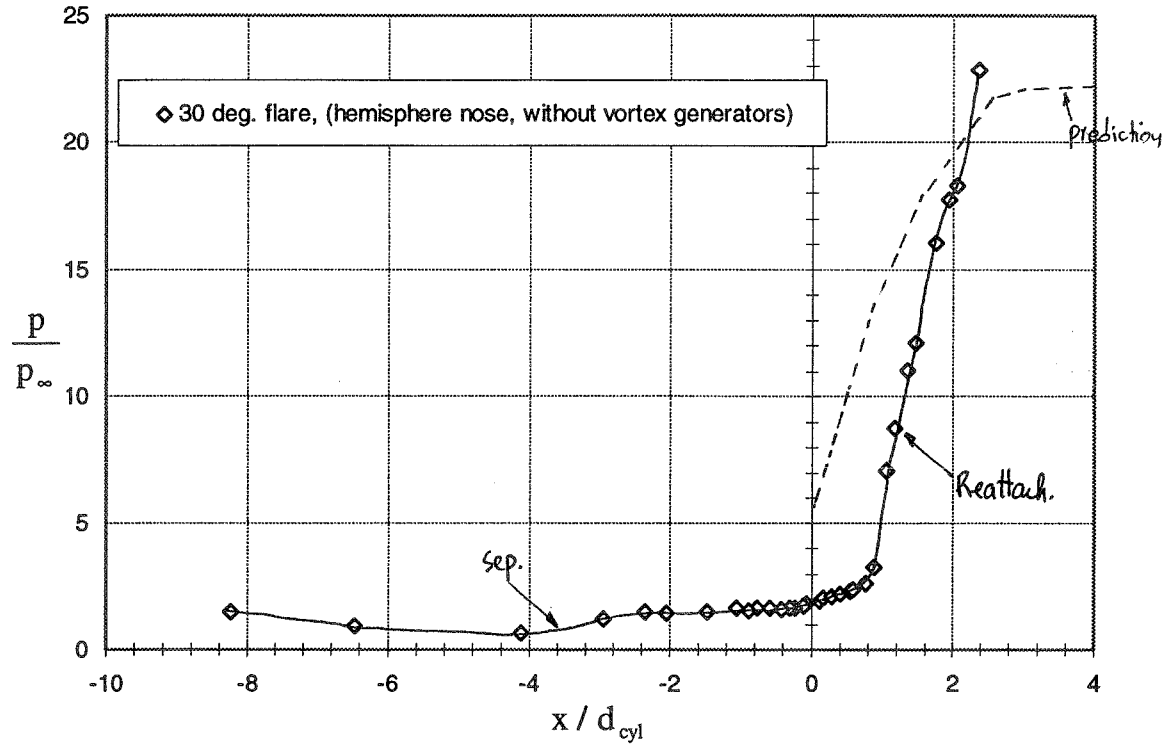

Fig. 5.35 Concluded

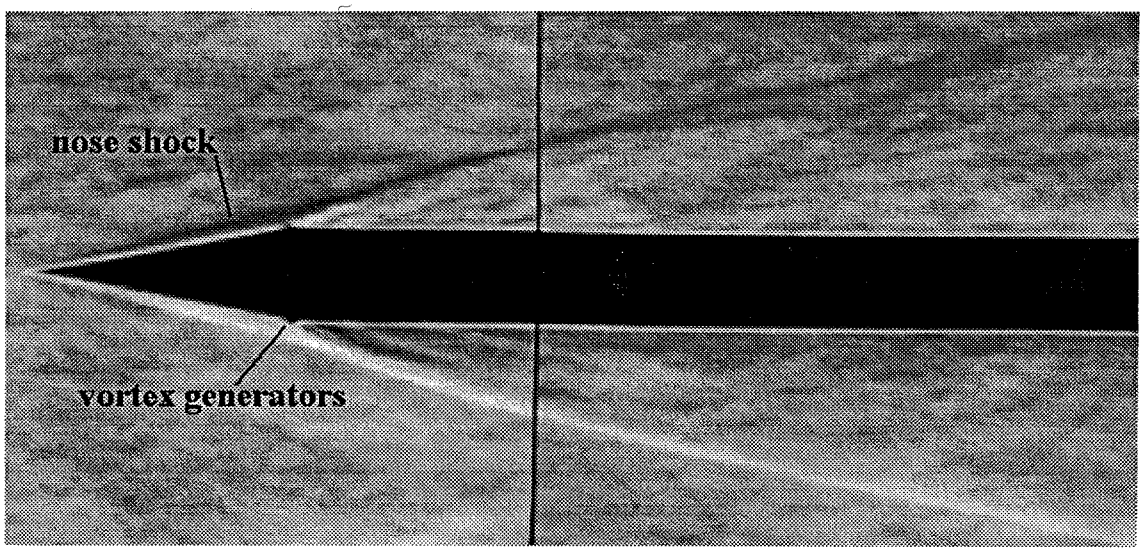

Fig. 5.36 Schlieren photo of the sharp cone cylinder (M_∞=8.2, Re_∞/cm=93000, turbulent boundary layer)

a) sharp cone nose cylinder, without vortex generators

b) sharp cone nose cylinder, with vortex generators

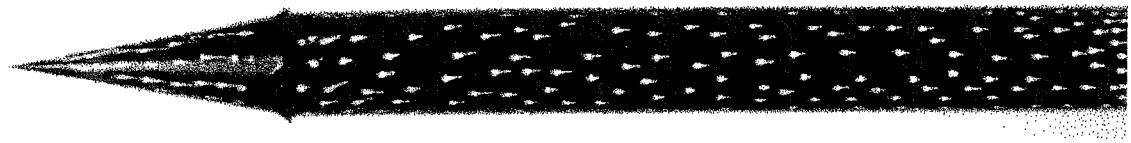

Fig. 5.37 The effect of turbulent boundary layer on the oil-dot flow visualisation of the sharp cone cylinder (M_∞=8.2, Re_∞/cm=93000)

a) sharp cone nose cylinder, without vortex generators

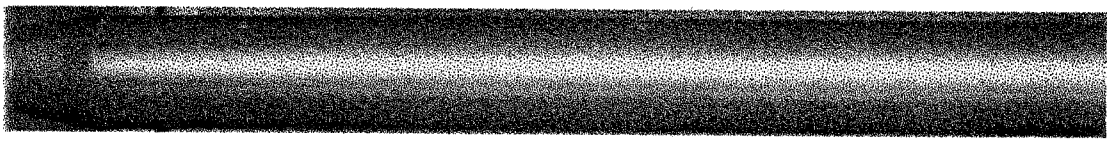

b) sharp cone nose cylinder, with vortex generators

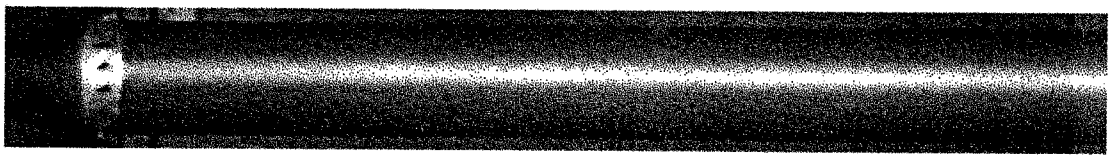

Fig. 5.38 The effect of turbulent boundary layer on the liquid-crystal flow visualisation of the sharp cone cylinder (M_∞=8.2, Re_∞/cm=93000)

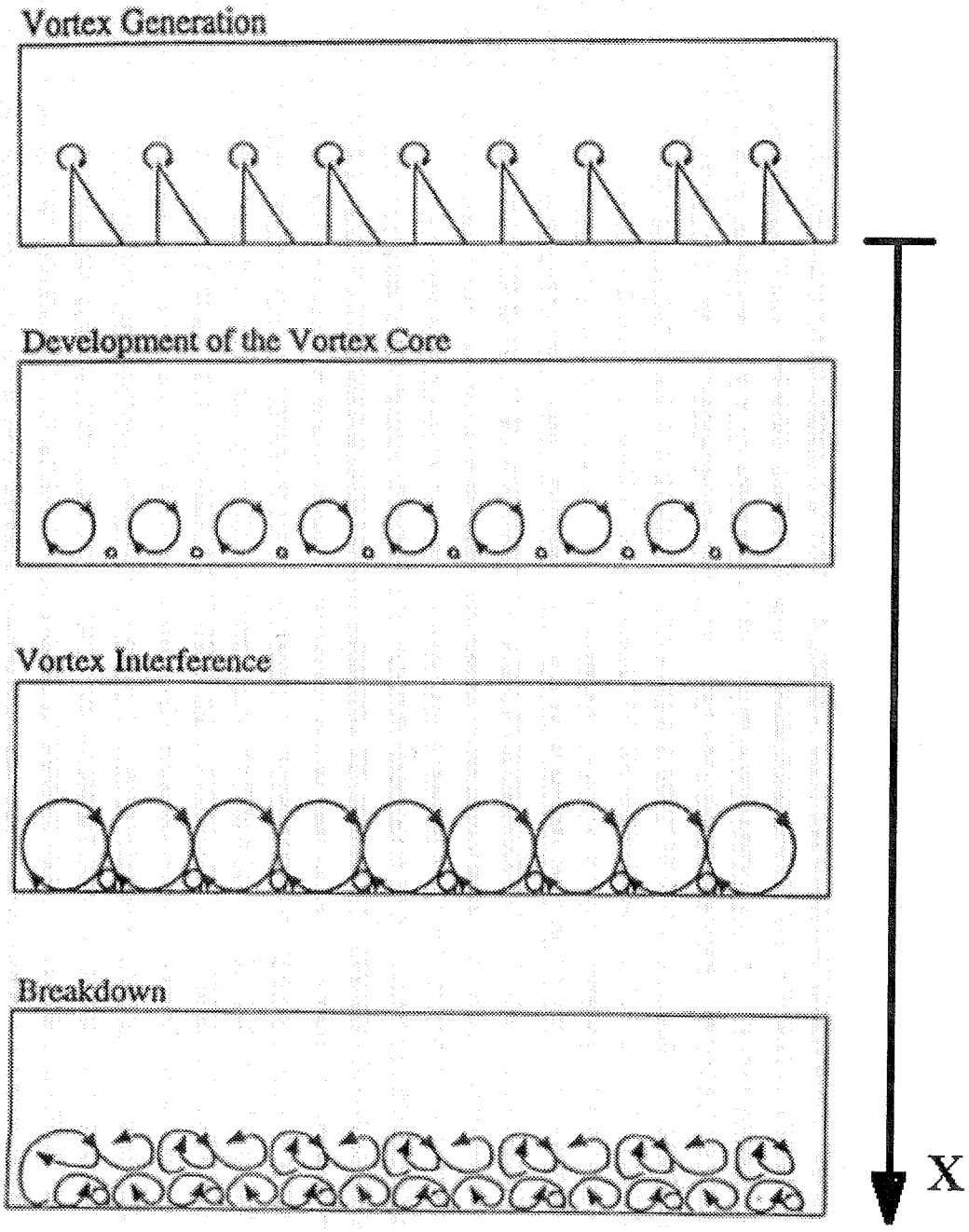

Fig. 5.39 The progress of vortex development and final break down (ref. 187)

i) schlieren picture

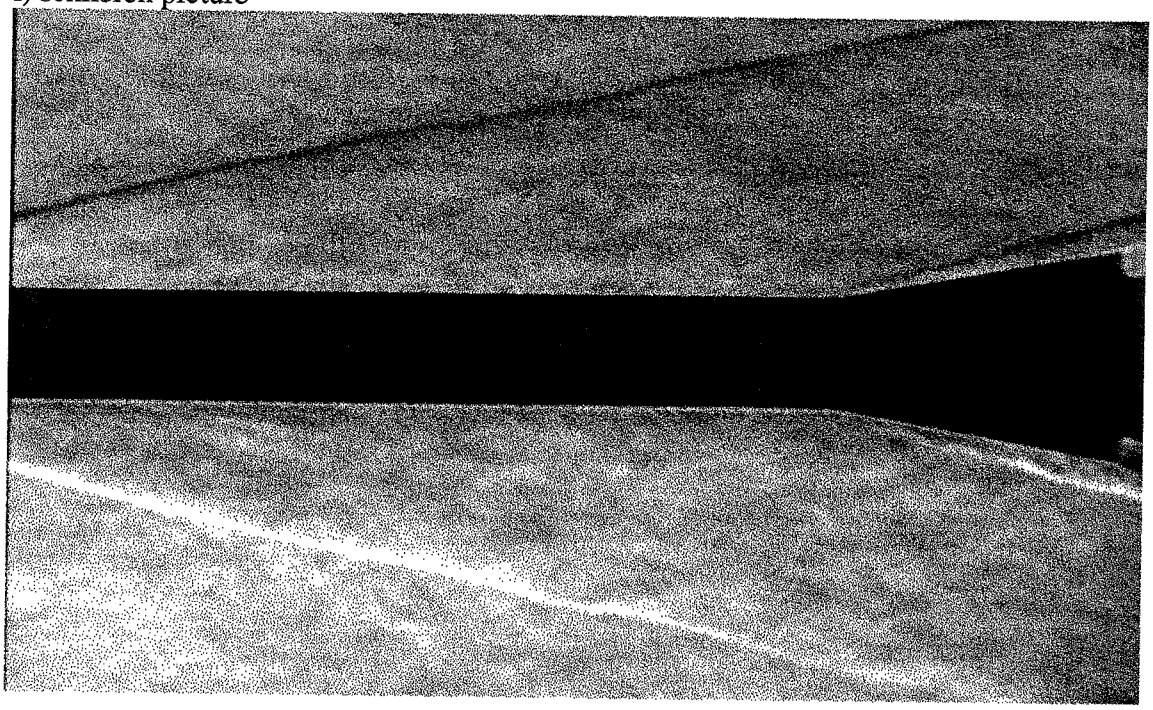

ii) liquid crystal picture

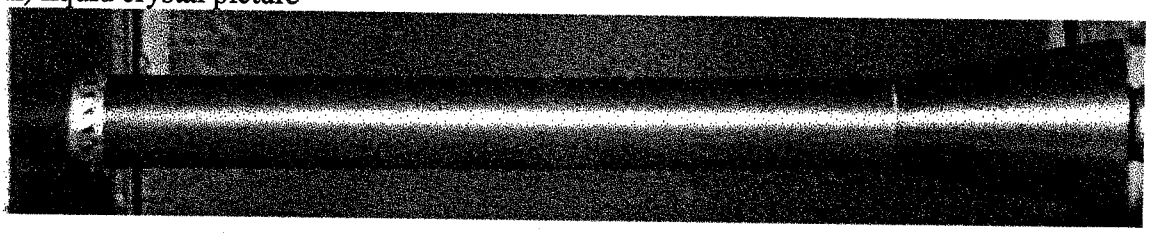

iii) oil-dot picture

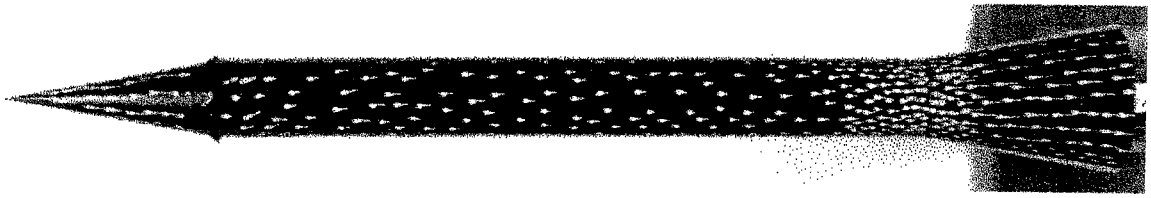

a) $\beta=10°$

Fig. 5.40 Schlieren, liquid-crystal and oil-dot flow visualisation and pressure measurements on sharp cone nose control flare configurations ($M_\infty=8.2$, $Re_\infty/cm=93000$, $L_{cyl}=15.3$ cm, turbulent boundary layer)

iv) pressure distribution

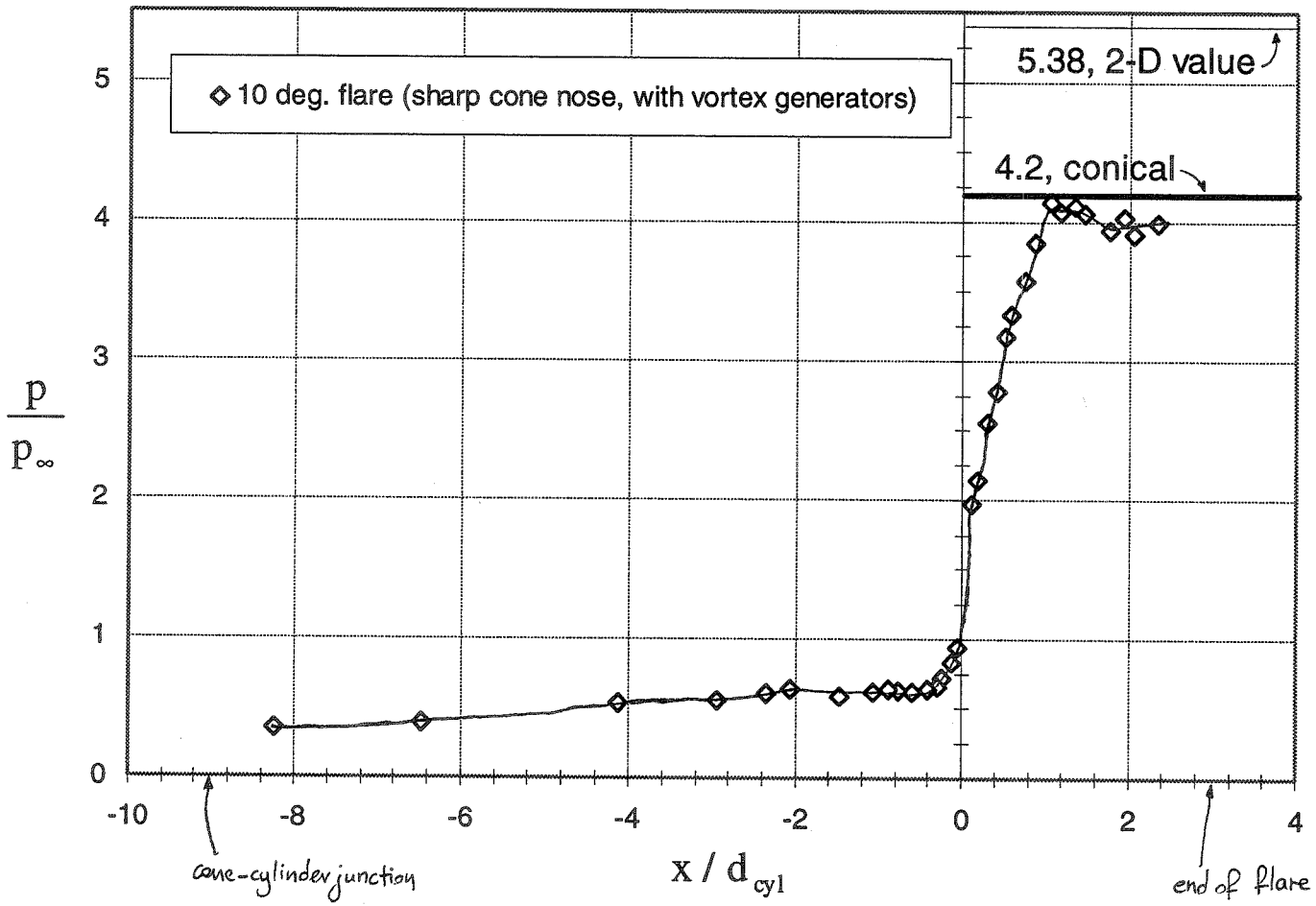

a) $\beta=10^{\circ}$

Fig. 5.40 Continue

i) schlieren picture

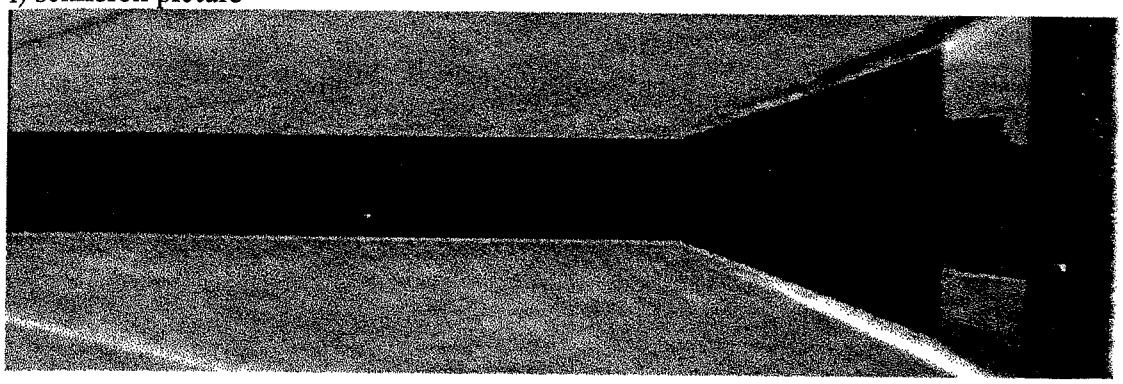

ii) liquid crystal picture

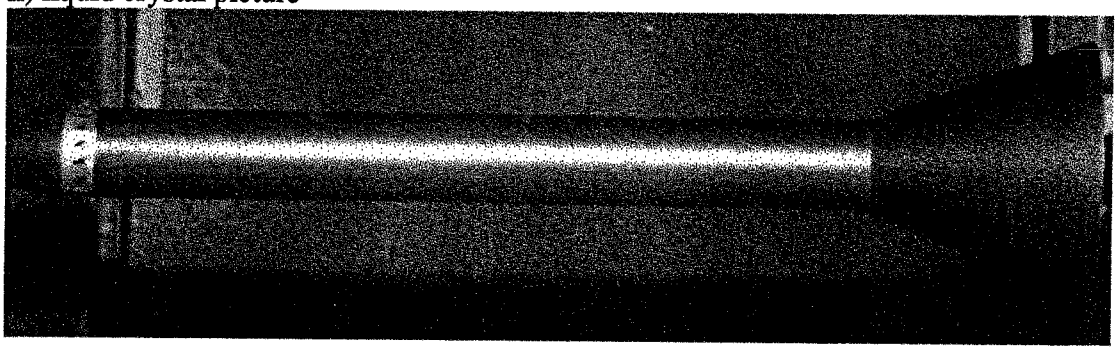

iii) oil-dot picture

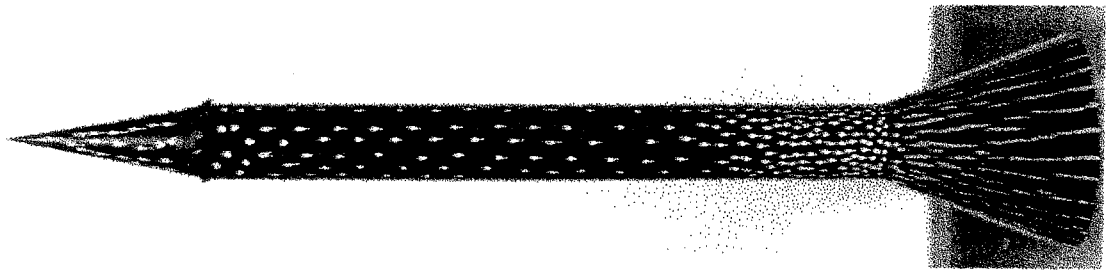

b) β=20°

Fig. 5.40 Continue

iv) pressure distribution

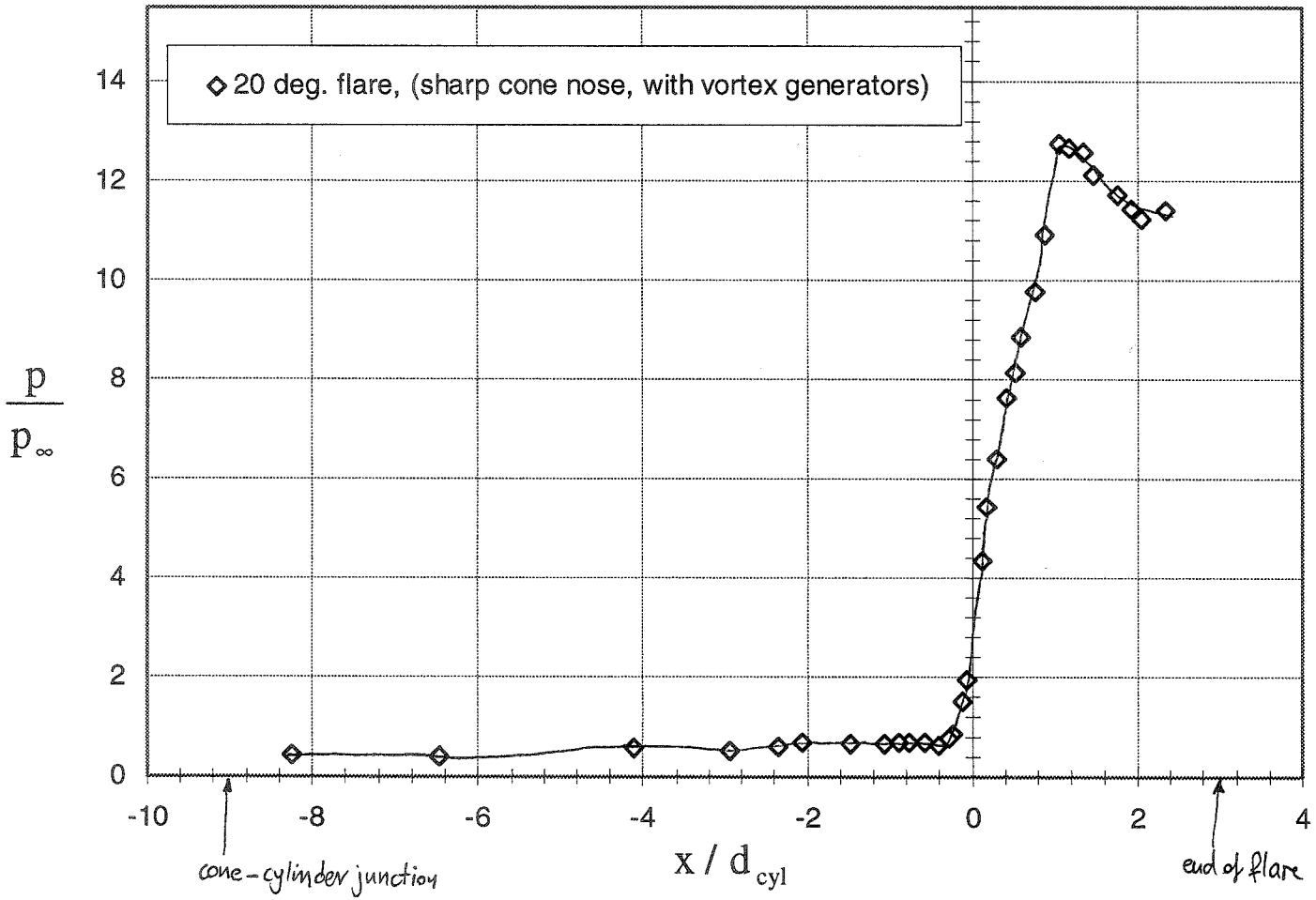

b) $\beta=20^{\circ}$

Fig. 5.40 Continue

i) schlieren picture

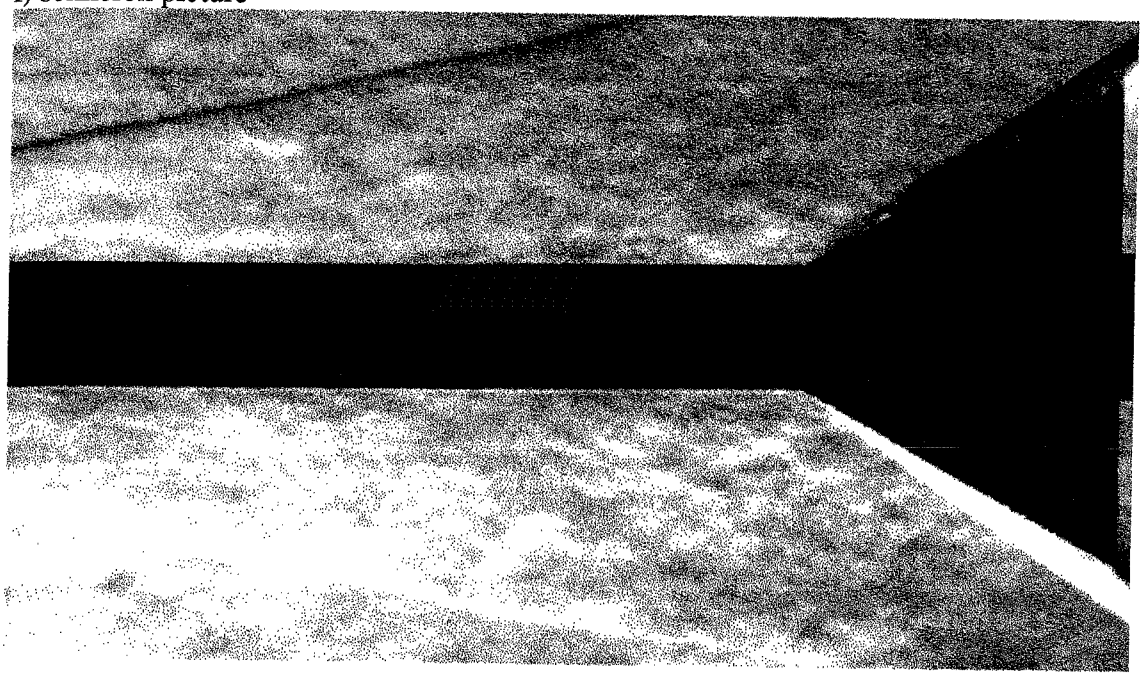

ii) liquid crystal picture

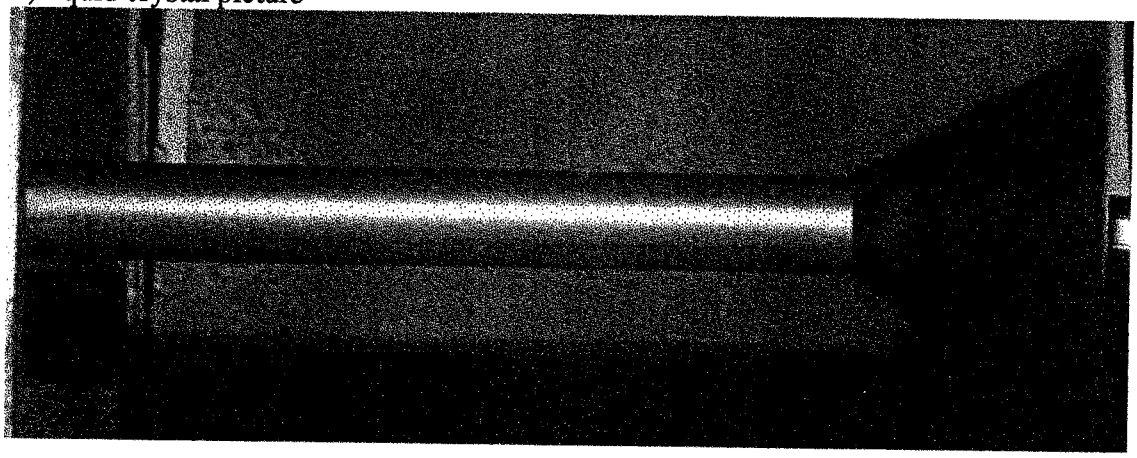

iii) oil-dot picture

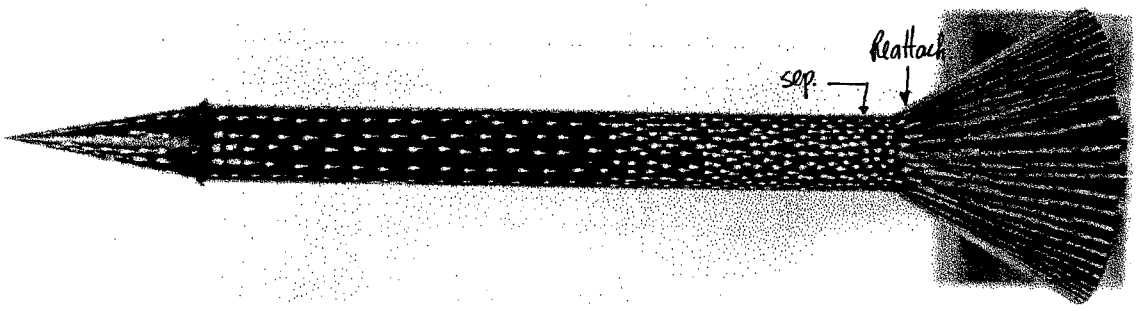

c) β=30°

Fig. 5.40 Continue

iv) pressure distribution

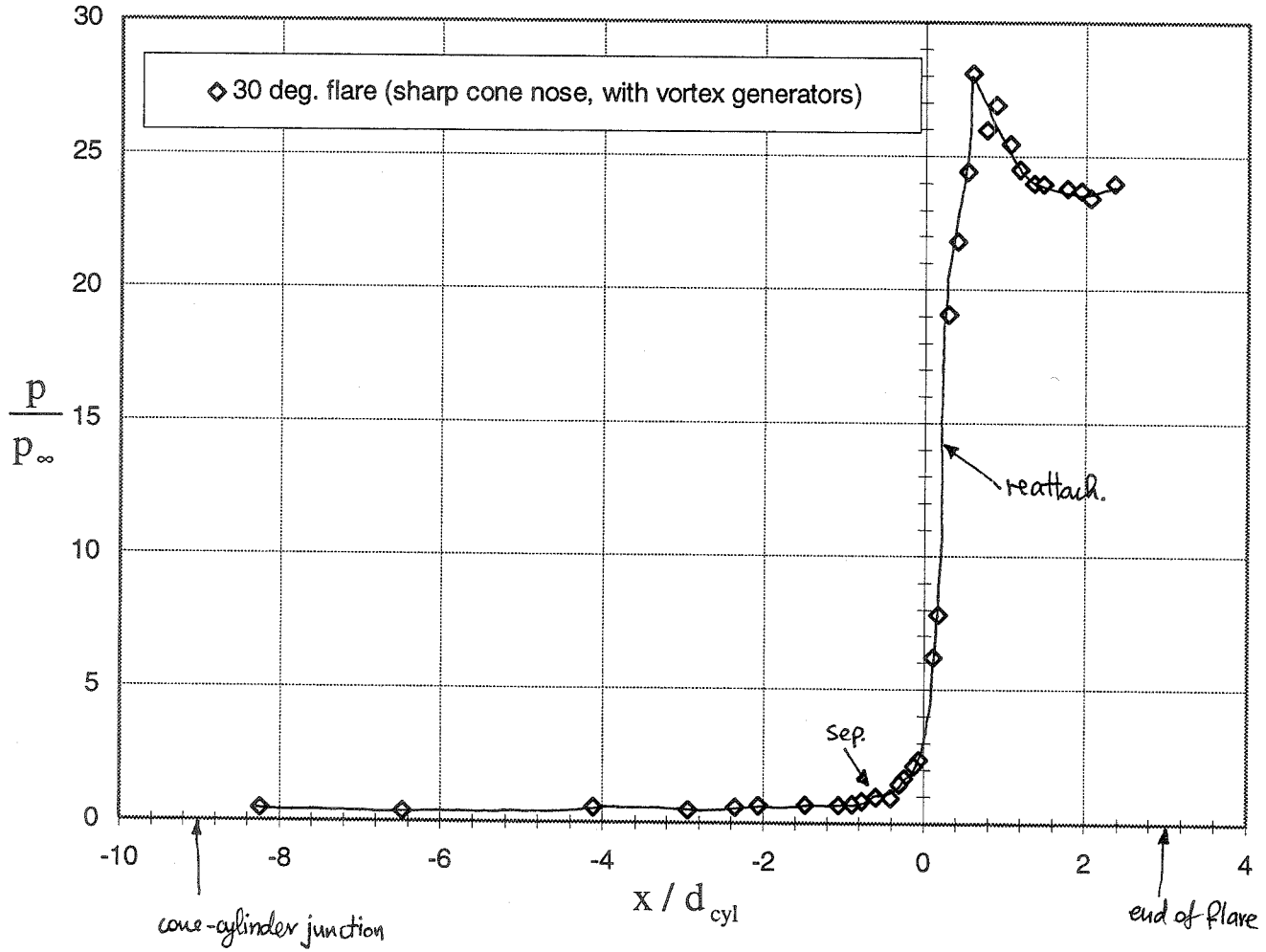

c) $\beta=30^{\circ}$

Fig. 5.40 Continue

i) schlieren picture

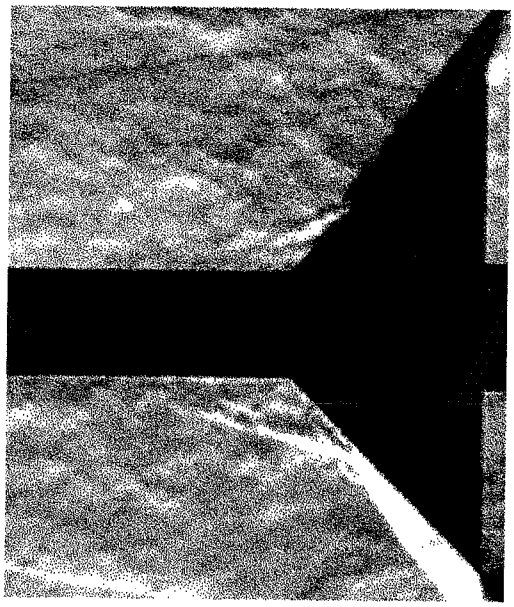

ii) liquid crystal picture

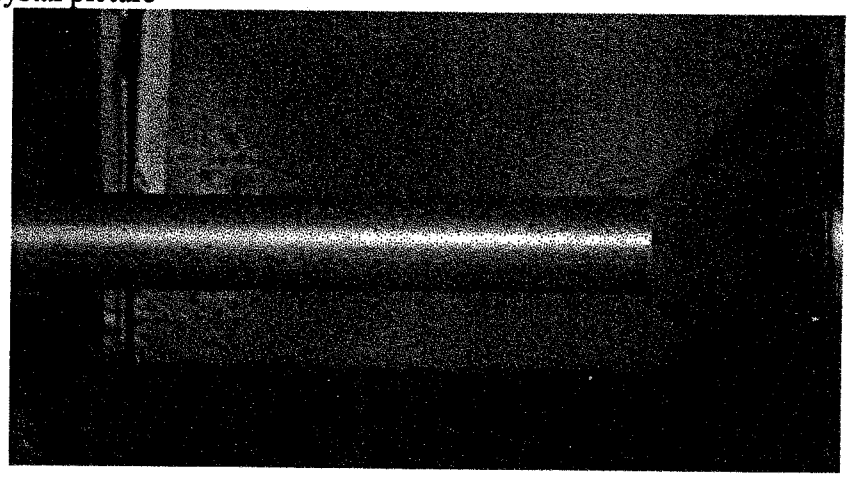

iii) oil-dot picture

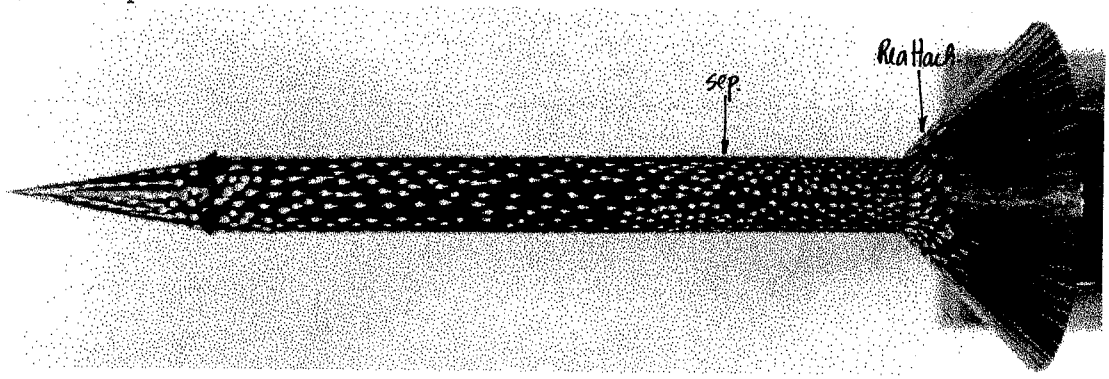

d) β=45°

Fig. 5.40 Continue

iv) pressure distribution

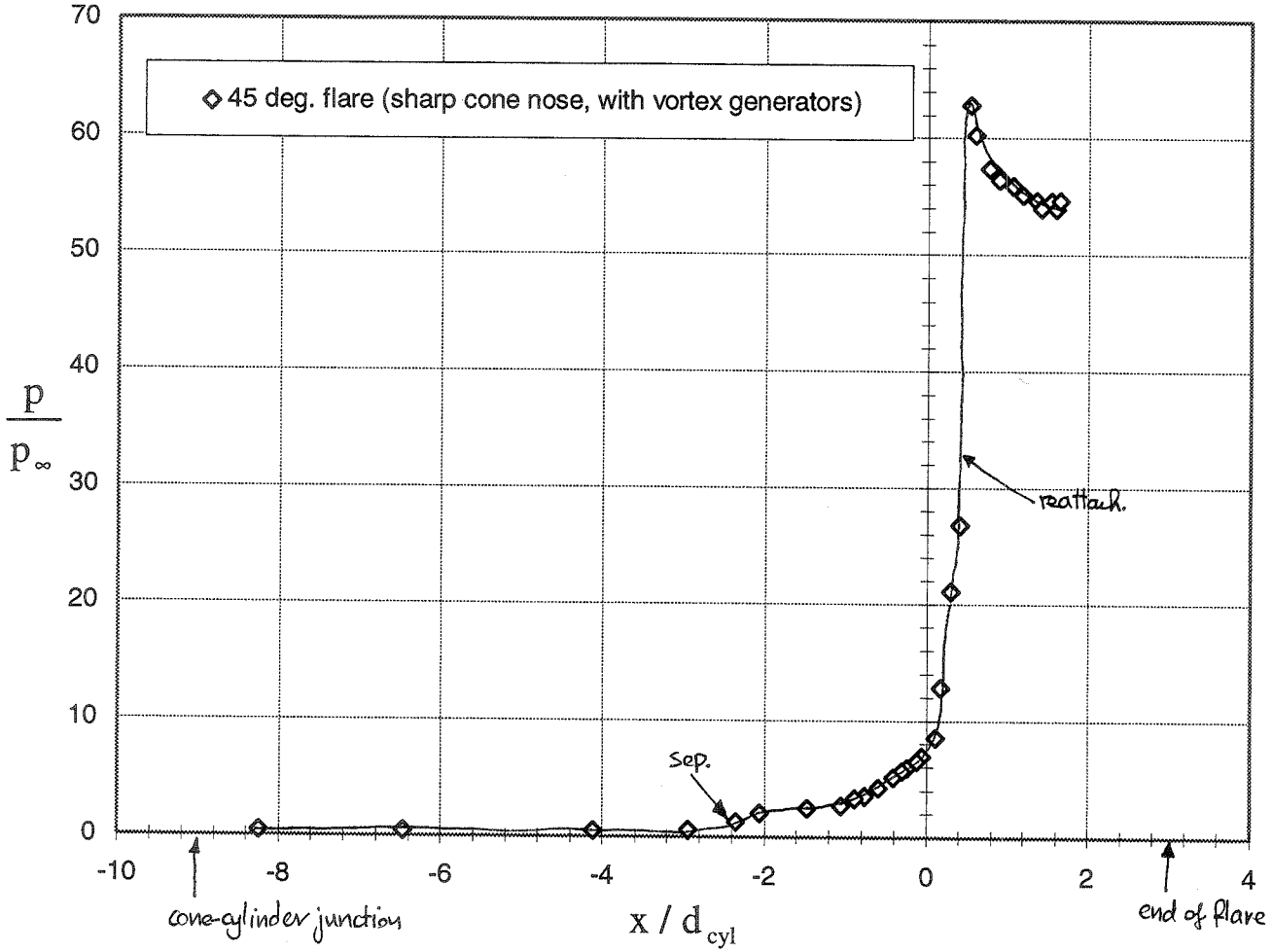

d) $\beta=45^{\circ}$

Fig. 5.40 Concluded

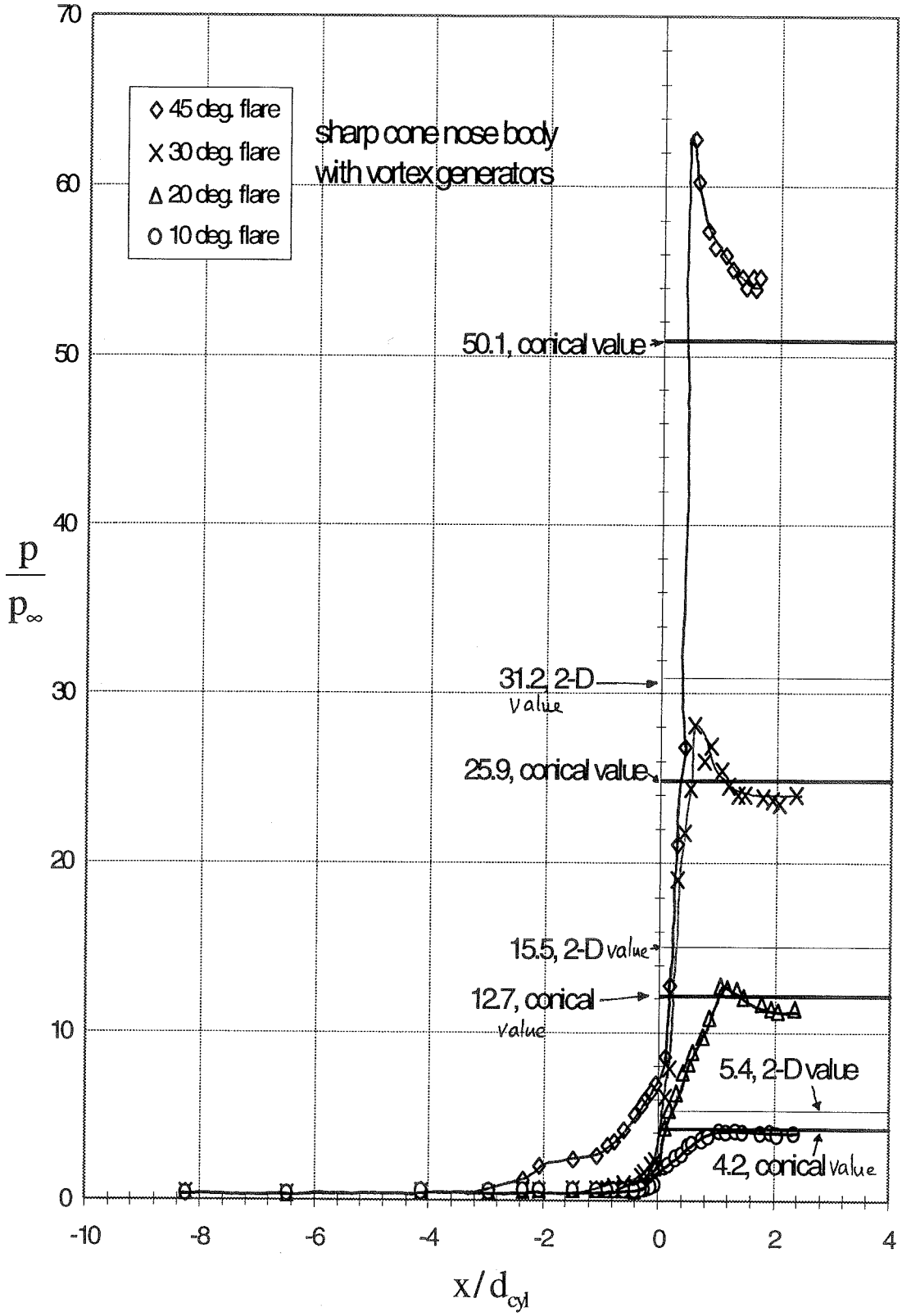

Fig. 5.41 Composite of pressure distributions (M_∞=8.2, Re_∞/cm=93000, sharp cone nose cylinder, turbulent boundary layer)

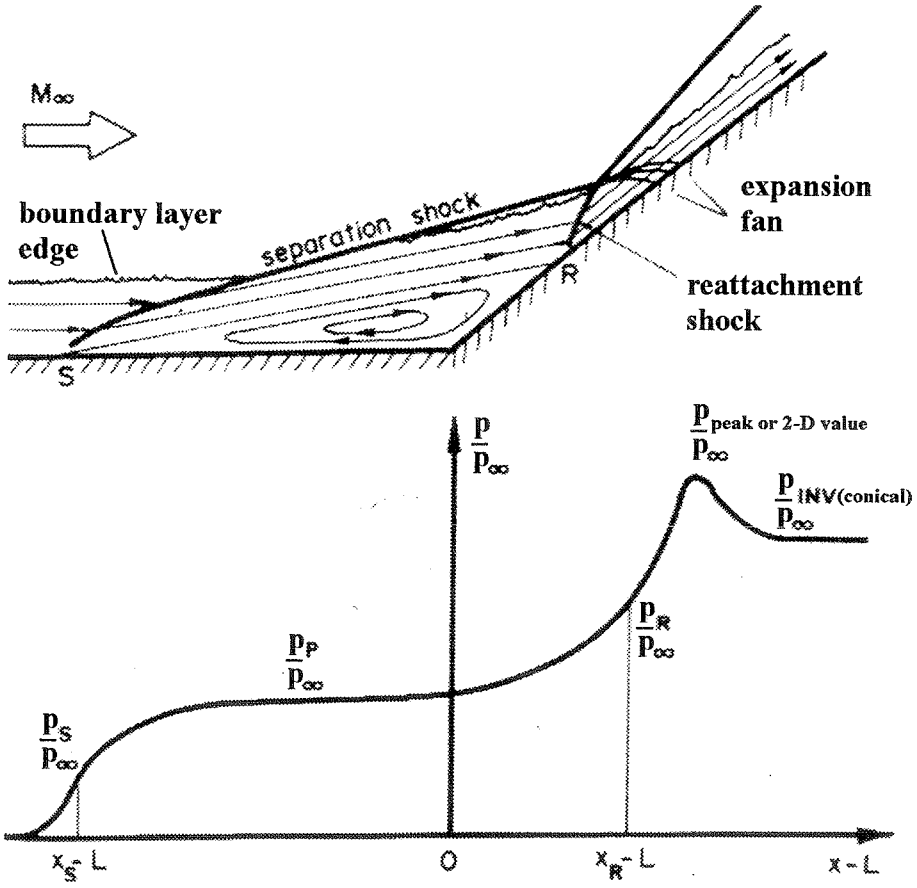

Fig. 5.42 Flowfield of a separated hypersonic turbulent boundary layer (ref. 37)

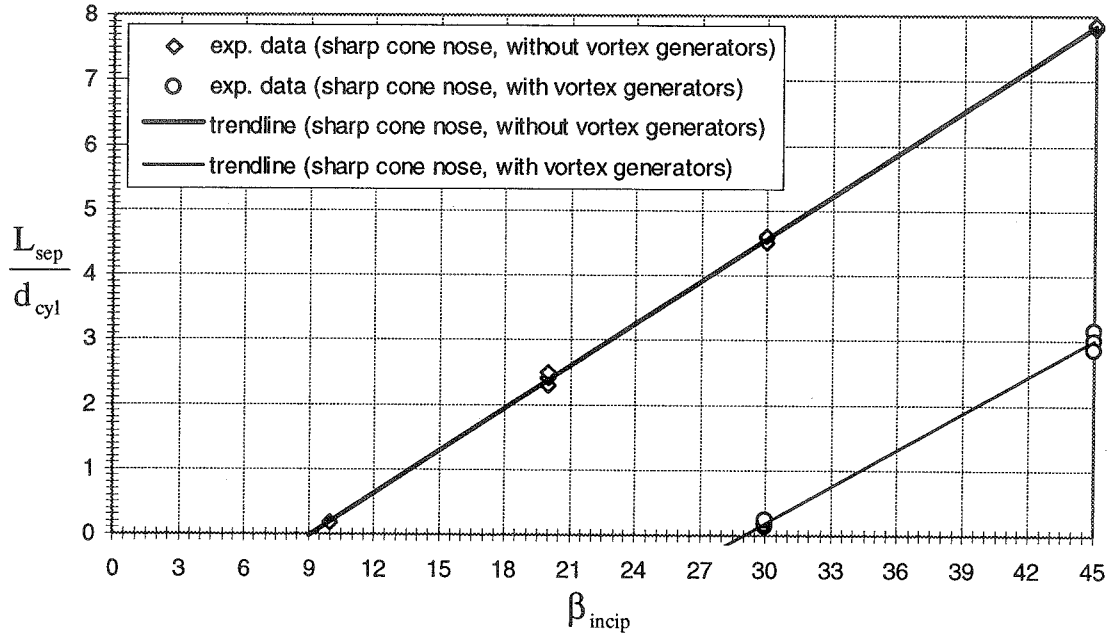

Fig. 5.43 Determination of incipient separation angle (turbulent boundary layer, sharp cone nose)

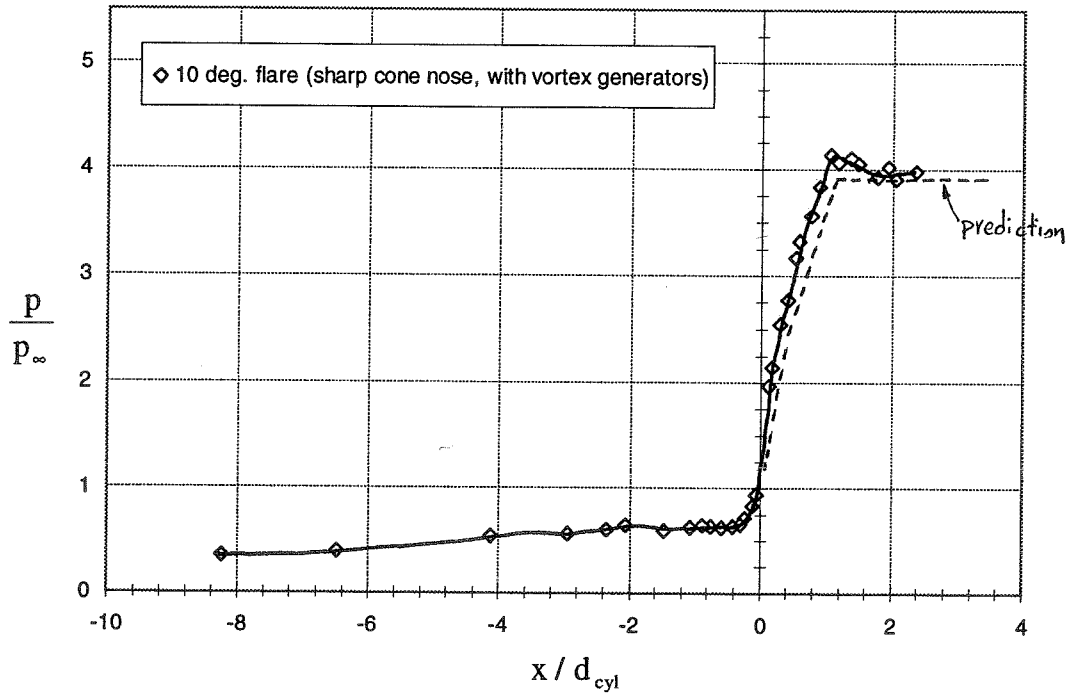

Fig. 5.44 Comparison of the experimental pressure distribution along the 10° flare with Elfstrom's[37] prediction model (M_∞=8.2, Re_∞/cm=93000, sharp cone nose, turbulent boundary layer)

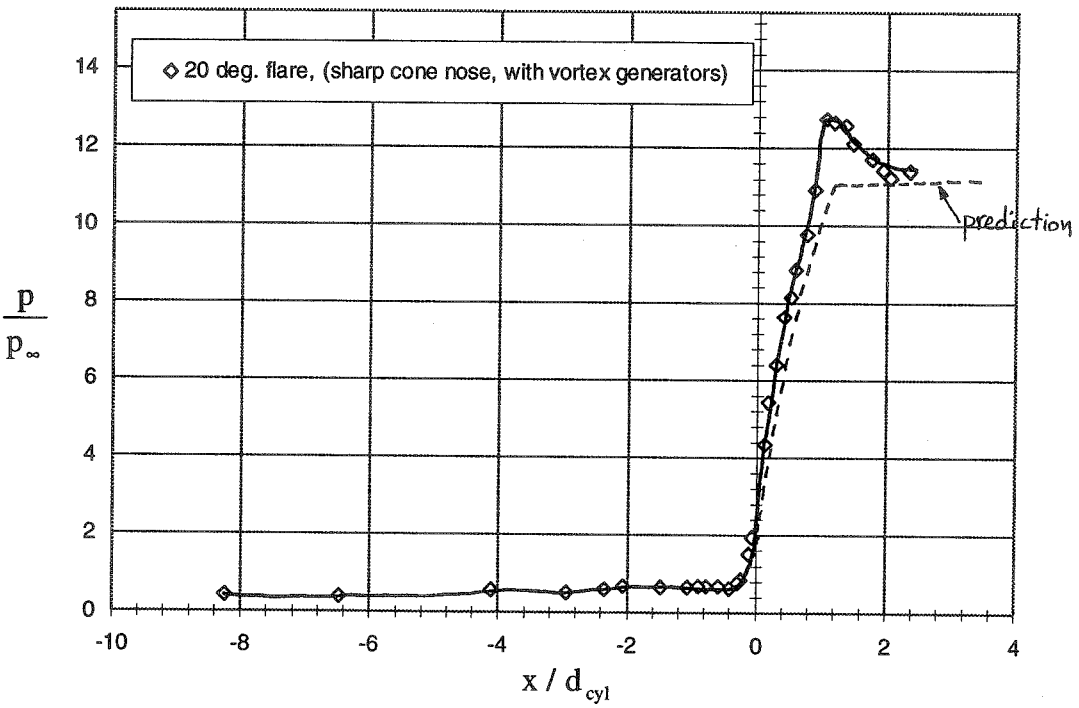

Fig. 5.45 Comparison of the experimental pressure distribution along the 20° flare with Elfstrom's[37] prediction model (M_∞=8.2, Re_∞/cm=93000, sharp cone nose, turbulent boundary layer)

i) sharp cone nose cylinder, with vortex generators

ii) hemisphere nose cylinder, with vortex generators

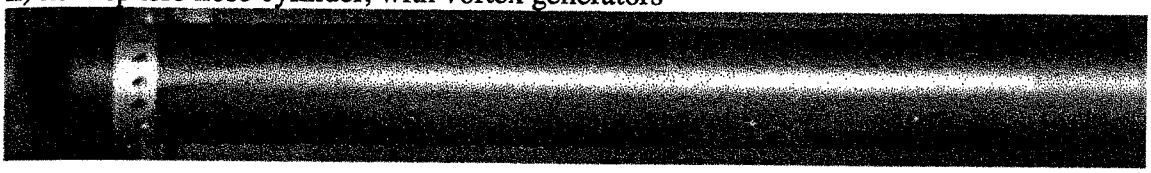

iii) hemisphere nose cylinder, without vortex generators

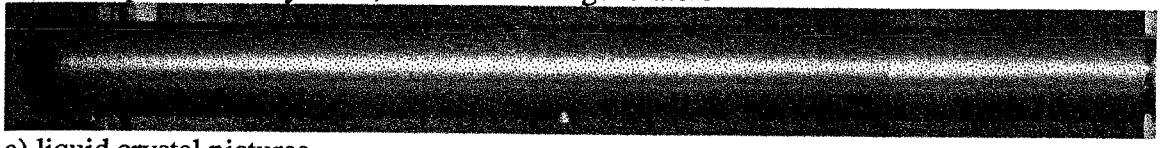

a) liquid crystal pictures

i) sharp cone nose cylinder, with vortex generators

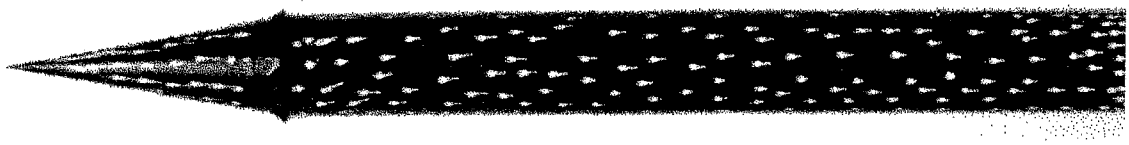

ii) hemisphere nose cylinder, with vortex generators

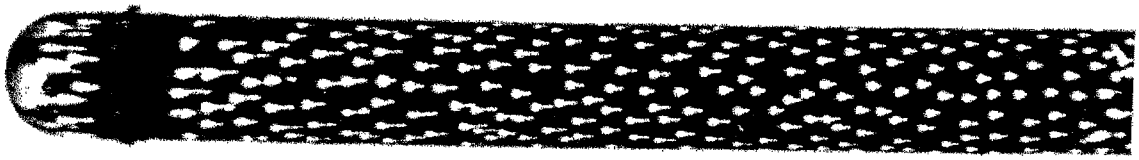

iii) hemisphere nose cylinder, without vortex generators

b) oil-dot pictures

Fig. 5.46 The effect of turbulent boundary layer on the oil-dot and liquid-crystal flow visualisation of the hemisphere cylinder (M_∞=8.2, Re_∞/cm=93000)

i) schlieren picture

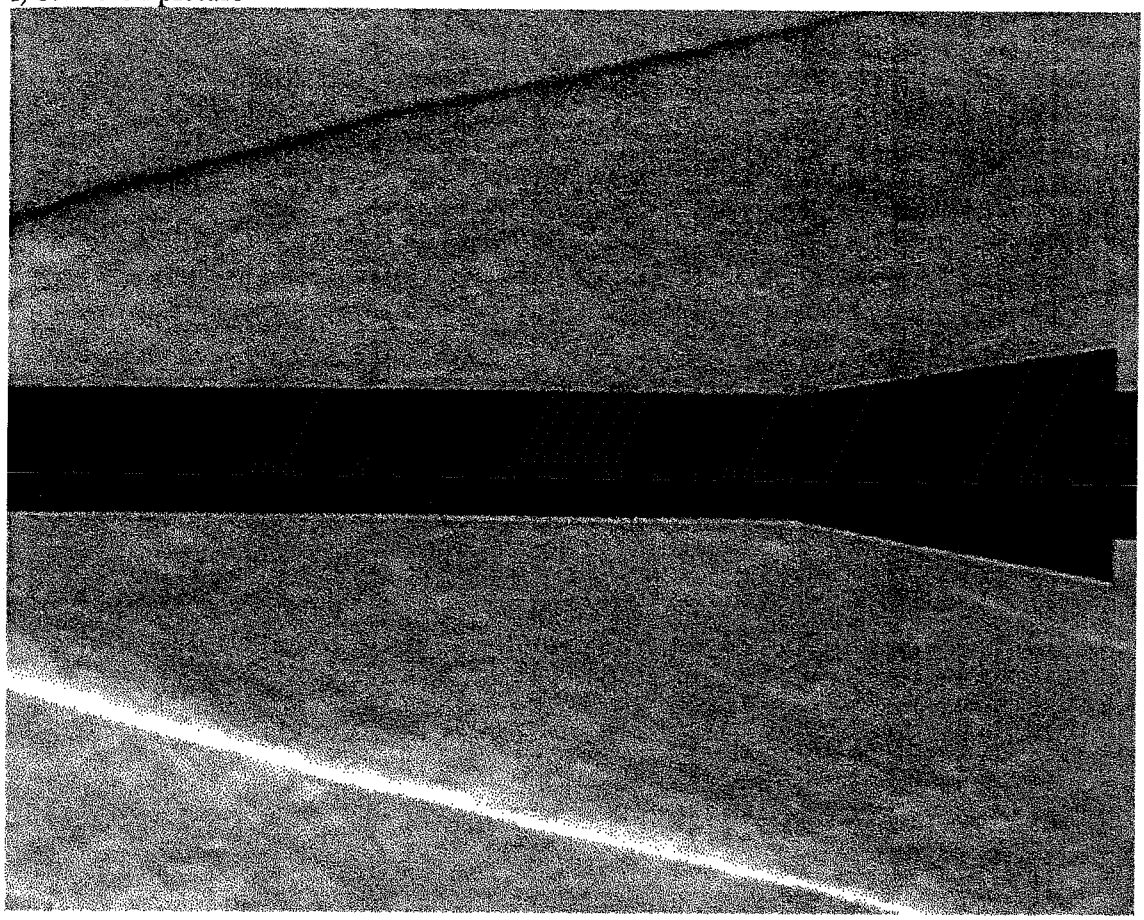

ii) liquid crystal picture

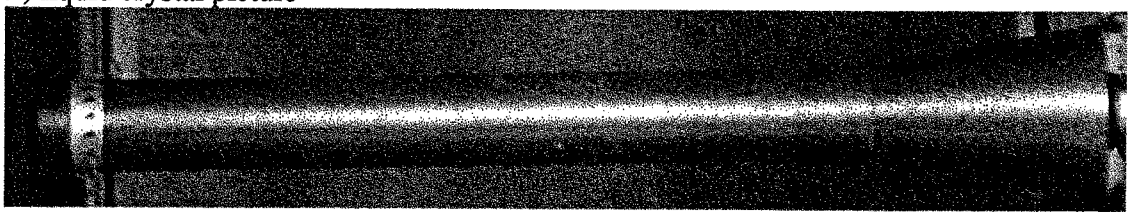

iii) oil-dot picture

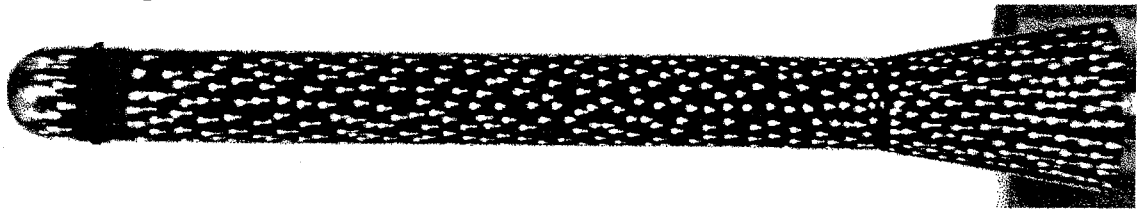

a) $\beta=10°$

Fig. 5.47 Schlieren, liquid-crystal and oil-dot flow visualisation and pressure measurements on hemisphere nose control flare configurations ($M_\infty=8.2$, $Re_\infty/cm=93000$, $L_{cyl}=15.3$ cm, $d_{cyl}=1.7$ cm, turbulent boundary layer)

iv) pressure distribution

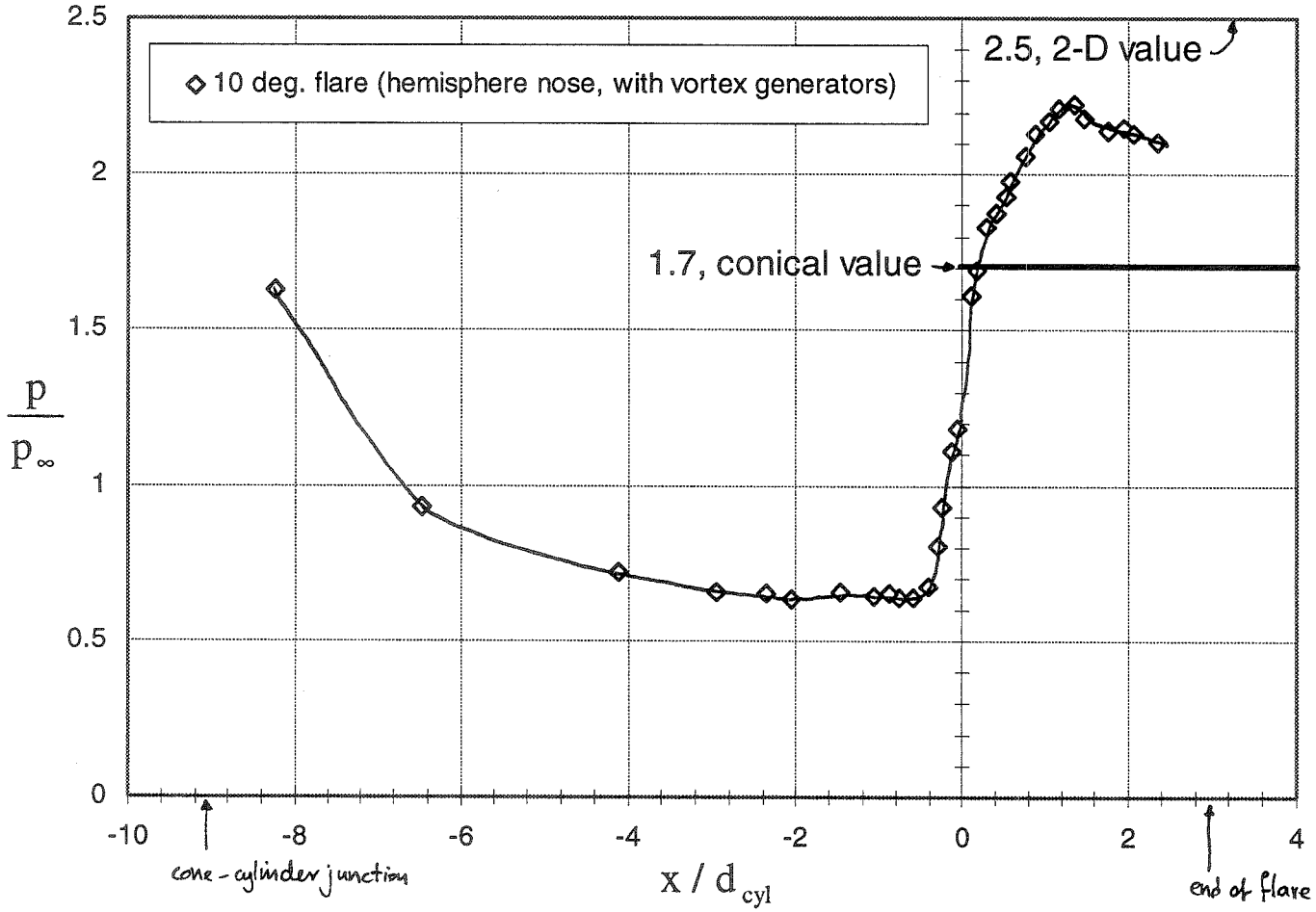

a) $\beta=10^{o}$

Fig. 5.47 Continue

i) schlieren picture

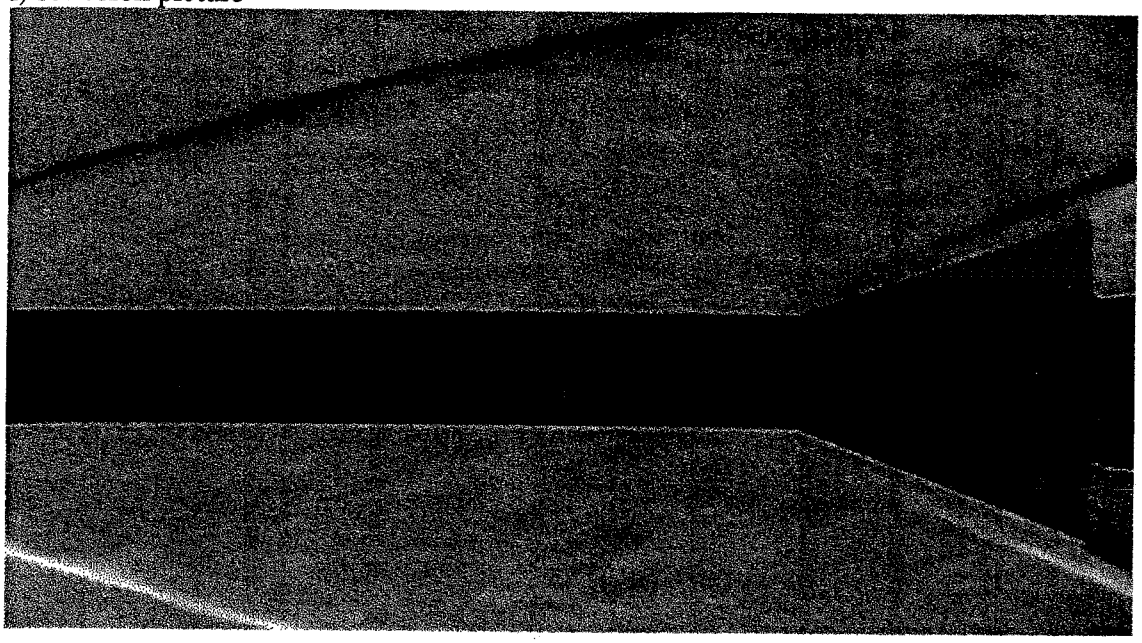

ii) liquid crystal picture

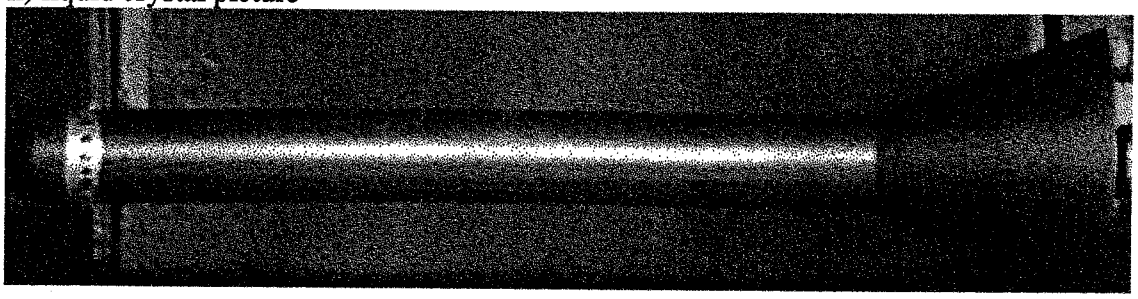

iii) oil-dot picture

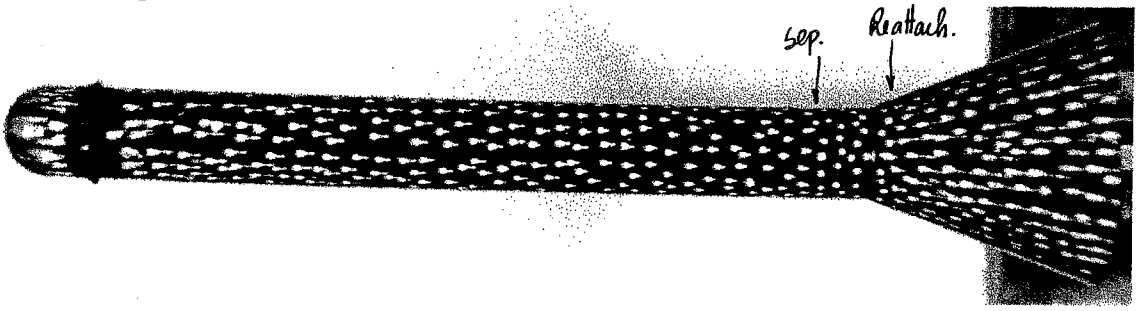

b) β=20°

Fig. 5.47 Continue

iv) pressure distribution

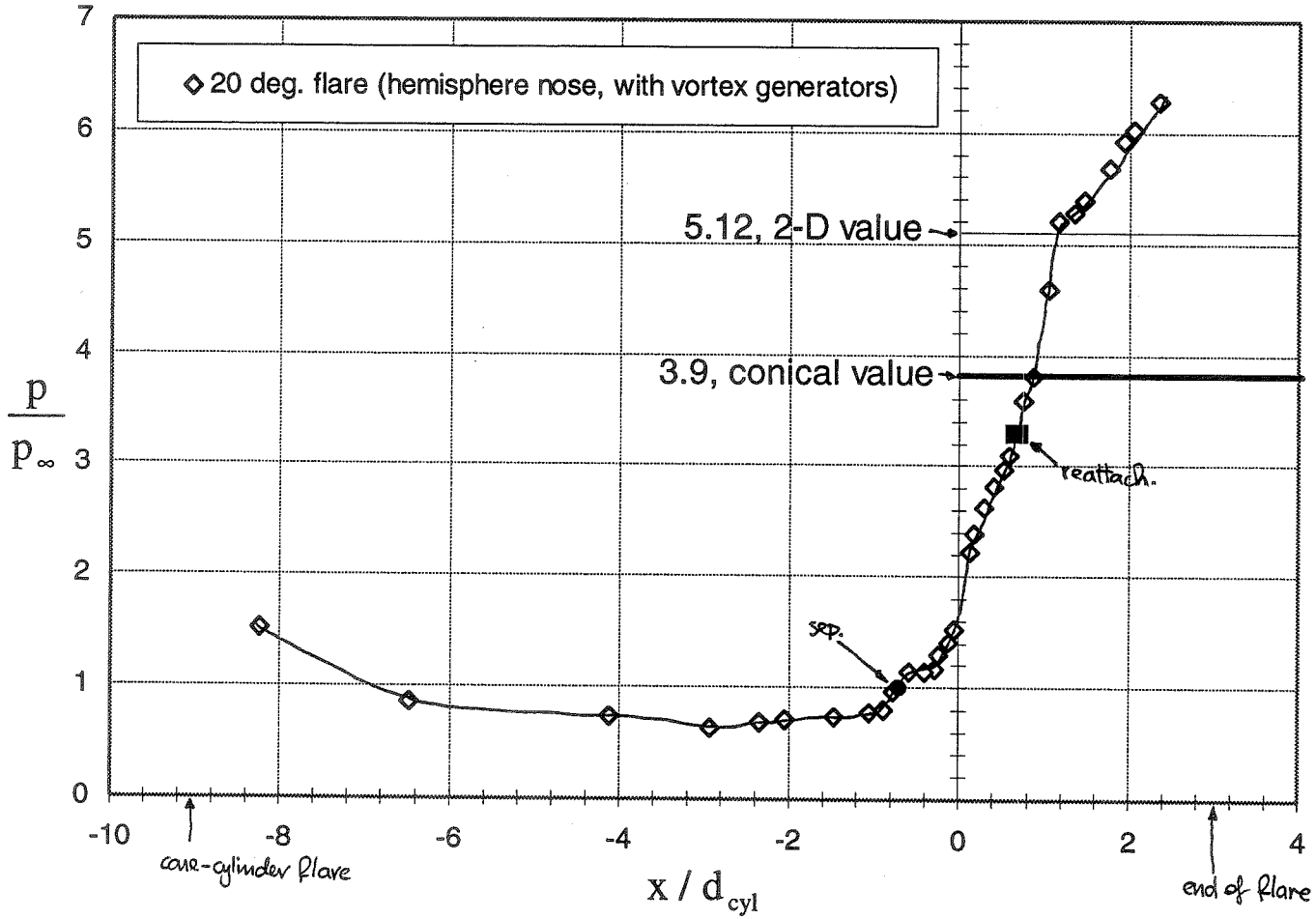

b) β=20°

Fig. 5.47 Continue

i) schlieren picture

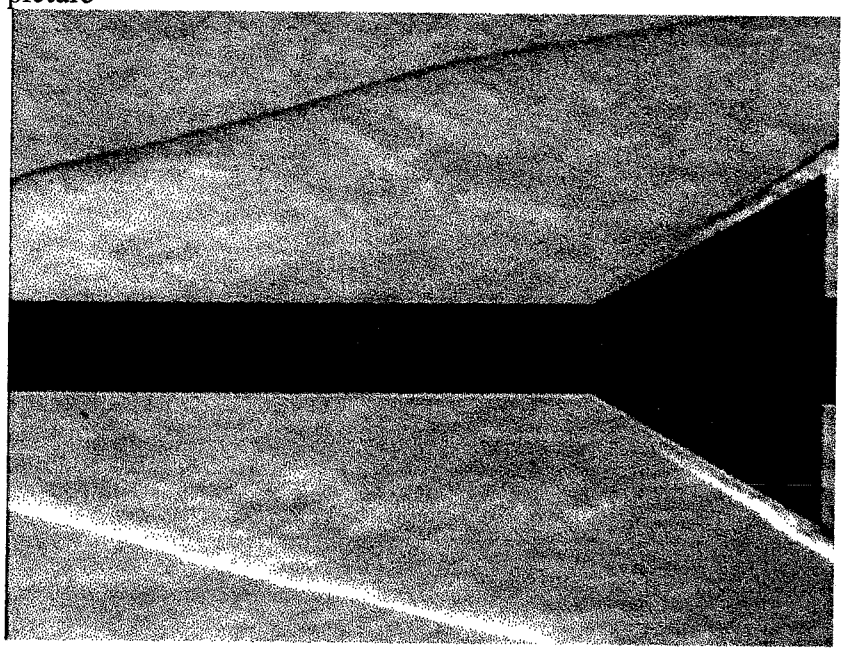

ii) liquid crystal picture

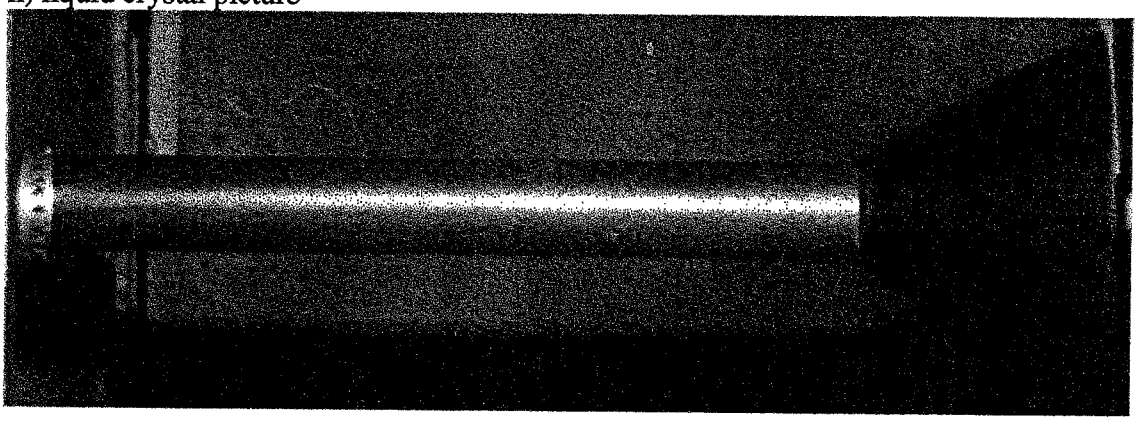

iii) oil-dot picture

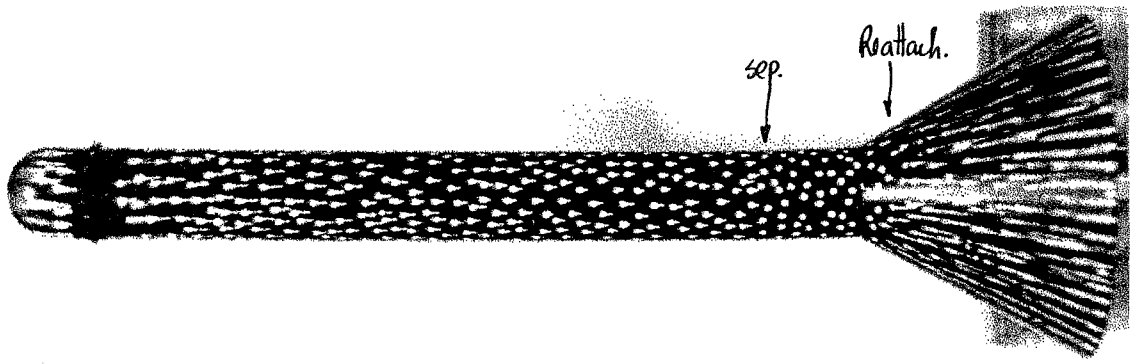

c) β=30°

Fig. 5.47 Continue

iv) pressure distribution

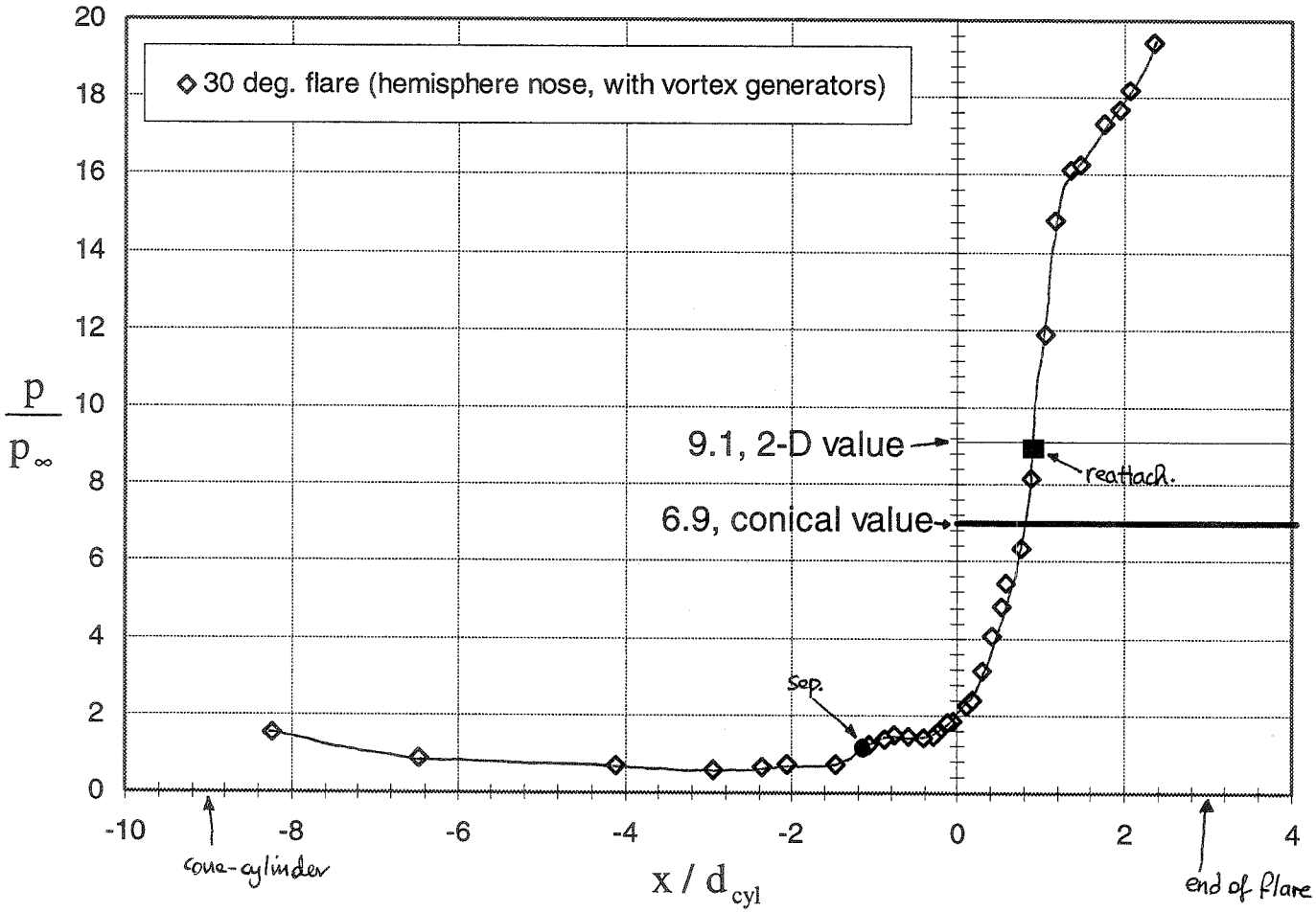

c) β=30°

Fig. 5.47 Continue

i) schlieren picture

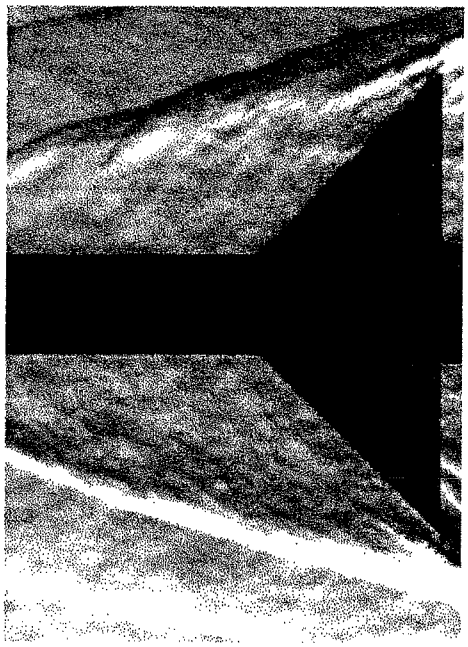

ii) liquid crystal picture

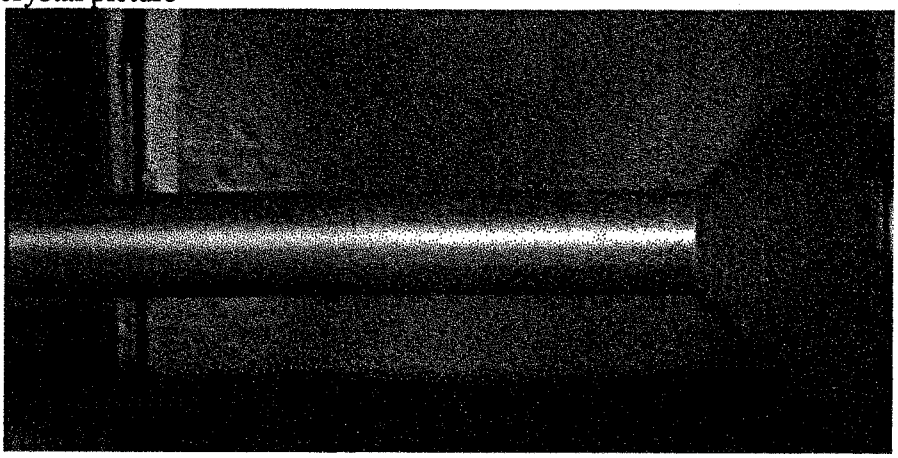

iii) oil-dot picture

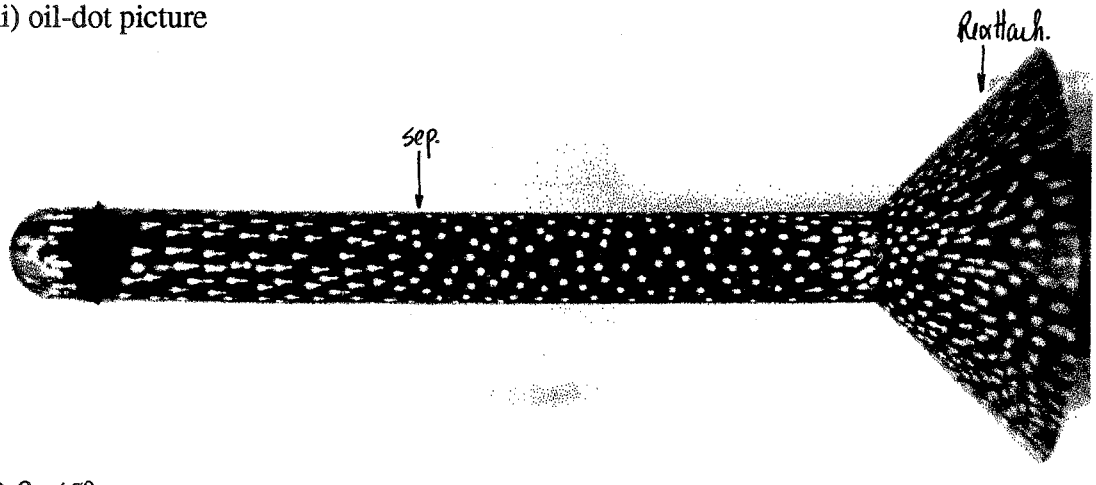

d) β=45°

Fig. 5.47 Continue

iv) pressure distribution

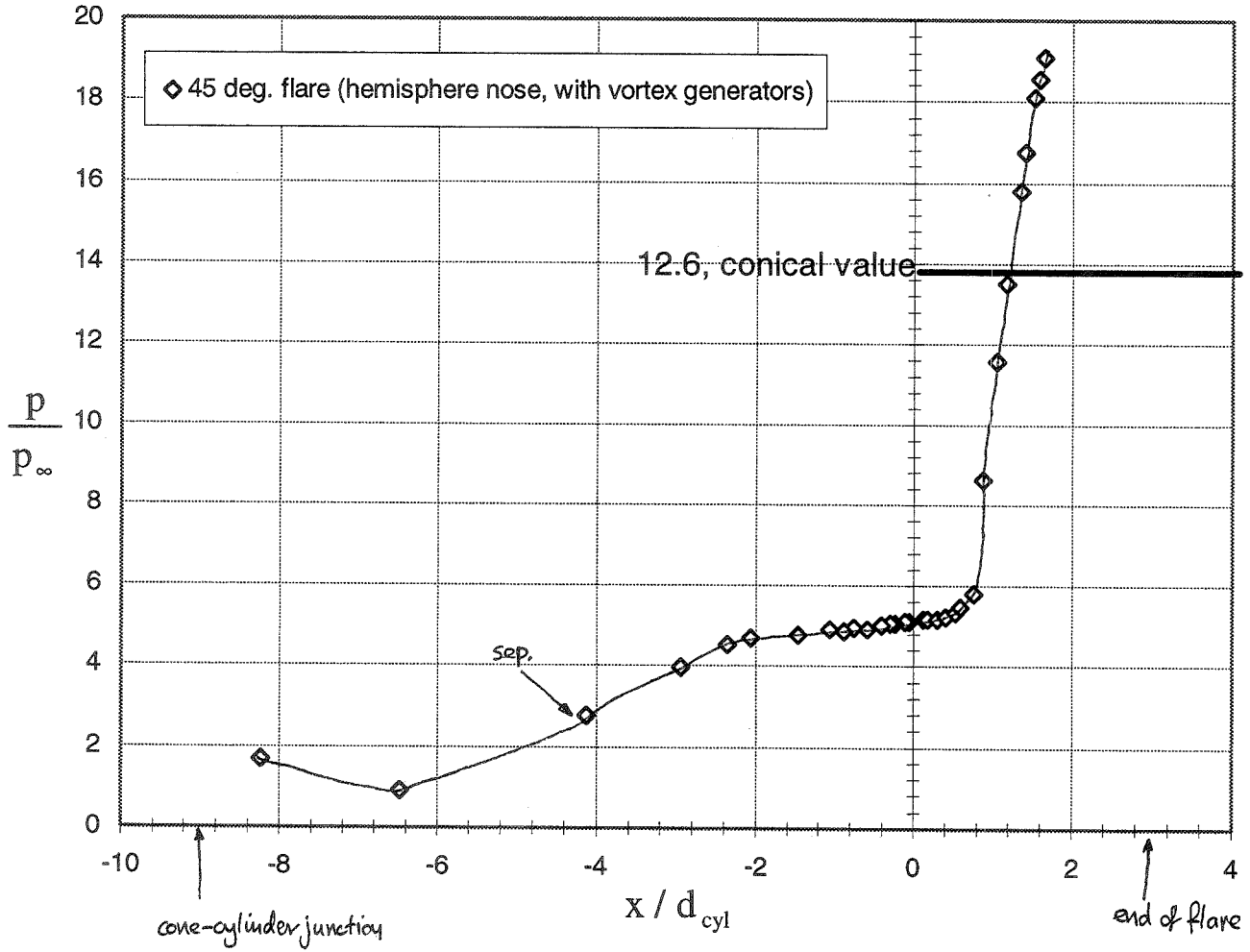

d) $\beta=45^{\circ}$

Fig. 5.47 Concluded

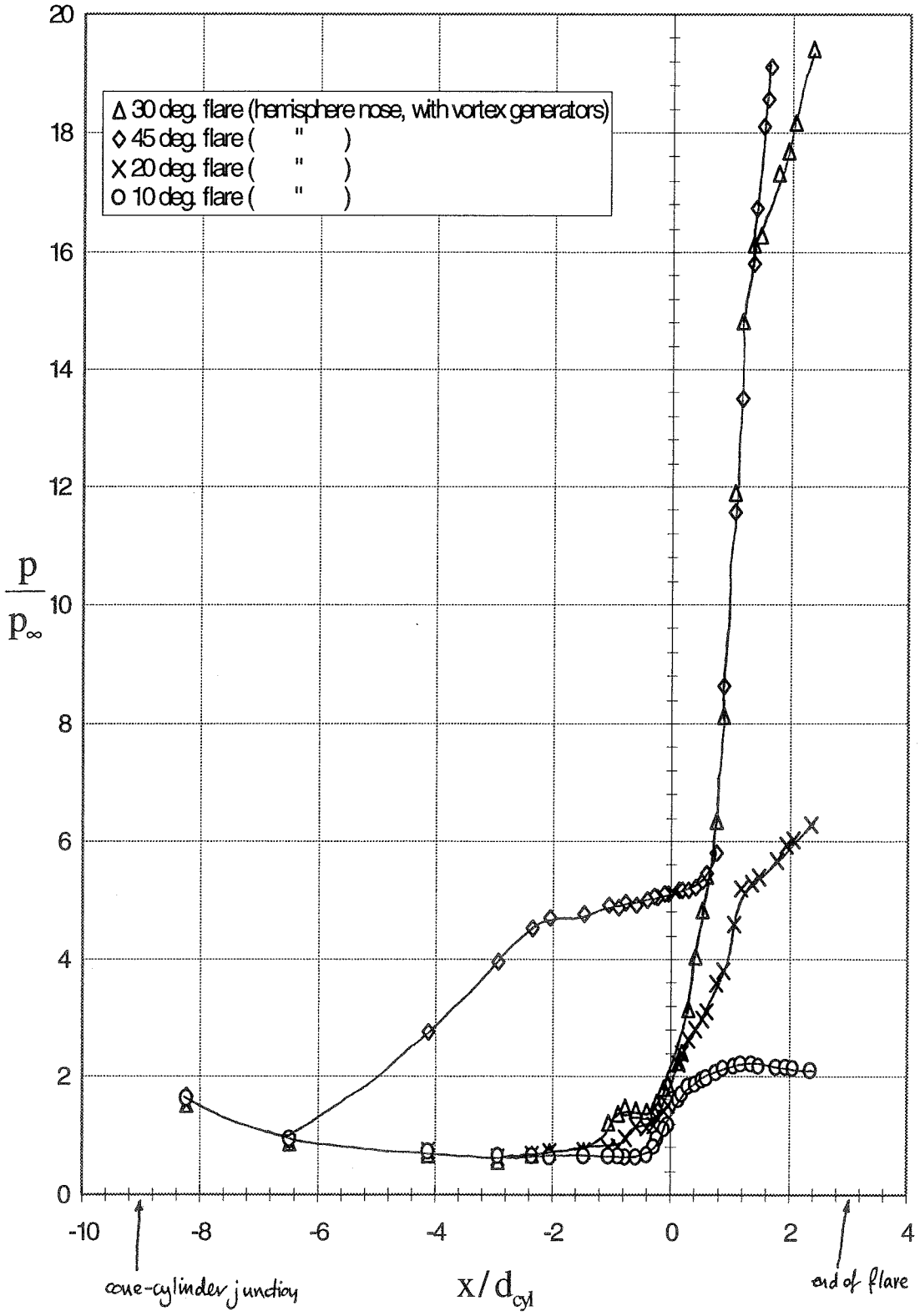

Fig. 5.48 Composite of pressure distributions (M_∞=8.2, Re_∞/cm=93000, hemisphere nose, turbulent boundary layer)

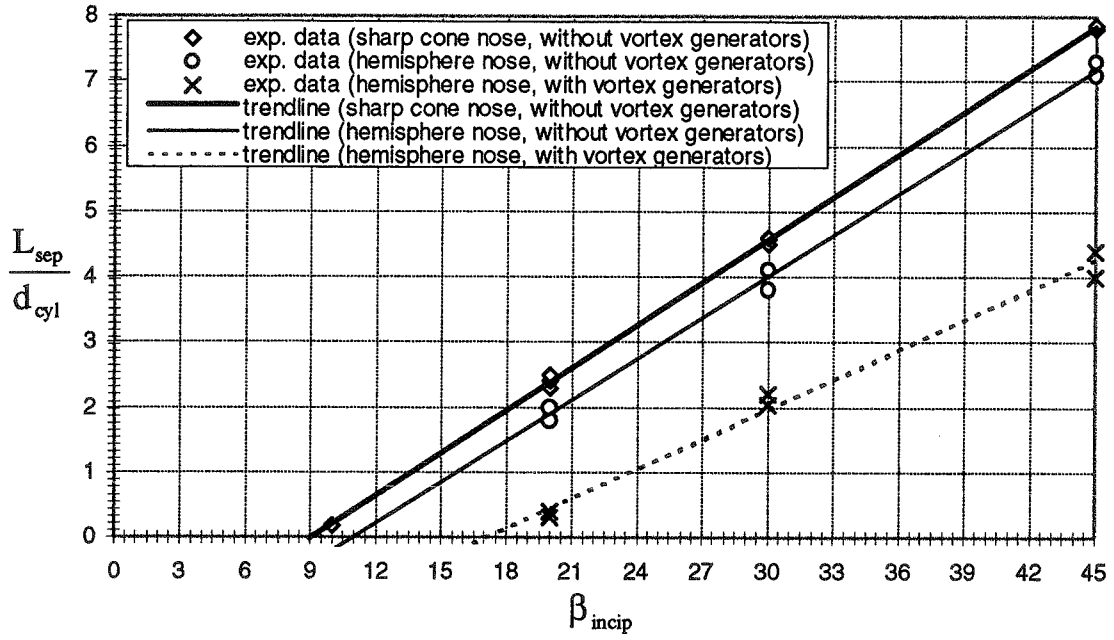

Fig. 5.49 Determination of incipient separation angle (turbulent boundary layer, hemisphere cone nose)

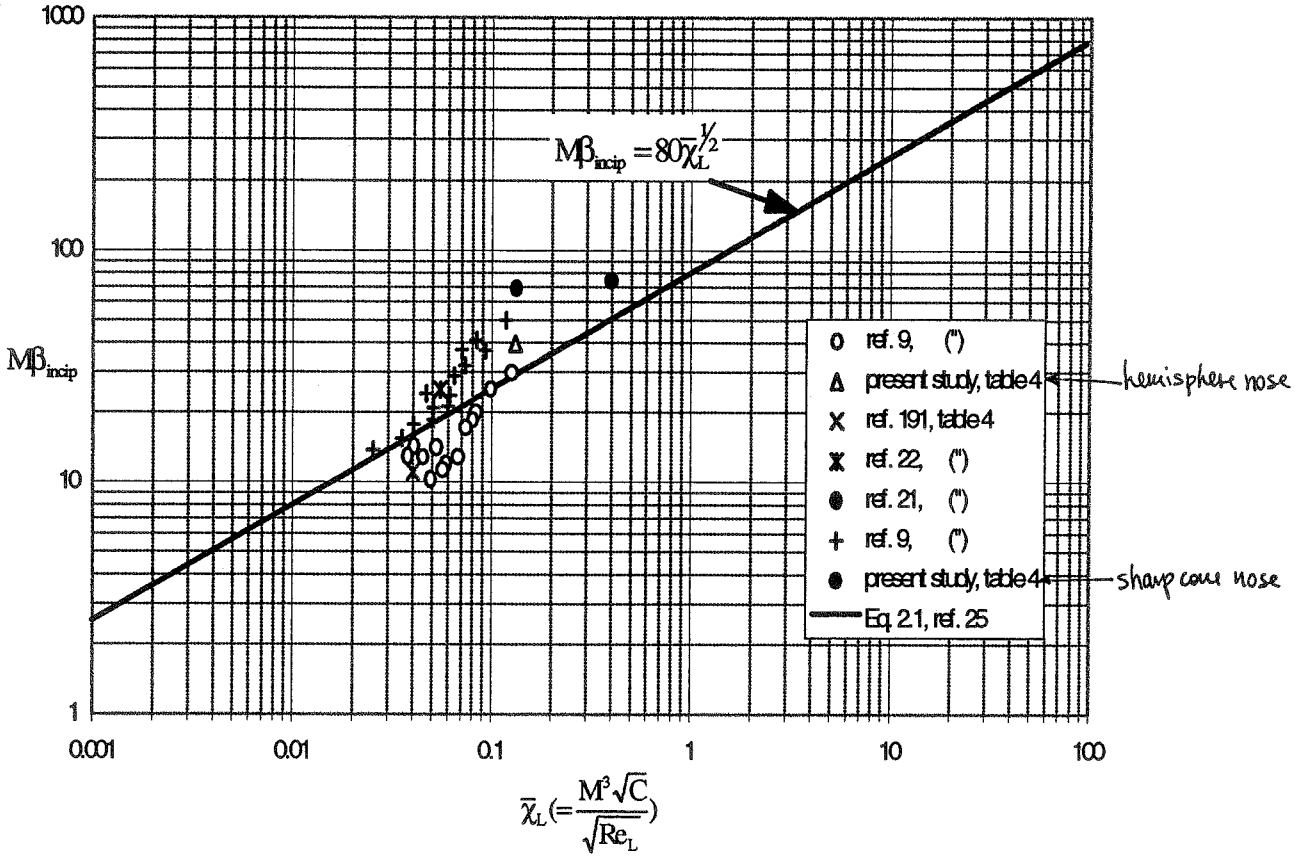

Fig. 5.50 Correlation of supersonic and hypersonic laminar incipient axisymmetric data

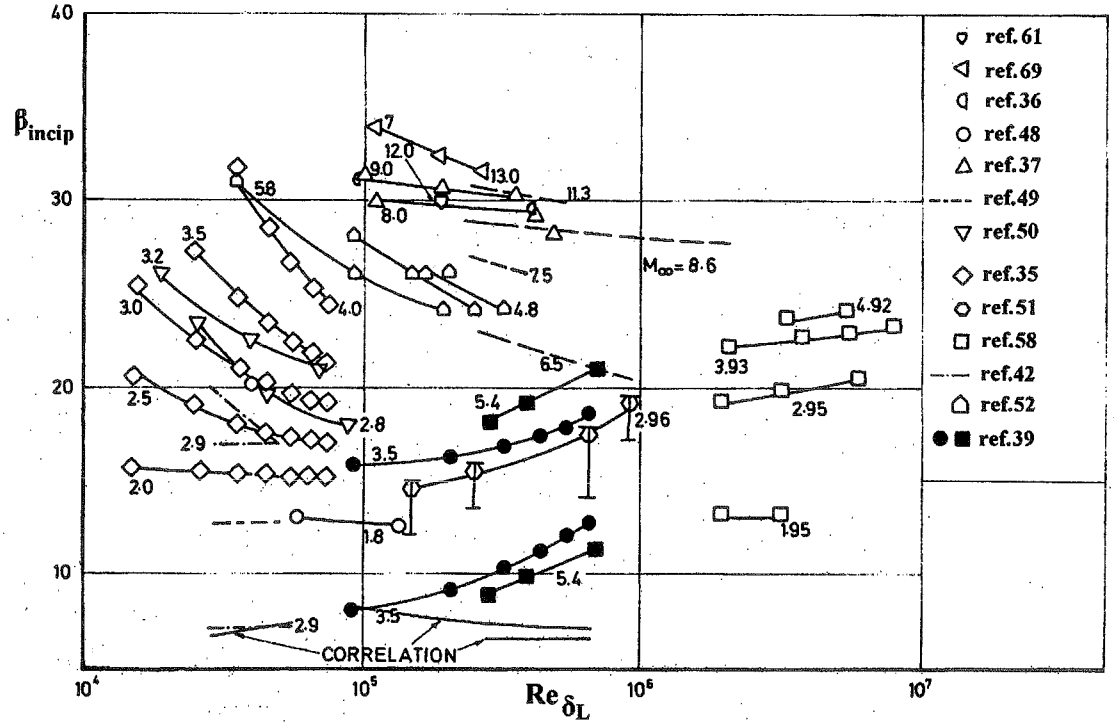

Fig. 2.5 Incipient separation at a wedge compression corner

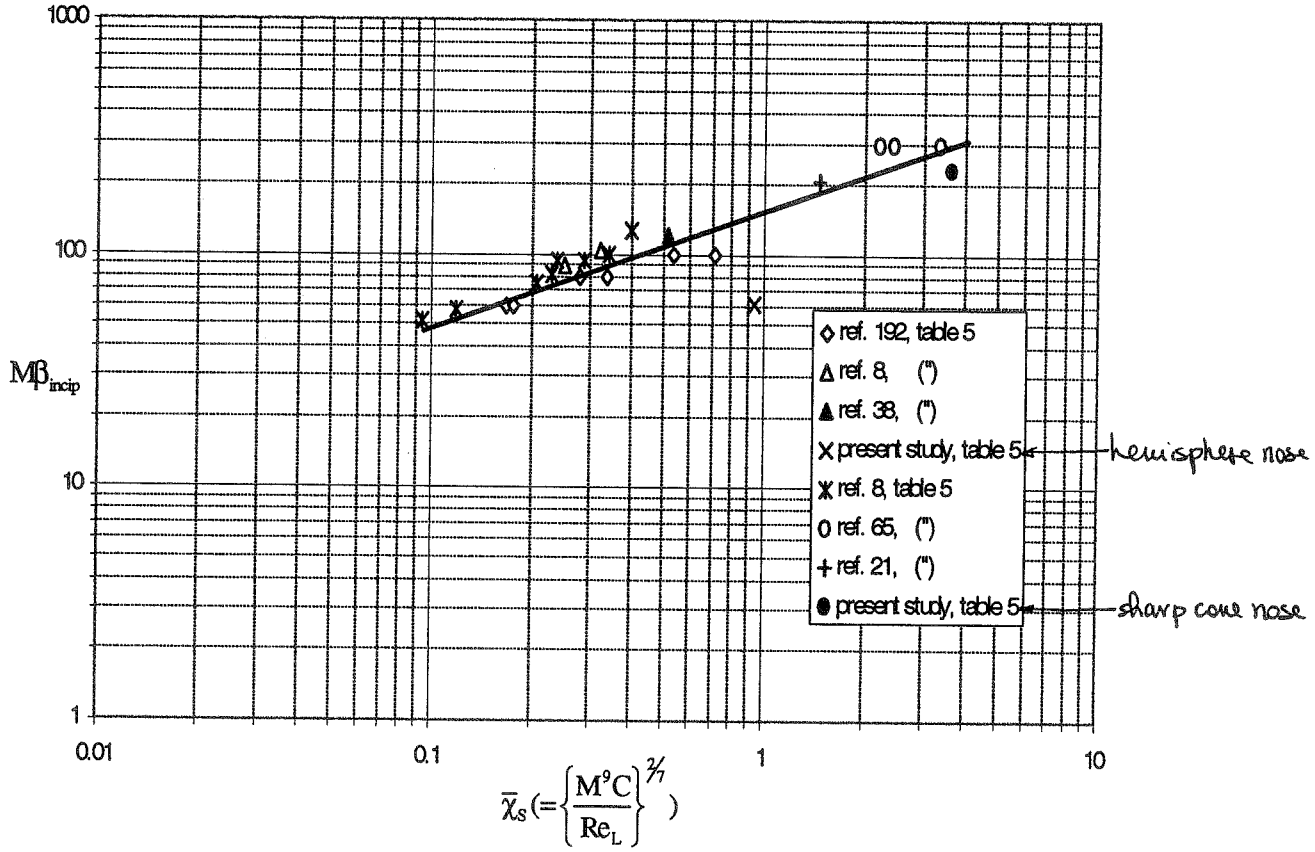

Fig. 5.51 Correlation of supersonic and hypersonic turbulent incipient axisymmetric data

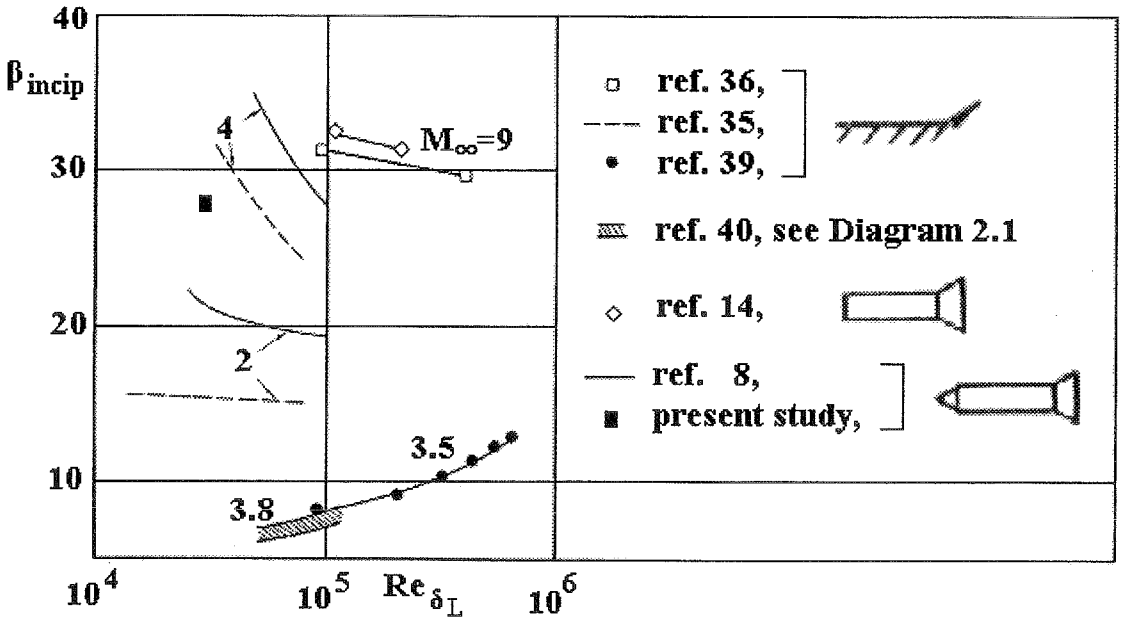

Fig. 5.52 Comparison of incipient separation angles for axi-symmetric configurations with 2-D results

APPENDIX A

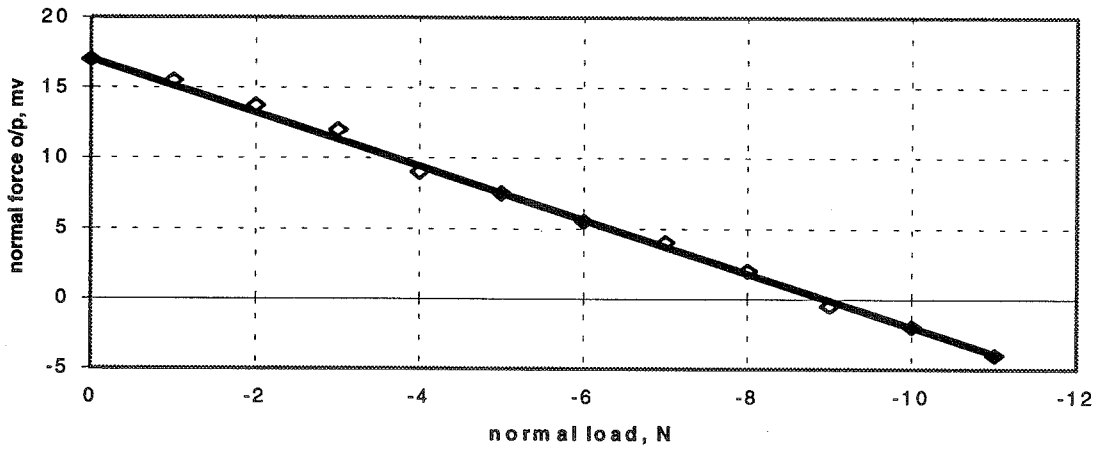

a) effect of normal load on normal channel

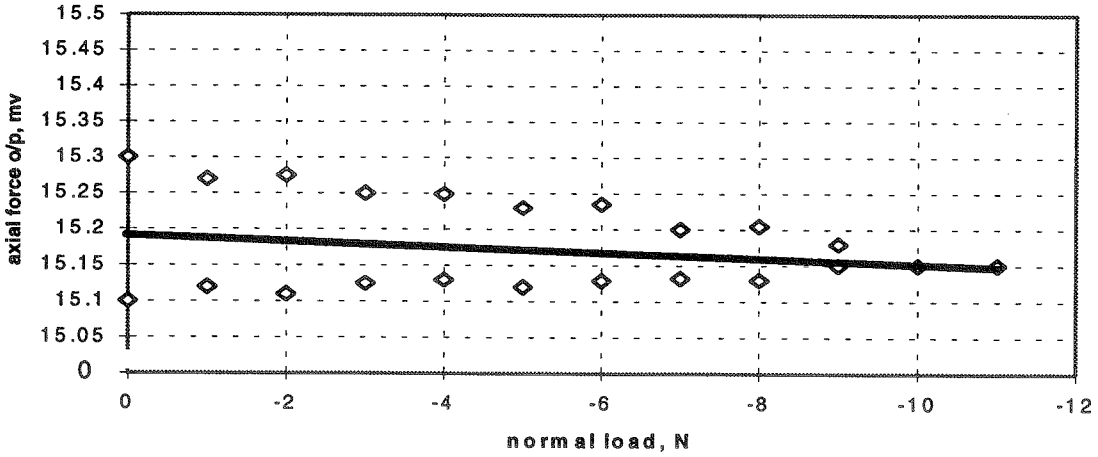

b) effect of normal load on axial channel

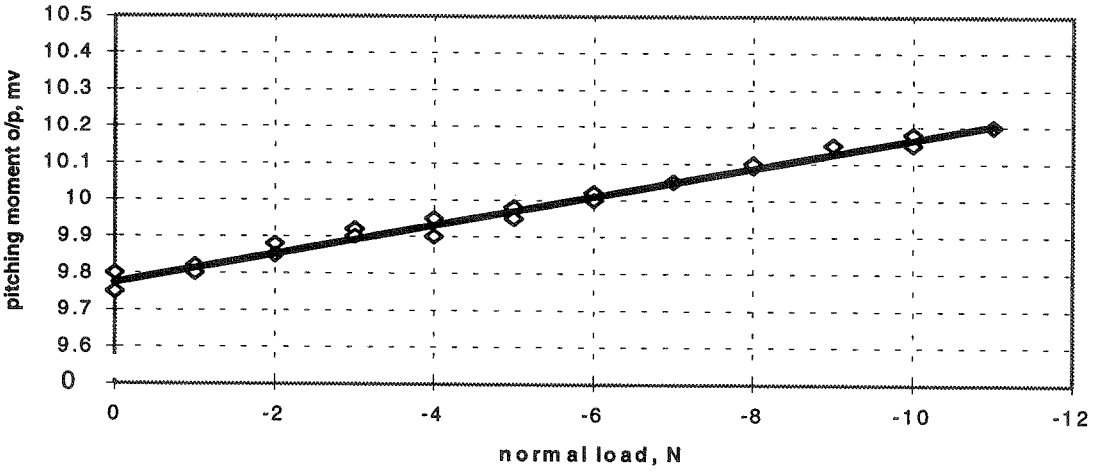

c) effect of normal load on pitching moment channel

Fig. A1 Calibration of the normal force loading

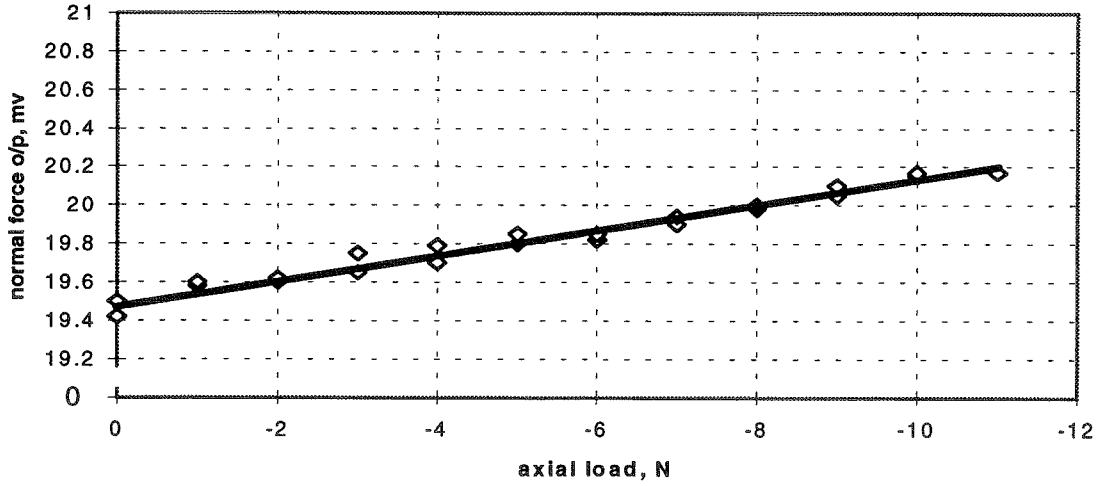

a) effect of axial load on normal channel

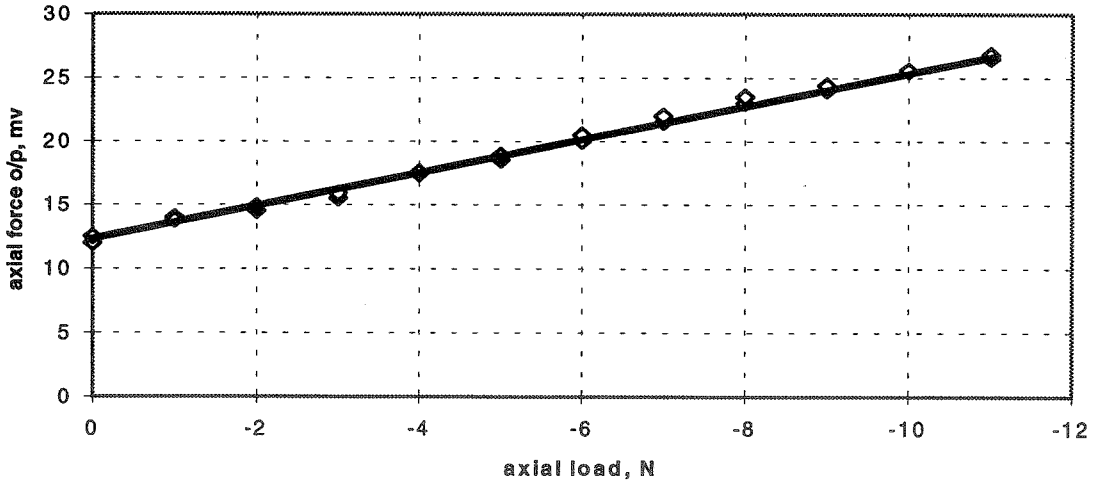

b) effect of axial load on axial channel

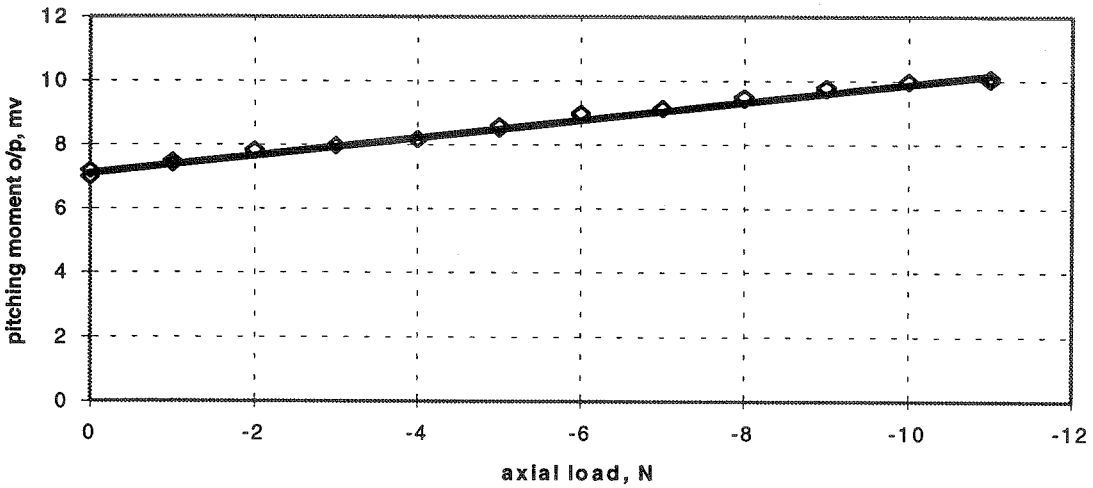

c) effect of axial load on pitching moment channel

Fig. A2 Calibration of the axial force loading

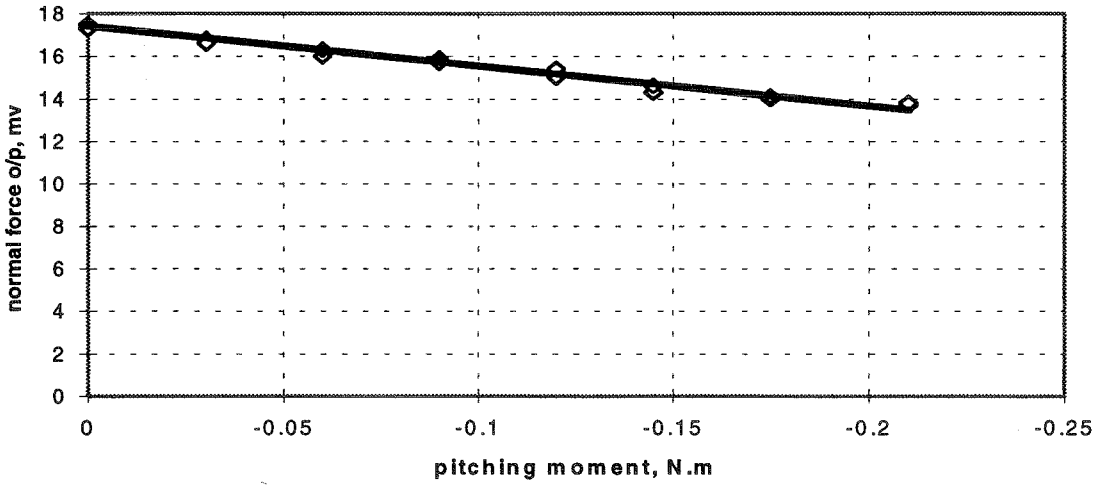

a) effect of pitching moment on normal channel

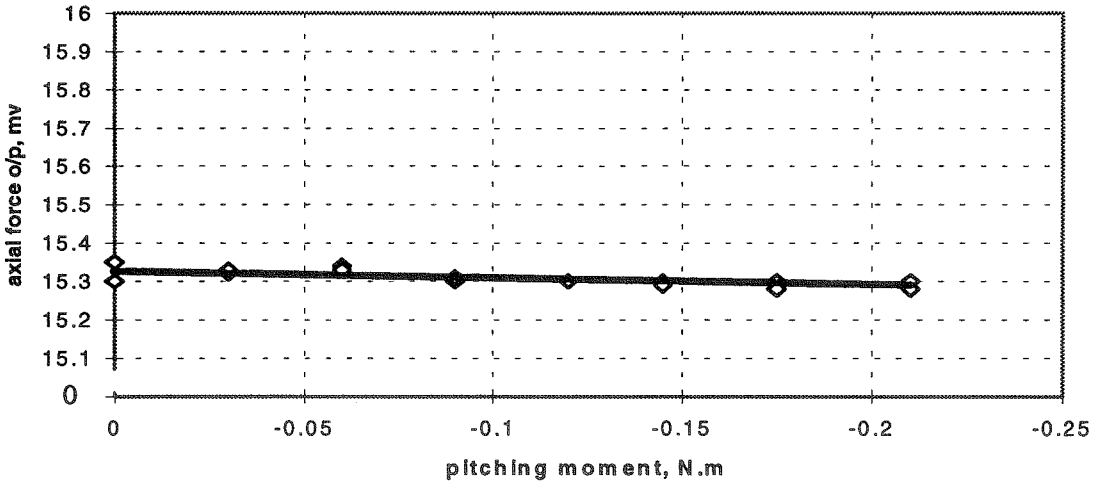

b) effect of pitching moment on axial channel

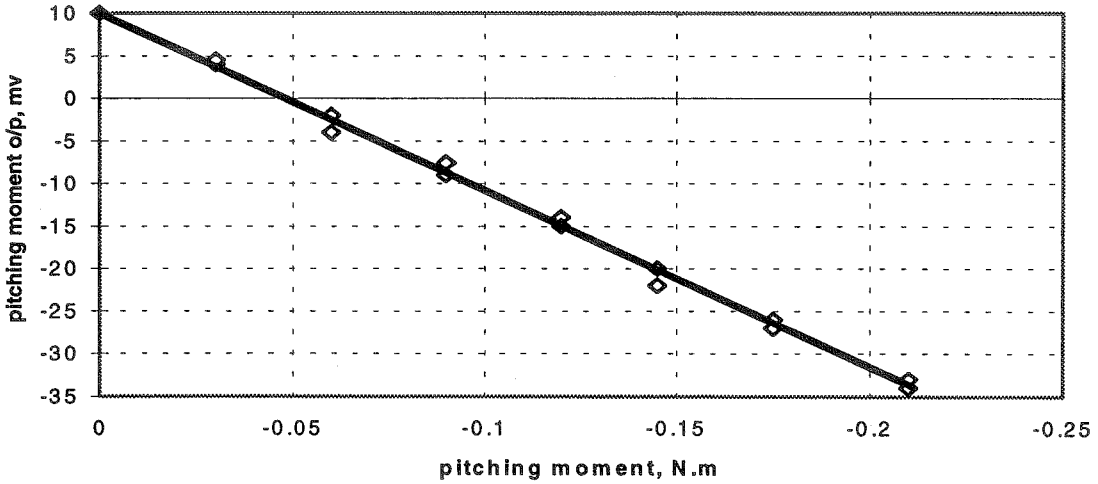

c) effect of pitching moment on pitching moment channel

Fig. A3 Calibration of the pitching moment loading

APPENDIX B

The Newtonian pressure coefficient of a right rhombic cone (derived using the method described in section 4.3.2) is:

$$C_p = 2\frac{\left[a\cos\alpha\cos\beta + L_S^2(\sin^2\varphi\sin\beta + \cos^2\varphi\sin\alpha\cos\beta) - \frac{4L_S^2}{a}\sin(135-\varphi)[\sin\varphi\sin\beta + \cos\varphi\sin\alpha\cos\beta]\right]^2}{\left[\left[(2L_S^2 + a)(\cos^2\varphi + \sin^2\varphi) + \frac{8L_S^4}{a}\cos\varphi\sin\varphi(\sin^3\varphi + \cos^3\varphi)\right]\times\left[\cos^2\alpha\cos^2\beta + \sin^2\beta + \sin^2\alpha\cos^2\beta\right]\right]} \quad \text{(B.1)}$$

APPENDIX C

a. This programme generates the surface grid of an elliptic cone with strakes

```
PROGRAM geometry
    DIMENSION xel(0:300,0:300), yel(0:300,0:300), coca(0:300)
    DIMENSION xeta(0:300)
C   This programme was written by Mr K. Kontis
C   a1= is the major semi-diameter of the base
C   b1= is the minor semi-diameter of the base
C   c1= is the length of the cone
C   x1= is the lower limit of the integration
C   x2= is the upper limit of the integration
C   e= is the eccentricity
C   circo= is the circumference at a particular station
C   dcirco= is an increament of the circumference
C   kxy= is the number of division of the circumference
C   kz= is the number of stations in the length
C   xel,yel,z1 are the coordinates on the body

    EXTERNAL funcd
    REAL a1,b1,c1,x1,x2,e,et,ef,es,eg,circo,dcirco,xacc
    OPEN (3, FILE='Surfstr.gr1')
    OPEN (4, FILE='check.out')
    pi=3.1415926536
    geo=0.005*pi
    x1=0.0

C   base main coordinates
    a0=0.02
    b0=0.0125
    c0=0.1875
C   station end coordinates
    c2=0.035
    b11=(c2/c0)*b0
    a2=(c2/c0)*a0
    e=sqrt(a2*a2-b11*b11)/(a2)
C   Simpson-trapezium iteration for front station
    cel=0
    cel1=(pi*57.5)/180
    CALL num(cel,cel1,rum1,a2,e)
    shark1=rum1
    cirhor=shark1-0.003
    dcirco=cirhor
    x2=((10*pi)/180)+geo
    xacc=(1.0E-4)*(x1+x2)/2
        CALL rtnewt(funcd,x1,x2,xacc,dcirco,a2,e)
        ROOT=rtnewt(funcd,x1,x2,xacc,dcirco,a2,e)
        ROOT1=pi/2-ROOT
    b13x=a2*cos(ROOT1)
    b13y=b11*sin(ROOT1)
    b14x=a2*cos((pi*32.5)/180)
    b14y=b11*sin((pi*32.5)/180)

C   Simpson-trapezium iteration for base station
    cel=0
    cel1=(pi*57.5)/180
    e=sqrt(a0*a0-b0*b0)/(a0)
```

```
      CALL num(cel,cel1,rum1,a0,e)
      circo5=rum1
      cirkos=circo5-0.003
      dcirco=cirkos
          x2=((50*pi)/180)+geo
          xacc=(1.0E-4)*(x1+x2)/2
          CALL rtnewt(funcd,x1,x2,xacc,dcirco,a0,e)
          ROOT=rtnewt(funcd,x1,x2,xacc,dcirco,a0,e)
          ROOT1=pi/2-ROOT
          xel(1,26)=a0*cos(ROOT1)
          yel(1,26)=b0*sin(ROOT1)
      xel(1,66)=a0*cos((pi*32.5)/180)
      yel(1,66)=b0*sin((pi*32.5)/180)
      disot=0.003
      umoth1=(yel(1,26)-yel(1,66))/(xel(1,26)-xel(1,66))
      umoth2=(-1)/umoth1
      coth1=(-1)*umoth2*xel(1,26)+yel(1,26)
      om1=1+umoth2*umoth2
      om2=-2*xel(1,26)-2*yel(1,26)*umoth2+2*umoth2*coth1
      om3a=xel(1,26)*xel(1,26)+yel(1,26)*yel(1,26)
      om3b=-2*yel(1,26)*coth1+coth1*coth1-disot*disot
      om3=om3a+om3b
          xel(1,34)=(-om2+sqrt((om2*om2)-4*om1*om3))/(2*om1)
          yel(1,34)=umoth2*xel(1,34)+coth1
      dd21=b13x*yel(1,34)*c0+xel(1,34)*yel(1,26)*c2+xel(1,26)*b13y*c0
      dd22=-b13x*yel(1,26)*c0-xel(1,34)*b13y*c0-xel(1,26)*yel(1,34)*c2
      dd2=dd21
      aa21=yel(1,34)*c0+yel(1,26)*c2+b13y*c0
      aa22=-yel(1,26)*c0-b13y*c0-yel(1,34)*c2
      aa2=aa21+aa22
      bb21=b13x*c0+xel(1,34)*c2+xel(1,26)*c0
      bb22=-b13x*c0-xel(1,34)*c0-xel(1,26)*c2
      bb2=bb21+bb22
      cc21=b13x*yel(1,34)+xel(1,34)*yel(1,26)+xel(1,26)*b13y
      cc22=-b13x*yel(1,26)-xel(1,34)*b13y-xel(1,26)*yel(1,34)
      cc2=cc21+cc22
      aa2=aa2/dd2
      bb2=bb2/dd2
      cc2=cc2/dd2
      DD2=dd2/dd2

C     cross-section divisions x-y plane
      kxy=16
C     axial stations divisions
      kz=64
      dc=c0/kz
      Z=c0
      WRITE(3,'(/1X,A)') 'Roots of xyz geometry:'
C     Loop for each station
      DO 400 J=1,(kz+1)
C     advance from A to B
      geo=0.005*pi
      a1=(Z/c0)*a0
      b1=(Z/c0)*b0
      e=sqrt(a1*a1-b1*b1)/(a1)
      uk1=(aa2*Z*a0)/c0
      uk2=(bb2*Z*b0)/c0
      uk3=DD2-cc2*Z
      uk4=((uk1/uk2)*(uk1/uk2))+1
      uk5=(-2)*((uk3*uk1)/(uk2*uk2))
      uk6=((uk3/uk2)*(uk3/uk2))-1
      thetaab=acos((-uk5+sqrt((uk5*uk5)-4*uk4*uk6))/(2*uk4))
```

```
      theta=(pi/2)-thetaab
      x2=(theta)+geo
      xel(J,26)=a1*cos(thetaab)
      yel(J,26)=b1*sin(thetaab)
      coca(26)=theta
   90 CONTINUE
      cel=0
      cel1=pi/2
      CALL num(cel,cel1,rum1,a1,e)
      circo1=rum1
      cel1=theta
      cel=0
      CALL num(cel,cel1,rum1,a1,e)
      circo2=rum1
      ulamda=(Z-c2)/(c0-c2)
      xel(J,34)=ulamda*(xel(1,34)-b13x)+b13x
      yel(J,34)=ulamda*(yel(1,34)-b13y)+b13y
      dista=(xel(J,34)-xel(J,26))*(xel(J,34)-xel(J,26))
      distb=(yel(J,34)-yel(J,26))*(yel(J,34)-yel(J,26))
      dist=sqrt(dista+distb)
      xel(J,0)=0
      yel(J,0)=b1
      dcoko=dist/(kxy/2)
      droth=dcoko
      dcirco=circo2-dcoko
      n=26
      x22=5
      xaccc=(1.0E-7)*(x1+x22)/2
      CALL ronewt(x1,x22,xaccc,dcoko,circo2,n)
      q=ronewt(x1,x22,xaccc,dcoko,circo2,n)

      ROOT=0.0
        DO 100 I=1,((kxy+10)-1)
          L=26-I
          M=L+1
          xacc=(1.0E-4)*(x1+x2)/2
          CALL rtnewt(funcd,x1,x2,xacc,dcirco,a1,e)
          ROOT=rtnewt(funcd,x1,x2,xacc,dcirco,a1,e)
           ROOT1=pi/2-ROOT
           xel(J,L)=a1*cos(ROOT1)
           yel(J,L)=b1*sin(ROOT1)
          coca(L)=ROOT
           rokas=coca(M)-ROOT
           x2=x2-rokas+geo
           droth=q*droth
           dcirco=dcirco-droth
  100     CONTINUE
  105     CONTINUE

      xel(J,66)=a1*cos((pi*32.5)/180)
      yel(J,66)=b1*sin((pi*32.5)/180)

      ditin=dist/(kxy/2)

      umoth1=(yel(J,26)-yel(J,66))/(xel(J,26)-xel(J,66))
      umoth2=(-1)/umoth1
      coth1=(-1)*umoth2*xel(J,26)+yel(J,26)
      coth2=(-1)*umoth2*xel(J,66)+yel(J,66)
      om1=1+umoth2*umoth2
      om2=-2*xel(J,26)-2*yel(J,26)*umoth2+2*umoth2*coth1
      distin=ditin
```

```
      DO 130 I=27,34
       om3a=xel(J,26)*xel(J,26)+yel(J,26)*yel(J,26)
       om3b=-2*yel(J,26)*coth1+coth1*coth1-distin*distin
       om3=om3a+om3b
       xel(J,I)=(-om2+sqrt((om2*om2)-4*om1*om3))/(2*om1)
       yel(J,I)=umoth2*xel(J,I)+coth1
       distin=distin+ditin
130     CONTINUE
   thetaab=pi*32.5/180
   thetos=(pi/2)-thetaab
   dista=(xel(J,34)-xel(J,26))*(xel(J,34)-xel(J,26))
   distb=(yel(J,34)-yel(J,26))*(yel(J,34)-yel(J,26))
   dist=sqrt(dista+distb)
   distin=dist/(kxy/2)
   gol1=distin
   gol2=distin
   ditin=0.0
   om1=1+umoth2*umoth2
   om2=-2*xel(J,66)-2*yel(J,66)*umoth2+2*umoth2*coth2

     DO 135 I=58,65
       dist=dist-ditin
       om3a=xel(J,66)*xel(J,66)+yel(J,66)*yel(J,66)
       om3b=-2*yel(J,66)*coth2+coth2*coth2-dist*dist
       om3=om3a+om3b
       xel(J,I)=(-om2+sqrt((om2*om2)-4*om1*om3))/(2*om1)
       yel(J,I)=umoth2*xel(J,I)+coth2
       ditin=distin
135     CONTINUE

   xel(J,46)=(0.5)*(xel(J,58)+xel(J,34))
   yel(J,46)=(0.5)*(yel(J,58)+yel(J,34))
   dista=(xel(J,46)-xel(J,34))*(xel(J,46)-xel(J,34))
   distb=(yel(J,46)-yel(J,34))*(yel(J,46)-yel(J,34))
   dist=sqrt(dista+distb)
   circo2=dist
   stretch=1.2
   umgrad=umoth1
   cont=(-1)*umgrad*xel(J,34)+yel(J,34)
   om1=1+umgrad*umgrad
   om2=-2*xel(J,34)-2*yel(J,34)*umgrad+2*umgrad*cont
   DO 136 k=0,12
    sp1=stretch+1
    sm1=stretch-1
    spm=sp1/sm1
    eta=REAL(k)/REAL(12)
    xeta(k)=((sp1-sm1*spm**(1-eta))/(1+spm**(1-eta)))
    xeta(k)=xeta(k)*circo2
136  CONTINUE
    k=1
   DO 138 I=35,45
       om3a=xel(J,34)*xel(J,34)+yel(J,34)*yel(J,34)
       om3b=-2*yel(J,34)*cont+cont*cont-(xeta(k)**2)
       om3=om3a+om3b
       xel(J,I)=(-om2+sqrt((om2*om2)-4*om1*om3))/(2*om1)
       yel(J,I)=umgrad*xel(J,I)+cont
       k=k+1
138     CONTINUE
   dista=(xel(J,46)-xel(J,58))*(xel(J,46)-xel(J,58))
   distb=(yel(J,46)-yel(J,58))*(yel(J,46)-yel(J,58))
   dist=sqrt(dista+distb)
   circo2=dist
```

```
      stretch=1.2
      umgrad=umoth1
      cont=(-1)*umgrad*xel(J,46)+yel(J,46)
      om1=1+umgrad*umgrad
      om2=-2*xel(J,46)-2*yel(J,46)*umgrad+2*umgrad*cont
      DO 139 k=0,12
       sp1=stretch+1
       sm1=stretch-1
       spm=sp1/sm1
       eta=REAL(12-k)/REAL(12)
       xeta(k)=1-(((sp1-sm1*spm**(1-eta))/(1+spm**(1-eta))))
       xeta(k)=xeta(k)*circo2
  139  CONTINUE
       k=1
       DO 157 I=47,57
          om3a=xel(J,46)*xel(J,46)+yel(J,46)*yel(J,46)
          om3b=-2*yel(J,46)*cont+cont*cont-(xeta(k)**2)
          om3=om3a+om3b
          xel(J,I)=(-om2+sqrt((om2*om2)-4*om1*om3))/(2*om1)
          yel(J,I)=umgrad*xel(J,I)+cont
          k=k+1
  157     CONTINUE

      cel=0
      cel1=(pi*57.5)/180
      CALL num(cel,cel1,rum1,a1,e)
      circo5=rum1
      cel=(pi*57.5)/180
      cel1=pi/2
      CALL num(cel,cel1,rum1,a1,e)
      circo14=rum1
      n=16
      x22=5
      dcoko=gol1
      dcirco=dcoko+circo5
      geo=0.105*pi
      x2=thetos+geo
      xaccc=(1.0E-7)*(x1+x22)/2
      CALL ronewt(x1,x22,xaccc,dcoko,circo14,n)
      q=ronewt(x1,x22,xaccc,dcoko,circo14,n)

         DO 170 I=67,82
          if (I.eq.82) then
           ROOT1=0
           xel(J,I)=a1*cos(ROOT1)
           yel(J,I)=b1*sin(ROOT1)
           goto 180
          endif
          xacc=(1.0E-4)*(x1+x2)/2
          CALL rtnewt(funcd,x1,x2,xacc,dcirco,a1,e)
          ROOT=rtnewt(funcd,x1,x2,xacc,dcirco,a1,e)
          ROOT1=pi/2-ROOT
          xel(J,I)=a1*cos(ROOT1)
          yel(J,I)=b1*sin(ROOT1)
          x2=ROOT+geo
          dcoko=q*dcoko
          dcirco=dcirco+dcoko
  170     CONTINUE
  180     CONTINUE

         DO 190 I=0,82
         K=164-I
```

```
        xel(J,K)=xel(J,I)
        yel(J,K)=-yel(J,I)
190     CONTINUE
    zar1=Z
    Z=Z-dc
    zar=Z
    hi=0.046
    Lar=J+1
    Kar=J
    if (zar.lt.hi) then
        goto 450
    endif
400 CONTINUE
450 CONTINUE
    Z=zar
    K=Kar
    DO 567 J=Lar,65
    DO 499 I=0,164
    xel(J,I)=xel(K,I)*(Z/zar1)
    yel(J,I)=yel(K,I)*(Z/zar1)
499 CONTINUE
    Z=Z-dc
567 CONTINUE
     Z=0
    K=65
    DO 600 J=1,65
    DO 590 I=0,164
    write(3,*) xel(K,I), -yel(K,I), Z
590 CONTINUE
    Z=Z+dc
    K=K-1
600 CONTINUE
    END

    FUNCTION fx(x,e,a1)
    REAL fx,x,a1,e
    fx=a1*sqrt(1-(e**2)*(sin(x)**2))
    return
    END

    FUNCTION fx1(x,e,a1)
    REAL fx1,x,a1,e
    fx1=a1*sqrt(1-(e**2)*(sin(x)**2))
    END

    FUNCTION rtnewt(funcd,x1,x2,xacc,dcirco,a1,e)
    INTEGER JMAX
    REAL rtnewt,x1,x2,xacc,a1,e,dcirco
    EXTERNAL funcd
    PARAMETER (JMAX=800)
    INTEGER j
    REAL df,dx,f
    rtnewt=0.5*(x1+x2)
    rtnewt=x2
    do 240 j=1,JMAX
     CALL funcd(x1,rtnewt,f,df,dcirco,a1,e)
     dx=f/df
     rtnewt=rtnewt-dx
     rtnewt1=x1-rtnewt
     rtnewt2=rtnewt-x2
     rtnewt12=rtnewt1*rtnewt2
    if (rtnewt12.lt.0) then
```

```
      pause 'rtnewt jumped out of brackets'
     endif
     if (abs(dx).lt.xacc) then
      return
     endif
240  continue
     pause 'rtnewt exceeded maximum iterations'
     END

     FUNCTION ronewt(x1,x22,xaccc,dcoko,circo2,n)
     INTEGER JMAX
     REAL ronewt,x1,x22,xaccc,dcoko,circo2
     PARAMETER (JMAX=800)
     INTEGER j
     REAL df,dx,f
     ronewt=0.5*(x1+x22)
     do 279 j=1,JMAX
     f=dcoko*(1-(ronewt**n))-circo2*(1-ronewt)
     df=(-1)*dcoko*n*(ronewt**(n-1))-circo2
     dx=f/df
      ronewt=ronewt-dx
      ronewt1=x1-ronewt
      ronewt2=ronewt-x22
      ronewt12=ronewt1*ronewt2
     if (ronewt12.lt.0) then
      pause 'ronewt jumped out of brackets'
     endif
     if (abs(dx).lt.xaccc) then
      return
     endif
279  continue
     pause 'ronewt exceeded maximum iterations'
     END

     SUBROUTINE funcd(x1,rtnewt,FN,DF,dcirco,a1,e)
     EXTERNAL fx,fx1
     CALL numinter(x1,rtnewt,ruminte,dcirco,a1,e)
     CALL fx1(rtnewt,e,a1)
     FN=ruminte
     DF=fx1(rtnewt,e,a1)
     return
     END

     SUBROUTINE numinter(x1,rtnewt,ruminte,dcirco,a1,e)
     PARAMETER(PI=3.1415926536)
     REAL ruminte,x1,rtnewt,dcirco,a1,e
     EXTERNAL fx
     CALL qsimp(fx,x1,rtnewt,s,a1,e)
     ruminte=s-dcirco
     rumintedf=s
     END

     SUBROUTINE num(cel,cel1,rum1,a1,e)
     REAL rum,a1,e
     EXTERNAL fx
     CALL qsimp(fx,cel,cel1,rum,a1,e)
     rum1=rum
     END

      SUBROUTINE qsimp(fx,x1,rtnewt,s,a1,e)
      INTEGER JMAX
      REAL x1,rtnewt,fx,s,EPS,a1,e
```

```
      EXTERNAL fx
      PARAMETER (EPS=1.e-4, JMAX=30)
      INTEGER j
      REAL os,ost,st
      ost=-1.e30
      os=-1.e30
      do 11 j=1,JMAX
        call trapzd(fx,x1,rtnewt,st,j,a1,e)
        s=(4*st-ost)/3
        if (ABS(s-os).LT.EPS*ABS(os)) return
        os=s
        ost=st
11    CONTINUE
      pause 'too many steps in qsimp'
      END

      SUBROUTINE trapzd(fx,a,b,s,n,a1,e)
      INTEGER n
      REAL a,b,s,fx
      EXTERNAL fx
      INTEGER it,j
      REAL del,sum,tnm,x
      if (n.eq.1) then
        CALL fx(a,e,a1)
        CALL fx(b,e,a1)
        fo1=fx(a,e,a1)
        fo2=fx(b,e,a1)
        s=0.5*(b-a)*(fo1-fo2)
      else
        it=2**(n-2)
        tnm=it
        del=(b-a)/tnm
        x=a+0.5*del
        sum=0.
        do 12 j=1,it
        CALL fx(x,e,a1)
           fo3=fx(x,e,a1)
            sum=sum+fo3
            x=x+del
12      CONTINUE
        s=0.5*(s+(b-a)*sum/tnm)
      endif
      return
      END
```

b. This programme generates the outer domain boundary surface

```
PROGRAM geometry
      DIMENSION xel(0:200), yel(0:200), xel1(0:200), yel1(0:200)
      DIMENSION thet1(0:100), thet2(0:100), xeta(0:300)
C     This programm was written by Mr K. Kontis
C     a1= is the major semi-diameter of the base
C     b1= is the minor semi-diameter of the base
C     c1= is the length of the cone
C     x1= is the lower limit of the integration
C     x2= is the upper limit of the integration
C     e= is the eccentricity
C     circo= is the circumference at a particular station
C     dcirco= is an increament of the circumference
C     kxy= is the number of division of the circumference
C     kz= is the number of stations in the length
```

```
C    xel,yel,z1 are the coordinates on the body

     EXTERNAL funcd
     REAL a1,b1,c1,x1,x2,e,et,ef,es,eg,circo,dcirco,xacc
     OPEN (3, FILE='OutStk.gr1')

     pi=3.1415926536
     a1=0.05
     c1=0.1875
     x20=0.3*pi
     x1=0.0
     kz=64
     dc=c1/kz
     z1=0.
     d=0.0325
     geo=0.005*pi

C    base main coordinates
     a0=0.02
     b0=0.0125
     c0=0.1875
C    station end coordinates
     c2=0.035
     b11=(c2/c0)*b0
     a2=(c2/c0)*a0
     e=sqrt(a2*a2-b11*b11)/(a2)
C    Simpson-trapezium iteration for front station
     cel=0
     cel1=(pi*57.5)/180
     CALL num(cel,cel1,rum1,a2,e)
     shark1=rum1
     cirhor=shark1-0.003
     dcirco=cirhor
     x2=((10*pi)/180)+geo
        xacc=(1.0E-4)*(x1+x2)/2
        CALL rtnewt(funcd,x1,x2,xacc,dcirco,a2,e)
        ROOT=rtnewt(funcd,x1,x2,xacc,dcirco,a2,e)
        ROOT1=pi/2-ROOT
     b13x=a2*cos(ROOT1)
     b13y=b11*sin(ROOT1)
     b14x=a2*cos((pi*32.5)/180)
     b14y=b11*sin((pi*32.5)/180)
C    Simpson-trapezium iteration for base station
     cel=0
     cel1=(pi*57.5)/180
     e=sqrt(a0*a0-b0*b0)/(a0)
     CALL num(cel,cel1,rum1,a0,e)
     circo5=rum1
     cirkos=circo5-0.003
     dcirco=cirkos
     x2=((50*pi)/180)+geo
     xacc=(1.0E-4)*(x1+x2)/2
        CALL rtnewt(funcd,x1,x2,xacc,dcirco,a0,e)
        ROOT=rtnewt(funcd,x1,x2,xacc,dcirco,a0,e)
        ROOT1=pi/2-ROOT
        xel(26)=a0*cos(ROOT1)
        yel(26)=b0*sin(ROOT1)
     xel(66)=a0*cos((pi*32.5)/180)
     yel(66)=b0*sin((pi*32.5)/180)
     disot=0.003
     umoth1=(yel(26)-yel(66))/(xel(26)-xel(66))
     umoth2=(-1)/umoth1
```

```
coth1=(-1)*umoth2*xel(26)+yel(26)
om1=1+umoth2*umoth2
om2=-2*xel(26)-2*yel(26)*umoth2+2*umoth2*coth1
om3a=xel(26)*xel(26)+yel(26)*yel(26)
om3b=-2*yel(26)*coth1+coth1*coth1-disot*disot
om3=om3a+om3b
    xel(34)=(-om2+sqrt((om2*om2)-4*om1*om3))/(2*om1)
    yel(34)=umoth2*xel(34)+coth1
disot=0.003
umoth1=(yel(26)-yel(66))/(xel(26)-xel(66))
umoth2=(-1)/umoth1
coth1=(-1)*umoth2*xel(66)+yel(66)
om1=1+umoth2*umoth2
om2=-2*xel(66)-2*yel(66)*umoth2+2*umoth2*coth1
om3a=xel(66)*xel(66)+yel(66)*yel(66)
om3b=-2*yel(66)*coth1+coth1*coth1-disot*disot
om3=om3a+om3b
    xel(58)=(-om2+sqrt((om2*om2)-4*om1*om3))/(2*om1)
    yel(58)=umoth2*xel(58)+coth1
xel(46)=0.5*(xel(34)+xel(58))
yel(46)=0.5*(yel(34)+d+yel(58)+d)
fecos1=yel(46)-umoth2*xel(46)
hlem1=umoth2
xel(46)=0.5*(xel(34)+xel(58))
yel(46)=0.5*(-yel(34)+d-yel(58)+d)
umoth1=(-yel(26)+yel(66))/(xel(26)-xel(66))
umoth2=(-1)/umoth1
fecos2=yel(46)-umoth2*xel(46)
hlem2=umoth2
dd21=b13x*yel(34)*c0+xel(34)*yel(26)*c2+xel(26)*b13y*c0
dd22=-b13x*yel(26)*c0-xel(34)*b13y*c0-xel(26)*yel(34)*c2
dd2=dd21+dd22
aa21=yel(34)*c0+yel(26)*c2+b13y*c0
aa22=-yel(26)*c0-b13y*c0-yel(34)*c2
aa2=aa21+aa22
bb21=b13x*c0+xel(34)*c2+xel(26)*c0
bb22=-b13x*c0-xel(34)*c0-xel(26)*c2
bb2=bb21+bb22
cc21=b13x*yel(34)+xel(34)*yel(26)+xel(26)*b13y
cc22=-b13x*yel(26)-xel(34)*b13y-xel(26)*yel(34)
cc2=cc21+cc22
aa2=aa2/dd2
bb2=bb2/dd2
cc2=cc2/dd2
DD2=dd2/dd2

WRITE(3,'(/1X,A)') 'Roots of xyz geometry:'
b1=0.055
uk4=(a1*a1*(hlem1**2)+b1*b1)
uk5=-2*b1*fecos1
outstruk6=((fecos1**2)-((a1*hlem1)**2))
thet1(I)=acos((-uk5+sqrt((uk5*uk5)-4*uk4*uk6))/(2*uk4))
velo2=thet1(I)-0.112011632
uk4=(a1*a1*(hlem2**2)+b1*b1)
uk5=-2*b1*fecos2
uk6=((fecos2**2)-((a1*hlem2)**2))
thet2(I)=acos((-uk5+sqrt((uk5*uk5)-4*uk4*uk6))/(2*uk4))
velo1=-1*(thet2(I)+0.059329656)

a1=0.05
b1=0.055
e=(sqrt(b1*b1-a1*a1))/b1
```

```
      e1=e
      cel=0
      theat=(pi/2)-velo2
      cel1=theat
      CALL num(cel,cel1,rum1,a1,e)
      circ11=rum1
      cel=theat
      cel1=pi/2
      CALL num(cel,cel1,rum1,a1,e)
      circ12=rum1
      cel=0
      cel1=pi/2
      CALL num(cel,cel1,rum1,a1,e)
      circo1=rum1
      theat1=(pi/2)+velo1
      cel=0
      cel1=theat1
      CALL num(cel,cel1,rum1,a1,e)
      circ22=rum1
      cel=theat1
      cel1=pi/2
      CALL num(cel,cel1,rum1,a1,e)
      circ29=rum
      circ33=circ12+circ29
      stretch=1.2
      DO 136 k=0,46
       sp1=stretch+1
       sm1=stretch-1
       spm=sp1/sm1
       eta=REAL(46-k)/REAL(46)
       xeta(k)=1-(((sp1-sm1*spm**(1-eta))/(1+spm**(1-eta))))
       xeta(k)=xeta(k)*circ11
  136  CONTINUE
      k=1
      xel(0)=0
      yel(0)=b1-d
      ROOT=0.0
      x2=0.15*pi
      dcirco=xeta(1)
      DO 310 I=1,46
           e=e1
           xacc=(1.0E-4)*(x1+x2)/2
           CALL rtnewt(funcd,x1,x2,xacc,dcirco,a1,e)
           ROOT=rtnewt(funcd,x1,x2,xacc,dcirco,a1,e)
           ROOT1=pi/2-ROOT
           xel(I)=a1*cos(ROOT1)
           yel(I)=b1*sin(ROOT1)-d
           x2=ROOT+x20
           k=k+1
           dcirco=dcirco+xeta(k)
  310      CONTINUE
      DO 311 k=0,72
       sp1=stretch+1
       sm1=stretch-1
       spm=sp1/sm1
       eta=REAL(k)/REAL(46)
       xeta(k)=(((sp1-sm1*spm**(1-eta))/(1+spm**(1-eta))))
       xeta(k)=xeta(k)*circ33
  311  CONTINUE
      dcirco=xeta(1)
      k=1
       DO 360 I=47,118
```

```
        if (ROOT.lt.(1.57077)) then
        e=e1
        xacc=(1.0E-4)*(x1+x2)/2
        CALL rtnewt(funcd,x1,x2,xacc,dcirco,a1,e)
        ROOT=rtnewt(funcd,x1,x2,xacc,dcirco,a1,e)
        if (ROOT.gt.(1.57077)) then
         dcirco=dcirco-circo1
         dcirco=dcirco+circo1
          x2=(pi/2)+x20
          goto 315
         endif
         ROOT1=pi/2-ROOT
         xel(I)=a1*cos(ROOT1)
         yel(I)=b1*sin(ROOT1)-d
         goto 340
        endif
315      CONTINUE
        e=e1
        xacc=(1.0E-4)*(x1+x2)/2
        CALL rtnewt(funcd,x1,x2,xacc,dcirco,a1,e)
        ROOT=rtnewt(funcd,x1,x2,xacc,dcirco,a1,e)
        ROOT1=pi/2-ROOT
         xel(I)=a1*cos(ROOT1)
         yel(I)=b1*sin(ROOT1)-d
340     CONTINUE
      x2=ROOT+x20
      k=k+1
      dcirco=dcirco+xeta(k)
360   CONTINUE
    DO 379 k=0,46
     sp1=stretch+1
     sm1=stretch-1
     spm=sp1/sm1
     eta=REAL(46-k)/REAL(46)
     xeta(k)=1-(((sp1-sm1*spm**(1-eta))/(1+spm**(1-eta))))
     xeta(k)=xeta(k)*circ11
379   CONTINUE
      k=1
     dcirco=circ22/(46)
      dcirco1=dcirco
      dcirco=dcirco+circ11+circ33
      DO 400 I=119,164
         e=e1
         xacc=(1.0E-4)*(x1+x2)/2
         CALL rtnewt(funcd,x1,x2,xacc,dcirco,a1,e)
         ROOT=rtnewt(funcd,x1,x2,xacc,dcirco,a1,e)
          ROOT1=pi/2-ROOT
          if (ROOT.gt.(3.14155)) then
           xel(164)=0
           yel(164)=-b1-d
           ROOT=pi
           goto 400
          endif
         xel(I)=a1*cos(ROOT1)
         yel(I)=b1*sin(ROOT1)-d
         x2=ROOT+x20
         dcirco=dcirco+dcirco1
400        CONTINUE
    kz=64
    dc=c1/kz
    gdc=dc
    dic1=3*dc
```

```
      del1=c1+dic1
      z1=4*dc
      z2=dc
      DO 567 J=1,64
      DO 499 I=0,164
      xol=(xel(I))*(z1/del1)
      yol=(yel(I))*(z1/del1)
      WRITE(3,*) xol,-yol,z2
  499 CONTINUE
      z1=z1+dc
      z2=z2+dc
  567 CONTINUE
       END

      FUNCTION fx(x,e,a1)
      REAL fx,x,a1,e
      fx=a1*sqrt(1-(e**2)*(sin(x)**2))
      return
      END

      FUNCTION fx1(x,e,a1)
      REAL fx1,x,a1,e
      fx1=a1*sqrt(1-(e**2)*(sin(x)**2))
      END

      FUNCTION rtnewt(funcd,x1,x2,xacc,dcirco,a1,e)
      INTEGER JMAX
      REAL rtnewt,x1,x2,xacc,a1,e,dcirco
      EXTERNAL funcd
      PARAMETER (JMAX=600)
      INTEGER j
      REAL df,dx,f
      rtnewt=0.5*(x1+x2)
      do 240 j=1,JMAX
       CALL funcd(x1,rtnewt,f,df,dcirco,a1,e)
       dx=f/df
       rtnewt=rtnewt-dx
       rtnewt1=x1-rtnewt
       rtnewt2=rtnewt-x2
       rtnewt12=rtnewt1*rtnewt2
      if (rtnewt12.lt.0) then
       pause 'rtnewt jumped out of brackets'
      endif
      if (abs(dx).lt.xacc) then
       return
      endif
  240 continue
      pause 'rtnewt exceeded maximum iterations'
      END

      SUBROUTINE funcd(x1,rtnewt,FN,DF,dcirco,a1,e)
      EXTERNAL fx,fx1
      CALL numinter(x1,rtnewt,ruminte,dcirco,a1,e)
      CALL fx1(rtnewt,e,a1)
      FN=ruminte
      DF=fx1(rtnewt,e,a1)
      return
      END

      SUBROUTINE numinter(x1,rtnewt,ruminte,dcirco,a1,e)
      PARAMETER(PI=3.1415926536)
      REAL ruminte,x1,rtnewt,dcirco,a1,e
```

```
      EXTERNAL fx
      CALL qsimp(fx,x1,rtnewt,s,a1,e)
      ruminte=s-dcirco
      rumintedf=s
      END

      SUBROUTINE num(cel,cel1,rum1,a1,e)
      REAL rum,a1,e
      EXTERNAL fx
      CALL qsimp(fx,cel,cel1,rum,a1,e)
      rum1=rum
      END

      SUBROUTINE qsimp(fx,x1,rtnewt,s,a1,e)
      INTEGER JMAX
      REAL x1,rtnewt,fx,s,EPS,a1,e
      EXTERNAL fx
      PARAMETER (EPS=1.e-4, JMAX=30)
      INTEGER j
      REAL os,ost,st
      ost=-1.e30
      os=-1.e30
      do 11 j=1,JMAX
        call trapzd(fx,x1,rtnewt,st,j,a1,e)
        s=(4*st-ost)/3
        if (ABS(s-os).LT.EPS*ABS(os)) return
        os=s
        ost=st
11    CONTINUE
      pause 'too many steps in qsimp'
      END
      SUBROUTINE trapzd(fx,a,b,s,n,a1,e)
      INTEGER n
      REAL a,b,s,fx
      EXTERNAL fx
      INTEGER it,j
      REAL del,sum,tnm,x
      if (n.eq.1) then
        CALL fx(a,e,a1)
        CALL fx(b,e,a1)
        fo1=fx(a,e,a1)
        fo2=fx(b,e,a1)
        s=0.5*(b-a)*(fo1-fo2)
      else
        it=2**(n-2)
        tnm=it
        del=(b-a)/tnm
        x=a+0.5*del
        sum=0.
        do 12 j=1,it
        CALL fx(x,e,a1)
           fo3=fx(x,e,a1)
            sum=sum+fo3
            x=x+del
12      CONTINUE
        s=0.5*(s+(b-a)*sum/tnm)
      endif
      return
      END
```

Awards

1. Bronze Medal of 47th International Astronautical Federation Congress for best student paper and presentation, Beijing, PR of China, October 1996.
2. Conference travel award to participate in the 14th Applied Aerodynamics Conference in New Orleans by the Royal Aeronautical Society and the Greek Ministry of Technology, June 1996.
3. First Prize for the best 20th ISTS student presentation and paper by the Japanese Council of Industry and Labour promotion of Gifu Aerospace Heavy Industries, May 1996.

List of Publications

1. Kontis, K., Qin, N., Stollery, J.L., "Computational and Experimental Investigation of Hypersonic Performance of a Lifting Elliptic Cone With and Without Strakes", 15th AIAA Applied Aerodynamic Conference Proceedings, Atlanta, USA, AIAA 97-2252, June 1997.
2. Kontis, K., Stollery, J.L., Edwards, J.A., "Hypersonic Effectiveness of Slender Lifting Elliptic Cones With and Without Strakes", 35th AIAA Aerospace Sciences Meeting and Exhibit, Reno, Nevada, USA, AIAA 97-0521, January 1997.
3. Kontis, K., "A Small Satellite Solution for Re-Entry Technology and Demonstration", 47th IAF Congress, Beijing, PR of China, ST-96-W.2.04, October 1996.
4. Kontis, K., Stollery, J.L., "Control Effectiveness of a Jet-Slender Body Combination at Hypersonic Speeds", 14th AIAA Applied Aerodynamics Conference Proceedings, New Orleans, LA, AIAA 96-2470, June 1996. (to be published in the Journal of Spacecraft and Rockets).
5. Kontis, K., "Control Jet-Slender Body Combination Performance Characteristics at Hypersonic Speeds", Proceedings of the 20th International Symposium on Space Technology and Science/11th International Astrodynamics Symposium, Gifu, Japan, 96-n-10, May 1996.
6. Kontis, K., "Investigation of the Flow over a Sharp Flat Plate with Compression Corner", COA/DAeS/9506, Cranfield University, 1995.

Papers

1.Control Effectiveness of a Jet-Slender Body Combination at Hypersonic Speeds

2.Hypersonic Effectiveness of Slender Lifting Elliptic Cones With and Without Strakes

3.Computational and Experimental Investigation of Hypersonic Performance of Lifting Elliptic Cone With and Without Strakes

AIAA 96-2470

Control Effectiveness of a Jet-Slender Body Combination at Hypersonic Speeds

Kontis, K, and Stollery, JL

14th AIAA Applied Aerodynamics Conference Proceedings, New Orleans, June 1996 and to be published in the Journal of Spacecraft and Rockets, Vol. 34, No. 6, November-December 1997

CONTROL EFFECTIVENESS OF A JET-SLENDER BODY COMBINATION AT HYPERSONIC SPEEDS

K Kontis* and J L Stollery†
College of Aeronautics, Cranfield University, Bedfordshire, MK43 0AL, UK

Abstract

The present investigation aims to determine the effects of jet control, on the aerodynamic characteristics, performance and stability of a 5^o semi-angle slender cone missile configuration. The tests were made in the College of Aeronautics hypersonic gun tunnel using both sharp and blunted cones. The study was conducted at a Mach number of 8.2 and a Reynolds number of 93500/cm, at pitch angles of -15^o to 15^o. The boundary layer was laminar. Air was used as the working gas for both the freestream and the sonic jet. The tests employed high speed schlieren photography to study the overall flow field. Quantitative studies of the effect of the jet have been made by pressure measurements. The forces were measured with a 3-component balance equipped with semi-conductor strain gauges.

Notation

A	area
C	Chapman-Rubesin constant
C_A	axial force coefficient
Cd	nose drag coefficient
C_m	pitching moment coefficient
C_N	normal force coefficient
C_p	pressure coefficient
$C_{p,max}$	stagnation pressure coefficient
d	diameter
L_1	measured total aerodynamic force with jet on
L_o	measured aerodynamic force with jet off
$F_{j,v}$	measured jet force without any external flow i.e. $M_\infty=0$
h	penetration height
K	amplification factor
L	total cone length
L_{sep}	separation distance
M	Mach number
P	pressure
$Re_{/cm}$	unit Reynolds number
T	temperature
x'	distance along the jet meridian from jet nozzle
x	distance from the nose
α	angle of attack (^{o})
γ	ratio of specific heats
δ_e	equivalent half cone angle
δ	cone semi-angle
ε	$(\gamma-1)/(\gamma+1)$
κ_ε	bluntness parameter, $M^3 Cd\ \varepsilon\ (d_n/x)$
φ	flow momentum flux
Φ	ray angle of sharp cone
χ	viscous interaction parameter, $M^3\sqrt{(C/Re_x)}$
χ_ε	$\varepsilon[0.664+1.73(T_w/T_o)]\ \chi$

Subscripts

b	at base
e	at jet exit
j	jet flow property
n	nose
o	total value
w	wall
1	condition behind a shock
2	condition ahead separation
∞	freestream

Introduction

Future defence weapons may include very high speed projectiles flying and manoeuvring over a wide incidence range. In situations where conventional aerodynamic surfaces cannot function properly, either due to the low density of the medium or to the considerable aerodynamic heating effects, secondary fluid injection is proposed as an attractive method of controlling the flight path. The Space Shuttle is a current example of the application of jet control for orbital flight manoeuvring. Even in cases where the interaction force becomes very small, as in rarefied flows, the jet thrust is still available for control. The complexity of flow fields created by jets interacting with external flows is such that the present understanding of them relies heavily on experimental data.

Experimental Set-up

Models

The general geometrical characteristics of the slender cone configurations are shown in figure 1. For the blunt cone, the bluntness ratio was 33.3% ($d_n/d_b=1/3$). The models were equipped with a single jet hole. Pressure models were equipped with tappings along the jet meridian.
The force model's air feed system used dual injection ports located in the horizontal axis plane of the models. In order to reduce the coupling forces between the jet feed system and the models, the pressure feed employed coiled tubes.

Gun Tunnel Facility

All the experiments were conducted in the College of Aeronautics gun tunnel. The tests were carried out with air as the working jet and freestream gas. An axisymmetric contoured nozzle provided a uniform flow at $M_\infty=8.2$ with a useful test jet diameter of 15.2 cm. The tunnel is equipped with a high speed single-pass schlieren system. This uses a high intensity microsecond duration argon spark source to illuminate density gradients in the flow. Pressure measurements were carried out using Kulite XCS-190 series, absolute pressure transducers. The forces were measured with a 3-component balance equipped with semi-conductor strain gauges. During the run, the working section is subjected to some mechanical vibrations. Due to the balance and models mass, these vibrations produce damped harmonic oscillations. Digital filters were designed,

---

* PhD Student
† Professor of Aerodynamics

Copyright © 1996 by K Kontis and J L Stollery. Published by the American Institute of Aeronautics and Astronautics, Inc. with permission.

in order to remove the natural frequency components from the test signals.

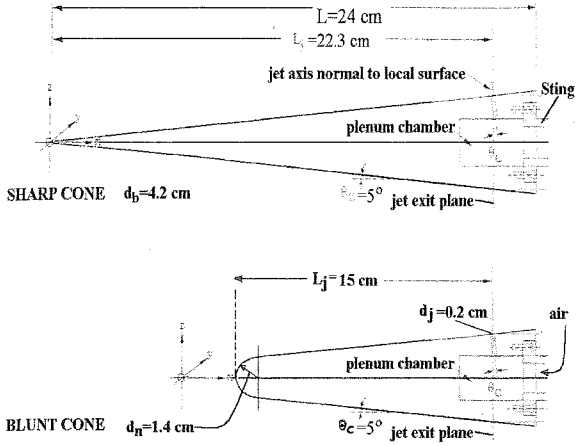

Fig.1 General geometry of the models

General Aspects of the Flow

Entropy Layer Effects

The introduction of bluntness modifies the aerodynamic properties of the flow over a slender body from that with an equivalent sharp nose. The bow shockwave stands off from the nose and is highly curved. These characteristics give rise to gradients in flow properties normal to the cone surface. The most important feature of the flow is that the streamtubes crossing the shock near the nose suffer a large entropy rise and then expand rapidly downstream. This entropy layer is a region of high temperature and low density. The result is total pressure losses due to the bow shock and lower local Mach number and unit Reynolds number in this layer than in the freestream. The entropy layer influences the local flow conditions for a large distance downstream. This entropy layer is eventually swallowed by the boundary layer but not in our experiments.

Effect of Nose Bluntness on Separation

Simpkins[1] found that the introduction of nose bluntness promotes separation, provided the boundary layer remains laminar. He did an experimental comparison of the interaction between a radial underexpanded jet and the hypersonic flow over a sharp and a blunt cone of semi-angle five degrees at a freestream Mach number of thirteen, with laminar boundary layers. Kumar and Stollery[2] identified some of the parameters which determine the upstream extent and lateral spreading of the separation front around an underexpanded transverse jet on a slender blunted cone. The interaction region was laminar.

Some experiments by Holden[3] on a sharp and blunt flat plate with a trailing edge flap (compression corner) showed that the extent of the laminar separated region was related to the viscous bluntness interaction parameter $\chi_\varepsilon/\kappa_\varepsilon^{2/3}$. The viscous bluntness interaction parameter ($\chi_\varepsilon/\kappa_\varepsilon^{2/3}$~M/$[d_n^{2/3}\sqrt{Re_x}]$) takes into account the relative effects of changes in Mach number and Reynolds number on the extent of the interaction. For $0.1 \le \chi_\varepsilon/\kappa_\varepsilon^{2/3} \le 0.5$, the introduction of leading edge bluntness promoted separation, while for $\chi_\varepsilon/\kappa_\varepsilon^{2/3} \le 0.1$, the leading edge bluntness resulted in a reduction in the extent of boundary layer separation. Holden's tests were entirely laminar.

Analytical Models

A combination of second order blast wave theory and Newtonian theory[4] was used to predict the pressure distribution on the blunt cone for $\alpha=0^o$,

$$\frac{P}{P_\infty}=\{0.067M_\infty^2\frac{\sqrt{Cd}}{(x/d_n)}+1.44\}+\gamma M_\infty^2\sin^2\delta\,, \qquad (1a)$$

For $\alpha>2.5^o$, another relation from Bade's paper[4] was used,

$$\frac{P}{P_\infty}=\frac{(\gamma+1)\gamma M_\infty^2\alpha^2}{2}[1+\frac{0.382}{\alpha^2}(\frac{2\varepsilon Cd}{(x/d_n)(\gamma+1)})^{2/3} \qquad (1b)$$

The nose drag coefficient was obtained by integrating the modified Newtonian flow pressure distribution over the hemispherical nose. For the modified Newtonian flow, Cd=0.964 for a hemisphere.

The pressure distribution over the sharp cone was predicted by a relation from the paper by Wells et al[5],

$$\frac{P}{P_\infty}=1+(\sin\delta\cos\alpha+\cos\delta\sin\alpha)^2\gamma M_\infty^2\,, \qquad (2)$$

Estimation of the Local Surface Mach Number

Blunt cone

1)$\alpha=0^o$

For a blunt body, the boundary layer streamtube is processed by the strong, near-normal section of the nose shockwave. From the Ames tables[6], the reservoir pressure downstream of a normal shock is given by the Rayleigh-pitot relationship. Assuming the flow at the edge of the boundary layer to be isentropic, the boundary layer edge Mach number is,

$$M_2=\sqrt{\frac{2}{\gamma-1}\{(\frac{P_{01}}{P_\infty}\frac{P_\infty}{P_2})^{(\gamma-1)/\gamma}-1\}}\,, \qquad (3)$$

P_2 is the measured pressure, (without the jet), at the jet location. P_{01}/P_∞ is given by the Rayleigh-pitot relationship.

2)$\alpha\neq0^o$

Cheng et al[7] have shown that the shock structure close to the axis of a blunt cone at incidence, $\alpha\neq0^o$, is determined by the shape of the nose. As with the zero incidence case, the surface streamtubes, on a blunt cone at incidence, are processed by a normal shock. Therefore, the reservoir pressure within these streamtubes can be approximated to that immediately downstream of a normal shock. This is given by the Rayleigh-pitot relationship. The Mach number on the blunt cone, at incidence, was determined by substituting from the Rayleigh-pitot relationship and the measured pressure, P_2, into equation 3.

Sharp cone

1)$\alpha=0^o$

From Brower's tables[8] for compressible flow, the local Mach number was interpolated, M_2= 7.39.

2)$\alpha<0^o$

High et al[9] used the concept of the equivalent cone (a right circular cone at zero incidence having the same freestream Mach number and a half cone angle equal to the angle between the freestream Mach number vector and the ray line on the cone under examination). δ_e was calculated by,

$$\delta_e=\sin^{-1}(\sin\delta\cos a\alpha+\cos\delta\sin\alpha\cos\Phi)\,, \qquad (4)$$

with $\Phi=0^o$ along the bottom generator and 180^o along the top generator. The local Mach number was calculated[9], for δ_e evaluated at Φ equal to 180^o. For $\Psi<1$,

$$M_2=M_\infty\cos\delta_e(1-\frac{\sin\delta_e}{M_\infty})^{0.5}\{[1+e^{-1-1.52\Psi}][1+(\frac{\Psi}{2})^2]\}^{-0.5}\,, \qquad (5)$$

if $\Psi \geq 1$,

$$M_2 = M_\infty \cos\delta_e \left(1 - \frac{\sin\delta_e}{M_\infty}\right)^{0.5} \left(1 + 0.35\Psi^{1.5}\right)^{-0.5}, \quad (6)$$

where Ψ is the hypersonic similarity parameter $M_\infty \sin\delta_e$.

3) $\alpha > 0^\circ$

A Prandtl-Meyer expansion was assumed from the freestream conditions to the surface values and since the flow is isentropic,

$$M_2 = \sqrt{\frac{2}{\gamma - 1}\left\{\left(1 + \frac{\gamma - 1}{2} M_\infty^2\right) / \left(\frac{P_2}{P_\infty}\right)^{(\gamma - 1)/\gamma} - 1\right\}}, \quad (7)$$

Results and Discussion

Description of the Jet Flow Field

The jet flow field interaction region is shown in figure 2. The experiments were conducted at $Re_\infty/cm = 93500$ with a jet reservoir pressure of $P_{oj} = 110$ psia. The freestream pressure was 0.137 psia, giving a ratio $P_{oj}/P_\infty \approx 800$. Thus the jet was sonic at exit and highly underexpanded. Due to the relatively high Mach number and the low Reynolds number, the initial boundary layer on the surface of the cones, in the absence of the jet, was laminar.

The jet plume presents an obstacle to the external flow, (figure 2), which causes a strong shock which causes the boundary layer upstream of the jet to separate. In contrast to the two-dimensional situation in which the entire external flow must go over the jet-induced obstruction, the flow can go around the three-dimensional jet. The flow field near the separation point is controlled by the interaction between the resultant free shear layer and the external stream.

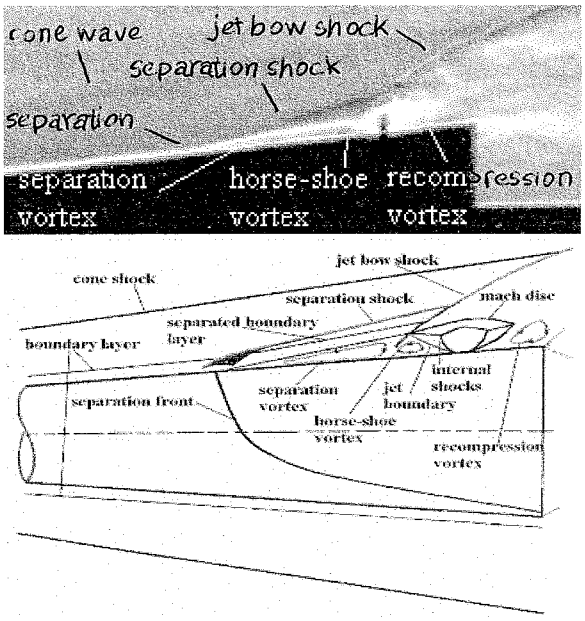

Fig.2 General structure of the interaction region for the sharp cone at $\alpha = 0^\circ$

As a result of high pressures downstream of the separation shock and mixing between the two streams, the jet is turned in the direction of the external flow, (figure 3). A three-dimensional shock structure forms in the jet plume as it is turned, bounded by a three-dimensional mixing layer. Some of the high pressure external air behind this separation shock flows downstream causing a high pressure region in front of the jet. From this high pressure region, the external air also flows radially outward along the surface of the cone, expanding to lower pressures. Finally this expanding reverse flow is terminated by a shock system. As the reverse flow continues outward from the jet it turns toward the downstream direction.

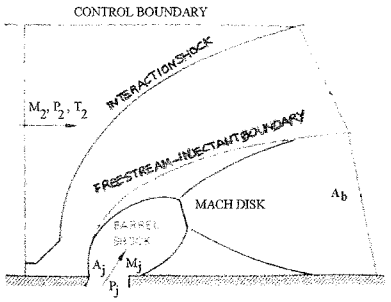

Fig.3 Model for jet injection into a hypersonic freestream, (ref. 14)

In order to satisfy the boundary conditions, at least two counter-rotating vortices must be present within the upstream separated region, (figure 2), the clockwise separation vortex in the separated flow region and the counterclockwise jet horse-shoe vortex in the region immediately upstream of the jet. Figure 4 suggests that there may be a set of vortices in the jet wake rotating around each other.

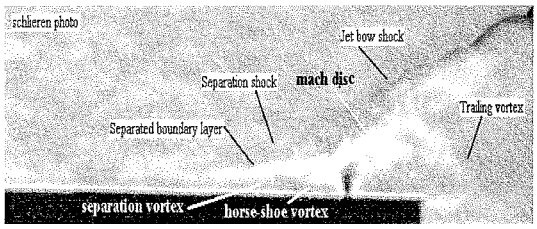

Fig.4 Trailing vortex structure

An important feature of interest is the strong shock which terminates the supersonic region of the jet (often referred to as the Mach disc or normal shock). The Mach disk is dish-shaped and in our experiments is parallel to the exit plane, (figures 2 and 4).

The absence of a separation shockwave along the 180° meridian in the schlieren photographs, (figures 5 and 6), means that the flow remains attached along this meridian and hence the shape of the separated region must be similar to that shown in figure 2.

Parameters for Data Presentation

a)In considering the general phenomenon of jet interaction, it is appropriate to define the control parameters of the problem. The ratio of jet to undisturbed flow momentum flux was used[10], ($d_b = 4.2$cm, $d_j = 0.2$cm, $\gamma_j = \gamma$, $M_j = 1$ and $P_{oj}/P_j = 1.892$),

$$\frac{\varphi_j}{\varphi_\infty} = \frac{\rho_j u_j^2 A_j}{\rho u_\infty^2 A_b} = \frac{P_j \gamma_j M_j^2 A_j}{P_\infty \gamma M_\infty^2 A_b} \sim \frac{P_j d_j^2}{P_\infty M_\infty^2 d_b^2} \sim \frac{P_{oj}}{P_2 M_2^2}, \quad (8)$$

where A_b is the base area of the cones.

b)The interaction force due to the pressure distribution induced on the body by the interaction between the jet and the cone flow can be represented in the form of an amplification factor, K,

$$K = L_1 / (L_0 + F_{j,v}), \quad (9)$$

Schlieren Visualisation Studies

Effect of Bluntness

It was found, (figures 5 and 6), that the introduction of nose bluntness effectively increases the jet size by reducing the local surface pressure ahead of the separation region. It also causes a delay in separation (e.g. figures 5d and 6d). The nose bluntness causes the boundary layer to grow by mutual interaction with the entropy layer and increases the magnitude of the favorable pressure gradient upstream of the jet and consequently, causes the velocity distribution in the boundary layer to be fuller close to the body. The reduced lengths of the separated regions are also evident from the pressure distributions (figure 7).

Substituting $d_n/x=0.0936$ (corresponding to the location of jet the orifice), Cd=0.964, $M_\infty=8.2$, $T_w=296K$, $T_o=1290K$, $\gamma_\infty=1.4$, $C\approx1$ and $Re_x=1.349x10^6$, into Holden's equations, it was found that $\chi_\varepsilon/\kappa_\varepsilon^{2/3}=0.0387$, which is lower than 0.1. Thus, Holden work also predicts a reduction of separation, at 0° incidence, for a blunt body, compared to the equivalent sharp body, although his theory is based on experiments on flat plates.

From Stetson's data[11] the distance needed for the boundary layer to swallow the entropy layer was calculated as 2 m. This means that for the blunt model tested here (L=16.7 cm) the whole flow field around the cone is influenced by the entropy layer.

The boundary-layer edge becomes totally invisible for the blunt cone (figures 5a and 5b). This is because the highly curved shock wave produces strong density gradients throughout the entire flow field that obscure the density gradients in the boundary layer, thus making the identification of separation of the flow very difficult.

The pressure measurements at zero incidence, (figure 8), with no jet, show that the effect of the nose bluntness is felt over the entire body length. The surface pressure distribution is reduced by the expansion at the shoulder to about 70 per cent of the sharp cone values. Because of the lower undisturbed surface pressure on the blunt cone, (figure 7), the jet pressure ratio, P_{oj}/P_2, is higher on the blunt cone than on the sharp cone and therefore, the jet penetration into the undisturbed flow will be greater in the blunt cone case (e.g. figures 5a and 6a). The difference between the two cones reduces as incidence decreases, (figures 5 and 6). This is because the bluntness effect on surface pressure distribution diminishes and approaches the equivalent sharp cone surface pressure near the jet as the angle of attack decreases, (figure 8).

The jet bow shock is closer to the jet for the sharp configuration, (e.g. figures 5d and 6d), this is due to the higher total pressure in the shock layer and the higher local stream velocity, (as the local surface Mach number is higher than for the blunt cone case). The oscillation of the bow wave ahead of the jet is apparent in all schlieren pictures and indicates the unsteady nature of the jet interaction with the separated shear layer.

Effect of Incidence

The effect of incidence is to decrease the local Mach number and increase the local Reynolds number along the windward ray. On the leeward ray, the local Mach number increases and the local Reynolds number decreases.

For the 'attached crossflow' case ($\alpha\leq\delta$), the schlieren pictures, (figures 5c, 5e, 6c and 6e), show a thickening of the boundary layer along the leeward meridian at an incidence of 5°. A decrease in heat transfer along the leeward meridian is expected[2], and it is due to the decrease in pressure in the leeward region of the cones, (figure 8).

Figure 8 shows a progressive decrease in cone pressure along the leeward meridian with incidence. The decrease in the local cone pressure along the leeward meridian with incidence effectively increases the local jet pressure ratio P_{oj}/P_2. The increased jet pressure ratio increases the diameter and penetration of the jet. This strengthens the interaction and promotes separation along the leeward meridian (figures 5 and 6). The increase in jet diameter also increases the jet bow shock stand-off distance (figures 5 and 6) and the diameter of the jet horseshoe vortex[2].

For the 'separated crossflow' case ($\alpha>\delta$), at incidences 10° and 15°, schlieren photographs, (figures 5a, 5b, 5f, 5g, 6a, 6b, 6f and 6g), show the establishment of a disturbed flow region over the leeward surface. This is probably, due to separation of the crossflow, resulting in the establishment of a pair of counter-rotating vortices, over the leeward region of the body. At these incidences, the leeward jet exhausts into a complex separated crossflow structure.

The density gradients associated with the crossflow vortices mask the gradients associated with the jet interaction region and thus make it difficult to observe the effects of the jet on the local flow field.

Schlieren pictures on the leeward side, (figures 6a and 6b), seem to show an increase in the strength of the crossflow vortices as the incidence increases from 10° to 15°. This was observed, as well, by other researchers[12,13] on experiments on a tangent ogive/cylinder configuration and on an elliptic cone configuration.

Equivalent Penetration Model

The schlieren pictures of the shock patterns produced by the jet injection, are reminiscent of the flow around a cylinder protruding from a solid surface. Based on this analogy, the modified equation of Zukoski et al[14] was used,

$$\left(\frac{A_b}{A_j}\right)^{\frac{1}{2}}=\frac{2.275}{M_2}\left(\frac{P_{oj}}{P_2C_p^*}\right)^{\frac{1}{2}}\left[1-\left(\frac{P_2}{P_{oj}}\right)^{\frac{2}{7}}\right]^{\frac{1}{4}}, \qquad (10)$$

$$C_p^*=\left(\frac{8.933M_2^2}{7M_2^2-1}\right)^{\frac{5}{2}}-\frac{1}{0.7M_2^2}, \qquad (11)$$

where A_b is the cross section area of the equivalent penetration model, (figure 9), and C_p^* is the pressure coefficient which corresponds to the stagnation pressure, of the equivalent cylinder protruding, behind a normal shock in the primary flow of Mach number, M_2. If a quarter sphere-half cylinder model is assumed then $A_b=\pi h^2/2$ (theory **A**), and if a spherical nosed cylinder is assumed then $A_b=\pi h^2$ (theory **B**), (figure 9).

The penetration height is characteristic of the scale of the disturbance produced by the jet. Figure 10 shows the comparison of the penetration heights, measured from the schlieren pictures, with each of the above theories. Theory **B** seems to agree better with the experimental findings of the blunt cone, while theory **A** seems to agree better with the experimental findings of the sharp cone. This is some indication of a different shape of disturbance. For the sharp cone the data correlates as,

$$\frac{h}{d_j}=\left[\frac{P_{oj}}{P_2M_2^2}\right]^{0.8}, \qquad (12)$$

and for the blunt cone,

$$\frac{h}{d_j}=0.7\left[\frac{P_{oj}}{P_2M_2^2}\right]^{0.6}, \qquad (13)$$

BLUNT CONE

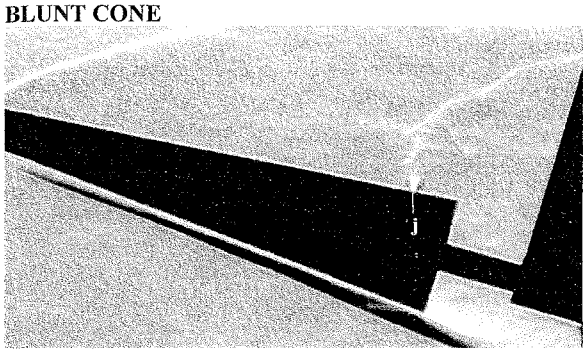

a)α=15°

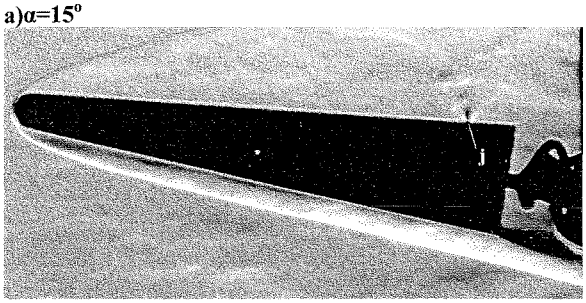

b)α=10°

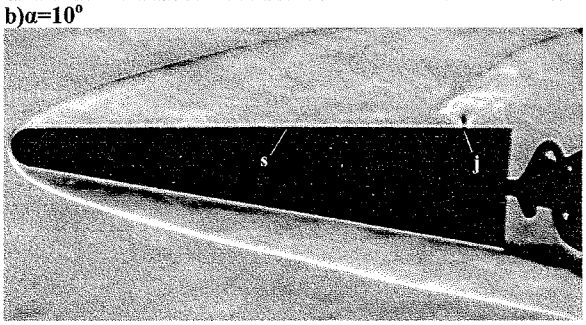

c)α=5°

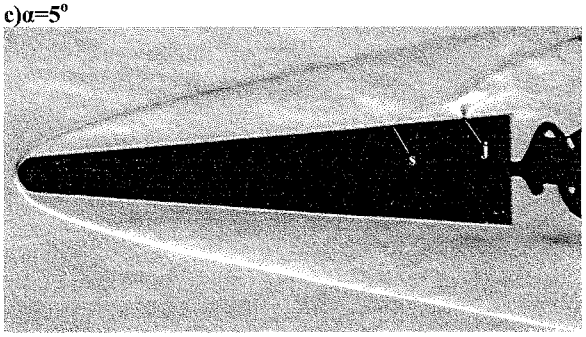

d)α=0°

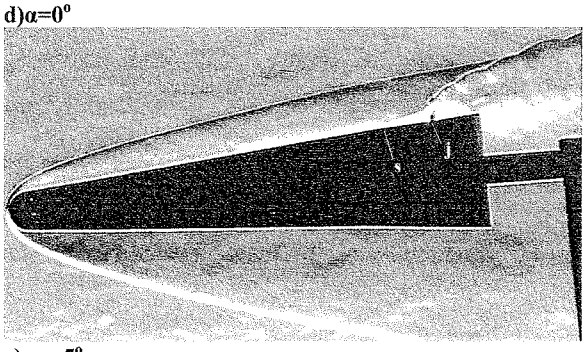

e)α= -5°

Fig.5 Schlieren visualisation studies for the blunt cone (continued overleaf)

SHARP CONE

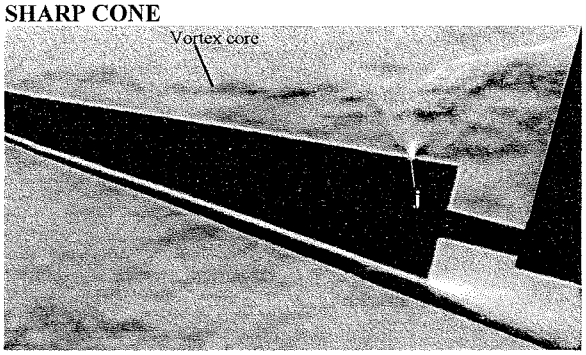

a)α=15°

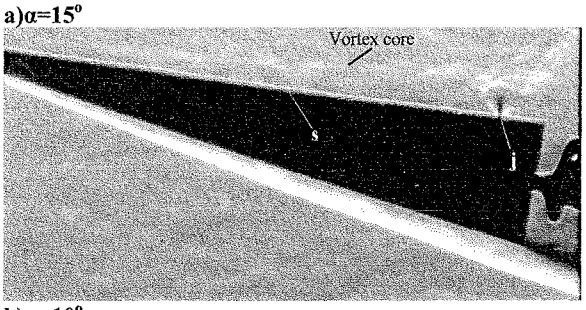

b)α=10°

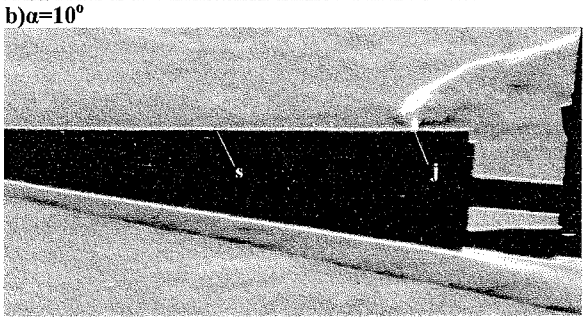

c)α=5°

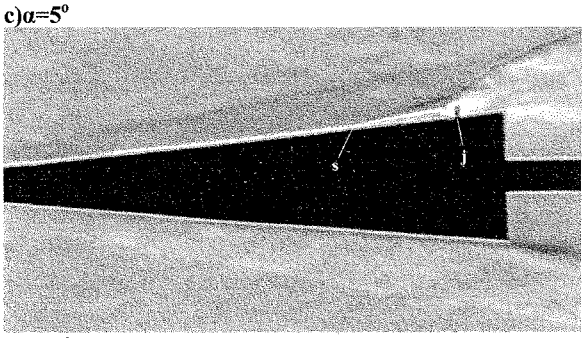

d)α=0°

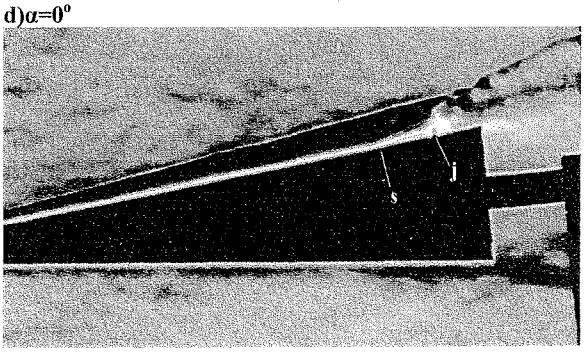

e)α= -5°

Fig.6 Schlieren visualisation studies for the sharp cone (continued overleaf)

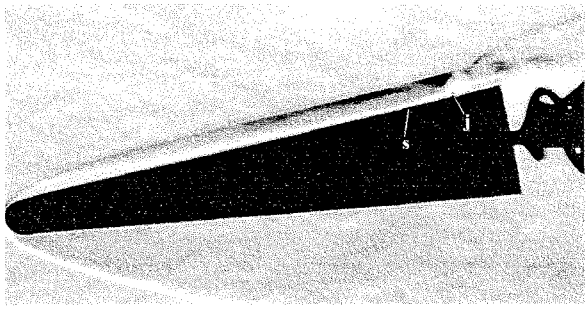

f)α= -10°

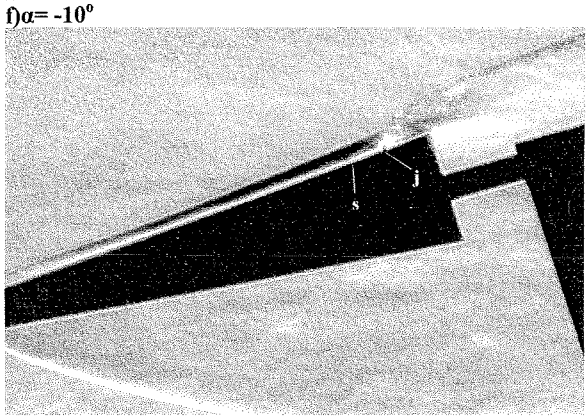

g)α= -15°

Fig.5 Schlieren visualisation studies for the blunt cone (concluded)

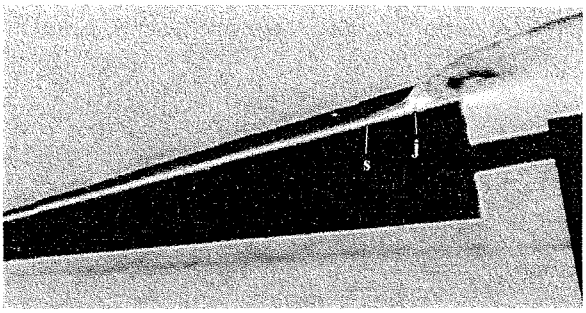

f)α= -10°

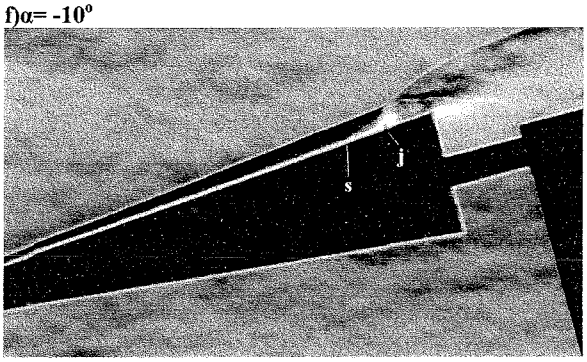

g)α= -15°

Fig.6 Schlieren visualisation studies for the sharp cone (concluded)

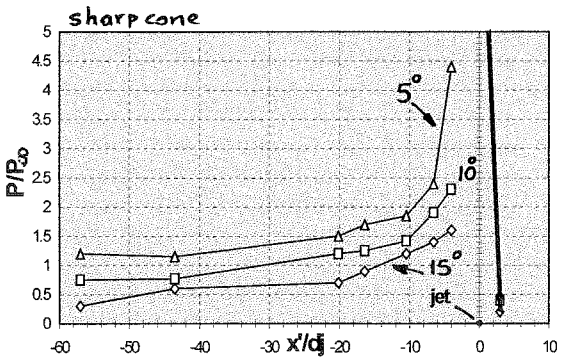

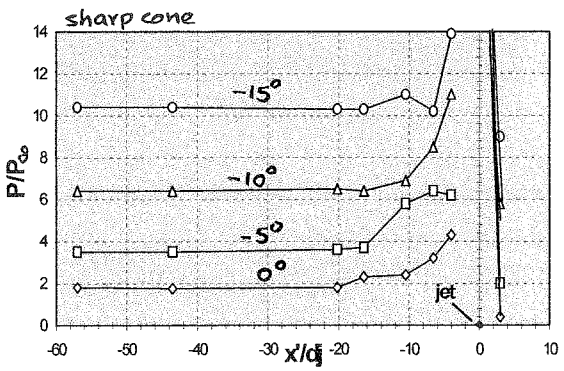

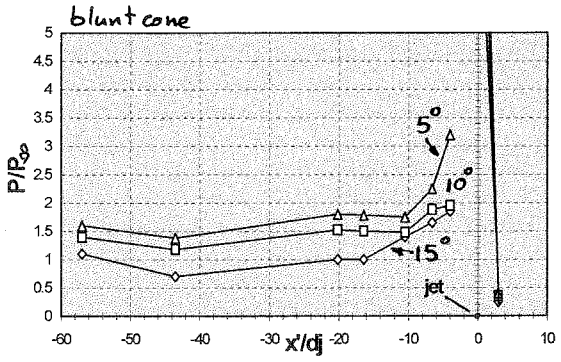

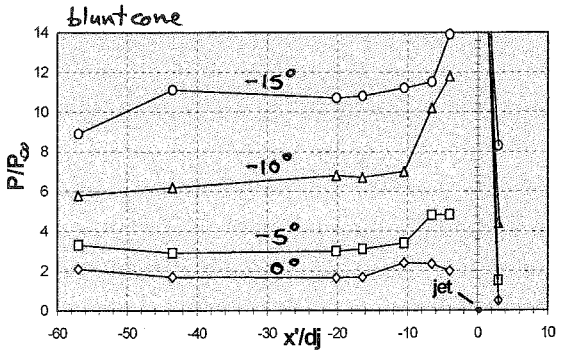

Fig.7 Pressure distributions in the interaction region (along the jet meridian)

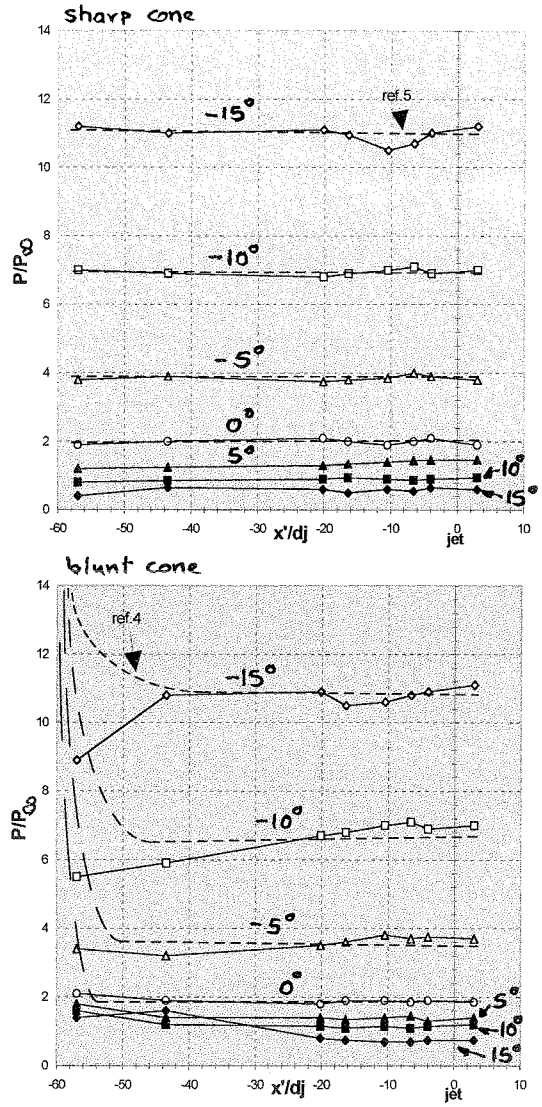

Fig.8 Pressure distributions with no jet

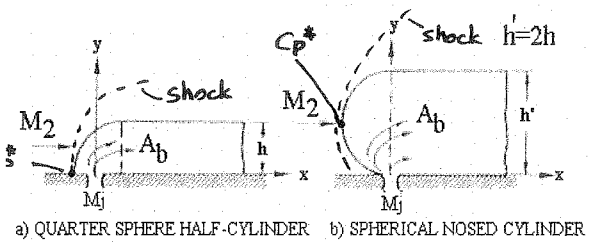

a) QUARTER SPHERE HALF-CYLINDER b) SPHERICAL NOSED CYLINDER

Fig.9 Models used for the jet penetration height prediction

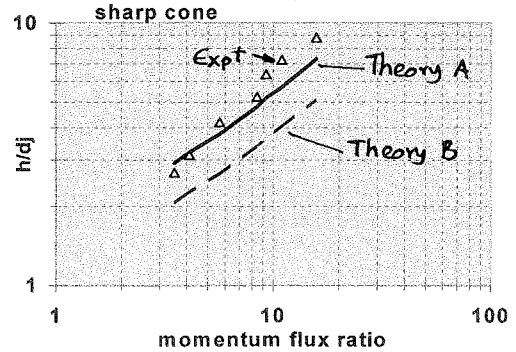

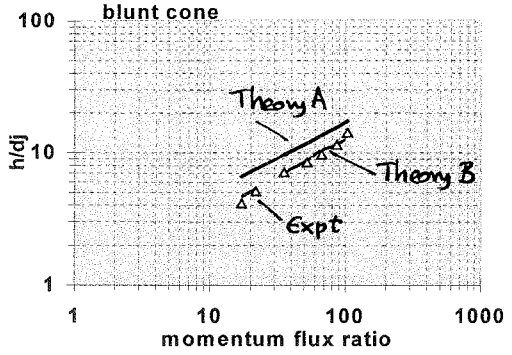

Fig.10 Correlation of jet penetration heights

Pressure Measurements

The distributions in the interaction region show a repeatability of ±5%. Separation was taken to be at the mid-point between the cone pressure and the plateau pressure levels. The location correlates well with schlieren observations of the location of the separation shock. By comparison of figures 7 and 8, it can be seen, that the resulting separation alters the surface pressure distribution ahead of the jet.

The separated flow region behind the jet makes a negative contribution to the control force, since near the base of the models the surface pressure was found to be consistently lower than the undisturbed cone values, (figure 7), as the primary flow expands around the jet. The separated flow ahead of the jet makes a positive contribution to the control force and this is the more significant effect resulting in amplification factors greater than unity.

The pressure along the jet meridian increases on the surface of the cones to the point at which the flow separates, then there is a further rise up to a pressure plateau. The pressure rises to a peak just ahead of the jet. The position of this peak corresponds with the location of the main reattachment ahead of the jet.

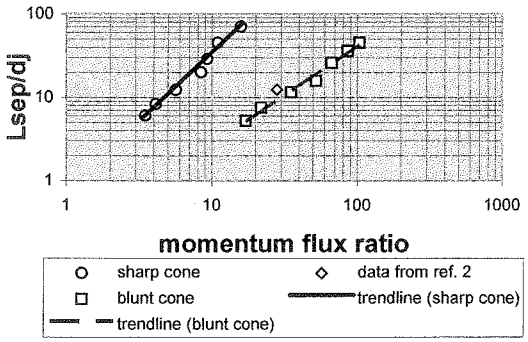

Fig.11 Correlation of the separated flow length along the jet meridian

Separation Length Correlation

A correlation of the length of separated flow along the jet meridian for the two cone configurations is shown in figure 11. The data correlates for the sharp cone as,

$$\frac{L_{sep}}{d_j} = 0.8\left[\frac{P_{oj}}{P_2 M_2^2}\right]^{1.6}, \qquad \textbf{(14a)}$$

and for the blunt cone,

$$\frac{L_{sep}}{d_j} = 0.18\left[\frac{P_{oj}}{P_2 M_2^2}\right]^{1.2}, \qquad \textbf{(14b)}$$

The correlation suggests that the length of the separated flow region increases with an increase in the jet to undisturbed flow surface value pressure ratio and a decrease in the local Mach number ahead the separation. The range of variables was limited and more data are required.

Force Measurements

The calculated force and moment values were non-dimensionalised using as reference values, the base area and base diameter. The pitching moment was measured at the moment reference point located at x'/d_j= -10.2 along the body axis measured from the jet nozzle.

The study of the effects of the jet interaction was conducted by first establishing a steady jet and then firing the tunnel. The normal force output is shown in figure 12. The presence of the jet at t=0 ms produces a negative force. The magnitude of this force is constant after 100 ms, because the jet plenum chamber becomes choked.

The firing of the tunnel initiates the aerodynamic forces and the increase in pressure in the interaction region augments the jet force. The completion of the tunnel run and the consequent removal of the augmentation force results in the force measured returning to the jet force level.

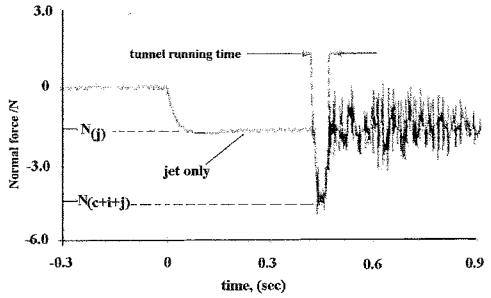

Fig.12 Effect of the jet and interaction on the force output

Estimation of Jet-only Contribution

Tests, with jet only, were performed, under near vacuum conditions, without running the gun tunnel. The jet thrust contributed a negative (downward) normal force, $C_{N(j)}$=-0.021, a positive (backward) axial force, $C_{A(j)}$=0.0042, and a positive (nose-up) pitching moment (due to the jet axis being aft of the moment centre), $C_{m(j)}$=0.0048.

Results

The aerodynamic coefficients measured on the cones, with and without the jet, are shown in figure 13.

SHARP CONE

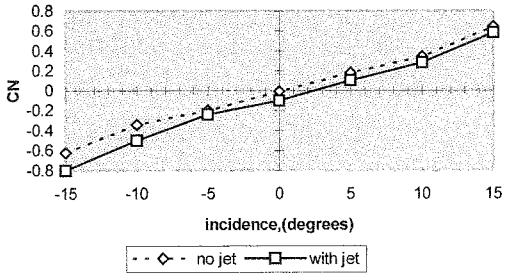

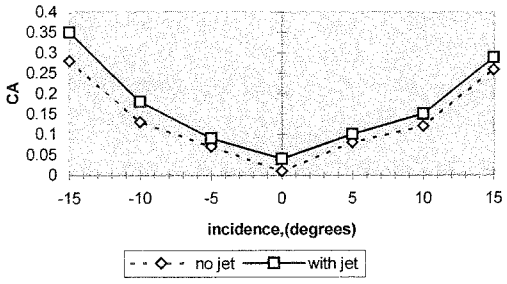

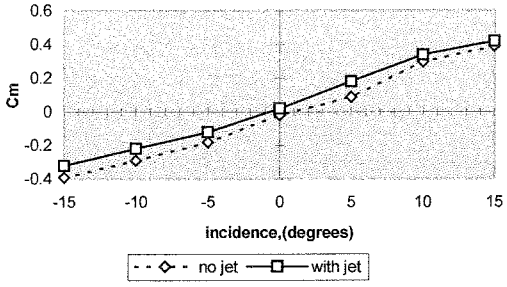

BLUNT CONE

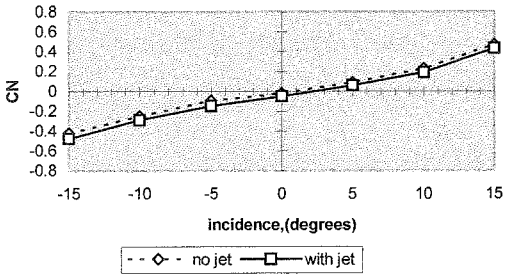

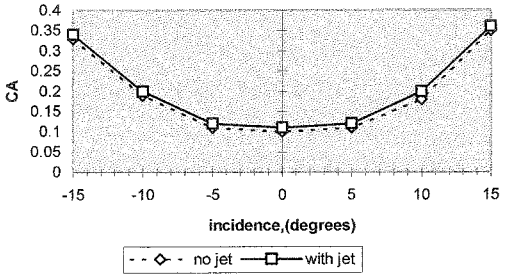

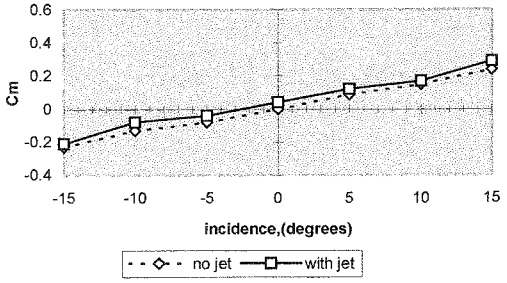

Fig.13 The effect of jet and jet interaction on the aerodynamic coefficients

The effect of the jet on the axial force coefficient is very small at all incidences. The effect of the jet is more pronounced on the normal force coefficient. The total induced force contributes a decrease at every incidence. The effect is to shift the normal coefficient curves to the right.

This shift is similar at all incidences, and each curve crosses the X-axis at approximately 2.5° incidence.

At $\alpha=0°$, a small normal force $C_{N(BluntCone)}$=-0.011 and a pitching moment $C_{m(BluntCone)}$=0.004 was measured on the blunt cone (in the absence of the jet), and a small normal force $C_{N(SharpCone)}$=-0.019 and a pitching moment $C_{m(SharpCone)}$=-0.0015 was measured on the sharp cone (in the absence of the jet). The forces and moments measured at 0° incidence, without the jet, are due to the centreline focusing effect associated with imperfections in the surface of the Mach 8.2 nozzle.

At $\alpha=0°$, the total normal force measured in the presence of the jet was $C_{N(BluntTotal)}$=-0.043 for the blunt cone and $C_{N(SharpTotal)}$ =-0.055 for the sharp cone (including the normal force on the cones). For the blunt cone, the combined jet and interaction normal force was -0.032 ($C_{N(BluntTotal)}$-$C_{N(BluntCone)}$). This compares with the jet only force of $C_{N(j)}$=-0.021. Thus, the interaction augments the total force generated by the jet by 52%. For the sharp cone, the combined jet and interaction normal force was -0.036 ($C_{N(SharpTotal)}$-$C_{N(SharpCone)}$). This compares with the jet only force of $C_{N(j)}$=-0.021. Thus, the interaction augments the total force generated by the jet by 72%.

The jet increases the moment on the cones (at $\alpha=0°$) from $C_{m(BluntCone)}$=0.004 (in the absence of the jet) to $C_{m(BluntTotal)}$=0.012 for the blunt cone, and from $C_{m(SharpCone)}$=-0.0015 (in the absence of the jet) to $C_{m(SharpTotal)}$=0.0075 for the sharp cone. Therefore, the combined jet/interaction pitching moment for the blunt configuration is 0.008 ($C_{m(BluntTotal)}$-$C_{m(BluntCone)}$). This compares with the jet only moment of $C_{m(j)}$=0.0048. Thus, the interaction augments the pitching moment generated by the jet by 66%. For the sharp cone, the combined jet/interaction pitching moment is 0.009 ($C_{m(SharpTotal)}$-$C_{m(SharpCone)}$). This compares with the jet only moment of $C_{m(j)}$=0.0048. Thus, the interaction augments the pitching moment generated by the jet by 87.5%.

At $\alpha>0°$, (nose up), the jet causes the centre of pressure to move forward. The main contribution towards the normal force and pitching moment comes from the region ahead of the jet. At $\alpha<0°$, (nose down), the jet causes the centre of pressure to move rearward. The main contribution towards the normal force and pitching moment comes from the vicinity of the jet and the region behind it.

The amplification factor, K, correlates well with the momentum flux ratio (figure 14). For the sharp cone the data correlates as,

$$K = 3.2\left[\frac{P_2 M_2^2}{P_{0j}}\right]^{0.3}, \qquad (15)$$

and for the blunt cone,

$$K = 4.2\left[\frac{P_2 M_2^2}{P_{0j}}\right]^{0.3}, \qquad (16)$$

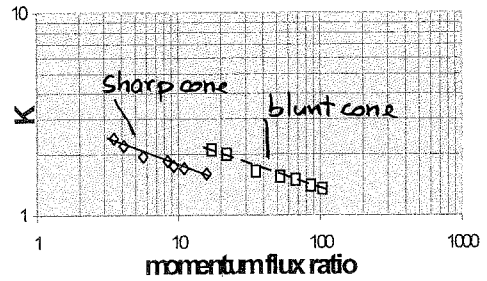

Fig.14 Correlation of amplification factor, K

Smaller amplification factors were deduced for the blunt cone. This is because the size of the separated region is reduced. A total of 50 to 160 percent augmentation of the jet thrust was measured.

Conclusions

1.The nose bluntness causes a delay in separation with respect to the equivalent sharp cone configuration.

2.The penetration height increases on the leeward side and decreases on the windward side as incidence is increased.

3.The jet penetration is less for the sharp cone.

4.The momentum flux ratio is an important control parameter.

5.The ensuing interaction causes a change in surface pressure around the injector. This pressure distribution modification results in a force which is between 50% to 160% larger than the nominal jet thrust.

6.The effect of the jet on the axial force coefficient is small.

7.The presence of the jet causes a rearward motion of the axial centre of pressure at negative incidences and a forward motion at positive incidences.

References

[1]Simpkins, P.:Hypersonic interactions about a slender cone induced by radial mass injection.AGARD CP-30, 1969.

[2]Kumar, D., Stollery, J.L. and Smith, A.:Hypersonic jet control effectiveness.AIAA 95-6066, 1995.

[3]Holden, M.:Experimental studies of shockwave-boundary layer interaction.AGARD AG-203, 1974.

[4]Bade, W. L.:Analytic formulas for conditions on blunt wedges in hypersonic flows.AIAA J., vol. 13, No. 9, 1975.

[5]Wells, W. and Armstrong, W.:Tables of aerodynamic coefficients obtained from developed Newtonian expressions for complete and partial conic and spherical bodies at combined angles of attack and sideslip with some comparisons with hypersonic experimental data.NASA TR R-127, 1961.

[6]Ames research staff:Equations, tables and charts for compressible flows.NACA Report 1135, 1952.

[7]Cheng, H. K., Hall, J. G., Golian, T. C., Hertzberg, A.:Boundary layer displacement and leading edge bluntness effects in high temperature hypersonic flow.
J. of the aerospace Sciences, vol. 28, 1961.

[8]Brower, W.:Theory, tables and data for compressible flow.New York:Hemisphere, 1990.

[9]High, W. and Blick, E.:Cone pressure distribution at large and small angles of attack.AIAA J., Vol. 2, No. 6, 1964.

[10]Powrie, H. E. G., Ball, G. J. and East, R. A.:Experimental study of the interaction of a two dimensional reaction control jet with a hypersonic flow.IUTAM Symposium/Marseille, France, 1992.

[11]Stetson, K. F:Effect of bluntness and angle of attack on boundary layer transition on cones and biconic configurations.AIAA 79-0269, 1979.

[12]Pagan, D., Molton, P. and Delery, J.:Basic experiments on a supersonic vortex flow around a missile body. Journal of Spacecraft and Rockets, vol. 29, 1992.

[13]Kontis, K. and Stollery J. L.:Hypersonic performance of a lifting elliptic cone with and without strakes.1996 Aerodynamics Research Forum, The Royal Aeronautical Society, 4/5 January, London.

[14]Zukoski, E. and Spaid, F.:Secondary injection of gases into a supersonic flow.AIAA J., Vol. 2, No. 4, 1964.

AIAA 97-0521

HYPERSONIC EFFECTIVENESS OF SLENDER LIFTING ELLIPTIC CONES WITH AND WITHOUT STRAKES

K Kontis, JL Stollery and JA Edwards
College of Aeronautics, Cranfield University,
Bedfordshire, MK43 0AL, UK

35th Aerospace Sciences Meeting & Exhibit
January 6-10, 1997 / Reno, NV

nission to copy or republish, contact the American Institute of Aeronautics and Astronautics
xander Bell Drive, Suite 500, Reston, VA 22091

HYPERSONIC EFFECTIVENESS OF SLENDER LIFTING ELLIPTIC CONES WITH AND WITHOUT STRAKES

K Kontis*, JL Stollery† and JA Edwards‡
College of Aeronautics, Cranfield University, Bedfordshire, MK43 0AL, UK

Abstract

Experimental data for two pairs of elliptic cones with and without strakes at Mach number 8.2 and unit Reynolds number of 9.3×10^6/m are presented. At this Reynolds number the boundary layer over the models was laminar. Surface flow visualisation and pressure measurements are made on one of the models to determine the effect of strakes. Force and moment data are presented for both pair of models.

Notation

C_D	drag coefficient
C_L	lift coefficient
C_Y	side force coefficient
C_m	pitching or yaw moment coefficient
C_p	pressure coefficient
D	drag
d_b	major axis diameter
$K_{\beta c}$	hypersonic similarity parameter, $M_\infty \beta_c$
$K_{\delta e}$	hypersonic similarity parameter, $M_\infty \delta_e$
L	lift
L	total cone length
M	Mach number
P	pressure
V	velocity
Y	side force
x	distance from the nose
x_{cp}	centre of pressure
α	angle of attack (^{o})
β	shock wave angle
γ	ratio of specific heats
δ	cone semi-angle
δ_e	equivalent half cone angle
θ_{xy}	elliptic cone half-angle measured in the horizontal plane
Φ	ray angle of sharp cone

Subscripts

∞	freestream
c	cone

Introduction

Future defence weapons may include very high speed projectiles flying and manoeuvring over a wide incidence range. The flow field about them can be complex and can feature extensive areas of separated flow and vortices. The designer must be aware of these effects, so that a suitable control system can be developed to manoeuvre the vehicle.

The present investigation aims:

- to compare right elliptic cone and power-law elliptic cone
- to determine the effects of strakes and to access whether improvements in lift coefficient are significant due to the containment of the windward flowfield
- to provide data for further CFD analysis
- to assist in the future design of realistic shapes for slender manoeuvring bodies.

Experimental Set-up

Models

The models tested were a pair of right elliptic cones and a pair of half-power-law elliptic cones (each pair comprises one with strakes and one without strakes). These models were 187.5 mm long and the ratio of major to minor axes was 1.6. The length to minor axis ratio was 7.5 for the right cones. The length to minor axis ratio was 11.2 for the half-power-law cones. The strakes were 3 mm square at base for the right cone and 1.7 mm square at base for the half-power-law cone (tapered, on height only, to zero at nose, for both cases). The general geometrical characteristics of the slender cone configurations are shown in figure 1. Pressure models were equipped with tappings along the windward/leeward meridian. The force models were made of jelutong wood for lightness. The CG (centre of gravity) position was 52 mm from base for right cones and 26 mm from base for half-power-law cones, indepedent of strakes, with masses of 49 grams and 56 grams for right

---

* PhD Student
† Emeritus Professor, Fellow of AIAA
‡ Visiting Professor, Senior Member of AIAA

copyright © 1996, British Crown Copyright MOD /DERA, UK. Published with the permission of the Controller of Her Britannic Majesty's Stationery Office.

cones and half-power-law cones, with strakes, respectively and 33 grams without strakes.

Gun Tunnel Facility

All the experiments were conducted in the College of Aeronautics hypersonic gun tunnel. Air is used as both driver and test gas. An axisymmetric contoured nozzle provides a flow at M_∞=8.2 with a useful core flow diameter of 152 mm and a Reynolds number of 9.3×10^6/m with test times of about 30 ms. At this Reynolds number the boundary layer is laminar. The tests were performed with right elliptic cones both in pitch and yaw angles of 0° to 20° and at same pitch angles range only for half-power-law elliptic cones.

The tests employed high speed schlieren photography to study the overall flow field in a standard Töepler configuration. Pressure measurements were carried out using Kulite XCS-190 series, absolute pressure transducers. The transducers were rigidly fixed at the foot of the model-mounting inside a housing.

The pressure transducers were calibrated linearly against a vacuum gauge during the test-section evacuation phase of each run. The outputs from the transducers, after suitable amplification were acquired on eight channels of Datalab transient recorder to obtain 4096 data points from each transducer channel at a rate of 50 KHz. The recorder output was acquired and analysed on a personal computer after the end of each run. The raw data was converted into ratios of local surface pressure to free stream static pressure.

Digital Filtering for Force Measurements

The forces were measured with a 3-component balance equipped with semi-conductor strain gauges. During the run, the working section is subjected to some mechanical vibrations. Due to the balance and models mass, these vibrations produce damped harmonic oscillations. Digital filters were designed, in order to remove the natural frequency components from the test signals.

Oil-dot Technique

The surface oil flow technique is not suitable for gun-tunnels because the oil film can not move in the short run duration. Discrete dots of a mixture consisting of linseed oil, silicon 4 oil and titanium dioxide powder with a few drops of orleic acid were applied on the matt black painted surface of the models.

During the run the oil dots flow in a direction depending upon the surface shear stress. Because of reduced shear stress in the regions of separated flow the oil dots do not move there. At reattachment flow regions the oil dots are wiped away because of the increase in shear stress there.

Analysis

Pressure Estimation

Cone Theory of Leung and Emanuel[1]

The theory of Leung and Emanuel was applied in pressure prediction along the windward meridian of the right elliptic cone (in pitch) without strakes assuming the concept of the equivalent cone (a right circular cone at zero incidence having the same freestream Mach number and a half cone angle equal to the angle between the freestream Mach number and the ray line on the cone under examination). δ_e was calculated by,

$$\delta_e=\sin^{-1}(\sin\delta\cos\alpha+\cos\delta\sin\alpha\cos\Phi) \quad (1)$$

with Φ=0° along the bottom generator and 180° along the top generator. In this case Φ was equal to 0°.

$$K_{\delta e}=M_\infty\delta_e \quad (2)$$

$$K_{\beta c}=\{1+[(\gamma+1)/2]\,K_{\delta e}^2\}^{1/2} \quad (3)$$

$$\frac{p}{p_\infty}=1+\gamma K_{\delta_e}^2\left\{\frac{1}{2}+\frac{1+[(\gamma+1)/2]K_{\delta_e}^2}{1+[(\gamma-1)/2]K_{\delta_e}^2}\ln\left(\frac{K_{\beta c}}{K_{\delta_e}}\right)\right\} \quad (4)$$

Newtonian Theory

Standard Newtonian theory was applied in the form,

$$\frac{p}{p_\infty}=1+(\cos\alpha\sin\theta_{xy})^2\gamma M_\infty^2 \quad (5)$$

Estimation of Aerodynamic Forces and Moments

Right Elliptic Cone Without Strakes

C_L, C_Y, C_D and C_m were calculated using the close form relations from Wells et al paper[2].

Right Elliptic Cone With Strakes

A theoretical prediction model was derived, based on the standard Newtonian theory. The strakes were assumed to be right rhombic cones of half-angle 0.7° and total length of 188 mm.

Any vortices caused by boundary layer separation and regions of trapped flow, such as at the strake-body junction were neglected. The contribution of strakes to the aerodynamic forces and moments was neglected if they are located inside the shadow region of the elliptic cone.

For purpose of integration cylindrical co-ordinates were assumed. The derivation started from the Newtonian relation $C_p=2\cos^2\eta$. The angle η is defined as the angle between the unit vector normal to the surface and the unit wind vector. The unit normal vector n was expressed as the gradient of the surface divided by its magnitude. The unit wind vector V was expressed in terms of the body axis. A close form of C_p for the right rhombic cone was derived. The contribution of each strake on the aerodynamic forces and moments was calculated by numerical integration using the pressure coefficient as determined by Newtonian theory. The individual forces and moments generated by the right elliptic cone and strakes were calculated then the total force and moment was derived. The lift coefficient for each incidence was predicted from

$$C_{Ltotal}=C_{Lstrakes}+C_{Lbody} \quad (6)$$

Similar expressions were used for the other aerodynamic coefficients.

This method for deriving the individual forces and moments fundamentally assumes that the forces and moments generated in the presence of strakes are equal to the sum of the individual components i.e. the algebraic sum of the forces and moments generated by the cone and the strakes. This method does not take into account the mutual interaction between the cone and the strakes flowfields.

Results and Discussion

Schlieren and Oil-dot Visualisation Studies

Right Elliptic Cone With and Without Strakes

The oil-dot surface visualisation technique captured successfully the cross-flow characteristics on the windward side and some details of the flow phenomena on the leeward side were seen, (figures 2 and 3). The strakes altered the surface flow characteristics and tended to inhibit the cross-flow on the windward side at all incidences tested.

Schlieren pictures for the right elliptic cone in pitch and yaw are shown in figures 4 and 5 respectively. No difference in schlieren pictures was observed due to inclusion of strakes. This is because any changes in the flowfield due to strakes addition are of small scale and they will not be visible in the schlieren pictures because of the main body obstruction.

The leading edge shock and attached laminar boundary layer, for $\alpha=0°$, can be seen in figures 4a and 5a. The distance between the shock wave and the body, for 0° incidence, is greater in the meridian plane containing the minor axis than in the meridian containing the major axis (figures 4a and 5a). The shock wave is not an ellipse similar to the body, but is 'pushed in' toward the major axis and 'pulled out' from the minor axis. This shape is because of the presence of a cross-flow from the high pressure sides at the ends of the major axis to the low pressure sides at the ends of the minor axis.

The effect of incidence is to decrease the local Mach number and increase the local Reynolds number along the windward ray. On the leeward ray, the local Mach number increases and the local Reynolds number decreases. With increasing angle of attack, there is the establishment of a disturbed flow region over the leeward meridian. This is probably, due to separation of the crossflow, resulting in the establishment of a pair of counter-rotating vortices, over the leeward region of the body.

At $\alpha=5°$ in pitch, the leeside flow separates close to the base of the model probably to form a pair of counter rotating vortices, (figures 2a and 4b). At $\alpha=5°$ in yaw, figure 3a shows that the flow is attached along the whole model and tends to converge along the leeward meridian. Figure 5b shows that the boundary layer thickens along the leeward meridian. There are no separated flow and vortices on the lee-side. A decrease in heat transfer along the leeward meridian is expected, and it is due to the decrease in pressure in the leeward region of the cones.

Stetson[3] found that the leeward flow over a circular cone separates at about 3/4 the cone half angle for sharp as well as a spherically blunted 5.6 degrees half-angle cones. In the present experiments, according to Stetson, the leeward flow should separate at incidence of 2.9° in pitch as the half-angle is 3.8° (angle corresponds to the vertical plane of symmetry, which includes the minor-axis). In yaw, the half-angle is 6.1° (angle corresponds to the vertical plane of symmetry, which includes the major-axis) and the leeward

flow should separate at 4.6°. In this case, Stetson predicts earlier the on-set of separation.
As incidence increases, schlieren and oil flow study showed that the separation point moves forward and by α=10° in pitch the separation region extends over the whole upper surface of the model, figure 4c, and about 4/5 of the length of the model, in yaw, figure 5c. The white line nearer the surface on the leeward side indicates the vortex core.
At α=15° in pitch and yaw, the vortex core is no longer visible, (figures 4d and 5d). This is probably because of the large expansion of the flow over the leeward side of the body reduces the local density beyond the sensitivity of the schlieren system. The oil dot results indicate that at that incidence the separation extends over the whole surface of the model in yaw, figure 3b. With growth of the pair of the symmetric vortices, the position of the vortex core rise.
At 20° incidence in pitch and yaw, the strakes inhibit the flow further. Schlieren pictures on the leeward side, seem to show an increase in the strength of the crossflow vortices as the incidence increases from 10° to 20°. This was observed, as well, by other researchers on experiments on a tangent ogive/cylinder configuration[4,5] and on an jet-cone configuration[6].

Half-power-law Elliptic Cone With and Without Strakes

Typical schlieren pictures for the power law body are shown in figure 6. No difference in schlieren pictures was found due to the inclusion of strakes. Figure 6a shows that at α=3° in pitch, the leeside flow separates close to the base of the body. The incidence at which the cross flow over a power law body separates will probably depend on the power law exponent.
As incidence increases the separation point moves forward and by α=9° in pitch, the separation region extends over the whole upper surface, figure 6b.

Pressure Measurements

Right Elliptic Cone With and Without Strakes

The pressure distributions show a repeatability of ±5%. Figure 7 shows a progressive decrease in cone pressure along the leeward meridian with incidence, in pitch. It was found that the addition of strakes caused a reduction of pressure on the leeward side and an increase of pressure on the windward side, figure 7. The pressure results without strakes on the windward side have been compared with standard Newtonian theory predictions and cone theory of Leung and Emanuel. Both theories predicted the experimental trends.

Forces and Moments Measurements

The sign convention used for the forces and moments measurements is shown in figure 8. An upward lift or side force (normal to the velocity vector), backward drag (parallel to the velocity vector) and a nose-up pitching or yaw moments were taken as positive.
The calculated forces were non-dimensionalised using the freestream dynamic head and the base area of the elliptic cones.
The moment values were non-dimensionalised using the freestream dynamic head, base area and base diameter. The pitching and yaw moments were measured at the moment reference point located at x/d_b=-1.3 and x/d_b=-1.0 along the body axis measured from the base for the right elliptic cone and half-power-law body respectively.
The strakes on the windward side of the body have negative dihedral and the other two on the leeward side have positive dihedral. Any interference between the flow over the body and that over the windward side of the anhedral strakes or over the leeward side of the dihedral strakes will result in changes in the aerodynamic characteristics of the straked configuration in comparison to the body alone configuration. Any interference effects on the leeward side of the anhedral strakes and that on the windward side of the dihedral strakes will be acting on a very small area of the body surface and will therefore not cause any significant changes in the aerodynamic characteristics.

Half-power-law Elliptic Cone

The results of the effect of strakes on the aerodynamic coefficients are presented in figure 9.
The effect of strakes addition is to shift the C_L-α curve upwards increasing C_L value at all incidences tested, figure 9a.
Figure 9a shows also the comparison of the power-law body without strakes results with those reported by Fournier and Spencer[7]. Fournier and Spencer performed their experiments using half-power-law elliptic cones

at M_∞= 4.63 and ratios of major to minor axes of 1.0 and 2.0. The ratio for the present results fall in between 1 and 2 obtained by Fournier and Spencer which follows the trend of increasing C_L with increasing ratio of major to minor axes. This increase in C_L is primarily due to the increased aspect ratio of the body. The effect of Mach number variation on the C_L-α curve seems to be negligible as concluded by Founier and Spencer for Mach numbers below 4.63. The C_L-α curve is non-linear, with its slope increasing with α and following the well known α^2 variation. The separation of leeside flow further increases the slope due to increased suction over the leeward side of the cone.

Figure 9a shows also the comparison with the results of Fox and Spencer[8] for the elliptic cone without strakes. The measurements by Fox and Spencer were obtained on a theoretical minimum-wave-drag body (volume and length constraints) of elliptic cross-section with ratio of major to minor axes of 2.0, however this body did not have a power-law longitudinal contour and the tests were conducted at M_∞=10.03. The minimum-wave-drag body consistently produces less lift than the half power law body of smaller ratio of major to minor axes.

Figure 9b shows that the addition of strakes increases the drag coefficient. Figure 9b shows also the variation of C_D with α at M_∞=4.63, 10.03 and 8.2. The drag measurements by Fournier and Spencer show that drag coefficient does not vary significantly with the ratio of major to minor axes, however a large reduction in C_D close to 0° incidence can be noticed. This is because of the reduction of base drag as Mach number increases from 4.63 to 8.2. The same figure compares the present drag measurements with that of Fox and Spencer. The two bodies have approximately same zero-lift drag but at higher incidences the half power-law body has significantly higher drag than the minimum wave-drag-body.

Figure 9c shows that at low incidences the addition of strakes does not cause any big change in pitching moment coefficient about the balance moment centre. At low incidences the effect of increased lift is accompanied by a downstream shift of centre of pressure. At higher incidences there is a bigger increase in pitching moment coefficient.

There is an overall increase in L/D ratio of approximately 17% because of the strakes addition.

The centre of pressure is located at 64% of total cone length from nose tip, for cone with strakes and 60% of total length from nose tip, for cone without strakes. According to slender body theory[9] the location of centre of pressure of power-law bodies is given by $x_{cp}/L=2n/(n+1)$, for $n\neq1$. For n=0.5, then $(x_{cp}/L)x100=67\%$ which is close to the experimental value without strakes. Any shift of centre of pressure as a eonsequence of the addition of strakes is constant with α.

Right Elliptic Cone With and Without Strakes

A comparison of experimental C_L, C_Y, C_D and C_m, in pitch and yaw, with theory is presented in figures 10 and 11 respectively. Theory predicted the experimental trends.

The effect of strakes addition is to shift the C_L-α and C_Y-α curves upwards increasing the C_Y and C_L values at all incidences tested, figures 10a and 11a. This increase is due to increased pressure over the lower side of the cone caused by increased amount of air entrapped by the strakes and because of the two strakes having negative dihedral create strong interference with the windward side of the body.

The cross flow component on the windward side remains very small due to the blockage created by the anhedral strakes and should therefore result in a constant pressure on the windward side of the body. Expansion of the flow over the leeward surfaces of the other two strakes having positive dihedral reduces the pressure on the leeward side of the body in comparison to the pressure there for the body alone configuration, figure 7. Surface pressure measurements by Reggiori[10] on a wing-cone configuration show these interference effects. It seems that the percentage increase of the side force coefficient due to strakes addition is higher than that of the lift coefficient.

Figures 10b and 11b show that strakes addition increases the drag coefficient, both in pitch and yaw. The increase in C_D is smaller at low incidences. The percentage increase of C_D in yaw is slightly higher than that in pitch.

Figures 10c and 11c show that at lower incidences the addition of strakes does not cause any big change in pitching and yaw moment coefficients about the balance moment centre. At low incidences the effect of increased lift and

side force is accompanied by a slight forward movement of the centre of pressure. At higher incidences there is a bigger increase in pitching and yaw moment coefficients, because lift and side force coefficients, for the cone with strakes over that without the strakes, continues to increase with α.

The L/D and Y/D ratios determine the overall aerodynamic efficiency of a lifting configuration. Lift, side force and drag coefficients increase with addition of strakes. Strakes gave an overall decrease in L/D and a slight increase in Y/D.

The maximum L/D, without strakes, is 4.5 and it occurs at incidence 5°, the maximum L/D, with strakes, is 3.8 and it occurs at the same incidence. The maximum Y/D, without strakes, is 2.4 and it occurs at incidence 8°, the maximum Y/D, with strakes, is 2.7 and it occurs at the same incidence. In all cases, the theoretical calculations predict the experimental trends but they overestimate the experimental values.

The centre of pressure is located at 68% of the total length, measured from nose tip, (with strakes), and 71%, (without strakes), in pitch. In yaw, the centre of pressure is located at 64% of the total length, measured from nose tip, (with strakes), and 66%, (without strakes). The addition of strakes moved the centre of pressure slightly forward at all incidences tested. Any shift in the centre of pressure as a consequence of addition of strakes is constant with α.

Conclusions

1.No gross external flow differences were detected from the schlieren pictures for models tested due to the addition of strakes.

2.The flow separates on the leeward side of the body to form a pair of counter rotating vortices at a low incidence for all models tested. The vortices grow with incidence.

3.Oil-dot visualisation demonstrates that the strakes alter the surface flow characteristics and tended to inhibit the cross-flow.

4.The addition of strakes caused a reduction of pressure on the leeward side and an increase of pressure on the windward side. The strakes produced a significant increase in the lift, side force and drag coefficients, in the incidence range of 0° to 20°.

5.Strakes gave an overall decrease in L/D for right cone in pitch, an increase in Y/D for right cone in yaw and increase in L/D for the half-power-law body.

6.The addition of strakes moved the centre of pressure slight forward for the right elliptic model and backwards for the power law body at all incidences tested.

Acknowledgements

The present investigation was supported under contract by the Defence Establishment and Research Agency of the United Kingdom.

References

[1]Leung, K. K. and Emanuel G.:Hypersonic Inviscid and viscous flow over a wedge and cone.Journal of Aircraft, vol. 32, no. 2, 1995.

[2]Wells, W. and Armstrong, W.:Tables of aerodynamic coefficients obtained from developed Newtonian expressions for complete and partial conic and spherical bodies at combined angles of attack and sideslip with some comparisons with hypersonic experimental data.NASA TR R-127, 1961.

[3]Stetson, K. F:Experimental results of laminar boundary layer separation on a slender cone at angle of attack at M_∞=14.2.WPAFB, ARL 71-0127, 1971.

[4]Peake, D. J. and Tobak, M.:Three-dimensional flows about simple components at angle of attack.AGARD LS-121, 1982.

[5]Pagan, D., Molton, P. and Delery, J.:Basic experiments on a supersonic vortex flow around a missile body.Journal of Spacecraft and Rockets, vol. 29, 1992.

[6]Kontis, K. and Stollery J. L.:Control effectiveness of a jet-slender body combination at hypersonic speeds.AIAA 96-2470, 1996.

[7]Fournier, R. H. and Spencer, B, Jr.:Supersonic aerodynamic characteristics of a series of related bodies of circular and elliptical cross section.NASA TN D-3539, 1966.

[8]Fox, C. H. Jr. and Spencer, B. Jr.:Hypersonic aerodynamic characteristics of low-wave-drag elliptical-body-tail combinations as affected by changes in stabiliser configuration.NASA TM X-1620, 1968.

[9]Sigal, A.:Methods of analysis and experiments for missiles with non-circular fuselages.Tactical Missile Aerodynamics, prediction methodology. Edited by Mendenhall, M. R., 2nd edition, 1992.

[10]Reggiori, A.:Lift and drag of wing-cone configuration in hypersonic flow.AIAA Journal, vol. 9, no. 4, 1971.

Figures

a)right elliptic cone

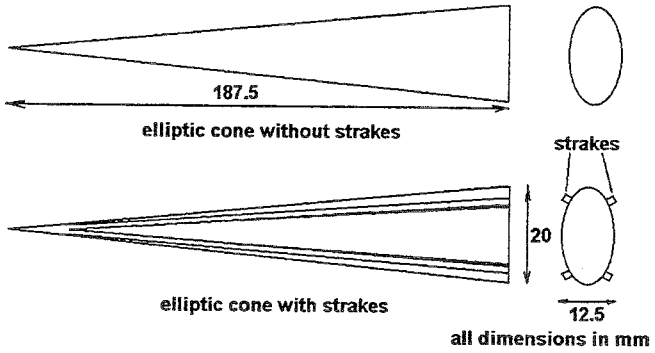

b)half-power-law elliptic cone

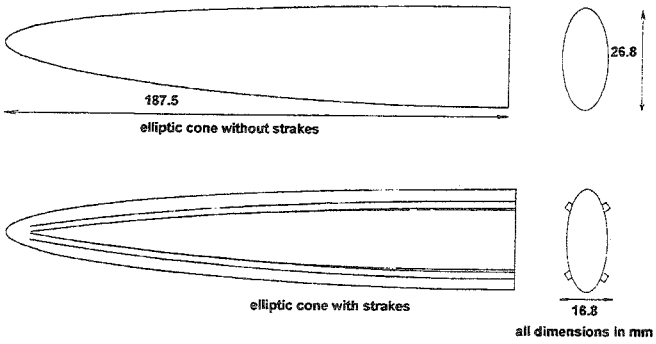

Fig.1General geometry of the models

a)α=5°

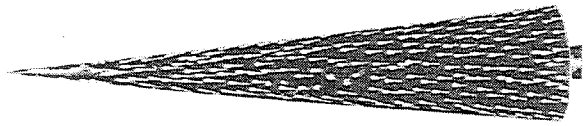

Windward side

Left side

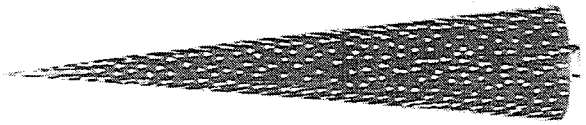

Leeward side

no-strakes

α=5°

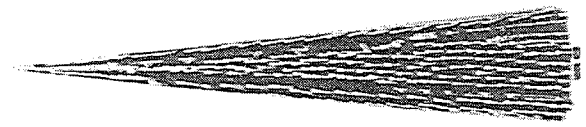

Windward side

Left side

Leeward side

with-strakes

b)α=15°

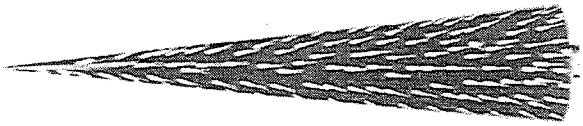

Windward side

Left side

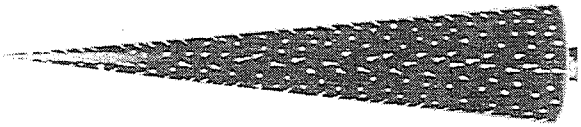

Leeward side

no-strakes

α=15°

Windward side

Left side

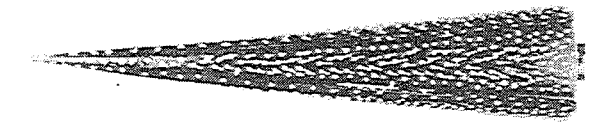

Leeward side

with-strakes

Fig.2Oil-dot studies (right elliptic cone in pitch)

a)α=5°

Windward side

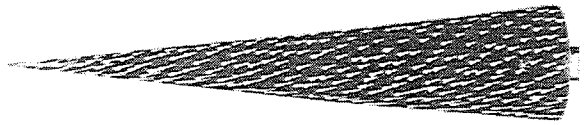

Left side

Leeward side

no-strakes

α=5°

Windward side

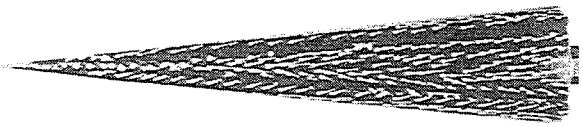

Left side

Leeward side

with-strakes

b)α=15°

Windward side

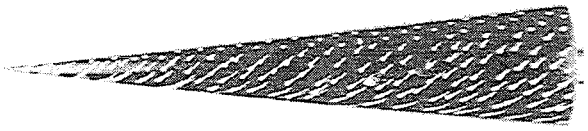

Left side

Leeward side

no-strakes

α=15°

Windward side

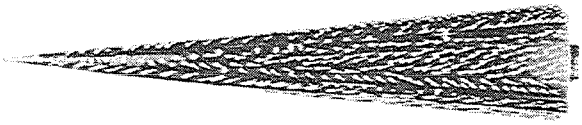

Left side

Leeward side

with-strakes

Fig.3Oil-dot studies (right elliptic cone in yaw)

a) α=0°

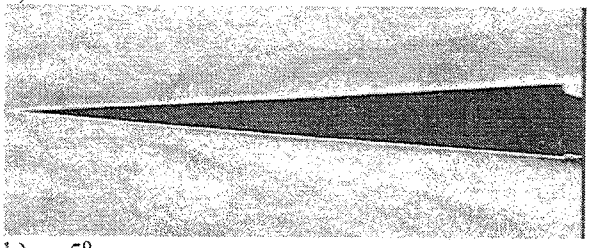

b) α=5°

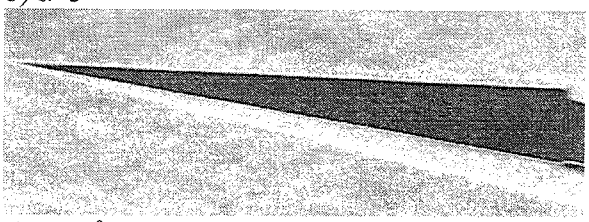

c) α=10°

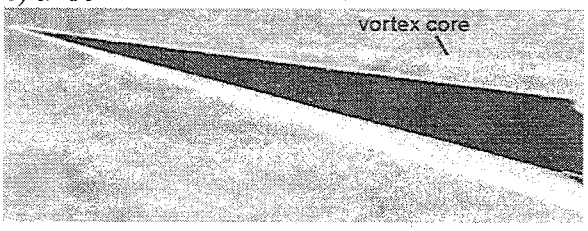

d) α=15°

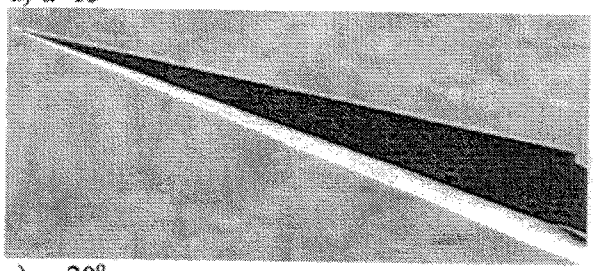

e) α=20°

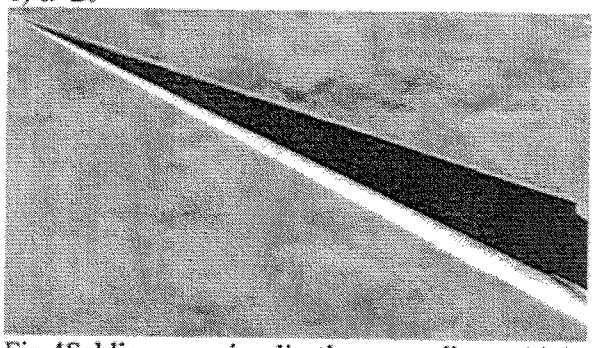

Fig.4Schlieren visualisation studies (right elliptic cone in pitch)

a) α=0°

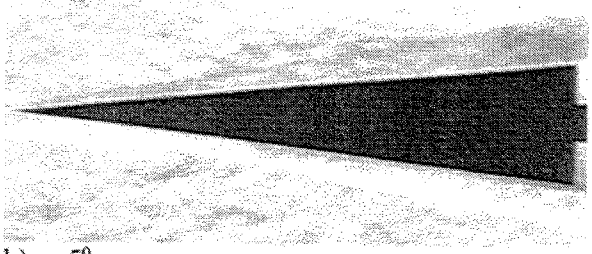

b) α=5°

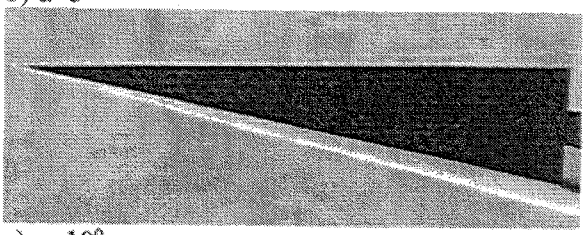

c) α=10°

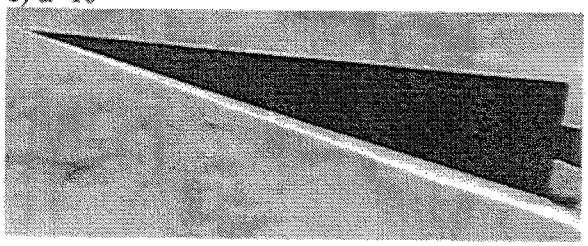

d) α=15°

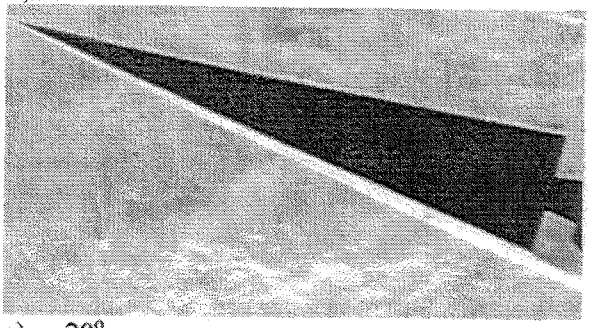

e) α=20°

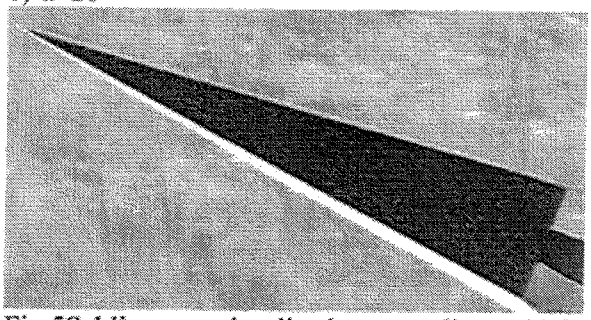

Fig.5Schlieren visualisation studies (right elliptic cone in yaw)

a) α=3°

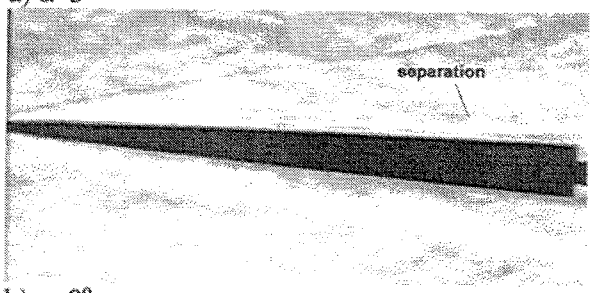

b) α=9°

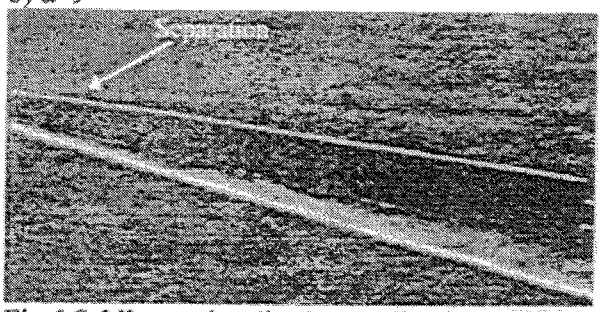

Fig.6 Schlieren visualisation studies (power-law-elliptic cone)

windward meridian

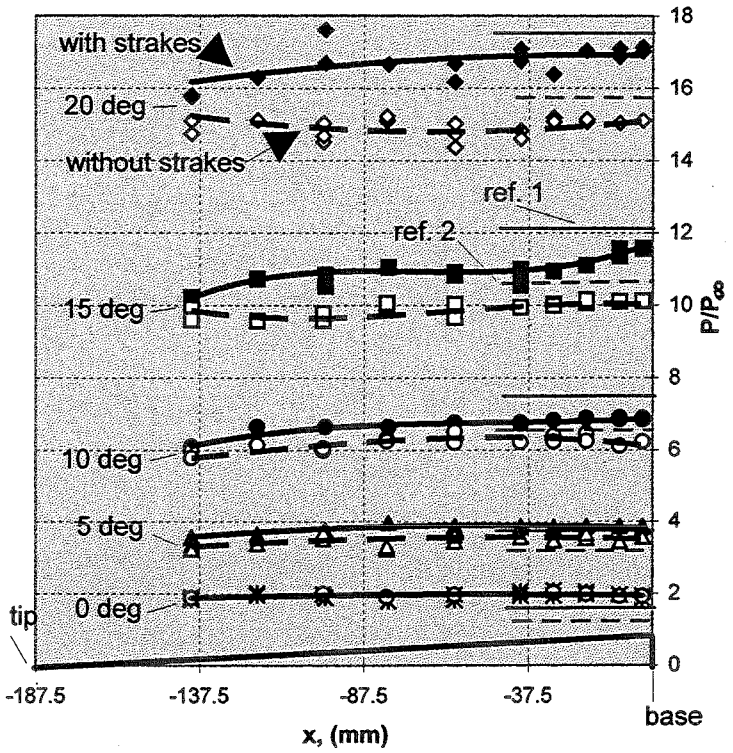

leeward meridian

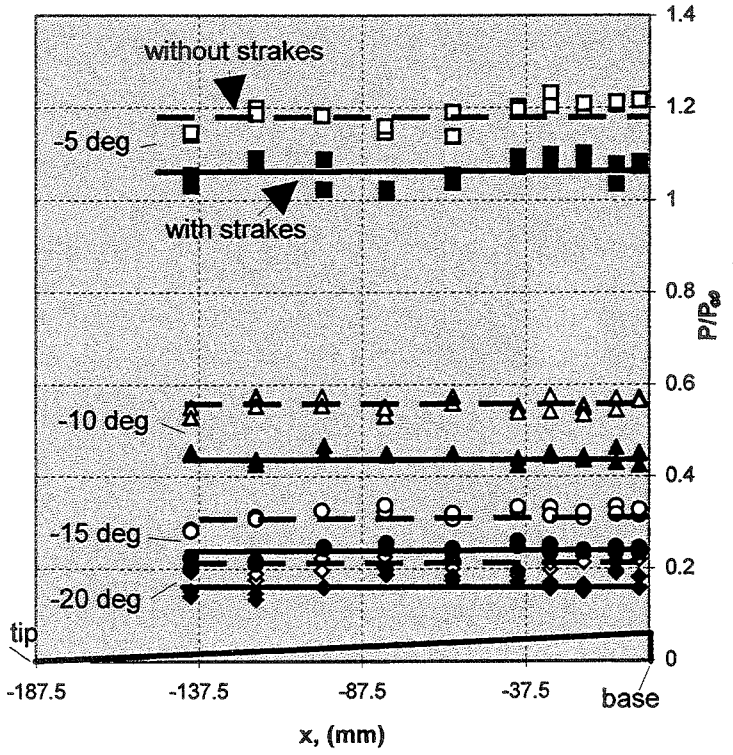

Fig.7Pressure distribution along the windward and leeward meridians (right elliptic cone in pitch)

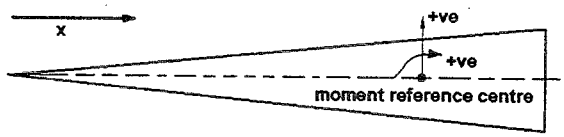

Fig.8Sign convention used for lift, side force, drag, pitching and yaw moments

a)

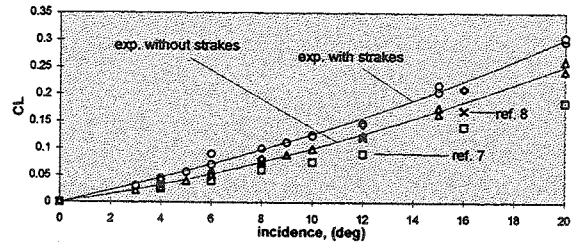

b)

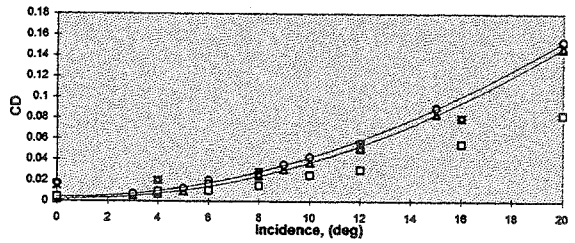

c)

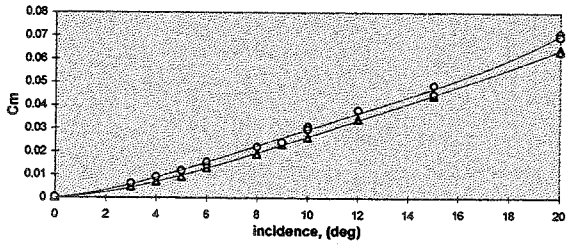

Fig.9 The effect of strakes on the aerodynamic coefficients (power-law elliptic cone)

a)

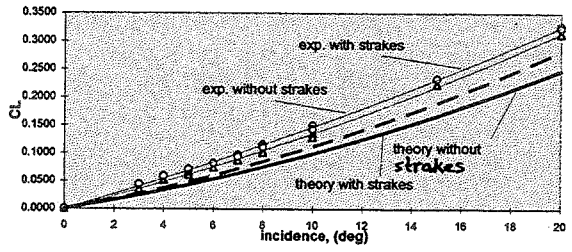

b)

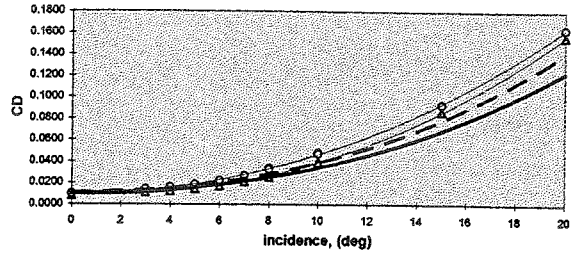

c)

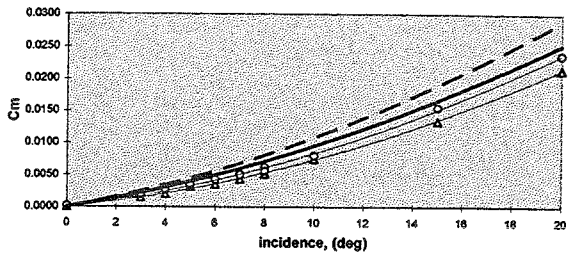

Fig.10The effect of strakes on the aerodynamic coefficients (right elliptic cone in pitch)

a)

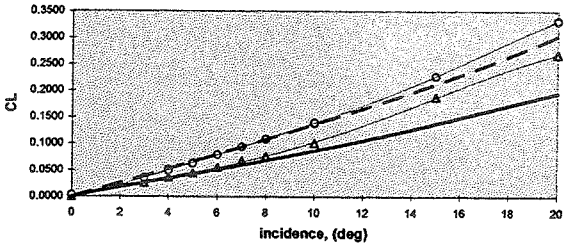

b)

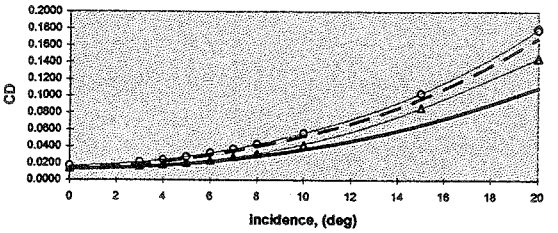

c)

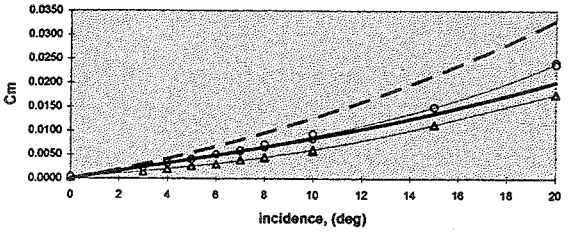

Fig.11 The effect of strakes on the aerodynamic coefficients (right elliptic cone in yaw)

AIAA 97-2252

Computational and Experimental Investigation of Hypersonic Performance of a Lifting Elliptic Cone With and Without Strakes

Kontis, K, Qin, N, and Stollery, JL

15th AIAA Applied Aerodynamic Conference Proceedings, Atlanta, USA, June 1997

COMPUTATIONAL AND EXPERIMENTAL INVESTIGATION OF HYPERSONIC PERFORMANCE OF A LIFTING ELLIPTIC CONE WITH AND WITHOUT STRAKES

K Kontis*, N Qin† and JL Stollery‡
Cranfield College of Aeronautics, Cranfield University, Bedfordshire, MK43 0AL, UK

Abstract

A side by side experimental and computational investigation was conducted on a pair of right elliptic cones with and without strakes at Mach number 8.2 and unit Reynolds number of 9.3×10^6/m. Aerodynamic pressure, force and moment measurements and flow visualisation results were obtained in the Cranfield College of Aeronautics hypersonic gun tunnel for laminar boundary layer conditions. Parabolized and iterative Navier-Stokes simulations were used to predict flowfields, pressures, forces and moments on the hypersonic configuration. Comparisons are made between experimental and computational results to evaluate the quality of each. A theoretical prediction model was derived, based on the standard Newtonian theory to estimate aerodynamic forces and moments on the elliptic cones.

Notation

C_D	drag coefficient
C_L	lift coefficient
C_m	pitching moment coefficient
C_p	pressure coefficient
d_b	major axis diameter
L	total cone length
M	Mach number
P	pressure
T	temperature
x	distance from the nose
α	angle of attack (^{o})

Subscripts

∞	freestream
c	cone
o	total value

Introduction

Future defence weapons may include very high speed projectiles flying and manoeuvring over a wide incidence range. The flowfield about them is very complex and features extensive areas of separated flow and vortices. The designer must be aware of these effects, so that a suitable control system can be developed to manoeuvre the vehicle.

In the conceptual design phase, a simple description of the aerodynamic characteristics is sufficient to assess candidate configurations. As the development process carries on, the complexity and detail required increases and the source of the data changes, from an almost exclusive reliance on engineering prediction methods, to a high dependence on results from detailed wind tunnel tests. There are obvious advantages in being able to proceed further with weapon development before limitations of available prediction methods force the designer to resort to expensive and time consuming wind tunnel tests. In recent years an increasing number of new weapon designs have included features, such as non-circular cross-section bodies, air intakes, or novel control concepts, which cannot usually be addressed using engineering prediction methods. These points, coupled with developments in computer technology and numerical methods, have focused attention on the application of computational fluid dynamics methods to weapon configurations.

Although in recent years the design of flight vehicles has been based increasingly upon computational simulation, wind tunnel experimentation continues to play the major role in aerodynamic analysis and design. This role, however, is changing because of significant improvements in the capability of, and confidence in, numerical simulations. For a small class of supersonic and hypersonic flow problems, high-quality numerical solutions are now believed to represent the physics of the problem more accurately than a wind tunnel experiment can simulate the free flight conditions. An example of this is the supersonic or hypersonic, laminar, perfect gas flow over a simple geometry at low angle of attack.

The realisation that certain flow fields can be computed more accurately than they can be measured experimentally must begin to change the relationship between computational and experimental aerodynamics. This paper addresses this changing relationship and seeks to improve the synergism between computational aerodynamics and wind tunnel experimentation. The physical and numerical approaches can each gain by using the strengths of one approach to offset the weaknesses of the other, and vice versa.

In experiments designed to validate CFD codes, experimentalists must develop a better understanding of the assumptions made in the numerical simulation so that experiments can be designed that match these assumptions. For example, in choosing a body geometry with which to validate a CFD code, a configuration should be chosen that eliminates

---

* PhD Research Assistant
† Senior Lecturer of CFD
‡ Professor of Aerodynamics

Copyright © 1997 by K Kontis, N Qin and JL Stollery. Published by the American Institute of Aeronautics and Astronautics, Inc. with permission.

unnecessary numerical difficulties. In the present experiment, this is achieved by requiring the strakes to extend to the nose of the body. Although this would be unrealistic in actual flight vehicle hardware, it allows a great simplification in body geometry description and outflow boundary conditions in the numerical simulation.

A large number of examples of viscous computations of body vortex flows, obtained using the full and thin-layer forms of the Reynolds Averaged Navier-Stokes (RANS) equations, have been reported in the literature[1-3]. These computations are generally very time consuming and are therefore not well suited for use in a design environment. The numerical solution of the Parabolized Navier-Stokes equations (PNS) provides an efficient means of obtaining viscous flow solutions for vehicle configurations in supersonic /hypersonic flight, and represents an attractive alternative to a time-marching RANS simulation. The PNS equations has the ability to model viscous effects, such as cross flow separation, and allow the use of a space-marching strategy, which reduces both computer execution times and memory requirements. The PNS approach has been successfully applied to a wide range of supersonic and hypersonic flow problems using a number of different solution strategies[4-6]. The computations of Degani and Schiff[6], obtained using a modified version of the non-iterative, finite-difference solver developed by Schiff and Steger[4], provide a good demonstration of the capabilities of PNS for the prediction of vortex flows around bodies at high incidence.

Many of the early PNS codes, employed central differencing and, as a result, required user defined damping terms to prevent oscillations when capturing shock waves. Several PNS solvers have been developed recently, which employ high resolution upwind schemes for the inviscid fluxes, these are inherently dissipative and alleviate the need to manually adjust damping terms. More recently, some of the PNS codes[7] are using an iterative procedure, where the unsteady term in the governing equations is retained and the steady state solution at each axial step is obtained via local pseudo time-marching. With this technique, reduction of linearization errors, improved robustness and ease of integration with a time-marching RANS solver can be achieved.

In the present study, a side by side numerical and experimental investigation has been done to determine the effect of strakes on the aerodynamic characteristics, performance and stability of a slender missile configuration.

The present investigation aims:

- to determine the effect of strakes and to access whether improvements in lift coefficient are significant due to the containment of the windward flowfield
- to provide data for code validation and further CFD analysis
- and to assist in the future design of realistic shapes for slender manoeuvring bodies.

The *CRAPNS3D*, high resolution, iterative, finite volume parabolized Navier-Stokes solver, based on the Osher approximate Riemann solver is used to generate solutions for the elliptic cones.

Experimental Investigation

Experimental Set-up and Model Geometry

All the experiments were conducted in the College of Aeronautics hypersonic gun tunnel. Air is used as both driver and test gas. An axisymmetric contoured nozzle provides a flow at M_∞=8.2, with a useful core flow diameter of 152 mm, a Reynolds number of 9.3×10^6/m, T_o=1290 K, T_∞=89 K, P_o=1570 psia (10.89×10^6 Pa) and P_∞=0.137 psi (950.3 Pa), with test times of about 30 ms. At this Reynolds number the boundary layer is laminar. The numerical simulations used an average wall temperature of 296 K. The tests were performed with right elliptic cones in pitch angles of 0° to 20°.

The tests employed high speed schlieren photography to study the overall flowfield in a standard Töepler configuration. Quantitative studies of the effect of strakes have been made by pressure measurements using Kulite XCS-190 series, absolute pressure transducers. For surface flow visualisation, discrete dots of a mixture consisting of linseed oil, silicon 4 oil, titanium dioxide powder and few drops of orleic acid were applied on the matt black painted surface of the models. During the run the oil dots flow in a direction depending upon the surface shear stress. Because of reduced shear stress in the regions of separated flow the oil dots do not move there. At reattachment flow regions the oil dots are wiped away because of the increase in shear stress there. Direct measurement of the effect of strakes on the aerodynamic performance has been made using a 3-component balance equipped with semi-conductor strain gauges. Digital filters were designed, in order to remove the natural frequency components from the test signals.

The models tested were a pair of right elliptic cones (it comprises one with strakes and one without strakes). These models were 187.5 mm long and the ratio of major to minor axes was 1.6. The length to minor axis ratio was 7.5. The strakes were 3 mm square at base (tapered, on height only, to zero at nose). The general geometrical characteristics of the slender cone configurations are shown in figure 1. Pressure models were equipped with tappings along the windward/leeward meridian. The force models were made of jelutong wood for lightness. The CG (centre of gravity) position was 52 mm from base, independent of strakes, with masses of 49 grams with strakes and 33 grams without strakes.

Computational Investigation

The numerical study employed a high resolution, iterative, finite volume PNS solver, *CRAPNS3D*, based upon Osher's flux vector difference splitting scheme for the spatial discretisation of the convective flux terms. The parabolized Navier-Stokes equations are a reduced form of the RANS equations which can be solved for a range of viscous flow problems using a space-marching procedure. The integral form of the three-dimensional, Reynolds-Averaged Navier-Stokes equations can be expressed as,

$$\frac{\partial}{\partial t}\int_V Q dV + \int_S (H.n) dS = 0 \qquad (1)$$

where **S** is the surface of the volume **V**, **n** is the outward unit vector normal to the surface, **Q** is the vector of conserved variables and **H** is the flux tensor. This approach is computationally more efficient than solving the RANS equations using a time-marching method, and can be used providing the following conditions are satisfied. Firstly, the flow must be steady and supersonic in the streamwise direction outside the viscous boundary layer, and secondly, there should be no streamwise reverse flow. Under these assumptions, the streamwise shear stress and heat transfer terms are neglected and the streamwise flux vector is modified to allow space-marching. The numerical method was developed by Qin and Richards[8] and it was extended to include the effects of turbulence by Birch, Qin and Jin[9]. In the following sections the main features of the method are highlighted.

The region of interest is discretized into small but finite hexahedral cells denoted by **i,j** and **k** (where i, j, k are the Cartesian unit vectors). The conservation integral is applied to cell **i,j,k** and it is assumed the tensor **H** remains constant across each face of the cell. The numerical integration procedure produces cell averaged flow properties, which are assigned to the centres of each of the hexahedral cells. The flux vectors are evaluated at the cell interfaces from the two distinct sets of state quantities on either side of the cell interface. Second or third order spatial accuracy is achieved via the MUSCL interpolation with a flux limiter to avoid oscillations at discontinuities such as shock waves. The Baldwin-Lomax[10] algebraic turbulence model with the modification proposed by Degani and Schiff[6] was employed to provide a turbulent contribution to the viscosity.

The inviscid fluxes are computed using the approximate Riemann solver of Osher[11]. This scheme has been demonstrated[12] to be effective in capturing both shock waves and shear layers in compressible viscous flows, and is preferred over the more popular Roe scheme for the following reasons. Firstly, it will not produce non-physical expansion shocks, which require an artificial fix. Secondly, the operator in the Osher scheme is continuously differentiable and offers the potential for smoother and faster convergence for iterative solutions. After transforming the governing equations from a system of partial differential equations to a system of ordinary differential equations in the streamwise marching co-ordinate, a fully implicit integration method is adopted[13]. The choice of an implicit marching strategy removes the need to consider stability restrictions when determining the size of the streamwise marching step. The viscous fluxes at the cell interfaces are evaluated using Gauss's theorem for the gradient at the cell interfaces. The streamwise fluxes are purely inviscid and the pressure terms are modified using the approach of Vigneron et al[14], to prevent upstream influence within the subsonic boundary layer and eliminate departure solutions. The streamwise flux is calculated in an upwind fashion using the states at the cell centres upstream.

A pseudo-time term is introduced to the set of non-linear equations. The pseudo-time dependent term is discretised using a first order accurate Euler explicit method. At each streamwise station the discretised equations are marched forward in pseudo-time, using a time step determined from the local CFL condition, until a converged steady state solution is obtained.

On the body surface the no-slip and isothermal wall conditions are applied. The values along the singular axis are obtained by averaging the values on the upper and lower symmetry planes, while at the outer boundary, the free stream condition is enforced. At the downstream boundary the values are extrapolated from inside the solution domain. The initial data at the first streamwise station are generated through iteration under the assumption that the flow is locally conical.

Theoretical Investigation

C_L, C_D and C_m for right elliptic cone without strakes were calculated using the close form relations from Wells et al paper[15]. A theoretical prediction model was derived, based on the standard Newtonian theory, to estimate C_L, C_D and C_m for right elliptic cone with strakes. The strakes were assumed to be right rhombic cones of half-angle 0.7° and total length of 188 mm. Any vortices caused by boundary layer separation and regions of trapped flow, such as at the strake-body junction were neglected. The contribution of strakes to the aerodynamic forces and moments was neglected if they are located inside the shadow region of the elliptic cone.

For purpose of integration cylindrical co-ordinates were assumed. The derivation started from the Newtonian relation $C_p=2\cos^2\eta$. The angle η is defined as the angle between the unit vector normal to the surface and the unit wind vector. The unit normal vector **n** was expressed as the gradient of the surface divided by its magnitude. The unit wind vector **V** was expressed in terms of the body axis. A close form of C_p for the right rhombic cone was derived. The contribution of each strake on the aerodynamic forces

and moments was calculated by numerical integration using the pressure coefficient as determined by Newtonian theory. The individual forces and moments generated by the right elliptic cone and strakes were calculated then the total force and moment was derived. The lift coefficient for each incidence was predicted from

$$C_{Ltotal}=C_{Lstrakes}+C_{Lbody} \quad (2)$$

Similar expressions were used for the other aerodynamic coefficients. This method for deriving the individual forces and moments fundamentally assumes that the forces and moments generated in the presence of strakes are equal to the sum of the individual components i.e. the algebraic sum of the forces and moments generated by the cone and the strakes. This method does not take into account the mutual interaction between the cone and the strakes flowfields.

Results and Discussion

Evaluation of Accuracy of Numerical Simulation

There are a number of factors which can influence the quality of vortex flow predictions. In this study, the sensitivity of the numerical solution to the computational was examined. Since the force and moment coefficients are the main parameters that are compared with experimental data, they are used as the representative factors for the grid sensitivity study. Smoothing and stabilising parameters were kept to a minimum during the grid sensitivity studies. The grid is refined in each direction of the three dimensions while holding the other two dimensions fixed. The computational grid was generated using algebraic techniques.

A 3D elliptic solver was used to remove any overlapping grid regions. The number of iterations were kept to the minimum to ensure orthogonality at the wall and good resolution near the corner regions. Computations were done using a number of grids ranging from a coarse grid, consisting of 40 axial, 40 radial and 100 circumferential points, to a fine grid with 100 points in axial and radial direction and 200 in circumferential direction. Intermediate grids have been studied, along with the effect of changing the degree of radial clustering. Figure 2 presents a study of the sensitivity of numerical results to grid density in each of the three co-ordinate directions. A better resolution of the vortical flowfield is obtained with the finer grid. However, the finer grid requires higher computer memory and more computing time leading to higher computing costs. The study showed sensitivity of the calculated forces and moment coefficients in the streamwise direction. This is attributed to the integration routines which have been used to evaluate the forces and moments. This is a conjecture.

The results of this study indicate that 165 grid points placed in the circumferential direction and 65 grid points in each of the other cross-flow plane directions are sufficient to resolve all of the flow features of interest. The grid used is shown in figure 3. This grid is highly clustered in the radial direction towards the wall and yields a typical value of $y+<1$ for the first cell off the body surface and in the streamwise direction near the nose. In the circumferential direction a uniform grid spacing was employed for the regions between the strakes. The grid on the strakes was stretched towards the strake's corner intersections with the elliptic surface.

Birch et al[9] assessed the effect of the simplifying assumptions, which are incorporated within the PNS solver, to enable the use of a space-marching strategy, by a computation using a time-marching RANS solver for comparison with the PNS solution. The agreement between the two codes was very good, justifying the use of the PNS approach for missile aerodynamics computational studies.

Flow Visualisation Studies

The typical flow field characteristics as predicted by the PNS solver at incidence, with strakes, are shown in figure 4. Figure 5 shows good agreement between numerical and experimental shock shape in the windward side of the elliptic cone with strakes. The experimental and computational study showed no difference in shock shape due to inclusion of strakes. Because any changes in the flowfield due to strakes addition are of small scale, they will not be visible in the schlieren pictures because of the main body obstruction.

The experimental leading edge shock and attached laminar boundary layer, for $\alpha=0°$, can be seen in figure 6. The distance between the shock wave and the body, for 0° incidence, is greater in the meridian plane containing the minor axis than in the meridian containing the major axis (figure 6). The shock wave is not an ellipse similar to the body, but is 'pushed in' toward the major axis and 'pulled out' from the minor axis. This shape is because of the presence of a cross-flow from the high pressure sides at the ends of the major axis to the low pressure sides at the ends of the minor axis. At very low angles of attack, the axial flow velocity is dominant and the flow is attached. There are no separated flow and vortices on the lee-side of the elliptic cone[16]. The boundary layer thickens along the leeward meridian. A decrease in heat transfer along the leeward meridian is expected, and it is due to the decrease in pressure in the leeward region of the cones. Stetson[17] found that the leeward flow over a circular cone separates at about 3/4 the cone half angle for sharp as well as a spherically blunted 5.6 degrees half-angle cones. In the present experiments, according to Stetson, the leeward flow should separate at incidence of 2.9° as the half-angle is 3.8° (angle corresponds to the vertical plane of symmetry, which includes the minor-axis).

The effect of incidence[16] is to decrease the local Mach number and increase the local Reynolds number along

the windward ray. On the leeward ray, the local Mach number increases and the local Reynolds number decreases. With increasing angle of attack, schlieren, oil flow[16] and numerical study showed the establishment of a disturbed flow region over the leeward meridian. The numerical simulation confirms that this is due to separation of the crossflow, resulting in the establishment of a pair of counter-rotating vortices, over the leeward region of the body, (figure 7). At low angles of attack, the flow is still attached over the front of the body[16]. The symmetric vortex pair and the point where the symmetric vortices originate moves from the base to the tip of body with increasing angle of attack[16]. At moderate incidences, the pair of vortices originates from the apex and extend to the base of the body on the leeside and beyond, (figures 4,5 and 8). The experimental study showed that with growth of the pair of the symmetric vortices, the position of the vortex core rises and the vortices increase in strength[16,18-20].

The oil-dot and numerical results, for the cone with strakes, compare well, (figure 8). Both studies captured successfully the cross-flow characteristics on the windward side and some details of the flow phenomena on the leeward side were seen. The numerical study predicted successfully the positions of separation and reattachment lines and managed to resolve the complicated flow in the corner region of strake with main body, (figure 9), to a much higher degree of resolution than the oil-flow study. The strakes altered the surface flow characteristics and tended to inhibit the cross-flow on the windward side, (figure 8). This is valied at all incidences tested experimentally and computationally.

By $\alpha=10°$ the separation region extends over the whole upper surface of the model[16]. At $\alpha=15°$, the vortex core is no longer visible, (figure 5). This is probably because of the large expansion of the flow over the leeward side of the body reduces the local density beyond the sensitivity of the schlieren system.

The numerical code predicted the complex vortex flowfield surrounding the cone, gave better understanding of the complicated nature of the flow and good indications of the shock shape and vortex core positions. Figure 10 and 11 show the base cross-flow Mach number and vorticity contours respectively. Some results of the no-strake case are shown in figure 7.

Pressure Measurements

The experimental pressure distributions show a repeatability of ±5%. Figure 12 shows a progressive decrease in cone pressure along the leeward meridian with incidence. Experimental and computational investigation showed that the addition of strakes caused a reduction of pressure on the leeward side and an increase of pressure on the windward side, figure 12. A good agreement was found between the experimental and computational pressure results, with and without strakes. The pressure results without strakes on the windward side have been compared with standard Newtonian theory predictions and cone theory of Leung and Emanuel[21]. Both theories predicted the experimental trends.

Forces and Moments Measurements

The sign convention used for the forces and moments measurements is shown in figure 13. An upward lift force (normal to the velocity vector), backward drag (parallel to the velocity vector) and a nose-up pitching moment were taken as positive.

The calculated forces were non-dimensionalised using the freestream dynamic head and the base area of the elliptic cones. The moment values were non-dimensionalised using the freestream dynamic head, base area and base diameter. The pitching moment was measured at the moment reference point located at $x/d_b=-1.3$ along the body axis measured from the base of the cones.

The strakes on the windward side of the body have negative dihedral and the other two on the leeward side have positive dihedral. Any interference between the flow over the body and that over the windward side of the anhedral strakes or over the leeward side of the dihedral strakes will result in changes in the aerodynamic characteristics of the straked configuration in comparison to the body alone configuration. Any interference effects on the leeward side of the anhedral strakes and that on the windward side of the dihedral strakes will be acting on a very small area of the body surface and will therefore not cause any significant changes in the aerodynamic characteristics.

A comparison of experimental C_L, C_D and C_m, with theory and computation is presented in figure 14. Theory and computation predicted the experimental trends successfully. Computation agrees better with experimental results.

The effect of strakes addition is to shift the C_L-α curve upwards increasing the C_L values at all incidences tested, figure 14. Computation and experimental results exhibit a good agreement with each other. This increase is due to increased pressure over the lower side of the cone caused by increased amount of air entrapped by the strakes and because of the two strakes having negative dihedral create strong interference with the windward side of the body. The cross flow component on the windward side remains very small due to the blockage created by the anhedral strakes and should therefore result in a constant pressure on the windward side of the body, (figure 12). Expansion of the flow over the leeward surfaces of the other two strakes having positive dihedral reduces the pressure on the leeward side of the body in comparison to the pressure there for the body alone configuration, (figure 12). Surface pressure measurements by Reggiori[22] on a wing-cone configuration show these interference effects.

Figure 14 shows that strakes addition increases the drag coefficient. The increase in C_D is smaller at low incidences. At these incidences, the addition of strakes does not cause any big change in pitching moment coefficients about the balance moment centre. At low incidences the effect of increased lift is accompanied by a slight forward movement of the centre of pressure. At higher incidences there is a bigger increase in pitching moment coefficients, because lift coefficient, for the cone with strakes over that without the strakes, continues to increase with α.

Conclusions

1.No gross external flow differences were detected from the schlieren pictures and the numerical simulation due to the addition of strakes.

2.Oil-dot and schlieren visualisation and PNS simulation show that the flow separates on the leeward side of the body to form a pair of counter rotating vortices at a low incidence. The vortices grow with incidence.

3.Oil-dot visualisation and numerical simulation demonstrate that the strakes alter the surface flow characteristics and tended to inhibit the cross-flow.

4.Both experimental and computational studies show that the addition of strakes caused a reduction of pressure on the leeward side and an increase of pressure on the windward side. PNS code predictions and experimental investigation results compare well.

5.The strakes produced a significant increase in the lift, drag and pitching moment coefficients, in the incidence range of 0° to 20°. Theory and computation predicted the experimental trends successfully. The numerical study shows a better agreement with experimental results.

6.In the experimental design stage, CFD can be used to identify important areas and important flow conditions before the model is cut, which can save unnecessary waste in the experimental tests. After data collection from the experiments, detailed numerical simulation can be conducted for the experimental conditions. In the present study, the simulation was able to provide flow field pictures to enhance the understanding of the flow problem.

Acknowledgements

The experimental part of the present investigation was supported under contract by the Defence Establishment and Research Agency of the United Kingdom.

References

[1]Graham, JE, and Hankey, WL. Computation of the Asymmetric Vortex Pattern for Bodies of Revolution. AIAA-82-0023, 1982.

[2]Borrel, M, d' Espiney, P, and Jouet, C. Three-Dimensional Thin-Layer and Space Marching Navier-Stokes Computations Using an Implicit MUSCL Approach: Comparisons with Experiments and Euler Computations. 9th GAMM Conference on Numerical Methods in Fluid Dynamics, 1991.

[3]Baysal, O, Fouladi, K, and Miller, DS. Computations of Supersonic Flows Over a Body at High Angles of Attack. AIAA Journal, Vol 27, No 4, 1989.

[4]Schiff, LB, and Steger, IL. Numerical Simulation of Steady Supersonic Viscous Flow. AIAA Journal, Vol 18, No 12, 1980.

[5]Jettmar, RU, and Kordulla W. Computation of Aerodynamic Forces on Bodies with Non-Circular Cross-Section in Supersonic Viscous Flow. AIAA-83-2077, 1983.

[6]Degani, D, and Schiff LB. Computation of Turbulent Supersonic Flows Around Pointed Bodies Having Crossflow Separation. Journal of Computational Physics, Vol 66, 1986.

[7]Greene, FA. An Upwind-Biased Space Marching Algorithm for Supersonic Viscous Flow. NASA TP-3068, 1991.

[8]Qin, N and Richards, BE. Finite Volume 3DNS and PNS Solutions of Hypersonic Viscous Flows Around a Delta Wing using Osher's Flux-Difference Splitting. Proceedings of a Workshop on Hypersonic Flows for Re-entry Problems, Vol 2, 1990.

[9]Birch, TJ, Qin, N and Jin, X. Computation of Supersonic Viscous Flows Around a Slender Body at Incidence. AIAA 94-1938, 1994.

[10]Baldwin, BS, and Lomax, H. Thin-Layel Approximation and Algebraic Turbulence Model for Separated Turbulent Flows. AIAA-78-257 (1978).

[11]Osher, S, and Chakravathy, SR. Upwind Schemes and Boundary Conditions with Applications to Euler Equations in General Co-ordinates. Journal of Computational Physics, Vol 50, 1983.

[12]Qin, N, Scriba, KW, and Richards, BE. Shock-Shock, Shock-Vortex Interaction and Aerodynamic Heating in Hypersonic Corner Flow. The Aeronautical Journal, Vol 95, No 945, 1991.

[13]Qin, N, Ludlow, D and Shaw, S. Calculation of Pitch Damping Coefficients using the PNS Equations in a Non-inertial Framework. Cranfield University, COA/9601, 1996.

[14]Vigneron, YC, Rakich, JV, and Tannehill, JC. Calculation of Supersonic Viscous Flow Over Delta Wings with Sharp Leading Edges. AIAA-78-1137, 1978.

[15]Wells, W and Armstrong, W. Tables of Aerodynamic Coefficients Obtained from Developed Newtonian Expressions for Complete and Partial Conic and Spherical Bodies at Combined Angles of Attack and Sideslip with some Comparisons with Hypersonic Experimental Data. NASA TR R-127, 1961.

[16]Kontis, K, Stollery, JL and Edwards, JA. Hypersonic Effectiveness of Slender Lifting Cones With and Without Strakes. AIAA-97-0521, 1997.

[17]Stetson, KF. Experimental Results of Laminar Boundary Layer Separation on a Slender Cone at

Angle of Attack at M_∞=14.2. WPAFB, ARL 71-0127, 1971.
[18]Peake, DJ and Tobak, M. Three-Dimensional Flows about Simple Components at Angle of Attack. AGARD LS-121, 1982.
[19]Pagan, D, Molton, P and Delery, J. Basic Experiments on a Supersonic Vortex Flow around a Missile Body. Journal of Spacecraft and Rockets, Vol 29, 1992.
[20]Kontis, K and Stollery JL. Control Effectiveness of a Jet-Slender Body Combination at Hypersonic Speeds. AIAA 96-2470, 1996.
[21]Leung, KK and Emanuel G. Hypersonic Inviscid and Viscous Flow over a Wedge and Cone. Journal of Aircraft, Vol 32, No 2, 1995.
[22]Reggiori, A. Lift and Drag of Wing-Cone Configuration in Hypersonic Flow. AIAA Journal, Vol 9, No 4, 1971.

Figures

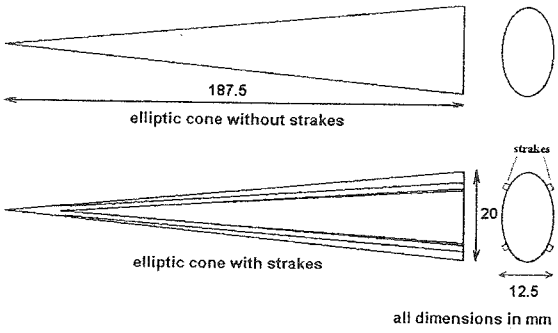

Fig.1 General geometry of the models

a)Lift coefficient

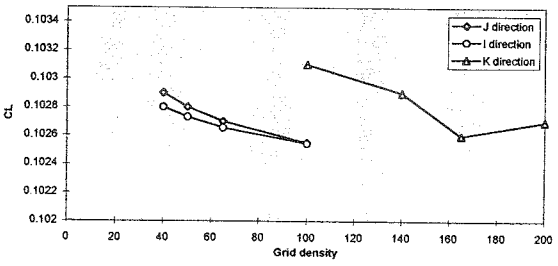

b)Drag coefficient

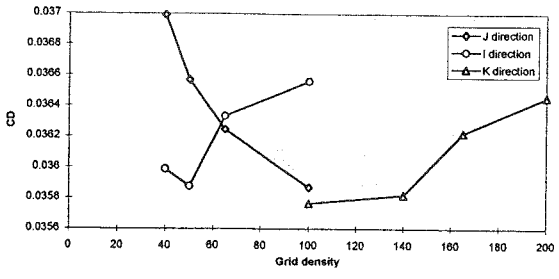

c)Pitching moment coefficient

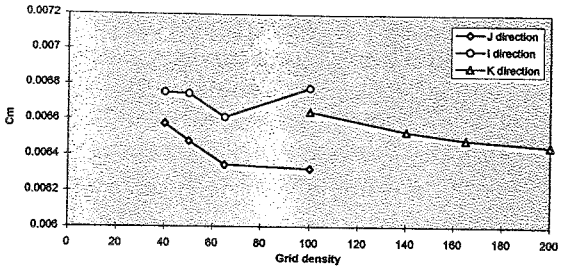

Fig.2 Grid sensitivity study (elliptic cone without strakes, 10° incidence)

a)Overall grid

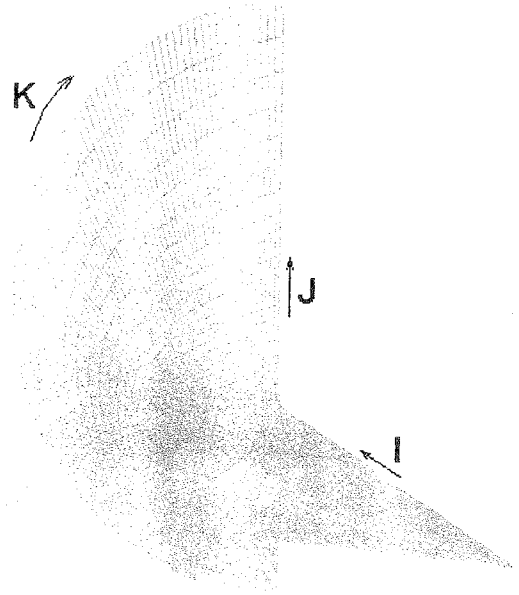

b)Grid detail near strake region

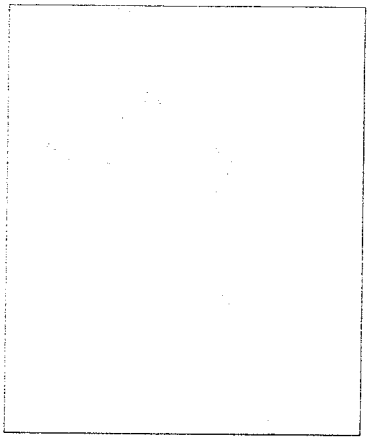

Fig.3 Computational grid

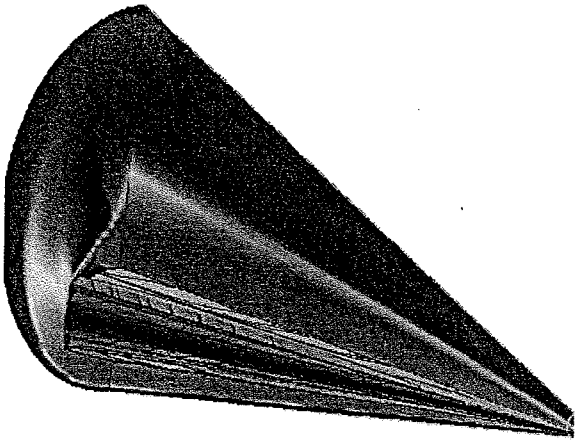

Fig.4 General flowfield characteristics (PNS, elliptic cone with strakes, 15° incidence)

a)PNS

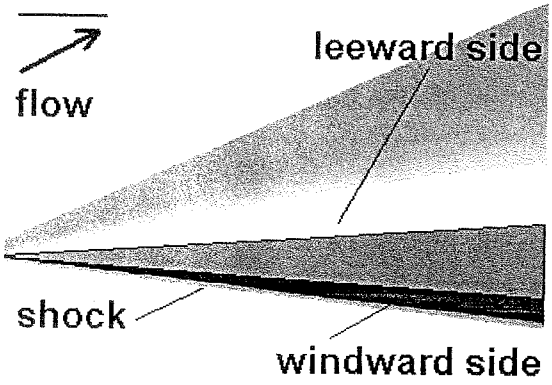

b)Experiment

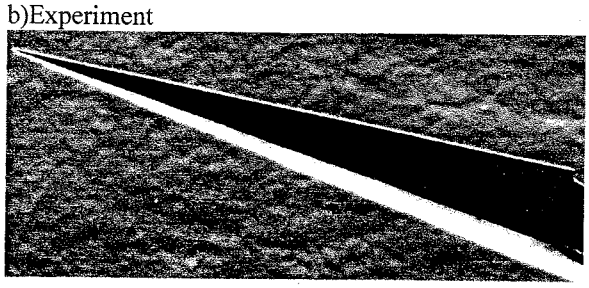

Fig.5 Elliptic cone with strakes at 15° incidence

a)Major-axis horizontal

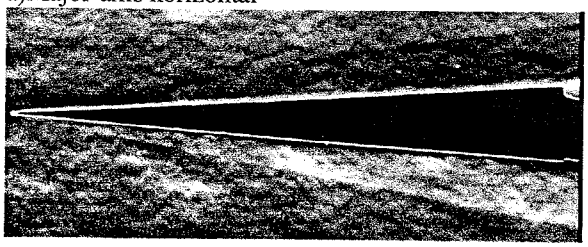

b)Major-axis vertical

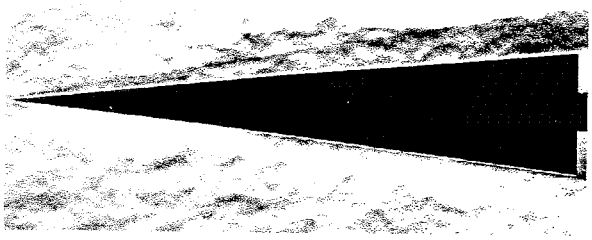

Fig.6 Elliptic cone without strakes at 0° incidence (experiment)

a)Velocity vectors, no-strakes

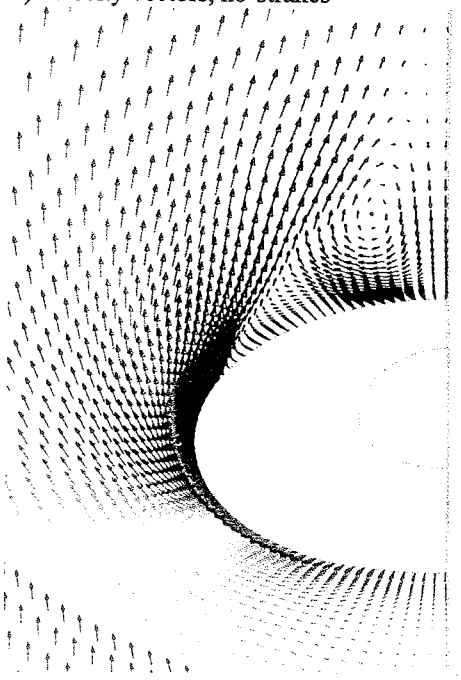

b)Velocity vectors, with-strakes

c)Pitot pressure, no-strakes

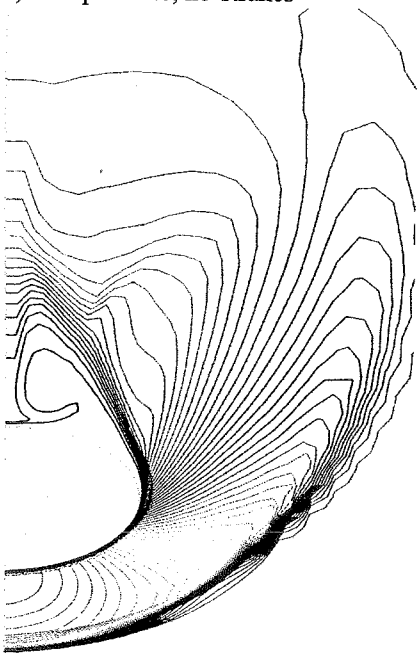

Fig.7 Elliptic cone at 15° incidence (PNS)

a)No-strakes, experiment

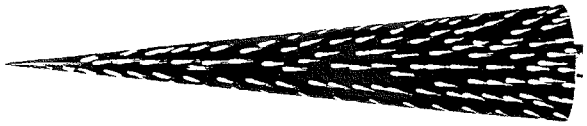

Windward side

Left side

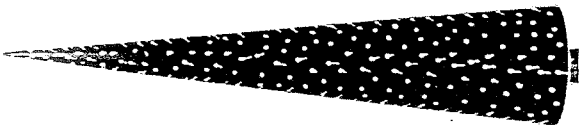

Leeward side

b)With-strakes, experiment

Windward side

Left side

Leeward side

c)With-strakes, PNS

Windward side

Left side

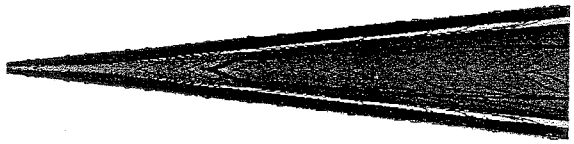

Leeward side

Fig.8 Surface flowfield characteristics at incidence 15°

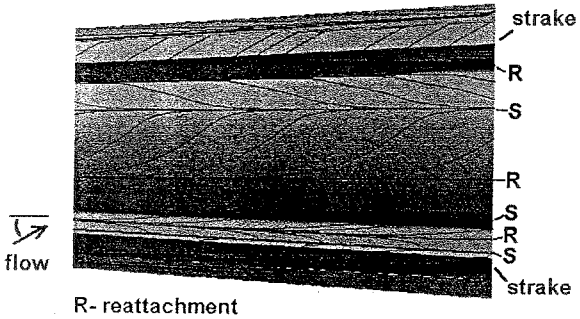

Fig.9 Close-up view of the effect of strakes in the surface flowfield (PNS, incidence 15°)

Fig.10 Base cross-flow Mach number contours (PNS, elliptic cone with strakes, incidence 15°)

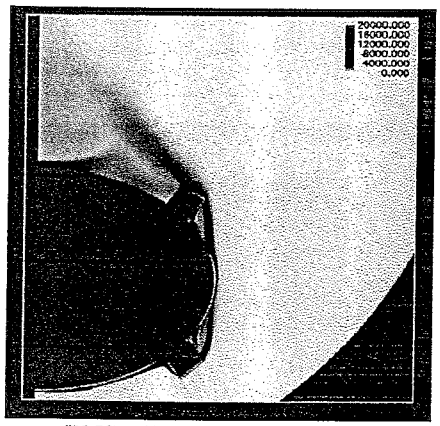

Fig.11 Base cross-flow vorticity contours (PNS, elliptic cone with strakes, incidence 15°)

a)Windward meridian

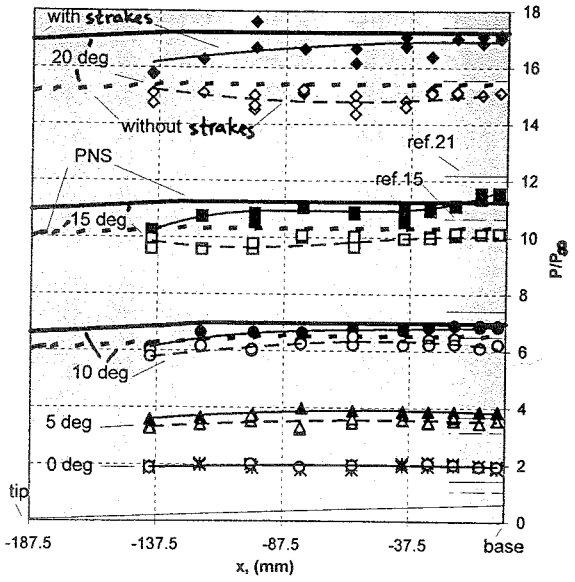

b)Leeward meridian

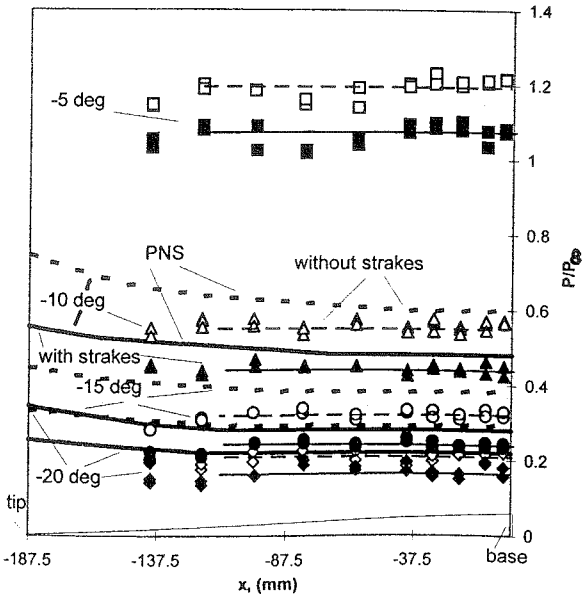

Fig.12 Experimental, numerical and theoretical pressure distributions with and without strakes

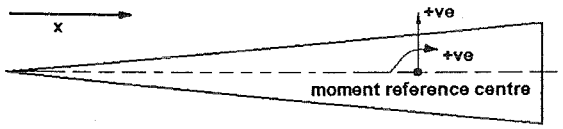

Fig.13 Sign convention used for lift, drag and pitching moment

a)

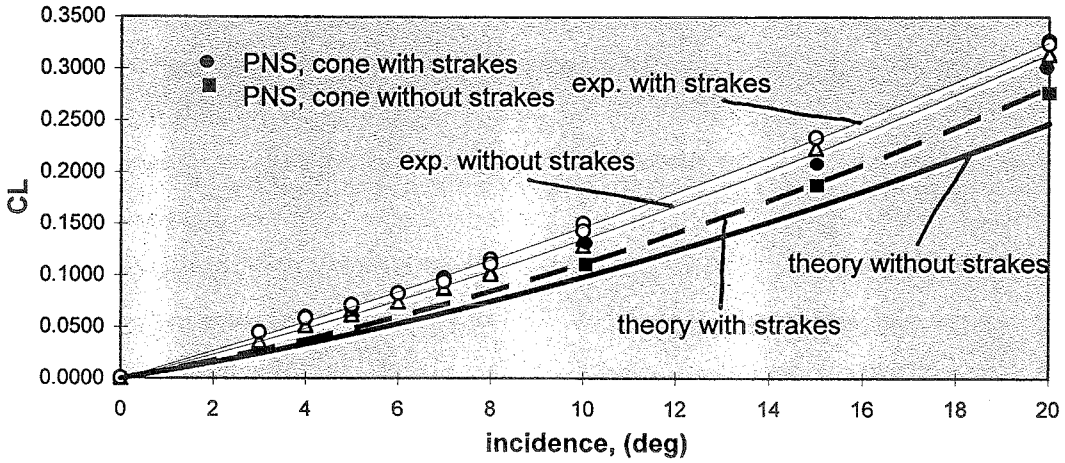

b)

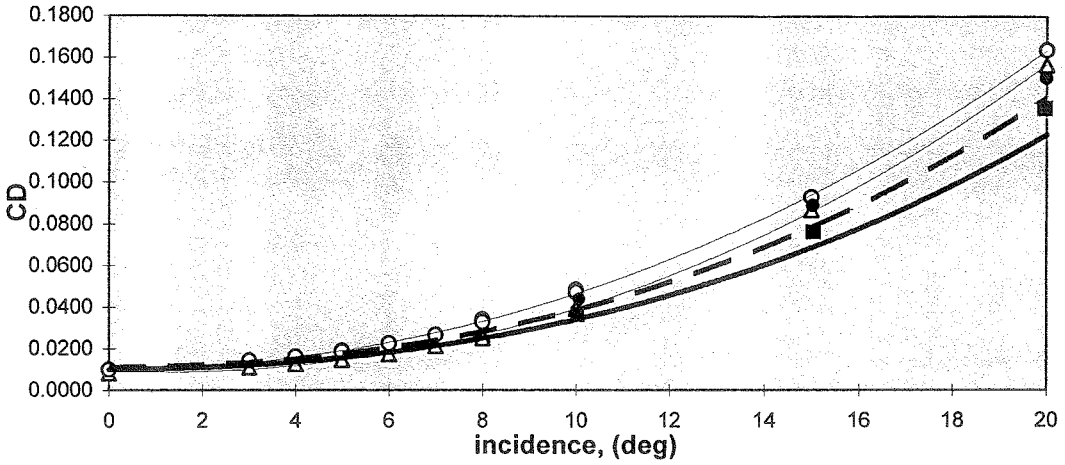

c)

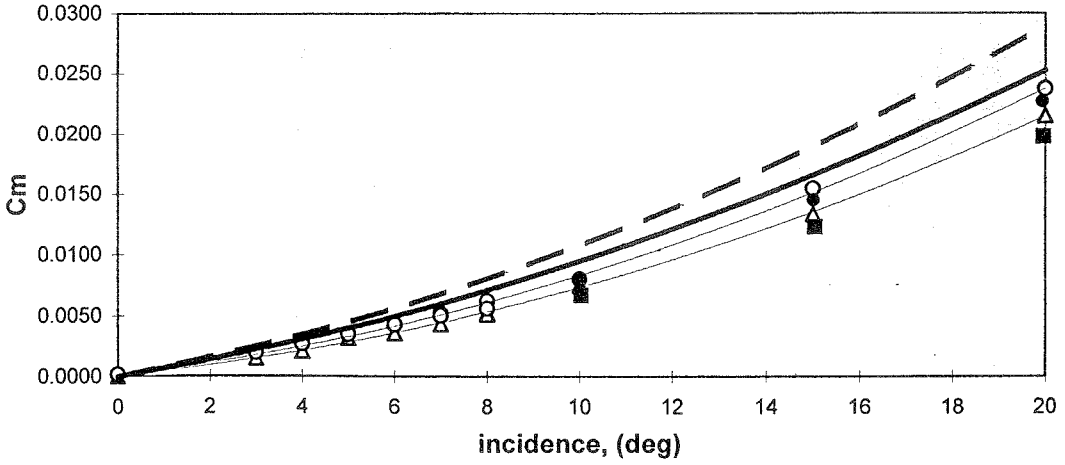

Fig.14 Experimental, numerical and theoretical demonstration of the effect of strakes on the aerodynamic coefficients